**Universidade do Minho**
Escola de Engenharia

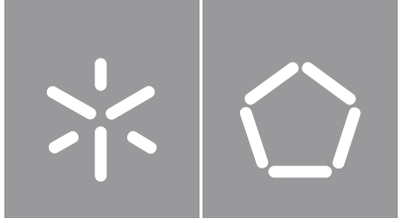
Nuno Alexandre Tavares de Campos Fernandes

# Development of a bioinspired knee orthosis for patients with knee osteoarthritis

July 2026

Development of a bioinspired knee orthosis for patients with knee osteoarthritis
Nuno Alexandre Tavares de Campos Fernandes
UMinho | 2026

Fundação para a Ciência e a Tecnologia
REPÚBLICA PORTUGUESA
Funded by the European Union
NextGenerationEU



**Universidade do Minho**
Escola de Engenharia

Nuno Alexandre Tavares de Campos Fernandes

# Development of a bioinspired knee orthosis for patients with knee osteoarthritis

Doctoral Thesis
Doctoral Program in Mechanical Engineering

Work Supervised by
**Professor Dr. Óscar Carvalho**
**Dr. Ana Leal**
**M. D. Betina Hinckel**

July 2026

**COPYRIGHT AND TERMS OF USE OF THIS WORK BY A THIRD PARTY**

This is academic work that can be used by third parties as long as internationally accepted rules and good practices regarding copyright and related rights are respected

Accordingly, this work may be used under the license provided below

If the user needs permission to make use of the work under conditions not provided for in the indicated licensing, they should contact the author through the RepositóriUM of Universidade do Minho.

**License granted to the users of this work**




Atribuição

CC BY

https://creativecommons.org/licenses/by/4.0/

# Acknowledgements

The completion of this thesis represents not only the outcome of several years of scientific work, but also the result of the support, patience, encouragement, and generosity of many people who accompanied me throughout this journey.

First, I would like to express my deepest gratitude to my girlfriend, Diana, for her constant support, understanding, and patience during the many demanding and lonely moments that inevitably accompanied this work. Her presence was fundamental throughout this process, particularly because she herself was also enrolled in a PhD programme and therefore understood, perhaps more than anyone, the sacrifices, uncertainties, and resilience required by this path. I am also sincerely grateful to her family, for their kindness, support, and encouragement during these years.

I would like to thank my supervisors, Professor Óscar, Ana Leal, and Betina Hinckel, for their guidance, availability, and contribution to the development of this work. I am especially grateful to Professor Óscar for continuously challenging me to go beyond my perceived limits, for recognizing my potential, and for valuing me not only as a researcher but also as a person. His trust, encouragement, and the opportunities he provided were essential in shaping both this thesis and my academic growth.

I also wish to thank my lab mates, who contributed to a stimulating and supportive research environment. A special word of appreciation goes to Shivam Sharma, for always believing in my potential and for the encouragement shared throughout this journey.

To my friends from the Azores, Fábio, Wilson, Henrique, Édi, Vânia, Juno, João, Mário, and Laura, I express my sincere gratitude for their friendship, companionship, and for some of the greatest summer vacations I could have asked for. Those moments of joy, distance, and simplicity were essential in restoring balance during the most demanding periods of this work.

I would also like to thank Engineer Filipe Dario Marques for teaching me how to use the tools in his workshop, for sharing his technical knowledge with generosity, and for the words of encouragement that helped me continue moving forward.

I am deeply grateful for the opportunity to teach during this period. Being part of the academic journey of many students was one of the most meaningful experiences of these years. Their curiosity, challenges, and growth reminded me of the broader purpose of academic life and gave additional meaning to the work developed in this thesis.

Finally, I acknowledge the support of the "Mechanobiological device to stimulate cartilage regeneration" (https://doi.org/10.54499/PTDC/EME-EME/1681/2021), "BrainStimMap—Mapping and modelling the transmission profile of optomechanical waves in the brain to optimize transcranial

stimulation against brain disorders" (https://doi.org/10.54499/PTDC/EME-EME/1681/2021) and "Development of 3D Printing Customized and Sensorized Low-Cost Phantoms for Radiotherapy Treatment" - COMPETE2030-FEDER-00775300 projects, as well as Fundação para a Ciência e a Tecnologia (FCT), for the scholarship (2022.11063.BD) that made this research possible. Their support was essential for the development and completion of this work.

To all those who, directly or indirectly, contributed to this journey, my sincere gratitude.

## STATEMENT OF INTEGRITY

I hereby declare having conducted this academic work with integrity. I confirm that I have not used plagiarism or any form of undue use of information or falsification of results along the process leading to its elaboration. I further declare that I have fully acknowledged the Code of Ethical Conduct of the University of Minho.

## DECLARATION ON THE USE OF ARTIFICIAL INTELLIGENCE (AI) TOOLS

I hereby declare having acted this academic work with integrity and confirm that I have not resorted to any form of undue use of AI tools, nor to the falsification or omission of information, sources, data, results or processes in any of the stages leading to its elaboration.

I further declare that any use of AI tools was done in a transparent and responsible manner, being duly noted in the work, and that I critically verified the accuracy of the content produced with their support, assuming full responsibility for what I submit.

I further declare that I have fully acknowledged the Code of Ethical Conduct of the University of Minho, as well as the applicable standards of academic integrity and data protection.

*“Waiting for the one*

*The day that never comes*

*When you stand up and feel the warmth*

*But the sunshine never comes, no*

*No, the sunshine never comes”*

**Metallica**, The day that never comes - Death Magnetic

# Desenvolvimento de uma ortótese bioinspirada para o joelho em pacientes com osteoartrite do joelho

## Resumo

A osteoartrite do joelho é uma doença degenerativa associada à degradação da cartilagem, dor, limitação funcional e redução da qualidade de vida. Embora as abordagens farmacológicas, cirúrgicas e de reabilitação atualmente disponíveis possam reduzir os sintomas, estas continuam limitadas na sua capacidade de regenerar a cartilagem e de fornecer estimulação mecânica personalizada para cada paciente. As terapias baseadas em ultrassons têm emergido como estratégias não invasivas promissoras para modular a mecanotransdução dos condrócitos. No entanto, a sua translação clínica é condicionada pela variabilidade anatómica, pela propagação acústica heterogénea nos tecidos biológicos e pela ausência de métodos sistemáticos para definir uma estimulação adaptada a cada paciente.

Esta tese investiga o desenvolvimento de uma estratégia personalizada baseada em ultrassons para a estimulação da cartilagem do joelho. O trabalho integra a caracterização de tecidos biológicos, modelação numérica, validação com fantomas médicos e desenvolvimento orientado para o dispositivo. As propriedades acústicas e mecânicas relevantes para a propagação de ondas (densidade, velocidade do som, atenuação, impedância acústica e difusividade sonora), são utilizados por modelos computacionais e para estimar a transmissão de ondas acústicas de um transdutor externo até à cartilagem.

Modelos 1D de ordem reduzida avaliam a transmissão acústica através de tecidos estratificados e identifica intervalos de frequência relevantes, enquanto simulações 2D e 3D anatomicamente informadas permitem avaliar distribuições de pressão, funções de transferência e a formação de ondas estacionárias. À escala microscópica, são desenvolvidos modelos multifísicos de elementos de volume representativo de condrócitos para investigar de que forma a excitação acústica pode induzir deformação celular e nuclear, estabelecendo uma ligação entre os campos de ultrassons aplicados externamente e mecanotransdução.

Fantomas anatómicos médicos são explorados como plataformas experimentais para o posicionamento de transdutores. Estes estudos suportam um fluxo de trabalho personalizado no qual a imagiologia médica fornece a geometria específica do paciente, a elastografia informa as propriedades dos tecidos, as simulações estimam parâmetros de estimulação adequados e os ensaios com fantomas validam o posicionamento do transdutor antes da geração de uma interface ortótica conformável.

**Palavras-chave:** Modelação multifísica e multiescala, Osteoartrite do joelho, Propagação de ondas acústicas em meios complexos, Regeneração da cartilagem, Ultrassons

# Development of a bioinspired knee orthosis for patients with knee osteoarthritis


## Abstract

Knee osteoarthritis is a degenerative joint disease associated with cartilage degradation, pain, functional impairment, and reduced quality of life. Although current pharmacological, surgical, and rehabilitation approaches can reduce symptoms, they remain limited in their capacity to promote cartilage regeneration or deliver patient-specific mechanical stimulation. Low-intensity ultrasound and vibration-based therapies have therefore emerged as promising non-invasive strategies to modulate chondrocyte mechanotransduction and cartilage homeostasis. However, their clinical translation is constrained by anatomical variability, heterogeneous acoustic wave propagation through biological tissues, and the absence of systematic methods to define stimulation parameters for individual patients.

This thesis investigates the development of a personalized ultrasound-based strategy for knee cartilage stimulation, supporting the design of a therapeutic orthosis for osteoarthritis management. The work integrates biological tissue characterization, numerical modelling, phantom-based validation, and device-oriented development. Acoustic and mechanical properties relevant to wave propagation, including density, speed of sound, attenuation, acoustic impedance and sound diffusivity, are examined to inform computational models and estimate the transmission of mechanical energy from an external transducer toward the cartilage.

Reduced-order one-dimensional models are used to evaluate acoustic transmission through layered tissues and identify relevant frequency ranges, while anatomically informed two- and three-dimensional simulations assess pressure distributions, transfer functions, standing wave formation, and the influence of transducer geometry and placement. At the microscale, multiphysics chondrocyte representative volume element models are developed to investigate how acoustic excitation may induce cellular and nuclear deformation, linking externally applied ultrasound fields with potential mechanotransductive responses.

Anatomical and tissue-mimicking phantoms are further explored as experimental platforms for transducer positioning and acoustic field validation. These studies support a personalized workflow in which medical imaging provides patient-specific geometry, elastography informs tissue properties, simulations estimate suitable stimulation parameters, and phantom experiments validate transducer placement before the generation of a conformal orthotic interface.



**Keywords:** Cartilage Regeneration, Knee Osteoarthritis, Ultrasound, Acoustic Wave Propagation in Complex Media, Multiphyisics and Multiscale Modelling

# Contents


**1 Introduction** **1**

1.1 Motivation . . . 2

1.2 Objectives and Research Questions . . . 5

1.3 Methodology and Expected Contributions . . . 8

1.4 Publications . . . 10

1.4.1 Journal Articles . . . 10

1.4.2 Book Chapter . . . 12

1.4.3 Conference Paper . . . 13

1.4.4 Software Tools . . . 13

1.5 Thesis Structure . . . 15

1.6 Bibliography . . . 17

**2 State of the Art** **20**

2.1 The Human Knee . . . 21

2.1.1 Knee Function and Anatomy . . . 21

2.1.2 Skin Function and Microstructure . . . 24

2.1.3 Adipose Tissue Function and Microstructure . . . 26

2.1.4 Muscle-Tendon Unit Function and Microstructure . . . 27

2.1.5 Ligaments Function and Microstructure . . . 29

2.1.6 Bone Function and Microstructure . . . 31

2.1.7 Articular Cartilage Function and microstructure . . . 33

2.1.8 Osteoarthritic Cartilage . . . 35

2.2 Existing treatments for knee osteoarthritis . . . 38

2.2.1 Conservative symptomatic treatments . . . 38

2.2.1.1 Mechanical Unloading . . . 39

2.2.1.2 Physical therapy and loading modulation . . . 42
2.2.1.3 Pharmacological approaches . . . 44
2.2.2 Biophysical Stimulation . . . 46
2.2.2.1 Ultrasound Stimulation . . . 46
2.2.2.2 Vibration Therapy . . . 48
2.2.2.3 Electromagnetic fields . . . 49
2.2.2.4 Shockwave Therapy . . . 51
2.2.3 Surgical Structural Interventions . . . 53
2.2.3.1 Microfracture . . . 53
2.2.3.2 Osteotomy . . . 55
2.2.3.3 Joint replacement . . . 56
2.3 Acoustic Wave propagation . . . 58
2.3.1 Wave Propagation in Homogeneous Media . . . 58
2.3.1.1 Linear Wave equation . . . 58
2.3.1.2 Linear Wave Propagation in Fluid Media . . . 59
2.3.1.3 Linear Wave Propagation in Solid Media . . . 64
2.3.1.4 Linear Wave propagation phenomena . . . 66
2.3.1.5 Nonlinear Wave equation . . . 70
2.3.2 Wave Propagation in Complex Media . . . 72
2.3.2.1 Hyperelastic Media . . . 72
2.3.2.2 Homogenization of Composite Materials . . . 74
2.3.2.3 Multiphysics Interfaces . . . 77
2.3.2.4 Vibroacoustics . . . 79
2.3.2.5 Poroelastic Wave Propagation . . . 83
2.3.2.6 Multiscale Wave Propagation . . . 89
2.3.3 From Wave Dissipation to Bioheat Transfer and Thermal Damage . . . 91
2.4 Biophysical Mechanisms of Cell Stimulation and Regeneration . . . 96
2.4.1 General Biophysical Mechanisms of Cell Stimulation . . . 96
2.4.2 Biophysical Mechanisms in Chondrocytes and Cartilage . . . 98
2.4.3 Implications for Wave-Based Therapies . . . 100
2.5 Computational models of acoustic Wave propagation . . . 103
2.5.1 Numerical Methods . . . 103

2.5.1.1 Finite-Element Method . . . 103
2.5.1.2 Finite-Difference Method . . . 106
2.5.1.3 Boundary-Element Method . . . 107
2.5.1.4 Discontinuous-Galerkin Method . . . 109
2.5.1.5 Fractional Derivatives Methods . . . 111
2.5.1.6 Absorbing Boundary Techniques . . . 113
2.5.2 Commercially Available Solutions . . . 116
2.5.3 Open-Source and Custom-Developed Frameworks . . . 119
2.5.4 Model Selection and Limitations . . . 120
2.6 Ultrasound Tissue-Mimicking Material Phantoms . . . 122
2.6.1 Purpose and Classification of Ultrasound Phantoms . . . 122
2.6.2 Standardized Tissue-Mimicking Phantoms . . . 123
2.6.3 Anatomically and Functionally Biomimetic Phantoms . . . 127
2.6.3.1 Skin Tissue Ultrasound Phantoms . . . 128
2.6.3.2 Adipose Tissue Ultrasound Phantoms . . . 130
2.6.3.3 Skeletal Muscle, Tendon, and Ligament Ultrasound Phantoms . . . 132
2.6.3.4 Bone Ultrasound Phantoms . . . 134
2.6.3.5 Cartilage Ultrasound Phantoms . . . 135
2.7 Techniques for ultrasound transmission and reception . . . 137
2.7.1 Fundamentals of Ultrasound Transduction . . . 137
2.7.1.1 Piezoelectric Effect and Electromechanical Coupling . . . 137
2.7.1.2 Alternative Transduction Mechanisms . . . 140
2.7.2 Ultrasound Transmission Techniques . . . 143
2.7.2.1 Transducer Design and Geometry . . . 143
2.7.2.2 Acoustic Coupling and Impedance Matching . . . 146
2.7.2.3 Excitation Signals and Driving Methods . . . 148
2.7.3 Ultrasound Reception Techniques . . . 150
2.7.3.1 Receiving Transducers and Sensitivity Considerations . . . 150
2.7.3.2 Signal Acquisition and Conditioning . . . 152
2.7.3.3 Advanced Detection Methods . . . 154
2.7.4 Calibration and Measurement Techniques . . . 156
2.7.4.1 Acoustic Field Characterization . . . 156

2.7.4.2 Hydrophone Calibration and Standards . . . 158
2.8 Bibliography . . . 161

**3 Conceptual Solution 193**

3.1 The fundamental paradox of articular cartilage regeneration . . . 194
3.2 Proposed Conceptual Design . . . 196
3.2.1 Material Characterization . . . 199
3.2.2 Computational Studies . . . 201
3.2.3 Structural Assembly . . . 203
3.2.4 Experimental Validation . . . 204
3.3 Development of medical devices . . . 206
3.4 Bibliography . . . 208

**4 Biological tissue characterization 210**

4.1 Introduction . . . 211
4.2 Materials and Methods . . . 215
4.2.1 Overview of Methodological Framework . . . 215
4.2.2 Biological Materials and Sample Preparation . . . 216
4.2.3 Experimental methods . . . 218
4.2.3.1 Density Measurement . . . 218
4.2.3.2 Ultrasound Transmission Setup . . . 219
4.2.3.3 Speed of Sound Measurement . . . 220
4.2.3.4 Attenuation Characterization . . . 220
4.2.3.5 Nonlinearity Parameter B/A . . . 221
4.2.4 Signal Processing . . . 222
4.2.5 Regression and Parameter Identification . . . 223
4.2.5.1 Attenuation Modelling . . . 223
4.2.5.2 Model Comparison . . . 224
4.2.6 Computational Modelling Framework . . . 225
4.2.6.1 Governing Equations . . . 225
4.2.6.2 Numerical Implementation (COMSOL) . . . 225
4.2.6.3 Geometry and Boundary Conditions . . . 226
4.2.6.4 Mesh and Stability Criteria . . . 227

4.2.7 Inverse Problem and Parameter Estimation . . . 228
4.2.8 Sound Diffusivity-Based Modelling Approaches . . . 229
4.3 Results . . . 231
4.3.1 Experimental Signal Characterization . . . 231
4.3.2 Experimental Acoustic Parameters Extraction . . . 234
4.3.2.1 Density . . . 234
4.3.2.2 Speed of Sound . . . 235
4.3.2.3 Attenuation . . . 236
4.3.2.4 Nonlinearity Parameter B/A . . . 237
4.3.3 Computational Model Validation . . . 238
4.3.4 Inverse Parameter Estimation . . . 239
4.3.4.1 Sound Diffusivity . . . 239
4.4 Discussion . . . 242
4.4.1 Experimental Acoustic Parameters Discussion . . . 242
4.4.2 Sound Diffusivity Regression Discussion . . . 247
4.4.3 General Discussion . . . 250
4.5 Conclusion . . . 251
4.6 Bibliography . . . 252

**5 Simulation of Acoustic Wave Propagation Through the Human Body 261**

5.1 Introduction to Acoustic Wave Simulation in Biological Systems . . . 262
5.1.1 Motivation and Role in Ultrasound-Based Therapies . . . 262
5.1.2 Challenges in Modelling Heterogeneous Biological Media . . . 264
5.2 Reduced-Order Modelling of Wave Propagation . . . 267
5.2.1 Governing Equations and Physical Assumptions . . . 267
5.2.2 Numerical Implementation Using Finite-Difference Time-Domain . . . 268
5.2.3 Results . . . 271
5.2.4 Discussion . . . 272
5.2.5 Conclusion . . . 273
5.3 Multi-Scale Patient-Specific Simulation Framework . . . 274
5.3.1 Overview of the Multi-Scale Modelling Strategy . . . 274
5.3.2 Computational MultiScale Modelling . . . 275
5.3.2.1 Articular Cartilage Geometry . . . 276

5.3.2.2 Patients' data for anatomic knee models . . . 277
5.3.3 Material Properties . . . 278
5.3.3.1 Articular Cartilage Material properties . . . 279
5.3.3.2 Biological Tissues Material properties . . . 281
5.3.4 Mesh and Boundary Conditions . . . 283
5.3.4.1 Representative volume element meshing . . . 283
5.3.4.2 Macroscale modelling . . . 284
5.3.5 Simulation Setup . . . 285
5.3.5.1 Modal analysis Setup . . . 286
5.3.5.2 Harmonic Analysis Setup . . . 286
5.3.5.3 Time-Explicit Simulations Setup . . . 287
5.3.6 Results . . . 289
5.3.6.1 Microscale Modal Analysis . . . 289
5.3.6.2 Microscale Frequency Response . . . 291
5.3.6.3 Macroscale Frequency Response . . . 296
5.3.6.4 Multiscale Coupled Frequency Response . . . 299
5.3.6.5 Multiscale Coupled Time-explicit Response . . . 301
5.3.7 Discussion . . . 304
5.3.8 Conclusions . . . 307
5.4 Concluding Remarks on Simulation Framework . . . 308
5.4.1 Summary of Key Findings . . . 308
5.4.2 Implications for Device Design and Optimization . . . 309
5.4.3 Future Directions in Multi-Scale Acoustic Modelling . . . 310
5.5 Bibliography . . . 312

**6 Experimental Validation Through Acoustic Medical Phantoms 320**

6.1 The Physical Role of Anatomical Phantoms in Ultrasound-based Therapies . . . 321
6.2 Development of specialized measuring equipment . . . 323
6.2.1 Physics, Materials and Methods . . . 323
6.2.1.1 Needle Hydrophone Physical Principles . . . 323
6.2.1.2 Material Screening via Numerical Simulation . . . 326
6.2.1.3 Experimental Evaluation of Material Properties . . . 330
6.2.1.4 Numerical Optimization and evaluation of Needle Elements . . . 331

6.2.1.5 Fabrication of Optimized Needle Designs . . . 335
6.2.1.6 Experimental Validation and Testing Methods . . . 337
6.2.2 Results . . . 338
6.2.2.1 Needle Horn Material Screening . . . 338
6.2.2.2 Aluminium Alloys Characterization . . . 339
6.2.2.3 Numerical Results . . . 340
6.2.2.4 Experimental results . . . 350
6.2.3 Discussion . . . 353
6.2.4 Conclusion . . . 356
6.3 Biological Tissues Tissue Mimicking Materials . . . 357
6.3.1 Theoretical Background . . . 357
6.3.1.1 Skin-Mimicking Materials . . . 357
6.3.1.2 Soft Tissue-Mimicking Materials . . . 358
6.3.1.3 Bone-Mimicking Materials . . . 359
6.3.2 Materials and Methods . . . 360
6.3.2.1 Material Selection . . . 361
6.3.2.2 Manufacture Process . . . 362
6.3.2.3 Experimental characterization Manufacturing . . . 366
6.3.3 Results and discussion . . . 370
6.3.3.1 Density . . . 370
6.3.3.2 Speed of Sound . . . 372
6.3.3.3 Attenuation . . . 375
6.3.3.4 Acoustic Impedance . . . 380
6.3.3.5 Limitations and Future Improvements . . . 383
6.4 Transducer characterization and optimization . . . 386
6.4.1 Materials and methods . . . 386
6.4.1.1 Ultrasound Transducer Selection and Description . . . 386
6.4.1.2 Experimental Characterization . . . 387
6.4.1.3 Numerical Characterization . . . 389
6.4.2 Results . . . 394
6.4.2.1 Initial Transducer Calibration and Validation . . . 394
6.4.2.2 Thermal Simulation of Transducer Coupling to Soft Tissue . . . 395

6.4.2.3 Transducer Calibration with Acrylic Tape . . . . . 402
6.5 Anatomical tissue phantom for ultrasound therapy delivery to the knee joint . . . . . 404
6.5.1 Materials and methods . . . . . 404
6.5.2 Results . . . . . 407
6.5.3 Conclusion . . . . . 410
6.6 Bibliography . . . . . 412

**7 Personalized Patient-Specific Image-Guided Acoustic Therapy Device Planning Workflow 420**
7.1 Rationale for Personalized Ultrasound Stimulation . . . . . 421
7.2 Overview of the Proposed Personalized Development Workflow . . . . . 424
7.2.1 Integration of Magnetical Resonance Imaging and Elastography . . . . . 426
7.2.2 Computational Branch: In Silico Therapy Planning . . . . . 427
7.2.3 Experimental Branch: Phantom-Based Transducer Validation . . . . . 428
7.2.4 Convergence Toward Personalized Device Generation . . . . . 430
7.3 Procedural Generation of the Personalized Orthosis . . . . . 432
7.4 Discussion . . . . . 436
7.4.1 Advantages of the Personalized Workflow . . . . . 436
7.4.2 Clinical and Translational Relevance . . . . . 438
7.4.3 Limitations of the Proposed Pipeline . . . . . 441
7.4.4 Future Integration with Market Regulations . . . . . 443
7.5 Bibliography . . . . . 447

**A Technical Drawings 452**

**B Supplemental Biological Tissue Validation Data 457**
B.1 Computational Model Validation . . . . . 458
B.1.1 Skin . . . . . 458
B.1.2 Adipose Tissue . . . . . 461
B.1.3 Skeletal Muscle ($\perp$ fibres) . . . . . 466
B.1.4 Skeletal Muscle ($\parallel$ fibers) . . . . . 469
B.1.5 Tendon . . . . . 474
B.1.6 Ligament . . . . . 478
B.1.7 Cartilage . . . . . 482

B.1.8 Trabecular Bone . . . . . 487
B.1.9 Cortical Bone . . . . . 492
B.2 Sound Diffusivity Regression Curves . . . . . 497

**C Supplemental Simulation Framework Data 500**
C.1 Imaging processing results . . . . . 501
C.2 Transfer Function Magnitude from Transducer to Cartilage for the Remaining Patients . . 504
C.3 Acoustic pressure distribution for the remaining patients . . . . . 508

**D Supplemental Experimental Validation Data 513**
D.1 Additional Tissue-mimicking Phantom Characterization Data . . . . . 514
D.1.1 Silicone Phantoms Additional Materials and Methods . . . . . 514
D.1.1.1 Computational Methods . . . . . 514
D.1.1.2 Material Characterization Methods . . . . . 522
D.1.2 Silicone Phantoms Additional Results and Discussion . . . . . 525
D.1.2.1 Tensile Testing and Composite Formulation Results . . . . . 525
D.1.2.2 Dynamic Mechanical Response Results . . . . . 530
D.1.2.3 Shear Wave Elastography Results . . . . . 533
D.1.3 Speed of Sound of Gelatine Phantoms . . . . . 536
D.2 Additional Tissue-mimicking Phantom Characterization Data . . . . . 538
D.3 Bibliography . . . . . 542

# List of abbreviations and acronyms

**ABC** Absorbing Boundary Condition. 114

**ACL** Anterior Cruciate Ligament. 22

**APDL** ANSYS Parametric Design Language. 117, 118

**ASI** Acoustic-Solid Interface. 77, 78, 289, 290, 291

**BEM** Boundary-Element Method. 107, 108, 109

**BOBYQA** Bound Optimization BY Quadratic Approximation. 228, 229

**CFL** Courant–Friedrichs–Lewy. 105, 107, 110, 227, 248, 266, 270, 285, 390, 391, 521

**CMUT** Capacitive Micromachined Ultrasonic Transducer. 140, 142

**CW** Continuous Wave. 148

**DGM** Discontinuous-Galerkin Method. 109, 110, 111, 120, 226, 285, 287

**ECM** Extracellular Matrix. xxv, 26, 46, 96, 98, 276, 279, 280, 281, 283, 286, 287, 288, 289, 291, 296

**EMAT** Electromagnetic Acoustic Transducers. 141, 142

**ESWT** Extracorporeal Shockwave Therapy. 51, 52

**f-ESWT** Focused-Extracorporeal Shockwave Therapy. 51, 52

**FDM** Finite-Difference Method. 106, 107, 267

**FDTD** Finite-Difference Time-Domain. xxv, xxxi, 267, 268, 269, 271, 273

**FEM** Finite-Element Method. 103, 104, 106, 107, 108, 109, 111, 120

**FFT** Fast Fourier Transform. xxvi, 223, 232, 233, 394, 402

**FRF** Frequency Response Function. xxv, xxvi, xxx, 291, 292, 293, 294, 295

**HA** Hyaluronic Acid. 44, 45

**HIFU** High Intensity Focused Ultrasound. 211, 321

**HTO** High tibial osteotomy. 55, 56

**IEC** International Electrotechnical Commission. 124

**KAM** Knee Adduction Moment. 39, 40, 41

**KOOS** Knee injury and Osteoarthritis Outcome Score. 39, 40, 50, 54, 55, 56

**LCL** Lateral Collateral Ligament. 22

**LDV** Laser Doppler Vibrometry. 155, 386, 387, 388, 390, 393, 394, 402, 403, 405, 406, 407, 408, 410, 538, 539, 540, 541

**LIPUS** Low-Intensity Pulsed Ultrasound. 46, 47, 100, 211, 305

**LWS** Longitudinal Wave Speed. 521

**MCL** Medial Collateral Ligament. 22

**MRI** Magnetic Resonance Imaging. 55, 278, 404, 421, 426, 427, 430, 438, 441, 501, 502, 503

**MTU** Muscle–Tendon Unit. 27, 29, 31

**NDT** Non-Destructive Testing. 334, 335

**NSAID** Non-Steroidal Anti-Inflammatory Drug. 44, 45

**OA** Osteoarthritis. xxv, 2, 7, 35, 36, 38, 39, 40, 41, 42, 44, 45, 46, 47, 48, 49, 50, 51, 53, 56, 194, 195, 274, 276, 277, 279, 281, 291, 294, 295, 296, 300, 302, 303, 305, 307, 308, 421

**PCL** Posterior Cruciate Ligament. 22

**PCM** Pericellular Matrix. 276, 277, 279, 280, 281, 283, 286, 291, 292, 293, 294, 296, 304

**PDE** Partial Differential Equation. 119, 120

**PDMS** Polydimethylsiloxane. 126, 129

**PEMF** Pulsed Electromagnetic Field. 49, 50, 51

**PML** Perfectly Matched Layer. 114, 115, 116

**PVA** Polyvinyl Alcohol. 126, 129, 136

**PVA-C** Polyvinyl Alcohol Cryogels. 126

**PVC** Polyvinyl Chloride. 126, 129

**PZT** Piezoelectric. 77, 78, 270, 324, 330, 338, 403, 521

**r-ESWT** Radial-Extracorporeal Shockwave Therapy. 51, 52

**RCT** Randomized Controlled Trial. 39, 40, 42, 45, 47, 49, 50, 54, 55

**RMS** Root Mean Square. xxv, xxx, 297, 298, 349, 508, 509, 510, 511, 512

**RUC** Repeating Unit Cell. xxxii, 518, 527, 528

**RVE** Representative Volume Element. 75, 77, 120, 274, 275, 276, 283, 284, 286, 287, 291, 518

**STL** Sound Transmission Loss. 271

**SWE** Shear Wave Elastography. 525

**SWs** Shear Wave Speed. 521, 525, 533, 534, 535, 536

**TKA** Total Knee Arthroplasty. 56, 57

**TMM** Tissue-Mimicking Material. xxvi, xxvii, xxxii, 123, 125, 126, 135, 321, 357, 358, 359, 361, 369, 371, 372, 373, 375, 376, 380, 381, 382, 383, 385, 409

**UKA** Unicompartmental Knee Arthroplasty. 56, 57

**UTMP** Ultrasound Tissue-Mimicking Phantoms. 122, 123, 124, 127, 128, 129, 130, 132, 133, 134, 135, 136, 203, 321, 322, 404

**VAS** Visual Analogue Scale. 39, 40, 42, 44, 47, 50, 52, 54, 56

**WBV** Whole-Body vibration. 48, 49

**WOMAC** Western Ontario and McMaster Universities Arthritis Index. 39, 40, 42, 44, 45, 47, 50, 52, 54, 56

# List of Figures


1 Biomechanical movements allowed by the knee join. . . . . 22
2 Relevant anatomic structures of the knee . . . . . 22
3 Main skin layers and its components . . . . . 25
4 Exemplification of Langer's lines . . . . . 25
5 Adipose tissue microstructure . . . . . 27
6 Hierarchical schematic of skeletal muscle organization . . . . . 28
7 Representation of the muscle–tendon interface . . . . . 29
8 Hierarchical organization of ligament tissue . . . . . 30
9 Bone hierarchical organization . . . . . 32
10 Comparison of bone microstructures . . . . . 33
11 Articular cartilage structure . . . . . 34
12 Creep response of cartilage under constant applied stress . . . . . 35
13 Comparison between healthy and osteoarthritic cartilage . . . . . 36
14 Mechanical unloading strategies using knee orthoses . . . . . 39
15 Lateral wedge insoles and foot orthoses . . . . . 41
16 Contralateral cane use . . . . . 42
17 low-intensity pulsed ultrasound . . . . . 46
18 Whole-body vibration . . . . . 48
19 Pulsed electromagnetic field device . . . . . 50
20 Extracorporeal shockwave therapy . . . . . 52
21 Microfracture technique in knee cartilage repair . . . . . 53
22 High tibial osteotomy . . . . . 55
23 Arthroplasty . . . . . 57
24 Acoustic wave propagation . . . . . 62
25 Acoustic wave propagation in solids . . . . . 64

26 Perfectly Rigid Boundary . . . 68
27 Perfectly Soft Boundary . . . 69
28 Diffraction of Acoustic Waves . . . 69
29 Linear and Nonlinear Wave Propagation . . . 70
30 Homogenization of composite materials . . . 75
31 One degree-of-freedom transmissibility . . . 80
32 Scattering, dispersion, local resonance, and mode conversion . . . 89
33 Cell regeneration process . . . 97
34 Biomechanical behavior of articular cartilage . . . 99
35 Contrast of anatomical complexity with experimental modelling . . . 124
36 Bidirectional operation of a piezoelectric transducer . . . 138
37 Cross-sectional representation of a piezoelectric transducer . . . 140
38 Representative microfabricated capacitive micromachined ultrasonic transducer . . . 141
39 Laser-based ultrasonic Propagation of an acoustic wave . . . 142
40 Schematic of an electromagnetic acoustic transducer . . . 143
41 Single-element ultrasonic transducer emitting converging acoustic waves . . . 144
42 Linear phased-array ultrasonic transducer . . . 145
43 Annular array transducer . . . 146
44 Ashby map of relevant acoustic properties of materials . . . 147
45 Time-domain signals and their corresponding frequency spectra . . . 149

46 Articular cartilage structure and its limited regenerative capacity . . . 194
47 Chondrocyte mechanotransduction . . . 196
48 Standing wave formation . . . 197
49 Ultrasound wave propagation in biological tissues . . . 198
50 Proposed conceptual design for localized acoustic stimulation . . . 199
51 Integrated workflow for general acoustic studies . . . 200
52 A dual-transducer ultrasonic setup for material characterization . . . 200
53 Three-stage computational framework . . . 202
54 Schematic representation of the assembled knee phantom . . . 203
55 Iterative validation workflow . . . 205
56 Medical device development pathway . . . 206

57 Integrated experimental–computational framework for acoustic characterization of biological tissues . . . 215
58 Biological Speciment Preparation . . . 218
59 Customized ultrasound transmission setup . . . 219
60 Comparison of unfiltered and filtered ultrasonic signals . . . 222
61 Axisymmetric computational domain . . . 226
62 Time-domain ultrasonic signals . . . 232
63 Time-of-flight and peak amplitude identification . . . 233
64 Frequency spectrum of the received signal . . . 233
65 Measured density of biological tissues . . . 234
66 Measured speed of sound in biological tissues . . . 235
67 Measured attenuation of biological tissues . . . 236
68 Measured nonlinearity parameter B/A of soft tissues . . . 238
69 Estimated sound diffusivity for soft tissues . . . 239
70 Estimated sound diffusivity for hard tissues . . . 240
71 Comparison of regression model performance ($R^2$) . . . 240

72 FDTD scheme illustrating the staggered grid formulation . . . 269
73 Representation of the simplified 1D acoustic propagation model . . . 270
74 Frequency-dependent sound transmission loss across tissue interfaces . . . 271
75 Multiscale modelling strategy . . . 275
76 Representative Volume Element of Cartilage . . . 276
77 Workflow for patient-specific knee model generation . . . 278
78 Patient-specific knee model for acoustic simulation . . . 284
79 Modal analysis of the healthy chondrocyte without ECM . . . 289
80 Modal analysis of the healthy chondrocyte with ECM . . . 290
81 Modal analysis of the OA chondrocyte with ECM . . . 291
82 Frequency response of a healthy chondrocyte . . . 292
83 Parametric FRF of healthy chondrocytes . . . 293
84 Frequency response of a OA chondrocyte . . . 294
85 Parametric FRF of OA chondrocytes . . . 295
86 Macroscale patient A frequency response function . . . 297
87 Macroscale patient A RMS pressure map . . . 298

88 Macroscale patients FRF . . . 299
89 Multiscale coupled FRF . . . 300
90 Time-explicit coupled FFT response . . . 302
91 Time-explicit transient pressure fields . . . 303

92 Ashby-style material selection map for the acoustic horn needle. . . . 326
93 Axisymmetric acoustic horn needle hydrophone model. . . . 330
94 Geometric configurations evaluated in the needle optimization study. . . . 332
95 Numerical model for directivity analysis. . . . 333
96 Frequency-domain calibration model for the horn needle hydrophone. . . . 335
97 Manufacturing process of the aluminium horn needle elements. . . . 336
98 Calibration setup for the horn needle hydrophone. . . . 337
99 Receiver sensitivity as a function of horn material impedance. . . . 338
100 Experimental acoustic properties of aluminium needle samples. . . . 339
101 Influence of needle length on receiver sensitivity. . . . 341
102 Influence of conical horn height on receiver sensitivity. . . . 343
103 Pressure field distribution within conical horn geometries. . . . 344
104 Influence of exponential horn height on receiver sensitivity. . . . 345
105 Pressure field distribution within exponential horn geometries. . . . 347
106 Simulated directivity patterns of the optimized horn needle hydrophone. . . . 348
107 Frequency-dependent receiver sensitivity of the optimized horn needle hydrophone. . . . 349
108 Comparison between experimental and numerical receiver sensitivity spectra. . . . 352
109 Structure of skin-mimicking material. . . . 358
110 Acoustic Impedance in Function of Angle of Incidence. . . . 360
111 Metamaterial for Bone Mimicking Effective Impedance. . . . 360
112 Skin-mimicking material manufacturing process. . . . 363
113 Skin-mimicking material sample configurations. . . . 363
114 Soft tissue TMM samples manufacturing process. . . . 364
115 Triangular pattern on PLA surface. . . . 365
116 PLA surface patterns. . . . 366
117 Acoustic TMM characterization setup. . . . 367
118 Matlab app interface for acoustic parameter extraction. . . . 367
119 Flowchart of the signal processing routine in the Matlab app. . . . 368

120 Density of skin TMM samples. . . . 370
121 Density of soft tissue TMM samples. . . . 371
122 Speed of sound in skin TMM samples. . . . 373
123 Speed of sound in soft tissue TMM samples. . . . 373
124 Attenuation of skin TMM samples. . . . 375
125 Attenuation of soft tissue TMM samples. . . . 376
126 Attenuation of PLA samples of different heights. . . . 377
127 Attenuation coefficient of PLA samples. . . . 378
128 Attenuation coefficient of PLA samples. . . . 379
129 Acoustic impedance of skin TMM samples. . . . 380
130 Acoustic impedance of soft tissue TMM samples. . . . 381
131 Acoustic impedance of PLA samples. . . . 382
132 28 kHz ultrasonic transducer . . . 387
133 Transducer support structure . . . 388
134 Transducer model . . . 389
135 Transducer–tissue coupling model . . . 390
136 Simulated acrylic tape configurations . . . 393
137 Experimental and numerical calibration of the transducer vibration response . . . 394
138 Acoustic field generated by the transducer in contact with soft tissue . . . 395
139 Transient temperature distribution during ultrasonic excitation . . . 396
140 Transient tissue damage distribution during ultrasonic excitation . . . 396
141 Temperature evolution and predicted tissue damage without attenuation layer. . . . 397
142 Temperature evolution and predicted tissue damage for different acrylic tape layers. . . . 398
143 Effect of acrylic tape layers on the acoustic pressure field. . . . 398
144 Temperature evolution for gap-modified six-layer acrylic tape configurations . . . 399
145 Predicted tissue damage for gap-modified six-layer acrylic tape configurations. . . . 400
146 Acoustic pressure distribution for the selected acrylic tape configuration. . . . 401
147 Calibration of the acylic tape-modified transducer vibration response . . . 402
148 Illustration of the anatomical knee phantom . . . 404
149 Sinusoidal pattern applied to the bone structures . . . 405
150 Design of the skin moulds . . . 405
151 Fabrication of the soft-tissue surrogate . . . 406

152 Experimental setup for acoustic testing of the anatomical knee phantom . . . . . 406
153 Angular dependence of vibration transmission to the left condyle. . . . . 407

154 Overview of the proposed personalized development workflow . . . . . 424
155 Phantom-informed placement of the therapeutic transducer . . . . . 432
156 Definition of orthosis boundary curves . . . . . 433
157 Procedural generation of the final personalized orthosis . . . . . 434
158 Classification of the developed ultrasound-based orthotic device . . . . . 444

159 Acoustic wave propagation in skin at $500$ kHz . . . . . 458
160 Acoustic wave propagation in skin at $1$ MHz . . . . . 459
161 Acoustic wave propagation in skin at $2$ MHz . . . . . 460
162 Acoustic wave propagation in skin at $4$ MHz . . . . . 460
163 Acoustic wave propagation in skin at $5$ MHz . . . . . 461
164 Acoustic wave propagation in adipose tissue at $500$ kHz . . . . . 462
165 Acoustic wave propagation in adipose tissue at $1$ MHz . . . . . 463
166 Acoustic wave propagation in adipose tissue at $2$ MHz . . . . . 464
167 Acoustic wave propagation in adipose tissue at $4$ MHz . . . . . 464
168 Acoustic wave propagation in adipose tissue at $5$ MHz . . . . . 465
169 Acoustic wave propagation in skeletal muscle ($\perp$ to fibers) at $500$ kHz . . . . . 466
170 Acoustic wave propagation in skeletal muscle ($\perp$ fibers) at $1$ MHz . . . . . 467
171 Acoustic wave propagation in skeletal muscle ($\perp$ fibers) at $2$ MHz . . . . . 468
172 Acoustic wave propagation in skeletal muscle ($\perp$ fibers) at $4$ MHz . . . . . 469
173 Acoustic wave propagation in skeletal muscle ($\perp$ fibers) at $5$ MHz . . . . . 470
174 Acoustic wave propagation in skeletal muscle ($\parallel$ fibers) at $500$ kHz . . . . . 471
175 Acoustic wave propagation in skeletal muscle ($\parallel$ fibers) at $1$ MHz . . . . . 471
176 Acoustic wave propagation in skeletal muscle ($\parallel$ fibers) at $2$ MHz . . . . . 472
177 Acoustic wave propagation in skeletal muscle ($\parallel$ fibers) at $4$ MHz . . . . . 473
178 Acoustic wave propagation in skeletal muscle ($\parallel$ fibers) at $5$ MHz . . . . . 474
179 Acoustic wave propagation in tendon at $500$ kHz . . . . . 475
180 Acoustic wave propagation in tendon at $1$ MHz . . . . . 475
181 Acoustic wave propagation in tendon at $2$ MHz . . . . . 476
182 Acoustic wave propagation in tendon at $4$ MHz . . . . . 477

183 Acoustic wave propagation in tendon at $5$ MHz . . . . . 478
184 Acoustic wave propagation in ligament at $500$ kHz . . . . . 479
185 Acoustic wave propagation in ligament at $1$ MHz . . . . . 480
186 Acoustic wave propagation in ligament at $2$ MHz . . . . . 480
187 Acoustic wave propagation in ligament at $4$ MHz . . . . . 481
188 Acoustic wave propagation in ligament at $5$ MHz . . . . . 482
189 Acoustic wave propagation in Cartilage at $500$ kHz . . . . . 483
190 Acoustic wave propagation in Cartilage at $1$ MHz . . . . . 484
191 Acoustic wave propagation in Cartilage at $2$ MHz . . . . . 485
192 Acoustic wave propagation in Cartilage at $4$ MHz . . . . . 485
193 Acoustic wave propagation in Cartilage at $5$ MHz . . . . . 486
194 Acoustic wave propagation in Trabecular Bone at $500$ kHz . . . . . 487
195 Acoustic wave propagation in Trabecular Bone at $1$ MHz . . . . . 488
196 Acoustic wave propagation in Trabecular Bone at $2$ MHz . . . . . 489
197 Acoustic wave propagation in Trabecular Bone at $4$ MHz . . . . . 490
198 Acoustic wave propagation in Trabecular Bone at $5$ MHz . . . . . 491
199 Acoustic wave propagation in Cortical Bone at $500$ kHz . . . . . 492
200 Acoustic wave propagation in Cortical Bone at $1$ MHz . . . . . 493
201 Acoustic wave propagation in Cortical Bone at $2$ MHz . . . . . 494
202 Acoustic wave propagation in Cortical Bone at $4$ MHz . . . . . 495
203 Acoustic wave propagation in Cortical Bone at $5$ MHz . . . . . 496
204 Frequency-dependent sound diffusivity for skin, adipose tissue, skeletal muscle . . . . . 497
205 Frequency-dependent sound diffusivity for tendon, ligament, and cartilage . . . . . 498
206 Frequency-dependent sound diffusivity for trabecular and cortical bone . . . . . 499

207 Patient A imaging processing results . . . . . 501
208 Patient B imaging processing results . . . . . 501
209 Patient C imaging processing results . . . . . 502
210 Patient D imaging processing results . . . . . 502
211 Patient E imaging processing results . . . . . 502
212 Patient F imaging processing results . . . . . 503
213 Patient G imaging processing results . . . . . 503
214 Patient H imaging processing results . . . . . 503

215 FRF for patient B knee . . . . . 504
216 FRF for patient C knee . . . . . 504
217 FRF for patient D knee . . . . . 505
218 FRF for patient E knee . . . . . 505
219 FRF for patient F knee . . . . . 506
220 FRF for patient G knee . . . . . 506
221 FRF for patient H knee . . . . . 507
222 RMS acoustic pressure distribution for Patient B . . . . . 508
223 RMS acoustic pressure distribution for Patient C . . . . . 509
224 RMS acoustic pressure distribution for Patient D . . . . . 510
225 RMS acoustic pressure distribution for Patient E . . . . . 510
226 RMS acoustic pressure distribution for Patient F . . . . . 511
227 RMS acoustic pressure distribution for Patient G . . . . . 511
228 RMS acoustic pressure distribution for Patient H . . . . . 512

229 Image-processing workflow for tensile test analysis. . . . . 523
230 Experimental setup for dynamic compressive testing. . . . . 524
231 Curve-fitting results for hyperelastic material models. . . . . 526
232 Independent loading cases applied to the repeating unit cell. . . . . 528
233 Young's modulus of skin and muscle phantoms. . . . . 529
234 Viscoelastic characterization of the phantom materials. . . . . 530
235 Shear wave elastography characterization of the phantom materials. . . . . 534
236 Measured speed of sound of the gelatin phantoms . . . . . 537
237 Point 1 experimental and simulated transducer responses . . . . . 538
238 Point 2 experimental and simulated transducer responses . . . . . 538
239 Point 3 experimental and simulated transducer responses . . . . . 539
240 Point 4 experimental and simulated transducer responses . . . . . 539
241 Point 5 experimental and simulated transducer responses . . . . . 540
242 Point 6 experimental and simulated transducer responses . . . . . 540
243 Point 7 experimental and simulated transducer responses . . . . . 541

# List of Tables


1 Ideal Mechanotransduction regimes . . . . . 97
2 Comparison of commercial software for multiphysic wave propagation . . . . . 117
3 Ideal parameters used for Ultrasound Tissue-Mimicking Phantoms. . . . . 124
4 Summary of Standardized Ultrasound Phantom Materials. . . . . 124
5 Ultrasound Phantoms Targeting Skin Tissue. . . . . 128
6 Ultrasound Phantoms Mimicking Adipose Tissue. . . . . 130
7 Ultrasound Phantoms Mimicking Skeletal Muscle, Tendons, and Ligaments. . . . . 132
8 Ultrasound Phantoms Mimicking Bone Tissue. . . . . 134

9 Summary of biological tissue samples used in this study. . . . . 216
10 Number of mesh elements used in the simulation domain for each biological tissue sample. 227
11 Overview of the parameter estimation limits. . . . . 229
12 Fitted power-law attenuation parameters ($\alpha_0$, $n$) . . . . . 237
13 Power-law regression parameters for sound diffusivity $\delta(f) = \delta_0 f^n$ in biological tissues. . . 241

14 Material parameters used for the simulation in 1D FDTD wave propagation. . . . . 269
15 Morphological parameters of chondrocytes . . . . . 276
16 Demographic and anthropometric characteristics of the subjects . . . . . 277
17 Chondrocyte's mechanical and acoustic material properties . . . . . 279
18 Biological tissues' mechanical and acoustic material properties . . . . . 281

19 Needle Material Selection Properties . . . . . 326
20 Needle Parameters evaluation . . . . . 332
21 Identification of the manufactured aluminium horn needle samples. . . . . 336
22 Wavelength-dependent needle horn length sensitivity behaviour . . . . . 342
23 Wavelength-dependent needle horn conical sensitivity behaviour . . . . . 343
24 Wavelength-dependent needle horn exponential sensitivity behaviour . . . . . 346

25 Soft Tissues TMM composition . . . . . 361
26 PLA Density . . . . . 372
27 PLA Speed of Sound . . . . . 374

28 Material parameters used for the fiber-reinforced RUC simulations. . . . . 518
29 Simulation parameters for dynamic mechanical compressive tests . . . . . 520
30 Fitted parameters for the five-parameter Mooney–Rivlin model. . . . . 527

# Chapter 1

# Introduction

## 1.1 Motivation

The present research emerges from the intersection of biomedical engineering, mechanical engineering, and physics, addressing the urgent need for innovative treatment approaches for knee osteoarthritis (OA).

Knee OA represents one of the most prevalent, disabling, and economically burdensome musculoskeletal disorders worldwide. In 2019, approximately 528 million people were living with osteoarthritis globally, representing a 113% increase since 1990, and the knee was the most frequently affected joint, with an estimated 365 million cases[1,2]. Global Burden of Disease estimates further indicate that osteoarthritis affected approximately 595 million people in 2020, corresponding to 7.6% of the global population, with projections suggesting that this number may approach one billion by 2050[3]. The disease is associated with chronic pain, cartilage degradation, impaired mobility, reduced quality of life, work limitations, and loss of independence, while approximately 344 million affected individuals experience moderate or severe disease levels that could benefit from rehabilitation[4]. Its economic burden is also substantial, with annual per-patient costs for knee osteoarthritis reported to range from approximately $9,801 in mild disease to $22,111 in severe disease, largely due to healthcare utilization, productivity losses, and disability-related costs[5]. Although pharmacological, surgical, and rehabilitation-based interventions may reduce symptoms or delay disease progression, they remain limited in their capacity to restore cartilage structure or provide controlled, patient-specific mechanical stimulation to the affected joint[6,7]. This unmet need has motivated increasing interest in non-invasive therapeutic strategies based on mechanical, vibrational, and ultrasound-mediated stimulation, particularly because cartilage is a mechanosensitive tissue whose cellular activity is strongly influenced by its mechanical environment.

From a biological and medical perspective, mechanical and acoustic stimulation have been investigated as potential modulators of cartilage metabolism, with several in vitro and in vivo studies reporting effects on chondrocyte proliferation, extracellular matrix synthesis, inflammatory regulation, matrix metalloproteinase activity, integrin-mediated mechanotransduction, and cartilage homeostasis[8–10]. These findings support the hypothesis that ultrasound-mediated mechanical energy may influence osteoarthritic tissues through non-thermal mechanisms, including acoustic radiation force, microstreaming, cavitation-related effects, membrane deformation, cytoskeletal remodeling, and activation of mechanosensitive biochemical pathways[8,9,11]. However, the biological response to these stimuli is not governed solely by the nominal parameters imposed at the actuator or transducer. Frequency, pressure amplitude, acoustic intensity, duty cycle, pulse repetition frequency, exposure

duration, spatial pressure distribution, and local tissue deformation all contribute to the resulting cellular response, indicating that ultrasound stimulation should be understood as a coupled physical–biological intervention rather than a purely empirical therapeutic input[8,9].

Despite this biological promise, the selection of stimulation parameters in the literature remains only partially optimized for cartilage mechanobiology. Many studies employ parameter ranges inherited from established diagnostic or therapeutic ultrasound practice, including frequencies in the MHz range and low spatial-average temporal-average intensities, rather than parameters derived from patient-specific wave propagation, cartilage-level energy deposition, or chondrocyte-scale mechanical response. For example, low-intensity pulsed ultrasound studies frequently adopt values close to the conventional LIPUS setting of approximately 1.5 MHz, 30–60 mW/cm$^2$, 20% duty cycle, and 1 kHz pulse repetition frequency[9,12]. These values are comparable to safety-oriented low-intensity ultrasound exposure regimes and overlap conceptually with the acoustic operating windows used in diagnostic ultrasonography and elastography, where ultrasound is primarily used to image tissues or estimate stiffness rather than to prescribe a controlled cartilage-level therapeutic stimulus[11,13]. Consequently, although ultrasound and vibration-based approaches have produced encouraging biological results, clinical outcomes remain heterogeneous, and some randomized trials have failed to demonstrate significant improvements in symptoms or cartilage preservation when pulsed low-intensity ultrasound was applied using generic treatment parameters[14]. Therefore, the therapeutic relevance of ultrasound or vibration-based stimulation depends not only on whether acoustic energy is generated externally, but also on whether an appropriate, quantifiable, and biologically meaningful mechanical stimulus reaches the target cartilage region.

This creates a fundamental engineering challenge. Between the external stimulation source and the articular cartilage, acoustic waves must propagate through a heterogeneous anatomical pathway composed of tissues with distinct density, stiffness, attenuation, acoustic impedance, anisotropy, and geometry. Skin, adipose tissue, muscle, tendons, ligaments, synovial fluid, cartilage, and bone may each modify the transmitted field through reflection, absorption, scattering, refraction, mode conversion, and local amplification. Therefore, the stimulus received by the cartilage may differ substantially from the programmed excitation, particularly when generic stimulation parameters or simplified placement strategies are used.

Modern engineering methods now provide the tools required to address this limitation. Full-wave numerical models, finite-element formulations, acoustic–structure interaction simulations, hydrophone-based field mapping, tissue-mimicking phantoms, and inverse design strategies can be used

to predict and engineer the internal acoustic field with high spatial precision. These approaches allow the investigator to estimate not only whether acoustic energy reaches the target tissue, but also the local pressure amplitude, intensity, phase distribution, focal position, frequency-dependent attenuation, and spatial pattern of mechanical loading within heterogeneous media. In focused ultrasound and neuromodulation, patient-specific simulations have already been used to predict pressure fields through complex anatomy, compensate for aberrations, optimize transducer positioning, and support treatment planning[15–18]. Similarly, acoustic holography, phased-array control, and model-based optimization demonstrate that the interior pressure field can be shaped, steered, and adapted to predefined target regions rather than being treated as an uncontrolled consequence of external excitation[19].

The literature thus contains important but often disconnected advances. Mechanical engineering and acoustics provide robust methods for modelling wave propagation, characterizing material properties, designing transducers, analysing acoustic impedance, estimating attenuation, acould field calculation techniques, and prescribing the amplitude and frequency required to obtain a desired internal stimulus. In parallel, biology and medicine provide essential knowledge regarding osteoarthritis pathology, cartilage mechanobiology, chondrocyte mechanotransduction, and the therapeutic potential of mechanical stimulation. However, these domains are frequently developed in isolation. Biological studies may report promising cellular or tissue-level outcomes without fully resolving the physical field delivered to the target region, while engineering studies may describe acoustic propagation or device performance without explicitly connecting these results to biologically meaningful stimulation conditions. The central opportunity, therefore, is to combine these two perspectives: to use engineering tools not only to generate ultrasound, but to define, predict, and control the cartilage-level mechanical stimulus that may activate relevant biological pathways.

This thesis is driven by the need to connect two complementary but often separated domains: mechanical engineering and acoustics, which provide the means to describe, predict, and control wave propagation, and biology and medicine, which define the cellular and clinical meaning of the stimulus being delivered. Its central premise is that the therapeutic value of acoustic and mechanical stimulation cannot be fully understood from the external excitation alone. It must instead be evaluated through the physical stimulus that actually reaches the biological target, its spatial and temporal characteristics, and its relationship with the mechanobiological pathways involved in cartilage homeostasis and degeneration. In this context, the present work is framed as a translational contribution, in which engineering methods are not treated as secondary technical supports, but as fundamental instruments for converting biological potential into a rational, reproducible, and patient-specific therapeutic strategy.

## 1.2 Objectives and Research Questions

The main objective of this thesis is to develop and evaluate an engineering-based framework for the design of a personalized ultrasound stimulation strategy for knee osteoarthritis. The work is motivated by the need to bridge acoustic wave propagation, biological tissue characterization, computational modelling, experimental validation, and device-oriented development. Rather than treating ultrasound stimulation as a generic external input, this thesis considers the therapeutic stimulus as a physical field that must be generated, transmitted, quantified, and controlled within a patient-specific anatomical environment.

As such, this thesis aims to establish a rational methodology for estimating how acoustic and mechanical energy propagates from an external transducer through the tissues of the knee and how this energy may reach the articular cartilage. This requires the integration of biological tissue properties, numerical models, anatomical geometries, tissue-mimicking phantoms, and transducer placement strategies. The broader purpose is to support the development of a non-invasive orthotic device capable of delivering controlled mechanical stimulation to cartilage regions affected by osteoarthritis.

The general objective of this thesis is to develop a personalized patient-specific workflow for ultrasound-based knee cartilage stimulation by combining biological tissue characterization, computational acoustic modelling, phantom-based validation, and device-oriented design. This framework is intended to support the definition of stimulation parameters, transducer positioning, and orthosis geometry required to deliver a controlled acoustic or mechanical stimulus to the target cartilage region.

The specific objectives of this thesis are defined as follows:

1. To review and consolidate the biological, clinical, and engineering foundations of ultrasound- and vibration-based stimulation for knee osteoarthritis, with particular emphasis on cartilage mechanobiology, chondrocyte mechanotransduction, and acoustic wave propagation in biological tissues;

2. To identify and develop a measurement method to analyse the acoustic and mechanical properties of biological tissues relevant to state-of-the-art simulation and characterization techniques;

3. To investigate how anatomical variability, tissue composition, transducer diameter, excitation frequency, and amplitude influence the acoustic pressure field reaching the articular cartilage.

4. To develop tissue-mimicking and anatomically representative phantoms that reproduce relevant acoustic and geometric characteristics of the knee, supporting experimental validation of transducer positioning and acoustic field delivery.

5. To develop a methodology able to validate numerical predictions and refine transducer configuration before device implementation.
6. To propose a personalized device-development workflow in which non-insasive measurement techniques converge toward a patient-specific therapeutic system.
7. To establish design recommendations for a non-invasive knee orthosis capable of positioning ultrasound transducers in a controlled manner and delivering reproducible stimulation to the target anatomical region.

Based on these objectives, the thesis is guided by the following research questions:

1. How can the acoustic and mechanical properties of knee-related biological tissues be incorporated into computational models of ultrasound propagation?
2. To what extent do tissue heterogeneity, acoustic impedance mismatch, attenuation, and anatomical geometry influence the transmission of ultrasound from an external transducer to the articular cartilage?
3. Can simplified one-dimensional or reduced-order models provide useful preliminary estimates of acoustic transmission through biological tissue layers before more complex patient-specific simulations are performed?
4. How does patient-specific knee anatomy affect the spatial distribution, magnitude, and frequency response of the acoustic field delivered to cartilage?
5. Which excitation parameters, including frequency, amplitude, duty cycle, and transducer diameter, most strongly influence the mechanical stimulus reaching the target cartilage region?
6. Can numerical acoustic simulations be used to identify patient-specific stimulation parameters that are more physically meaningful than generic ultrasound settings derived from conventional diagnostic or therapeutic practice?
7. Can tissue-mimicking phantoms be designed to reproduce the relevant acoustic behaviour of biological tissues and support validation of transducer performance?
8. To what extent can phantom-based experiments validate the predicted acoustic field and assist in optimizing transducer placement for knee stimulation?

9. How can computational and experimental branches be integrated into a unified workflow for personalized ultrasound therapy planning?

10. What design principles should guide the development of an orthotic device intended to hold ultrasound transducers in patient-specific positions while ensuring comfort, reproducibility, and non-invasive use?

The central hypothesis of this thesis is that ultrasound-based stimulation for knee OA can be made more rational, reproducible, and patient-specific by combining acoustic modelling, biological tissue characterization, and phantom-based validation. More specifically, it is hypothesized that the therapeutic relevance of ultrasound stimulation depends not only on the nominal parameters imposed at the transducer, but on the local mechanical stimulus effectively delivered to the cartilage after propagation through patient-specific tissues.

From this perspective, the knee should not be treated as a homogeneous medium, nor should the stimulation protocol be defined solely by generic frequency and intensity values. Instead, the acoustic field should be planned using anatomical geometry, tissue properties, and model-based estimation of local pressure, attenuation, reflection, and energy distribution. This hypothesis supports the development of a personalized workflow in which engineering tools become essential for translating biological mechanostimulation concepts into a controllable therapeutic device.

## 1.3 Methodology and Expected Contributions

This thesis adopts an interdisciplinary methodology that combines biological tissue characterization, acoustic wave propagation modelling, computational simulation, phantom-based validation, and device-oriented development. The methodological structure reflects the central premise of the work: ultrasound-based stimulation for knee osteoarthritis should not be defined only by nominal parameters imposed at the transducer, but by the physical stimulus effectively delivered to the target cartilage region after propagation through patient-specific anatomical tissues.

The proposed methodology is therefore organized as a progressive workflow, moving from the identification of relevant biological and acoustic parameters to the numerical and experimental validation of ultrasound delivery strategies. This structure allows the thesis to connect mechanobiological requirements with engineering design decisions, supporting the development of a rational and patient-specific approach for therapeutic knee stimulation.

As such, it is centered on four complementary stages. The first stage establishes the biological and physical foundations of the problem, with emphasis on knee osteoarthritis, cartilage mechanobiology, chondrocyte mechanotransduction, and the acoustic properties of biological tissues relevant for state-of-the-art applications. The second stage develops computational models capable of estimating acoustic transmission through simplified and anatomically informed tissue domains. The third stage introduces experimental validation through tissue-mimicking and anatomical phantoms, allowing the predicted acoustic fields and transducer configurations to be evaluated under controlled laboratory conditions. The fourth stage integrates the computational and experimental findings into a device-oriented workflow for the design of a personalized knee orthosis.

This methodological sequence is intended to reduce the distance between biological hypothesis and engineering implementation. Rather than treating the transducer as an isolated actuator, the thesis considers the complete therapeutic pathway: the generation of acoustic energy, its propagation through heterogeneous tissues, its interaction with anatomical interfaces, and its final delivery to cartilage.

The expected contributions of this thesis are organized into scientific, methodological, and translational contributions.

From a scientific perspective, this thesis contributes to the understanding of acoustic propagation through complex heterogeneous media (knee tissues). By analysing the influence of tissue properties, anatomical geometry, acoustic impedance mismatch, attenuation, and transducer configuration, the work provides insight into how externally generated acoustic energy may be modified before reaching the articular cartilage. This contributes to a more physically grounded interpretation of ultrasound-based

cartilage stimulation.

From a methodological perspective, the thesis proposes an integrated framework combining tissue characterization, reduced-order modelling, patient-specific simulation, phantom validation, and device-oriented design. This framework addresses a key limitation in the current literature: the frequent separation between biological studies of mechanostimulation and engineering studies of acoustic field generation. By connecting these domains, the work provides a structured methodology for estimating the actual stimulus delivered to the biological target. The use of computational models to support the definition of stimulation parameters. Instead of relying solely on conventional ultrasound settings, the thesis explores how frequency, amplitude, transducer diameter, and placement may be selected according to the acoustic response of the anatomical pathway. This may support the future development of more rational and individualized stimulation protocols.

From an experimental perspective, the thesis contributes to the development and use of tissue-mimicking and anatomical phantoms for therapeutic ultrasound validation. These phantoms provide a controlled platform for testing transducer placement, acoustic coupling, and internal field distribution. They also create an intermediate validation step between numerical modelling and clinical or preclinical application.

From a device-development perspective, the thesis proposes a workflow for the generation of a personalized orthotic system for knee stimulation. By linking medical imaging, simulation, phantom testing, and procedural design, the work supports the creation of a device capable of delivering ultrasound stimulation in a controlled, reproducible, and patient-specific manner.

Finally, from a translational perspective, the thesis contributes to the broader field of personalized therapeutic ultrasound. Its central contribution is not limited to the design of a specific device, but rather to the establishment of a strategy for connecting actuator-level input, tissue-level propagation, cartilage-level stimulation, and mechanobiological relevance. In this sense, the thesis seeks to transform ultrasound-based cartilage stimulation from an empirical intervention into a model-informed therapeutic approach.

## 1.4 Publications

Nuno Alexandre Tavares de Campos Fernandes is a PhD candidate in Mechanical Engineering at the University of Minho, affiliated with Centre for MicroElectroMechanical Systems (CMEMS) and an Invited Assistant Professor at the same institution. His work is positioned at the intersection of mechanical engineering, acoustics, wave propagation, multiphysics modelling, biomedical technologies and advanced materials. His scientific output includes 23 scientfic outputs and the development of 3 software tools, with citation metrics of h-index 4 and 42 citations in Scopus, and h-index 5 and 60 citations in Google Scholar. He has co-supervised 17 MSc dissertations, received 2 awards and/or honours, and participated in 1 project as a PhD Student Fellow and 4 projects as a Researcher. His main research interests include wave propagation in complex heterogeneous media, ultrasound-based stimulation, acoustic transmission, numerical modelling, acoustic and thermal insulation, recycled materials, footwear waste valorisation, and sustainable engineering solutions.

### 1.4.1 Journal Articles

- **Nuno A. T. C. Fernandes**, Filipe Dario Marques, Shivam Sharma, Óscar Carvalho, "Wavelength-Scaled Design and Validation of an Aluminum Horn Needle Hydrophone Attachment for Ex Vivo Transcranial Ultrasound Applications" in Journal of Vibration and Engineering Technologies (Q1 - Acoustics and Ultrasonics), 2026 (Accepted).

- **Nuno A. T. C. Fernandes**, Betina Hinckel, Ana Leal, Óscar Carvalho, "A Multi-Scale 3D–2D Coupled Model of Patient-Specific Acoustic Wave Propagation for Mechanotransduction Stimulation of Healthy and Osteoarthritic Knee Articular Cartilage" in Biomechanics and Modeling in Mechanobiology (Q1 - Mechanical Engineering/Modelling and Simulation), 2026 (In Review).

- **Nuno A. T. C. Fernandes**, Shivam Sharma, Ana Arieira, Betina Hinckel, Filipe Silva, Ana Leal, Óscar Carvalho, "Experimental Validation of Time-Explicit Ultrasound Propagation Models with Sound Diffusivity or Viscous Attenuation in Biological Tissues Using COMSOL Multiphysics" in Bioenegineering (Q2 - Bioengineering), August 2025. `https://doi.org/10.3390/bioengineering12090946`

- **Nuno A. T. C. Fernandes**, Diana I. Alves, Diana P. Ferreira, Maria Monteiro, Ana Arieira, Betina Hinckel, Filipe Silva, Ana Leal, Óscar Carvalho, "Sustainable Tunable Anisotropic Ultrasound Medical Phantoms for Skin, Skeletal Muscle, and Other Fibrous Biological Tissues Using Natural

Fibers and a BioElastomeric Matrix" in Journal of Composites Science (Q1 - Engineering (miscellaneous)), June 2025. https://doi.org/10.3390/jcs9070370

- **Nuno A. T. C. Fernandes**, Ana Arieira, Betina Hinckel, Filipe Samuel Silva, Óscar Carvalho, Ana Leal "Unlocking the Secrets of Knee Joint Unloading: A Systematic Review and Biomechanical Study of the Invasive and Non-Invasive Methods and Their Influence on Knee Joint Loading" in Rheumato, June 2025. https://doi.org/10.3390/rheumato5030008

- **Nuno A. T. C. Fernandes**, Óscar Carvalho, Ana Leal, Filipe Samuel Silva, "The effect that Lower Limb orthoses have on cartilage on patients with knee osteoarthritis: a narrative review" in Prosthetics and Orthotics International (Q2 - Rehabilitation, Health Professions (miscellaneous)), April 2022. https://doi.org/10.1097/PXR.0000000000000128

- Tiago Cunha, **Nuno A. T. C. Fernandes**, Delfim Soares, Óscar Carvalho, "Tunable Cellular Structures with Damping for Industry-Ready Dynamic Load Management in Bus Applications" in Applied Sciences (Q2 - Engineering (miscellaneous)), February 2026. https://doi.org/10.3390/app16041772

- Ana Z Santos, Sofia Rocha, **Nuno A. T. C. Fernandes**, Diana I. Alves, Diana P. Ferreira, Sofia M. Costa, Jorge Padrão, Óscar Carvalho, "Sustainable Shear Wave Elastography Medical Phantoms: Waste-Based Fibrous Structures for Medical Applications" in Textiles (Q1 - Materials Science (miscellaneous)), January 2026. https://doi.org/10.3390/textiles6010006

- Shivam Sharma, **Nuno A. T. C. Fernandes**, Óscar Carvalho, "A Frequency-Dependent and Nonlinear, Time-Explicit Five-Layer Human Head Numerical Model for Realistic Estimation of Focused Acoustic Transmission Through the Human Skull for Noninvasive High-Intensity and High-Frequency Transcranial Ultrasound Stimulation: An Application to Neurological and Psychiatric Disorders" in Bioengineering (Q2 - Bioengineering), October 2025. https://doi.org/10.3390/bioengineering12111161

- Diana I. Alves, Renato Guimarães, Sofia M. Costa, **Nuno A. T. C. Fernandes**, Óscar Carvalho, Raul Fangueiro, Diana P. Ferreira, "An Innovative Solution for Post-Consumer Footwear Waste: Nonwoven Fibrous Structures with Thermal and Acoustic Insulation Properties" in Materials (Q2 - Materials Science (miscellaneous)), October 2025. https://doi.org/10.3390/ma18204765

- Ana Z. Santos, Sofia Rocha, Beatriz Carneiro, **Nuno A. T. C. Fernandes**, Jorge Padrão, Óscar Carvalho, "Current state of elastography research in multiple anatomical structures and respective phantoms" in Physica Medica (Q2 - Biophysics), October 2025. https://doi.org/10.1016/j.ejmp.2025.105192

- Susana O. Catarino, **Nuno A. T. C. Fernandes**, Francisca Monteiro, Sofia Oliveira, Filipa Fernandes, Filipe S. Silva, Óscar Carvalho, "Unraveling the potential of transcranial photobiomodulation and ultrasound stimulation for brain therapeutics: an introduction" in Brain Stimulation (Q1 - Biophysics, Neurology (Clinical), Neuroscience (miscellaneous)), January 2025. https://doi.org/10.1016/j.brs.2024.12.121

- Diana I. Alves, Óscar Carvalho, **Nuno A. T. C. Fernandes**, Livia Consentino, Adilson C Paula Junior, Raul Fangueiro, Diana P. Ferreira, "Upcycling of industrial footwear waste into nonwoven fibrous structures with thermal and acoustic insulation properties" in Journal of Environmental Management (Q1 - Environmental Engineering), June 2024. https://doi.org/10.1016/j.jenvman.2024.121363

### 1.4.2 Book Chapter

- **Nuno A. T. C. Fernandes**, Diana I. Alves, Francisco Ruivo, Diana P. Ferreira, Óscar Carvalho, "Green Vibrations: Dynamic Stiffness and Constitutive Modelling of Recycled Nonwoven Materials for Sustainable Vibration Damping in Flooring", in WASTES: Solutions, Treatments and Opportunities, May 2026. https://doi.org/10.1007/978-3-032-14960-2_113

- **Nuno A. T. C. Fernandes**, Gabriela Couto, Shivam Sharma, Óscar Carvalho, "Development of a Tuneable Helmholtz Resonator Metamaterial for Acoustic Notch Filtering Attenuation and Ventilation Using 3D Printing" in Proceedings of ICOVP and WMVC 2025, January 2026. https://doi.org/10.1007/978-3-032-11549-2_4

- **Nuno A. T. C. Fernandes**, Ana Arieira, Betina Hinckel, Filipe S. Silva, Ana Leal, Óscar Carvalho, "A Python FDTD Method Algorithm for 1D Planar Acoustic Wave Propagation: Simulating High-Frequency Ultrasound in the Brain and Beyond" in Proceedings of ICOVP and WMVC 2025, January 2026. https://doi.org/10.1007/978-3-032-13225-3_39

- **Nuno A. T. C. Fernandes**, Ana Rita Amorim, Barbara Silva, Joana Freitas, João P. Mendonça, "TAB-Med: Automated Pill Dispenser in Residential Environments" in Innovations in Mechanical Engineering, January 2022. https://doi.org/10.1007/978-3-030-79165-0_34
- Anabela Pereira, Vanessa F. Cardoso, Marcos Martins, **Nuno A. T. C. Fernandes**, Óscar Carvalho, "Development of a Hydrophone for Measuring the Propagation of Acoustic Waves in Biological Tissues" in "Acoustic Wave Propagation in Proceedings of ICOVP and WMVC 2025, January 2026. https://doi.org/10.1007/978-3-032-11549-2_63
- Ana Isabel Ribeiro; Tiago Azevedo, Mariana P. Barreiros, Ana Catarina Silva, Diego Chaves, **Nuno A. T. C. Fernandes**, Óscar Carvalho, Raul Fangueiro, Diana P. Ferreira, "Aqueous Solutions for Sustainable Elastane Degradation in Textile Recycling" in Advances in the Textile and Clothing Research, 2026. https://doi.org/10.1007/978-3-032-20865-1_13

### 1.4.3 Conference Paper

- **Nuno A. T. C. Fernandes**, Maria Inês Cardoso, Maria Cândida Vilarinho, Óscar Carvalho, "NATURAL FIBRE COMPOSITES FOR SOUND INSULATION: A SUSTAINABLE SOLUTION FOR BUILDING ACOUSTICS" in ICNF 2025, 2025.
- **Nuno A. T. C. Fernandes**, Filipe S. Silva, Ana Leal, Óscar Carvalho, "Development of a Tuneable Helmholtz Resonator Metamaterial for Acoustic Notch Filtering Attenuation and Ventilation Using 3D Printing" in International Workshop on Additive Manufacturing and Sustainability, 2024.
- **Nuno A. T. C. Fernandes**, Syn Schmitt, Oleksandr V. Martynenko, "Modelling and Validation of the 3D Muscle-Tendon Unit with solid Finite Elements in LS-DYNA for Active Human Body Model applications" in IRCOBI 2019, 2019.
- Elina Marinho, Diego chaves, Joana C. Araújo, Tiago azevedo, Diana I. Alves, Renato guimarães, **Nuno A. T. C. Fernandes**, Óscar Carvalho, Raul Fangueiro, "PRODUCTION OF NONWOVEN STRUCTURES FROM NOVEL NATURAL FIBERS: INNOVATION AND SUSTAINABILITY" in ICNF 2025, 2025.

### 1.4.4 Software Tools

- **Nuno A. T. C. Fernandes**, "MATLAB Post-Processing Tool for Ultrasound Transmission Measurements in Soft Tissue and Tissue-Mimicking Samples", 2026.

https://doi.org/10.5281/zenodo.20334690

- **Nuno A. T. C. Fernandes**, "Cauchy Stress Tensile Test Post-Processing for SkinMimicking Materials", 2026. https://doi.org/10.5281/zenodo.20369771
- **Nuno A. T. C. Fernandes**, "1D FDTD Planar Acoustic Wave Propagation", 2026. https://doi.org/10.5281/zenodo.20445080

## 1.5 Thesis Structure

This thesis is organized into seven chapters, following the progression of the research from the definition of the scientific problem and theoretical background to the development, validation, and integration of the proposed therapeutic strategy.

Chapter 1 introduces the research topic and establishes the scientific and clinical context of the thesis. It presents the motivation for the study, defines the main objectives and research questions, and describes the methodological framework adopted throughout the work.

Chapter 2 presents the state of the art related to the main themes addressed in the thesis. The chapter reviews the literature on wave propagation in complex heterogeneous media, the biomechanical and biological aspects of knee osteoarthritis, the mechanobiological stimulation of cartilage tissues, and current therapeutic approaches and biomedical devices for joint rehabilitation and treatment. This chapter is supported by two publications authored by the candidate as main author[6,7], as well as one co-authored publication related to elastography and tissue assessment[20].

Chapter 3 introduces the conceptual solution proposed in this thesis. It presents the design rationale of the therapeutic approach, describing the principles underlying the combination of mechanical unloading of the knee joint with controlled mechanical or acoustic stimulation. The chapter positions the proposed device concept within a broader personalized medicine framework, in which anatomical information, tissue properties, computational modelling, and device design are integrated to support patient-specific stimulation.

Chapter 4 focuses on the characterization stage of the research. It presents the experimental characterization of relevant materials and biological tissue analogues, with particular emphasis on the mechanical and acoustic properties required to inform numerical models, phantom development, and device design. These properties include density, speed of sound, attenuation, acoustic impedance, and related parameters relevant to wave propagation. The work described in this chapter supported a main-author publication[21] and the development of a software tool for estimating the acoustic properties of biological tissues from experimental data[22]. This tool was subsequently used in later stages of the investigation.

Chapter 5 addresses the in silico modelling developed in this thesis. Computational models are introduced to simulate acoustic wave propagation in heterogeneous media and to analyse the interaction between mechanical vibrations, acoustic waves, and multiphysical interfaces in biological and engineered materials. The chapter includes reduced-order and finite-difference time-domain approaches, supporting the estimation of transmitted acoustic fields and the evaluation of stimulation conditions

relevant to cartilage-targeted therapy. The work presented in this chapter resulted in one main-author publication[23], an additional article currently under review, and the development of a software tool for simulating planar acoustic wave propagation through multilayer media using the finite-difference time-domain method[24], that was awarded the ICOVP and WMC 2025 best paper award.

Chapter 6 describes the development and validation of medical phantoms designed to reproduce selected mechanical and acoustic characteristics of biological tissues. These phantoms provide controlled and repeatable experimental platforms for studying wave propagation, validating acoustic field predictions, and evaluating stimulation mechanisms under laboratory conditions. The chapter also addresses the role of tissue-mimicking materials in bridging computational modelling and device validation. The work described in this chapter is associated with two main-author publications[25,26], an accepted publication, and two co-authored publications related to shear-wave elastography and hydrophone-based acoustic measurements[27,28]. In addition, this stage included the development of software tools for tissue-mimicking phantom design and acoustic property characterization[22], as well as for the post-processing of tensile test data and determination of the Cauchy stress tensor[29].

Chapter 7 presents the development of the device prototype and the proposed unified workflow for personalized therapeutic stimulation. The chapter details the design, fabrication, and integration of the orthotic system, including its role in positioning the stimulation source relative to the knee joint. It also describes the tests performed to evaluate the mechanical behaviour of the prototype and its potential to deliver controlled mechanical or ultrasonic stimulation. Finally, the chapter consolidates the methodological contributions of the thesis into an integrated development strategy that combines imaging, tissue characterization, computational simulation, phantom validation, and patient-specific device generation.

## 1.6 Bibliography

[1]W. H. Organization, *WHO Model List of Essential Medicines - 23rd list*, World Health Organization, (2023) https://www.who.int/publications/i/item/WHO-MHP-HPS-EML-2023.02 (visited on 01/14/2026).

[2]W. H. Organization, "58ª ASAMBLEA MUNDIAL DE LA SALUD", in (May 25, 2005).

[3]J. D. Steinmetz and et al., "Global, regional, and national burden of osteoarthritis, 1990–2020 and projections to 2050: a systematic analysis for the Global Burden of Disease Study 2021", Lancet Rheumatol. **5**, e508–e522 (2023) 10.1016/S2665-9913(23)00163-7.

[4]World Health Organization, *Osteoarthritis*, (2023) https://www.who.int/news-room/fact-sheets/detail/osteoarthritis (visited on 05/29/2026).

[5]M. Langworthy, V. Dasa, and A. I. Spitzer, "Knee osteoarthritis: disease burden, available treatments, and emerging options", Ther. Adv. Musculoskelet. Dis. **16**, 1759720X241273009 (2024) 10.1177/1759720X241273009.

[6]N. A. T. C. Fernandes, A. Arieira, B. Hinckel, F. S. Silva, Ó. Carvalho, and A. Leal, "Unlocking the Secrets of Knee Joint Unloading: A Systematic Review and Biomechanical Study of the Invasive and Non-Invasive Methods and Their Influence on Knee Joint Loading", Rheumato **5**, 8 (2025) 10.3390/rheumato5030008.

[7]N. Fernandes, F. S. Silva, Ó. Carvalho, and A. Leal, "Effect of lower limb orthoses on cartilage in patients with knee osteoarthritis: A narrative review", **47** (2022).

[8]S. Oliveira, R. Andrade, F. Silva, J. Espregueira-Mendes, B. Hinckel, A. Leal, and Ó. Carvalho, "Effects and mechanotransduction pathways of therapeutic ultrasound on healthy and osteoarthritic chondrocytes: a systematic review of in vitro studies", Osteoarthritis Cartilage **31**, 317–339 (2023) 10.1016/j.joca.2022.07.014.

[9]J. Zhou, E. Ning, L. Lu, H. Zhang, X. Yang, and Y. Hao, "Effectiveness of low-intensity pulsed ultrasound on osteoarthritis: molecular mechanism and tissue engineering", Front. Med. **11**, 1292473 (2024) 10.3389/fmed.2024.1292473.

[10]S. Dupont, L. Morsut, M. Aragona, E. Enzo, S. Giulitti, M. Cordenonsi, F. Zanconato, J. Le Digabel, M. Forcato, S. Bicciato, N. Elvassore, and S. Piccolo, "Role of YAP/TAZ in mechanotransduction", Nature **474**, 179–183 (2011) 10.1038/nature10137.

[11]M. Guan, X. Zhang, X. Li, B. Liao, W. Han, J. Tan, Z. Wang, L. Wang, J. Shen, X. Han, and D. Bai, "Research Progress of Osteoarthritis Treatment by Low Intensity Pulsed Ultrasound", Smart Med. **4**, e70003 (2025) 10.1002/smmd.70003.

[12]R. McCarthy, L. Jeffcott, and R. McCartney, "Ultrasound speed in equine cortical bone: Effects of orientation, density, porosity and temperature", J. Biomech. **23**, 1139–1143 (1990) 10.1016/0021-9290(90)90006-O.

[13]K. Nightingale, "Acoustic Radiation Force Impulse (ARFI) Imaging: A Review", Curr. Med. Imaging Rev. **7**, 328–339 (2011) 10.2174/157340511798038657.

[14]C. McCarthy and G. Camci-Unal, "Low Intensity Pulsed Ultrasound for Bone Tissue Engineering", Micromachines **12**, 1488 (2021) 10.3390/mi12121488.

[15]B. E. Treeby and B. T. Cox, "K-Wave: MATLAB toolbox for the simulation and reconstruction of photoacoustic wave fields", J. Biomed. Opt. **15**, 021314 (2010) 10.1117/1.3360308.

[16]B. E. Treeby, E. Z. Zhang, A. S. Thomas, and B. T. Cox, "Measurement of the Ultrasound Attenuation and Dispersion in Whole Human Blood and its Components From 0–70 MHz", Ultrasound Med. Biol. **37**, 289–300 (2011) 10.1016/j.ultrasmedbio.2010.10.020.

[17]M. K. Sigona, T. J. Manuel, M. A. Phipps, K. B. Boroujeni, R. L. Treuting, T. Womelsdorf, and C. F. Caskey, "Generating Patient-Specific Acoustic Simulations for Transcranial Focused Ultrasound Procedures Based on Optical Tracking Information", IEEE Open J. Ultrason. Ferroelectr. Freq. Control **3**, 146–156 (2023) 10.1109/OJUFFC.2023.3318560.

[18]N. Richards, D. Christensen, J. Hillyard, M. Kline, S. Johnson, H. Odéen, and A. Payne, "Evaluation of acoustic-thermal simulations of in vivo magnetic resonance guided focused ultrasound ablative therapy", Int. J. Hyperthermia **41**, 2301489 (2024) 10.1080/02656736.2023.2301489.

[19]O. A. Sapozhnikov, S. A. Tsysar, V. A. Khokhlova, and W. Kreider, "Acoustic holography as a metrological tool for characterizing medical ultrasound sources and fields", J. Acoust. Soc. Am. **138**, 1515–1532 (2015) 10.1121/1.4928396.

[20]A. Z. Santos, S. Rocha, B. Carneiro, N. A. Fernandes, J. Padrão, and Ó. Carvalho, "Current state of elastography research in multiple anatomical structures and respective phantoms", Phys. Med. **138**, 105192 (2025) 10.1016/j.ejmp.2025.105192.

[21]N. A. T. C. Fernandes, S. Sharma, A. Arieira, B. Hinckel, F. Silva, A. Leal, and Ó. Carvalho, "Experimental Validation of Time-Explicit Ultrasound Propagation Models with Sound Diffusivity or Viscous Attenuation in Biological Tissues Using COMSOL Multiphysics", Bioengineering **12**, 946 (2025) 10.3390/bioengineering12090946.

[22]N. A. T. C. Fernandes, *Nnunofernandes/Ultrasound-Wave-Material-Characterization: First Release*, version 1.0.1, Zenodo, May 21, 2026, 10.5281/ZENODO.20334339.

[23]N. A. T. C. Fernandes, A. Arieira, B. Hinckel, F. Silva, A. Leal, and Ó. Carvalho, "A Python FDTD Method Algorithm for 1D Planar Acoustic Wave Propagation: Simulating High-Frequency Ultrasound in the Brain and Beyond", in *Proceedings of ICOVP and WMVC 2025*, Vol. 197, edited by Z. Dimitrovová, P. Biswas, and T. A. N. Silva (Springer Nature Switzerland, Cham, 2026), pp. 391–401, 10.1007/978-3-032-13225-3_39.

[24]N. A. T. C. Fernandes, *Nnunofernandes/1D-FDTD-Multilayer-Acoustic-Wave-Planar-Propagation: 1.0.1*, version 1.0.1, Zenodo, May 29, 2026, 10.5281/ZENODO.20445080.

[25]N. A. T. C. Fernandes, D. I. Alves, D. P. Ferreira, M. Monteiro, A. Arieira, F. Silva, B. Hinckel, A. Leal, and Ó. Carvalho, "Sustainable Tunable Anisotropic Ultrasound Medical Phantoms for Skin, Skeletal Muscle, and Other Fibrous Biological Tissues Using Natural Fibers and a Bio-Elastomeric Matrix", J. Compos. Sci. **9**, 370 (2025) 10.3390/jcs9070370.

[26]N. A. T. C. Fernandes, D. I. Alves, D. P. Ferreira, A. Arieira, F. Silva, B. Hinckel, A. Leal, and Ó. Carvalho, "MICRO AND MACROMECHANICAL MODELLING AND SIMULATION OF BIO ELASTOMERIC COMPOSITES REINFORCED WITH NATURAL FIBRES FOR CRANIAL SKIN ULTRASOUND MEDICAL PHANTOMS", (2025) 10.13140/RG.2.2.17942.05440.

[27]A. Z. Santos, S. Rocha, N. A. T. C. Fernandes, D. I. Alves, D. P. Ferreira, S. M. Costa, J. Padrão, and Ó. Carvalho, "Sustainable Shear Wave Elastography Medical Phantoms: Waste-Based Fibrous Structures for Medical Applications", Textiles **6**, 6 (2026) 10.3390/textiles6010006.

[28]A. Pereira, V. Cardoso, M. Martins, and N. A. T. C. Fernandes, "Development of a hydrophone for measuring the propagation of acoustic waves in biological tissues", in *Proceedings of ICOVP & WMVC 2025. ICOVP & WMVC 2025*, Lecture Notes in Mechanical Engineering (Springer, Cham, 2025), 10.1007/978-3-032-11549-2_63.

[29]N. A. T. C. Fernandes, *Nnunofernandes/Cauchy-Stress-Tensile-Test-Post-Processing: First Release*, version 1.0.0, Zenodo, May 24, 2026, 10.5281/ZENODO.20369750.

# Chapter 2

# State of the Art

All the necessary concepts from different multidisciplanry fields that are relevant for the present work have been introduced in this chapter. This chapter is supported by two first-author publications by the candidate[1,2], together with a collaborative publication addressing elastography-based tissue assessment[3].

## 2.1 The Human Knee

The human knee is a complex synovial joint that plays a central role in load transmission, mobility, and stability of the lower limb. Structurally, it is primarily composed of the articulations between the femur, tibia, and patella, stabilized by a network of ligaments, menisci, and surrounding musculature. Functionally, the knee operates as a modified hinge joint, permitting flexion–extension while accommodating limited rotational and translational motions. This apparent simplicity conceals a highly intricate biomechanical system in which forces several times greater than body weight are routinely transmitted during daily activities such as walking, stair climbing, and jumping. The distribution of these loads is mediated by the menisci and the articular cartilage, which together ensure efficient stress dissipation and joint congruency.

During this section, the functional roles of the knee, its main anatomical constituents, and their contribution to joint stability and load distribution will be described. In addition to its structural and functional characterization, particular attention will be given to the changes that occur in the knee joint under pathological conditions, specifically osteoarthritis.

### 2.1.1 Knee Function and Anatomy

The knee joint is the largest synovial joint in the human body, shaping the mechanical interface between the femur, tibia, and patella. It consists of two primary articulations: the tibiofemoral joint, responsible for load-bearing, and the patellofemoral joint, which enhances the efficiency of the extensor mechanism. Functionally, the knee behaves as a modified hinge joint, allowing flexion–extension with superimposed rotational and translational degrees of freedom, enabling complex movements such as gait and squatting. Beyond mobility, its primary roles include withstanding body weight, maintaining postural stability, and transmitting loads between the upper and lower limb segments[4], as can be seen in figure 1. During daily activities, the joint is subjected to substantial mechanical demands, requiring an integrated response from its osseous, cartilaginous, and soft tissue structures.

At the macroscale, the knee is composed of bones, articular cartilage, menisci, ligaments, and tendons, each contributing to its mechanical function (figure 2). The menisci play a central role in load

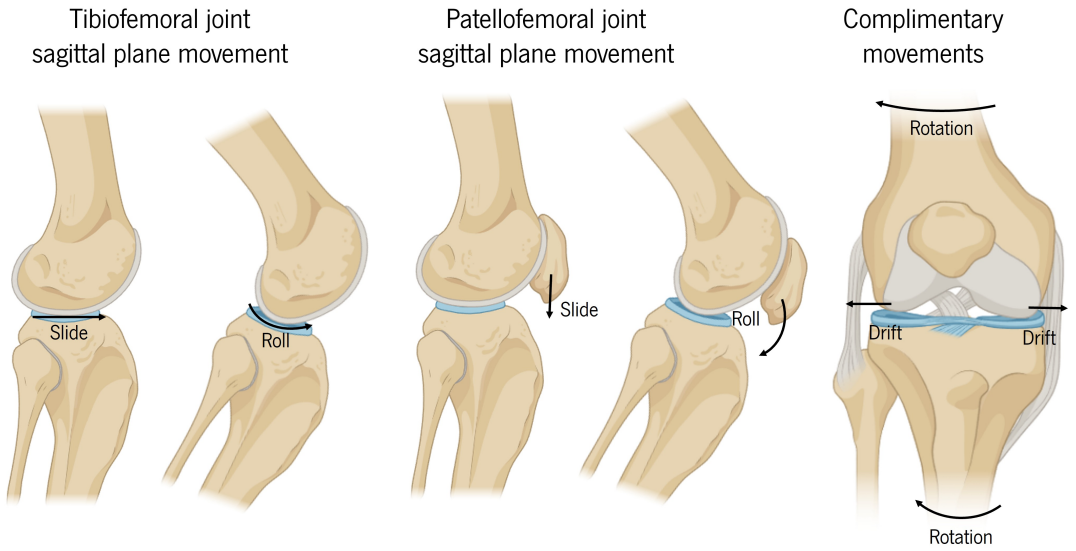



Figure 1: Biomechanical movements allowed by the knee join.

distribution, shock absorption, and joint stabilization. Their wedge-shaped geometry increases joint congruency, allowing efficient transmission of compressive forces while reducing peak contact stresses on the cartilage[5]. Quantitatively, the menisci can transmit a significant portion of the applied load (often exceeding $50\%$), redistributing stresses and protecting the underlying cartilage from degeneration[6]. Additionally, their circumferential collagen architecture enables the development of localized stresses, which convert axial loads into tensile forces along the meniscal structure, further enhancing load-bearing capacity[7]. Beyond load transmission, the menisci also contribute to joint lubrication, proprioception, and secondary stabilization, particularly in controlling anteroposterior and rotational motions[8].

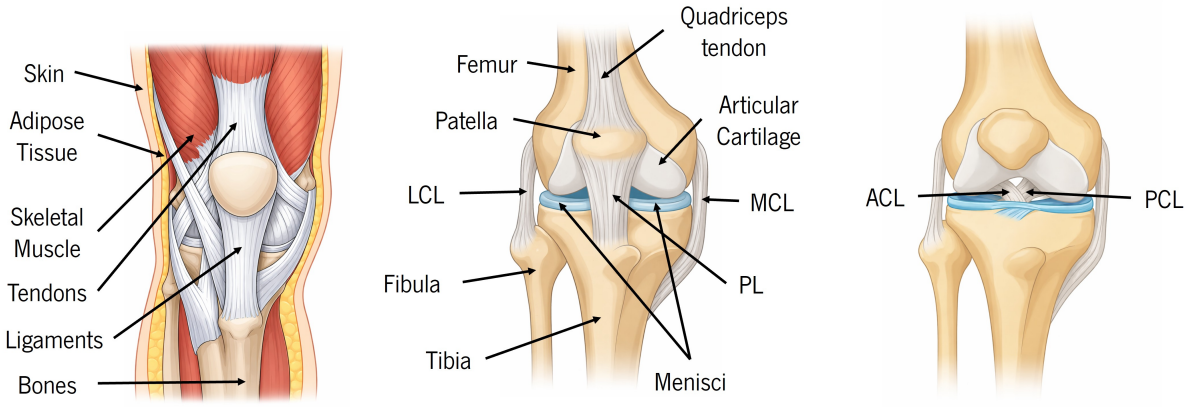



Figure 2: Relevant anatomic structures of the knee for the present work.

Joint stability is primarily governed by the ligamentous system, which constrains excessive motion and ensures coordinated kinematics. The anterior cruciate ligament (ACL) and posterior cruciate ligament (PCL) regulate anterior–posterior translation of the tibia relative to the femur, while the medial collateral ligament (MCL) and lateral collateral ligament (LCL) provide resistance to valgus and varus stresses,

respectively[9]. These ligaments act as passive load-bearing elements that become engaged under specific loading conditions, redistributing forces and maintaining joint alignment. Importantly, their mechanical response is coupled with the surrounding structures; for example, alterations in meniscal integrity can increase ligament loading, highlighting the interdependence of joint components[10]. In parallel, smaller ligamentous structures, such as the meniscofemoral ligaments, contribute to fine-tuning joint stability and controlling meniscal motion[11].

The tendinous structures surrounding the knee, particularly the quadriceps tendon and the patellar tendon, shape the extensor mechanism, which is essential for force transmission during movement. The quadriceps muscle group generates force that is transmitted through the patella and patellar tendon to extend the knee, effectively converting muscular contraction into joint motion while increasing mechanical leverage[12]. This mechanism not only enables locomotion but also plays a critical role in absorbing and redistributing loads during dynamic activities. Collectively, the coordinated interaction between bones, cartilage, menisci, ligaments, and tendons establishes the knee as a highly optimized biomechanical system, capable of sustaining large and repetitive loads while preserving joint integrity.

From a purely mechanical perspective, the knee does not simply withstand body weight in a static sense, it amplifies and redistributes it through internal forces generated by muscles, ligaments, and joint geometry. Under static conditions such as quiet standing, the load transmitted through the knee joint is approximately equal to body weight, typically ranging between 0.8 and 1.5 times body weight depending on posture and weight distribution[13]. At a global scale, human body weight exhibits significant variability, however, the average adult human body mass is commonly reported in the range of approximately 60–70 kg. When disaggregated by sex, adult males typically average around 70 kg, while females average closer to 60 kg, reflecting differences in body composition and height[14].

Even in static equilibrium, internal forces arising from muscle co-contraction and ligament tension contribute significantly to joint contact forces. Indeed, biomechanical analyses indicate that ligament and muscle forces together can account for a substantial portion of the total joint load, with ligaments alone contributing up to a comparable order of magnitude relative to external loading in certain conditions[15]. Consequently, any increase in body mass translates almost directly into increased joint loading, establishing body weight as a primary determinant of long-term mechanical stress on the knee.

However, the true mechanical challenge of the knee emerges under dynamic conditions, where loads are no longer static but oscillatory, transient, and often nonlinear. During walking, peak knee joint forces typically reach approximately 2–3 times body weight, arising from the combined effects of ground reaction forces and muscle activation during the stance phase[16]. As activity intensity increases, these

loads rise significantly: stair negotiation and jogging can elevate forces to around 3–4 times body weight, while running may induce peak loads exceeding 5–8 times body weight depending on speed and biomechanics[13,17]. These dynamic loads are not continuous but cyclic, with thousands of loading cycles occurring daily, introducing a fatigue-like mechanical environment at the tissue level. Importantly, the temporal characteristics of loading, such as rate, frequency, and repetition—become as critical as magnitude, influencing cartilage mechanobiology and potentially driving either adaptive remodelling or degenerative processes. Thus, the knee operates not merely as a passive load-bearing structure, but as a dynamic system constantly balancing between stability, mobility, and mechanical resilience under fluctuating physiological demands.

### 2.1.2 Skin Function and Microstructure

The skin is the largest organ of the human body, accounting for approximately $8–20\%$ of total body mass and shaping the primary interface between the organism and its external environment. Its functions are multifaceted, encompassing mechanical protection, thermoregulation, sensory perception, immune defense, and maintenance of fluid balance. At a fundamental level, the skin acts as a physical, chemical, and biological barrier, preventing the ingress of pathogens, shielding underlying tissues from mechanical damage and ultraviolet radiation, and regulating water loss[18]. In parallel, it serves as a sensory organ through an extensive network of mechanoreceptors, thermoreceptors, and nociceptors distributed across its layers, enabling the detection of external stimuli and contributing to protective reflexes and environmental interaction[19].

From a structural perspective, the skin exhibits a hierarchical organization composed of three layers: the epidermis, dermis, and hypodermis, each with distinct composition and function (figure 3). The epidermis, the outermost layer, is a stratified squamous epithelium primarily composed of keratinocytes that undergo continuous renewal, creating a waterproof and mechanically resilient barrier[18]. Beneath it, the dermis provides the bulk of the skin's mechanical strength and elasticity, consisting of a dense connective tissue matrix rich in collagen (predominantly type I) and elastin fibers, along with blood vessels, lymphatics, and nerve endings[20]. The hypodermis, composed mainly of adipose and loose connective tissue, acts as a cushioning layer, contributing to impact absorption and energy dissipation while anchoring the skin to underlying structures[19,20]. This multilayered architecture enables the skin to exhibit complex mechanical behavior, combining stiffness, extensibility, and viscoelasticity across scales.

A defining feature of skin mechanics is its anisotropic behavior, largely governed by the orientation of collagen fibers within the dermis. This anisotropy is macroscopically described by Langer's lines, which

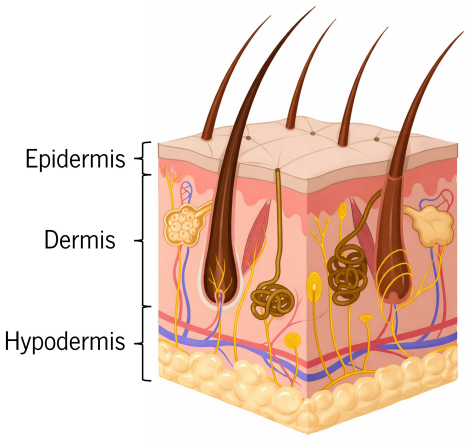



Figure 3: The three main skin layers and its components.

represent the natural directions of tension in the skin and correspond to the preferential alignment of dermal collagen bundles[21,22]. These lines reflect the intrinsic mechanical architecture of the tissue and have direct implications for deformation, stress distribution, and failure behavior. Experimental studies have demonstrated that the mechanical properties of skin are strongly dependent on loading direction relative to Langer's lines, confirming their structural basis in collagen organization[23]. From a mechanical standpoint, this means that skin does not respond uniformly to loading, but instead exhibits direction-dependent stiffness and extensibility, a characteristic that must be considered when analyzing wave propagation, mechanical stimulation, or device–tissue interaction.

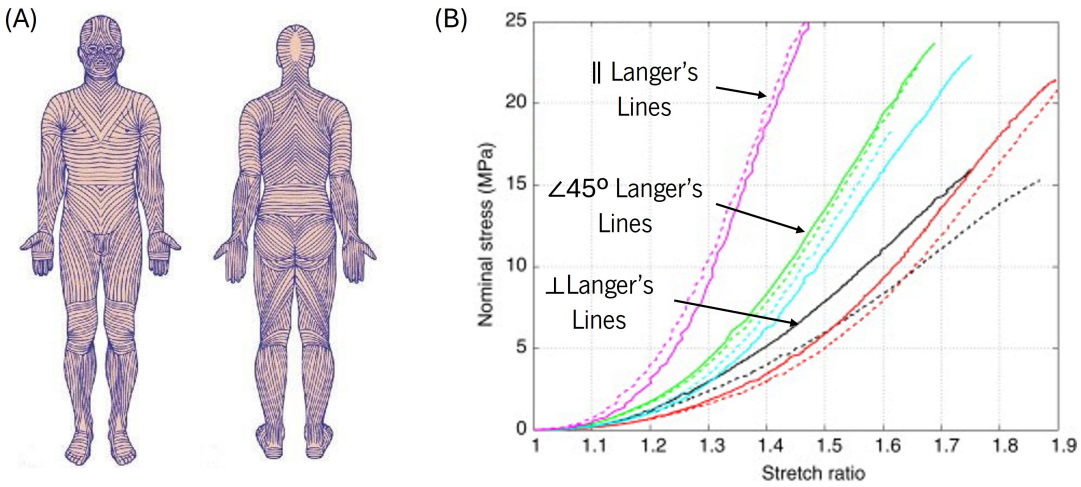



Figure 4: Exemplification of Langer's lines with (A) demonstrating how it's typically spread in the body and (B) demonstrating how the Stress-Strain relation changes in accordance to Langer's lines, adapted from[23].

This structure–function relationship is particularly relevant in the context of external stimulation, where mechanical or acoustic inputs must propagate through a layered, anisotropic, and viscoelastic medium before reaching deeper tissues. Understanding this complex interface is therefore essential for accurately modelling energy transmission and for designing effective non-invasive therapeutic strategies.

### 2.1.3 Adipose Tissue Function and Microstructure

Adipose tissue is a specialized loose connective tissue that serves essential roles in energy storage, mechanical protection, and systemic metabolic regulation. It is primarily composed of adipocytes, withstood by a heterogeneous stromal vascular fraction that includes fibroblasts, endothelial cells, immune cells, and progenitor cells. Beyond its role as a lipid reservoir, adipose tissue is also an active endocrine organ, secreting adipokines and cytokines that regulate energy homeostasis, inflammation, and insulin sensitivity. From a mechanical standpoint, adipose tissue also functions as a shock-absorbing and cushioning layer, protecting underlying structures by redistributing applied loads. This dual metabolic–mechanical role imposes specific structural requirements, linking its composition directly to both physiological and biomechanical performance[24].

At the microstructural level, adipose tissue exhibits a highly organized architecture characterized by clusters of adipocytes embedded within a three-dimensional extracellular matrix (ECM). Each adipocyte is dominated by a broad lipid droplet that occupies most of the cell volume, necessitating structural withstand to prevent mechanical disruption. This support is provided by a base membrane rich in type IV collagen that encapsulates individual adipocytes, creating a protective mechanical interface between the intracellular lipid core and the surrounding environment[24,25]. At the tissue scale, adipocytes are arranged in lobular structures interconnected by a collagen fiber network, which contributes to both mechanical stability and load distribution. The ECM itself is composed of multiple components, including collagens (types I, III, and IV), fibronectin, and laminin, which together create a compliant yet structured environment that regulates cell adhesion, signalling, and mechanical integrity[26].

Functionally, the extracellular matrix plays a central role in modulating adipose tissue behavior, both mechanically and biologically. It acts as a scaffold that distributes stresses across the tissue, reducing localized deformation at the cellular level while enabling large macroscopic strains. At the same time, the ECM is dynamically remodelled during tissue expansion, allowing for adipocyte hypertrophy and hyperplasia while maintaining structural coherence[24,25]. Both adipocytes and adipose-derived stem cells are mechanosensitive, responding to changes in ECM stiffness and mechanical loading through alterations in gene expression, differentiation pathways, and metabolic activity[28,29]. This responsiveness indicates that adipose tissue is not merely a passive mechanical buffer but an active participant in mechanotransduction processes, capable of adapting its structure and function in response to physical stimuli.

In the context of external mechanical or acoustic stimulation, adipose tissue acts as an intermediate propagation medium, influencing attenuation, dispersion, and spatial distribution of energy before it

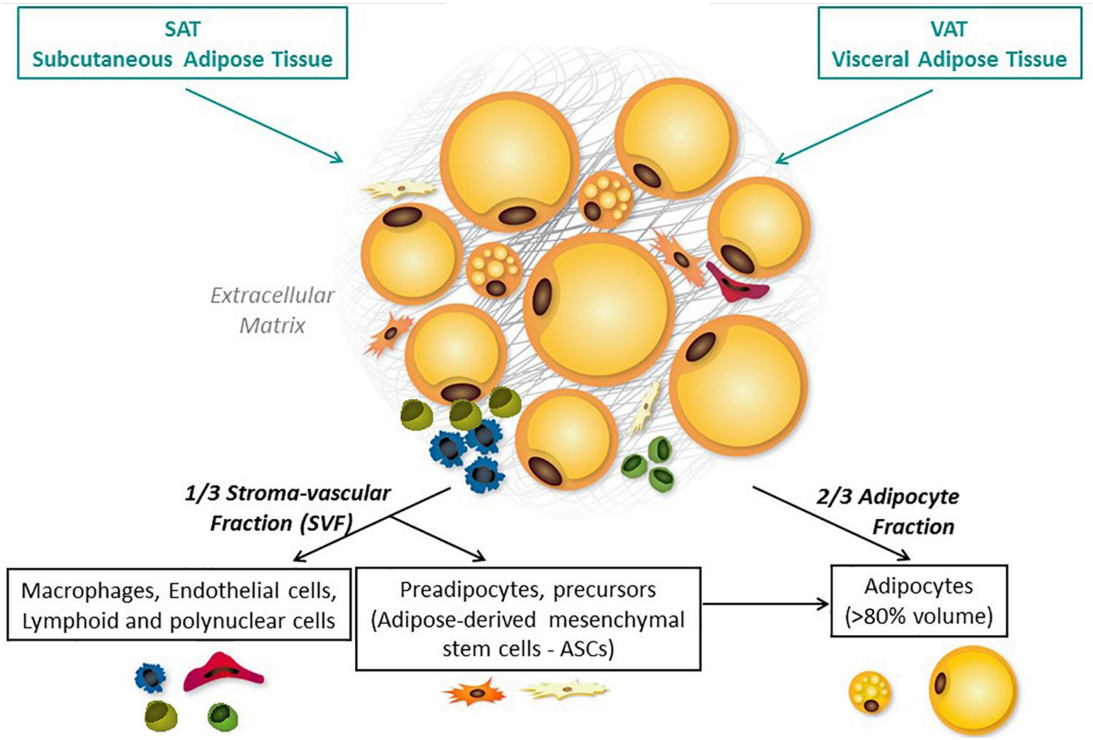



Figure 5: Adipose tissue microstructure, adapted from[27].

reaches deeper tissues.

### 2.1.4 Muscle-Tendon Unit Function and Microstructure

The muscle–tendon unit (MTU) is a highly integrated biomechanical system responsible for force generation, transmission, and movement control. At a fundamental level, skeletal muscle actively generates force through actin–myosin cross-bridge cycling, while tendons passively transmit this force to the skeleton, enabling joint motion and contributing to locomotor efficiency[30,31]. This division of roles, however, is not purely sequential but synergistic: tendons act as elastic energy storage elements, absorbing and releasing mechanical energy during cyclic activities such as walking and running, thereby improving mechanical efficiency and reducing metabolic cost[31]. Additionally, the MTU plays a critical role in shock absorption, force modulation, and proprioception, with specialized structures such as the Golgi tendon organ sensing tension and contributing to neuromuscular control[30]. Thus, the MTU operates as a dynamic system where active and passive components continuously interact to regulate force, stability, and movement.

From a macroscale structural perspective, the MTU is composed of muscle fibers organized into fascicles, surrounded by connective tissue layers (endomysium, perimysium, and epimysium), which merge into the tendon—a dense regular connective tissue that connects muscle to bone. This hierarchical organization enables efficient force transmission not only longitudinally, along the primary

axis of contraction, but also laterally through the extracellular matrix, distributing loads across the tissue and enhancing mechanical robustness (figure 6).

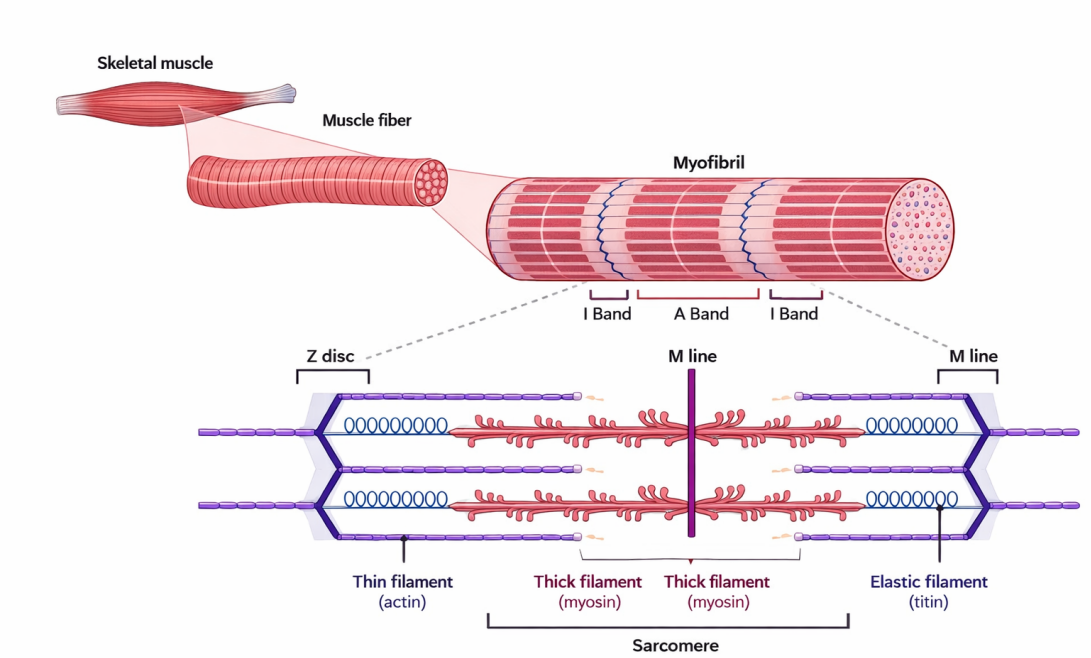



Figure 6: Hierarchical schematic of skeletal muscle organization, illustrating the transition from whole muscle to fiber, myofibril, and the sarcomere, highlighting the arrangement of actin, myosin, and titin filaments.

The transition between muscle and tendon occurs at the muscle–tendon junction, a specialized interface where intracellular contractile forces are transmitted to the extracellular collagen network via protein complexes such as integrins and the dystrophin associated complex. This interface is characterized by a highly folded geometry, increasing surface area and reducing stress concentrations, thereby ensuring efficient and safe force transfer between tissues of markedly different mechanical properties[32], as can be observed in figure 7.

Tendons, in contrast, are dominated by a highly organized extracellular matrix composed primarily of type I collagen fibers arranged in parallel along the direction of loading[33]. This alignment confers exceptional tensile strength and stiffness in the longitudinal direction, while maintaining lower stiffness transversely, reinforcing their anisotropic nature. The collagen fibrils themselves exhibit a hierarchical structure with characteristic crimp patterns that contribute to the nonlinear stress–strain response observed in tendons[34]. This crimped configuration allows initial deformation at low strains, followed by progressive fiber recruitment and stiffening under higher loads, enabling both flexibility and strength. Furthermore, the continuity and alignment of collagen fibers are critical for efficient load transfer, as they ensure that forces generated in the muscle are transmitted with minimal dissipation to the skeletal system.

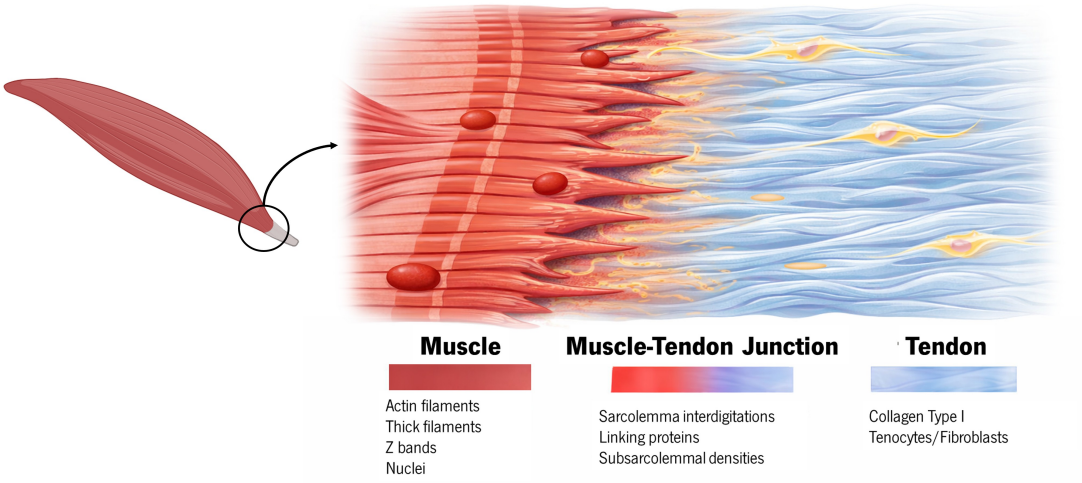



Figure 7: Representation of the muscle–tendon interface illustrating the gradual structural and functional transition from contractile muscle fibers to collagen-rich tendon.

The MTU can be understood as a fiber-reinforced, anisotropic composite system in which structure and function are tightly coupled across scales. The directional organization of muscle fibers and tendon collagen not only governs mechanical behavior but also influences how mechanical and acoustic waves propagate through the tissue. This anisotropy, combined with the complex hierarchical architecture and the presence of specialized interfaces play a decisive role in modulating stress distribution, energy transmission, and mechanobiological responses, making the MTU a critical component in both physiological function and therapeutic stimulation contexts.

### 2.1.5 Ligaments Function and Microstructure

Ligaments are dense fibrous connective tissues that connect bone to bone and play a fundamental role in joint stability, motion guidance, and load distribution. Their primary function is to constrain excessive or non-physiological joint motion while permitting controlled kinematics within a safe range. Rather than acting as rigid restraints, ligaments behave as passive load-bearing elements that progressively engage under increasing deformation, contributing to joint stiffness and redistributing loads across articulating structures. This behavior is intrinsically linked to their viscoelastic nature, enabling time-dependent responses such as creep, stress relaxation, and energy dissipation, which are essential for damping mechanical loads during repetitive or dynamic activities[35]. In addition, ligaments are mechanosensitive tissues that adapt structurally to mechanical stimuli, modifying their composition and organization in response to changes in loading conditions, thereby maintaining joint homeostasis over time[36].

At the microstructural level, ligaments exhibit a hierarchical organization typical of load-bearing

collagen tissues. Their extracellular matrix is dominated by type I collagen, which serves as the principal structural component responsible for tensile strength and force transmission[37]. This collagen is organized across multiple length scales, from tropocollagen molecules to fibrils, fibers, and fascicles, creating a continuous fibrous network embedded within a proteoglycan matrix[38], as can be observed in figure 8. Such hierarchical structuring enables efficient transfer of mechanical loads from the macroscopic to the microscopic scale while preserving structural integrity. In addition to collagen, ligaments contain elastin and other matrix components that contribute to elasticity, resilience, and recovery following deformation. Importantly, the cellular component plays a regulatory role in maintaining and remodelling this matrix, although the bulk mechanical behavior is largely governed by the extracellular architecture[39].

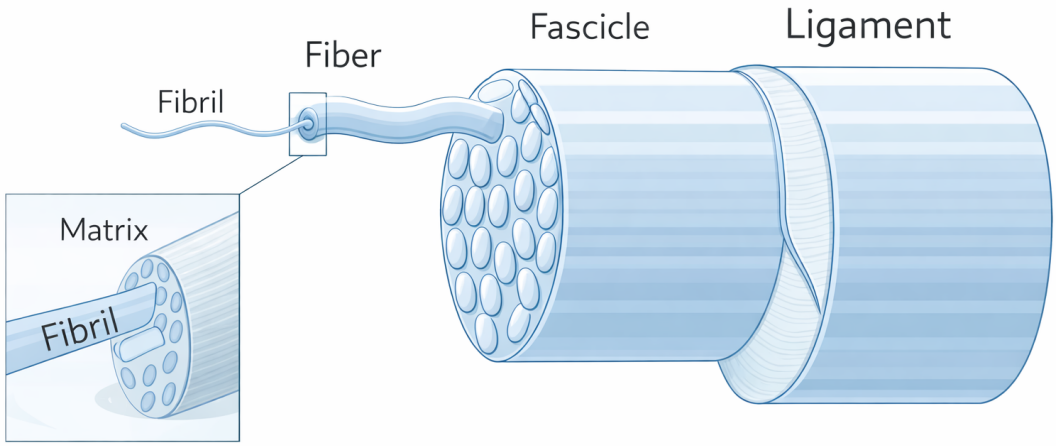



Figure 8: Hierarchical organization of ligament tissue, illustrating the transition from the macroscopic structure to its fibrillar and matrix components.

A defining feature of ligament mechanics is their pronounced anisotropy, which arises from the preferential alignment of collagen fibers along the primary loading direction. Experimental and computational studies have demonstrated that collagen fibers in ligaments are strongly oriented in specific directions, resulting in significantly higher stiffness and strength along the fiber axis compared to transverse directions[40]. This anisotropic organization is not uniform throughout the tissue; instead, regional variations in fiber orientation and density produce heterogeneous mechanical responses and localized stress distributions. At smaller scales, collagen fibrils exhibit a crimped configuration, which underlies the characteristic nonlinear stress–strain behavior. During initial loading, the crimp straightens

with minimal resistance, followed by progressive fiber recruitment and increased stiffness as the fibers align with the load direction[35]. This mechanism allows ligaments to combine flexibility at low strains with high strength at higher strains, an essential feature for accommodating physiological motion while preventing injury.

Similarly to the MTU, ligaments can be interpreted as anisotropic, fiber-reinforced composite materials optimized for tensile load transmission and joint stabilization. Their hierarchical collagen architecture, directional fiber alignment, and viscoelastic matrix collectively define their mechanical response across scales. This organization also has important implications for wave propagation and mechanical stimulation, as the directional dependence of stiffness and structural heterogeneity influence how mechanical energy is transmitted and dissipated within the tissue.

### 2.1.6 Bone Function and Microstructure

The bone is a multifunctional biological composite that provides structural support, protects vital organs, and enables movement through its interaction with the musculoskeletal system. Mechanically, bone must simultaneously exhibit high stiffness to sustain loads, sufficient strength to resist fracture, and adequate toughness to dissipate energy under dynamic conditions. These properties are achieved through a hierarchical organization spanning multiple length scales, from nanostructured mineralized collagen fibrils to whole-organ geometry[41,42]. Functionally, bone adapts continuously to mechanical stimuli through remodelling processes governed by osteoblasts and osteoclasts, allowing it to optimize its architecture in response to loading conditions. This adaptive behavior ensures that bone is not a static material, but a dynamic system capable of maintaining mechanical competence under varying physiological demands[41].

At the macroscale, bone is broadly classified into two distinct types: cortical (compact) bone and trabecular (cancellous) bone, each fulfilling complementary mechanical roles (figure 9). Cortical bone shapes the dense shell of long bones and is primarily responsible for structural rigidity and load-bearing capacity. It exhibits relatively low porosity (typically $5–15\%$) and high stiffness, with a Young's modulus on the order of $10–20$ GPa[43]. In contrast, trabecular bone is a porous, lattice-like structure located in the epiphyses of long bones and in vertebral bodies, with porosity often exceeding $70–90\%$. This architecture, composed of interconnected plates and rods (trabeculae), enables efficient load distribution while minimizing mass. Trabecular bone plays a critical role in transferring loads from articular surfaces to cortical bone and is frequently the primary load-bearing structure in regions such as the spine[41]. Mechanically, it is less stiff but more deformable and energy-absorbing than cortical bone, contributing to

shock attenuation and structural resilience[44].

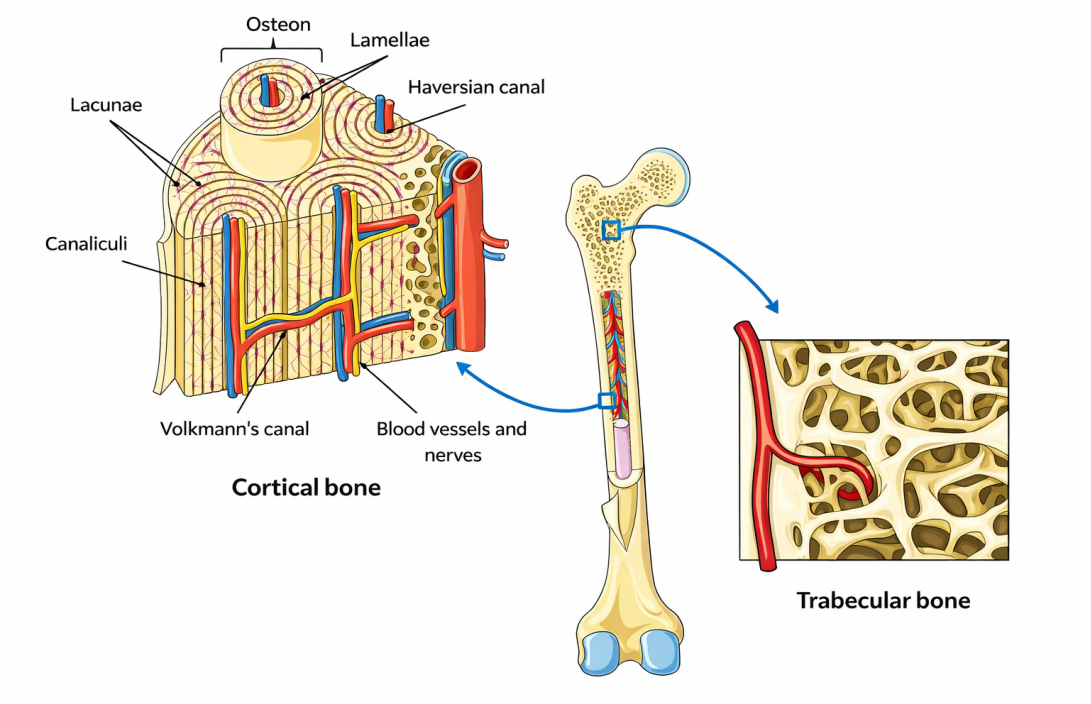



Figure 9: Bone hierarchical organization, illustrating the microstructural features of cortical bone alongside the porous architecture of trabecular bone and its spatial distribution within a long bone.

At the microstructural level, both cortical and trabecular bone share a common fundamental building block: the mineralized collagen fibril. These fibrils consist of type I collagen reinforced by hydroxyapatite nanocrystals, creating a composite material in which the organic phase provides toughness and the mineral phase provides stiffness and strength[42]. These fibrils are organized into lamellae, which in cortical bone are arranged into osteons—cylindrical structures aligned along the primary loading direction—while in trabecular bone they shape the internal struts and plates of the lattice[45]. This hierarchical arrangement, observed in figure 10 enables efficient load transfer across scales and contributes to the remarkable combination of mechanical properties observed in bone. Importantly, the orientation of both collagen fibers and mineral crystals is not random but highly organized, reflecting the mechanical environment experienced by the tissue.

A defining characteristic of bone is its pronounced anisotropy, meaning that its mechanical properties depend strongly on the direction of loading. In cortical bone, stiffness and strength are significantly higher along the longitudinal axis of the bone compared to transverse directions, a consequence of the preferential alignment of collagen fibers and mineral crystals along the primary loading direction[46]. Similarly, trabecular bone exhibits anisotropy at the architectural level: the orientation and connectivity of trabeculae are aligned with principal stress trajectories, resulting in direction-dependent mechanical behavior. This anisotropy can be quantitatively described using

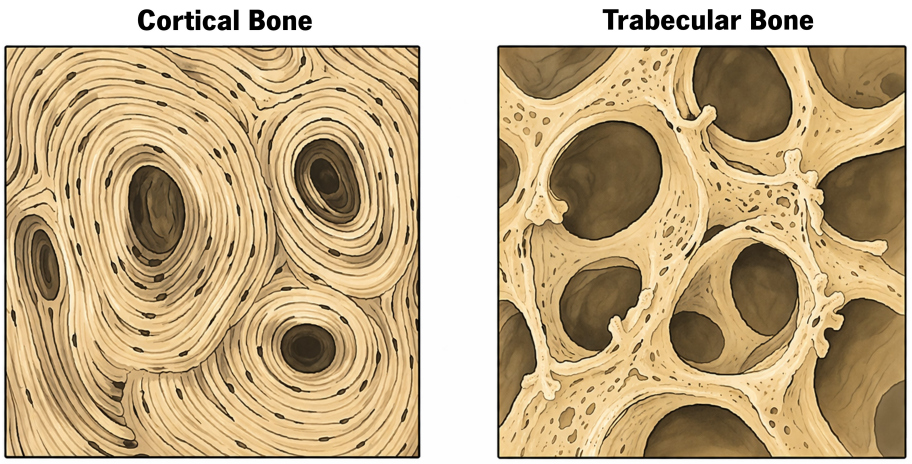



Figure 10: Comparison of bone microstructures illustrating the dense, concentric organization of cortical bone alongside the porous, interconnected architecture of trabecular bone.

orthotropic or transversely isotropic models, reflecting the presence of preferred structural directions within the tissue[47]. Experimental studies further show that the degree of anisotropy is often greater in trabecular bone than in cortical bone, due to its highly heterogeneous and directional architecture[48].

This interplay between cortical rigidity and trabecular adaptability allows the skeleton to efficiently manage complex loading scenarios, from static weight support to dynamic impacts. Moreover, the directional organization of its microstructure plays a critical role in governing not only mechanical performance but also the propagation of mechanical and acoustic waves through the tissue.

### 2.1.7 Articular Cartilage Function and microstructure

Articular cartilage is a highly specialized connective tissue that covers the articulating surfaces of synovial joints, where it performs the dual function of load transmission and frictionless motion. Its primary mechanical role is to distribute compressive loads while minimizing stress concentrations on the underlying subchondral bone, thereby protecting the joint during repetitive activities such as walking and running[49,50]. In addition, cartilage exhibits remarkable tribological properties, with an extremely low coefficient of friction, enabling smooth articulation over millions of loading cycles. From a biological perspective, cartilage is an avascular, aneural, and alymphatic tissue, meaning it lacks blood vessels, nerves, and lymphatic drainage. This absence of vascularization severely limits its regenerative capacity, as nutrient transport occurs primarily through diffusion and fluid flow within the matrix[49]. Consequently, cartilage operates in a delicate balance between mechanical function and limited biological repair, making it particularly vulnerable to degeneration under altered loading conditions.

At the microstructural level, cartilage is a biphasic (or more precisely, poro-viscoelastic) material composed of a solid extracellular matrix and an interstitial fluid phase. The solid matrix consists mainly

of type II collagen fibers and proteoglycans, particularly aggrecan, which are highly negatively charged and attract water molecules[49]. This results in a tissue that is typically composed of up to $70–80\%$ water, a feature that is central to its mechanical behavior. Under compressive loading, fluid pressurization within the matrix withstand a significant portion of the applied load, while the collagen network constrains deformation and provides tensile integrity[51]. Structurally, cartilage is organized into distinct zones (superficial, middle, deep, and calcified), each characterized by different collagen orientations and cellular distributions, leading to depth-dependent mechanical properties[52], as is demonstrated in figure 11. In the superficial zone, collagen fibers are aligned parallel to the joint surface to resist shear stresses, while in deeper zones they are oriented more perpendicularly, enhancing compressive load support.

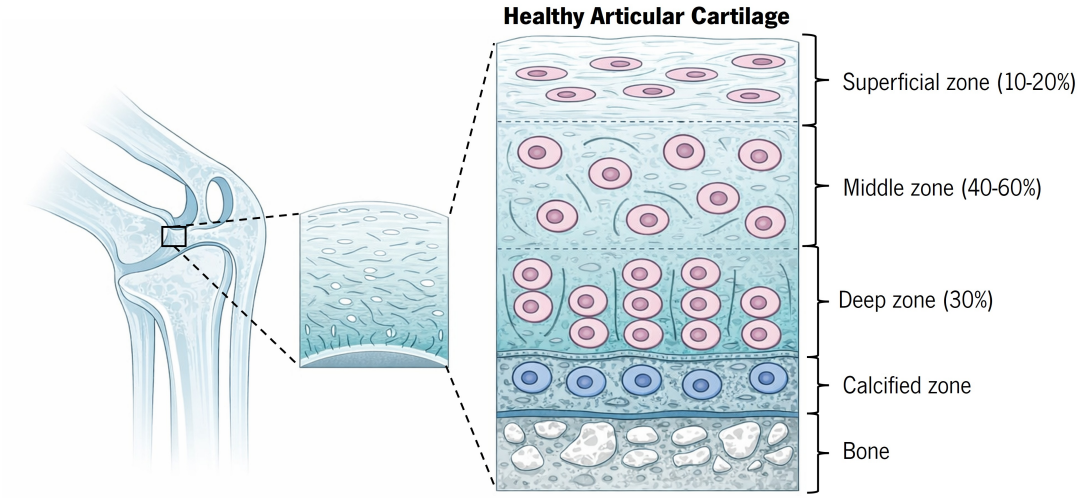



Figure 11: Articular cartilage structure, showing its zonal organization from the superficial layer to the calcified interface and underlying subchondral bone.

Mechanically, the behavior of cartilage is commonly represented using combinations of springs and dashpots, reflecting its viscoelastic nature. Simple models such as the Kelvin–Voigt model describe cartilage as a parallel arrangement of an elastic spring (representing the solid matrix) and a viscous damper (representing fluid flow and internal friction). In reality, cartilage exhibits more complex poroelastic behavior, where time-dependent deformation arises from fluid exudation and redistribution within the porous matrix. For example, under a constant load (creep), cartilage deformation evolves over time as fluid gradually flows out of the tissue, while under constant deformation (stress relaxation), the internal stress decreases as fluid pressure dissipates[52], as can be observed in figure 12.

A defining feature of cartilage is its anisotropy and inhomogeneity, arising from the organized orientation of collagen fibers and the zonal variation in composition. Mechanical properties such as stiffness, permeability, and strength vary with direction and depth, reflecting the alignment of collagen

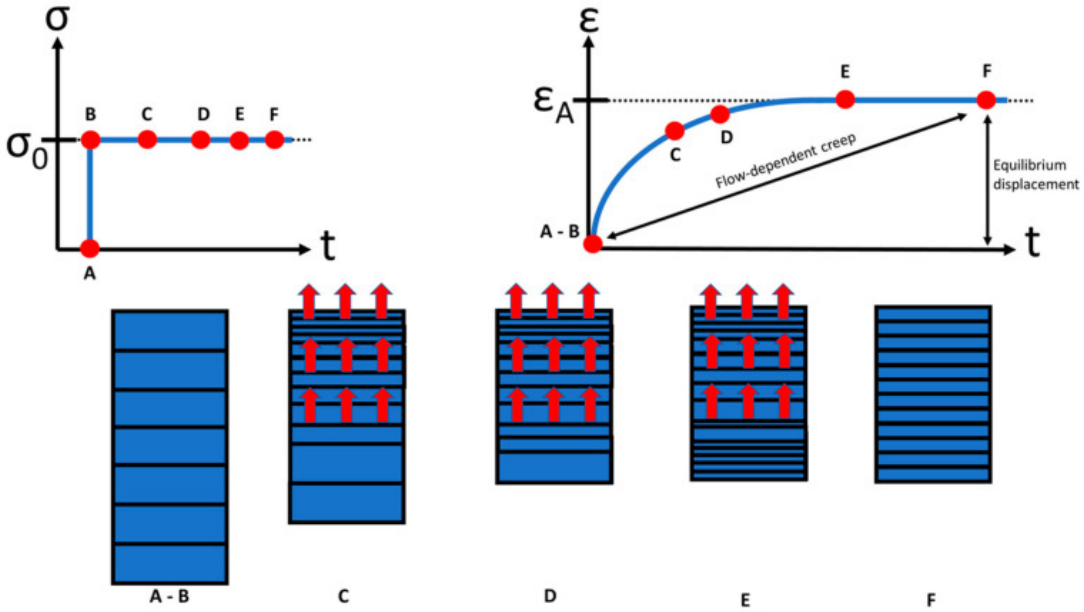



Figure 12: A constant stress $\sigma_0$ applied to a sample of AC (top left); creep response $\varepsilon$ of the sample under the constant applied stress $\sigma$ (top right). The boxes below the loading and creep curves (A to F) illustrate that creep is accompanied by fluid exudation from the tissue. At equilibrium ($t \leftarrow \infty$), fluid flow ceases, and the load is borne entirely by the solid matrix (F)[52].

and the distribution of proteoglycans and water[49]. This anisotropic structure enables cartilage to simultaneously resist compressive, tensile, and shear forces, adapting its response depending on the direction and magnitude of loading. From a structure–function perspective, cartilage can thus be understood as a hydrated, fiber-reinforced composite with strong coupling between its microstructure and mechanical performance. This complex organization not only governs load-bearing and lubrication but also plays a critical role in the propagation and attenuation of mechanical and acoustic waves, making cartilage a key tissue in both joint biomechanics and mechanobiological stimulation contexts.

### 2.1.8 Osteoarthritic Cartilage

In healthy conditions, articular cartilage maintains a finely tuned balance between its extracellular matrix composition and mechanical function, enabling efficient load distribution, low friction, and long-term durability. This homeostasis is primarily governed by the integrity of the collagen network and the high concentration of proteoglycans, which together sustain fluid pressurization and mechanical resilience. However, in OA, this balance is progressively disrupted through a combination of biochemical and mechanical alterations. One of the earliest microstructural changes is the depletion of proteoglycans, which reduces the tissue's ability to retain water and generate osmotic swelling pressure, thereby compromising its ability to resist compressive loads. Concurrently, the collagen network becomes disorganized and degraded, leading to a loss of structural integrity and increased susceptibility to damage (figure 13). These changes are accompanied by chondrocyte dysfunction, including altered

metabolism and increased production of matrix-degrading enzymes, further accelerating tissue breakdown.[53].

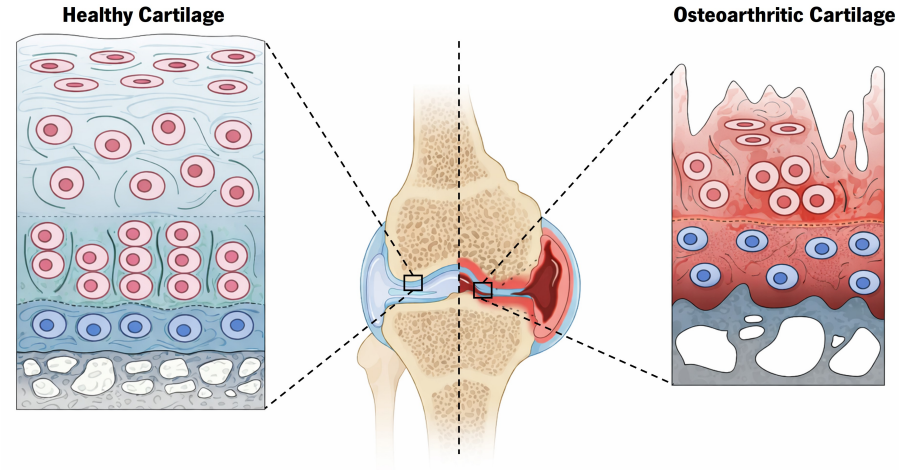



Figure 13: Comparison between healthy and osteoarthritic cartilage, highlighting the transition from organized, stratified tissue to a degraded structure characterized by surface irregularities, altered cellular distribution, and disruption of the cartilage–bone interface.

From a mechanical standpoint, these microstructural alterations translate into a marked deterioration of cartilage performance. Osteoarthritic cartilage exhibits reduced stiffness, diminished load-bearing capacity, and increased permeability, which together impair its ability to sustain fluid pressurization under loading. As a result, the tissue experiences greater deformation and higher friction during articulation, increasing stress on both the cartilage itself and the underlying subchondral bone. This creates a self-reinforcing cycle: as mechanical function degrades, abnormal loading patterns further exacerbate structural damage, promoting the progression of the disease. Additionally, fatigue phenomena such as microcrack formation and propagation become more prominent under cyclic loading, contributing to the gradual loss of cartilage thickness and mechanical competence[54].

A critical factor underlying the limited recovery of cartilage is its avascular, aneural, and alymphatic nature. Unlike most biological tissues, cartilage lacks a direct blood supply, relying instead on diffusion and fluid flow for nutrient transport and waste removal. This severely restricts the ability of the tissue to mount an effective healing response following injury. Consequently, damage to cartilage—whether due to mechanical overload or degenerative processes—tends to accumulate over time rather than being repaired. Even current clinical repair strategies often result in the formation of fibrocartilage, which lacks the mechanical properties of native hyaline cartilage and is prone to further degradation. Moreover, the intrinsic repair process is inherently slow and inefficient due to the absence of vascularization, making complete functional regeneration extremely challenging[55].

From a broader perspective, OA can thus be understood as a failure of the cartilage system to maintain its structure–function relationship under sustained mechanical and biological stress. The transition from

healthy to diseased cartilage is not abrupt but gradual, driven by subtle microstructural changes that progressively compromise mechanical behavior.

## 2.2 Existing treatments for knee osteoarthritis

Knee OA is a progressive, multifactorial joint disease that remains without a definitive therapy, and current treatment strategies are therefore primarily aimed at symptom control, functional improvement, and delay of disease progression. Contemporary management follows a multimodal and hierarchical approach, combining conservative interventions, pharmacological treatments, biophysical stimulation techniques, and, in advanced stages, surgical procedures such as osteotomy or joint replacement. Despite the wide range of available options, a recurring limitation across the literature is that most treatments provide only partial and often temporary relief, with highly variable effectiveness between patients.

A critical challenge in evaluating these treatments lies in the nature of the outcome measures employed. The majority of clinical studies rely on patient-reported outcomes, such as pain and functional scores, rather than direct quantitative assessments of joint structure or mechanics. Consequently, while many interventions demonstrate statistically significant improvements in symptoms, their ability to modify the underlying biological or structural progression of OA remains unclear. This creates a fundamental gap in the field: treatments are regularly validated based on how patients feel, rather than on measurable changes in cartilage, subchondral bone, or joint mechanics.

Within this context, the following sections critically examine the existing treatment landscape for knee OA, emphasizing not only their reported clinical outcomes but also the extent to which they are supported by objective, quantitative evidence across different scales of investigation.

### 2.2.1 Conservative symptomatic treatments

Conservative and symptom-modifying treatments form the foundation of clinical management for knee OA, particularly in early and moderate stages of the disease. These approaches encompass non-surgical strategies such as mechanical unloading, exercise therapy, pharmacological management and lifestyle modification. While widely recommended in clinical guidelines, their effectiveness is primarily evaluated through patient-reported outcomes, such as pain and functional scores, rather than objective structural or biomechanical changes[1,2]. This reliance on relative and subjective metrics introduces significant challenges in assessing their true therapeutic impact.

#### 2.2.1.1 Mechanical Unloading

Mechanical unloading strategies represent one of the most conceptually grounded non-invasive approaches for managing knee OA, aiming to redistribute joint loads and reduce compartment-specific stress. These interventions are based in biomechanical principles, yet their clinical evaluation reveals a striking imbalance between mechanistic rationale and quantitative evidence of effectiveness.

Valgus (medial unloading) and varus (lateral unloading) knee braces are designed to apply corrective external moments to counteract malalignment and redistribute joint loads (figure 14). Biomechanical studies consistently demonstrate that such devices can reduce the knee adduction moment (KAM), a commonly used surrogate for medial compartment loading. Systematic reviews report that most studies ($20$ out of $24$) observe reductions in KAM, with some reporting decreases on the order of $13\%$ during gait[56].

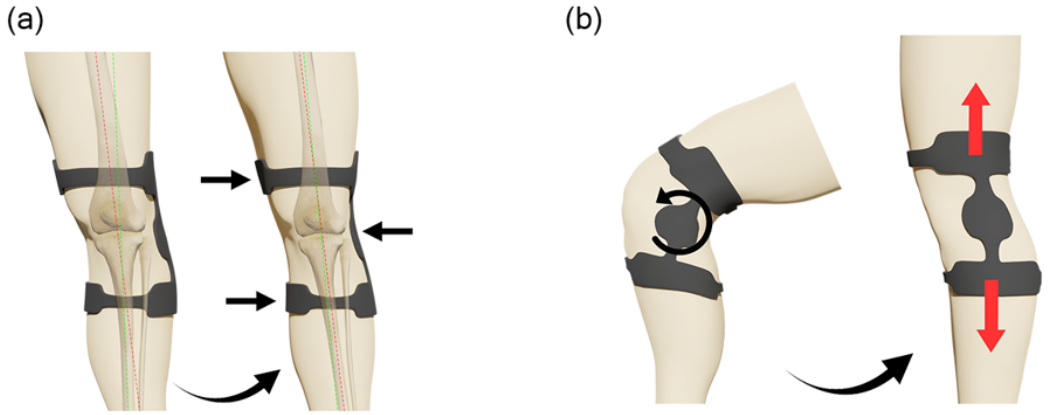



Figure 14: Mechanical unloading strategies using knee orthoses: (a) valgus/varus offloading braces redistribute joint loads by shifting the mechanical axis away from the affected compartment; (b) distraction–rotation braces combine joint separation and controlled rotation to reduce compressive forces and improve joint alignment during movement.

Despite this consistent biomechanical effect, the translation to clinical outcomes is far less robust. Randomized controlled trials (RCTs) indicate modest improvements in patient-reported outcomes. For example, improvements in pain scores of approximately $9\%$ and functional gains of only 4 points on a $100$-point scale have been reported[57]. However, systematic evidence remains inconclusive: meta-analyses suggest that braces may improve walking distance, but show little or no consistent improvement in validated functional scores, with very low certainty regarding pain reduction[58].

More importantly, the overwhelming majority of brace studies rely on Western Ontario and McMaster Universities Arthritis Index (WOMAC), Knee injury and Osteoarthritis Outcome Score (KOOS), or Visual Analogue Scale (VAS) (pain and function), Gait parameters (walking speed, step length), KAM as a surrogate biomechanical metric[2]. As such, Direct structural outcomes are rarely assessed. As highlighted in recent systematic analyses, non-invasive unloading strategies lack quantitative evaluation

of cartilage thickness or joint space width, even though these are the most relevant markers of disease progression[1].

There has only been one study in a post-surgical context that reported where unloading braces have been associated with increases in cartilage repair tissue thickness (0.4 mm vs –0.1 mm at 24 months) following microfracture[59]. However, this evidence is limited, highly specific, and not representative of general OA populations.

A fundamental assumption underlying the use of knee orthotics is that externally applied forces are effectively transmitted through the soft tissues to alter internal joint loading, particularly at the cartilage level. However, despite decades of research on knee OA and orthotic interventions, there is a significant and unresolved gap in the literature regarding how this load transfer actually occurs across the different biological layers of the joint system.

From a mechanical standpoint, knee braces operate through principles such as the three-point pressure system, generating external moments intended to reduce compartmental loading. While this mechanism is well described at a macroscopic level, the pathway through which these forces propagate (from the brace–skin interface, through subcutaneous tissues, muscles, ligaments, and finally to the articular cartilage) remains poorly understood[60].

Even computational efforts, such as finite element models of orthoses, primarily focus on brace efficiency, stiffness, and joint kinematics, rather than resolving the full pathway of stress propagation through biological tissues[61]. Experimental studies, on the other hand, are typically limited to external measurements or simplified cadaver models, which do not capture the complex, dynamic behavior of living tissues[1].

Lateral wedge insoles and foot orthoses are also widely used and aim to modify ground reaction forces and reduce medial compartment loading through alterations in foot alignment (figure 15). Biomechanical studies consistently report immediate reductions in KAM of approximately $5–10\%$ during walking[62].

However, clinical outcomes again show substantial variability. Some RCTs report improvements in pain and function, while others demonstrate no significant effect compared to control conditions, particularly in advanced OA populations[57]. Meta-analytical comparisons indicate that insoles and knee braces produce similar improvements in pain and function, with no statistically significant difference between interventions[63].

Once again, A key limitation lies in the nature of outcome measures. Across studies, the primary endpoints are pain scores (VAS, WOMAC, KOOS), functional tests (chair rise time) and indirect biomechanical measurements KAM. The reported primary outcomes aren't consistent and vary widely

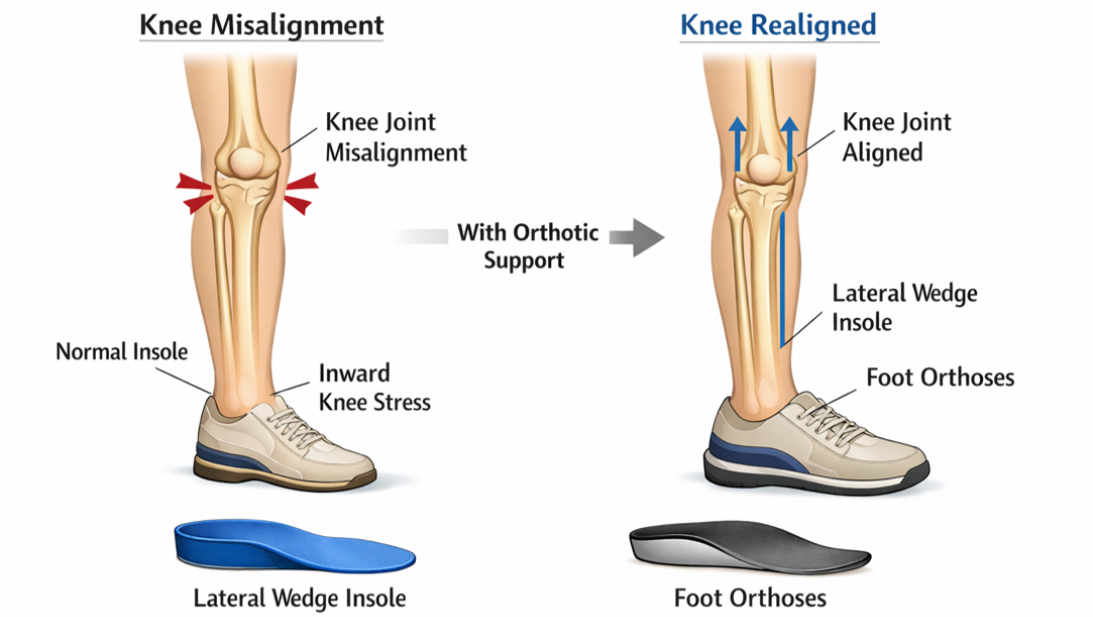



Figure 15: Lateral wedge insoles and foot orthoses alter plantar pressure to realign the lower limb, reducing medial knee loading. By inducing a valgus moment and stabilizing foot mechanics, they redistribute forces across the knee and improve gait biomechanics.

across studies, with a mix of subjective clinical scores and indirect biomechanical metrics, further complicating interpretation. Longitudinal studies suggest that the biomechanical effects of insoles may not persist over time, and there is little evidence demonstrating sustained structural benefit[64]. As with bracing, direct measurements of cartilage morphology are largely absent.

Assistive devices such as canes aim to reduce joint loading by redistributing body weight during gait, typically through contralateral use (figure 16).

While biomechanical principles suggest a reduction in joint forces, the available clinical evidence is comparatively sparse. Systematic reviews indicate that cane use probably reduces pain and may slightly improve function, but the certainty of evidence is low, and the number of high-quality studies is limited. Importantly, most studies focus exclusively on pain reduction and functional improvement rather than direct quantification of joint loading or structural changes[58].

Unlike braces and insoles, even surrogate biomechanical metrics such as KAM are rarely reported in cane studies[58]. This further exacerbates the lack of quantitative understanding of their effectiveness.

All the described strategies remain essential in conservative OA management due to their safety, accessibility, and biomechanical rationale. However, the current body of evidence reveals a lack of standardized, objective, and quantitative metrics capable of linking mechanical intervention to structural outcomes.

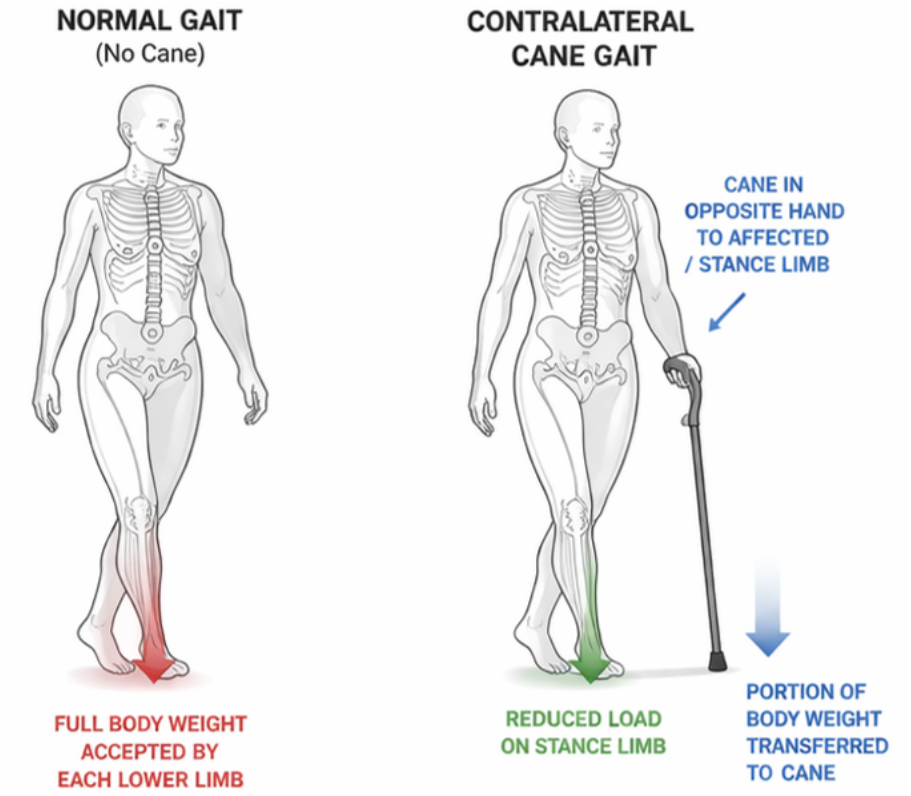



Figure 16: Contralateral cane use redistributes body weight during gait, transferring part of the load to the upper limb and reducing joint loading on the affected stance leg.

#### 2.2.1.2 Physical therapy and loading modulation

Physical therapy and loading modulation strategies are among the most widely prescribed non-invasive interventions for knee OA, encompassing muscle strengthening, neuromuscular training, and controlled mechanical stimulation. These approaches are based on the premise that modifying muscular support, joint kinematics, and dynamic loading patterns can reduce symptoms and potentially influence disease progression. However, a critical analysis of recent scientific literature reveals that their effectiveness is predominantly evaluated through patient-reported outcomes, with a persistent lack of direct quantitative evidence linking these interventions to structural or mechanistic changes within the joint.

Strengthening interventions, particularly targeting the quadriceps, represent the most extensively studied component of physical therapy in knee OA. RCTs consistently demonstrate improvements in pain and function following structured strengthening programs. For example, a home-based quadriceps strengthening program resulted in a $22.5\%$ reduction in WOMAC pain scores and a $17.4\%$ improvement in physical function, compared to minimal changes in control groups[65]. Similarly, multiple recent trials and meta-analyses confirm that quadriceps strengthening produces significant reductions in pain and improvements in functional outcomes, typically assessed using WOMAC or VAS scales[66]. These findings are further supported by reported increases in muscle strength of approximately $26\%$ alongside improved

self-reported pain and function[67].

Despite these consistent clinical improvements, the relationship between increased muscle strength and joint mechanics remains unclear. A two-centre randomized controlled trial demonstrated that while quadriceps strengthening significantly improved symptomatic and functional outcomes, it did not alter knee joint biomechanics during walking, including joint loading patterns[68]. Similarly, other studies report that improvements in pain and function occur independently of measurable changes in muscle strength or joint loading, suggesting that the mechanisms underlying symptom relief are not directly linked to mechanical changes[69]. These findings highlight a critical disconnect: strengthening interventions improve what patients feel, but not necessarily what the joint experiences mechanically.

This disconnect becomes even more evident in long-term and high-intensity training studies. A large randomized clinical trial involving $377$ participants found that high-intensity strength training did not produce significant improvements in knee pain or joint compressive forces compared to low-intensity training or control interventions over $18$ months[70]. This study included one of the few attempts to incorporate a quantitative structural parameter (joint space width) yet reported no significant differences between groups, indicating that even prolonged mechanical loading interventions may not translate into measurable structural changes.

Neuromuscular training, which focuses on improving joint stability, proprioception, and movement patterns, follows a similar trend. Studies comparing different exercise modalities (weight-bearing versus non-weight-bearing training) consistently show similar improvements in pain and function across interventions, without clear superiority of one approach over another[71]. These outcomes are again predominantly assessed using subjective measures, with limited incorporation of objective biomechanical or structural endpoints. While neuromuscular training is hypothesized to reduce aberrant loading and improve joint alignment, direct quantification of these effects at the cartilage level is largely absent.

Controlled mechanical stimulation, including structured loading protocols and resistance-based exercise, further illustrates the limitations of current evaluation frameworks. Although such interventions are designed to modulate joint loading in a controlled manner, their effectiveness is typically inferred from improvements in pain, range of motion, and functional scores. Even when biomechanical variables are included, they are generally limited to indirect measures such as joint torque, gait parameters, or muscle activation patterns[72,73]. Direct assessment of cartilage response is rarely performed.

The current body of evidence suggests that physical therapy and loading modulation strategies are effective in improving symptoms and functional capacity, but their ability to modify joint structure or

disease progression remains uncertain, once again focusing on patient-reported outcomes. Studies that systematically integrate patient-reported outcomes, biomechanical analysis, and direct structural measurements, the effectiveness of physical therapy in knee OA are need to close this gap. This gap once again accentuates the need for a more comprehensive, multiscale evaluation framework capable of linking external loading strategies to internal tissue response, thereby providing a clearer understanding of how these interventions influence disease progression.

#### 2.2.1.3 Pharmacological approaches

Pharmacological approaches remain a central component of knee OA management, particularly when conservative mechanical and physical interventions fail to provide sufficient symptomatic relief. The most commonly used modalities include non-steroidal anti-inflammatory drugs (NSAIDs), intra-articular corticosteroid injections, and hyaluronic acid (HA) viscosupplementation. While these treatments are widely prescribed and supported by extensive clinical research, their evaluation is overwhelmingly based on patient-reported outcomes rather than direct quantitative measures of joint structure. As a result, a critical limitation emerges: despite large volumes of data, the true physiological effectiveness of these interventions remains difficult to quantify.

NSAIDs are the most frequently used pharmacological agents in knee OA, acting through inhibition of cyclooxygenase enzymes and subsequent reduction of inflammatory mediators. Large-scale meta-analyses demonstrate that NSAIDs provide statistically significant reductions in pain; however, the magnitude of this effect is consistently modest. For instance, pooled analyses report standardized mean differences of approximately $0.23$–$0.32$ for pain reduction compared to placebo[74,75]. These values correspond to small-to-moderate effect sizes, often near or below thresholds of minimal clinically important difference. Indeed, when stricter criteria are applied, no NSAID treatment consistently achieves clinically meaningful improvement[76].

Responder analyses further illustrate the limited magnitude of benefit. Approximately $50$–$60\%$ of patients achieve moderate pain relief (larger than $30\%$ reduction), while only $20$–$30\%$ achieve substantial relief (larger than $70\%$)[77]. This indicates that a significant proportion of patients experience only partial or negligible benefit. Moreover, longitudinal studies highlight that effect sizes may decrease over time, suggesting limited durability of treatment effects[74]. NSAID studies almost exclusively rely on WOMAC, VAS, or similar subjective scales, with virtually no direct assessment of cartilage thickness or joint structure. Even large observational cohorts investigating long-term NSAID use focus primarily on symptom progression rather than structural endpoints[78].

Intra-articular corticosteroid injections represent a more targeted pharmacological approach, aiming to reduce synovial inflammation and provide rapid pain relief. Clinical studies confirm that corticosteroids are effective in the short term, with approximately $73\%$ of patients responding within two weeks. However, this effect is transient: only $29\%$ of patients maintain improvement at six months, indicating a rapid decline in efficacy[79]. This has been further demonstrated as recent articles report that corticosteroids provide superior pain relief in the first $2$–$6$ weeks, but their benefits diminish thereafter[80]. Some longitudinal studies suggest that repeated corticosteroid injections may be associated with increased risk of radiographic OA progression and future joint replacement, raising questions about their long-term safety. Despite these concerns, most clinical trials continue to evaluate corticosteroids using short-term pain relief and functional scores, with minimal incorporation of imaging-based metrics. Thus, even for a treatment directly administered into the joint space, quantitative assessment of cartilage response remains largely absent[79].

HA viscosupplementation is intended to restore the viscoelastic properties of synovial fluid, thereby improving joint lubrication and shock absorption. Clinical trials report reductions in pain and improvements in function, often measured through WOMAC scores. For example, RCTs demonstrate reductions in WOMAC pain of approximately $18$–$23$ mm over six months, indicating moderate symptomatic improvement[81]. Compared to corticosteroids, HA tends to produce slower onset but longer-lasting effects, with benefits extending up to 6 months in some studies[80]. However, as with NSAIDs and corticosteroids, the magnitude and clinical relevance of these improvements remain uncertain. Network meta-analyses indicate that while HA may reach the lowest threshold for clinical significance ($0.20$), it frequently fails to meet more conservative criteria. Furthermore, comparisons with NSAIDs suggest similar overall effectiveness, reinforcing the notion that these treatments operate within a narrow therapeutic range[76].

In contrast, direct quantitative parameters are rarely assessed. Even when imaging is used, it is typically not the primary endpoint, and longitudinal structural changes are rarely reported. This reliance on subjective measures introduces a fundamental limitation. Pain and function scores are influenced not only by physiological changes but also by psychological and contextual factors. Indeed, recent analyses recommend that up to $75\%$ of pain reduction observed in OA trials may be attributable to placebo effects, further complicating interpretation[82]. Additionally, substantial uncertainty in effect size estimates across all pharmacological treatments are reported, even in long-term studies[83].

### 2.2.2 Biophysical Stimulation

Biophysical stimulation represents an emerging class of non-invasive therapeutic strategies that aim to modulate biological processes through the application of physical energy, rather than chemical or structural intervention. These approaches are based on the principle that mechanical or electromagnetic stimuli can directly interact with cellular structures, particularly at the membrane level, triggering intracellular signalling pathways associated with tissue repair, anti-inflammatory responses, and extracellular matrix synthesis. In contrast to conventional conservative treatments, which primarily alter the external mechanical environment of the joint, biophysical stimulation seeks to directly influence chondrocyte activity and joint homeostasis through mechanotransduction mechanisms (further explained in section 2.4).

#### 2.2.2.1 Ultrasound Stimulation

Ultrasound stimulation, particularly in the form of low-intensity pulsed ultrasound (LIPUS), illustrated in figure 17, has gained increasing attention as a non-invasive biophysical strategy for knee OA, due to its ability to deliver mechanical energy at the tissue and cellular levels. The therapeutic rationale is rooted in mechanotransduction: acoustic pressure waves induce micromechanical perturbations at the cell membrane, activating intracellular signalling pathways associated with ECM synthesis, anti-inflammatory responses, and cell survival.

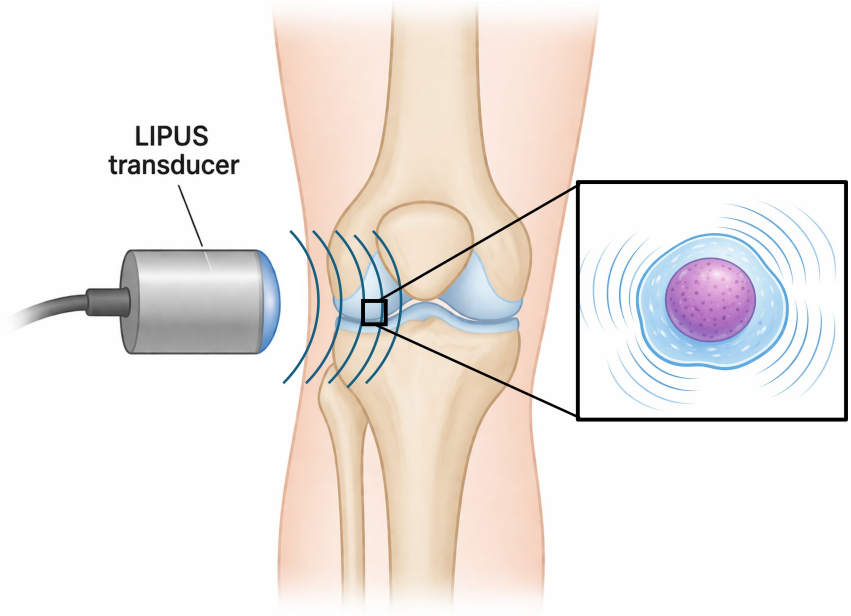



Figure 17: Schematic representation of low-intensity pulsed ultrasound applied to the knee joint, illustrating acoustic wave propagation through the tissue and the resulting vibrational response at the chondrocyte level.

A substantial body of in vitro evidence demonstrates that ultrasound stimulation can directly

influence chondrocyte behavior. Studies using human OA chondrocytes show that LIPUS reduces apoptosis and significantly increases the expression of key cartilage matrix components, including type II collagen and aggrecan, through pathways involving transcription factors such as SOX9[84]. Similarly, experimental work on cartilage explants indicates that ultrasound can stimulate chondrocyte proliferation and matrix production, with increases in cell cluster formation of up to 4.8-fold in certain conditions, suggesting a strong anabolic response at the tissue level[85].

These findings are further supported by molecular studies showing that ultrasound stimulation modulates catabolic and inflammatory pathways, including suppression of MMP-13 expression and enhancement of cartilage-specific gene expression. More recent investigations extend these mechanisms to include autophagy activation, calcium signalling, and mitochondrial regulation, highlighting a complex network of intracellular responses that collectively promote cartilage homeostasis[86].

Beyond isolated cell systems, in vivo preclinical models consistently report chondroprotective effects. Animal studies demonstrate that ultrasound stimulation can reduce cartilage degeneration, decrease apoptosis, and restore anabolic–catabolic balance in osteoarthritic joints[87]. Additional evidence indicates that LIPUS enhances cartilage repair when combined with regenerative strategies, such as mesenchymal stem cell therapies, by promoting exosome release and chondrogenic differentiation[88].

However, when transitioning to clinical studies, a clear shift in evaluation methodology becomes apparent. A substantial portion of clinical research on ultrasound stimulation focuses on patient-reported outcomes, particularly pain and function. RCTs consistently demonstrate improvements in these domains. For instance, focused LIPUS has been shown to produce significant reductions in VAS pain scores and improvements in WOMAC and quality-of-life indices, alongside increased ambulation speed, following short-term treatment protocols[89,90]. Similarly, wearable long-duration ultrasound systems have demonstrated symptomatic relief in placebo-controlled trials, further reinforcing the perception that ultrasound is effective in reducing pain and improving function[91].

In contrast, the use of direct quantitative structural parameters, such as cartilage thickness or joint morphology, remains limited and inconsistent across studies. While preclinical studies demonstrate clear effects on cartilage metabolism and tissue repair mechanisms[92] clinical studies rarely confirm these effects through objective measurements.

A few RCTs have attempted to address this gap using imaging techniques. For example, a randomized placebo-controlled pilot study reported an increase in medial tibial cartilage thickness of approximately $90\ \mu$m ($95\%$ CI: $1$–$200\ \mu$m) in patients receiving LIPUS after multiple treatment sessions[93]. However, other RCTs have reported no significant differences between treatment and control

groups, despite improvements in pain and function[94,95].

A key limitation underlying this discrepancy is the heterogeneity of ultrasound protocols, including variations in frequency, intensity, duty cycle, treatment duration, and delivery method. Recent clinical trials explicitly acknowledge the need to determine optimal dosing and application parameters before definitive conclusions can be drawn[93]. This lack of standardization further complicates the comparison of results across studies and contributes to the variability in reported outcomes.

#### 2.2.2.2 Vibration Therapy

Vibration therapy has emerged as a non-invasive biophysical intervention in knee OA, encompassing whole-body vibration (WBV), localized mechanical stimulation, and protocols defined by frequency-dependent loading regimes. The fundamental premise is that oscillatory mechanical signals can modulate neuromuscular function, joint loading, and potentially cartilage metabolism (figure 18).

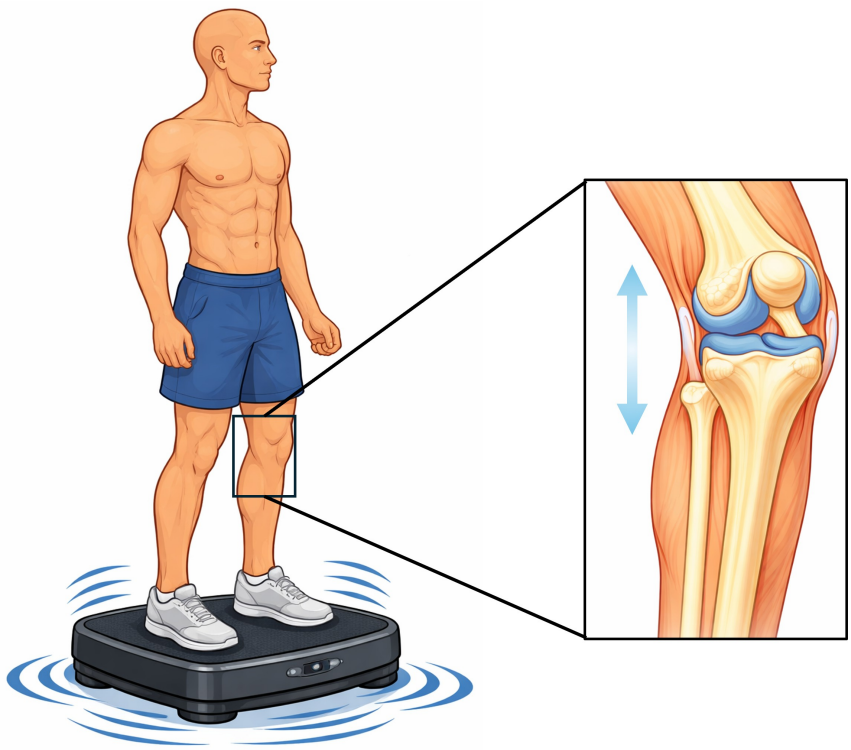


Figure 18: Whole-body vibration involves standing on an oscillating platform that transmits mechanical vibrations through the body, inducing rapid muscle contractions and small cyclic displacements at the joints, including the knee.

At the clinical level, WBV is the most extensively studied modality. Randomized controlled trials and meta-analyses consistently report improvements in pain, functional performance, and muscle strength, particularly when WBV is combined with conventional rehabilitation or strengthening exercises. A recent meta-analysis of randomized trials ($n = 559$ patients) reported moderate effect sizes for pain reduction ($SMD = 0.46$) and functional improvement ($SMD = 0.51$), alongside improvements in Timed Up

and Go performance and quadriceps strength[96]. Similarly, more recent systematic reviews confirm that WBV significantly reduces pain (mean difference −0.43) and improves functional outcomes compared to standard rehabilitation[97]. These findings are reinforced by individual trials demonstrating improvements in proprioception, neuromuscular control, and muscle performance, suggesting that vibration acts primarily through neuromuscular and functional pathways rather than direct joint modification[98].

A limited number of RCTs have attempted to evaluate cartilage response to vibration. In controlled human studies, WBV has been shown to prevent reductions in tibial cartilage thickness during unloading conditions, suggesting sensitivity of cartilage to mechanical vibration stimuli[99]. Animal studies provide more direct insight into structural effects but reveal conflicting results. For example, in murine OA models, low-frequency WBV has been shown to exacerbate cartilage degradation, with only minor effects on subchondral bone[100]. Conversely, other preclinical studies report that vibration can increase cartilage thickness or improve subchondral bone microarchitecture, depending on frequency and loading conditions[101].

These findings highlight a critical feature of vibration therapy, where its effects are highly dependent on frequency, amplitude, and exposure duration. This leads directly to the concept of frequency-dependent effects, which is one of the most important yet unresolved aspects of vibration therapy. As such, experimental studies indicate that low-magnitude, low-frequency vibration may promote anabolic responses and improve tissue adaptation. On the other hand, higher frequencies or inappropriate loading regimes may induce catabolic responses or accelerate degeneration. This dual behavior is consistent across preclinical models and is increasingly recognized in clinical analyses. Even meta-analytical studies note that different frequency protocols produce variable clinical outcomes, contributing to heterogeneity and uncertainty in effectiveness[96,102].

Taken together, while vibration therapy demonstrates consistent improvements in patient-reported outcomes and functional performance, the absence of standardized protocols and uniform direct quantitative evidence of cartilage-level effects prevents a clear determination of whether these interventions merely alleviate symptoms or meaningfully influence the underlying structural progression of osteoarthritis.

#### 2.2.2.3 Electromagnetic fields

Electromagnetic field stimulation, most commonly delivered as Pulsed Electromagnetic Fields (PEMFs), has been investigated as a non-invasive biophysical intervention for knee OA because it can expose the joint to time-varying electromagnetic signals without imposing direct mechanical contact or

pharmacological burden. The rationale is that PEMFs may influence inflammatory activity, chondrocyte metabolism, subchondral bone remodelling, and muscle performance.

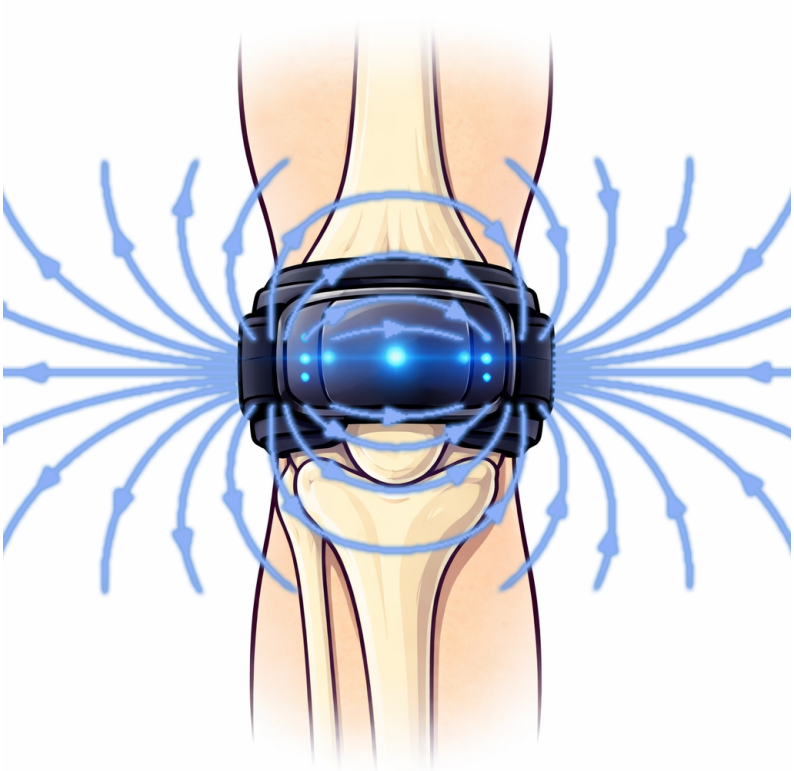


Figure 19: Pulsed electromagnetic field device applied to the knee joint, generating a spatially distributed magnetic field (blue arrows) that penetrates surrounding tissues and may stimulate cellular activity within the joint.

At the clinical scale, most recent studies continue to evaluate PEMFs through pain, symptoms, and function. The dominant endpoints are WOMAC, VAS, KOOS, quality-of-life scores, and performance tests such as chair-rise or gait-related tasks. It was found that in end-stage knee OA PEMF combined with home-based exercise improved pain and knee muscle strength and showed only a "promising tendency" for better performance-based physical function; the principal conclusions were therefore framed around symptoms and muscle performance, not cartilage repair. As such, PEMF as a conservative adjunct capable of improving pain and strength, which reflects how the modality is usually clinically interpreted[103,104]. However, it has also been demonstrated in RCTs that 8 weeks of PEMF significantly improved knee extensor strength at 6 months, but it did not significantly improve cartilage thickness, minimum joint space width, lower-limb physical function, or knee-specific patient-reported outcomes up to 12 months[103,105].

At the tissue and organ scale, direct quantitative evidence is scarcer in humans but widely reported in animal models. It has been reported that PEMF exposure has been associated with reduced cartilage fibrillation, improved cartilage histology, mitigation of subchondral bone abnormalities, and preservation of cartilage integrity, with frequency-dependent responses reported in some models. Preclinical findings

demonstrated decreased joint inflammation and cartilage degradation where osteoarthritic guinea pig and rat where exposed to PEMF, which alleviated cartilage fibrillation, reduced subchondral bone changes, or preserved cartilage integrity. PEMF has also been reported to improve cartilage metabolic homeostasis and reduced OA pathology in a destabilization model, including better histological appearance and reduced proteoglycan loss. These outcomes are more direct than clinical pain scores because they evaluate the tissue itself. However, they remain largely preclinical, and therefore they validate biological plausibility more than they validate real-world clinical effectiveness in human knee OA[106,107].

At the cellular and molecular scale, the evidence is even more favorable to PEMFs. PEMF-induced modulation of inflammatory signalling, oxidative stress, apoptosis, and matrix metabolism in has been reported in cartilage-related systems. PEMFs may suppress inflammatory cascades, reduce catabolic activity, and support anabolic or homeostatic cartilage responses. The proposed targets include NF-κB-related inflammatory signalling, apoptosis pathways, and chondrocyte metabolic regulation. This explains why PEMFs continue to attract attention despite equivocal structural clinical data: in vitro and molecular studies provide a coherent mechanistic story in which electromagnetic stimulation can influence the biology of cartilage degeneration. Yet the translational bridge remains incomplete. A strong signal at the molecular level does not guarantee that clinically practical treatment regimens will generate measurable improvements in cartilage thickness or joint-space preservation in patients[103,106,108].

Unfortunately, studies are irregular in terms of signal characteristics, including frequency, waveform, intensity, exposure duration, total treatment period, and anatomical target. Optimal treatment regimens remain undefined and dose–response relationships are still insufficiently characterized. This heterogeneity makes it difficult to compare studies directly and contributes to the recurrent pattern in which some studies report pain reduction while others show limited or no structural benefit. Even if PEMFs do have a biologically meaningful therapeutic window, the field has not yet converged on a standard protocol capable of consistently producing clinically and structurally relevant outcomes[105,107].

#### 2.2.2.4 Shockwave Therapy

Extracorporeal shockwave therapy (ESWT - figure 20) has emerged as a non-invasive biophysical intervention for knee OA, delivered either as focused shockwaves (f-ESWT) or radial shockwaves (r-ESWT). These modalities differ in their physical characteristics: focused waves concentrate energy at a specific depth, enabling interaction with subchondral bone and cartilage interfaces, whereas radial waves disperse energy more superficially. Both approaches are hypothesized to induce mechanotransductive responses, including stimulation of tissue remodelling, modulation of inflammation, and promotion of angiogenesis.

However, given that articular cartilage is avascular, the relevance of angiogenic stimulation should be confined to surrounding tissues such as subchondral bone and synovium, rather than cartilage itself.



Figure 20: Extracorporeal shockwave therapy applied to the knee, where externally generated acoustic pulses are transmitted through soft tissues to target the joint and surrounding structures.

Clinically, the overwhelming majority of studies evaluate ESWT using patient-reported outcomes and functional metrics. It is reported that ESWT leads to significant reductions in pain and improvements in function, typically assessed using WOMAC, VAS, or similar scales in the short term (less than 12 weeks), with relatively low complication rates[109], and may outperform some conventional therapies under specific conditions[110]. Comparative studies between f-ESWT and r-ESWT also show consistent symptomatic benefits. Both modalities significantly reduce pain and improve functional performance, with some evidence suggesting that focused ESWT produces greater reductions in VAS pain ($-4.5$ vs. $-2.6$ points) and superior improvements in functional tests such as the 6-minute walk test[111]. However, similar to other conservative interventions, these measures do not directly quantify internal joint mechanics or cartilage loading. Even when biomechanical parameters are included, they typically reflect global functional performance rather than localized cartilage stress or contact forces.

At the tissue and structural scale, the evidence becomes significantly more limited. Only a small subset of studies attempts to evaluate objective changes beyond symptoms. Some clinical investigations report reductions in supra patellar effusion or inflammatory markers following ESWT, recommending a measurable effect on joint environment. However, direct structural parameters such as cartilage thickness, joint space width, or cartilage composition are rarely assessed in human studies. This represents a major limitation, particularly given that ESWT is often proposed as a therapy capable of promoting tissue remodelling[112]. Animal studies consistently report that ESWT can reduce cartilage degradation, improve histological cartilage structure and slow OA progression. These effects are regularly attributed to enhanced subchondral bone remodelling, increased vascularization, and modulation of inflammatory pathways. Nonetheless, these findings remain largely confined to controlled experimental settings and have not been robustly translated into clinical studies with direct structural endpoints[113].

In vitro and preclinical studies suggest that shockwaves can stimulate angiogenesis, osteogenesis, and tissue remodelling, particularly in bone and tendon tissues. However, the application of these mechanisms to cartilage is inherently complex due to its avascular nature. While subchondral bone and synovial tissues may respond to angiogenic stimuli, the direct impact on chondrocytes and cartilage matrix remains less clearly defined, and is typically inferred rather than directly measured[110].

Until future studies integrate direct structural measurements with clinical and mechanistic outcomes, shockwave therapy will remain a promising yet quantitatively underdefined intervention in knee osteoarthritis.

### 2.2.3 Surgical Structural Interventions

Surgical structural interventions represent the most invasive stage in the treatment spectrum of knee OA, typically reserved for patients in whom conservative and pharmacological strategies fail to provide adequate symptom relief or functional restoration. These approaches aim to directly modify or replace the structural components of the joint, either by correcting underlying biomechanical abnormalities, attempting tissue repair, or substituting the joint entirely[114,115]. In contrast to non-invasive therapies, which act by modulating the external or biological environment of the joint, surgical interventions seek to redefine the mechanical architecture of the system itself, restoring alignment, redistributing loads, or replacing degenerated surfaces with engineered components.

#### 2.2.3.1 Microfracture

Microfracture is one of the most widely used surgical techniques for the treatment of focal cartilage defects in the knee and is frequently considered a first-line marrow stimulation procedure. The technique involves perforating the subchondral bone to induce bleeding and release mesenchymal stem cells, which subsequently form a repair tissue within the defect (figure 21).

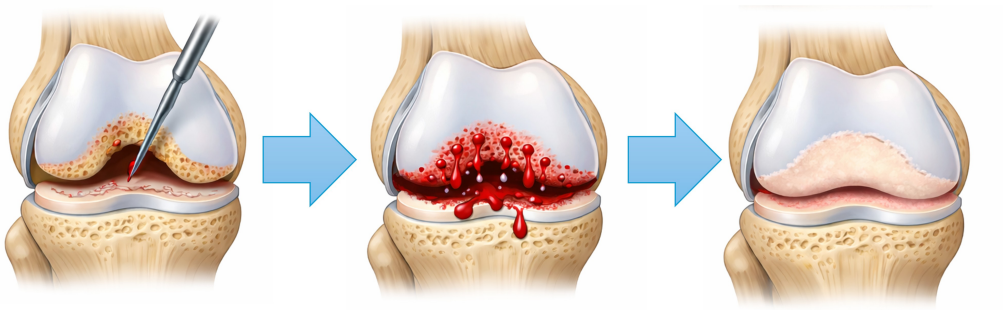


Figure 21: Microfracture technique in knee cartilage repair: perforation of the subchondral bone induces bleeding and release of mesenchymal stem cells, forming a reparative fibrocartilaginous tissue within the defect.

Although the conceptual goal is cartilage regeneration, the resulting tissue is predominantly fibrocartilage, which differs mechanically and structurally from native hyaline cartilage and is generally considered less durable[116].

It has been observed in RCTs that microfracture has been consistently associated with improvements in symptoms and function, particularly in the short to mid-term. Numerous studies report significant gains in patient-reported outcomes such as KOOS, WOMAC, and VAS scores following the procedure. Patients undergoing microfracture show significant improvements in pain and function scores over several years, comparable to other cartilage repair techniques in small defects[117]. However, long-term evidence challenges the durability of these improvements. A large registry-based study with a 10-year follow-up found that microfracture showed no significant association with improved patient-reported outcomes compared to no surgical treatment, indicating that initial symptomatic benefits may not persist over time[118]. Similarly, longitudinal analyses show that clinical scores often peak within the first year and gradually decline, returning toward baseline levels over longer follow-up periods[119].

At the tissue and structural scale, microfracture has been evaluated using imaging modalities such as MRI, particularly through scoring systems. These studies provide some of the most direct quantitative insights into cartilage repair. Early postoperative imaging frequently demonstrates partial defect filling, with approximately $70\%$ of cases showing more than $50\%$ filling at around 2 years, suggesting an initial reparative response. However, this structural improvement does not necessarily persist. Long-term imaging studies reveal progressive degeneration, deterioration of repair tissue, and radiographic progression of osteoarthritis, typically beginning within 5 years postoperatively[119]. 2hile alternative techniques may show significant increases in cartilage thickness (1 mm over several years), microfracture regularly demonstrates no statistically significant change in cartilage thickness over time, despite improvements in patient-reported outcomes[117].

Emerging evidence proposes that microfracture may not prevent, and may even be associated with, progression toward osteoarthritis, particularly in larger defects. Recent analyses report high rates of OA progression and poor long-term healing in medium-to-large defects, raising concerns about the long-term efficacy of the procedure. This further reinforces the notion that microfracture may function primarily as a symptom-modifying intervention rather than a disease-modifying strategy[120].

The current evidence suggests that while microfracture can stimulate a repair response and improve patient-reported outcomes, it does not reliably produce durable, quantitatively measurable restoration of cartilage structure. As such, it remains a widely used but structurally limited intervention, highlighting the need for approaches capable of bridging the gap between symptom relief and true tissue regeneration.

#### 2.2.3.2 Osteotomy

High tibial osteotomy (HTO), is a joint-preserving surgical procedure aimed at redistributing load across the knee by correcting malalignment, most commonly shifting load from the medial to the lateral compartment in varus knees. Unlike pharmacological or purely symptomatic interventions, osteotomy directly targets the mechanical axis of the limb, thereby modifying the boundary conditions under which cartilage degeneration occurs. From a conceptual standpoint, it represents one of the clearest examples of a mechanics-driven intervention in osteoarthritis (figure 22).

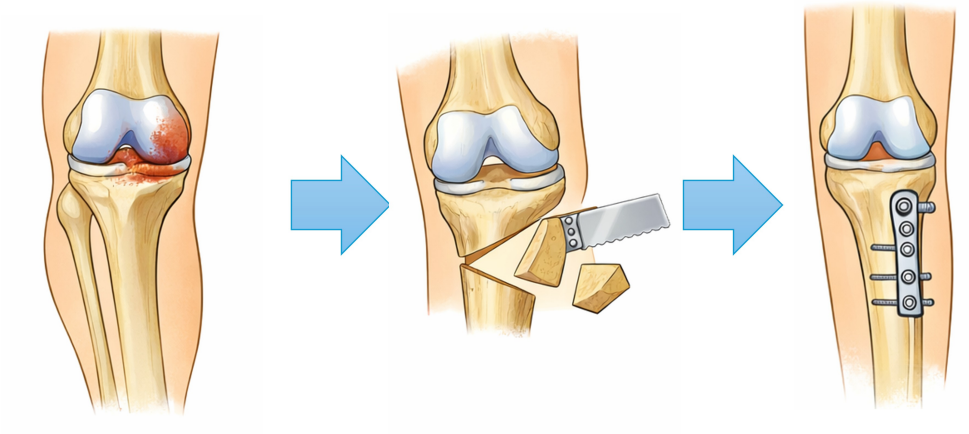


Figure 22: High tibial osteotomy: correction of knee malalignment by tibial wedge resection and fixation, redistributing load away from the degenerated compartment.

HTO is consistently associated with substantial improvements in patient-reported outcomes. RCTs demonstrate that patients undergoing HTO exhibit significant improvements in KOOS scores, with increases on the order of $25$ points compared to $9$ points in non-surgical management, indicating a clinically meaningful benefit in pain, symptoms, and function. These improvements are typically sustained over mid-term follow-up and are often interpreted as evidence of successful intervention. Functional outcomes, including walking capacity and activity levels, similarly improve following surgery[121].

Through the use of $3$ T MRI and $3D$ MRI analysis, recent RCTs using these techniques report that HTO can reduce the rate of cartilage loss, with one study showing a $2\%$ decrease in cartilage thickness in the HTO group versus $9\%$ in controls over two years, corresponding to a between-group difference of approximately $0.18$ mm. This suggests that osteotomy may have a protective effect on cartilage, slowing degeneration rather than reversing it[121].

Other studies report that cartilage thickness may continue to decrease following HTO, particularly in regions such as the patellofemoral joint, likely due to altered biomechanics after realignment[122]. Furthermore, comparative analyses indicate that while HTO improves symptoms and joint space width, it

may not produce significant increases in cartilage thickness, and observed changes may reflect the natural progression of the disease rather than true regeneration[123]. As such, HTO may redistribute load sufficiently to improve symptoms and slow degeneration, but it does not consistently demonstrate quantitative cartilage restoration.

An increase in joint space width is often reported following HTO, which are interpreted as indirect evidence of improved joint condition. However, this measure is influenced by multiple factors, including alignment and joint positioning, and does not provide a direct measure of cartilage morphology. As such, reliance on radiographic metrics introduces uncertainty when attempting to infer true structural changes[124].

Osteotomy occupies a unique position in the treatment landscape of knee OA as a mechanically driven, joint-preserving surgical intervention. It consistently improves patient-reported outcomes and has a clear biomechanical rationale based on load redistribution. Current evidence suggests that osteotomy may delay degeneration rather than reverse it, functioning as a mechanical strategy to manage disease progression rather than a true regenerative intervention. This highlights the need for future studies integrating precise biomechanical modelling, quantitative imaging, and long-term structural evaluation, in order to fully understand how mechanical realignment translates into tissue-level outcomes.

#### 2.2.3.3 Joint replacement

Joint replacement, most commonly total knee arthroplasty (TKA) and unicompartmental knee arthroplasty (UKA), represents the definitive surgical intervention for end-stage knee OA, in which the diseased articular surfaces are replaced by prosthetic components (figure 23). Unlike all previously discussed treatments, joint replacement does not attempt to preserve or regenerate cartilage; rather, it eliminates the native cartilage entirely and substitutes joint function through engineered materials.

As such, the framework for evaluating its effectiveness is fundamentally different. Joint replacement consistently produces the largest improvements in pain and function among all OA treatments. Recent studies report using WOMAC, KOOS and VAS pain score that approximately $90$–$94\%$ of patients experience significant improvement in quality of life and are satisfied with surgical outcomes, although $8$–$27\%$ remain dissatisfied, often due to persistent pain or functional limitations[125,126]. On the other hand, studies investigating the relationship between patient reported outcomes and performance-based functional tests demonstrate weak correlations ($r = 0.00$–$0.30$), indicating that improvements reported by patients do not necessarily correspond to measurable changes in physical function, underlining that even in a procedure as structurally transformative as joint replacement, clinical success is largely defined

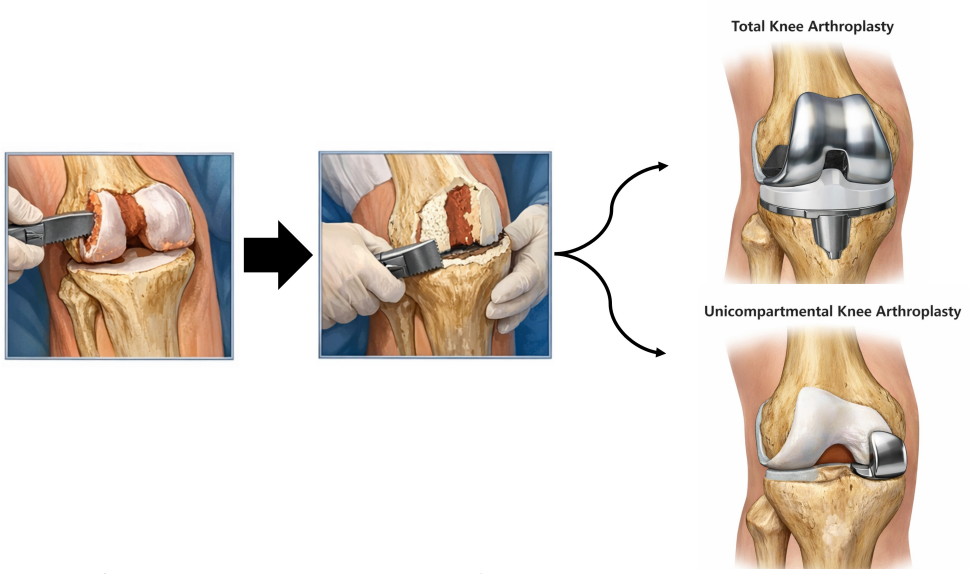



Figure 23: Comparison of surgical approaches in knee arthroplasty. Initially, both approaches requite bone resection and preparation prior to implant placement, while total knee arthroplasty (right, top) involves complete resurfacing of the femoral and tibial joint surfaces, an on the other hand unicompartmental knee arthroplasty (right, bottom) replaces only the affected compartment.

by perception rather than objective mechanical performance[126].

It has also been reported that patients experience rapid improvement in physical activity within the first 6 weeks postoperatively, followed by slower recovery over several months[127]. Most patients eventually have to perform revision surgery, with patients with TKA had a higher threshold for revision compared with UKA[128].

At the tissue and interface scale, joint replacement introduces a complex interaction between prosthetic materials and biological tissues, including bone–implant integration and soft tissue adaptation. However, clinical studies rarely quantify these interactions directly. Instead, they are inferred through imaging or clinical symptoms. It has been demonstrated that the status of preoperative cartilage does not significantly affect postoperative outcomes patient reported outcomes, reinforcing the notion that outcomes are largely independent of the original tissue state. This further emphasizes that joint replacement shifts the focus away from cartilage biology toward prosthetic function and patient perception[129].

Current evidence suggests that while joint replacement is highly effective in relieving symptoms, its evaluation remains largely patient-centered and outcome-driven, with insufficient integration of continuous, quantitative biomechanical metrics capable of fully characterizing joint performance over time.

## 2.3 Acoustic Wave propagation

Acoustic wave propagation provides the fundamental physical basis for understanding how mechanical energy is transmitted through biological tissues and engineered materials. Wave propagation can be described across multiple regimes, ranging from linear propagation in homogeneous media to nonlinear, attenuated, and multiscale phenomena in complex structures. However, real systems rarely conform to ideal assumptions. Biological tissues, in particular, exhibit strong heterogeneity, fluid–solid coupling, viscoelasticity, and hierarchical organization, which significantly influence wave transmission, attenuation, and interaction with structures.

This section establishes the theoretical framework required to analyze such phenomena, beginning with classical wave equations and extending toward nonlinear, multiphysics, and multiscale formulations. These concepts are directly relevant to the present thesis, as they underpin the design and optimization of vibroacoustic stimulation strategies for cartilage regeneration. In this context, understanding how acoustic waves propagate, interact with tissue interfaces, and couple with mechanical structures is essential for identifying effective stimulation regimes and ensuring both efficacy and safety of the proposed therapeutic approach.

### 2.3.1 Wave Propagation in Homogeneous Media

Wave propagation in homogeneous media constitutes the fundamental framework for understanding how mechanical disturbances travel through matter. A homogeneous medium is characterized by spatially uniform physical properties, such as density, elasticity, and compressibility. Under these conditions, the governing equations describing wave motion become significantly simpler, allowing analytical solutions that reveal the essential physical mechanisms behind wave propagation. These simplified models serve as the foundation upon which more complex descriptions are later developed.

#### 2.3.1.1 Linear Wave equation

Wave phenomena arise in many areas of physics and are often governed by equations that share a similar mathematical structure. In its most general form, the classical wave equation describes how a disturbance propagates in space and time. For a scalar field $\phi(x,t)$, the linear wave equation can be written as equation 1

$$\nabla^2\phi = \frac{1}{c^2}\frac{\partial^2\phi}{\partial t^2} \tag{1}$$

where $c$ is the propagation velocity, $\nabla^2$ is the Laplacian operator and $t$ is time. This equation describes the propagation of disturbances that travel with finite velocity without changing their fundamental form in an ideal lossless medium. Although simple in appearance, this equation underlies many physical phenomena, ranging from electromagnetic radiation to mechanical disturbances in solids and fluids[130].

A similar mathematical structure also emerges in acoustics and mechanical vibrations. In this thesis the term acoustic waves will be used to refer to disturbances that propagate through a material medium due to mechanical motion of its particles. In many areas of the literature these phenomena are referred to as mechanical waves. However, because the branch of physics that traditionally studies wave propagation in fluids and compressible media is acoustics, the terminology adopted here follows that convention.

Although electromagnetic and acoustic waves share a similar mathematical description, their physical nature differs fundamentally. Electromagnetic waves correspond to oscillations of electric and magnetic fields that can propagate even in vacuum[130]. Acoustic waves, on the other hand, require a material medium and arise from oscillations of pressure, density, and particle velocity[131].

#### 2.3.1.2 Linear Wave Propagation in Fluid Media

The acoustic wave equation is typically derived from the fundamental equations of continuum mechanics and fluid dynamics[132,133]. The propagation of acoustic disturbances in a fluid medium can be derived from the fundamental conservation laws of continuum mechanics. In the classical approach, acoustics is treated as the study of small-amplitude perturbations superimposed on a fluid initially at rest or in a state of uniform equilibrium. Under these assumptions, the governing equations of fluid dynamics may be linearized, leading to the well-known acoustic wave equation.

The derivation begins with the equations of conservation of mass and conservation of momentum., together with a constitutive relation linking pressure and density.

The general continuity equation for a compressible fluid is given by equation 2

$$\frac{\partial \rho}{\partial t} + \nabla \cdot (\rho \mathbf{v}) = 0 \tag{2}$$

where ($\rho$) is the fluid density and (**v**) is the particle velocity vector. This equation states that the rate of increase of mass inside an infinitesimal control volume plus the net mass flux leaving that volume must vanish.

The equation of motion for a compressible Newtonian fluid is given by the Navier–Stokes equation (equation 3),

$$\rho \left( \frac{\partial \mathbf{v}}{\partial t} + \mathbf{v} \cdot \nabla \mathbf{v} \right) - \nabla p + \mu \nabla^2 \mathbf{v} + \left( \mu_B + \frac{1}{3} \mu \right) \nabla (\nabla \cdot \mathbf{v}) + \rho \mathbf{f} \tag{3}$$

where ($p$) is pressure, ($\mu$) is the dynamic shear viscosity, ($\mu_B$) is the bulk viscosity, and (**f**) is the body force per unit mass.

For the classical derivation of the acoustic wave equation, several simplifying assumptions are introduced. First, body forces are neglected (**f** $= 0$). Second, viscous effects are assumed to be negligible in comparison with inertial and pressure forces, so that the fluid may be approximated as inviscid ($\mu = 0$, $\mu_B = 0$). Under these assumptions, Equation 3 reduces to the Euler equation (equation 4),

$$\rho \left( \frac{\partial \mathbf{v}}{\partial t} + \mathbf{v} \cdot \nabla \mathbf{v} \right) = -\nabla p \tag{4}$$

where the conservation of linear momentum is expressed in an inviscid compressible fluid.

As an acoustic wave travels through the medium it creates a compression and rarefaction zone as can be seen in figure 24.

It is assumed that as the acoustic propagates, only small perturbations are performed in the medium. Thus, the field variables are decomposed into an equilibrium part (equation 5) and a small perturbation part (equation 6),

$$\rho = \rho_0 + \rho' \tag{5}$$

$$p = p_0 + p' \tag{6}$$

where $\rho_0$ and $p_0$ are the equilibrium density and pressure, respectively, and $\rho'$, $p'$, and $\mathbf{v}'$ are the corresponding acoustic perturbations. The equilibrium fluid is assumed to be initially at rest, hence the mean velocity is null. The perturbations are assumed to be small compared with the equilibrium quantities, such that equation 7 is not violated.

$$|\rho'| \ll \rho_0, \qquad |p'| \ll p_0, \qquad |\mathbf{v}'| \text{ is small} \tag{7}$$

This small-amplitude assumption permits linearization of the governing equations by neglecting products of perturbation terms.

Substituting equations 5, 6 and 7 into equation 2 yields equation 8.

$$\frac{\partial(\rho_0 + \rho')}{\partial t} + \nabla \cdot [(\rho_0 + \rho')\mathbf{v}'] = 0 \tag{8}$$

Assuming that the equilibrium density $\rho_0$ is constant in time, it is possible to further simplify equation 8 into equation 9.

$$\frac{\partial \rho'}{\partial t} + \nabla \cdot (\rho_0 \mathbf{v}' + \rho' \mathbf{v}') = 0 \tag{9}$$

Expanding the divergence term gives equation 10.

$$\frac{\partial \rho'}{\partial t} + \nabla \cdot (\rho_0 \mathbf{v}') + \nabla \cdot (\rho' \mathbf{v}') = 0 \tag{10}$$

Since $\rho'\mathbf{v}'$ is the product of two small perturbations, it is a second-order quantity and may be neglected in the linear approximation. Furthermore, if $\rho_0$ is spatially uniform, then equation 11 is assumed.

$$\nabla \cdot (\rho_0 \mathbf{v}') = \rho_0 \nabla \cdot \mathbf{v}' \tag{11}$$

Therefore, the linearized continuity equation becomes 10 equation 12.

$$\frac{\partial \rho'}{\partial t} + \rho_0 \nabla \cdot \mathbf{v}' = 0 \tag{12}$$

This relation states that local changes in density are associated with the divergence of the acoustic particle velocity field.

Just like the continuity equation could be simplified, the same rationale can be applied to the Navier–Stokes momentum equation. Substituting equations 5, 6 and 7 into equation 3 yields equation 13.

$$(\rho_0 + \rho') \left( \frac{\partial \mathbf{v}'}{\partial t} + \mathbf{v}' \cdot \nabla \mathbf{v}' \right) = -\nabla (p_0 + p') \tag{13}$$

Expanding the right-hand side of equation 13 yields equation 14.

$$(\rho_0 + \rho') \left( \frac{\partial \mathbf{v}'}{\partial t} + \mathbf{v}' \cdot \nabla \mathbf{v}' \right) = -\nabla p_0 - \nabla p' \tag{14}$$

In equilibrium, the background pressure is constant or spatially uniform in the absence of external loading, so that equation 15 must be true.

$$\nabla p_0 = 0 \tag{15}$$

Moreover, the terms $\rho' \cdot \frac{\partial \mathbf{v}'}{\partial t}$ and $\mathbf{v}' \cdot \nabla \mathbf{v}'$ are second-order perturbation terms and are neglected in the linear approximation. Equation 14 therefore reduces to Equation 16.

$$\rho_0 \frac{\partial \mathbf{v}'}{\partial t} = -\nabla p' \tag{16}$$

This is the linearized momentum equation. It shows that fluid particles accelerate in response to spatial gradients of acoustic pressure.

At this stage, equation 12 and equation 16 involve three unknown acoustic variables: $\rho'$, $p'$, and $\mathbf{v}'$. A third relation is therefore required. As the acoustic wave travels through the medium, a small compression and rarefaction zone is formed as it propagates throughout the medium as is exemplified in figure 24

Since both of these zones have got the same amplitude, the net heat exchange can be considered null ($Q = 0$), and thus the system can be considered adiabatic. For small adiabatic perturbations this equation can be written as equation 17,

$$p' = c^2 \cdot \rho' \tag{17}$$

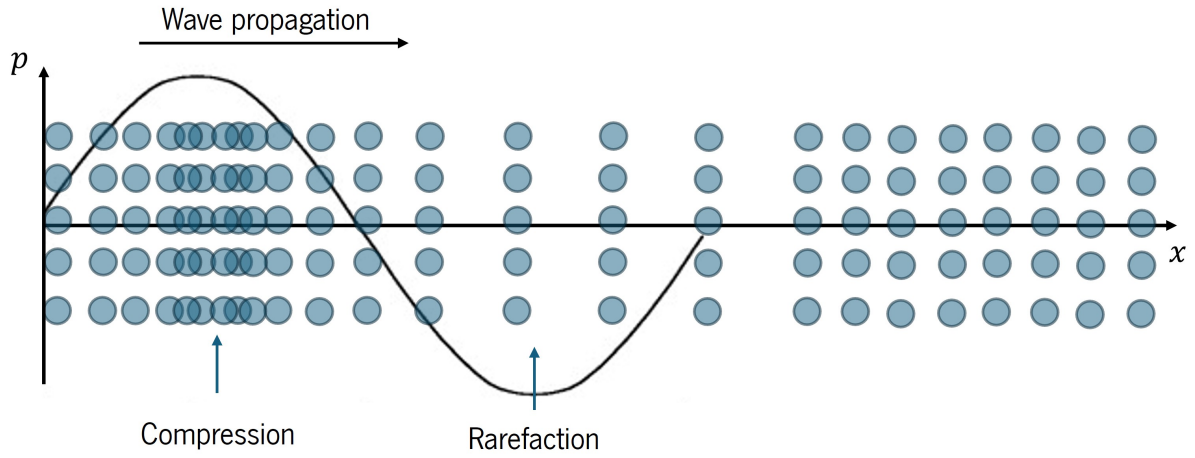



Figure 24: Illustration demonstrating how a generic acoustic wave travels through the medium.

where $c$ is the speed of sound (wave speed), defined by the thermodynamic derivative in equation 18,

$$c^2 = \left(\frac{\partial p}{\partial \rho}\right)_s \tag{18}$$

with the subscript $s$ denoting constant entropy.

Equation 17 is the linearized constitutive relation for acoustic propagation in a compressible fluid.

The acoustic wave equation may now be obtained by combining equation 12, equation 16 and equation 17.

First, take the divergence of equation 16, writing equation 19

$$\rho_0 \frac{\partial}{\partial t}(\nabla \cdot \mathbf{v}') = -\nabla \cdot (\nabla p') \tag{19}$$

Since $\nabla \cdot (\nabla p') = \nabla^2 p'$, equation 19 becomes equation 20

$$\rho_0 \frac{\partial}{\partial t}(\nabla \cdot \mathbf{v}') = -\nabla^2 p' \tag{20}$$

Rearranging equation 12 to express the divergence of velocity, it can be written as equation 21.

$$\nabla \cdot \mathbf{v}' = -\frac{1}{\rho_0}\frac{\partial \rho'}{\partial t} \tag{21}$$

Differentiating equation 21 with respect to time, equation 22 is obtained

$$\frac{\partial}{\partial t}(\nabla \cdot \mathbf{v}') = -\frac{1}{\rho_0}\frac{\partial^2 \rho'}{\partial t^2} \tag{22}$$

Substituting equation 22 into equation 20 gives equation 23

$$\rho_0 \left(-\frac{1}{\rho_0}\frac{\partial^2 \rho'}{\partial t^2}\right) = -\nabla^2 p' \tag{23}$$

which can be further simplified to equation 24

$$\frac{\partial^2 \rho'}{\partial t^2} = \nabla^2 p' \tag{24}$$

With equation 17 it is possible to infer equation 25

$$p' = c^2 \rho' \qquad \Rightarrow \qquad \rho' = \frac{p'}{c^2} \tag{25}$$

Therefore, equation 26 is true.

$$\frac{\partial^2 \rho'}{\partial t^2} = \frac{1}{c^2} \frac{\partial^2 p'}{\partial t^2} \tag{26}$$

Substituting equation 24 into equation 26 , and simplifying notation so that $p' = p$ yields equation 27,

$$\nabla^2 p = \frac{1}{c^2} \cdot \frac{\partial^2 p}{\partial t^2} \tag{27}$$

which is the classical acoustic wave propagation equation written in terms of pressure fluctuations.

This equation admits a general solution for one dimension given by D'Alembert's formula, representing the pressure field as given in equation 28,

$$p(x,t) = F(x - ct) + G(x + ct) \tag{28}$$

where $F(x - ct)$ represents a wave travelling in the positive direction and $G(x + ct)$ a wave travelling in the negative direction, with $F$ and $G$ representing arbitrary functions determined by the initial conditions of pressure and particle velocity.

Simultaneously, The particle velocity field in the medium is related to the pressure gradient through the linearized momentum equation 20,obtaining equation 29,

$$\nabla p = -\rho_0 \frac{\partial \mathbf{v}}{\partial t} \tag{29}$$

which can be expressed component-wise as as equation 30,

$$\frac{\partial p(x,t)}{\partial x_j} = -\rho_0 \frac{\partial v_j(x,t)}{\partial t} \tag{30}$$

where $j$ denotes the spatial component of the velocity vector.

This derivation shows that acoustic propagation emerges naturally from the interaction between two fundamental mechanisms. The first is the conservation of mass, which relates compressions and rarefactions of the medium to local fluid motion. The second is the conservation of momentum, which

relates particle acceleration to pressure gradients. The constitutive relation closes the system by linking pressure and density fluctuations through the compressibility of the medium.

From a physical standpoint, a local compression increases pressure, the resulting pressure gradient drives particle motion, and this motion redistributes mass, generating successive compressions and rarefactions that travel through the medium as a wave. The speed of that propagation is governed by the compressibility and inertia of the medium, represented by the speed of sound $c$.

The speed of sound is thus a property of the medium, and equation 18 can be rewritten relating to the physical properties of said medium. In the case of ideal gases, it is expressed as equation 31,

$$c = \sqrt{\gamma \frac{p}{\rho}} \tag{31}$$

where $\gamma$ is the ratio of specific heats $\frac{C_p}{C_v}$, $p$ is pressure and $\rho$ is the gas density.

For liquid fluids, the speed of sound is expressed as equation 32,

$$c = \sqrt{\frac{K}{\rho}} \tag{32}$$

where $K$ is the bulk modulus of the fluid and $\rho$ is the density of the fluid.

The value of $c$ in water is approximately $1480 m/s$[134] which is quite similar to that of biological soft tissues $1460 - 1655 m/s$[135].

These relations link acoustic propagation to the compressibility and inertia of the medium, explaining why sound travels much faster in liquids and solids than in gases.

#### 2.3.1.3 Linear Wave Propagation in Solid Media

In solid media the propagation of acoustic disturbances is governed by the equations of elasticity rather than fluid dynamics[136]. Unlike fluids, which admit only longitudinal wave propagation, solids can sustain both volumetric compression and shear deformation, which leads to the existence of multiple wave types (figure 25). Consequently, the speed of sound in solids depends not only on density but also on the elastic constants of the material.

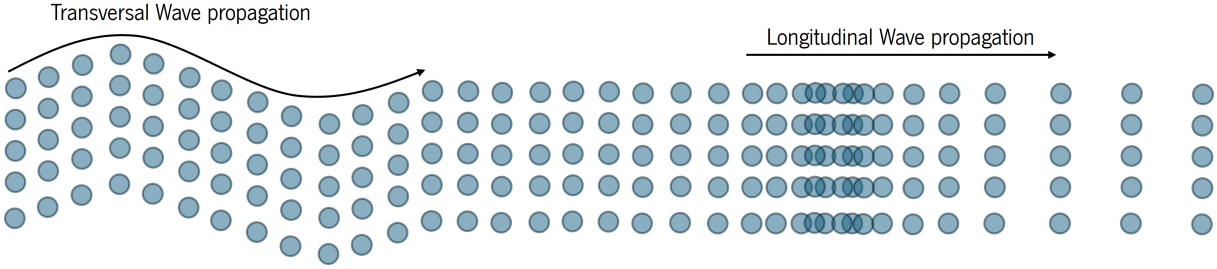



Figure 25: Illustration demonstrating how a generic transversal and longitudinal acoustic wave travel through the medium.

This relation is expressed through the most general form of the wave equation in an isotropic solid, known as the Navier–Cauchy equation 33,

$$\rho\frac{\partial^2\mathbf{u}}{\partial t^2} = (\lambda+\mu)\nabla(\nabla\cdot\mathbf{u}) + \mu\nabla^2\mathbf{u} \tag{33}$$

where **u** is a displacement vector field ($u_x, u_y, u_z$), $\rho$ is the density of the solid, $\lambda$ and $\mu$ are Lamé elastic constants, $\nabla(\nabla\cdot u)$ is the gradient of volumetric strain and $\nabla^2\mathbf{u}$ is the vector of Laplacian displacement. Equation 27 can be thought of as being a special case of equation 33 where $\mu$ tends to zero, meaning that the solid behaves like a fluid, since fluids cannot sustain shear stresses.

Unlike fluids, the displacement field in solids can be decomposed into two independent wave types: longitudinal (compressional) waves and transverse (shear) waves.

Longitudinal waves correspond to compressional waves where particle motion occurs parallel to the direction of propagation. Taking the divergence of the equation33 leads to the wave equation governing volumetric motion, equation 34,

$$\nabla^2(\nabla\cdot\mathbf{u}) = \frac{1}{c_L^2}\cdot\frac{\partial^2(\nabla\cdot\mathbf{u})}{\partial t^2} \tag{34}$$

where the longitudinal wave velocity is expressed by equation 35,

$$c_L = \sqrt{\frac{\lambda+2\mu}{\rho}} \tag{35}$$

These waves correspond to compressions and rarefactions, similar to acoustic waves in fluids. Solids can also support transverse waves, where particle motion is perpendicular to the direction of propagation. These waves cannot exist in fluids because fluids cannot sustain shear stress. Taking the curl of the equation 33 leads to the shear wave equation 36,

$$\nabla^2(\nabla\cdot\mathbf{u}) = \frac{1}{c_T^2}\cdot\frac{\partial^2(\nabla\cdot\mathbf{u})}{\partial t^2} \tag{36}$$

where the shear wave velocity is expressed by equation 37,

$$c_T = \sqrt{\frac{\mu}{\rho}} \tag{37}$$

It is possible to rewrite equation 35 and equation 37 using the elastic constants of solids employed in many engineering contexts, the Young's modulus and Poisson's ratio, rewriting them as equation 38 and equation 39,

$$c_L = \sqrt{\frac{E(1-\nu)}{\rho(1+\nu)(1-2\nu)}} \tag{38}$$

$$c_T = \sqrt{\frac{E}{2\rho(1+\nu)}} \tag{39}$$

where $E$ is Young's Modulus and $\nu$ is Poisson's ratio.

Wave propagation speed in solids depends on the balance between elastic stiffness and inertia. Materials with higher elastic moduli resist deformation more strongly and therefore transmit mechanical disturbances faster. Conversely, higher density increases inertia and tends to reduce wave speed.

If we apply the solid-wave equation using realistic Young's modulus values reported in the literature with $E = 10 - 50kPa$, $\rho = 1000kg/m^3$, and $\nu = 0.49$, $c_L \approx 20\text{–}50m/s$[137], which is not in accordance with the previously stated literature of $c_L = 1460 - 1655m/s$[135]. The reason is that soft biological tissues do not behave as simple elastic solids. Soft tissues are composed of $60\text{–}80\%$ water, a porous extracellular matrix and fluid-filled cellular structures. Because of this, compressional waves propagate primarily through the fluid phase, whose bulk modulus is close to that of water. Water has a sound speed of about 1500 m/s, which explains why most soft tissues exhibit similar longitudinal wave speeds[138].

By applying the same rationale to transverse wave speed, a value of $c_T \approx 1 - 10m/s$ is obtained which is in accordance with the literature[138].

As such, it is common to model soft tissues as fluids and solid tissues as solids for general wave propagation in the human body. However, for elastography, which requires transversal wave calculations, more complex models have to be used, as will be described in section 2.3.2.

#### 2.3.1.4 Linear Wave propagation phenomena

When an acoustic wave propagates through a medium and encounters boundaries, heterogeneities, or obstacles, several physical phenomena may occur. These include reflection, refraction, transmission, absorption, diffraction, and impedance-controlled interactions at interfaces. Understanding these phenomena is fundamental for describing wave behavior in heterogeneous materials and biological tissues[130,131].

In section 2.3.1.2, it was demonstrated how the wave equation (27) could be derived in the time domain. However, in order to understand concepts in wave propagation phenomena, it's important to first understand how this equation is analysed in the frequency domain. If we apply the Fourier transform, assuming there is a sound pressure spectrum ($p(x,t) \Leftrightarrow P(x,\omega)$), Helmholtz equation (40) is obtained,

$$\nabla^2 P(x,\omega) = -\frac{\omega^2}{c^2} P(x,\omega) \Leftrightarrow \nabla^2 P(x,\omega) = -k^2 P(x,\omega) \tag{40}$$

where $k = \omega/c$ is the wave number.

The previously obtained equation 30 relates the velocity of a particle in the medium with pressure. By applying the Fourier transform, it is possible to obtain a new relation linking the spectrum of the pressure gradient with the spectrum of particle velocity, as expressed in equation 41,

$$\partial_j P(x,\omega) = -i\rho\omega V_j(x,\omega) \Leftrightarrow V_j(x,\omega) = \frac{i}{\rho\omega}\partial_j P(x,\omega) \tag{41}$$

where j indicates direction.

One of the most significant quantities governing wave interaction with interfaces is the acoustic impedance of a medium, expressed through equation 42,

$$Z_j(\omega) = \frac{P(\omega)}{V_j(\omega)} \tag{42}$$

which expresses specific acoustic impedance ($Z_j$) in function of the particles pressure and velocity, meaning that it is direction dependent Considering a plane wave propagating in a single direction, equation 28 as equation 43 in the frequency domain,

$$p(x,\omega) = F(\omega)e^{-ikx} \tag{43}$$

and equation 30, can be expressed as equation 44,

$$v_x(x,\omega) = \frac{i}{\rho\omega}\frac{\partial p(x,\omega)}{\partial x} = \frac{F(\omega)}{\rho c}e^{-ikx} \tag{44}$$

which if it is replaced in equation 42, the normal impedance in planar wave propagation can be expressed through Equation 45.

$$Z = \frac{p}{v_x} = \rho c \tag{45}$$

Acoustic impedance ($Z$) quantifies the relationship between pressure and particle velocity and governs reflection and transmission at interfaces. When a wave encounters an interface between two media with different impedances, part of the wave energy is reflected and part is transmitted.

When a plane wave travelling in medium 1 reaches an interface with medium 2,the ratio of reflected and transmitted amplitudes depends on the impedance mismatch between the two media, where the pressure reflection coefficient ($R$) is given by equation 46,

$$R = \frac{Z_2 - Z_1}{Z_2 + Z_1} \tag{46}$$

and the transmission coefficient ($T$) is given by equation 47,

$$T = \frac{2Z_2}{Z_1 + Z_2} \tag{47}$$

where $Z_1$ is the impedance of medium 1 and $Z_2$ is the impedance of medium 2. The fraction of amplitude reflected increases as the difference between impedances increases.

When a wave crosses an interface between two media with different propagation velocities, its direction of propagation changes according to Snell's law in equation 48,

$$\frac{sin\theta_1}{c_1} = \frac{sin\theta_2}{c_2} \tag{48}$$

where $c_1$ and $c_2$ are the wave speeds in each medium and $\theta_1$ and $\theta_2$ are the incident and refracted angle respectively. Refraction occurs because the wavefront propagates at different speeds in each medium.

As the acoustic wave encounters boundaries, it will influence how it interacts with surfaces. There are two types of perfect boundary surfaces that are typically inserted when modelling an acoustic medium: perfectly hard (rigid) boundary and perfectly soft boundary.

A perfectly hard sound boundary corresponds to a rigid surface where particle velocity is zero ($v = 0$), leading to an infinite impedance ($Z = \infty$). An example of this type of boundary is when an acoustic wave is propagating in air and encounters a wall that is much more rigid than the medium it is propagating in. Under this condition, the wave is reflected with no phase change in pressure, as is exemplified in figure 26.

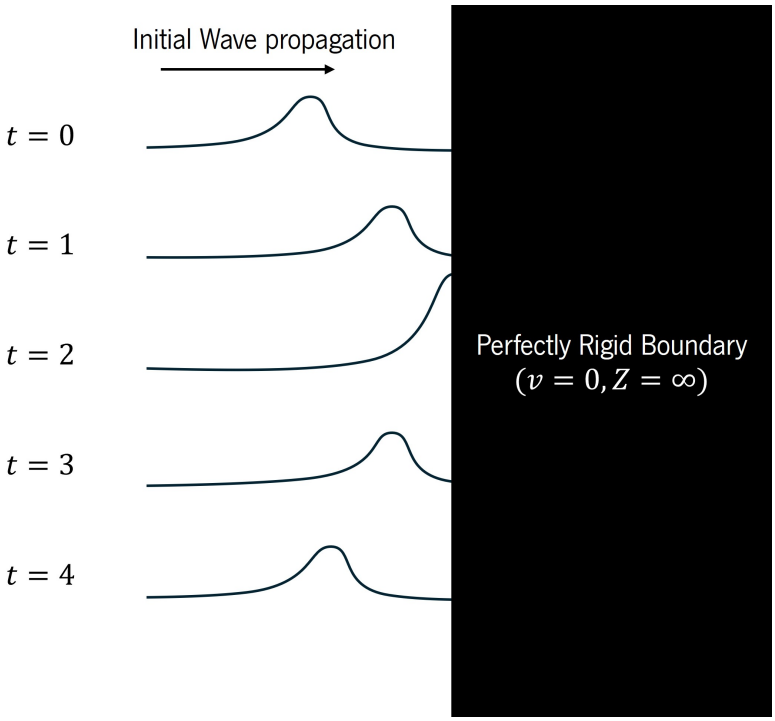



Figure 26: Exemplification of how an acoustic pulse is reflected when it encounters a perfectly rigid boundary.

In contrast, a perfectly soft sound boundary corresponds to a pressure-release surface where acoustic pressure vanishes ($p = 0$), resulting in a null impedance ($Z = 0$). A practical example where this happens in reality is an the open end of a tube, where pressure outside is much smaller than the pressure

inside that can be considered almost null. This type of boundary produces a reflected wave with a phase inversion, as is exemplified in figure 27.

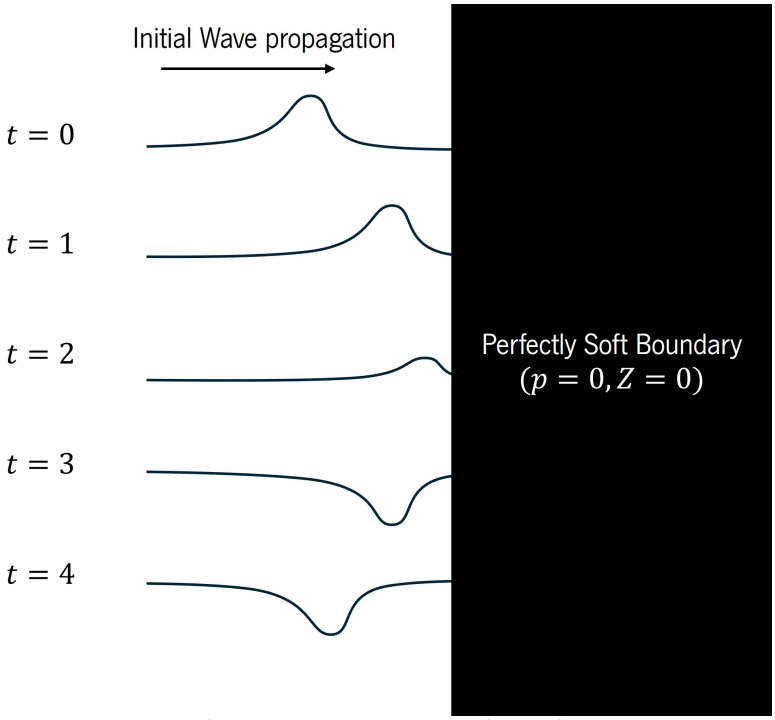



Figure 27: Exemplification of how an acoustic pulse is reflected when it encounters a perfectly soft boundary.

Under specific conditions, bending and spreading occur when acoustic waves encounter obstacles or apertures with dimensions comparable to the wavelength. This phenomenon is called diffraction, and it becomes significant when $\lambda \approx d$, where$\lambda$ is the wavelength and $d$ is the characteristic size of the obstacle or aperture. Under such conditions, waves do not propagate strictly along geometrical acoustic paths but spread into shadow regions, as can be observed in figure 28.

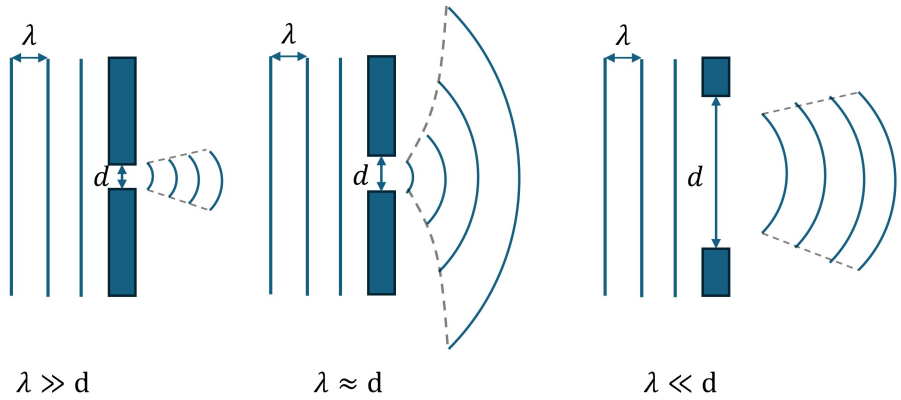



Figure 28: Illustration of the diffraction of acoustic waves, taking into account several aperture sizes in relation to the wavelength.

Although in ideal conditions, acoustic wave attenuation can be ignored, in reality, part of their energy is dissipated due to mechanisms such as viscous losses, internal friction, and scattering. However, this process is neglected in equation 27 because the process is considered in lossless and inviscid conditions.

As such, in order to account for the attenuation, an *ad hoc* term is typically inserted to artificially account attenuation, modifying equation 27 into equation 49,

$$\nabla^2 p = \frac{1}{c^2}\frac{\partial^2 p}{\partial t^2} + \frac{2\alpha}{c}\frac{\partial p}{\partial t} \tag{49}$$

where $\alpha$ is the attenuation coefficient. By introducing this additional term, energy dissipation is artificially introduced, causing the amplitude to decrease as the wave propagates.

#### 2.3.1.5 Nonlinear Wave equation

The classical acoustic wave equation presented in 2.3.1.2 assumes that wave amplitudes are sufficiently small so that all governing relations can be linearized. However, when wave the finite-amplitudes become sufficiently large that $\frac{p}{p_0}$ is not negligible nor infinitesimal, the assumptions used to linearize the governing equations are no longer valid. The full equations of fluid dynamics or elasticity are inherently nonlinear, and nonlinear effects must be retained. In nonlinear propagation the waveform gradually distorts during propagation, generating higher harmonics and potentially leading to shock formation[139]. The difference between a linear wave propagation and nonlinear wave propagation can be observed in figure 29.

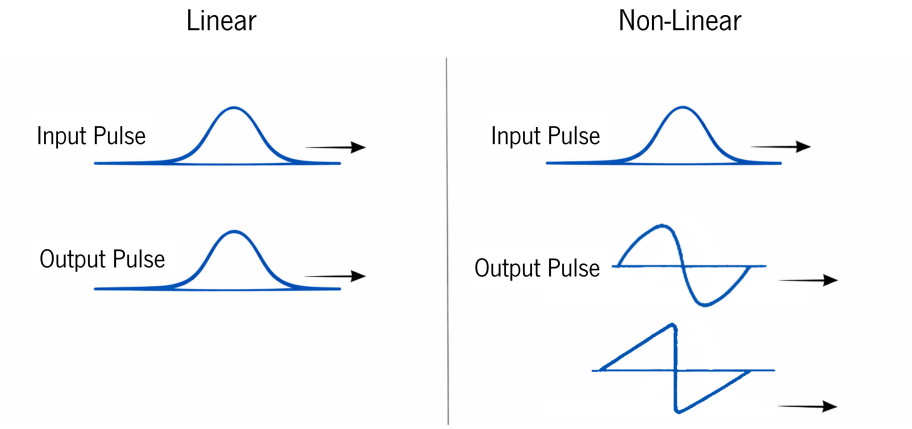



Figure 29: Linear and nonlinear wave propagation.

The origin of acoustic nonlinearity lies primarily in the nonlinear relationship between pressure and density in compressible media. Instead of assuming a strictly linear equation of state, the pressure–density relation can be expanded using a Taylor series around the equilibrium state, as observed in equation 50,

$$p - p_0 = A\left(\frac{\rho - \rho_0}{\rho_0}\right) + \frac{B}{2}\left(\frac{\rho - \rho_0}{\rho_0}\right)^2 + \ldots \tag{50}$$

where $A$ is the linear term of the equation of state and $B$ the second-order nonlinear coefficient. Equation 50, theoretically continues infinitely, but the first two right hand terms are used to define the

nonlinearity parameter as equation 51,

$$\frac{B}{A} \tag{51}$$

which quantifies the degree of thermodynamic nonlinearity of the medium. This parameter reflects how strongly the sound speed varies with local pressure fluctuations. Typical values of $B/A$ in biological media range from approximately 5 to 10, significantly larger than those of ideal gases, indicating strong nonlinear behaviour[135]. In many formulations a modified parameter is used as is demonstrated in equation 52,

$$\beta = 1 + \frac{B}{2A} \tag{52}$$

which appears directly in nonlinear acoustic wave equations.

Starting from the continuity equation (equation 2) and momentum conservation (equation 3), nonlinear propagation can be derived by retaining second-order terms that were neglected in the linear approximation. When these nonlinear terms are retained and combined with the nonlinear equation of state (equation 50), the resulting governing equation contains additional quadratic terms in pressure.

One of the most widely used nonlinear models is the Westervelt equation, which incorporates both nonlinear effects and viscous attenuation, resulting in equation 53,

$$\nabla^2 - \frac{1}{c_0^2}\frac{\partial^2 p}{\partial t^2} + \frac{\delta}{c_0^4}\frac{\partial^3 p}{\partial t^3} = -\frac{\beta}{\rho_0 c_0^4}\frac{\partial^2 p^2}{\partial t^2} \tag{53}$$

where $\delta$ represents sound diffusivity and is related to the wave attenuation. The nonlinear term on the right-hand side represents the self-interaction of the acoustic pressure field, which causes waveform distortion and harmonic generation.

The sound diffusivity term $\delta$ accounts for dissipative processes due to viscosity and thermal conduction. It is defined as 54,

$$\delta = \frac{1}{\rho_0}\left(\frac{4}{3}\mu + \mu_B\right) + \frac{k}{\rho_0}\left(\frac{1}{c_v} - \frac{1}{c_p}\right) \tag{54}$$

where $\mu$ is the shear viscosity, $\mu_B$ is the bulk viscosity, $k$ is the thermal conductivity and $c_v$ and $c_p$ is the specific heats at constant volume and pressure. The sound diffusivity describes the rate at which acoustic energy spreads and dissipates due to viscous and thermal mechanisms within the medium.

In other instances, it's possible to extend equation 53, and incorporate elements that account for diffraction, Nonlinear waveform distortion due to finite amplitude and thermoviscous absorption within the medium. This leads to Khokhlov–Zabolotskaya–Kuznetsov equation, which is particularly suited for describing directional beams such as those produced by ultrasonic transducers, as is demonstrated in equation 55,

$$\frac{\partial^2}{\partial z \partial \tau} = \frac{c_0}{2}\nabla^2_{\perp p} + \frac{\delta}{2c_0^3}\frac{\partial^3 p}{\partial \tau^3} + \frac{\beta}{2\rho_0 c_0^3}\frac{\partial^2 p^2}{\partial \tau^2} \tag{55}$$

where $z$ is the propagation direction, $\tau = t - \frac{z}{c_0}$ is the retarded time coordinate and $\nabla_\perp^2$ is the transverse Laplacian operator describing diffraction. This equation is derived as a parabolic approximation of equation 53 under the assumption that the acoustic field propagates predominantly in one direction (usually denoted as the $z$-axis). Such an approximation simplifies the full nonlinear wave equation while retaining the main physical mechanisms governing wave propagation.

The nonlinear acoustic models provide a more accurate description of wave propagation in media where wave amplitudes are sufficiently large that linear approximations are no longer valid. These phenomena are particularly relevant in high-intensity ultrasound, nonlinear elastography, and biomedical ultrasound applications where finite-amplitude waves interact with biological tissues.

### 2.3.2 Wave Propagation in Complex Media

Wave propagation in complex media include materials whose internal structure, composition, or multiphysics behavior cause waves to deviate from the predictions of classical homogeneous models. The investigation of wave propagation in complex media is inherently interdisciplinary, combining acoustics, solid mechanics, fluid mechanics, materials science, and numerical modelling. Through the integration of theoretical analysis, computational simulation, and experimental validation, it becomes possible to understand how waves interact with heterogeneous structures and to exploit these interactions in applications ranging from medical imaging and therapeutic ultrasound to nondestructive testing and acoustic metamaterials. Examples include porous materials, biological tissues, composites, metamaterials, and heterogeneous geological structures. Because such media involve multiple interacting mechanisms (elastic, viscous, fluidic, and structural) wave propagation must often be analyzed across multiple spatial scales.

#### 2.3.2.1 Hyperelastic Media

Hyperelastic materials are a class of nonlinear elastic solids whose mechanical response is derived from a strain energy density function. Unlike linear elastic materials, where stress is proportional to strain, hyperelastic materials can undergo large deformations while maintaining reversible mechanical behavior. Such models are commonly used to describe rubbers, biological tissues, and soft polymers[140]. The study of wave propagation in hyperelastic media therefore requires a formulation that accounts for finite deformation and nonlinear constitutive relations[141].

Considering the deformation of a continuum body is described by the motion present in equation 56,

$$\mathbf{x} = \chi(\mathbf{X}, t) \tag{56}$$

where **X** denotes the position of a material particle in the reference configuration and **x** denotes its position in the current configuration.

The deformation gradient tensor is defined as equation 57,

$$\mathbf{F} = \frac{\partial \mathbf{x}}{\partial \mathbf{X}} \tag{57}$$

which describes the local transformation of material line elements. The determinant of the deformation gradient in $\mathbf{J} = def(\mathbf{F})$ represents the local change in volume during deformation.

For hyperelastic materials the stress is derived from a strain energy density function $W$, which depends on the deformation gradient or on invariants of the strain tensor.

The first Piola–Kirchhoff stress tensor is obtained as equation 58,

$$\mathbf{P} = \frac{\partial \mathbf{W}}{\partial \mathbf{F}} \tag{58}$$

while the Cauchy stress tensor may be written as equation 59,

$$\sigma = \frac{1}{J}\mathbf{P}\mathbf{F}^T \tag{59}$$

In many applications, the strain energy function is expressed in terms of the invariants of the right Cauchy–Green deformation tensor as $\mathbf{C} = \mathbf{F}^T\mathbf{F}$. As such, the invariants of **C** are defined as equation 60.

$$I_1 = tr(\mathbf{C}), I_2 = \frac{1}{2}\left[\left(tr(\mathbf{C})^2\right) - tr\left(\mathbf{C^2}\right)\right], I_3 = det\left(\mathbf{C}\right) \tag{60}$$

Many hyperelastic models are constructed as functions of these invariants. The models utilized in this thesis will be described in section D.1.1.1.

The acoustic wave equation for a deformable continuum follows from the balance of linear momentum. In the reference configuration it can be written as equation 61.

$$\rho_0 \frac{\partial^2 \mathbf{u}}{\partial t^2} = \nabla x \cdot \mathbf{P} = \nabla x \cdot \frac{\partial W}{\partial \mathbf{F}} \tag{61}$$

Wave propagation in hyperelastic media is commonly analyzed using the theory of incremental motion superimposed on a finite deformation. In this approach, a small dynamic perturbation is superimposed on a statically deformed configuration.

If the total motion be written as equation 62,

$$x = x_0 + \mathbf{u}(\mathbf{X}, t) \tag{62}$$

where $x_0$ represents the finite static deformation and **u** represents a small incremental displacement associated with the propagating wave.

Linearizing the governing equations with respect to the incremental motion leads to the governing equation for wave propagation in hyperelastic materials under finite deformation, equation 63,

$$\rho_0 \frac{\partial^2 u_i}{\partial t^2} = A_{ijkl} \frac{\partial^2 u_k}{\partial X_j \partial X_l} \tag{63}$$

where $A_{ijkl}$ is the fourth-order incremental elasticity tensor, which depends on the pre-deformation state of the material and on the derivatives of the strain energy function.Thus, the incremental elasticity tensor is given by equation 64.

$$A_{ijkl} = \frac{\partial^2 W}{\partial F_{ij} \partial F_{kl}} \tag{64}$$

If a plane wave travels through a hyperelastic material, substituting it into equation 63, leads to a generalized eigenvalue problem

$$\rho_0 \omega^2 A_i = A_{ijkl} k_j k_l A_k \tag{65}$$

As such, the waves speeds can be obtained deduced from equation 66 for an hyperelastic material,

$$c = \frac{\omega}{|\mathbf{k}|} \tag{66}$$

which depends on the direction of propagation, the state of deformation, and the derivatives of the strain energy function.

An important consequence of hyperelastic behavior is the acoustoelastic effect, whereby the propagation speed of waves depends on the stress state of the material. Because the incremental elasticity tensor $A_{ijkl}$ depends on the pre-existing deformation, wave velocities vary with applied strain.

#### 2.3.2.2 Homogenization of Composite Materials

Composite materials consist of two or more constituent phases with distinct mechanical properties combined to produce a heterogeneous medium. Typical examples include fiber–reinforced polymers, layered laminates, and biological tissues with fibrous reinforcement. Because the elastic properties vary spatially at the microstructural scale, the propagation of mechanical waves in composites differs fundamentally from that in homogeneous solids. In order to analyze such materials, it is often necessary to employ homogenization techniques that allow the heterogeneous medium to be represented by an equivalent continuum with effective properties[142].

Simplifying equation 33, we can represent wave propagation in solids through a displacement field $\mathbf{u}(\mathbf{x}, t)$ with the governing equation 67,

$$\rho \frac{\partial^2 \mathbf{u}}{\partial t^2} = \nabla \cdot \sigma \tag{67}$$

where $\sigma$ is the stress tensor.

The stress–strain relationship for an elastic material given by Hooke's law can be written as equation 68,

$$\sigma_{ij} = C_{ijkl}\varepsilon_{kl} \tag{68}$$

where $C_{ijkl}$ represents the fourth-order elastic stiffness tensor and $\varepsilon_{kl}$ is the strain tensor defined as equation 69

$$\varepsilon_{kl} = \frac{1}{2}\left(\frac{\partial u_k}{\partial x_l} + \frac{\partial u_l}{\partial x_k}\right) \tag{69}$$

Substituting equation 68 and equation 69 into equation 67 leads to the general elastodynamic wave equation presented in equation 70.

$$\rho\frac{\partial^2 u_i}{\partial t^2} = \frac{\partial}{\partial x_j}\left(C_{ijkl}\frac{\partial u_k}{\partial x_l}\right) \tag{70}$$

For homogeneous isotropic materials the stiffness tensor reduces to the Lamé formulation, yielding the classical Navier equation. However, in composite materials the stiffness tensor varies spatially due to the presence of different phases, with $C_{ijkl} = C_{ijkl}(\mathbf{x})$.

This spatial heterogeneity complicates the analysis of wave propagation because the mechanical properties change at the scale of the microstructure.

To address this difficulty, composite materials are typically studied using homogenization methods. The central idea is that the heterogeneous microstructure can be replaced by an equivalent homogeneous medium with effective material properties, provided that the characteristic wavelength of the propagating wave is significantly larger than the microstructural length scale, as be observed in figure 30.

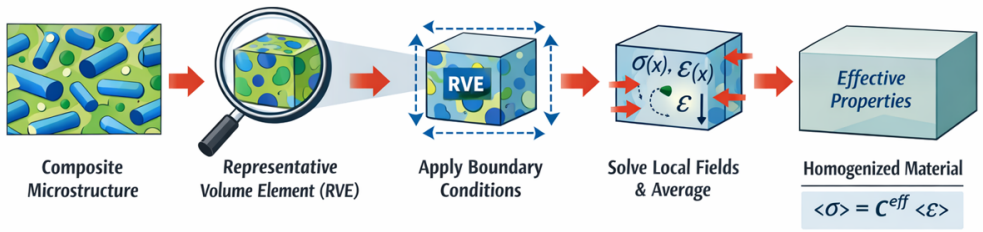



Figure 30: Depiction of the procedure typically taken to represent a composite material through its homogenized properties using a representative volume element.

The homogenization process relies on the definition of a Representative Volume Element (RVE). The RVE is a small region of material that statistically captures the microstructural features of the composite, including the distribution of phases, fiber orientation, and volume fractions.

Let  denote the volume of the RVE. Thus, the average strain over the RVE can be defined as equation 71

$$\langle\varepsilon_{ij}\rangle = \frac{1}{V}\int_V \varepsilon_{ij}dV \tag{71}$$

Similarly, the average stress can be defined as equation 72.

$$\langle \sigma_{ij} \rangle >= \frac{1}{V} \int_V \sigma_{ij} dV \tag{72}$$

The homogenized constitutive relationship for the equivalent continuum may thus be written as equation 73,

$$\langle \sigma_{ij} \rangle = C^{eff}_{ijkl} \langle \varepsilon_{ij} \rangle \tag{73}$$

where $C^{eff}_{ijkl}$ is the effective stiffness tensor of the composite.

Once the effective elastic constants have been determined, the composite can be treated as an equivalent homogeneous medium at the macroscopic scale. Thus, in the macroscopic scale, equation 70 can be written as equation 74,

$$\rho_{eff} \frac{\partial^2 u_i}{\partial t^2} = \frac{\partial}{\partial x_j} \left( C^{eff}_{ijkl} \frac{\partial u_k}{\partial x_l} \right) \tag{74}$$

where $\rho_{eff}$ is the effective density of the composite, typically obtained as a volume-weighted average of the constituent densities, given by equation 75

$$\rho_{eff} = \sum_n = v_n \rho_n \tag{75}$$

with $v_n$ representing the volume fraction of phase $n$.

For isotropic homogenized composites, the effective elastic constants may be expressed in terms of effective Lamé parameters $\lambda_{eff}$ and $\mu_{eff}$. In this case, the wave equation reduces to the classical form presented in equation 76.

$$\rho_{eff} \frac{\partial^2 \mathbf{u}}{\partial t^2} = (\lambda_{eff} + \mu_{eff}) \nabla (\nabla \cdot \mathbf{u}) + \mu_{eff} \nabla^2 \mathbf{u} \tag{76}$$

From this formulation, the effective longitudinal and transversal wave speed in the composite medium can be obtained as equation 77 and equation 77 respectively.

$$c_L = \sqrt{\frac{\lambda_{eff} + 2\mu_{eff}}{\rho_{eff}}} \tag{77}$$

$$c_T = \sqrt{\frac{\mu_{eff}}{\rho_{eff}}} \tag{78}$$

These expressions show that wave propagation in composite materials depends on the effective elastic constants derived from the microstructure.

The homogenization framework introduces a clear separation between two characteristic length scales. At the microscopic scale, the composite consists of individual constituents whose properties vary

spatially. At the macroscopic scale, the material behaves as an equivalent continuum characterized by effective elastic parameters. When the wavelength of the propagating disturbance is much larger than the dimensions of the RVE, the wave interacts primarily with the homogenized medium rather than with individual microstructural features.

However, when the wavelength becomes comparable to the characteristic microstructural length scale, scattering, dispersion, and local resonance effects may occur. In such cases, homogenized models may no longer be sufficient and more advanced multiscale or periodic formulations are required to accurately capture wave propagation phenomena[143].

#### 2.3.2.3 Multiphysics Interfaces

Wave propagation in real systems rarely occurs within a single physical domain. Instead, waves often interact with interfaces separating different media, where distinct governing equations apply. These multiphysics interfaces are regions where physical quantities such as stress, pressure, displacement, and electric fields must satisfy compatibility and equilibrium conditions. In vibroacoustic systems, two interfaces are of particular importance: the acoustic–solid interface (ASI) and the solid–piezoelectric (PZT) interface.

At the interface between a fluid and a solid domain, the governing equations differ. In the fluid, wave propagation is typically described in terms of acoustic pressure $p$, whereas in the solid, it is described in terms of displacement $u$ and stress $\sigma$. The interface conditions ensure continuity of physical quantities across the boundary[144].

The acoustic pressure in the fluid acts as a normal stress on the solid surface. Therefore, equilibrium of forces requires equation 79,

$$\sigma \cdot \mathbf{n} = -p \cdot \mathbf{n} \tag{79}$$

where **n** denotes the unit normal vector at the interface.

This condition ensures that the stress exerted by the fluid on the solid is balanced by the stress within the solid.

Similarly, the normal component of the particle velocity in the fluid must match the normal velocity of the solid boundary. In the fluid, particle velocity **v** is related to pressure through the linearized momentum equation 80.

$$\rho_f \partial \frac{\partial \mathbf{v}}{\partial t} = -\nabla p \tag{80}$$

At the interface, the kinematic condition becomes equation 81.

$$\mathbf{v} \cdot \mathbf{n} = \frac{\partial \mathbf{u}}{\partial t} \cdot \mathbf{n} \tag{81}$$

This condition enforces that there is no separation or interpenetration between the fluid and the solid.

The interaction at the interface is strongly governed by the acoustic impedance of each medium. A mismatch in impedance leads to partial reflection and transmission of the wave. At an ASI, the solid typically has a much higher impedance than the fluid, resulting in significant reflection and limited transmission unless coupling layers are introduced.

At ASIs, the coupling occurs between pressure waves and structural vibrations. However, at solid–piezoelectric interfaces, the coupling extends further, linking mechanical deformation with electrical fields. These interactions enable the conversion of energy between different physical domains[145].

PZT materials introduce an additional level of coupling, as they convert mechanical deformation into electrical charge and vice versa. The constitutive relations for a linear piezoelectric material are given by equation 82 and equation 83,

$$\mathbf{S} = \mathbf{s}^E\mathbf{T} + \mathbf{d}^T\mathbf{E} \tag{82}$$

$$\mathbf{D} = \mathbf{dT} + \varepsilon^T\mathbf{E} \tag{83}$$

where **S** is the strain tensor, **T** is the stress tensor,**E** is the electric field, **D** is the electric displacement, $\mathbf{s}^E$ is the compliance tensor at constant electric field, **d** is the piezoelectric coupling tensor and $\varepsilon^T$ is the permittivity tensor at constant stress.

At the interface between a solid structure and a piezoelectric material, continuity of displacement (equation 84) and stress (equation 85) must be satisfied.

$$\mathbf{u}_{solid} = \mathbf{u}_{PZT} \tag{84}$$

$$\sigma_{solid} \cdot \mathbf{n} = \sigma_{PZT} \cdot \mathbf{n} \tag{85}$$

These conditions ensure mechanical compatibility and equilibrium across the interface.

In addition to mechanical continuity, electrical conditions must also be satisfied. The electric displacement normal to the interface must be continuous, ensuring equation 86.

$$\mathbf{D}_1 \cdot \mathbf{n} = \mathbf{D}_3 \cdot \mathbf{n} \tag{86}$$

Understanding the governing equations and boundary conditions at these interfaces is therefore essential for accurately modelling wave propagation and for optimizing the performance of vibroacoustic systems.

#### 2.3.2.4 Vibroacoustics

Vibroacoustics describes the interaction between structural vibration and acoustic wave propagation in the surrounding medium. In essence, a mechanical structure may vibrate due to an applied dynamic force, and this vibration may in turn radiate sound into the surrounding medium. Conversely, an acoustic wave propagating through a fluid or solid medium may exert dynamic pressure on a structure and induce its vibration. Vibroacoustic phenomena therefore emerge from the coupling between mechanical motion and wave-induced excitation[146].

The starting point for the study of mechanical vibrations is typically Newton's second law[147]. For a single-degree-of-freedom mechanical system can be reduced to three elements: a mass that represents inertia, a damping element that represents dissipation and an elastic element that represents stiffness. The sum of these three elements must be equal to any external force as represented in equation 87,

$$m\frac{\partial^2 x}{\partial t^2} + c\frac{\partial x}{\partial t} + kx = F(t) \tag{87}$$

where $m$ represents the structure effective mass, $c$ the damping coefficient and $k$ stiffness.

In the absence of an external force ($F(t) = 0$), free vibration occurs and equation 87 becomes equation 88.

$$m\frac{\partial^2 x}{\partial t^2} + c\frac{\partial x}{\partial t} + kx = 0 \tag{88}$$

If we neglect damping ($c = 0$), equation 88 is further simplified into equation 89.

$$m\frac{\partial^2 x}{\partial t^2} + kx = 0 \tag{89}$$

Assuming that there is a harmonic solution of the form $x(t) = Xe^{i\omega t}$ that can solve equation 89, by substituting it, equation 90 is obtained,

$$(-m\omega^2 + k)Xe^{i\omega t} = 0 \tag{90}$$

where $\omega$ is the angular frequency of the system ($\omega = 2\pi f$).

Since $Xe^{i\omega t} \neq 0$ equation 90 can be simplified to equation 91.

$$-m\omega^2 + k = 0 \tag{91}$$

By rewriting this in function of angular frequency, we obtain equation 92,

$$\omega_n = \sqrt{\frac{k}{m}} \tag{92}$$

where $\omega_n$ is the natural frequency of the structure.

If we consider that an external force is applied through harmonic forcing described by $F(t) = F_0 \sin(\omega t)$, equation 87 becomes equation 93.

$$m\frac{\partial^2 x}{\partial t^2} + c\frac{\partial x}{\partial t} + kx = F_0 \sin(\omega t) \tag{93}$$

Admitting that the movement of $x$ can be described once again through $x(t) = Xe^{i\omega t}$, the displacement amplitude steady-state harmonic response is given by equation 94.

$$X = \frac{F_0}{\sqrt{(k - m\omega^2)^2 + (c\omega)^2}} \tag{94}$$

It is possible to rewrite equation 94 as equation 95 resorting to $\omega_n$, the natural frequency given by equation 92,

$$X = \frac{F_0/k}{\sqrt{(1 - r^2)^2 + (2\zeta r)^2}} \tag{95}$$

where $\zeta$ is the damping ratio given by $\zeta = \frac{c}{2m\omega_n}$ and $r$ is frequency ratio between the current excitation frequency and natural frequency ($r = \frac{\omega}{\omega_m}$).

If we plot equation 95 considering an arbitrary constant $F_0$, $k$ and $\zeta$, with $X$ in function of $r$, figure 31 is obtained.

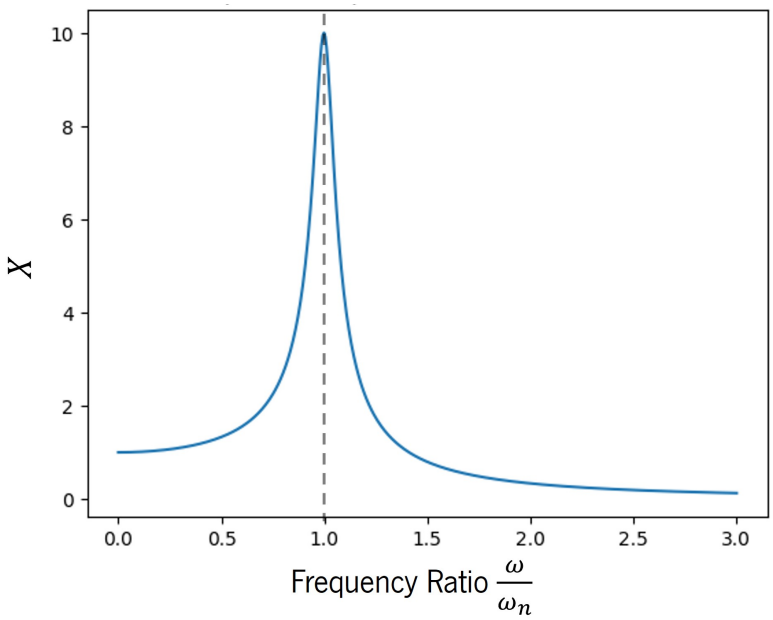



Figure 31: Plot illustrating how the amplitude is transmitted in a one degree-of-freedom structure as a function of the frequency ratio.

By observing figure 31 and relating it to equation 95 it is possible to observe that when the excitation frequency approaches the natural frequency, that is, when $\rightarrow 1$, the term $(1 - r^2)^2$ tends towards zero. This means that the denominator becomes very small, and therefore the response amplitude becomes very large. If we consider and ideal undamped case $(\zeta = 0)$, at resonance $(r = 1)$, the denominator vanishes completely and the theoretical amplitude tends to infinity $(X \rightarrow \infty$ when $\omega = \omega_n)$.

Of course, real systems never reach infinity due to damping, nonlinearities, boundary effects, and material limitations intervene. But the central truth remains: a structure is most dynamically vulnerable when the forcing frequency coincides with one of its natural frequencies.

In vibroacoustic problems, the external force $F(t)$ may be generated by an acoustic field rather than by direct mechanical contact. If an acoustic pressure field $p(t)$ acts over an area $A$, the equivalent forcing term is $F(t) = p(t)A$. If the incident pressure is harmonic then it can be represented as $p(t) = p_0 \sin(\omega t)$, and the applied force becomes $F(t) = p_0 A \sin(\omega t)$.

Substituting into equation 87, it becomes equation 96.

$$m\frac{\partial^2 x}{\partial t^2} + c\frac{\partial x}{\partial t} + kx = p_0 A \sin(\omega t) \tag{96}$$

When a wave propagates through a bounded medium, it may reflect at boundaries. The superposition of an incident wave and a reflected wave travelling in opposite directions may generate a standing wave.

Considering an incident harmonic wave characterized by equation 97,

$$u_i(x,t) = A \sin(\omega_t - kx) \tag{97}$$

and a reflected harmonic wave given by equation 98,

$$u_r(x,t) = A \sin(\omega_t + kx) \tag{98}$$

the total displacement is given by equation 99.

$$u(x,t) = u_i + u_r \tag{99}$$

By using the trigonometric identity $\sin(\alpha - \beta) + \sin(\alpha + \beta) = 2 \sin\alpha \cos\beta$ and replacing it in equation 99, equation 100 is obtained.

$$u(x,t) = 2A \sin(\omega t) \cos(kx) \tag{100}$$

Equation 100 is the classical expression for a standing wave. Unlike a travelling wave, the spatial and temporal parts are separable. The term $\sin(\omega t)$ governs temporal oscillation, whereas $\cos(kx)$ governs the spatial distribution of amplitude.

This means that some points called nodes remain motionless, when $\cos(kx) = 0$ while other points, called antinodes, oscillate with maximum amplitude, when $|\cos(kx) = 1|$. Thus, the wave no longer transports energy uniformly along the medium. Instead, energy becomes spatially organized into fixed oscillatory patterns.

Standing waves become especially important when the geometry of the medium allows only certain wavelengths. For a one-dimensional domain of length , resonance occurs when the boundary conditions permit a wave pattern that “fits” exactly inside the domain.

If a medium fixed at both ends is considered, the admissible wavelengths are $L = n\frac{\lambda_n}{2}$, with $n = 1, 2, 3, ....$ If we consider $\lambda_n = \frac{2L}{n}$, and relate wavelength with speed of sound through $c = f\lambda$, the corresponding resonant frequencies are given by equation 101,

$$f_n = \frac{nc}{2L} \tag{101}$$

which give the natural frequencies of the bounded medium in function of the speed of sound.

Now the key link with vibroacoustics appears. If an acoustic standing wave develops such that its oscillation frequency matches the natural frequency of a mechanical structure, the acoustic field becomes an efficient external excitation source. In other words, if $\omega_{acoustic} = \omega_{n,structure}$ then the forcing generated by the acoustic field may induce structural resonance.

More precisely, the standing wave creates spatial regions of high oscillatory pressure, especially near antinodes. If the structure is located in such a region, the acoustic pressure loading may be sufficiently strong to excite the structure dynamically. The response will be maximum when the wave field has a strong local amplitude, and the excitation frequency coincides with one of the natural frequencies of the structure.

Thus, the acoustic wave acts as a periodic external force, and resonance emerges through the same mechanism already shown in the equation 96.

Vibroacoustic phenomena arise from the dynamic interaction between structural mechanics and wave propagation. Mechanical structures are governed by equations of motion whose response becomes highly amplified near their natural frequencies, as demonstrated by the forced vibration solution. Meanwhile, acoustic waves propagating in bounded media may reflect and interfere, producing excitations and interfaces and standing wave patterns characterized by nodes and antinodes. When the frequency of such an acoustic field coincides with the natural frequency of a mechanical structure, the acoustic pressure acts as an external harmonic excitation capable of inducing resonance. This coupling mechanism is central to many engineering and biomedical problems, as it governs the transfer of vibrational energy from acoustic fields to solid structures and strongly influences the resulting dynamic response.

#### 2.3.2.5 Poroelastic Wave Propagation

The propagation of mechanical waves in biological tissues cannot always be described adequately by considering the medium as either a purely elastic solid or a purely compressible fluid. Many tissues, including cartilage, bone, tendon, ligament, muscle and hydrated soft connective tissues, exhibit a biphasic structure composed of a deformable solid matrix saturated by interstitial fluid. In these materials, wave propagation results from the coupled motion of the solid skeleton and the pore fluid. Poroelastic theory therefore provides a natural extension of the wave equations previously introduced for solids and fluids, since it combines elastic deformation, fluid pressure, relative fluid flow and viscous dissipation within a single continuum framework. The classical formulation was established by Biot for fluid-saturated porous solids and remains the most widely used theoretical basis for acoustic and mechanical wave propagation in porous media [148–150]. Its relevance has also been recognized in biological tissues, particularly in cancellous bone, cartilage and other hydrated fibrous tissues, where porosity, permeability and solid–fluid coupling strongly influence mechanical response [151, 152].

A saturated poroelastic medium may be represented by two interpenetrating continua: an elastic porous skeleton and a viscous fluid occupying the connected pore space. Let $\phi$ denote the porosity, $\mathbf{u}$ the displacement field of the solid skeleton, and $\mathbf{U}$ the displacement field of the pore fluid. The relative fluid displacement is commonly defined as equation 102,

$$\mathbf{w} = \phi\left(\mathbf{U} - \mathbf{u}\right), \tag{102}$$

where $\mathbf{w}$ describes the fluid motion relative to the deforming solid frame. This definition is useful because the medium does not behave as two independent phases: the deformation of the solid skeleton changes the pore volume, while the resulting fluid pressure induces stresses back onto the skeleton. The volumetric strain of the solid frame is shown in equation 103,

$$e = \nabla \cdot \mathbf{u}, \tag{103}$$

and the variation of fluid content may be written as equation 104,

$$\zeta = -\nabla \cdot \mathbf{w}. \tag{104}$$

The minus sign indicates that a positive fluid content variation corresponds to fluid accumulation within the representative volume. In a poroelastic material, the stress state is governed not only by the strain of the solid skeleton but also by the pressure of the pore fluid. For an isotropic, linear poroelastic material, the total stress tensor may be written as equation 105,

$$\boldsymbol{\sigma} = 2G\boldsymbol{\varepsilon} + \lambda e\mathbf{I} - \alpha p\mathbf{I}, \tag{105}$$

where $G$ and $\lambda$ are the Lamé parameters of the drained solid frame, $\boldsymbol{\varepsilon}$ is the infinitesimal strain tensor, $p$ is the pore pressure, $\mathbf{I}$ is the identity tensor, and $\alpha$ is the Biot coefficient. The Biot coefficient quantifies the degree of coupling between pore pressure and skeletal stress. For a fully dense solid, $\alpha \to 0$, and the equation reduces to the classical elastic stress–strain relation. For highly porous or compliant matrices, $\alpha$ approaches unity, meaning that pore pressure contributes strongly to the total stress.

The pore pressure is related to the fluid content variation and the volumetric deformation of the solid skeleton by equation 106,

$$p = M\left(\zeta - \alpha e\right), \tag{106}$$

where $M$ is the Biot modulus. This parameter represents the storage stiffness of the saturated porous medium and depends on the compressibility of the solid grains, the pore fluid and the porous frame. A common expression is equation 107,

$$\frac{1}{M} = \frac{\alpha - \phi}{K_s} + \frac{\phi}{K_f}, \tag{107}$$

where $K_s$ is the bulk modulus of the solid constituent and $K_f$ is the bulk modulus of the pore fluid. The Biot coefficient may be expressed as equation 108,

$$\alpha = 1 - \frac{K_b}{K_s}, \tag{108}$$

where $K_b$ is the drained bulk modulus of the porous skeleton. These relations show that poroelasticity naturally bridges the solid and fluid descriptions. If the pores are absent or the fluid pressure is negligible, the response tends toward classical elasticity. If the solid frame is extremely compliant and the fluid dominates the compressibility, the response approaches that of a pressure-driven acoustic fluid.

The governing equations are obtained by applying momentum balance to the coupled solid–fluid system. In Biot's low-frequency formulation, the equations of motion may be written as equation 109 and equation 110

$$\nabla \cdot \boldsymbol{\sigma} = \rho \frac{\partial^2 \mathbf{u}}{\partial t^2} + \rho_f \frac{\partial^2 \mathbf{w}}{\partial t^2}, \tag{109}$$

$$-\nabla p = \rho_f \frac{\partial^2 \mathbf{u}}{\partial t^2} + m \frac{\partial^2 \mathbf{w}}{\partial t^2} + b \frac{\partial \mathbf{w}}{\partial t}. \tag{110}$$

The average density of the saturated medium is given by equation 111.

$$\rho = (1 - \phi)\rho_s + \phi \rho_f \tag{111}$$

where $\rho_s$ and $\rho_f$ are the densities of the solid and fluid phases, respectively, $m$ is an inertial coupling parameter often related to tortuosity, and equation 112 defines the viscous drag coefficient $b$,

$$b = \frac{\eta}{\kappa} \tag{112}$$

where $\eta$ is the dynamic viscosity of the pore fluid and $\kappa$ is the intrinsic permeability of the porous skeleton. Equation 109 describes the motion of the solid frame under the action of total stress, while equation 110 describes the relative fluid motion driven by pressure gradients, inertial coupling and viscous resistance. The term $b\partial\mathbf{w}/\partial t$ is particularly important in biological tissues, since low permeability may generate strong viscous dissipation and substantial attenuation.

Substituting equations 105 and 106 into the momentum equations gives the coupled displacement–pressure form of the poroelastic wave problem shown in equations 113 and 114,

$$G\nabla^2\mathbf{u} + (\lambda + G)\nabla(\nabla \cdot \mathbf{u}) - \alpha\nabla p = \rho\frac{\partial^2\mathbf{u}}{\partial t^2} + \rho_f\frac{\partial^2\mathbf{w}}{\partial t^2}, \tag{113}$$

$$-\nabla p = \rho_f\frac{\partial^2\mathbf{u}}{\partial t^2} + m\frac{\partial^2\mathbf{w}}{\partial t^2} + b\frac{\partial\mathbf{w}}{\partial t}, \tag{114}$$

guaranteeing that the solid and fluid motions are fully coupled through the pore pressure. The pore pressure can be explicitly expressed in terms of the displacement fields by rearranging equation 106 and substituting the definitions of $\zeta$ and $e$ from equations 104 and 103, respectively. This yields equation 115.

$$p = M\left[-\nabla \cdot \mathbf{w} - \alpha\nabla \cdot \mathbf{u}\right]. \tag{115}$$

These equations demonstrate the central difference between poroelastic wave propagation and wave propagation in a single-phase solid. In an elastic solid, longitudinal and shear waves are governed only by the stiffness and density of the medium. In a poroelastic material, longitudinal deformation also generates pressure gradients, which drive relative fluid flow. This fluid flow produces viscous energy loss and modifies the effective stiffness and inertia of the medium.

The wave modes of a poroelastic medium can be identified by decomposing the displacement field into scalar and vector potentials. For longitudinal motion, the fields are irrotational and may be represented as equation 116.

$$\mathbf{u} = \nabla\varphi, \qquad \mathbf{w} = \nabla\psi. \tag{116}$$

Assuming time-harmonic plane-wave solutions of the form shown in equation 117,

$$\{\varphi, \psi, p\} = \left\{\hat{\varphi}, \hat{\psi}, \hat{p}\right\} e^{i(\omega t - \mathbf{k}\cdot\mathbf{x})}, \tag{117}$$

where $\omega$ is the angular frequency and $\mathbf{k}$ is the wave vector, the governing equations lead to a dispersion relation for compressional waves. In compact form, this relation may be expressed as equation 118.

$$\begin{vmatrix} (\lambda + 2G + \alpha^2 M)k^2 - \rho\omega^2 & \alpha M k^2 - \rho_f\omega^2 \\ \alpha M k^2 - \rho_f\omega^2 & M k^2 - m\omega^2 - i\omega b \end{vmatrix} = 0. \tag{118}$$

Solving equation 118 yields two compressional modes rather than the single longitudinal mode observed in a classical elastic solid. The first is the fast compressional wave, in which the solid skeleton and pore fluid move approximately in phase. This mode is analogous to the conventional longitudinal wave in an elastic solid, but its velocity is modified by the presence of the pore fluid and by the undrained stiffness of the medium. The second is the slow compressional wave, in which the fluid and solid phases move partially out of phase. This mode is strongly affected by permeability, viscosity and frequency, and it is usually highly attenuated in low-permeability biological tissues. The existence of these two compressional waves is one of the defining predictions of Biot theory[149,150].

The complex wavenumber may be written as equation 119,

$$k = k_r + ik_i, \tag{119}$$

where $k_r$ controls phase propagation and $k_i$ controls spatial attenuation. The corresponding phase velocity and attenuation coefficient are given by equations 120 and 121,

$$c_p = \frac{\omega}{k_r}, \tag{120}$$

$$\alpha_{\text{att}} = k_i. \tag{121}$$

Thus, unlike purely elastic wave propagation, poroelastic wave propagation is intrinsically dispersive and dissipative. The phase velocity and attenuation are frequency-dependent because the relative motion between fluid and solid depends on the competition between inertial and viscous effects. At low frequencies or low permeability, viscous drag forces the fluid and solid to move nearly together, producing an undrained response. At higher frequencies, or when permeability is sufficiently high, relative fluid motion becomes more significant, increasing attenuation and altering wave speed.

For shear waves, the motion is divergence-free and is given by equation 122.

$$\nabla \cdot \mathbf{u} = 0, \qquad \nabla \cdot \mathbf{w} = 0. \tag{122}$$

Since shear deformation does not produce a volumetric change, it does not directly generate pore pressure in the isotropic linear formulation. The shear response is therefore governed mainly by the stiffness of the solid skeleton, although the inertia and viscous interaction of the pore fluid can still influence attenuation and dispersion. In the limiting case where the fluid is locked to the skeleton, the shear wave velocity is descrybed by equation 123,

$$c_s \approx \sqrt{\frac{G}{\rho}}, \tag{123}$$

where $\rho$ is the saturated mixture density. This expression resembles the classical shear-wave velocity in solids, but with the density of the saturated medium rather than the density of the dry skeleton. In more general dynamic formulations, shear propagation is also affected by tortuosity, permeability and viscous drag.

An important limiting case is the undrained condition, in which relative fluid flow is negligible (equation 124). This condition is often relevant for wave propagation in low-permeability tissues or at high frequencies, where the fluid does not have sufficient time to redistribute during the passage of the wave.

$$\mathbf{w} \approx \mathbf{0}. \tag{124}$$

Under this condition, the fluid remains trapped within the pores during the time scale of wave propagation. From equation 115, the pore pressure becomes directly proportional to the volumetric strain of the solid frame, as shown in equation 125.

$$p \approx -\alpha M \nabla \cdot \mathbf{u}. \tag{125}$$

Substitution into Equation 105 gives an effective undrained elastic response, with an undrained bulk modulus (equation 126) that is larger than the drained bulk modulus of the skeleton due to the contribution of fluid pressurization,

$$K_u = K_b + \alpha^2 M, \tag{126}$$

where equation 108 can be used to express $\alpha$ in terms of the drained bulk modulus $K_b$ and the solid grain bulk modulus $K_s$, where equation 127 gives the drained bulk modulus in terms of the Lamé parameters.

$$K_b = \lambda + \frac{2}{3}G. \tag{127}$$

The corresponding fast compressional wave velocity may be approximated as equation 128,

$$c_{p,u} = \sqrt{\frac{K_u + \frac{4}{3}G}{\rho}}. \tag{128}$$

This result shows how poroelasticity merges the solid and fluid descriptions: the elastic skeleton provides shear resistance, while the trapped pore fluid increases the apparent compressional stiffness. This mechanism is particularly relevant in hydrated tissues subjected to rapid dynamic loading, where the fluid does not have sufficient time to redistribute.

The opposite limiting case is the drained condition, in which fluid pressure dissipates rapidly and does not contribute significantly to the total stress (equation 129).

$$p \approx 0. \tag{129}$$

The compressional wave velocity then tends toward that of the drained elastic skeleton, as shown in equation 130.

$$c_{p,d} = \sqrt{\frac{K_b + \frac{4}{3}G}{\rho}}. \tag{130}$$

The difference between Eqs. (128) and (130) highlights the role of fluid pressurization. In rapidly loaded or low-permeability media, the tissue appears stiffer because the interstitial fluid supports part of the compressive load. In slowly loaded or highly permeable media, the pressure relaxes and the response becomes closer to that of the solid matrix alone.

For biological tissues, poroelastic wave propagation is especially relevant because the apparent mechanical and acoustic properties depend on hydration, permeability, extracellular matrix composition and loading frequency. Cartilage, for example, consists of a collagen–proteoglycan solid matrix saturated with interstitial fluid. Under dynamic loading, fluid pressurization contributes substantially to load support, while relative fluid motion contributes to energy dissipation. Similarly, cancellous bone may be interpreted as a porous mineralized structure saturated by marrow, making poroelastic models useful for describing ultrasonic propagation and attenuation in trabecular architectures [151, 152]. In fibrous tissues, anisotropy further modifies the coupling between elastic deformation and fluid flow, meaning that wave speed and attenuation may depend on propagation direction relative to collagen alignment [152].

In the context of ultrasound-based therapeutic stimulation, poroelasticity provides a physically consistent framework for describing how acoustic energy is transmitted through hydrated, heterogeneous tissues. A purely fluid model captures pressure waves but neglects the shear resistance and structural deformation of the matrix. A purely elastic solid model captures skeletal deformation but neglects fluid pressure, permeability-driven dissipation and phase-dependent motion. Poroelastic theory combines both descriptions by allowing pressure waves, matrix deformation and interstitial flow to coexist. This is particularly important when estimating the mechanical stimulus delivered to tissues such as cartilage, where chondrocytes are embedded in a hydrated extracellular matrix and may respond not only to strain but also to pressure gradients, fluid flow and frequency-dependent deformation.

Therefore, poroelastic wave propagation may be understood as the natural intermediate case between acoustic propagation in fluids and elastic propagation in solids. Its governing equations reduce to classical elasticity when fluid effects are negligible, and they approach fluid-like acoustic behavior when the solid frame provides limited shear resistance. Between these limits, the coupled solid–fluid interaction produces fast and slow compressional waves, frequency-dependent attenuation, dispersion and fluid-pressure-mediated stiffening. These features make poroelasticity particularly relevant for

modelling wave propagation in biological tissues and for interpreting the transmission of therapeutic mechanical energy through complex hydrated structures.

#### 2.3.2.6 Multiscale Wave Propagation

In some particular situations, wave propagation cannot be accurately described using a single-scale continuum model. This limitation arises when the characteristic wavelength of the propagating disturbance becomes comparable to the internal structural length scales of the material. In such cases, the assumptions underlying homogenization break down, and the medium can no longer be represented by effective properties alone. Instead, a multiscale modelling strategy must be employed to capture the interaction between waves and the underlying microstructure[153].

As discussed previously, homogenization techniques rely on the assumption that the wavelength $\lambda$ s significantly larger than the characteristic microstructural length $l_c$. Under this condition, the wave interacts with the material as effectively homogeneous, and its propagation can be described using averaged material properties.

However, when $\lambda \approx l_c$ or even $\lambda < l_c$, the wave interacts directly with the microstructure. This interaction leads to phenomena such as scattering, dispersion, local resonance, and mode conversion (figure 32), which cannot be captured by classical homogenized models.

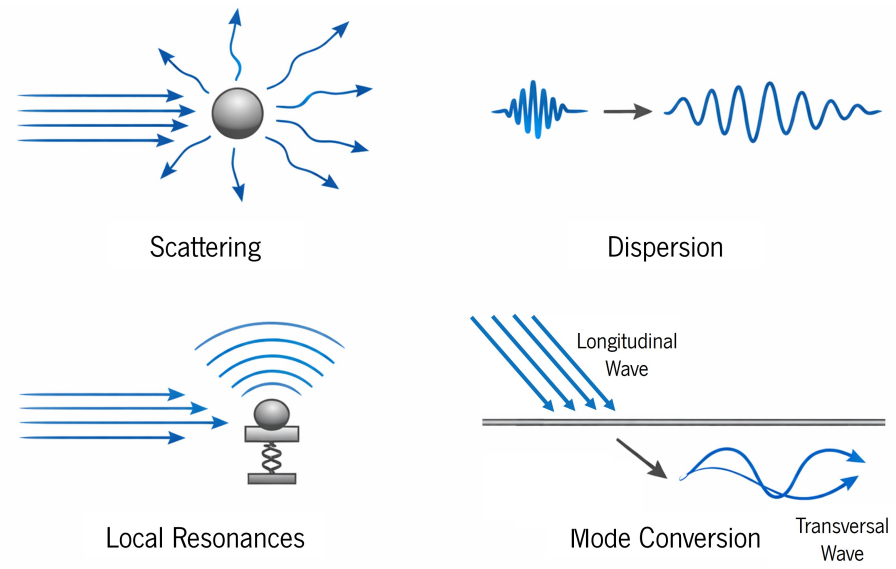



Figure 32: Depiction of scattering, dispersion, local resonance, and mode conversion effects that can occur at the microscale.

To address this, a multiscale formulation is used the displacement field is expressed as a function of both macroscopic and microscopic spatial variables. As such equation 131 is used,

$$\varepsilon = \frac{l_c}{L} \tag{131}$$

where a small parameter $\varepsilon$, represents the ratio between microstructural and macroscopic length scales. As such, two spatial variable are defined in equation 132.

$$\mathbf{x} \rightarrow \text{macroscopic coordinate}, \mathbf{y} = \frac{\mathbf{x}}{\varepsilon} \rightarrow \text{microscopic coordinate} \tag{132}$$

The displacement field is then expanded as an asymptotic series as in equation 133.

$$\mathbf{u}(\mathbf{x}, t) = \mathbf{u}_0(\mathbf{x}, \mathbf{y}, t) + \varepsilon \mathbf{u}_1(\mathbf{x}, \mathbf{y}, t) + \varepsilon^2 \mathbf{u}_2(\mathbf{x}, \mathbf{y}, t) + ... \tag{133}$$

This expansion allows the separation of wave behavior into contributions arising from different scales.

Substituting equation 133 in equation 70, it can be written as equation 134.

$$\rho(\mathbf{x}) \frac{\partial^2 u_i}{\partial t^2} = \frac{\partial}{\partial x_j} \left( C_{ijkl}(\mathbf{x}) \frac{\partial u_k}{\partial x_l} \right) \tag{134}$$

At leading order, one obtains the microscale equilibrium problem, which governs the local response within the representative microstructure. At higher orders, macroscopic behavior emerges, incorporating the influence of the microstructure on wave propagation.

A key outcome of multiscale wave analysis is the emergence of dispersion relations, where wave velocity depends on frequency. For periodic media, applying Bloch–Floquet theory leads to wave solutions of the form presented in equation 135

$$\mathbf{u}(\mathbf{x}, t) = \mathbf{U}(\mathbf{x}) e^{i(\mathbf{k} \cdot \mathbf{x} - \omega t)} \tag{135}$$

where $\mathbf{U}(\mathbf{x})$ is periodic over the unit cell of the microstructure.

Substituting into the governing equations yields a dispersion relation $\omega = \omega(\mathbf{k})$ which reflects how the internal structure of the material influences wave propagation. Unlike homogeneous media, where wave speed is constant, multiscale media exhibit frequency-dependent behavior, including band gaps where wave propagation is not permitted.

An important feature of multiscale wave propagation is the coupling between micro- and macro-scales. Local resonances within the microstructure can significantly affect the global response of the material. This is particularly relevant in materials with hierarchical or porous structures, such as biological tissues and engineered metamaterials.

The effective behavior at the macroscale is therefore not simply an average of the microscale properties, but rather the result of complex interactions between scales. These interactions may lead to enhanced attenuation, anisotropy, or selective filtering of certain frequency ranges.

### 2.3.3 From Wave Dissipation to Bioheat Transfer and Thermal Damage

The propagation of acoustic or elastic waves in biological tissues is generally accompanied by energy dissipation. In an ideal lossless medium, the mechanical energy carried by the wave is reversibly exchanged between kinetic and potential forms. However, real tissues exhibit viscosity, structural damping, scattering, relaxation processes, and, in porous media, frictional losses associated with relative fluid–solid motion. These mechanisms attenuate the propagating wave and convert part of its mechanical energy into heat. Consequently, wave propagation, heat transfer, and tissue damage are coupled phenomena: the wave field determines the local rate of energy absorption, this absorbed energy increases tissue temperature, and the resulting thermal history may lead to reversible or irreversible biological effects.

If the wave propagates through an attenuating medium, the intensity decreases with distance according to equation 136,

$$I(x) = I_0 e^{-2\alpha x}, \tag{136}$$

where $I_0$ is the incident intensity and $\alpha$ is the amplitude attenuation coefficient expressed in nepers per unit length. The factor $2\alpha$ appears because intensity is proportional to the square of the pressure amplitude. The local rate of acoustic energy converted into heat per unit volume may then be obtained from the spatial loss of intensity, as shown in equation 137,

$$Q_{\text{abs}} = -\frac{\mathrm{d}I}{\mathrm{d}x} = 2\alpha I. \tag{137}$$

Thus, for a plane wave in a homogeneous attenuating medium, the volumetric heat source generated by acoustic absorption is shown in equation 138.

$$Q_{\text{abs}} = \frac{2\alpha p_{\text{rms}}^2}{\rho c}. \tag{138}$$

This expression provides the direct link between the dissipative wave equation and the thermal problem. The attenuation coefficient controls how rapidly acoustic energy is removed from the propagating field, while the absorbed power density defines the source term that drives the temperature rise.

In more general three-dimensional problems, the absorbed power density may be expressed from the divergence of the time-averaged intensity vector as shown in equation 139,

$$Q_{\text{abs}} = -\nabla \cdot \langle \mathbf{I} \rangle, \tag{139}$$

where $\langle \mathbf{I} \rangle$ is the time-averaged acoustic intensity. For a linear acoustic field, this vector is given by equation 140,

$$\langle \mathbf{I} \rangle = \frac{1}{2} \mathrm{Re}\left(p \mathbf{v}^*\right), \tag{140}$$

where $p$ is the complex acoustic pressure, $\mathbf{v}$ is the particle velocity, $(\cdot)^*$ denotes the complex conjugate, and $\mathrm{Re}(\cdot)$ represents the real part. This form is particularly useful in numerical models because the heat source can be calculated directly from the simulated pressure and velocity fields, without reducing the problem to one-dimensional plane-wave propagation.

The same reasoning can be extended to elastic or poroelastic waves. In a viscoelastic solid, mechanical dissipation is associated with stress–strain hysteresis. The rate of mechanical energy converted into heat per unit volume can be written as equation 141,

$$Q_{\mathrm{mech}} = \left\langle \boldsymbol{\sigma} : \dot{\boldsymbol{\varepsilon}} \right\rangle_{\mathrm{diss}}, \tag{141}$$

where $\boldsymbol{\sigma}$ is the stress tensor, $\dot{\boldsymbol{\varepsilon}}$ is the strain-rate tensor, : denotes the double contraction, and $\langle \cdot \rangle_{\mathrm{diss}}$ indicates the time-averaged dissipative component. For harmonic loading in a linear viscoelastic material, the dissipated power density can be related to the imaginary part of the complex stiffness tensor, as shown in equation 142,

$$Q_{\mathrm{mech}} = \frac{\omega}{2} \boldsymbol{\varepsilon}_0^* : \mathbf{C}'' : \boldsymbol{\varepsilon}_0, \tag{142}$$

where $\omega$ is the angular frequency, $\boldsymbol{\varepsilon}_0$ is the complex strain amplitude, and $\mathbf{C}''$ is the loss component of the complex stiffness tensor. In a poroelastic medium, additional heat generation may arise from viscous drag between the pore fluid and the solid skeleton. If $\mathbf{w}$ denotes the relative fluid displacement, the corresponding dissipative contribution can be represented as equation 143,

$$Q_{\mathrm{poro}} = b \left\langle \frac{\partial \mathbf{w}}{\partial t} \cdot \frac{\partial \mathbf{w}}{\partial t} \right\rangle, \tag{143}$$

where $b = \eta / \kappa$ is the viscous drag coefficient, $\eta$ is the dynamic viscosity of the pore fluid, and $\kappa$ is the intrinsic permeability of the porous matrix. Therefore, regardless of whether the tissue is modelled as acoustic, elastic, viscoelastic or poroelastic, the dissipated mechanical energy can be introduced into the thermal problem as a volumetric heat source.

The temperature evolution in living tissue is commonly described using the Pennes bioheat equation [154]. In its general form, this equation is written as equation 144,

$$\rho_t c_t \frac{\partial T}{\partial t} = \nabla \cdot \left(k_t \nabla T\right) + \rho_b c_b \omega_b \left(T_b - T\right) + Q_{\mathrm{met}} + Q_{\mathrm{ext}}, \tag{144}$$

where $T$ is the tissue temperature, $\rho_t$ is the tissue density, $c_t$ is the tissue specific heat capacity, $k_t$ is the thermal conductivity, $\rho_b$ is the blood density, $c_b$ is the blood specific heat capacity, $\omega_b$ is the blood

perfusion rate, $T_b$ is the arterial blood temperature, $Q_{\text{met}}$ is the metabolic heat generation rate, and $Q_{\text{ext}}$ is the external heat source. In the present context, the external source is defined by wave absorption in equation 145,

$$Q_{\text{ext}} = Q_{\text{abs}}, \tag{145}$$

or, in a more general dissipative mechanical formulation, by equation 146,

$$Q_{\text{ext}} = Q_{\text{mech}} + Q_{\text{poro}} + Q_{\text{scat}} + Q_{\text{relax}}, \tag{146}$$

where $Q_{\text{scat}}$ and $Q_{\text{relax}}$ represent heat generated by scattering-related losses and molecular relaxation mechanisms, respectively, when these effects are explicitly considered. This formulation establishes the energy pathway from wave attenuation to tissue heating.

For short exposure times or weakly perfused tissues, perfusion and metabolic heat may sometimes be neglected as a first approximation. Equation 144 then reduces to equation 147,

$$\rho_t c_t \frac{\partial T}{\partial t} = \nabla \cdot (k_t \nabla T) + Q_{\text{abs}}. \tag{147}$$

If heat conduction is also neglected locally over a very short time interval, the initial temperature rise rate becomes equation 148,

$$\frac{\partial T}{\partial t} \approx \frac{Q_{\text{abs}}}{\rho_t c_t}. \tag{148}$$

Substituting equation 138 gives equation 149,

$$\frac{\partial T}{\partial t} \approx \frac{2\alpha p_{\text{rms}}^2}{\rho_t c_t \rho c}. \tag{149}$$

This expression shows that, under simplified local conditions, temperature rise increases with attenuation and pressure amplitude, and decreases with the volumetric heat capacity of the tissue. Although this approximation does not replace the full bioheat equation, it is useful for interpreting the direct thermal consequence of wave absorption.

The thermal field obtained from equation 144 can subsequently be linked to tissue injury models. A widely used approach is the Arrhenius thermal damage model, which describes damage accumulation as a thermally activated kinetic process[155]. The accumulated damage parameter $\Omega$ is defined as equation 150,

$$\Omega(t) = \int_0^t A \exp\left(-\frac{E_a}{RT(\tau)}\right) \mathrm{d}\tau, \tag{150}$$

where $A$ is the frequency factor, $E_a$ is the activation energy for thermal injury, $R$ is the universal gas constant, and $T(\tau)$ is the absolute temperature history in kelvin. The Arrhenius model is highly sensitive to temperature because the reaction rate increases exponentially with increasing $T$. Therefore, short

exposures at high temperature may produce damage comparable to longer exposures at lower temperature.

The damage parameter $\Omega$ can be related to the fraction of undamaged tissue. If $C_0$ is the initial concentration of undamaged biological material and $C(t)$ is the concentration remaining after exposure, as shown in equation 151.

$$\Omega(t) = \ln\left(\frac{C_0}{C(t)}\right). \tag{151}$$

The corresponding fraction of damaged tissue is shown in equation 152,

$$D(t) = 1 - e^{-\Omega(t)}. \tag{152}$$

A commonly used interpretation is that $\Omega = 1$ corresponds to approximately $63\%$ damage (equation 152)

$$D = 1 - e^{-1} \approx 0.632. \tag{153}$$

This threshold is often used as an indicator of irreversible thermal injury, although the specific values of $A$ and $E_a$ depend on tissue type, injury mechanism and experimental calibration.

Combining the wave equation, the bioheat equation and the Arrhenius model gives a sequential multiphysics framework. First, the dissipative wave problem is solved to obtain the pressure, velocity, displacement or strain fields. Second, the local mechanical energy loss is converted into a volumetric heat source. Third, the bioheat equation is solved to determine the transient temperature distribution. Finally, the temperature history is inserted into the Arrhenius integral to estimate the probability or extent of thermal damage. This sequence may be written schematically as shown in equation 154.

$$\{p, \mathbf{v}, \mathbf{u}, \boldsymbol{\varepsilon}\} \rightarrow Q_{\text{abs}} \rightarrow T(\mathbf{x}, t) \rightarrow \Omega(\mathbf{x}, t). \tag{154}$$

For ultrasound-based therapies, this chain is particularly important because the intended biological stimulus may be mechanical, thermal or a combination of both. Low-intensity stimulation generally aims to avoid harmful temperature elevations while still producing biologically relevant mechanical cues. In contrast, ablative ultrasound intentionally exploits absorption-induced heating to generate controlled thermal damage. In either case, safety assessment requires that the dissipated wave energy be evaluated in relation to the thermal response of the tissue and the time-dependent accumulation of damage.

The complete coupled formulation can therefore be summarized as equations 155-158.

$$\mathcal{L}_{\text{wave}}(p, \mathbf{v}, \mathbf{u}) = 0, \tag{155}$$

$$Q_{\text{abs}} = -\nabla \cdot \langle \mathbf{I} \rangle, \tag{156}$$

$$\rho_t c_t \frac{\partial T}{\partial t} = \nabla \cdot (k_t \nabla T) + \rho_b c_b \omega_b \left(T_b - T\right) + Q_{\text{met}} + Q_{\text{abs}}, \tag{157}$$

$$\Omega(t) = \int_0^t A \exp\left(-\frac{E_a}{RT(\tau)}\right) \mathrm{d}\tau. \tag{158}$$

Here, $\mathcal{L}_{\text{wave}}$ denotes the selected dissipative wave operator, which may correspond to acoustic, elastic, viscoelastic or poroelastic propagation. This formulation makes explicit that attenuation is not merely a loss of useful wave amplitude, but also a source of thermal loading. Therefore, the same material properties that determine wave transmission, namely attenuation, density, sound speed, viscosity, permeability and thermal properties, also influence the biological safety of the exposure.

In the context of patient-specific ultrasound stimulation, this coupling provides a direct computational route for defining safe operating conditions. The wave model estimates the spatial distribution of acoustic or mechanical energy, the bioheat equation predicts whether the delivered energy produces relevant temperature elevations, and the Arrhenius model evaluates whether the thermal dose approaches damaging levels. This is especially relevant near bone, cartilage and highly attenuating soft tissues, where local absorption, reflection and standing-wave formation may produce spatially heterogeneous heating. Consequently, linking dissipative wave propagation to bioheat transfer and thermal damage is essential for distinguishing mechanically effective stimulation from thermally unsafe exposure.

## 2.4 Biophysical Mechanisms of Cell Stimulation and Regeneration

Biology, when observed closely enough, stops being "soft". It becomes mechanics, fields, gradients—forces interacting with structures. Cells are not passive entities waiting for biochemical instruction; they are active sensors of their physical environment. They interpret deformation, pressure, fluid flow, and electromagnetic cues as information. In this sense, regeneration is not only a biochemical process resulting from the interaction between cells and their surroundings.

Biophysics describe how forces, material properties, and fields (mechanical, osmotic, electrical, acoustic, and thermal) are sensed, integrated, and converted into biochemical and transcriptional programs that bias cells toward survival, proliferation, migration, differentiation, matrix synthesis, or (when excessive) damage and apoptosis[156].

This section reviews the current state of the art regarding the biophysical mechanisms that govern cell stimulation and regeneration, first from a general perspective and subsequently with a specific focus on chondrocytes and cartilage tissue.

### 2.4.1 General Biophysical Mechanisms of Cell Stimulation

Cells are embedded within a complex microenvironment composed of the ECM, interstitial fluids, and neighbouring cells. This environment imposes mechanical, electrical, and transport-related stimuli that are continuously sensed and transduced into biochemical responses through a process known as mechanotransduction.

Mechanotransduction refers to the conversion of physical stimuli into intracellular biochemical signals. This process is primarily mediated by integrins and focal adhesions, which mechanically couple the ECM to the cytoskeleton, cytoskeletal structures (actin filaments, microtubules, intermediate filaments), mechanosensitive ion channels (e.g., Piezo1/2, TRPV4) and primary cilia, acting as mechanosensory organelles[157,158].

Across cell types, the most consistently supported theory for mechanotransduction is a multi-scale process, described in figure 33.

The biophysical regulation of cell regeneration can be understood as a hierarchical cascade in which external physical cues are progressively translated into biological outcomes. Initially, cells are exposed to extrinsic stimuli arising from their microenvironment, including ECM stiffness, geometric confinement, interstitial fluid flow, mechanical pressure, osmotic fluctuations, endogenous or applied electric fields,

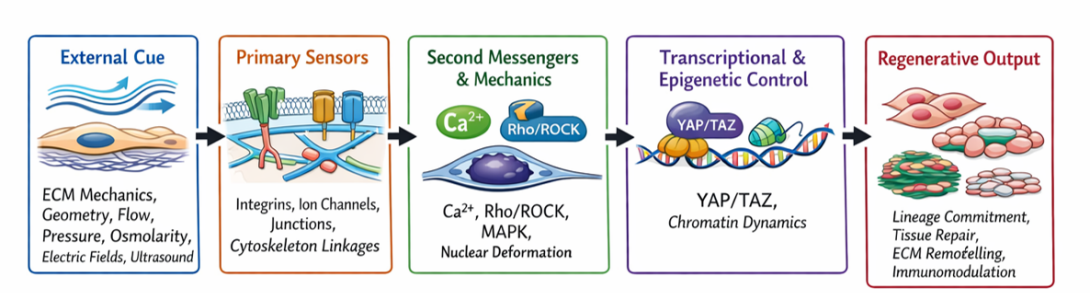



Figure 33: Depiction of the regeneration process, including the five main stages: external cue, primary sensors, second messengers and mechanics, transcriptional and epigenetic control and regenerative output.

and acoustic perturbations such as ultrasound[159,160]. Ideal stimulation regimes are further described in Table 1.

Table 1: Ideal Mechanotransduction regimes reported in the literature for cell stimulation.

| **Stimulation Type** | | **Parameters** | **Reference** |
|---|---|---|---|
| Mechanical | Static | Stimulation: 1-10 % strain<br>Catabolic/apoptotic response: 15–20% strain | [161–163] |
| | Dynamic | Frequency: 0.1–2 Hz<br>Amplitude: 2–8% strain<br>Exposure time: 1–4 h/day | [162–164] |
| | Vibration | Frequency: 1-100 Hz<br>Acceleration: 0.1–1 g, optimally 0.3–0.5 g<br>Amplitude: 10–100 μm<br>Exposure time: 10–60 min/day | [165, 166] |
| | Acoustic | Frequency: 1–1.5 MHz<br>Intensity: 30–100 mW/cm$^2$<br>Amplitude: 10–150 kPa<br>Duty cycle:20%<br>Exposure time: 10–20 min/day | [167, 168] |
| Fluid Induced shear Stress | | Frequency: 0.5–2 Hz<br>Enhanced stimulation: up to 5 Pa<br>Cytotoxic range: >10–20 Pa<br>Interstitial flow velocities: 0.1–10 μm/s | [169–171] |
| Electrical and Electromagnetic Stimulation | | Electric field strength: 10–100 mV/mm<br>Current density: 1–100 μA/cm$^2$ | [172, 173] |

These inputs are detected by primary mechanosensors, including integrin-based focal adhesions—where forces on the order of $1–10$ nN are transmitted through the so-called molecular clutch—mechanosensitive ion channels such as Piezo1/2 and TRPV4 (activated by membrane tensions of a few mN/m or strains of $5–10\%$), cell–cell junctions, and the coupled cytoskeleton–nucleus system via the LINC complex[174–178].

The activation of these sensors initiates a set of second messengers and intracellular mechanical responses, notably transient increases in intracellular calcium (often $2–3\times$ baseline), activation of Rho/ROCK pathways regulating actomyosin contractility (generating intracellular stresses in the kPa

range), and engagement of MAPK/ERK signalling cascades. Concurrently, forces are transmitted to the nucleus, inducing measurable deformations (on the order of micrometers) and remodelling of the nuclear lamina[179–182].

These processes collectively drive transcriptional and epigenetic regulation, prominently through mechanosensitive transcriptional co-activators such as YAP/TAZ, whose nuclear localization is favored on stiffer substrates ($10$–$20$ kPa), as well as through alterations in chromatin organization and accessibility that encode a form of "mechanical memory"[161,178,183–185].

Ultimately, this integrated signalling network determines the regenerative output, guiding lineage commitment, modulating extracellular matrix synthesis (e.g., collagen and proteoglycan production increases of $20$–$100\%$ under optimal stimulation), activating tissue repair programs, and shaping immunomodulatory responses. In this framework, regeneration emerges not as a direct consequence of a single stimulus, but as the result of a finely tuned, multiscale transduction of physical information into biological function.

### 2.4.2 Biophysical Mechanisms in Chondrocytes and Cartilage

Cartilage is biological tissue. Its avascular and aneural nature means that mechanical and physical stimuli are the only regulators of cell function.

Chondrocytes exist within a highly specialized ECM composed primarily of collagen type II and proteoglycans, as has been explained in section 2.1.7. Their behavior is tightly coupled to mechanical loading conditions.

Mechanical loading plays a fundamental role in the maintenance of cartilage homeostasis, acting not merely as a boundary condition but as a primary regulator of chondrocyte function. Under physiological conditions, cartilage is subjected to dynamic compressive strains typically in the range of $5$–$10\%$ at frequencies around $0.1$–$2$ Hz, corresponding to daily activities such as walking. Within this regime, dynamic compression has been consistently shown to stimulate the synthesis of key extracellular matrix components, particularly glycosaminoglycans and collagen type II, with reported increases in matrix production ranging from $20\%$ to $100\%$ depending on loading parameters[186–188].

In contrast, static loading—despite involving similar magnitudes of strain—tends to suppress anabolic activity and may even promote catabolic signalling pathways. When mechanical loading exceeds physiological thresholds, typically above $15$–$20$ MPa in terms of contact stress or beyond $15\%$ strain, cartilage begins to exhibit degenerative behavior associated with osteoarthritis. Importantly, chondrocytes do not sense compressive forces directly; rather, they respond to the resulting deformation

of the extracellular matrix and the pressurization-driven flow of interstitial fluid, as described by the biphasic theory of cartilage[189,190]

This fluid–solid interaction is central to the poroelastic nature of cartilage. With a permeability on the order of $10^{-15}$ to $10^{-16}$ m$^2$, cartilage behaves as a load-bearing structure in which up to $90\%$ of the applied stress is supported by fluid pressurization. Mechanical compression induces fluid exudation and reabsorption (figure 34), generating interstitial fluid velocities typically between $1$ and $50$ $\mu$m/s. This flow produces shear stresses at the cellular level in the range of $0.01$–$1$ Pa, values that are sufficient to activate mechanotransduction pathways. Beyond mechanical stimulation, this fluid movement also enhances the transport of nutrients, ions, and signalling molecules within the avascular cartilage matrix. The coupling between matrix deformation and fluid flow thus represents a fundamental mechanism by which mechanical information is conveyed to chondrocytes[191,192].

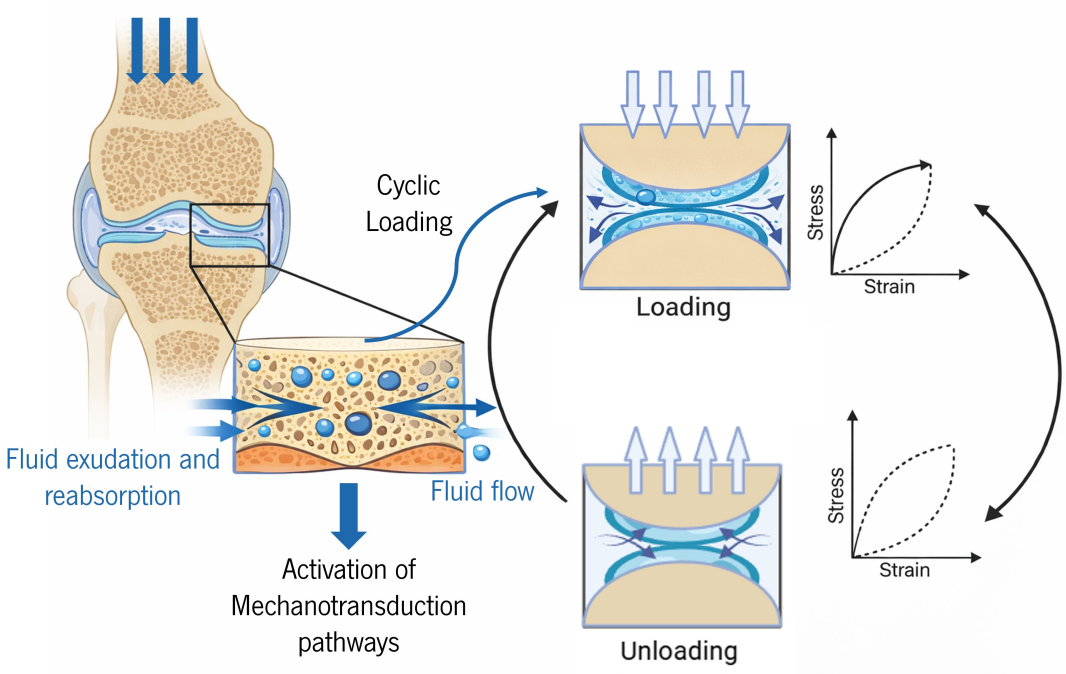



Figure 34: Schematic illustration of the biomechanical behavior of articular cartilage under loading and unloading conditions.

At the cellular level, chondrocytes are highly sensitive to osmotic and ionic changes induced by mechanical loading. The osmolarity of cartilage typically ranges between $350$ and $450$ mOsm, and mechanical compression can induce fluctuations of approximately $\pm 50$–$100$ mOsm. These changes alter local ion concentrations and activate mechanosensitive ion channels such as TRPV4 and Piezo1/2, which are known to respond to membrane strains of approximately $5$–$10\%$. Activation of these channels leads to transient increases in intracellular calcium, often reaching levels two to three times higher than baseline, which in turn drives anabolic signalling pathways associated with matrix synthesis. In this context, osmotic stress should not be interpreted as a secondary effect, but rather as an integral

component of the mechanobiological signal[193–195].

In addition to purely mechanical stimuli, acoustic stimulation has emerged as a promising non-invasive approach for cartilage regeneration, in the form of Low-Intensity Pulsed Ultrasound(LIPUS). Typical LIPUS parameters include frequencies in the range of $1–1.5$ MHz and intensities around 30 mW/cm$^2$. Under these conditions, LIPUS has been shown to increase the expression of collagen type II and aggrecan by approximately $20–80\%$, enhance chondrocyte proliferation, and reduce inflammatory mediators such as IL-1$\beta$ by up to $50\%$. The underlying mechanisms involve activation of integral-mediated signalling pathways, increased intracellular calcium levels, and stimulation of growth factor pathways such as TGF-. These effects are thought to arise from a combination of acoustic streaming (with fluid velocities on the order of $10–100$ μm/s) and stable cavitation phenomena[92,196–198].

Similarly, low-frequency mechanical vibrations have been shown to influence chondrocyte behavior and cartilage regeneration. Vibrational stimuli in the range of $10–60$ Hz, with accelerations between $0.1$ and $0.5$ g and displacement amplitudes on the order of $10–100$ μm, have been associated with enhanced chondrogenic differentiation of mesenchymal stem cells, increased extracellular matrix deposition, and modulation of inflammatory pathways. Reported increases in chondrogenic markers such as SOX9 and COL2A1 range from $25\%$ to $70\%$, while matrix production may increase by $20–50\%$ under optimal conditions. However, these effects are highly dependent on the specific combination of frequency and amplitude, with higher frequencies ($80–100$ Hz) or excessive accelerations potentially inducing catabolic responses and matrix degradation. This dual behavior suggests that chondrocytes respond to vibrational stimuli in a nonlinear manner, potentially governed by resonance-like interactions between the applied stimulus and the intrinsic mechanical properties of the cell–matrix system[199–202].

Taken together, these observations reinforce the notion that cartilage regeneration is not driven by the mere presence of mechanical or physical stimuli, but by their precise tuning within specific biophysical windows. The response of chondrocytes emerges from the interplay between solid deformation, fluid flow, ionic transport, and dynamic loading, forming a tightly coupled system in which physics and biology are inseparable.

### 2.4.3 Implications for Wave-Based Therapies

Across all scales, a consistent pattern emerges: cells respond not merely to the presence of stimuli, but to their spatiotemporal structure. Frequency, amplitude, and coupling with the surrounding medium define whether a stimulus becomes regenerative or degenerative.

For cartilage, this becomes even more critical due to its multiphase nature. Mechanical waves

propagating through such a medium may interact with its intrinsic length scales, potentially leading to local resonance phenomena, enhanced energy localization and frequency-dependent biological responses as has been explained in section 2.3.2.6. This dual-phase interaction enables the simultaneous induction of matrix deformation, fluid flow, and pressure gradients, effectively coupling multiple mechanotransduction pathways. As a result, a single wave-based stimulus can activate integrin-mediated signalling, ion channel responses, and osmotic effects concurrently. This multiphysics coupling represents a significant advantage over conventional mechanical loading strategies, which often target only one aspect of the system.

From a design perspective, the frequency of the applied wave emerges as a central parameter. At low frequencies ($10–100$ Hz), the response is dominated by bulk tissue deformation and fluid redistribution, making this regime particularly suitable for stimulating mechanosensitive pathways associated with cytoskeletal tension and matrix synthesis. At higher frequencies (kHz–MHz range), as in ultrasound, the wavelength becomes comparable to microstructural features of the tissue, enabling localized phenomena such as acoustic streaming, microscale pressure gradients, and potentially even resonance effects at the cellular or subcellular level. Although still insufficiently understood, there is growing evidence that such frequency-dependent interactions may enhance energy localization and increase the efficiency of stimulation.

However, the same parameters that enable therapeutic effects also define the boundaries of safety. Excessive intensities, inappropriate frequencies, or prolonged exposure can shift the cellular response from anabolic to catabolic. For example, vibrational stimuli around $80–100$ Hz or accelerations exceeding $1$ g have been associated with increased expression of matrix-degrading enzymes, while high-intensity ultrasound can induce thermal effects or inertial cavitation, leading to tissue damage. This underscores the necessity of identifying optimal stimulation windows, where the delivered energy is sufficient to trigger mechanotransduction without crossing into regimes of biological stress[203,204].

Despite the promising outcomes reported in the literature, a fundamental limitation persists: the lack of a unified theoretical framework linking wave propagation in complex, heterogeneous tissues to cellular-level responses. Current approaches often treat mechanical, acoustic, and electrical stimuli independently, neglecting the inherently coupled nature of these phenomena. In particular, the role of impedance mismatches, reflection, attenuation, and scattering in determining local energy distribution remains underexplored in the context of mechanobiology. Furthermore, the possibility that cells or their surrounding microenvironments may exhibit resonance-like behavior, selectively amplifying specific frequency components, represents an open and compelling research direction.

Ultimately, the effectiveness of wave-based therapies depends on the ability to operate within the narrow corridor defined by biology: low amplitude, dynamic, and precisely modulated stimuli. Within these limitations, waves become not a disturbance, but a sound that only cells can understand.

## 2.5 Computational models of acoustic Wave propagation

Acoustic wave propagation, when transposed from theory to real-world media, quickly evolves into a complex problem without an immediate solution. Biological tissues, composite materials, and multiphase systems introduce heterogeneity, anisotropy, frequency-dependent attenuation, and strong multiphysics couplings that render analytical solutions either intractable or excessively simplified. As a result, computational models emerge not merely as a convenience, but as a necessity, serving as the bridge between governing physical laws and observable phenomena. These models enable the resolution of wave fields across spatial and temporal scales, capturing interactions between pressure waves, solid deformation, and energy dissipation mechanisms. However, no single numerical approach is universally optimal; each formulation makes specific assumptions, strengths, and limitations that condition its applicability. Consequently, the study of acoustic wave propagation in complex media is inseparable from the careful selection and critical understanding of the computational frameworks used to approximate it.

### 2.5.1 Numerical Methods

Numerical methods for acoustic wave propagation are not selected arbitrarily, but are intrinsically tied to the physical regime in which the wave problem is posed. The nature of the medium (homogeneous or heterogeneous, fluid or solid), the frequency range of interest, and the presence of nonlinearities or multiphysics couplings all influence the mathematical form of the governing equations and, consequently, the suitability of a given discretization strategy. For instance, frequency-domain formulations are often preferred for steady-state, linear issues, whereas time-domain approaches become essential when dealing with transient phenomena, broadband excitations, or nonlinear wave evolution. Similarly, high-frequency regimes impose stringent requirements on spatial resolution and numerical stability, favoring methods capable of accurately capturing dispersion and discontinuities, while high attenuation or viscoelastic media may require alternative formulations, such as fractional derivative models, to reproduce experimentally observed behavior. These aspects, and the implications they have on the selection and performance of different numerical approaches, will be explored in detail throughout this section.

#### 2.5.1.1 Finite-Element Method

The Finite Element Method (FEM) is a numerical technique for obtaining approximate solutions to boundary value problems governed by partial differential equations. Its central idea lies in transforming a

continuous problem defined over a domain into a discrete system of algebraic equations by subdividing the domain into a finite number of smaller, non-overlapping elements[205].

Considering the general acoustic wave equation (equation 27) in a lossless fluid domain $\Omega$ as equation 159

$$\nabla \cdot \left(\frac{1}{\rho}\nabla p\right) - \frac{1}{K}\frac{\partial^2 p}{\partial t^2} = 0 \tag{159}$$

where $p(\mathbf{x}, t)$ is the acoustic pressure, $\rho$ is the density and $K$ is the bulk modulus of the medium. If harmonic time dependence is assumed where the acoustic pressure can be defined as $p(\mathbf{x}, t) = \hat{p}(\mathbf{x}e^{i\omega t})$, equation 159 can be rewritten as 160,

$$\nabla \cdot \left(\frac{1}{\rho}\nabla \hat{p}\right) - \frac{\omega^2}{K}\hat{p} = 0 \tag{160}$$

which is a modified form of the Helmholtz equation (equation 40). As such, this approximation can be used for both harmonic time-dependent and frequency-dependent analysis.

The FEM formulation begins by expressing this equation in its weak (variational) form. Multiplying by a test function $v$ and integrating over the domain, leading to equation 161.

$$\int_\Omega v\nabla \cdot \left(\frac{1}{\rho}\nabla \hat{p}\right) d\Omega + \int_\Omega v\frac{\omega^2}{K}\hat{p}d\Omega = 0 \tag{161}$$

Applying integration by parts (Green's theorem), the weak form in equation 161 becomes equation 162

$$\int_\Omega \frac{1}{\rho}v \cdot \nabla \hat{p}d\Omega - \int_{d\Omega} v\frac{1}{\rho}\nabla \hat{p} \cdot \mathbf{n}dT + \int_\Omega \frac{\omega^2}{K}vd\Omega = 0 \tag{162}$$

At this stage, boundary conditions emerge naturally. Neumann boundary conditions prescribe the normal derivative of the field, such as an imposed acoustic velocity or pressure gradient at the boundary, obeying equation 163[206].

$$\frac{1}{\rho}\nabla \hat{p} \cdot \mathbf{n} = g \text{ with } \partial\Omega_N \tag{163}$$

These conditions appear explicitly in the boundary integral term. In contrast, Dirichlet boundary conditions impose the value of the field itself, following equation 164,

$$\hat{p} = \overline{p} \text{ with } \partial\Omega_D \tag{164}$$

and are enforced directly on the solution space by constraining the corresponding nodal degrees of freedom[206].

The domain $\Omega$ is the discretized into finite elements, and the unknown pressure field is approximated using interpolation functions in the form of $N_i(\mathbf{x})$, obeying equation 165.

$$\hat{p}(\mathbf{x}) \approx \sum_{i=1}^{N} N_i(\mathbf{x})p_i \tag{165}$$

Using a Galerkin formulation ($v = N_j$) and assembling contributions from all elements leads to the global system represented in equation 166,

$$\mathbf{Kp} - \omega^2 \mathbf{Mp} = \mathbf{f} \tag{166}$$

where **K** is the stiffness matrix and **M** is the mass matrix, arising from spatial gradients and inertial effects, respectively.

In time-domain formulations, the system can be written as equation 167.

$$\mathbf{M}\frac{\partial^2 \mathbf{p}}{\partial t^2} + \mathbf{kp} = \mathbf{f}(t) \tag{167}$$

At this point, a fundamental distinction arises when compared to typical mechanical structural problems. For wave propagation problems, particularly at high frequencies or in large domains, explicit time integration have to be adopted. This is because they avoid solving large coupled linear systems at each time step, making them computationally efficient and well-suited for transient wave phenomena. However, this efficiency comes at the cost of conditional stability.

As such, Explicit schemes must satisfy the Courant–Friedrichs–Lewy (CFL) condition, which imposes a limit on the time step $\Delta t$ through equation 168,

$$\Delta t <= \frac{h}{c} \tag{168}$$

where $h$ is the characteristic element size and $c$ is the wave speed. Physically, this condition ensures that information does not propagate across more than one element within a single time step. If violated, the numerical solution becomes unstable, leading to non-physical growth of the wave field. In essence, the CFL condition enforces a causality constraint at the discrete level: the numerical domain of dependence must contain the physical one.

Another important aspect distinguishing wave problems from classical static or low-frequency analyses is the notion of convergence. In traditional finite element analysis, mesh convergence is assessed by refining the mesh until the solution stabilizes[205]. However, in wave propagation problems, accuracy is governed by resolution relative to the wavelength. A commonly accepted criterion is to use a minimum number of elements per wavelength (typically 6–10 for linear elements), ensuring that the oscillatory nature of the solution is adequately captured. Excessive refinement beyond this requirement does not necessarily improve accuracy and may instead increase numerical dispersion or computational cost. Therefore, wave problems are less concerned with classical mesh convergence and more with dispersion-controlled discretization[206].

From a practical standpoint, the application of FEM in engineering follows a structured workflow that reflects both the physics of the problem and the numerical constraints of the method. This process typically begins with the definition of the geometry and the identification of the relevant physical domains, followed by the assignment of material properties, including density, elastic or acoustic parameters, and attenuation characteristics when applicable. Appropriate boundary and initial conditions are then specified to represent the physical system, including sources, constraints, and absorbing boundaries where necessary. The domain is subsequently discretized into a mesh, whose resolution must be chosen in accordance with the wavelength of interest to ensure accurate wave representation. After selecting the appropriate formulation (frequency-domain or time-domain) and corresponding solver settings, the system of equations is assembled and solved. Finally, the results are post-processed and interpreted, often involving field visualization, frequency response analysis, or extraction of quantities of interest such as pressure amplitudes, transmission coefficients, or energy distributions. This workflow is inherently iterative, as insights from the solution frequently lead to refinements in geometry, mesh design, or modelling assumptions to better capture the underlying physical behaviour.

In general for linear, frequency and time-dependent formulations that are predicted to occur in short time and domains, this method is preferred. The methods discussed in the next sections are typically adopted when the studied problem cannot be studied with these constraints.

#### 2.5.1.2 Finite-Difference Method

The Finite Difference Method (FDM) is a numerical technique based on the direct discretization of the governing differential equations by replacing continuous derivatives with algebraic approximations defined on a set of discrete grid points. In contrast to the FEM, which relies on a variational formulation and unstructured meshes, FDM operates most naturally on structured grids and is particularly well-suited for problems defined over regular geometries and homogeneous or weakly heterogeneous media.

The core idea of FDM is to approximate the temporal and spatial derivatives using finite differences[207]. For example, in a one-dimensional domain (equation 30), the second-order time derivative at a grid point $x_i$ and time $t^n$ can be approximated using a central difference scheme, as is presented in equation 169

$$\frac{\partial^2 p}{\partial t^2} \approx \frac{p_i^{n+1} - 2p_i^n + p_i^{n-1}}{\Delta t^2} \tag{169}$$

Similarly, the second-order spatial derivative is approximated as equation 170

$$\frac{\partial^2 p}{\partial x^2} \approx \frac{p_i^{n+1} - 2p_i^n + p_i^{n-1}}{\Delta x^2} \tag{170}$$

Substituting equation 169 and equation 170 into the 1D wave equation (equation 30) yields the explicit equation 171.

$$p^{n+1} = 2p_i^n - p_i^{n-1} + \left(\frac{c\Delta t}{\Delta x}\right)^2 \left(p_{i+1}^n - 2p_i^n + p_{i-1}^n\right) \tag{171}$$

This expression allows the wave field to be advanced in time using only previously computed values, making FDM particularly attractive for time-domain simulations due to its simplicity and computational efficiency.

Once again, this explicit formulation is conditionally stable and must satisfy the CFL condition (equation 168) and in higher dimensions becomes more restrictive.

An important limitation of FDM arises from its reliance on structured grids, which restricts its applicability to simple geometries or requires complex grid generation techniques for irregular domains. Additionally, the method can suffer from numerical dispersion, where different frequency components propagate at incorrect speeds due to discretization errors. As with FEM, accuracy is therefore governed by the number of grid points per wavelength rather than classical mesh convergence, typically requiring at least $10–15$ points per wavelength for acceptable precision in wave propagation problems[207].

Despite these limitations, FDM remains widely used in acoustics, particularly in large-scale simulations, seismic wave modelling, and problems where computational efficiency is critical. Its straightforward implementation and natural compatibility with explicit time integration make it a powerful tool for capturing transient wave phenomena, provided that stability and dispersion constraints are carefully managed.

#### 2.5.1.3 Boundary-Element Method

The Boundary Element Method (BEM) is a numerical technique that reformulates partial differential equations into equivalent boundary integral equations, thereby reducing the dimensionality of the problem by one. In the context of acoustic wave propagation, this reduction is particularly advantageous, as it allows the solution of exterior radiation and scattering problems without the need to discretize the entire volume domain. Instead, only the boundary of the domain is discretized, leading to a significant reduction in computational effort for problems involving unbounded media[208].

Considering Helmholtz equation (equation 160) governing time-harmonic acoustic pressure $\hat{p}(\mathbf{x})$ in a homogeneous, isotropic fluid domain. As such, the fundamental solution (Green's function) for the Helmholtz equation in three dimensions is given by equation 172,

$$G(\mathbf{x}, \xi) = \frac{e^{ik|\mathbf{x}-\xi|}}{4\pi|\mathbf{x}-\xi|} \tag{172}$$

which represents the acoustic response at point **x** due to a unit point located at $\xi$.

The BEM formulation is thus derived from Green's second identity applied to $\hat{p}$ and $G$, yielding the boundary integral equation 173

$$c(\xi)\hat{p}(\xi) + \int_{\partial\Omega} \hat{p}(\mathbf{x}) \frac{\partial G(\mathbf{x}, \xi)}{\partial n} d\Gamma = \int_{\partial\Omega} \frac{\partial \hat{p}(\mathbf{x})}{\partial n} G(\mathbf{x}, \xi) d\Gamma \tag{173}$$

where $\partial/\partial n$ denotes differentiation along the outward normal, $c(\xi)$ is a coefficient depending on the location of $\xi$ (typically $1/2$for smooth boundaries) and $d\Gamma$ is the differential surface elements at the boundaries.

This integral equation expresses the pressure field entirely in terms of boundary values of pressure $\hat{p}$ and its normal derivative $\partial\hat{p}/\partial n$, which correspond physically to acoustic pressure and normal particle velocity, respectively[209].

To obtain a numerical solution, the boundary $\partial\Omega$ is discretized into elements, and the field variables are approximated using the interpolation functions in equation 174.

$$\hat{p}(\mathbf{x}) \approx \sum_{j=i}^{N} N_j(\mathbf{x}) p_j, \frac{\partial \hat{p}}{\partial n}(\mathbf{x}) \approx \sum_{j=1}^{N} N_j(\mathbf{x}) q_j \tag{174}$$

Substituting equation 174 into equation 173 and enforcing it at discrete collocation points leads to a system of equation 175

$$\mathbf{Hp} = \mathbf{Gq} \tag{175}$$

where **H** and **G** are fully populated (dense) matrices arising from the boundary integrals of the kernel and its normal derivative, and **p** and **q** are vectors of nodal pressure and normal velocity values.

Unlike FEM, where matrices are sparse due to local support of shape functions, BEM matrices are dense because each boundary node interacts with every other node through the Green's function. This leads to higher memory requirements and computational cost for large-scale problems, although techniques such as the Fast Multipole Method can be employed to mitigate this issue.

One of the principal advantages of BEM in acoustics is its natural satisfaction of the Sommerfeld radiation condition, presented in equation 176,

$$\lim_{r\to\infty} r \left( \frac{\partial \hat{p}}{\partial t} - ik\hat{p} \right) = 0 \tag{176}$$

which ensures that waves propagate outward without artificial reflections at infinity. This makes BEM particularly suitable for exterior problems such as scattering, radiation, and noise propagation in open domains, where truncation of the computational domain would otherwise introduce spurious reflections.

However, BEM also presents several limitations. The formulation is generally restricted to linear, homogeneous media, as the Green's function must be known analytically. This makes it less suitable

for problems involving strong material heterogeneity, nonlinear effects, or multiphysics coupling, where domain-based methods such as FEM are more appropriate. Additionally, the presence of singular integrals in the formulation requires careful numerical treatment, particularly when the source point coincides with the boundary.

In practice, BEM is often coupled with FEM in hybrid approaches, where FEM is used to model complex interior regions and BEM handles the unbounded exterior domain. This combination leverages the strengths of both methods: the flexibility of FEM in handling complex materials and the efficiency of BEM in representing infinite domains.

#### 2.5.1.4 Discontinuous-Galerkin Method

The Discontinuous-Galerkin method (DGM) is a FEM formulation that combines features of classical Galerkin methods and finite volume schemes, allowing for discontinuities of the solution field across element interfaces. This property makes DGM particularly well-suited for wave propagation problems, where sharp gradients, material discontinuities, and high-frequency content demand both numerical stability and local conservation[210].

Considering the acoustic wave equation (equation 27) over a domain over a domain $\Omega$, in order to construct a DGM formulation, the domain is partitioned into a set of non-overlapping elements $\Omega_e$, such that equation 177 is obeyed.

$$\Omega = \bigcup_{e=1}^{N_e} \Omega_e \tag{177}$$

Unlike classical FEM, the solution $p$ is approximated independently within each element, allowing for discontinuities across inter-element boundaries. The approximation within each element is written as equation 178,

$$p^h|_{\Omega_e}(\mathbf{x}, t) = \sum_{i=1}^{N_p} N_i^{(e)}(\mathbf{x}) p_i^{(e)}(t) \tag{178}$$

where $N_I^{(e)}$ are local shape functions and $p_i^{(e)}$ are element-specific degrees of freedom.

The governing equation is multiplied by a test function $v$, also defined locally within each element, and integrated over $\Omega_e$ as displayed in equation 179.

$$\int_{\Omega_e} v \frac{1}{c^2} \frac{\partial^2 p^h}{\partial t^2} d\Omega - \int_{\Omega_e} v \nabla p^h d\Omega = 0 \tag{179}$$

Applying integration by parts to the Laplacian term yields equation 180.

$$\int_{\Omega_e} v \frac{1}{c^2} \frac{\partial^2 p^h}{\partial t^2} d\Omega + \int_{\Omega_e} \nabla v \cdot \nabla p^h d\Omega - \int_{\partial\Omega_e} v \nabla p^h \cdot \mathbf{n} d\Gamma = 0 \tag{180}$$

At this point, a key distinction from standard FEM emerges. Since $p^h$ is discontinuous across element boundaries, the normal flux $\nabla p^h \cdot \mathbf{n}$ is not uniquely defined on interfaces. To resolve this, numerical fluxes are introduced, replacing the boundary term with a consistent and stable approximation.

If $[p]$ denotes the jump of the solution across an interface, and $\{\cdot\}$ denotes the average. A common choice for the numerical flux in acoustic problems is based on a central or upwind scheme. The DGM weak formulation can then be written as equation 181

$$\int_{\Omega_e} v \frac{1}{c^2} \frac{\partial^2 p^h}{\partial t^2} d\Omega + \int_{\Omega_e} \nabla v \cdot \nabla p^h d\Omega - \int_{\partial\Omega_e} v \hat{\nabla} p \cdot \mathbf{n} d\Gamma = 0 \tag{181}$$

where $\hat{\nabla} p$ is the numerical flux, constructed to ensure stability and inter-element coupling.

A widely used formulation for wave problems is the interior penalty DGM method, where additional stabilization terms are introduced in equation 182

$$\sum_e \Big[ \int_{\Omega_e} \frac{1}{c^2} v \frac{\partial^2 p^h}{\partial t^2} d\Omega + \int_{\Omega_e} \nabla v \cdot \nabla p^h d\Omega - \int_{\partial\Omega_e} \Big( \Big\{ \nabla p^h \Big\} \cdot \mathbf{n} v + \Big\{ \nabla v \Big\} \cdot \mathbf{n} p^h \Big) d\Gamma + \int_{\partial\Omega_e} \frac{\eta}{h} [p^h][v] d\Gamma \Big] = 0 \tag{182}$$

where $\eta$ is a stabilization parameter and $h$ is the characteristic element size.

The penalty term enforces weak continuity across interfaces while maintaining the flexibility of discontinuous approximations.

For time-domain simulations, the semi-discrete system takes the form of equation 183

$$\mathbf{M} \frac{\partial^2 \mathbf{p}}{\partial t^2} + \mathbf{K}_{DG} \mathbf{p} = \mathbf{f} \tag{183}$$

where $\mathbf{K}_{DG}$ includes both element-wise stiffness contributions and interface flux terms. Due to the element-local nature of DGM, the mass matrix $\mathbf{M}$ is typically block-diagonal, enabling efficient inversion and making the method particularly attractive for explicit time integration schemes.

Unlike the methods described in the previous section the CFL condition is altered, taking the form of equation 184

$$\Delta t <= \frac{h}{(2p+1)c} \tag{184}$$

where $p$ is the polynomial order of the approximation. Higher-order elements improve accuracy but impose stricter time step restrictions.

The DGM is especially advantageous in wave propagation problems for several reasons. First, its ability to handle discontinuities makes it well-suited for heterogeneous media and sharp material interfaces, such as those encountered in biological tissues or composite materials. Second, the use of

numerical fluxes provides enhanced control over stability and allows the method to mimic physically correct wave transmission and reflection at interfaces. Third, its local formulation facilitates parallelization and scalability, which is essential for large-scale simulations.

Moreover, DGM exhibits favourable dispersion properties, particularly when high-order polynomial bases are employed, making it highly effective for high-frequency wave propagation. Unlike standard FEM, which may suffer from spurious oscillations or require additional stabilization, DG naturally accommodates complex wave phenomena, including reflections, refractions, and mode conversions.

However, for highly attenuating media (like biological tissues), the DGM remains applicable, but its suitability depends on how attenuation is modelled. In media where attenuation is introduced through classical viscous or damping terms, DGM can incorporate these effects without fundamental difficulty. However, in cases where attenuation follows complex frequency-dependent or power-law (which is common in biological tissues) additional formulations, such as fractional derivative models or auxiliary differential equations, are required. In such scenarios, DGM can still be employed, but the computational cost increases, and stability constraints may become more restrictive. Moreover, in strongly attenuating regimes where wave amplitudes decay rapidly, the advantages of DGM in capturing high-frequency content become less critical, and alternative methods optimized for diffusive or heavily damped behavior may be more efficient, since all the methods described so far tend to demonstrate a behaviour in which the amplitude suddenly increases exponentially, often referred to as a "simulation blow-up".

#### 2.5.1.5 Fractional Derivatives Methods

Classical models of acoustic wave propagation typically assume integer-order temporal and spatial derivatives, leading to attenuation mechanisms that are either frequency-independent or proportional to integer powers of frequency. However, experimental observations in complex media consistently demonstrate power-law attenuation of the form $\alpha(f) \propto f^y$, with $0 < y < 2$. Such behaviour cannot be accurately captured using standard viscous or relaxation-based models without introducing a large number of fitting parameters. Fractional derivative methods provide a compact and physically consistent framework to model these phenomena by incorporating memory effects and nonlocality directly into the governing equations[211].

Modifying the classical wave propagation equation (equation 27), a fractional damping term can be inserted, originating equation 185,

$$\nabla^2 p - \frac{1}{c^2}\frac{\partial^2 p}{\partial t^2} - \tau \frac{\partial^{1+\gamma} p}{\partial t^{1+\gamma}} = 0 \tag{185}$$

where $\tau$ is a material parameter and $\gamma \in (0, 1)$ controls the frequency dependence of attenuation. The operator $\frac{\partial^{1+\gamma}}{\partial t^{1+\gamma}}$ is a fractional derivative, which generalizes classical differentiation to non-integer order.

Several definitions of fractional derivatives exist, with the most commonly used in wave propagation being the Caputo derivative[212]. The Caputo fractional derivative of order $\alpha \in (0, 1)$ is defined as equation 186

$$ {}^{c}D_t^{\alpha} p(t) = \frac{1}{\Gamma(1-\alpha)} \int_0^t \frac{\frac{dp(\tau)}{\tau}}{(t-\tau)^{\alpha}} d\tau \tag{186} $$

where $\Gamma(\cdot)$ is the Gamma function, in which it is possible to observe that the rate of change at time $t$ depends on the entire history of the field. Physically, this corresponds to materials with hereditary behavior, where energy dissipation is distributed over time rather than occurring instantaneously.

In the frequency domain, fractional derivatives introduce a complex, frequency-dependent term. For harmonic solutions $p(t) \leftarrow e^{i\omega t}$, the fractional derivative satisfies equation 187,

$$ \frac{\partial^{\alpha}}{\partial t^{\alpha}} \leftarrow (i\omega^{\alpha} \tag{187} $$

which to the modified Helmholtz Equation in equation 188

$$ \nabla^2 \hat{p} + k^2(\omega)\hat{p} = 0 \tag{188} $$

where the complex wave number is given by equation 189

$$ k^2(\omega) = \frac{\omega^2}{c^2} + i\tau\omega^{1+\gamma} \tag{189} $$

This formulation naturally produces attenuation following a power-law in frequency, consistent with experimental observations in soft tissues and porous media.

An alternative and widely used formulation is the fractional Laplacian model, which introduces spatial fractional derivatives to account for scattering and anomalous diffusion effects as demonstrated in equation 190,

$$ \frac{\partial^2 p}{\partial t^2} + \eta(-\nabla^2)^{\beta/2} \frac{\partial p}{\partial t} - c^2 \nabla^2 p = 0 \tag{190} $$

where $(-\nabla^2)^{\beta/2}$ is the fractional Laplacian operator and $\beta \in (0, 2)$. This operator models long-range spatial interactions, making it particularly suitable for media with strong heterogeneity and multiple scattering, where wave propagation deviates from classical diffusion or ballistic transport.

Numerical implementation of fractional derivative models presents significant challenges due to their nonlocal nature. In time-domain simulations, the evaluation of fractional derivatives requires storing the full-time history of the solution, leading to high memory and computational costs. To mitigate this, the most

employed strategy is using Grünwald–Letnikov approximations, which discretize the fractional derivative using weighted sums of past values in equation 191

$$D_t^\alpha p^n \approx \frac{1}{\Delta t^\alpha} \sum_{k=0}^{n} w_k^{(\alpha)} p^{n-k} \tag{191}$$

In spatial fractional formulations, spectral methods or matrix-transfer techniques are often used to evaluate the fractional Laplacian efficiently.

Fractional derivative methods are particularly powerful in modeling highly attenuating and scattering media, where classical wave equations fail to reproduce observed behavior. In biological tissues, for example, attenuation often follows $\alpha(f) \approx f^y$, reflecting complex microstructural interactions such as viscous losses, scattering by inhomogeneities, and structural relaxation. Similarly, in porous or composite materials, multiple scattering events lead to anomalous transport that can be effectively captured using fractional spatial operators.

However, these advantages come at a cost. Fractional models are computationally intensive, require careful numerical treatment to ensure stability, and introduce parameters that may lack direct physical interpretation. Additionally, coupling fractional models with multiphysics formulations can be nontrivial.

Despite these challenges, fractional derivative methods provide a fundamentally richer framework for describing wave propagation in complex media. Rather than forcing physical behavior into integer-order models, they embrace the intrinsic nonlocality and memory effects of real materials, offering a more faithful representation of attenuation, dispersion, and scattering phenomena across multiple scales.

#### 2.5.1.6 Absorbing Boundary Techniques

One of the main problems in the numerical simulation of acoustic wave propagation lies in the treatment of unbounded domains. Many physically relevant problems, including radiation, scattering, and transmission through open media, are posed in domains that extend effectively to infinity. However, domain-based numerical methods require truncation of the computational domain to a finite region. If this truncation is introduced as physical limit, the artificial outer boundary reflects outgoing waves back into the computational domain, thereby contaminating the solution with non-physical echoes. Absorbing boundary techniques are therefore introduced to emulate open-space radiation and minimize spurious reflections from the numerical boundary[213].

The mathematical foundation of absorbing boundaries is closely related to the Sommerfeld radiation condition explored in equation 176. This condition enforces that the solution behaves asymptotically as an outward-propagating wave. In finite computational domains, absorbing boundary techniques seek to reproduce this asymptotic behavior at a truncated boundary $\Gamma_a$.

A first class of absorbing boundaries is given by local absorbing boundary conditions (ABCs), also referred to as non-reflecting or radiation boundary conditions. The simplest form is the first-order impedance boundary condition, obtained by approximating the Sommerfeld condition locally as equation 192,

$$\frac{\partial \hat{p}}{\partial n} = ik\hat{p} \text{ on } \Gamma_a \tag{192}$$

where $\partial/\partial n$ denotes the derivative in the outward normal direction. In the time domain, the corresponding condition may be written as equation 193.

$$\frac{\partial p}{\partial n} + \frac{1}{c}\frac{\partial p}{\partial t} = 0 \tag{193}$$

This equation states that the normal gradient of the field at the artificial boundary is proportional to its time derivative, thereby allowing waves to leave the domain with minimal reflection if they strike the boundary approximately at normal incidence. Although simple and computationally inexpensive, first-order absorbing boundary conditions are only exact for planar waves impinging normally on the boundary. Their performance deteriorates for oblique incidence, curved wavefronts, and high-frequency scattering fields.

To improve absorption, higher-order absorbing boundary conditions can be introduced. For example, the Bayliss–Turkel conditions for circular or spherical truncation boundaries provide asymptotic expansions of the outgoing solution. In two dimensions, a second-order condition may be written as equation 194.

$$\frac{\partial \hat{p}}{\partial r} = ik\hat{p} - \frac{1}{2r}\hat{p} \tag{194}$$

These conditions improve the approximation of outgoing cylindrical or spherical waves, but they remain local approximations and are still limited in strongly heterogeneous or highly scattering problems, where the wave field near the boundary is not well represented by a simple asymptotic form.

A more robust strategy is provided by the Perfectly Matched Layer (PML), which has become the most widely used absorbing boundary technique in computational wave propagation. The key idea of the PML is not to impose an approximate boundary condition directly, but instead to surround the physical domain with an artificial absorbing layer in which the governing equations are modified so that outgoing waves decay exponentially without reflection at the interface between the physical domain and the absorbing region.

The classical derivation of the PML is based on a complex stretching of the spatial coordinates. For example, in one dimension, the spatial coordinate $x$ is transformed into a complex coordinate $\tilde{x}$ according to equation 195,

$$\tilde{x}(x) = int_0^x s_x(\xi)d\xi \tag{195}$$

where equation 196 must be obeyed,

$$s_x(x) = 1 + \frac{\sigma_x(x)}{i\omega} \tag{196}$$

Here, $\sigma_x(x) \geq 0$ is an attenuation profile that is zero inside the physical domain and positive within the absorbing layer. Under this transformation, spatial derivatives are modified to equation 197.

$$\frac{\partial}{\partial x} \leftarrow \frac{1}{s_x(x)} \frac{\partial}{\partial x} \tag{197}$$

In multiple dimensions, the Helmholtz equation (equation 40) thus becomes equation 198,

$$\frac{\partial}{\partial x}\Big(\frac{1}{s_x}\frac{\partial \hat{p}}{\partial x}\Big) + \frac{\partial}{\partial y}\Big(\frac{1}{s_y}\frac{\partial \hat{p}}{\partial y}\Big) + \frac{\partial}{\partial z}\Big(\frac{1}{s_z}\frac{\partial \hat{p}}{\partial z}\Big) + k^2 s_x s_y s_z \hat{p} = 0 \tag{198}$$

with appropriate tensorial forms depending on the formulation. Because the transformation is designed to be perfectly matched at the interface, a wave entering the PML does not experience an impedance mismatch and therefore, in the continuous setting, generates no reflection. Once inside the layer, the imaginary part of the stretched coordinate causes exponential attenuation.

In practical implementations, the attenuation profile $\sigma(x)$ is usually chosen as a polynomial function over the thickness $L_{PML}$ of the absorbing layer, as stated in equation 199,

$$\sigma(x) = \sigma_{max}\Big(\frac{x}{L_{PML}}\Big)^m \tag{199}$$

where $m$ is typically between 2 and 4. The maximum damping $\sigma_{max}$ is selected to achieve a target reflection coefficient $R$, often estimated by equation 200

$$\sigma_{max} \approx -\frac{(m+1)c}{2L_{PML}} \ln R \tag{200}$$

This relation shows that stronger attenuation and thicker layers reduce reflections, but also increase computational cost. An excessively strong or abruptly varying attenuation profile may itself introduce numerical reflections due to discrete mismatch, so the profile must be designed smoothly.

In the time domain, PML formulations require auxiliary variables or split-field representations. For instance, the first-order acoustic system in equations 201 and 202,

$$\frac{\partial p}{\partial t} + k\nabla v = 0 \tag{201}$$

$$\frac{\partial v}{\partial t} + \nabla p = 0 \tag{202}$$

may be modified in the PML region by introducing damping terms separately in each direction, yielding equations 203 and 204,

$$\frac{\partial p}{\partial t} + k\Big(\frac{\partial v_x}{\partial x} + \frac{\partial v_y}{\partial y} + \frac{\partial v_z}{\partial z}\Big) + \sigma_p p = 0 \tag{203}$$

$$\rho \frac{\partial v_x}{\partial t} + \frac{\partial p}{\partial x} + \sigma_x \rho v_x = 0 \tag{204}$$

with analogous equations for $v_y$ and $v_z$. More advanced unsplit PML formulations have been developed to improve numerical stability, especially in anisotropic or dispersive media.

Despite its conceptual elegance, the PML is not universally perfect in the discrete sense. In numerical practice, reflections may arise due to discretization error, insufficient layer thickness, abrupt parameter variation, anisotropy, grazing incidence, or strong heterogeneity near the interface. In addition, PML performance may degrade in media with strong evanescent content, backward waves, or certain dispersive constitutive laws. For these reasons, the PML must be carefully tuned and validated.

In highly scattering media, absorbing boundaries become more challenging because the outgoing field approaching the artificial boundary is no longer dominated by a single coherent wavefront. Instead, it may consist of multiple scattered components with a broad angular distribution and locally varying phase structure. Under such conditions, low-order absorbing boundary conditions perform poorly, since they are derived under assumptions of locally planar or spherical outgoing waves. PMLs remain the preferred option because they absorb a wide range of incidence angles and wavefront shapes more effectively. Nevertheless, in strongly scattering problems it is advisable to place the absorbing layer sufficiently far from the primary scattering region so that the field entering the absorber is less contaminated by near-field effects and sharp local heterogeneities.

In highly attenuating media, the role of absorbing boundaries changes somewhat. Because the physical medium already dissipates energy, spurious reflections from the outer boundary may be partially masked by natural attenuation. However, this does not eliminate the need for absorbing boundaries, particularly in frequency-domain problems or in simulations where even weak reflected waves may alter interference patterns or bias local response measures. In attenuating media, the PML attenuation profile must be designed consistently with the physical damping of the medium. If the physical attenuation is already strong, a thinner PML may sometimes suffice; however, if the constitutive behavior is dispersive or follows a non-classical attenuation law, the PML formulation must remain compatible with the underlying wave model. For example, in fractional or viscoacoustic media, standard PML derivations may require extension to preserve both absorption and stability.

### 2.5.2 Commercially Available Solutions

The simulation of acoustic wave propagation in biological tissues cannot be reduced to a single governing equation or a single physical domain. What appears, at first glance, as a pressure wave travelling through a medium is, in reality, a layered interaction between acoustics, structural mechanics,

and biological material behavior. Biological tissues are heterogeneous, anisotropic, and dissipative, often exhibiting viscoelastic or poroelastic characteristics. As a result, acoustic waves do not simply propagate; they are continuously transformed through coupling mechanisms that redistribute energy between pressure, deformation, and internal dissipation.

At the macroscopic scale, wave propagation through the knee involves transmission across multiple tissue layers such as skin, adipose tissue, muscle, and cartilage, each characterized by distinct acoustic impedances, attenuation laws, and mechanical responses. At smaller scales, particularly within cartilage, the problem evolves into a coupled multiphysics system in which acoustic pressure fields induce mechanical deformation in the extracellular matrix, which in turn governs the mechanical stimulation of embedded chondrocytes. This introduces the necessity of fluid–structure interaction, viscoelastic constitutive modelling, and potentially biphasic or poroelastic formulations. In fluid-like regions, acoustic pressure is typically governed by linear or nonlinear wave equations, while in solid domains, the elastodynamic equation governs displacement fields. At their interface, continuity of stress and velocity must be enforced, making the problem inherently coupled.

Single-physics solvers fail to capture these interactions, particularly at interfaces where most of the relevant physics occurs. The transmission of energy into cartilage, the formation of localized amplification zones, and the resulting mechanotransduction effects all depend on accurate coupling between acoustic and structural domains. Additionally, biological tissues exhibit frequency-dependent attenuation, often described by empirical power laws, and may require nonlinear formulations such as the Westervelt equation when dealing with higher acoustic intensities. These requirements necessitate a simulation environment capable of handling multiple interacting physical phenomena within a unified framework. A summary of the capabilities of the most competent commercial multiphysics is available in table 2.

Table 2: Comparison of available commercial software solutions for multiphysic simulation of wave propagation.

| **Feature** | **Comsol** | **ANSYS** | **k-Wave** | **Abaqus** |
|---|---|---|---|---|
| Linear Acoustics | Fully incorporated | Harmonic response (frequency domain), more options available in APDL | Fully incorporated | Harmonic response (frequency domain) |

| | | | | |
|---|---|---|---|---|
| Nonlinear Acoustics | Westervelt equation (fluid, but can be coupled)* | Available through APDL and Fluent module | Not natively implemented | N/A |
| Acoustic-Structure Interaction | Fully incorporated | Fully incorporated | N/A | Limited |
| Frequency-dependent Attenuation | Not natively implemented, but can be modelled through equations | Limited to material models | Fully implemented | Limited to material models |
| Arbitrary Multiphysics Coupling | Variety of options | limited through system coupling | N/A | Limited |
| Frequency-domain Response | Fully incorporated | Fully incorporated | Fully incorporated | Limited in vibroacoustics |
| Time- dependent propagation | Fully incorporated | Mostly through APDL | Fully integrated | Not available in vibroacoustics |

*In theory custom partial differential equations are allowed, so the user can implement any variation

As such, multiphysics software platforms are commonly employed to address such problems, each offering different capabilities and limitations in the context of acoustic wave propagation. COMSOL Multiphysics provides a highly integrated environment in which linear and nonlinear acoustics can be solved in both frequency and time domains, with strong support for fully coupled acoustic–structure interaction, and several arbitrary multiphysics coupling. It allows the implementation of frequency-dependent attenuation models, including thermoviscous losses and user-defined power-law formulations, and enables seamless coupling with structural mechanics, piezoelectricity, and thermal effects. However, this flexibility comes at a significant computational cost, particularly for nonlinear transient simulations[214].

ANSYS, through its Mechanical and Fluent environments, also supports acoustic simulations, although its multiphysics capabilities are more fragmented, with most of the features necessary being only available through its more advanced through its ANSYS Parametric Design Language (APDL). Linear acoustics can be addressed in both frequency-domain harmonic analyses and time-dependent transient

simulations, while nonlinear acoustics is not natively supported and typically requires indirect approaches. Acoustic–structure interaction is available but less intuitive to implement, and attenuation is generally introduced through material damping models such as Rayleigh damping or viscoelastic Prony series. While ANSYS is highly robust in structural mechanics, its integration of advanced acoustic physics is comparatively limited[215,216].

The k-Wave toolbox, implemented in MATLAB, is specifically designed for acoustic wave propagation and offers efficient time-domain solvers capable of handling both linear and nonlinear acoustic equations. It supports frequency-dependent attenuation through power-law absorption models and is particularly well-suited for ultrasound simulations in heterogeneous media. However, it does not provide a full framework for structural mechanics or fluid–structure interaction, limiting its applicability when solid deformation plays a critical role[217].

Abaqus, while highly advanced in nonlinear solid mechanics, provides only limited capabilities for acoustic wave propagation. Linear acoustic analyses can be performed, and time-dependent formulations are available, but nonlinear acoustics is not natively supported. Acoustic–structure interaction can be modelled, although it is not optimized for high-frequency wave propagation problems. As such, Abaqus is more suitable for problems where structural nonlinearity dominates rather than acoustic propagation[218].

### 2.5.3 Open-Source and Custom-Developed Frameworks

Open-source and custom-developed frameworks offer a fundamentally different philosophy compared to commercial multiphysics platforms, privileging flexibility and mathematical generality over out-of-the-box convenience.

Among these, FEniCS stands out as a powerful environment for implementing custom Partial-Differential Equation (PDE)-based models using the finite element method. Its formulation language allows researchers to define weak forms directly, enabling the implementation of classical linear acoustics, fully nonlinear formulations, and advanced attenuation models, including fractional Laplacians or time-fractional derivatives. This makes FEniCS particularly well-suited for research contexts where standard constitutive models are insufficient, such as modelling power-law attenuation in soft tissues or coupling microscale viscoelastic effects with macroscale wave propagation. However, this flexibility comes at the cost of requiring the user to explicitly implement interface conditions, stabilization techniques for high-frequency problems, and efficient time-integration schemes for transient nonlinear simulations[219,220].

Similarly, FEniCSx extends these capabilities with improved parallelism and performance, making it

more suitable for large-scale three-dimensional simulations or multiscale problems involving RVE[221–224].

Another relevant open-source framework is deal.II, which provides a highly optimized and flexible C++ environment for solving complex PDE systems. While less concise than FEniCS in terms of formulation, deal.II excels in handling high-order discretizations, adaptive mesh refinement, and large-scale parallel computations, which are critical for resolving wave phenomena across multiple spatial scales. Its modular structure facilitates the implementation of DGM, which are particularly advantageous for wave propagation problems involving strong material contrasts and interface discontinuities[225,226].

Another emerging tool is MFEM, which emphasizes high-performance computing and supports advanced discretization techniques, including DGM and mixed FEM. MFEM allows for the implementation of coupled multiphysics systems and is particularly suited for large-scale simulations where computational efficiency is critical. However, similar to deal.II, it requires a more substantial programming effort and deeper numerical expertise[227–229].

Open-source frameworks offer near-total freedom to define the governing physics, enabling the development of novel models—such as multiscale, fractional, or strongly nonlinear wave propagation in heterogeneous biological media—but require substantial expertise in numerical methods and computational implementation. Commercial tools, on the other hand, provide robust and user-friendly environments for standard multiphysics problems but may limit innovation when the underlying physics deviates from established formulations. For research problems at the frontier of biomechanics and acoustics (such as the fractional derivative method or some nonlinear wave formulations) open-source and custom-developed approaches often become not just advantageous, but necessary.

### 2.5.4 Model Selection and Limitations

During the course of this thesis, COMSOL Multiphysics was employed as the primary computational framework to model acoustic wave propagation in biological tissues under a multiphysics perspective. Its flexibility in handling coupled physical phenomena enabled the construction of representative models spanning from macroscopic wave transmission through layered tissues to localized mechanical responses.

In addition to standard built-in physics interfaces, a custom solver was developed within Python to address one-dimensional planar wave propagation. This approach was adopted to isolate and analyze fundamental wave phenomena under controlled conditions, providing a reduced-order yet physically meaningful representation of acoustic transmission. This custom formulation allowed systematic investigation of wave behavior while maintaining consistency with the broader multiphysics framework used in higher-dimensional models. The 1D solver therefore served both as a validation tool and as a

computationally efficient platform for parametric studies, supporting the interpretation and calibration of more complex simulations performed throughout the thesis.

## 2.6 Ultrasound Tissue-Mimicking Material Phantoms

Ultrasound tissue-mimicking phantoms (UTMP) represent a fundamental bridge between theoretical modelling, computational simulation, and experimental validation in biomedical acoustics. Their development is driven by the need to reproduce, under controlled and reproducible conditions, the complex physical behavior of biological tissues when subjected to acoustic wave propagation. In modern biomedical engineering, where ultrasound is employed not only for imaging but also for therapeutic interventions and mechanobiological stimulation, phantoms have become indispensable tools for both research and clinical translation.

### 2.6.1 Purpose and Classification of Ultrasound Phantoms

From a functional standpoint, UTMP have three functions: calibration and quality assurance of imaging systems, training and procedural simulation, and validation of computational and experimental methodologies. In diagnostic ultrasound, phantom-based calibration ensures that imaging systems produce consistent and accurate representations of tissue structures, minimizing operator-dependent variability and enabling inter-device comparability. This is particularly relevant given that ultrasound imaging quality is strongly influenced by acquisition conditions and operator expertise. Tissue-mimicking phantoms provide a standardized environment in which system performance can be quantitatively assessed[230].

In parallel, UTMP play a critical role in medical training and procedural rehearsal, particularly for ultrasound-guided interventions such as biopsies, catheter placements, and minimally invasive therapies. The ability to replicate both the acoustic response and mechanical behavior of tissues enables realistic simulation environments, allowing clinicians to develop and refine skills without ethical or safety concerns associated with in vivo experimentation. This educational role has gained increasing importance as ultrasound-based procedures continue to expand across medical specialties[230].

A further and equally significant role of UTMP lies in the validation of numerical models and the development of emerging ultrasound technologies. Computational models of wave propagation in biological tissues often rely on simplifying assumptions—such as homogeneity, linear elasticity, or isotropy—that do not fully capture the intrinsic complexity of living tissues. Experimental validation using phantoms allows these models to be systematically assessed and refined. In this context, phantoms serve as controlled physical analogs, enabling the study of acoustic phenomena such as attenuation, scattering, and nonlinear propagation under reproducible conditions[231].

At the material level, UTMP are typically designed to replicate key acoustic properties of soft tissues, including speed of sound, acoustic impedance, attenuation coefficient, and backscatter behavior. Achieving this requires the use of engineered tissue-mimicking materials (TMM), which are commonly polymer-based systems formulated using water, oil, or hybrid solvent matrices. Recent systematic reviews have shown that these materials can be broadly categorized into water-based, oil-based, and oil-in-hydrogel systems, each offering distinct advantages in terms of acoustic fidelity, stability, and manufacturability[231].

Despite these advances, a central challenge persists: no single phantom can simultaneously replicate all relevant aspects of biological tissues, which are inherently heterogeneous, anisotropic, and multiphysical. Real tissues exhibit complex interactions between solid and fluid phases, frequency-dependent viscoelastic behavior, and hierarchical structural organization across multiple length scales. As a consequence, phantom design inevitably involves trade-offs between physical accuracy, experimental control, and practical feasibility.

This inherent compromise motivates the classification of ultrasound phantoms into two principal categories: standardized (calibration-oriented) phantoms discussed in section 2.6.2 and anatomically and functionally biomimetic phantoms discussed in section 2.6.3

### 2.6.2 Standardized Tissue-Mimicking Phantoms

Standardized UTMP represent the most controlled and reproducible class of experimental media used in biomedical ultrasonics. Their design is guided not by anatomical realism, but by the need to isolate and reproduce specific acoustic phenomena under well-defined and repeatable conditions. In this sense, they form a “controlled world,” where variability is minimized and physical parameters are intentionally constrained, as is observed in figure 35.

The design of standardized UTMP is fundamentally driven by four key requirements: reproducibility, well-defined acoustic properties, long-term stability, and compliance with international standards.

Reproducibility is critical, as standardized UTMP are frequently used for calibration and benchmarking across different devices and laboratories. Consequently, fabrication protocols must yield consistent material properties across batches. Modern reviews emphasize that ideal tissue-mimicking materials should exhibit reproducible fabrication methods and tuneable acoustic and mechanical properties[231].

Closely related is the requirement for well-characterized acoustic properties, including speed of sound, attenuation, and impedance. These parameters must be measurable, stable, and adjustable to

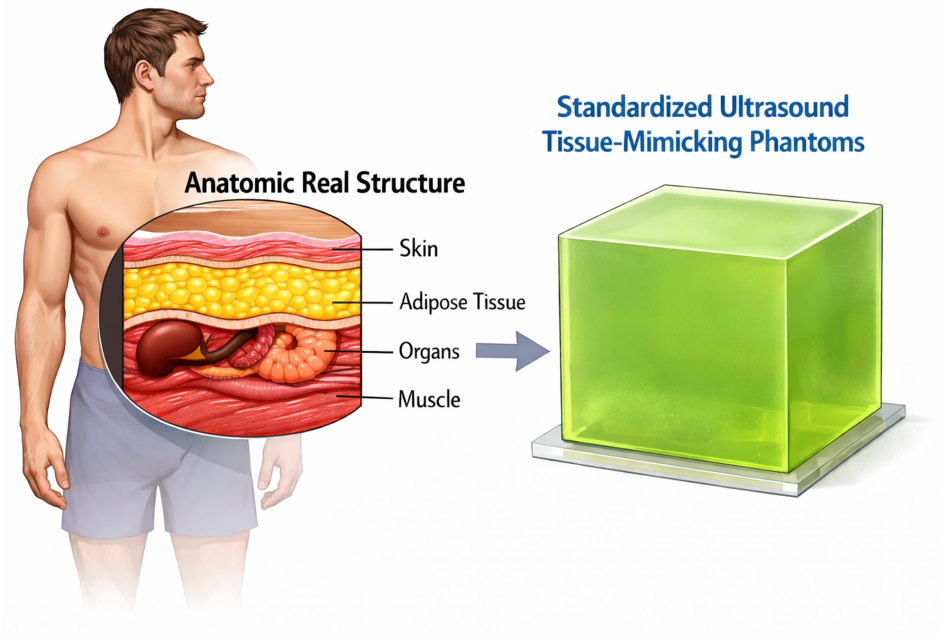



Figure 35: Representation contrasting anatomical complexity with controlled experimental modelling: a multilayered human tissue structure is simplified into a homogeneous gelatin-based standardized tissue-mimicking phantom.

match reference tissue values, underlining that standardized UTMP are engineered systems rather than biologically inspired constructs. Typically, adopted parameters are described in table 3.

Table 3: Ideal parameters used for Ultrasound Tissue-Mimicking Phantoms.

| **Speed of Sound (m/s)** | **Attenuation (dB/cm/MHz)** | **Normal Acoustic impedance (MRayl)** | **Backscattering** |
|---|---|---|---|
| 1540 | 0.5–1 | 1.5–1.7 | Must be present |

These parameters govern wave propagation, reflection, and energy dissipation. Experimental studies consistently show that successful phantoms achieve values within narrow tolerances of biological tissues[232].

These parameters are set by standards that are primarily developed by the International Electrotechnical Commission (IEC)[233–235]. These documents specify that ultrasound systems must be tested using standardized UTMPwith acoustic and thermal properties representative of human soft tissue. In addition, IEC standards define measurement protocols, such as beam characterization, thermal testing, and output power evaluation, all of which rely on phantom-based setups.

In order to achieve these properties, a relatively small set of material systems dominates the landscape of standardized ultrasound phantoms. These are described in table 4.

Table 4: Summary of Standardized Ultrasound Phantom Materials.

| Material | Speed of Sound (m/s) | Attenuation (dB/cm/MHz) | Frequency Range (MHz) | Fabrication Method | Reference |
|---|---|---|---|---|---|
| IEC Agar TMM | 1547–1548 | $0.40f + 0.0076f^2$ | 10–47 | Agar + graphite casting | [236] |
| Multi-material TMM | 1500–1600 | 0.4–1.2 | 1–10 | Composite mixing | [237] |
| Agar | 1500–1540 | 0.5–1 | 2–15 | Gel casting | [238] |
| Water-based TMM | 1540 | 0.5–1 | 1–15 | Hydrogel systems | [231] |
| PVA hydrogel | 1500–1550 | 0.4–1 | 1–10 | Freeze–thaw cycles | [239] |
| PVA-C | 1528–1531 | 0.5–0.8 | 3 | Freeze–thaw + molding | [240] |
| Agar phantom | 1520–1540 | 0.075–0.28 | 1–10 | Gel casting | [241] |
| Gelatin | 1540 | 0.6 | 1–10 | Gelation | [242] |
| Mixed TMM | 1500–1600 | 0.4–1.2 | 1–15 | Multi-material | [243] |
| Polyacrylamide | 1500 | 0.3–0.8 | 1–10 | Polymerization | [244] |
| Agar/PVA/PAA | 1480–1540 | 0.3–1 | 1–10 | Gel casting | [245] |
| PVA-C | 1520–1540 | 0.2–0.6 | 1–5 | Freeze–thaw | [246] |
| Agar/PVA mix | 1500–1550 | 0.5–1 | 1–10 | Composite gels | [247] |
| PDMS/silicone | 1000–1400 | low | 1–5 | 3D printing + casting | [248] |
| Agar/PVA hybrid | 1500–1540 | tuneable | 1–10 | Additive manufacturing molds | [249] |
| PVA-C | 1520–1540 | 0.1–0.3 | 1–10 | Freeze–thaw | [250] |
| Carbomer gel | 1567 | 0.6 | 1 | Hydrogel mixing | [232] |

| | | | | | |
|---|---|---|---|---|---|
| PVC plastisol | 1400–1500 | tuneable | 1–10 | Polymer mixing | [251] |
| Gelatin-alginate | 1520 | low | 1–10 | Gel formation | [252] |
| Composite TMM | 1500–1550 | tuneable | 1–10 | Polymer composites | [253] |
| Fiber-reinforced TMM | 1086–1127 | 0.13–0.76 | 1–5 | Composite fabrication | [254] |

Analyzing the data, Most studies report values of sound speed clustered between approximately $1500$ and $1560$ m/s, with attenuation coefficients typically ranging from $0.5$ to $1$ dB/cm/MHz. This consistency reflects a long-standing optimization effort within the field, driven by the need to reproduce the canonical acoustic properties of soft biological tissues. Water-based systems, in particular, demonstrate a remarkable ability to achieve these targets, as their intrinsic composition closely resembles that of biological tissues, which are predominantly aqueous[231,236,238–242,245–247,249,250,252]. As a result, materials such as agar, gelatin, and polyvinyl alcohol (PVA) have become the benchmark for acoustic fidelity, enabling reliable calibration, imaging validation, and inter-device comparison.

Among these, agar and gelatin-based phantoms have historically dominated due to their simplicity, low cost, and excellent agreement with target acoustic parameters. However, poor long-term stability fundamentally limits their effectiveness. These materials are prone to dehydration, microbial degradation, and mechanical instability, which restricts their use to short-term or controlled laboratory conditions[236,238,241,242,245,247,249,252]. In contrast, polyvinyl alcohol cryogels (PVA-C) represent a significant advancement, offering improved durability and tuneability through freeze–thaw processing. By adjusting the number of freeze–thaw cycles, it is possible to control both mechanical stiffness and acoustic properties, making PVA one of the most versatile and widely adopted materials in recent studies. Consequently, PVA-based systems occupy a unique position in the field, balancing acoustic realism with enhanced structural stability[240,246,250].

Synthetic polymer systems, including silicone, Polydimethylsiloxane (PDMS), urethane, and Polyvinyl Chloride (PVC) plastisol, exhibit an inverse behavior. These materials are highly stable, mechanically robust, and suitable for long-term or repeated use, particularly in training and industrial applications. However, their intrinsic acoustic properties often deviate from those of biological tissues, particularly in

terms of sound speed and attenuation. As a result, they require the incorporation of additives to achieve acceptable acoustic performance. This necessity introduces additional complexity, as tuning acoustic properties through fillers may alter density, impedance, and mechanical behavior, thereby decoupling the relationship between acoustic and structural realism[237,243–245,248,253,254].

The introduction of scattering agents and additives plays a critical role in refining the acoustic behavior of these materials. Substances such as graphite, silica, aluminum oxide, and lipid emulsions are widely used to control backscatter and attenuation. By adjusting the concentration and distribution of these inclusions, researchers can effectively tune the frequency-dependent attenuation and scattering characteristics of the phantom. This approach allows standardized phantoms to reproduce not only bulk acoustic parameters but also more subtle wave–material interactions. However, the use of additives introduces trade-offs, as modifications intended to improve acoustic realism may inadvertently affect mechanical properties or long-term stability[237,243,247].

Despite the overall success of standardized phantoms in matching key acoustic parameters, no material system simultaneously satisfies all relevant criteria. Water-based hydrogels excel in acoustic fidelity but lack durability, while synthetic polymers provide stability at the expense of acoustic realism. Hybrid and composite systems attempt to bridge this gap, combining different material phases to achieve a balance between properties. Although promising, these approaches remain constrained by the inherent difficulty of reproducing the complex, multiphysical behavior of biological tissues within a single engineered material.

More critically, the limitations of standardized UTMP extend beyond material selection to their underlying design. Most systems are homogeneous and isotropic, whereas real tissues exhibit hierarchical heterogeneity and anisotropic behavior due to structural organization, such as fiber alignment in muscle and connective tissues. Furthermore, standardized UTMP are typically modelled as linear materials, neglecting nonlinear acoustic effects that become significant at higher intensities or in therapeutic applications. Perhaps most importantly, they fail to reproduce fluid–solid interactions, which are central to the behavior of many biological tissues, particularly those exhibiting poroelastic or viscoelastic characteristics.

### 2.6.3 Anatomically and Functionally Biomimetic Phantoms

In contrast to standardized UTMP, anatomically and functionally biomimetic UTMP are designed to reproduce not only the acoustic properties of biological tissues, but also their structural organization, mechanical response, and multiphysical behavior. This shift reflects a growing understanding in the

literature that matching bulk acoustic parameters alone is insufficient to replicate the true interaction between ultrasound waves and living tissues. Instead, tissue response emerges from a complex interplay of geometry, heterogeneity, and coupled physical processes, which must be considered explicitly in phantom design.

While standardized phantoms are primarily used for calibration and validation, biomimetic systems are intended to simulate realistic clinical scenarios, including anatomical complexity and tissue-specific responses. This is particularly relevant in applications such as ultrasound-guided interventions, elastography, and therapeutic ultrasound, where both mechanical and acoustic fidelity are required[243]. In the following subsections UTMP specifically designed for the relevant biological tissues will be discussed.

#### 2.6.3.1 Skin Tissue Ultrasound Phantoms

The development of UTMP specifically targeting skin tissue has received increasing attention in recent years in both diagnostic and therapeutic applications. Unlike standardized UTMP phantoms, skin presents a unique challenge due to its layered architecture, moderate stiffness, and relatively high attenuation, which strongly influence wave transmission, reflection, and scattering at the body's interface with the external environment. Ideally, the UTMP should reach a speed of sound of $1622.11 - 1687.75$ m/s and an attenuation of $1.096$ dB/cm/MHz[135]. A summary of recent developments can be found in table 5.

Table 5: Ultrasound Phantoms Targeting Skin Tissue.

| **Phantom Type** | **Material** | **Speed of Sound (m/s)** | **Attenuation (dB/cm/MHz)** | **Key Features** | **Reference** |
|---|---|---|---|---|---|
| Multilayer skin phantom (Epidermis–dermis–hypodermis) | Agar + gelatin + additives | $1530$–$1540$ | $0.5$–$1$ | Tuneable mechanical/acoustic | [255] |
| Anisotropic phantom (Fibrous skin mimic) | Silicone + natural fibres | $1086$–$1127$ | $0.13$–$0.76$ | Anisotropy modelling | [254] |

| | | | | | |
|---|---|---|---|---|---|
| Melanoma phantom (Skin lesion model) | Gel-based | 1520–1540 | 0.5–1 | Dermatological imaging | [256] |
| Thyroid phantom (Skin layer included) | Polyacrylamide mix | 1500–1540 | 0.5–1 | Interventional training | [256] |
| Optical-acoustic phantom (Skin layer) | Silicone/fibrin | 1400–1550 | 0.3–1 | Multimodal | [257] |
| Prostate phantom (Skin layer inluded) | PVC | 1400–1500 | 0.3–0.8 | Needle interaction | [258] |
| Multiple location (skin inlcuded) | PVA | 1520–1540 | 0.1–0.3 | Mechanical realism | [250] |
| Dynamic phantom (Skin-like responsive layer) | Hydrogel composite | 1540 | 0.5–0.1 | Dynamic tissue response | [259] |

Similar to what observed in standardized UTMP, the materials utilized demonstrate the same trend, where water-based hydrogels (agar, gelatin, PVA) are widely utilized in skin-mimicking applications. These materials are consistently selected due to their ability to reproduce key acoustic parameters such as sound velocity and attenuation. Studies confirm that such hydrogels exhibit acoustic properties close to those of skin, making them suitable for superficial imaging applications, once again matching the desired Speed of Sound and Attenuation[250,255,256,259]. In particular the research performed by[255] stood out, where each skin layer is independently tuned in terms of mechanical, optical, and acoustic properties, achieving behavior comparable to real human skin. This indicates that, skin modelling is starting to be approached no longer as a homogeneous approximation, but rather as a stratified system with depth-dependent properties.

Conversely, synthetic materials such as silicone, PDMS, and PVC plastisol are widely used when

mechanical robustness and longevity are required. These materials provide stable and reusable phantom structures, particularly for training and interventional simulations. However, their acoustic properties are inherently less representative of skin tissue[254,257,258]. Standardized UTMP primarily focused on acoustic matching, but newer approaches attempt to incorporate viscoelasticity and anisotropy, reflecting the fibrous and heterogeneous nature of skin. However, achieving this remains challenging.

The findings suggest that despite the different materials utilized, none of them seem to be able the ideal speed of sound, with even the highest registered materials having lower values than what was expected. The progression observed across the data reflects a transition from simple acoustic matching toward increasingly sophisticated models that incorporate structural and mechanical realism. However, this progression also exposes the inherent difficulty of replicating skin has a complex, hierarchical interface between the external environment and the internal body.

#### 2.6.3.2 Adipose Tissue Ultrasound Phantoms

Adipose tissue presents a distinct challenge in UTMP design due to its low acoustic impedance, relatively low speed of sound of $1435.66 - 1487.88$ m/s, and moderate attenuation of $0.7264$ dB/cm/MHz[135], which differs significantly from the averaged soft tissue parameters discussed in section 2.6.2. These differences are sufficient to strongly influence wave refraction, focusing, and image quality, particularly in patients with high body fat percentages. Thus, adipose-mimicking phantoms are essential for studying image degradation, attenuation effects, and wave distortion in realistic clinical scenarios. Recent progress can be observed in table 6.

Table 6: Ultrasound Phantoms Mimicking Adipose Tissue.

| **Phantom Type** | **Material** | **Speed of Sound (m/s)** | **Attenuation (dB/cm/MHz)** | **Key Features** | **Reference** |
|---|---|---|---|---|---|
| Emulsion gel phantom | Agar + evaporated milk | 1450–1540 | 0.3–1.5 | Fat fraction control | [260] |
| Oil-gel phantom | styrene-ethylene/butylene-styrene + paraffin oil | 1480 | 0.03 | Mimics fatty breast refraction | [261] |

| | | | | | |
|---|---|---|---|---|---|
| Agarose fat phantom | Agarose + lipid emulsions | 1480–1520 | 0.5–1.2 | Controlled scattering | [262] |
| Gelatin fat-mimic | Gelatin + oil droplets | 1450–1500 | 0.4–1.0 | Simple fat dispersion | [262] |
| Silicone fat phantom | Silicone + mineral oil | 1400–1500 | 0.3–0.8 | Stable, tunable | [263] |
| PVA composite phantom | PVA + oil inclusions | 1500–1540 | 0.5–1 | Tunable stiffness | [262] |
| Oil-in-gel phantom | Gel + lipid droplets | 1450–1520 | 0.5–1.2 | Fat droplet simulation | [264] |
| Liver-Fat phantom | Agar + milk | 1450–1500 | 0.5–1.5 | Steatosis modeling | [265] |
| Fatty tissue phantom | Oil-in-gel emulsionsk | 1480–1550 | 0.3–1.5 | Computational model validation | [266] |

The most consistent observation across studies is that increasing lipid content leads to a decrease in sound speed and an increase in attenuation, directly aligning with known properties of biological fat[260–265]

Oil-based systems demonstrate high effectiveness in mimicking wave refraction at fat–tissue interfaces. These systems reproduce the key physical condition that defines adipose tissue: a lower speed of sound relative to surrounding tissues, which induces refraction and focusing errors in ultrasound imaging. This makes them particularly valuable for studying imaging artifacts and reconstruction errors in heterogeneous media[261–264].

Hydrogel-based systems offer greater control over acoustic tuning and are widely used due to their versatility. By incorporating lipid emulsions, these materials can replicate both attenuation and scattering effects associated with adipose tissue. However, studies indicate that their performance is highly dependent on emulsion stability and distribution, which can introduce variability in long-term experiments[260,262,265].

Synthetic materials such as silicone and PVC provide improved durability and mechanical stability but require significant modification to achieve realistic acoustic properties. Their lower intrinsic sound speed

can be advantageous for mimicking fat, but attenuation behaviour often needs to be artificially adjusted[263].

Another critical insight is that adipose tissue is best understood as a heterogeneous composite medium, rather than a homogeneous material. Studies modelling adipose tissue as dispersed droplets within a continuous matrix demonstrate improved agreement with experimental observations, particularly in terms of attenuation and scattering behavior. This suggests that future phantom designs should increasingly adopt multiphase and microstructural approaches, rather than relying on bulk property matching alone[265].

As such, adipose tissue phantoms are most effective when they embrace the fundamental nature of adipose tissue, not as a uniform medium, but as a dispersive, lossy, and structurally heterogeneous system. Current approaches approximate this behavior with varying degrees of success, but the full replication of adipose tissue, particularly its interaction with surrounding tissues and its role in wave distortion, remains an open challenge.

#### 2.6.3.3 Skeletal Muscle, Tendon, and Ligament Ultrasound Phantoms

UTMP designed to replicate skeletal muscle, tendons, and ligaments occupy a particularly demanding niche within biomedical ultrasonics. Unlike isotropic soft tissues, these structures are inherently fibrous, anisotropic, and mechanically stiff, with acoustic properties that depend strongly on fiber orientation and hierarchical organization. The ideal skeletal muscle ($\perp$ fibers), skeletal muscle ($\parallel$ fibers), tendon and ligament values for speed of sound are $1541.42 - 1582.94$, $1564.34 - 1633.02$, $1798 - 1856.86$ and $1621.39 - 1705.97$ m/s and attenuation of $1.150$, $2.870$, $4.617$ and $1.489$ dB/cm/MHz respectively[135]. This anisotropy directly affects wave propagation, attenuation, and scattering, making it essential for phantoms to reproduce not only bulk acoustic parameters, but also direction-dependent behavior. Table 7 compiles representative studies where phantoms were specifically designed or adapted to mimic fibrous tissues such as skeletal muscle, tendons, and ligaments.

Table 7: Ultrasound Phantoms Mimicking Skeletal Muscle, Tendons, and Ligaments.

| Phantom Type | Material | Speed of Sound (m/s) | Attenuation (dB/cm/MHz) | Key Features | Reference |
|---|---|---|---|---|---|
| Anisotropic muscle phantom | Silicone + natural fibers | 1086–1127 | 0.13–0.76 | Fiber-induced anisotropy | [254] |

| | | | | | |
|---|---|---|---|---|---|
| Layered muscle phantom | Gelatin + fiber alignment | 1540 | 0.5–1 | Directional wave propagation | [267] |
| Simplified muscle phantom | Gelatin + aluminium powder | 1549.8 | 1.14 | Directional wave propagation | [268] |
| Fat–muscle–ligament composite phantom | Oil-in-gel emulsions + fibrous inclusions | 1480–1550 | 0.3–1.5 | Multi-tissue modeling; includes interfaces relevant for ligaments | [269] |

Unlike isotropic tissues, these structures are governed by anisotropy, where acoustic and mechanical properties vary significantly depending on direction relative to fiber orientation. This is particularly evident in skeletal muscle, where wave propagation differs along and across fibers, and even more pronounced in tendons, where highly aligned collagen structures produce elevated stiffness and attenuation. Experimental data confirms that attenuation in skeletal muscle varies with fibre orientation, while tendons exhibit significantly higher attenuation due to their dense fibrous structure[135].

Compared with the soft tissues explored in the previous categories, there is a significantly reduced number of articles that introduce anisotropy in their UTMP. Although the same trend was observed when compared with the materials previously, where hydrogels had the best match for speed of sound, and silicone not being able to reach the desired speed, they are increasingly supplemented with aligned fibers, which introduce anisotropy and improve mechanical realism, allowing control over directional stiffness and wave propagation, making such composites significantly more representative of real muscle and connective tissues[254,267,269].

Tendon and ligament phantoms present an even greater challenge. These tissues exhibit higher sound speeds and significantly higher attenuation, reflecting their dense collagen composition. As of this date, these properties have yet to be replicated, since it not only stiffer materials but also highly aligned fiber architectures, which are difficult to fabricate consistently.

As such, although significant progress has been made through the use of fiber-reinforced composites and multilayer systems, current approaches still represent approximations. The full replication of fibrous

tissues remains an open problem.

#### 2.6.3.4 Bone Ultrasound Phantoms

Bone UTMP represent one of the most demanding categories in biomedical ultrasonics due to the extreme contrast in acoustic properties relative to soft tissues, as well as the strong influence of microstructure and porosity on wave propagation. Cortical bone typically exhibits longitudinal wave speeds above $2152.58 - 2498.18$ m/s and an attenuation of $1.784$ dB/cm/MHz, while trabecular bone has longitudinal wave speeds of $3080.67 - 3307.23$ m/s and an attenuation of $6.779$ dB/cm/MHz, introducing significant scattering and attenuation due to its porous architecture[135]. Modern bone UTMP are presented in table 8.

Table 8: Ultrasound Phantoms Mimicking Bone Tissue.

| **Phantom Type** | **Material** | **Speed of Sound (m/s)** | **Attenuation (dB/cm/MHz)** | **Key Features** | **Reference** |
|---|---|---|---|---|---|
| Composite bone phantom | Polymer + ceramic composite | 2500–3500 | 5–15 | Cortical + trabecular mimic | [270] |
| Cortical bone phantom | Synthetic composite cylinders | 2500–2600 | 5–10 | Axial wave propagation study | [271] |
| Porous bone phantom | 3D printed porous polymer | 2000–3500 | 5–20 | Porosity-controlled structure study | [272] |
| Skull phantom | Multilayer bone phantom | 1700–2600 | 5–15 | Cortical vs trabecular layers | [273] |
| Cortical plate phantom | Solid composite plates (short glass fibers + epoxy matrix) | 2500–3500 | 5–12 | Guided wave propagation | [274] |

Unlike soft tissues, where acoustic properties can be approximated using homogeneous hydrogels, bone requires the explicit consideration of porosity, mineralization, and hierarchical organization. Material-wise, composite systems combining polymers with mineral fillers provide the most realistic approximation of cortical bone[270,271,274]. These systems achieve sound speeds in the range of 2500–3500 m/s and high attenuation values. However, they are often brittle and difficult to fabricate, limiting their practical use. In contrast, polymer foams and porous materials offer greater flexibility and are particularly effective for mimicking trabecular bone, where scattering dominates wave propagation[272,273].

Another important observation is the role of frequency-dependent behavior. Guided wave studies show that different frequency regimes probe different aspects of bone: low frequencies are sensitive to global geometry, while higher frequencies interact more strongly with microstructure[271]. This aspect is still underexplored and reinforces the need for phantoms that can accurately reproduce both bulk and microstructural properties across a range of frequencies.

Despite these advances, no current phantom fully captures the complete behavior of bone. This is mainly due to the fact that bone exhibits a fundamentally different wave propagation behavior compared to soft biological tissues due to its solid, elastic, and anisotropic nature. In contrast to soft tissues—often reasonably approximated as fluids supporting primarily longitudinal waves, bone supports both longitudinal and transverse wave modes. As a result, wave propagation in bone involves not only multiple wave modes, but also phenomena such as mode conversion, dispersion, and direction-dependent velocities, especially at interfaces and within porous trabecular structures. This complexity stands in stark contrast to soft tissues, where the absence of shear rigidity justifies fluid-like assumptions and simplifies wave modelling. Consequently, treating bone as a fluid-like medium is fundamentally inadequate, as it neglects the rich spectrum of mechanical interactions that govern acoustic wave transmission in solid, heterogeneous structures.

#### 2.6.3.5 Cartilage Ultrasound Phantoms

The current body of literature on UTMP reveals that while substantial progress has been made for soft tissues such as liver, fat, and skeletal muscle, cartilage remains comparatively underrepresented and insufficiently developed as a dedicated phantom target. Standardized TMM consistently emphasize acoustic matching, yet these benchmarks are largely derived from bulk soft tissues properties and are not directly applicable to cartilage, which exhibits distinctly higher speed of sound ($1598.85$–$1702.75$ m/s), and markedly elevated attenuation ($4.336$ dB/cm/MHz)[135]. As a result, many widely used phantom

formulations—particularly agar-, gelatin-, or PVA-based systems—fail to reproduce the combined acoustic and mechanical profile required for realistic cartilage simulation.

No studies were found to have attempted to explicitly develop cartilage-specific UTMP. This highlights a broader issue: the field has largely prioritized acoustic matching in isolation, without adequately addressing the structural and poroelastic complexity that governs cartilage behavior under ultrasound.

A further limitation is the absence of UTMP that capture the depth-dependent anisotropy and zonal organization of articular cartilage. Native cartilage exhibits a highly organized architecture, with collagen fibers transitioning from parallel to perpendicular orientations across its thickness. This structural heterogeneity strongly influences ultrasound scattering, attenuation, and wave propagation, particularly in high-frequency imaging and elastography. Yet, existing UTMP designs are overwhelmingly homogeneous and isotropic, making them unsuitable for validating advanced techniques aimed at characterizing cartilage integrity, degeneration, or repair. Consequently, there is a disconnect between the capabilities of modern ultrasound methods and the simplified phantoms used to validate them.

As Such, there is a need for novel UTMP for advancing quantitative ultrasound approaches in orthopedics and rheumatology, particularly for early detection of cartilage degeneration and for monitoring tissue-engineered constructs.

## 2.7 Techniques for ultrasound transmission and reception

Ultrasound transmission and reception techniques collectively define how acoustic energy is generated, propagated, and ultimately captured to extract meaningful information about a medium. These processes are intrinsically coupled: the manner in which a wave is emitted determines its interaction with the medium, while the receiving system dictates how faithfully the resulting signals are interpreted. In complex and heterogeneous environments this interplay becomes critical, as attenuation, scattering, and nonlinear effects continuously reshape the wave field. This section therefore examines the fundamental principles and technologies underlying ultrasound transmission and reception, emphasizing how transducer design, excitation strategies, coupling mechanisms, detection methods, and signal conditioning together establish the complete acoustic measurement chain.

### 2.7.1 Fundamentals of Ultrasound Transduction

Ultrasound transduction lies at the core of any system that seeks to generate, control, and interpret acoustic wave propagation in complex media. At its essence, a transducer defines how energy is introduced into the system and how returning wave fields are captured, effectively shaping both the initial boundary conditions and the measurable response of the acoustic domain. In the context of this thesis, where wave propagation through heterogeneous biological tissues is of primary interest, the choice of transduction mechanism is a fundamental aspect that influences frequency content, bandwidth, spatial resolution, coupling efficiency, and ultimately the interaction with the target medium. This section therefore examines the fundamental principles governing ultrasound transduction by exploring multiple classes of transducers, each rooted in distinct physical coupling mechanisms.

#### 2.7.1.1 Piezoelectric Effect and Electromechanical Coupling

Within the framework of ultrasound transduction, the piezoelectric effect is the fundamental mechanism that enables the conversion between electrical excitation and acoustic wave generation. Ultrasonic transducers operate precisely because certain materials can directly translate an applied alternating voltage into mechanical vibrations at ultrasonic frequencies, and reciprocally convert incident acoustic waves into measurable electrical signals. This bidirectional conversion defines the core of ultrasonic transmission and reception systems, positioning piezoelectric materials as the central interface between electronic control and wave propagation in biological media.

At its most fundamental level, the piezoelectric effect arises in non-centrosymmetric materials,

where mechanical deformation induces a redistribution of internal charges, producing an electric displacement field. Conversely, when an electric field is applied, these materials undergo a strain proportional to the field intensity. This duality enables the same device to function both as an actuator (transmitter) and as a sensor (receiver), a principle that underpins most conventional ultrasound systems (figure 36). In practical ultrasonic transducers, an alternating electrical signal is applied to a piezoelectric element, typically operating near its resonant frequency, causing periodic expansion and contraction that generates pressure waves in the surrounding medium[275].

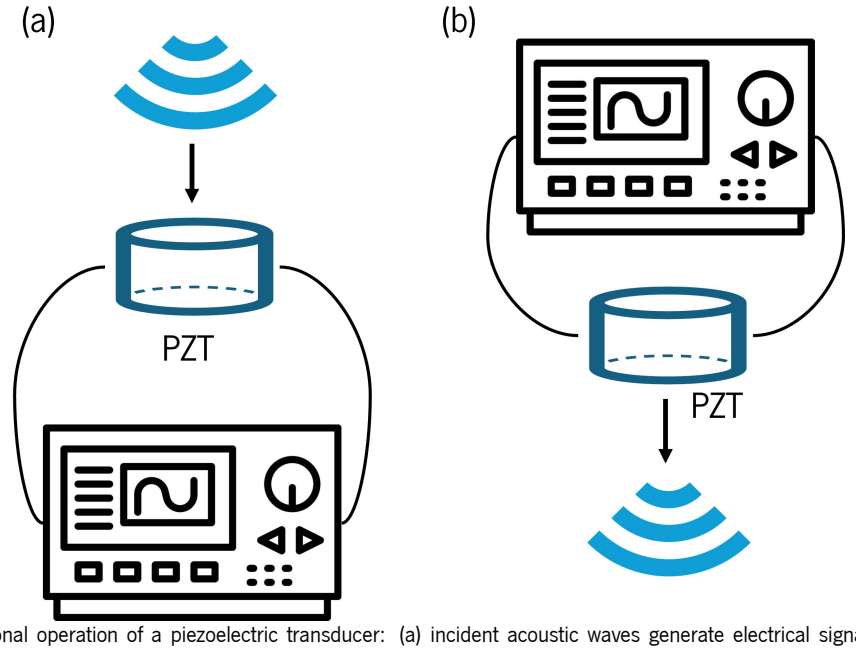



Figure 36: Bidirectional operation of a piezoelectric transducer: (a) incident acoustic waves generate electrical signals through inverse deformation (reception mode) and (b) electrical excitation induces mechanical vibrations that emit ultrasonic waves (transmission mode).

The constitutive behavior of piezoelectric materials is typically described through a set of coupled linear equations, expressed in tensor form, which relate mechanical stress **T**, strain **S**, electric field **E**, and electric displacement **D**. Their most common representation is presented in equation 205

$$\mathbf{S} = \mathbf{s}^{\mathbf{E}}\mathbf{T} + \mathbf{d}^{\mathbf{T}}\mathbf{E}, \mathbf{D} = \mathbf{d}\mathbf{T} + \varepsilon^{\mathbf{T}}\mathbf{E} \tag{205}$$

where $\mathbf{s}^{\mathbf{E}}$ is the elastic compliance at constant electric field, $\varepsilon^{\mathbf{T}}$ is the permittivity at constant stress, and **d** is the piezoelectric coupling tensor. These relations formalize the duality of the phenomenon: mechanical loading generates electric displacement, and electric fields induce strain. The tensorial nature of these coefficients reflects the intrinsic anisotropy of piezoelectric crystals, where coupling strength depends strongly on crystallographic orientation and polarization direction.

A central parameter governing the performance of ultrasound transducers is the electromechanical coupling coefficient, $k$, which quantifies the efficiency of energy conversion between electrical and

mechanical domains. In the context of ultrasound, this coefficient directly influences the amplitude of the generated acoustic pressure during transmission and the sensitivity during reception. Physically, it represents the fraction of input energy that is converted into useful acoustic energy, with higher values indicating more efficient transduction. The coupling coefficient is mode-dependent, with different values associated with longitudinal ($k_{33}$), transverse ($k_{31}$), and thickness ($k_t$) modes, reflecting the directional nature of the electromechanical interaction[276].

In practical transducer design, the electromechanical coupling is closely linked to resonance and anti-resonance phenomena. Ultrasonic transducers are typically operated near their natural frequencies, where the mechanical response is maximized, allowing efficient radiation of acoustic energy. The difference between resonance and anti-resonance frequencies provides a direct measure of the effective coupling coefficient, and this relationship is frequently used in both analytical modelling and experimental characterization of transducers. The existence of multiple vibrational modes further implies that transducer performance is inherently frequency-dependent, with different modes contributing to bandwidth, directivity, and efficiency[277].

Beyond intrinsic material properties, electromechanical coupling in ultrasound systems is strongly influenced by device architecture and boundary conditions (figure 37). At its core lies the piezoelectric element, where electrical energy is converted into mechanical vibrations and, in reverse, incoming acoustic waves are transformed back into electrical signals. Behind it, the backing material is highly attenuating material, designed to absorb backward-propagating waves and the vibration of the piezoelectric element, thereby reducing ringing and shortening the pulse, which improves axial resolution at the cost of some efficiency. Encasing the structure, the acoustic insulator prevents lateral energy leakage, forcing the vibration to remain directed forward, while also contributing to mechanical isolation from the housing. The matching layer, positioned at the front face, acts as an impedance bridge between the high acoustic impedance of the PZT and the much lower impedance of the propagating medium, as without it, most of the wave would reflect back. Surrounding everything, the metallic case provides structural integrity and protection, while also serving as part of the electrical grounding system. The electrical shield further ensures signal integrity by minimizing electromagnetic interference, preserving the fidelity of both transmitted and received signals. Finally, the wire establishes the electrical pathway, delivering excitation to the transducer and carrying the returning signal back to the acquisition system[275].

Within the broader context of ultrasound transduction, the piezoelectric effect can be understood as the physical mechanism that allows electrical control systems to interact with mechanical wave phenomena. It

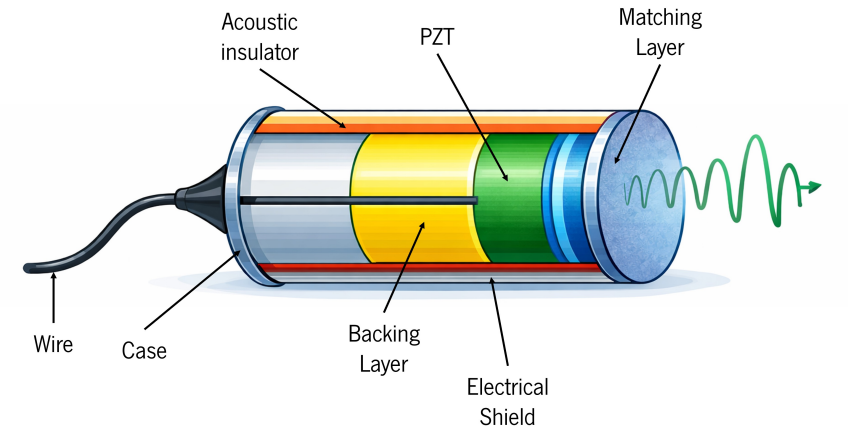



Figure 37: Cross-sectional representation of a piezoelectric transducer, illustrating the internal layered structure responsible for efficient electromechanical conversion and ultrasonic wave emission.

is the point where abstract signals become physical vibrations, and where returning echoes are translated back into measurable data.

#### 2.7.1.2 Alternative Transduction Mechanisms

Although piezoelectric materials dominate conventional ultrasound systems, alternative transduction mechanisms have emerged that challenge this paradigm by exploiting fundamentally different physical couplings. These approaches utilize alternative mechanisms acoustic waves are generation and detection, particularly in regimes where miniaturization, bandwidth, coupling conditions, or multiphysics integration impose limitations on traditional designs. In the context of ultrasound wave propagation, these mechanisms must ultimately satisfy the same requirement: the efficient conversion between an external excitation (electrical, optical, or magnetic) and a mechanical pressure field capable of propagating through heterogeneous media.

Capacitive micromachined ultrasonic transducers (CMUTs) represent one of the most mature alternatives to piezoelectric devices, operating on an electrostatic rather than electromechanical polarization principle. A typical CMUT consists of a micromachined membrane suspended over a vacuum cavity, forming a parallel-plate capacitor with the substrate (figure 38). When a DC bias voltage is applied and superimposed with an AC excitation, electrostatic forces induce membrane vibration, generating ultrasonic waves in the surrounding medium. Conversely, incoming acoustic waves deform the membrane, producing variations in capacitance that are converted into electrical signals. This mechanism fundamentally shifts the transduction process from bulk material deformation to surface-controlled electrostatic actuation, enabling precise control over vibration modes and frequency response[278,279].

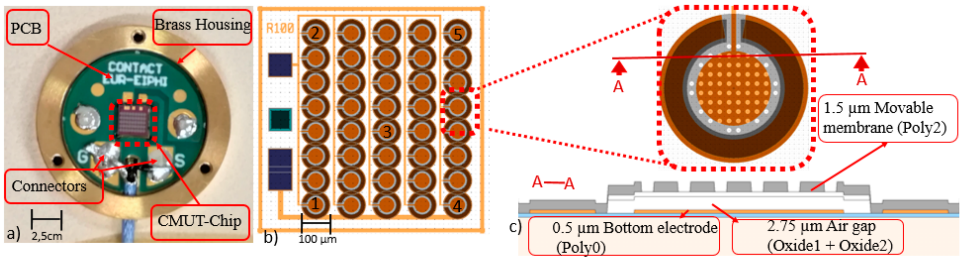



Figure 38: Representative microfabricated capacitive micromachined ultrasonic transducer: (a) packaged device showing PCB, connectors, and brass housing; (b) array layout of individual cells; (c) cross-sectional view detailing the membrane, air gap, and electrodes that enable electrostatic actuation and acoustic wave generation/detection.[279].

Optoacoustic and laser-based ultrasound generation introduces a fundamentally different paradigm, where acoustic waves are generated through thermoelastic expansion induced by optical absorption 39. In this mechanism, a short laser pulse is absorbed by a material—either a dedicated absorber layer or the biological tissue itself—resulting in rapid localized heating and subsequent expansion, which launches a wave into the medium. This process, often referred to as the photoacoustic effect, bypasses the need for direct mechanical actuation and instead leverages energy conversion between optical and mechanical domains. The resulting acoustic waves retain the propagation characteristics of conventional ultrasound, including reflection, scattering, and attenuation in heterogeneous media, but their origin is fundamentally different[280]. One of the key advantages of optoacoustic generation lies in its ability to achieve extremely high bandwidth and spatial resolution, as the temporal profile of the generated acoustic pulse is directly related to the laser pulse duration, often in the nanosecond regime. This enables the generation of broadband ultrasonic waves that can capture fine structural details. Additionally, optical methods allow for remote or non-contact generation of ultrasound, which can be particularly advantageous in scenarios where physical coupling is difficult or undesirable. On the detection side, optical ultrasound sensors offer ultra-high sensitivity and wide bandwidth, overcoming limitations associated with the size-dependent sensitivity of piezoelectric sensors. However, these systems are inherently dependent on optical access, and their performance can be affected by scattering and absorption in the propagation media, which limits penetration[281].

Magnetostrictive and electromagnetic acoustic transducers (EMATs) introduce yet another layer of abstraction, where ultrasound generation arises from magnetic-field-induced strain or Lorentz-force-driven motion in conductive materials (figure 40). In magnetostrictive systems, ferromagnetic materials undergo dimensional changes when subjected to a varying magnetic field, producing mechanical vibrations at ultrasonic frequencies. These vibrations then propagate as elastic waves through the material. In EMATs, the interaction between an induced current and a static magnetic field generates Lorentz forces, directly exciting mechanical waves without physical contact. This

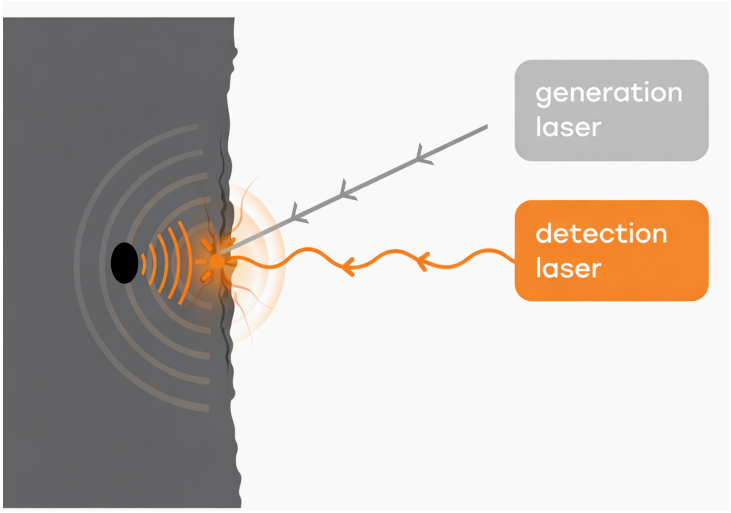



Figure 39: Laser-based ultrasonic Propagation of an acoustic wave. Since a single laser can't send and read a wave, a generation laser induces acoustic waves near the interest zone, while a detection laser measures the returning surface response.

non-contact nature distinguishes EMATs from both piezoelectric and capacitive systems, eliminating the need for coupling media and enabling operation in harsh environments. From the standpoint of wave propagation, EMATs are particularly versatile, capable of generating a wide range of wave modes, including bulk longitudinal waves, shear waves, and guided waves such as Lamb and surface waves. This versatility arises from the ability to tailor the spatial distribution of electromagnetic forces through coil and magnet design, effectively shaping the initial conditions of the propagating acoustic field. However, this flexibility comes at the cost of lower transduction efficiency compared to piezoelectric systems, as well as limitations to conductive or magnetostrictive materials, restricting their applicability in soft biological tissues. Although magnetostrictive approaches remain highly relevant in structural health monitoring and non-destructive evaluation, where contactless operation and mode selectivity are critical, for propagation in biological tissues its usefulness is quite limited, since biological tissues are not inherently magnetic[282].

Emerging approaches continue to blur the boundaries between these transduction mechanisms, often combining multiple physical principles to overcome individual limitations. Hybrid systems, such as CMUT-based photoacoustic sensors or optically interrogated MEMS devices, leverage the strengths of each domain to achieve enhanced sensitivity, bandwidth, and integration. Optical ring resonators embedded within micromachined membranes, for example, enable purely optical detection of ultrasonic vibrations, eliminating electrical noise sources and enabling unprecedented sensitivity at micro- and nanoscale dimensions. Similarly, flexible and conformable transducers based on micromachined architectures are expanding the applicability of ultrasound to wearable and implantable devices, where traditional rigid piezoelectric elements are unsuitable[283]

In the broader context of ultrasound wave propagation, these alternative transduction mechanisms do

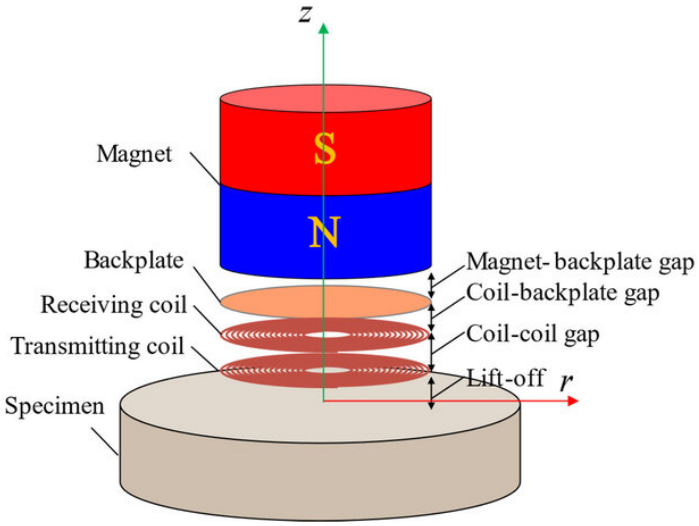



Figure 40: Schematic of an electromagnetic acoustic transducer showing the magnet, backplate, transmitting and receiving coils, and key spacing parameters governing wave generation and detection in the specimen[282].

not alter the governing physics of the acoustic field itself, but they redefine the boundary conditions through which that field is generated and sensed. The choice of transduction mechanism therefore becomes a question not only of efficiency, but of compatibility with the physical environment, desired frequency content, spatial resolution, and system integration.

## 2.7.2 Ultrasound Transmission Techniques

Ultrasound transmission techniques define how acoustic energy is generated, shaped, and launched into a propagation medium, establishing the initial conditions that govern all subsequent wave behavior. The characteristics of this field, including its frequency content, spatial distribution, intensity, and directionality, are not incidental but are directly determined by the transmission methodology employed. This section therefore examines the fundamental techniques used to transmit ultrasound, focusing on how transducer geometry, beamforming strategies, coupling mechanisms and excitation signals collectively shape the emitted wave and determine its interaction with the medium.

### 2.7.2.1 Transducer Design and Geometry

The design and geometry of an ultrasound transducer define the spatial and temporal characteristics of the generated acoustic field, acting as the primary boundary condition from which wave propagation emerges. In essence, the geometry of the transducer governs how mechanical vibrations are distributed in space, which in turn determines beam shape, focusing capability, penetration depth, and resolution. As such, transducer design allows a controlled manipulation of wavefront formation.

Single-element transducers represent the most fundamental configuration, consisting of a monolithic piezoelectric element that vibrates uniformly when exautocited. In these systems, the emitted acoustic field is largely dictated by the aperture diameter and operating frequency, with beam divergence arising from diffraction effects. The near-field (Fresnel zone) and far-field (Fraunhofer zone) behavior are directly linked to these geometric parameters, with the beam initially narrowing before diverging as it propagates. In practice, the performance of single-element transducers is strongly influenced by geometric parameters such as the radius of curvature and aperture size, which determine focal depth and beam width. A critical distinction in transducer design lies between focused and unfocused sources, which fundamentally alters how acoustic energy is distributed in space. Unfocused transducers emit waves that diverge naturally due to diffraction, resulting in a broad beam with lower amplitude at any given point. Focusing can be achieved geometrically, through curved transducer surfaces or acoustic lenses, or electronically, through phased array beamforming techniques.

Focused single-element transducers are typically achieved either by mechanically shaping the piezoelectric element into a concave geometry or by adding an acoustic lens, enabling concentration of acoustic energy at a predefined focal point, as is illustrated in figure 41. High-frequency designs ($50$–$100$ MHz) demonstrate that careful selection of matching layers, backing materials, and curvature allows for bandwidths exceeding $50\%$ while maintaining high sensitivity, highlighting the delicate balance between geometric constraints and acoustic performance. Despite their simplicity and high sensitivity, single-element transducers lack electronic beam steering capabilities, requiring mechanical movement to scan a region of interest, which limits their applicability in dynamic or real-time imaging scenarios[284,285].

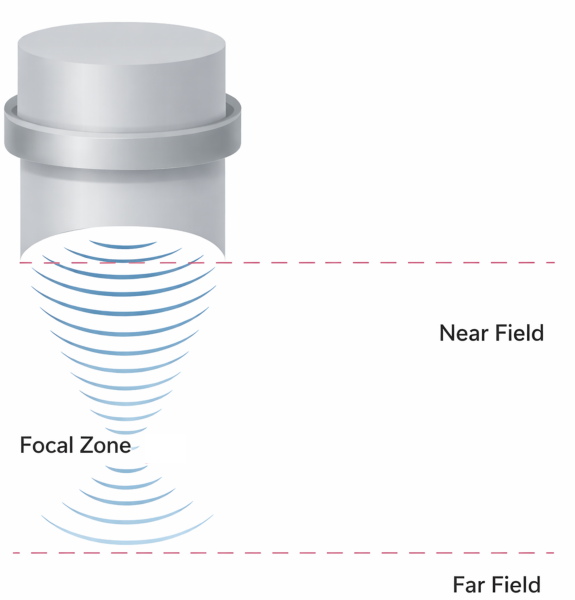



Figure 41: Single-element ultrasonic transducer emitting converging acoustic waves, illustrating the formation of a focal zone within the near field and the transition to the far field beyond.

To overcome these limitations, array-based transducers introduce spatial discretization of the aperture into multiple independently controlled elements, enabling dynamic control of the emitted wavefront. Linear arrays, one of the most widely used configurations in medical ultrasound, consist of a one-dimensional arrangement of elements that can be sequentially or simultaneously activated to generate and receive acoustic waves (figure 42). By applying time delays across the array, constructive interference can be engineered to produce focused beams and steer them laterally without mechanical motion. This principle, known as beamforming, allows linear arrays to image two-dimensional planes efficiently, making them suitable for applications such as soft tissue imaging and real-time diagnostics. Phased array transducers extend this concept by allowing full electronic control over both beam steering and focusing through precise timing of element excitation. Each element in the array emits a wave with a controlled phase delay, resulting in constructive interference along a desired direction and destructive interference elsewhere. This enables the formation of steerable and dynamically focused beams, effectively transforming the transducer into an acoustic antenna. The focal spot size and beam direction are governed by parameters such as aperture size, wavelength, and focal length, with relationships analogous to electromagnetic antenna theory. Phased arrays are particularly advantageous in applications requiring deep penetration and precise targeting, such as therapeutic ultrasound and neuromodulation, where beam steering must compensate for heterogeneous tissue structures. Optimization of phased array geometry involves trade-offs between spatial resolution, power efficiency, and the suppression of side lobes, which can lead to unintended energy deposition[286–288].

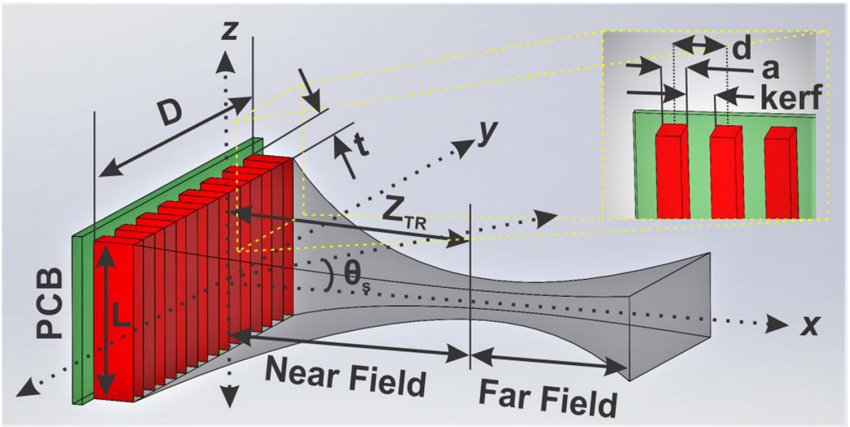



Figure 42: Linear phased-array ultrasonic transducer showing element geometry (pitch, kerf, thickness) and beam steering/focusing, illustrating near-field formation and divergence into the far field.[286].

Annular arrays represent a distinct class of transducer geometry, characterized by concentric ring elements rather than linear arrangements. This configuration preserves axial symmetry, making it particularly suitable for applications requiring high-resolution focusing along a central point (figure 43). Each ring can be driven independently, allowing dynamic focusing along the axial direction while

maintaining a symmetric beam profile. Studies have demonstrated that annular arrays can achieve improved depth-of-field and enhanced focusing performance compared to single-element transducers, particularly in high-frequency imaging applications. Furthermore, the distribution of excitation across concentric elements can be analysed in the wave number domain, revealing how specific geometries influence mode selection and beam focusing through spectral filtering of the acoustic field. This calls attention to the deep connection between geometry and wave physics, where the spatial arrangement of elements effectively defines the frequency and directionality content of the emitted waves[289,290].

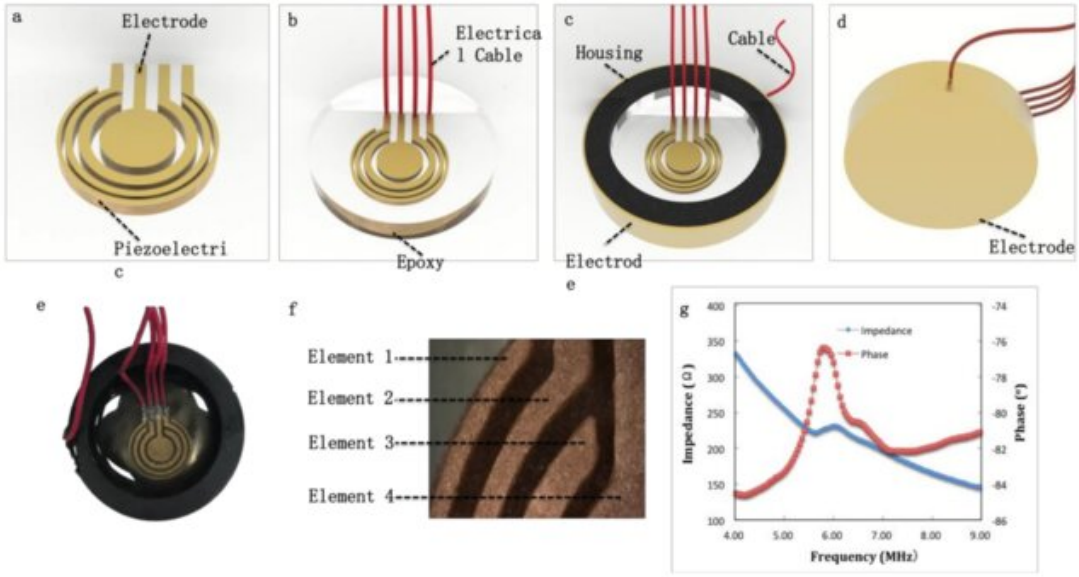



Figure 43: Schematic and experimental realization of an annular array transducer, showing (a–d) Structure of annular array transducer, (e) Optical image of annular array transducer, (f) Four elements of annular array and (g) Element's spectrum of impedance and phase[291].

The geometry of an ultrasound transducer defines the initial conditions of wave propagation, shaping not only the emitted field but also the interaction with the medium. Whether through the simplicity of a single-element device, the flexibility of linear and phased arrays, or the symmetry of annular configurations, transducer design is an exercise in controlling interference, diffraction, and energy distribution

#### 2.7.2.2 Acoustic Coupling and Impedance Matching

The efficiency of ultrasound transmission into the desired media is fundamentally governed by acoustic coupling and impedance matching, which together define how much of the generated mechanical energy is effectively radiated into the propagation medium. In practical systems, a severe mismatch exists between the acoustic impedance of the transducer's active material (typically $> 10$ MRayl) and that of soft tissues or fluids, which are typically around $1–2$ MRayl. This disparity leads to strong reflections at the interface, causing energy to be trapped within the transducer, increasing reverberation, reducing signal-to-noise ratio, and distorting the emitted waveform. Consequently,

impedance matching becomes a central requirement that directly controls transmission efficiency, bandwidth, and the temporal fidelity of the acoustic pulse[292,293].

Acoustic impedance governs the partition of energy at material interfaces. Figure 44 illustrates the relationship between longitudinal wave speed and density of materials (the main variables for normal incidence impedance). When a wave encounters a boundary between two media with different impedances, part of the energy is reflected and part is transmitted, with the transmission coefficient strongly dependent on the impedance ratio. In the extreme case of a large mismatch, such as between a piezoelectric element and air or soft tissue, nearly all the energy is reflected, severely limiting acoustic radiation. To mitigate this, matching layers are introduced between the transducer and the medium, designed to provide a gradual transition in impedance. Theoretically, optimal transmission occurs when the impedance of the matching layer is the geometric mean of the transducer and the medium, and its thickness corresponds to one-quarter of the acoustic wavelength, ensuring constructive interference of transmitted waves[292].

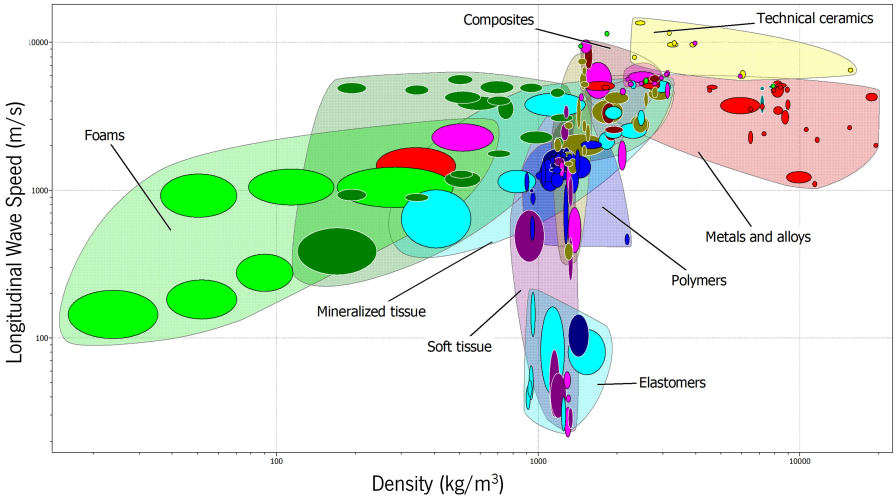



Figure 44: Ashby map illustrating the distribution of material classes in terms of acoustic impedance, highlighting the overlap between biological tissues and engineering materials, and enabling comparative selection for acoustic matching and wave transmission applications.

In practice, matching layers are often implemented as single or multiple layers of polymer composites, epoxies, or engineered materials with tailored acoustic properties. These layers act not only as impedance bridges but also as spectral filters, shaping the frequency response of the transducer. Experimental studies have demonstrated that the thickness and composition of matching layers significantly influence bandwidth and sensitivity, with quarter-wavelength designs typically providing optimal performance in pulse-echo systems. More recent developments have introduced gradient impedance materials and metamaterials, where impedance varies continuously across the layer thickness, enabling broader bandwidth and reduced insertion loss by minimizing internal reflections.

Such approaches highlight the shift from discrete matching strategies to engineered acoustic continua, where the interface itself becomes a designed propagation medium[294,295].

Energy transmission efficiency at interfaces is therefore not an abstract concept but a measurable quantity that directly determines how much acoustic power contributes to wave propagation. In layered systems, such as a transducer with backing, matching layers, and coupling medium, the total transmitted energy is the cumulative result of multiple reflection–transmission events. Each interface acts as a partial barrier, and inefficient matching leads to cascading energy losses. From a system-level perspective, the transmitted intensity can be interpreted as the product of transmission coefficients across all interfaces, meaning that even modest mismatches can significantly degrade overall efficiency. This is particularly critical in biomedical applications, where attenuation in tissue further reduces the available energy, making efficient initial transmission essential for maintaining sufficient signal levels at depth[293].

Acoustic coupling extends beyond solid layers to include the medium between the transducer and the target, particularly in biomedical applications where gels, water, or other coupling agents are used to eliminate air gaps. Even a thin air layer can drastically reduce transmission due to its extremely low acoustic impedance relative to solids and liquids. Coupling media therefore serve to maintain continuity of acoustic impedance, ensuring efficient transfer of energy into the tissue. In fluidic and microscale systems, the coupling layer itself can act as a resonant element, influencing the overall system response depending on its thickness and material properties, effectively becoming part of the acoustic design[296].

In the context of ultrasound propagation through biological tissues, where heterogeneity and attenuation dominate, the design of coupling and matching layers becomes a fundamental requirement for controlling how energy penetrates, propagates, and interacts with complex structures.

#### 2.7.2.3 Excitation Signals and Driving Methods

The effectiveness of impedance matching is dependent not only on the media it travels but also on the excitation signal used to drive the transducer, as different excitation regimes interact differently with the transducer's frequency response. Figure 45 describes the typically used signals.

Continuous wave (CW) excitation represents the simplest case, where a steady sinusoidal signal drives the transducer at a fixed frequency. Under CW operation, the system reaches a steady-state response, and impedance matching primarily determines the amplitude of the transmitted wave. In such cases, matching layers can be optimized for a narrow frequency band, maximizing energy transfer at the operating frequency. However, CW excitation is inherently limited in temporal resolution and is therefore less suitable for imaging applications where time-of-flight information is required[297].

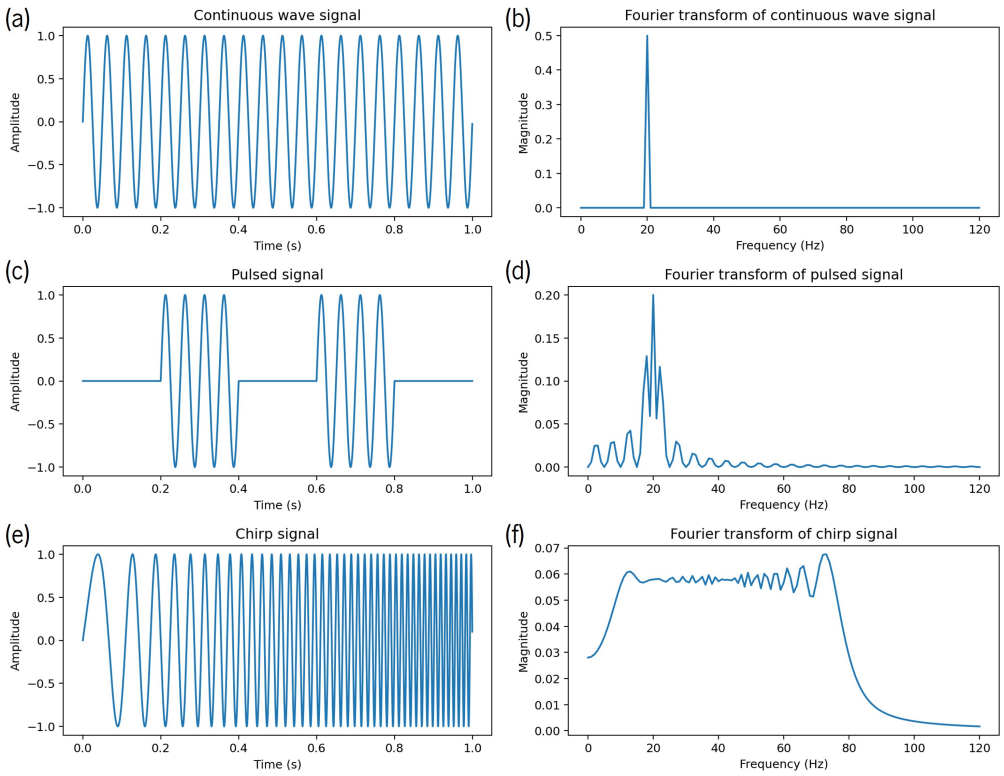



Figure 45: Time-domain signals and their corresponding frequency spectra where (a–b) continuous wave showing a single dominant frequency component, (c–d) pulsed signal exhibiting spectral spreading due to time localization, and (e–f) chirp signal with a broadband frequency distribution reflecting its time-varying frequency content.

In contrast, pulsed excitation and burst modulation introduce transient signals with finite duration, enabling the extraction of spatial information through echo timing. In this regime, impedance matching plays a more complex role, as the transducer must support a broad frequency spectrum to generate short pulses with high axial resolution. The presence of matching layers influences not only transmission efficiency but also the temporal response of the system, affecting ring-down and pulse length. Studies have shown that matching layers act as bandpass filters, enhancing bandwidth in short-pulse excitation while potentially reducing peak amplitude compared to long-pulse excitation. This introduces a fundamental trade-off between sensitivity and resolution: increasing bandwidth improves spatial resolution but may reduce the amplitude of the transmitted and received signals[297].

Advanced excitation techniques, such as frequency sweeps and chirp signals, further expand the interaction between impedance matching and signal design. Chirp excitation, in which the frequency is varied over time, allows the transmission of long-duration signals with controlled frequency content, which can later be compressed in post-processing to achieve high resolution. This approach effectively decouples energy transmission from resolution, enabling higher signal-to-noise ratios without sacrificing spatial detail. The design of matching layers becomes critical in this context, as the transducer must efficiently transmit and receive across a wide frequency range. Techniques such as coded excitation and pulse compression

rely on the ability to shape the excitation spectrum to match the transducer's transfer function, maximizing energy transfer while preserving signal fidelity[298].

The choice of excitation directly influences bandwidth, penetration depth, signal-to-noise ratio, and resolution. These signal characteristics, in turn, interact with the intrinsic response of the transducer and the surrounding medium, forming a coupled system where electrical input, mechanical vibration, and acoustic radiation are inseparable. Consequently, the design of excitation methods cannot be treated independently from transducer geometry and impedance matching; rather, it must be approached as part of an integrated framework that governs how ultrasound energy is generated, transmitted, and ultimately interpreted within complex, attenuating media.

## 2.7.3 Ultrasound Reception Techniques

Ultrasound reception techniques define how propagating acoustic fields are captured, converted, and interpreted after their interaction with a medium, completing the physical loop initiated during transmission. Unlike transmission, where the wave is deliberately imposed, reception deals with signals that have been altered by attenuation, scattering, nonlinear effects, and multiple interface interactions, often arriving with reduced amplitude and distorted spectral content. The role of the receiving system is therefore not only to detect these returning waveforms but to preserve their physical meaning with sufficient fidelity to enable accurate interpretation. In this sense, reception is inherently constrained by sensitivity and bandwidth, as well as by the ability to discriminate between useful signals and noise introduced both by the medium and the acquisition chain.

This section explores the fundamental principles governing ultrasound reception, focusing on the design and performance of receiving transducers, signal acquisition and conditioning, and advanced detection methodologies.

### 2.7.3.1 Receiving Transducers and Sensitivity Considerations

The reception of ultrasound signals constitutes the inverse problem of transmission: rather than imposing a controlled mechanical disturbance, the receiving transducer must often detect weak, distorted pressure fields that have propagated through attenuating and heterogeneous media. In this context, sensitivity becomes the defining performance metric, as it determines the minimum detectable amplitude variation and ultimately governs signal-to-noise ratio, spatial resolution, and penetration depth. Unlike transmission, where energy can be actively supplied, reception is constrained by the returning waves, making the efficiency of electromechanical conversion and noise suppression critical to system

performance. Consequently, the design of receiving transducers is inherently a balance between sensitivity, bandwidth, directivity, and physical dimensions.

Piezoelectric receivers remain the most widely used detection mechanism in ultrasound systems due to their direct and efficient conversion of pressure variations into electrical signals. When subjected to an incident acoustic wave, the resulting stress within the piezoelectric material generates an electric displacement proportional to the received amplitude, producing a measurable voltage output. This principle underlies devices such as hydrophones, which are specifically designed to measure acoustic pressure fields in fluids. In such systems, the receiving element is often optimized differently from transmitting elements: rather than maximizing output power, the design prioritizes sensitivity and fidelity of pressure detection across a given frequency range. For instance, piezoelectric hydrophones operating in resonance mode exhibit high sensitivity but limited bandwidth, whereas those operating in hydrostatic mode provide a flatter frequency response at the cost of reduced sensitivity[299].

Lead zirconate titanate remains a common choice due to its high piezoelectric coefficients and robustness, offering strong sensitivity to weak acoustic signals and good high-frequency response. However, polymer-based materials such as PVDF are often preferred in broadband applications due to their lower acoustic impedance and improved matching with fluids, which enhances energy transfer and reduces reflections. Composite materials, such as piezoelectric single crystal–polymer structures, have demonstrated the ability to combine high sensitivity with wide bandwidth by tailoring the internal microstructure to optimize electromechanical coupling[299,300].

Sensitivity is commonly quantified in terms of voltage response per unit pressure (V/Pa), and is fundamentally limited by both intrinsic material properties and extrinsic noise sources. Thermal noise, electronic noise in amplification circuits, and environmental interference all contribute to the noise floor, defining the minimum detectable signal. In high-performance systems, the concept of noise-equivalent pressure is often used, representing the pressure level that produces a signal equal to the noise level. Advanced sensing technologies, including optical detection systems, have demonstrated significantly lower values compared to traditional piezoelectric sensors, highlighting the ongoing evolution of ultrasound reception technologies toward higher sensitivity and miniaturization.

A critical design trade-off in receiving transducers lies between broadband and narrowband detection. Narrowband receivers are typically designed to operate near a specific resonance frequency, where the electromechanical response is maximized. This results in high sensitivity and strong signal amplification at that frequency, making such devices suitable for applications where the signal frequency is well-defined, such as continuous wave Doppler systems or resonant sensing. However, this comes at the cost of limited

frequency response, reducing the ability to accurately capture transient signals or broadband waveforms. The non-flat frequency response of resonant receivers can also introduce distortion in the detected signal, complicating interpretation and post-processing.

In contrast, broadband receivers aim to maintain a relatively flat frequency response over a wide range of frequencies, enabling accurate detection of short pulses and complex waveforms. This is particularly important in imaging and pulse-echo applications, where axial resolution depends on the temporal width of the received signal. Broadband detection allows for shorter pulse durations and improved spatial resolution, but typically results in lower peak sensitivity compared to resonant systems. As demonstrated in experimental studies of broadband hydrophones, achieving both high sensitivity and wide bandwidth requires careful optimization of material composition, thickness, and backing conditions, often involving trade-offs between these competing objectives[299].

The influence of geometry and size further complicates sensitivity considerations. As transducers are miniaturized, their sensitivity generally decreases due to reduced active area and lower energy capture. This limitation is particularly evident in piezoelectric systems, where sensitivity scales with volume, posing challenges for high-resolution imaging systems that require small detector elements. Emerging technologies, such as optical microcavity-based sensors, have demonstrated the potential to overcome this limitation by achieving extremely high sensitivity even at sub-micron scales, with bandwidths extending into the hundreds of MHz. These developments suggest that future ultrasound systems may increasingly rely on hybrid or non-piezoelectric detection mechanisms to achieve both high spatial resolution and sensitivity.

Another important aspect of receiving transducer performance is directivity, which describes the angular dependence of sensitivity. Omnidirectional receivers capture acoustic energy from all directions, providing uniform sensitivity but limited spatial selectivity. Directional receivers, on the other hand, enhance sensitivity in specific directions, improving signal discrimination and reducing noise from unwanted sources. The directivity pattern is determined by the geometry and size of the transducer relative to the wavelength, with larger apertures generally providing narrower beam patterns and higher directional sensitivity.

#### 2.7.3.2 Signal Acquisition and Conditioning

The process of signal acquisition and conditioning in ultrasound receivers represents the critical transition between physical wave detection and meaningful data interpretation. Once an acoustic wave has been converted into an electrical signal by the receiving transducer, this signal is typically of very low

amplitude, often in the microvolt to millivolt range, and is superimposed with multiple sources of noise and distortion. As such, raw signals are rarely suitable for direct digitization or analysis. Signal conditioning therefore serves as an essential intermediary stage, where amplification, filtering, impedance adaptation, and noise mitigation are applied to preserve the integrity of the acoustic information while adapting it to the requirements of downstream electronics and processing systems .

Amplification constitutes the first and most critical step in signal conditioning, as it directly influences both signal resolution and signal-to-noise ratio. In ultrasound systems, preamplifiers are often placed as close as possible to the transducer element to minimize signal degradation due to cable losses and electromagnetic interference. This is particularly important in array-based systems, where small, high-impedance elements are susceptible to signal attenuation before reaching the main processing unit. Integrated front-end electronics, such as application-specific integrated circuits, have been shown to significantly improve SNR by locally amplifying echo signals prior to transmission, thereby preserving weak signals that would otherwise be lost. Experimental implementations further demonstrate that even modest preamplification stages can substantially enhance detection performance; for example, the integration of a high-bandwidth operational amplifier in a PVDF receiver system was shown to improve SNR by stabilizing and boosting the received signal before processing. These findings highlight that amplification is not merely about increasing signal amplitude, but about preserving information fidelity in the presence of unavoidable losses[301,302].

Filtering represents the second fundamental pillar of signal conditioning, acting to isolate relevant frequency components while suppressing noise and interference. In ultrasound systems, the received signal typically occupies a well-defined frequency band centred around the transducer's operating frequency, whereas noise sources may span a much broader spectrum. Band-pass filtering is therefore commonly employed to retain only the frequency range of interest, eliminating low-frequency drift and high-frequency electronic noise. Additionally, antialiasing filters are essential prior to analog-to-digital conversion, ensuring that frequency components above half the sampling rate do not introduce spectral distortion. More specialized filtering techniques are also used depending on the application; for instance, subharmonic and superharmonic filtering can selectively isolate nonlinear responses from contrast agents, enhancing signal specificity in biomedical imaging. These filtering strategies effectively shape the spectral content of the signal, ensuring that only meaningful acoustic information is retained for further analysis[303–305].

The acquisition chain is further influenced by the architecture of the data acquisition system, which includes analog-to-digital converters , sampling strategies, and synchronization with transmission events.

The dynamic range of the acquisition system is a key parameter, as it determines the ability to resolve weak echoes in the presence of strong reflections. Systems with high dynamic range can detect signals several orders of magnitude smaller than the maximum input, which is essential in medical ultrasound where reflections from deep tissues are significantly attenuated. Advanced acquisition techniques, such as time-delay sampling and compressed sensing approaches, have been developed to reduce data rates while maintaining signal fidelity, though these methods often require careful SNR management to avoid degradation of reconstructed signals[306].

Noise sources in ultrasound receivers are diverse and originate from both physical and electronic domains. Thermal noise, arising from the random motion of charge carriers in electronic components, sets a fundamental lower bound on detectable signal levels. Electronic noise from amplifiers, analog-to-digital converters' quantization noise, and electromagnetic interference from external stimuli further contribute to signal degradation. Additionally, acoustic noise introduces complexity that cannot be removed solely through electronic conditioning. In practical systems, these noise sources combine to define the overall noise floor, against which the useful signal must be distinguished. As such, optimizing the signal-to-noise ratio is therefore a central objective in ultrasound receiver design, requiring coordinated strategies across multiple levels of the system. At the hardware level, low-noise amplifiers, impedance matching, and shielding techniques are employed to minimize electronic noise contributions. At the system level, array configurations and beamforming techniques can improve SNR by coherently combining signals from multiple elements, effectively reinforcing the desired signal while suppressing uncorrelated noise. Signal processing techniques further enhance SNR, including averaging, matched filtering, and coded excitation schemes, which distribute energy over time and recover it through correlation-based methods. Recent advances in computational approaches, including deep learning-based denoising and adaptive filtering, have demonstrated the ability to improve signal-to-noise ratio without sacrificing spatial resolution, highlighting the increasing role of data-driven methods in ultrasound signal conditioning[306,307].

#### 2.7.3.3 Advanced Detection Methods

Beyond conventional piezoelectric receivers, advanced detection methods have been developed to overcome intrinsic limitations in sensitivity, bandwidth, spatial resolution, and measurement fidelity. These approaches are particularly relevant in high-frequency, nonlinear, or high-intensity ultrasound regimes, where conventional sensors may suffer from spatial averaging, limited dynamic range, or physical constraints.

Hydrophones constitute the reference standard for quantitative ultrasound field measurements, particularly in calibration, safety assessment, and high-fidelity acoustic characterization. These devices operate by converting local pressure variations in a fluid medium into electrical signals, typically via piezoelectric or optical mechanisms. Three primary classes of hydrophones are commonly distinguished: needle, membrane, and fibre-optic hydrophones. Needle hydrophones, characterized by small sensitive elements (often tens to hundreds of micrometers in diameter), offer high spatial resolution and are particularly suited for mapping highly localized acoustic fields, such as focused ultrasound beams. Their compact geometry minimizes spatial averaging effects, enabling accurate measurement of high-frequency and nonlinear waveforms; however, this comes at the cost of reduced sensitivity and increased susceptibility to noise[308].

Membrane hydrophones, in contrast, utilize thin polymer films stretched over a supporting structure, providing improved sensitivity and broader bandwidth due to better acoustic impedance matching with water. These devices are widely used in diagnostic ultrasound calibration but can suffer from spatial averaging when the sensitive area is large relative to the wavelength[309]. Fibre-optic hydrophones represent a more recent advancement, employing optical interferometry or reflectance-based sensing to detect pressure-induced changes in refractive index or optical path length. These sensors exhibit exceptional bandwidth and can withstand extremely high amplitude levels, making them particularly suitable for high-intensity focused ultrasound and cavitation[308,310]. Hydrophone performance is strongly influenced by frequency-dependent sensitivity and directivity, requiring careful calibration and correction methods to ensure accurate measurements across wide frequency ranges[309].

Optical detection methods, particularly laser Doppler vibrometry (LDV), offer a fundamentally different approach by enabling non-contact measurement of ultrasonic waves through surface vibration analysis. LDV systems operate based on the Doppler shift of reflected laser light, which encodes the velocity of a vibrating surface induced by incident acoustic waves. This technique allows for high sensitivity and spatial resolution without physically loading the measurement surface, eliminating perturbations introduced by contact-based sensors[311].

In ultrasound applications, LDV has been increasingly employed for detecting photoacoustic signals and surface wave propagation, particularly in scenarios where conventional sensors cannot be attached, such as delicate biological tissues or microscale devices. Recent developments in silicon photonics-based LDV systems have demonstrated the capability to perform non-contact ultrasound detection with sufficient sensitivity to reconstruct two-dimensional acoustic images, highlighting the potential of optical vibrometry in next-generation imaging systems. However, LDV-based methods are

inherently limited by optical access requirements and sensitivity to surface reflectivity, which can constrain their applicability in deeply embedded or optically scattering media.

## 2.7.4 Calibration and Measurement Techniques

Ultrasound calibration and measurement techniques establish the quantitative foundation upon which all experimental, diagnostic, and therapeutic applications are built. While transmission and reception define how acoustic waves are generated and detected, calibration ensures that these processes are physically meaningful, linking measured electrical signals to absolute acoustic quantities such as pressure, intensity, and power. In the absence of proper calibration, ultrasound systems operate in a relative domain, where comparisons may be possible, but absolute interpretation becomes unreliable. This section therefore addresses the principles and methodologies used to characterize and calibrate ultrasound systems, focusing on acoustic field measurements and sensor calibration procedures.

### 2.7.4.1 Acoustic Field Characterization

Accurate acoustic field characterization is a fundamental requirement in ultrasound research and applications, as it is the only to cross from qualitative to quantitative data. In modern ultrasound systems, particularly in high-frequency and high-intensity regimes, characterization is typically expressed through three primary descriptors: acoustic pressure, acoustic intensity, and acoustic power. These quantities are intrinsically interconnected, yet each provides distinct insight into wave propagation phenomena, energy transport, and interaction with complex media. Recent advances in measurement methodologies have emphasized the need for high spatial and temporal resolution, as well as minimal perturbation of the field.

Acoustic pressure remains the most direct and fundamental quantity measured in ultrasound field characterization, as it represents the local mechanical perturbation driving wave propagation. In practice, pressure fields are most commonly measured using hydrophones, which provide localized detection of pressure amplitude with high sensitivity. However, recent studies have highlighted limitations associated with hydrophone-based measurements, particularly the spatial averaging effect, whereby finite sensor size leads to underestimation of peak amplitude in highly focused or nonlinear fields[312,313]. This effect becomes increasingly significant in High intensity focused ultrasound, where nonlinear propagation leads to steep pressure gradients and shock formation. Experimental investigations have demonstrated that peak pressures exceeding tens of megapascals can be measured using fibre-optic hydrophones, but accurate quantification requires correction for spatial averaging and

frequency-dependent sensitivity autocitecanneyAcousticCharacterizationHigh2008. To address these limitations, recent research has introduced non-contact optical methods, such laser deflection techniques, capable of reconstructing pressure fields with high spatial resolution and without disturbing the acoustic field. These methods exploit the relationship between pressure-induced refractive index variations and optical wave propagation, enabling full-field reconstruction of acoustic pressure distributions in both linear and nonlinear regimes[314,315].

Acoustic intensity provides a measure of the rate of energy transport through a medium and is typically defined as the time-averaged product of pressure and particle velocity. In experimental practice, intensity is often derived from pressure measurements under assumptions of plane wave propagation, although this approximation breaks down in strongly focused or nonlinear fields. In such cases, intensity must be calculated using spatial integration or numerical reconstruction methods based on measured pressure distributions. Recent work has demonstrated the use of acoustic holography and re-radiation techniques to reconstruct three-dimensional intensity fields from planar pressure measurements, enabling accurate estimation of energy distribution even in complex beamforming scenarios. These approaches are particularly valuable in array-based systems, where the superposition of multiple elements creates intricate interference patterns that cannot be captured through single-point measurements alone. Furthermore, nonlinear propagation introduces harmonic generation, which redistributes energy across the frequency spectrum and complicates intensity estimation, requiring broadband measurement techniques and frequency-resolved analysis[316].

Acoustic power, representing the total energy emitted by a transducer per unit time, provides a global measure of system output and is particularly relevant in safety and regulatory contexts. Unlike pressure and intensity, which are local quantities, acoustic power is typically determined through spatial integration of intensity over a surface enclosing the domain. In experimental settings, power measurements are often performed using radiation force balances or calorimetric methods, which infer acoustic power from the mechanical force exerted on an absorbing target or from temperature rise in a medium. However, in high-frequency and highly focused systems, direct measurement of power can be challenging due to spatial confinement of the beam and nonlinear attenuation. As a result, hybrid approaches combining pressure measurements, numerical modelling, and inverse methods are increasingly employed to estimate acoustic power with high accuracy. Recent studies emphasize that accurate power estimation requires careful consideration of beam geometry, attenuation, and reflection losses, particularly in heterogeneous media where energy redistribution occurs along the propagation path[317,318].

A key challenge in acoustic field characterization lies in the coupling between these three quantities.

Pressure measurements provide the most accessible experimental data, but intensity and power are derived quantities that depend on assumptions regarding wave propagation and medium properties. In linear, homogeneous media, these relationships are straightforward; however, in biological tissues or strongly nonlinear regimes, the propagation becomes significantly more complex. For example, nonlinear effects such as waveform distortion and shock formation lead to asymmetry between compressional and rarefaction phases, altering the relationship between peak pressure and time-averaged intensity. Similarly, attenuation and scattering redistribute energy spatially, meaning that local intensity measurements may not directly reflect total emitted power[312].

Recent advances in acoustic field characterization have therefore focused on integrating experimental and computational approaches to overcome these limitations. Combined measurement–modelling frameworks, where experimentally measured pressure fields are used to calibrate numerical models, have been shown to provide accurate predictions of intensity and power distributions in both linear and nonlinear regimes[312]. Additionally, emerging optical and tomographic techniques enable full-field characterization with discrete spatial resolution, offering new possibilities for capturing the complex structure of ultrasound fields in realistic environments[315],

#### 2.7.4.2 Hydrophone Calibration and Standards

The accurate use of hydrophones for ultrasound field characterization fundamentally relies on rigorous calibration procedures that ensure traceability, reproducibility, and physical validity of measured acoustic quantities. Hydrophone calibration establishes the relationship between the measured electrical output and the true acoustic pressure, typically expressed as a complex, frequency-dependent sensitivity function. This calibration is not a single-point adjustment but a broadband characterization that must account for amplitude and phase response across the operational frequency range. International standards provide the formal framework for this process, ensuring consistency across laboratories and applications. In particular, the IEC 62127 series defines procedures for the use of calibrated hydrophones in ultrasonic field measurements, including requirements for bandwidth, sensitivity characterization, and uncertainty estimation in medical ultrasound applications[319]. Complementarily, the IEC 60565 standard series establishes methods for absolute and relative calibration of hydrophones in free-field conditions, including reciprocity-based primary calibration techniques that provide traceability to fundamental electrical standards[320].

Calibration methodologies can be broadly categorized into absolute (primary) and comparative (secondary) approaches. Absolute calibration techniques, such as the three-transducer reciprocity

method, allow the determination of hydrophone sensitivity without reliance on pre-calibrated reference devices, instead deriving sensitivity directly from electrical measurements and known physical relationships. These methods are typically implemented in controlled laboratory environments and form the basis of national metrology institute standards. In contrast, relative calibration methods involve comparison with a reference hydrophone whose sensitivity is already known and traceable to primary standards, enabling more practical calibration workflows for routine measurements[320]. Recent developments have further introduced optical interferometric calibration techniques, which directly relate acoustic pressure to displacement measurements, offering potential improvements in accuracy and bandwidth, particularly at higher frequencies[309].

A central challenge in hydrophone measurements, explicitly addressed in IEC 62127, is the finite size of the hydrophone sensing element, which leads to spatial averaging effects. Unlike an ideal point receiver, a real hydrophone integrates pressure over its active field, effectively smoothing spatial variations in the acoustic field. This results in systematic underestimation of peak pressures, particularly in highly focused beams or nonlinear fields where steep gradients and localized maxima are present. The magnitude of this effect depends on the ratio between the hydrophone element size and the acoustic wavelength, becoming increasingly significant at higher frequencies and in tightly focused fields. Modern standards therefore require the application of spatial averaging corrections, which can be derived either analytically or numerically based on the known spatial response of the hydrophone[319].

Equally critical is the correction for frequency-dependent sensitivity, as hydrophones do not exhibit uniform response across their operational bandwidth. The frequency response of a hydrophone is influenced by material properties, geometry, backing conditions, and internal resonances, resulting in amplitude and phase variations that distort the measured signal. IEC standards explicitly require that calibration data be provided as a function of frequency, enabling the reconstruction of the true pressure waveform through deconvolution or frequency-domain correction. In broadband or pulsed ultrasound applications, where signals contain a wide range of frequency components, failure to apply frequency response corrections can lead to significant distortion of waveform shape, peak pressure, and derived quantities such as intensity. Advanced calibration techniques therefore incorporate complex sensitivity functions, allowing both magnitude and phase corrections to be applied to measured signals, ensuring accurate reconstruction of transient waveforms[319].

The interplay between spatial averaging and frequency response is particularly important in nonlinear ultrasound fields, where harmonic generation redistributes energy across the spectrum and creates highly localized pressure gradients. In such conditions, calibration must account simultaneously

for spatial filtering effects and frequency-dependent attenuation of higher harmonics, requiring high-resolution calibration data and sophisticated correction algorithms. IEC 62127 explicitly addresses these limitations by defining procedures for estimating measurement uncertainty associated with finite bandwidth and element size, reinforcing the need for comprehensive calibration strategies. Furthermore, modern calibration practices increasingly integrate numerical modelling with experimental measurements, allowing correction factors to be tailored to specific measurement techniques and transducer geometries[319].

## 2.8 Bibliography

[1]N. A. T. C. Fernandes, A. Arieira, B. Hinckel, F. S. Silva, Ó. Carvalho, and A. Leal, "Unlocking the Secrets of Knee Joint Unloading: A Systematic Review and Biomechanical Study of the Invasive and Non-Invasive Methods and Their Influence on Knee Joint Loading", Rheumato **5**, 8 (2025) 10.3390/rheumato5030008.

[2]N. Fernandes, F. S. Silva, Ó. Carvalho, and A. Leal, "Effect of lower limb orthoses on cartilage in patients with knee osteoarthritis: A narrative review", **47** (2022).

[3]A. Z. Santos, S. Rocha, B. Carneiro, N. A. Fernandes, J. Padrão, and Ó. Carvalho, "Current state of elastography research in multiple anatomical structures and respective phantoms", Phys. Med. **138**, 105192 (2025) 10.1016/j.ejmp.2025.105192.

[4]A. R. Nochehdehi, F. Nemavhola, S. Thomas, and H. J. Maria, *Cartilage Tissue and Knee Joint Biomechanics* (Elsevier, United Kingdom, 2024), 10.1016/C2020-0-03993-9.

[5]E. S. Mameri, S. P. Dasari, L. M. Fortier, F. G. Verdejo, S. Gursoy, A. B. Yanke, and J. Chahla, "Review of Meniscus Anatomy and Biomechanics", Curr. Rev. Musculoskelet. Med. **15**, 323–335 (2022) 10.1007/s12178-022-09768-1.

[6]P. S. Walker, S. Arno, C. Bell, G. Salvadore, I. Borukhov, and C. Oh, "Function of the medial meniscus in force transmission and stability", J. Biomech. **48**, 1383–1388 (2015) 10.1016/j.jbiomech.2015.02.055.

[7]M. S. Kim, Y. In, H. Kim, J. Jeong, and S. Sohn, "Why Hoop Tension Matters: A Biomechanical Perspective on Medial Meniscus Posterior Root Tears—A Narrative Review", Bioengineering **12**, 638 (2025) 10.3390/bioengineering12060638.

[8]D. J. Cognetti and A. Bedi, "Biomechanics of the Meniscus and Meniscal Injury", Oper. Tech. Orthop. **35**, 101180 (2025) 10.1016/j.oto.2025.101180.

[9]J. Li, H. Liu, M. Song, F. Lin, Z. Zhao, Z. Wang, L. Hou, G. Zhao, and W. Ren, "Biomechanical characteristics of ligament injuries in the knee joint during impact in the upright position: a finite element analysis", J. Orthop. Surg. **19**, 630 (2024) 10.1186/s13018-024-05064-5.

[10]A. Hussain, M. Madraswala, J. Koh, and F. Amirouche, "Anterior Cruciate Ligament Mechanical Response to Load in the Setting of Changes to the Medial Meniscus", Bioengineering **12**, 74 (2025) 10.3390/bioengineering12010074.

[11]C. M. Gupte, A. M. Bull, R. Thomas, and A. A. Amis, “A review of the function and biomechanics of the meniscofemoral ligaments”, Arthrosc. J. Arthrosc. Relat. Surg. **19**, 161–171 (2003) 10.1053/jars.2003.50011.

[12]S. Andrikoula, A. Tokis, H. S. Vasiliadis, and A. Georgoulis, “The extensor mechanism of the knee joint: an anatomical study”, Knee Surg. Sports Traumatol. Arthrosc. **14**, 214–220 (2006) 10.1007/s00167-005-0680-3.

[13]R. H. Miller, W. Brent Edwards, and K. J. Deluzio, “Energy expended and knee joint load accumulated when walking, running, or standing for the same amount of time”, Gait Posture **41**, 326–328 (2015) 10.1016/j.gaitpost.2014.10.009.

[14]S. C. Walpole, D. Prieto-Merino, P. Edwards, J. Cleland, G. Stevens, and I. Roberts, “The weight of nations: an estimation of adult human biomass”, BMC Public Health **12**, 439 (2012) 10.1186/1471-2458-12-439.

[15]C. A. Frigo and L. Donno, “The Effects of External Loads and Muscle Forces on the Knee Joint Ligaments during Walking: A Musculoskeletal Model Study”, Appl. Sci. **11**, 2356 (2021) 10.3390/app11052356.

[16]D. D. D’Lima, B. J. Fregly, S. Patil, N. Steklov, and C. W. Colwell, “Knee joint forces: prediction, measurement, and significance”, Proc. Inst. Mech. Eng. [H] **226**, 95–102 (2012) 10.1177/0954411911433372.

[17]R. L. Lenhart, D. G. Thelen, C. M. Wille, E. S. Chumanov, and B. C. Heiderscheit, “Increasing Running Step Rate Reduces Patellofemoral Joint Forces”, Med. Sci. Sports Exerc. **46**, 557–564 (2014) 10.1249/MSS.0b013e3182a78c3a.

[18]M. Yousefifard, Mandy Alhajj, Adegbenro O. Fakoya, and Sandeep Sharma, *Anatomy, Skin (Integument), Epidermis*, (Jan. 2026) https://www.ncbi.nlm.nih.gov/books/NBK470464/.

[19]Z. Lotfollahi, “The anatomy, physiology and function of all skin layers and the impact of ageing on the skin”, Wound Pract. Res. **32** (2024) 10.33235/wpr.32.1.6-10.

[20]S. A. Mohamed and R. Hargest, “Surgical anatomy of the skin”, Surg. Oxf. **40**, 1–7 (2022) 10.1016/j.mpsur.2021.11.021.

[21]M. Pawlaczyk, M. Lelonkiewicz, and M. Wieczorowski, “Age-dependent biomechanical properties of the skin”, Adv. Dermatol. Allergol. **5**, 302–306 (2013) 10.5114/pdia.2013.38359.

[22]Xing Liang and S. Boppart, "Biomechanical Properties of *In Vivo* Human Skin From Dynamic Optical Coherence Elastography", IEEE Trans. Biomed. Eng. **57**, 953–959 (2010) 10.1109/TBME.2009.2033464.

[23]A. Ní Annaidh, K. Bruyère, M. Destrade, M. D. Gilchrist, and M. Otténio, "Characterization of the anisotropic mechanical properties of excised human skin", J. Mech. Behav. Biomed. Mater. **5**, 139–148 (2012) 10.1016/j.jmbbm.2011.08.016.

[24]E. C. M. Mariman and P. Wang, "Adipocyte extracellular matrix composition, dynamics and role in obesity", Cell. Mol. Life Sci. **67**, 1277–1292 (2010) 10.1007/s00018-010-0263-4.

[25]N. Alkhouli, J. Mansfield, E. Green, J. Bell, B. Knight, N. Liversedge, J. C. Tham, R. Welbourn, A. C. Shore, K. Kos, and C. P. Winlove, "The mechanical properties of human adipose tissues and their relationships to the structure and composition of the extracellular matrix", Am. J. Physiol.-Endocrinol. Metab. **305**, E1427–E1435 (2013) 10.1152/ajpendo.00111.2013.

[26]F. J. Ruiz-Ojeda, A. Méndez-Gutiérrez, C. M. Aguilera, and J. Plaza-Díaz, "Extracellular Matrix Remodeling of Adipose Tissue in Obesity and Metabolic Diseases", Int. J. Mol. Sci. **20**, 4888 (2019) 10.3390/ijms20194888.

[27]C. Bourgeois, J. Gorwood, A. Barrail-Tran, C. Lagathu, J. Capeau, D. Desjardins, R. Le Grand, A. Damouche, V. Béréziat, and O. Lambotte, "Specific Biological Features of Adipose Tissue, and Their Impact on HIV Persistence", Front. Microbiol. **10**, 2837 (2019) 10.3389/fmicb.2019.02837.

[28]C. L. Frosti, S. P. Connelly, and M. D. Layne, "Mechanobiology of Adipose Tissue Remodeling", Tissue Eng. Part A, 19373341251405218 (2025) 10.1177/19373341251405218.

[29]S. P. Blade, D. J. Falkowski, S. N. Bachand, S. J. Pagano, and L. Chin, "Mechanobiology of Adipocytes", Biology **13**, 434 (2024) 10.3390/biology13060434.

[30]J. A. Trotter, "Structure–function considerations of muscle–tendon junctions", Comp. Biochem. Physiol. A. Mol. Integr. Physiol. **133**, 1127–1133 (2002) 10.1016/S1095-6433(02)00213-1.

[31]A. Arampatzis, L. Mademli, T. Reilly, M. I. Lambert, L. Bosquet, J.-P. Richalet, T. Busso, B. Mettauer, S. Gréciano, B. Geny, F. Magkos, and B. Knechtle, "Tendon", in *Encyclopedia of Exercise Medicine in Health and Disease*, edited by F. C. Mooren (Springer Berlin Heidelberg, Berlin, Heidelberg, 2012), pp. 843–849, 10.1007/978-3-540-29807-6_260.

[32]S. Tong, Y. Sun, B. Kuang, M. Wang, Z. Chen, W. Zhang, and J. Chen, "A Comprehensive Review of Muscle–Tendon Junction: Structure, Function, Injury and Repair", Biomedicines **12**, 423 (2024) 10.3390/biomedicines12020423.

[33]N. Pien, H. Krzyslak, S. Shastry Kallaje, J. Van Meerssche, D. Mantovani, C. De Schauwer, P. Dubruel, S. Van Vlierberghe, and C. Pennisi, "Tissue engineering of skeletal muscle, tendons and nerves: A review of manufacturing strategies to meet structural and functional requirements", Appl. Mater. Today **31**, 101737 (2023) 10.1016/j.apmt.2023.101737.

[34]M. Franchi, A. Trirè, M. Quaranta, E. Orsini, and V. Ottani, "Collagen Structure of Tendon Relates to Function", Sci. World J. **7**, 404–420 (2007) 10.1100/tsw.2007.92.

[35]A. Biewener, "Tendons and Ligaments: Structure, Mechanical Behavior and Biological Function", in *Collagen*, edited by P. Fratzl (Springer US, Boston, MA, 2008), pp. 269–284, 10.1007/978-0-387-73906-9_10.

[36]J. H.-C. Wang, Q. Guo, and B. Li, "Tendon Biomechanics and Mechanobiology—A Minireview of Basic Concepts and Recent Advancements", J. Hand Ther. **25**, 133–141 (2012) 10.1016/j.jht.2011.07.004.

[37]P. P. Provenzano and R. Vanderby, "Collagen fibril morphology and organization: Implications for force transmission in ligament and tendon", Matrix Biol. **25**, 71–84 (2006) 10.1016/j.matbio.2005.09.005.

[38]S. P. Reese, S. A. Maas, and J. A. Weiss, "Micromechanical models of helical superstructures in ligament and tendon fibers predict large Poisson's ratios", J. Biomech. **43**, 1394–1400 (2010) 10.1016/j.jbiomech.2010.01.004.

[39]N. Hammer, D. Huster, S. Fritsch, C. Hädrich, H. Koch, P. Schmidt, F. Sichting, M. F.-X. Wagner, and A. Boldt, "Do Cells Contribute to Tendon and Ligament Biomechanics?", PLoS ONE **9**, edited by S. Bhattacharya, e105037 (2014) 10.1371/journal.pone.0105037.

[40]S. Zhang, V. Zarei, B. A. Winkelstein, and V. H. Barocas, "Multiscale mechanics of the cervical facet capsular ligament, with particular emphasis on anomalous fiber realignment prior to tissue failure", Biomech. Model. Mechanobiol. **17**, 133–145 (2018) 10.1007/s10237-017-0949-8.

[41]E. F. Morgan, G. U. Unnikrisnan, and A. I. Hussein, "Bone Mechanical Properties in Healthy and Diseased States", Annu. Rev. Biomed. Eng. **20**, 119–143 (2018) 10.1146/annurev-bioeng-062117-121139.

[42]L. Al-Qudsy, Y.-W. Hu, H. Xu, and P.-F. Yang, "Mineralized Collagen Fibrils: An Essential Component in Determining the Mechanical Behavior of Cortical Bone", ACS Biomater. Sci. Eng. **9**, 2203–2219 (2023) 10.1021/acsbiomaterials.2c01377.

[43]C. Ma, T. Du, X. Niu, and Y. Fan, "Biomechanics and mechanobiology of the bone matrix", Bone Res. **10**, 59 (2022) 10.1038/s41413-022-00223-y.

[44]M. Bittner-Frank, A. G. Reisinger, O. G. Andriotis, D. H. Pahr, and P. J. Thurner, "Cortical and trabecular mechanical properties in the femoral neck vary differently with changes in bone mineral density", JBMR Plus **8**, ziae049 (2024) 10.1093/jbmrpl/ziae049.

[45]M. Georgiadis, R. Müller, and P. Schneider, "Techniques to assess bone ultrastructure organization: orientation and arrangement of mineralized collagen fibrils", J. R. Soc. Interface **13**, 20160088 (2016) 10.1098/rsif.2016.0088.

[46]E. Novitskaya, S. Lee, V. A. Lubarda, and J. McKittrick, "Initial anisotropy in demineralized bovine cortical bone in compressive cyclic loading–unloading", Mater. Sci. Eng. C **33**, 817–823 (2013) 10.1016/j.msec.2012.11.006.

[47]R. Oftadeh, M. Perez-Viloria, J. C. Villa-Camacho, A. Vaziri, and A. Nazarian, "Biomechanics and Mechanobiology of Trabecular Bone: A Review", J. Biomech. Eng. **137** (2015) 10.1115/1.4029176.

[48]M. Asgari, J. Abi-Rafeh, G. N. Hendy, and D. Pasini, "Material anisotropy and elasticity of cortical and trabecular bone in the adult mouse femur via AFM indentation", J. Mech. Behav. Biomed. Mater. **93**, 81–92 (2019) 10.1016/j.jmbbm.2019.01.024.

[49]R. Karpinski, A. Prus, J. Baj, S. Radej, M. Prz□dka, P. Krakowski, and K. Jonak, "Articular Cartilage: Structure, Biomechanics, and the Potential of Conventional and Advanced Diagnostics", Appl. Sci. **15**, 6896 (2025) 10.3390/app15126896.

[50]E. Belluzzi, S. Todros, A. Pozzuoli, P. Ruggieri, E. L. Carniel, and A. Berardo, "Human Cartilage Biomechanics: Experimental and Theoretical Approaches towards the Identification of Mechanical Properties in Healthy and Osteoarthritic Conditions", Processes **11**, 1014 (2023) 10.3390/pr11041014.

[51]N. S., D. A., and J. Carlos, "Mechanical Behavior of Articular Cartilage", in *Injury and Skeletal Biomechanics*, edited by T. Goswami (InTech, Aug. 1, 2012), 10.5772/48323.

[52]J. Eschweiler, N. Horn, B. Rath, M. Betsch, A. Baroncini, M. Tingart, and F. Migliorini, "The Biomechanics of Cartilage—An Overview", Life **11**, 302 (2021) 10.3390/life11040302.

[53]S. P. Hiruthyaswamy, A. Bose, A. Upadhyay, T. Raha, S. Bhattacharjee, I. Singha, S. Ray, N. M. Nicky Macarius, P. Viswanathan, and K. Deepankumar, "Molecular signaling pathways in osteoarthritis and biomaterials for cartilage regeneration: a review", Bioengineered **16**, 2501880 (2025) 10.1080/21655979.2025.2501880.

[54]P. Krakowski, A. Rejniak, J. Sobczyk, and R. Karpinski, "Cartilage Integrity: A Review of Mechanical and Frictional Properties and Repair Approaches in Osteoarthritis", Healthcare **12**, 1648 (2024) 10.3390/healthcare12161648.

[55]M. Mostakhdemin, A. Nand, and M. Ramezani, "Articular and Artificial Cartilage, Characteristics, Properties and Testing Approaches—A Review", Polymers **13**, 2000 (2021) 10.3390/polym13122000.

[56]W. Petersen, A. Ellermann, T. Zantop, I. V. Rembitzki, H. Semsch, C. Liebau, and R. Best, "Biomechanical effect of unloader braces for medial osteoarthritis of the knee: a systematic review", Arch. Orthop. Trauma Surg. **136**, 649–656 (2016) 10.1007/s00402-015-2388-2.

[57]T. M. van Raaij, M. Reijman, R. W. Brouwer, S. M. A. Bierma-Zeinstra, and J. A. N. Verhaar, "Medial Knee Osteoarthritis Treated by Insoles or Braces: A Randomized Trial", Clin. Orthop. Relat. Res. **468**, 1926–1932 (2010) 10.1007/s11999-010-1274-z.

[58]F. Moller, L. Ortíz-Muñoz, and S. Irarrázaval, "Offloader knee braces for knee osteoarthritis", Medwave **21**, e8114–e8114 (2021) 10.5867/medwave.2021.01.8114.

[59]H. Matsuno, K. M. Kadowaki, and H. Tsuji, "Generation II knee bracing for severe medial compartment osteoarthritis of the knee", Arch. Phys. Med. Rehabil. **78**, 745–749 (1997) 10.1016/S0003-9993(97)90083-6.

[60]R. Parween, D. Shriram, R. E. Mohan, Y. H. D. Lee, and K. Subburaj, "Methods for evaluating effects of unloader knee braces on joint health: a review", Biomed. Eng. Lett. **9**, 153–168 (2019) 10.1007/s13534-019-00094-z.

[61]B. Pierrat, J. Molimard, P. Calmels, L. Navarro, and S. Avril, *Efficiency and comfort of knee braces: A parametric study based on computational modelling*, version 1, (2014) 10.48550/ARXIV.1409.5756, https://arxiv.org/abs/1409.5756 (visited on 03/31/2026), pre-published.

[62]R. S. Hinman, C. Payne, B. R. Metcalf, T. V. Wrigley, and K. L. Bennell, "Lateral wedges in knee osteoarthritis: What are their immediate clinical and biomechanical effects and can these predict a three-month clinical outcome?", Arthritis Rheum. **59**, 408–415 (2008) 10.1002/art.23326.

[63]M. Khosravi, T. Babaee, A. Daryabor, and M. Jalali, "Effect of knee braces and insoles on clinical outcomes of individuals with medial knee osteoarthritis: A systematic review and meta-analysis", Assist. Technol. **34**, 501–517 (2022) 10.1080/10400435.2021.1880495.

[64]P. Jindasakchai, C. Angthong, P. Panyarachun, P. Rajbhandari, and N. Rungrattanawilai, "Therapeutic significance of insoles in patients with knee osteoarthritis", Eur. Rev. Med. Pharmacol. Sci. **27**, 5023–5030 (2023) 10.26355/eurrev_202306_32619.

[65]S. C. O'Reilly, K. R. Muir, and M. Doherty, "Effectiveness of home exercise on pain and disability from osteoarthritis of the knee: a randomised controlled trial", Ann. Rheum. Dis. **58**, 15–19 (1999) 10.1136/ard.58.1.15.

[66]D. D. Hegde, K. Hadya Ananda, and N. Vavachan, "Effectiveness of Quadriceps Strength Training in Adults With Knee Osteoarthritis: A Systematized Review", Musculoskeletal Care **23**, e70134 (2025) 10.1002/msc.70134.

[67]M. Hall, R. Hinman, T. Wrigley, J. Kasza, B.-W. Lim, and K. Bennell, "Knee extensor strength gains mediate symptom improvement in knee osteoarthritis: secondary analysis of a randomised controlled trial", Osteoarthritis Cartilage **26**, 495–500 (2018) 10.1016/j.joca.2018.01.018.

[68]P. DeVita, J. Aaboe, C. Bartholdy, J. M. Leonardis, H. Bliddal, and M. Henriksen, "Quadriceps-strengthening exercise and quadriceps and knee biomechanics during walking in knee osteoarthritis: A two-centre randomized controlled trial", Clin. Biomech. **59**, 199–206 (2018) 10.1016/j.clinbiomech.2018.09.016.

[69]H. R. Bokaeian, A. H. Bakhtiary, M. Mirmohammadkhani, and J. Moghimi, "Quadriceps strengthening exercises may not change pain and function in knee osteoarthritis", J. Bodyw. Mov. Ther. **22**, 528–533 (2018) 10.1016/j.jbmt.2017.06.013.

[70]S. P. Messier, S. L. Mihalko, D. P. Beavers, B. J. Nicklas, P. DeVita, J. J. Carr, D. J. Hunter, M. Lyles, A. Guermazi, K. L. Bennell, and R. F. Loeser, "Effect of High-Intensity Strength Training on Knee Pain and Knee Joint Compressive Forces Among Adults With Knee Osteoarthritis: The START Randomized Clinical Trial", JAMA **325**, 646 (2021) 10.1001/jama.2021.0411.

[71]K. Bennell, R. Nelligan, A. Kimp, S. Schwartz, J. Kasza, T. Wrigley, B. Metcalf, P. Hodges, and R. Hinman, "What type of exercise is most effective for people with knee osteoarthritis and co-morbid obesity?: The TARGET randomized controlled trial", Osteoarthritis Cartilage **28**, 755–765 (2020) 10.1016/j.joca.2020.02.838.

[72]D. Hryvniak, R. P. Wilder, J. Jenkins, and S. M. Statuta, "Therapeutic Exercise", in *Braddom's Physical Medicine and Rehabilitation* (Elsevier, 2021), 291–315.e4, 10.1016/B978-0-323-62539-5.00015-1.

[73]J. W. Atchison, R. B. Tolchin, B. S. Ross, and J. E. Eubanks, "Manipulation, Traction, and Massage", in *Braddom's Physical Medicine and Rehabilitation* (Elsevier, 2021), 316–337.e7, 10.1016/B978-0-323-62539-5.00016-3.

[74]R. J. Holt, J. G. Fort, A. Y. Grahn, J. D. Kent, and A. E. Bello, "Onset and durability of pain relief in knee osteoarthritis: Pooled results from two placebo trials of naproxen/esomeprazole combination and celecoxib", Phys. Sportsmed. **43**, 200–212 (2015) 10.1080/00913847.2015.1074852.

[75]J. M. Bjordal, A. E. Ljunggren, A. Klovning, and L. Slørdal, "Non-steroidal anti-inflammatory drugs, including cyclo-oxygenase-2 inhibitors, in osteoarthritic knee pain: meta-analysis of randomised placebo controlled trials", BMJ **329**, 1317 (2004) 10.1136/bmj.38273.626655.63.

[76]A. Concoff, J. Rosen, F. Fu, M. Bhandari, K. Boyer, J. Karlsson, T. A. Einhorn, and E. Schemitsch, "A Comparison of Treatment Effects for Nonsurgical Therapies and the Minimum Clinically Important Difference in Knee Osteoarthritis: A Systematic Review", JBJS Rev. **7**, e5–e5 (2019) 10.2106/JBJS.RVW.18.00150.

[77]R. A. Moore, O. A. Moore, S. Derry, P. M. Peloso, A. R. Gammaitoni, and H. Wang, "Responder analysis for pain relief and numbers needed to treat in a meta-analysis of etoricoxib osteoarthritis trials: bridging a gap between clinical trials and clinical practice", Ann. Rheum. Dis. **69**, 374–379 (2010) 10.1136/ard.2009.107805.

[78]Z. Salis and A. Sainsbury, "Association of long-term use of non-steroidal anti-inflammatory drugs with knee osteoarthritis: a prospective multi-cohort study over 4-to-5 years", Sci. Rep. **14**, 6593 (2024) 10.1038/s41598-024-56665-3.

[79]R. Wu, Y. Ma, M. Li, Q. Li, Z. Deng, Y. Chen, Q. Zheng, and G. Fu, "Baseline Knee Pain Predicts Long-Term Response of Intra-Articular Steroid Injection in Symptomatic Knee Osteoarthritis: Data from OAI", CARTILAGE **14**, 144–151 (2023) 10.1177/19476035221144745.

[80]Adnan Haider, Prem Chand, Abdul Aleem, Ali Muhammad, Saoud Javed, and Yazdan Bin Kamran, "Meta Analysis on Outcomes of Intra Articular Knee Injections: Hyaluronic Acid and Corticosteroid for Knee Osteoarthritis", J. Health Wellness Community Res., e1032 (2025) 10.61919/c6d0sh59.

[81]F. Berenbaum, J. Grifka, S. Cazzaniga, M. D'Amato, G. Giacovelli, X. Chevalier, F. Rannou, L. C. Rovati, and E. Maheu, "A randomised, double-blind, controlled trial comparing two intra-articular hyaluronic acid preparations differing by their molecular weight in symptomatic knee osteoarthritis", Ann. Rheum. Dis. **71**, 1454–1460 (2012) 10.1136/annrheumdis-2011-200972.

[82]J. M. Borst, S. Ruoss, I. Palmer, T. Smith, K. Kalunian, and S. R. Ward, "Placebo Effect Sizes in Clinical Trials of Knee Osteoarthritis Using Intra-Articular Injections of Biologic Agents", Arthritis Care Res. **77**, 998–1006 (2025) 10.1002/acr.25526.

[83]D. Gregori, G. Giacovelli, C. Minto, B. Barbetta, F. Gualtieri, D. Azzolina, P. Vaghi, and L. C. Rovati, "Association of Pharmacological Treatments With Long-term Pain Control in Patients With Knee Osteoarthritis: A Systematic Review and Meta-analysis", JAMA **320**, 2564 (2018) 10.1001/jama.2018.19319.

[84]W. Ding, D. Du, and S. Chen, "LIPUS promotes synthesis and secretion of extracellular matrix and reduces cell apoptosis in human osteoarthritis through upregulation of SOX9 expression", Int. J. Clin. Exp. Pathol. **13**, 810–817 (2020).

[85]C. M. Korstjens, R. H. H. Van Der Rijt, G. H. R. Albers, C. M. Semeins, and J. Klein-Nulend, "Low-intensity pulsed ultrasound affects human articular chondrocytes in vitro", Med. Biol. Eng. Comput. **46**, 1263 (2008) 10.1007/s11517-008-0409-9.

[86]M. Guan, X. Zhang, X. Li, B. Liao, W. Han, J. Tan, Z. Wang, L. Wang, J. Shen, X. Han, and D. Bai, "Research Progress of Osteoarthritis Treatment by Low Intensity Pulsed Ultrasound", Smart Med. **4**, e70003 (2025) 10.1002/smmd.70003.

[87]H. Ye, D. Li, X. Wei, L. Yu, and L. Jia, "Focused low-intensity pulsed ultrasound alleviates osteoarthritis via restoring impaired FUNDC1-mediated mitophagy", iScience **26**, 107772 (2023) 10.1016/j.isci.2023.107772.

[88]P. Xia, Q. Wang, J. Song, X. Wang, X. Wang, Q. Lin, K. Cheng, A. Chen, and X. Li, "Low-Intensity Pulsed Ultrasound Enhances the Efficacy of Bone Marrow–Derived MSCs in Osteoarthritis Cartilage Repair by Regulating Autophagy-Mediated Exosome Release", CARTILAGE **13**, 19476035221093060 (2022) 10.1177/19476035221093060.

[89]L. Jia, Y. Wang, J. Chen, and W. Chen, “Efficacy of focused low-intensity pulsed ultrasound therapy for the management of knee osteoarthritis: a randomized, double blind, placebo-controlled trial”, Sci. Rep. **6**, 35453 (2016) 10.1038/srep35453.

[90]F. A. Khadour, Y. A. Khadour, and N. S. K. Alharbi, “Synergistic effects of low-intensity pulsed ultrasound and extracorporeal shock wave therapy in knee osteoarthritis: clinical outcomes and biochemical mechanisms”, J. Orthop. Surg. **20**, 942 (2025) 10.1186/s13018-025-06384-w.

[91]D. O. Draper, D. Klyve, R. Ortiz, and T. M. Best, “Effect of low-intensity long-duration ultrasound on the symptomatic relief of knee osteoarthritis: a randomized, placebo-controlled double-blind study”, J. Orthop. Surg. **13**, 257 (2018) 10.1186/s13018-018-0965-0.

[92]J. Zhou, E. Ning, L. Lu, H. Zhang, X. Yang, and Y. Hao, “Effectiveness of low-intensity pulsed ultrasound on osteoarthritis: molecular mechanism and tissue engineering”, Front. Med. **11**, 1292473 (2024) 10.3389/fmed.2024.1292473.

[93]A. Loyola-Sánchez, J. Richardson, K. A. Beattie, C. Otero-Fuentes, J. D. Adachi, and N. J. MacIntyre, “Effect of Low-Intensity Pulsed Ultrasound on the Cartilage Repair in People With Mild to Moderate Knee Osteoarthritis: A Double-Blinded, Randomized, Placebo-Controlled Pilot Study”, Arch. Phys. Med. Rehabil. **93**, 35–42 (2012) 10.1016/j.apmr.2011.07.196.

[94]A. Karakas, M. A. Şahin, H. Ellidokuz, B. Dilek, and Ö. Şenocak, “THU0435 ASSESING THE EFFECTS OF PULSED ULTRASOUND TREATMENT ON PAIN, FUNCTIONALITY, SYNOVIAL FLUID AND CARTILAGE THICKNESS, IN KNEE OSTEOARTHRITIS”, Ann. Rheum. Dis. **78**, 506–507 (2019) 10.1136/annrheumdis-2019-eular.6322.

[95]A. D. Sawitzke, C. G. Jackson, K. Carlson, M. D. Bizien, M. Leiner, D. J. Reda, T. Sindowski, C. Hanrahan, R. G. Spencer, C. K. Kwoh, S. J. Lee, K. Hose, L. Robin, D. W. Cain, M. D. Taylor, N. Bangerter, M. Finco, and D. O. Clegg, “Effect of Pulsed Low-Intensity Ultrasonography on Symptom Relief and Tibiofemoral Articular Cartilage Thickness Among Veterans Affairs Enrollees With Knee Osteoarthritis: A Randomized Clinical Trial”, JAMA Netw. Open **5**, e220632 (2022) 10.1001/jamanetworkopen.2022.0632.

[96]C. G. Qiu, C. S. Chui, S. K. H. Chow, W.-H. Cheung, and R. M. Y. Wong, “Effects of Whole-Body Vibration Therapy on Knee Osteoarthritis: A Systematic Review and Meta-Analysis of Randomized Controlled Trials”, J. Rehabil. Med. **54**, jrm00266 (2022) 10.2340/jrm.v54.2032.

[97]Y. Peng, Q. Qi, C. L. Lee, Y. L. Tay, S. C. Chai, and M. A. Ahmad, “Effects of whole-body vibration training as an adjunct to conventional rehabilitation exercise on pain, physical function and disability

in knee osteoarthritis: A systematic review and meta-analysis", PLOS ONE **20**, edited by S. Rogan, e0318635 (2025) 10.1371/journal.pone.0318635.

[98]T. Trans, J. Aaboe, M. Henriksen, R. Christensen, H. Bliddal, and H. Lund, "Effect of whole body vibration exercise on muscle strength and proprioception in females with knee osteoarthritis", The Knee **16**, 256–261 (2009) 10.1016/j.knee.2008.11.014.

[99]E. Moreira-Marconi, Y. Teixeira-Silva, A. G. D. Meirelles, M. C. Moura-Fernandes, P. Lopes-Souza, A. Reis-Silva, R. M. Marchon, E. D. O. Guedes-Aguiar, L. L. Paineiras-Domingos, D. D. C. De Sá-Caputo, M. E. D. S. Melo-Oliveira, B. B. M. D. Oliveira, M. A. D. S. Gama, R. Alvim-Oliveira, D. Batouli-Santos, A. C. R. Lacerda, V. A. Mendonça, V. L. Xavier, L. P. D. Oliveira, A. D. P. Mozella, B. Sañudo, A. Seixas, R. Taiar, D. Cochrane, and M. Bernardo-Filho, "Effect of Whole-Body Vibration on the Functional Responses of the Patients with Knee Osteoarthritis by the Electromyographic Profile of the Vastus Lateralis Muscles during the Five-Repetition Chair Stand Test: A Randomized Crossover Trial", Appl. Sci. **10**, 4302 (2020) 10.3390/app10124302.

[100]H. Wang, C. Zhang, S. Zhu, C. Gao, Q. Gao, R. Huang, S. Liu, X. Wei, H. Zhang, Q. Wei, and C. He, "Low-frequency whole-body vibration can enhance cartilage degradation with slight changes in subchondral bone in mice with knee osteoarthritis and does not have any morphologic effect on normal joints", PLOS ONE **18**, edited by L. Han, e0270074 (2023) 10.1371/journal.pone.0270074.

[101]W. Junbo, L. Sijia, C. Hongying, L. Lei, and W. Pu, "Effect of low-magnitude different-frequency whole-body vibration on subchondral trabecular bone microarchitecture, cartilage degradation, bone/cartilage turnover, and joint pain in rabbits with knee osteoarthritis", BMC Musculoskelet. Disord. **18**, 260 (2017) 10.1186/s12891-017-1579-0.

[102]X. Li, X.-Q. Wang, B.-L. Chen, L.-Y. Huang, and Y. Liu, "Whole-Body Vibration Exercise for Knee Osteoarthritis: A Systematic Review and Meta-Analysis", Evid. Based Complement. Alternat. Med. **2015**, 1–11 (2015) 10.1155/2015/758147.

[103]K. K. L. Lau, A. S. C. Chen, C. H. Y. Fu, J. P. Ng, M. T. Y. Ong, P. S. H. Yung, and P. P. Y. Lui, "Pulsed Electromagnetic Field Therapy for Mild-to-Moderate Knee Osteoarthritis: A Double-Blind, Randomized, Placebo-Controlled Clinical Trial", J. Cachexia Sarcopenia Muscle **17**, e70199 (2026) 10.1002/jcsm.70199.

[104]Q.-w. Wang, M. T.-y. Ong, G. C.-w. Man, A. Franco-Obregón, B. C.-y. Choi, P. P.-y. Lui, D. T. P. Fong, J.-h. Qiu, X. He, J. P. Ng, and P. S.-h. Yung, "The effects of pulsed electromagnetic field therapy on

muscle strength and pain in patients with end-stage knee osteoarthritis: a randomized controlled trial", Front. Med. **11**, 1435277 (2024) 10.3389/fmed.2024.1435277.

[105]L. Cianni, E. Di Gialleonardo, D. Coppola, G. Capece, E. Libutti, M. Nannerini, G. Maccauro, and R. Vitiello, "Current Evidence Using Pulsed Electromagnetic Fields in Osteoarthritis: A Systematic Review", J. Clin. Med. **13**, 1959 (2024) 10.3390/jcm13071959.

[106]A. Kaadan, S. Salati, R. Cadossi, and R. Aaron, "Regulation of Inflammatory Responses by Pulsed Electromagnetic Fields", Bioengineering **12**, 474 (2025) 10.3390/bioengineering12050474.

[107]S. Zhou, H. Wen, X. He, X. Han, and H. Li, "Pulsed electromagnetic field ameliorates the progression of osteoarthritis via the Sirt1/NF-$\kappa$B pathway", Arthritis Res. Ther. **27**, 33 (2025) 10.1186/s13075-025-03492-0.

[108]B. Masante, S. Gabetti, J. C. Silva, G. Putame, S. Israel, C. Bignardi, and D. Massai, "Insights into bone and cartilage responses to pulsed electromagnetic field stimulation: a review with quantitative comparisons", Front. Bioeng. Biotechnol. **13**, 1557572 (2025) 10.3389/fbioe.2025.1557572.

[109]J. Avendaño-Coy, N. Comino-Suárez, J. Grande-Muñoz, C. Avendaño-López, and J. Gómez-Soriano, "Extracorporeal shockwave therapy improves pain and function in subjects with knee osteoarthritis: A systematic review and meta-analysis of randomized clinical trials", Int. J. Surg. **82**, 64–75 (2020) 10.1016/j.ijsu.2020.07.055.

[110]P.-C. Liao, S.-H. Chou, and C.-L. Shih, "A systematic review of the use of shockwave therapy for knee osteoarthritis", J. Orthop. **56**, 18–25 (2024) 10.1016/j.jor.2024.04.020.

[111]N.-Y. Ko, C.-N. Chang, C.-H. Cheng, H.-K. Yu, and G.-C. Hu, "Comparative Effectiveness of Focused Extracorporeal versus Radial Extracorporeal Shockwave Therapy for Knee Osteoarthritis—Randomized Controlled Study", Int. J. Environ. Res. Public. Health **19**, 9001 (2022) 10.3390/ijerph19159001.

[112]I. J. Choi, J. H. Jeon, W. H. Choi, and H.-E. Yang, "Effects of extracorporeal shockwave therapy for mild knee osteoarthritis: A pilot study", Medicine (Baltimore) **102**, e36117 (2023) 10.1097/MD.0000000000036117.

[113]J.-H. Kim, J.-Y. Kim, C.-M. Choi, J.-K. Lee, H.-S. Kee, K.-I. Jung, and S.-R. Yoon, "The Dose-Related Effects of Extracorporeal Shock Wave Therapy for Knee Osteoarthritis", Ann. Rehabil. Med. **39**, 616 (2015) 10.5535/arm.2015.39.4.616.

[114]H. Madry, "Surgical therapy in osteoarthritis", Osteoarthritis Cartilage **30**, 1019–1034 (2022) 10.1016/j.joca.2022.01.012.

[115]P. Brumat, O. Kunšič, S. Novak, U. Slokar, J. Pšenica, M. Topolovec, R. Mihalič, and R. Trebše, "The Surgical Treatment of Osteoarthritis", Life **12**, 982 (2022) 10.3390/life12070982.

[116]D. J. Haslhofer, J. Shatrov, M. Jones, W. Abdul, A. Motesharei, S. V. Ball, and A. Williams, "Microfracture for full-thickness chondral lesions of the knee in elite athletes leads to high return-to-play rates", Knee Surg. Sports Traumatol. Arthrosc., ksa.12808 (2025) 10.1002/ksa.12808.

[117]Y.-Y. Kuo, S.-Q. Chiu, W.-P. Chang, C.-Y. Chen, C.-H. Chen, C.-K. Liaw, C.-A. Tan, and P.-W. Weng, "A prospective randomized controlled trial comparing biphasic cartilage repair implant with microfracture in small chondral lesions of knee: findings at five-year-follow-up", J. Orthop. Surg. **20**, 73 (2025) 10.1186/s13018-024-05392-6.

[118]S. Kjennvold, J. H. Røtterud, M. Forssblad, L. Engebretsen, A. Årøen, and S. Ulstein, "Debridement or Microfracture for Full-Thickness Cartilage Lesions in Anterior Cruciate Ligament Reconstruction: A 10-Year Cohort Study of 326 Patients in Norway and Sweden", Orthop. J. Sports Med. **13**, 23259671251381340 (2025) 10.1177/23259671251381340.

[119]A. E. Weber, P. H. Locker, E. N. Mayer, G. L. Cvetanovich, A. K. Tilton, B. J. Erickson, A. B. Yanke, and B. J. Cole, "Clinical Outcomes After Microfracture of the Knee: Midterm Follow-up", Orthop. J. Sports Med. **6**, 2325967117753572 (2018) 10.1177/2325967117753572.

[120]V. Gopinatth, G. R. Jackson, D. C. Touhey, J. Chahla, M. V. Smith, M. J. Matava, R. H. Brophy, and D. M. Knapik, "Microfracture for medium size to large knee chondral defects has limited long-term efficacy: A systematic review", J. Exp. Orthop. **11**, e70060 (2024) 10.1002/jeo2.70060.

[121]T. B. Birmingham, C. A. Primeau, R. F. Moyer, D. M. Bryant, J. Ma, K. M. Leitch, W. Wirth, R. Degen, A. M. Getgood, R. B. Litchfield, K. R. Willits, F. Eckstein, and J. R. Giffin, "High Tibial Osteotomy for Medial Compartment Knee Osteoarthritis: A Randomized Trial With Parallel Preference Arm", Ann. Intern. Med. **178**, 1238–1248 (2025) 10.7326/ANNALS-25-00920.

[122]Y. Fuchioka, N. Ozeki, H. Koga, T. Nakamura, Y. Nakagawa, M. Amemiya, A. Asami, H. Katano, and I. Sekiya, "3D-MRI evaluation of cartilage thickness changes and their location in the patellofemoral joint after open wedge high tibial osteotomy for knee osteoarthritis: A retrospective cohort study", PLOS One **20**, edited by S. Han, e0333961 (2025) 10.1371/journal.pone.0333961.

[123]M. Jansen, S. Maschek, R. van Heerwaarden, S. Mastbergen, W. Wirth, F. Lafeber, and F. Eckstein, "Changes in Cartilage Thickness and Denuded Bone Area after Knee Joint Distraction and High Tibial Osteotomy-Post-Hoc Analyses of Two Randomized Controlled Trials", J. Clin. Med. **10** (2021) 10.3390/jcm10020368.

[124]H.-S. Moon, C.-H. Choi, J.-H. Yoo, M. Jung, T.-H. Lee, J.-W. Byun, and S.-H. Kim, "An Increase in Medial Joint Space Width After Medial Open-Wedge High Tibial Osteotomy Is Associated With an Increase in the Postoperative Weight-Bearing Line Ratio Rather Than With Cartilage Regeneration: Comparative Analysis of Patients Who Underwent Second-Look Arthroscopic Assessment", Arthroscopy **37**, 657 (2021) 10.1016/j.arthro.2020.09.042.

[125]M. Lughi, "Evaluation of patients' satisfaction after knee arthroplasty", Joints **3** (2025) 10.26355/joints_20258_1583.

[126]B. G. Hill, S. Shah, W. E. Moschetti, and P. L. Schilling, "Do Patient-Reported Outcomes Reflect Objective Measures of Function? Implications for Total Knee Arthroplasty", J. Arthroplasty **38**, S162–S168.e3 (2023) 10.1016/j.arth.2023.04.049.

[127]Y. Zhang, A. Folarin, C. Stewart, H. Kim, R. Zhong, S. Sun, and R. J. Dobson, *Preoperative Decline and Postoperative Recovery of Wearable-Derived Physical Activity Over a Four-Year Perioperative Period in Total Knee and Hip Arthroplasty: Evidence from the All of Us Research Program*, version 1, (2026) 10.48550/ARXIV.2603.05741, https://arxiv.org/abs/2603.05741 (visited on 04/01/2026), pre-published.

[128]M. Vella-baldacchino, A. Bottle, J. Cobb, and A. D. Liddle, "Patient-reported outcomes following patellofemoral and total knee replacement: an analysis of the 6–18 months postoperative period from the National Joint Registry", Acta Orthop. **97** (2026) 10.2340/17453674.2025.45115.

[129]D. W. Lee, D. H. Ro, H.-S. Han, and M. C. Lee, "Patella Cartilage Status Does Not Affect the Clinical Outcomes of Non-resurfaced Patella in Mobile-Bearing Total Knee Arthroplasty", Clin. Orthop. Surg. **16**, 242 (2023) 10.4055/cios22253.

[130]S. Nettel, *Wave Physics* (Springer Berlin Heidelberg, Berlin, Heidelberg, 2009), 10.1007/978-3-540-87908-4.

[131]A. D. Pierce, *Acoustics: an introduction to its physical principles and applications*, 1989 ed (Acoustical Society of America, Woodbury, N.Y, 1989), 678 pp.

[132]D. T. Blackstock, *Fundamentals of physical acoustics*, A Wiley-Interscience Publication (Wiley, New York, NY, 2000), 541 pp.

[133]L. E. Kinsler, ed., *Fundamentals of acoustics*, 4th ed (Wiley, New York, 2000), 548 pp.

[134]S. Temkin, *Elements of acoustics* (Published by the Acoustical Society of America through the American Institute of Physics, Woodbury, NY, 2001), 515 pp.

[135]N. A. T. C. Fernandes, S. Sharma, A. Arieira, B. Hinckel, F. Silva, A. Leal, and Ó. Carvalho, "Experimental Validation of Time-Explicit Ultrasound Propagation Models with Sound Diffusivity or Viscous Attenuation in Biological Tissues Using COMSOL Multiphysics", Bioengineering **12**, 946 (2025) 10.3390/bioengineering12090946.

[136]K. F. Graff, ed., *Wave motion in elastic solids* (Dover Publications, New York, 1991), 649 pp.

[137]P. N. T. Wells and H.-D. Liang, "Medical ultrasound: imaging of soft tissue strain and elasticity", J. R. Soc. Interface **8**, 1521–1549 (2011) 10.1098/rsif.2011.0054.

[138]M. Cè, N. C. D'Amico, G. M. Danesini, C. Foschini, G. Oliva, C. Martinenghi, and M. Cellina, "Ultrasound Elastography: Basic Principles and Examples of Clinical Applications with Artificial Intelligence—A Review", BioMedInformatics **3**, 17–43 (2023) 10.3390/biomedinformatics3010002.

[139]M. F. Hamilton and D. T. Blackstock, eds., *Nonlinear Acoustics* (Springer Nature Switzerland, Cham, 2024), 10.1007/978-3-031-58963-8.

[140]H. B. Khaniki, M. H. Ghayesh, R. Chin, and M. Amabili, "Hyperelastic structures: A review on the mechanics and biomechanics", Int. J. Non-Linear Mech. **148**, 104275 (2023) 10.1016/j.ijnonlinmec.2022.104275.

[141]A. Amendola, J. De Castro Motta, and L. Vergori, "Wave propagation in compressible hyperelastic solids in the presence of powerless internal forces", Int. J. Eng. Sci. **214**, 104294 (2025) 10.1016/j.ijengsci.2025.104294.

[142]S. Li and E. Sitnikova, *Representative volume elements and unit cells: concepts, theory, applications and implementation*, Woodhead Publishing Series in Composites Science and Engineering (Elsevier, Duxford Cambridge, 2020).

[143]A. H. Nayfeh, ed., *Wave propagation in layered anisotropic media: with applications to composites*, North-Holland Series in Applied Mathematics and Mechanics v. 39 (Elsevier, Amsterdam New York, 1995), 332 pp.

[144]G. Sandberg and R. Ohayon, eds., *Computational aspects of structural acoustics and vibration*, CISM Courses and Lectures no. 505 (Springer, Wien ; New York, 2008), 276 pp.

[145]E. M. Dede, J. Lee, and T. Nomura, *Multiphysics Simulation: Electromechanical System Applications and Optimization*, Simulation Foundations, Methods and Applications (Springer London, London, 2014), 10.1007/978-1-4471-5640-6.

[146]D. J. Nefske, S. A. Hambric, and S. H. Sung, eds., *Engineering vibroacoustic analysis: methods and applications* (John Wiley & Sons Inc, Chichester, West Sussex, United Kingdom, 2016), 1 p., 10.1002/9781118693988.

[147]S. S. Rao, *Mechanical vibrations*, Sixth edition in SI Units, global edition (Pearson, Harlow, United Kingdom, 2018), 1 p.

[148]M. A. Biot, "Mechanics of Deformation and Acoustic Propagation in Porous Media", J. Appl. Phys. **33**, 1482–1498 (1962) 10.1063/1.1728759.

[149]M. A. Biot, "Theory of Propagation of Elastic Waves in a Fluid-Saturated Porous Solid. II. Higher Frequency Range", J. Acoust. Soc. Am. **28**, 179–191 (1956) 10.1121/1.1908241.

[150]M. A. Biot, "Theory of Propagation of Elastic Waves in a Fluid-Saturated Porous Solid. I. Low-Frequency Range", J. Acoust. Soc. Am. **28**, 168–178 (1956) 10.1121/1.1908239.

[151]S. C. Cowin, "Bone poroelasticity", J. Biomech. **32**, 217–238 (1999) 10.1016/S0021-9290(98)00161-4.

[152]S. Kulkarni and S. L. Wunder, "Moduli of ordered polymer composites prepared by colloidal crystallization of nano- and micro-SiO2 spheres in crosslinked methacrylate resins", Mech. Mater. **43**, 643–653 (2011) 10.1016/j.mechmat.2011.08.009.

[153]A. B. Movchan, N. V. Movchan, I. S. Jones, and D. J. Colquitt, *Mathematical Modelling of Waves in Multi-Scale Structured Media*, 1st ed. (Chapman and Hall/CRC, Nov. 9, 2017), 10.1201/9781315155388.

[154]H. H. Pennes, "*Analysis of Tissue and Arterial Blood Temperatures in the Resting Human Forearm*", J. Appl. Physiol. **1**, 93–122 (1948) 10.1152/jappl.1948.1.2.93.

[155]J. A. Pearce, "Relationship between Arrhenius models of thermal damage and the CEM 43 thermal dose", in , edited by T. P. Ryan (Feb. 12, 2009), p. 718104, 10.1117/12.807999.

[156]X. Di, X. Gao, L. Peng, J. Ai, X. Jin, S. Qi, H. Li, K. Wang, and D. Luo, "Cellular mechanotransduction in health and diseases: from molecular mechanism to therapeutic targets", Signal Transduct. Target. Ther. **8**, 282 (2023) 10.1038/s41392-023-01501-9.

[157]D. E. Ingber, "Cellular mechanotransduction: putting all the pieces together again", FASEB J. **20**, 811–827 (2006) 10.1096/fj.05-5424rev.

[158]V. Vogel and M. Sheetz, "Local force and geometry sensing regulate cell functions", Nat. Rev. Mol. Cell Biol. **7**, 265–275 (2006) 10.1038/nrm1890.

[159]F. Martino, A. R. Perestrelo, V. Vinarský, S. Pagliari, and G. Forte, "Cellular Mechanotransduction: From Tension to Function", Front. Physiol. **9**, 824 (2018) 10.3389/fphys.2018.00824.

[160]D. E. Jaalouk and J. Lammerding, "Mechanotransduction gone awry", Nat. Rev. Mol. Cell Biol. **10**, 63–73 (2009) 10.1038/nrm2597.

[161]A. J. Engler, S. Sen, H. L. Sweeney, and D. E. Discher, "Matrix Elasticity Directs Stem Cell Lineage Specification", Cell **126**, 677–689 (2006) 10.1016/j.cell.2006.06.044.

[162]T. J. Knobloch, S. Madhavan, J. Nam, S. Agarwal Jr., and S. Agarwal, "Regulation of Chondrocytic Gene Expression by Biomechanical Signals", Crit. Rev. Eukaryot. Gene Expr. **18**, 139–150 (2008) 10.1615/CritRevEukarGeneExpr.v18.i2.30.

[163]T. D. Brown, "Techniques for mechanical stimulation of cells in vitro: a review", J. Biomech. **33**, 3–14 (2000) 10.1016/S0021-9290(99)00177-3.

[164]D. E. Discher, P. Janmey, and Y.-l. Wang, "Tissue Cells Feel and Respond to the Stiffness of Their Substrate", Science **310**, 1139–1143 (2005) 10.1126/science.1116995.

[165]E. Ozcivici, Y. K. Luu, B. Adler, Y.-X. Qin, J. Rubin, S. Judex, and C. T. Rubin, "Mechanical signals as anabolic agents in bone", Nat. Rev. Rheumatol. **6**, 50–59 (2010) 10.1038/nrrheum.2009.239.

[166]L. Xie, J. M. Jacobson, E. S. Choi, B. Busa, L. R. Donahue, L. M. Miller, C. T. Rubin, and S. Judex, "Low-level mechanical vibrations can influence bone resorption and bone formation in the growing skeleton", Bone **39**, 1059–1066 (2006) 10.1016/j.bone.2006.05.012.

[167]D. Dalecki, "Mechanical Bioeffects of Ultrasound", Annu. Rev. Biomed. Eng. **6**, 229–248 (2004) 10.1146/annurev.bioeng.6.040803.140126.

[168]F. Padilla, R. Puts, L. Vico, and K. Raum, "Stimulation of bone repair with ultrasound: A review of the possible mechanic effects", Ultrasonics **54**, 1125–1145 (2014) 10.1016/j.ultras.2014.01.004.

[169]P. F. Davies, "Flow-mediated endothelial mechanotransduction", Physiol. Rev. **75**, 519–560 (1995) 10.1152/physrev.1995.75.3.519.

[170]C. Hahn and M. A. Schwartz, "Mechanotransduction in vascular physiology and atherogenesis", Nat. Rev. Mol. Cell Biol. **10**, 53–62 (2009) 10.1038/nrm2596.

[171]Y.-S. J. Li, J. H. Haga, and S. Chien, "Molecular basis of the effects of shear stress on vascular endothelial cells", J. Biomech. **38**, 1949–1971 (2005) 10.1016/j.jbiomech.2004.09.030.

[172]M. Zhao, B. Song, J. Pu, T. Wada, B. Reid, G. Tai, F. Wang, A. Guo, P. Walczysko, Y. Gu, T. Sasaki, A. Suzuki, J. V. Forrester, H. R. Bourne, P. N. Devreotes, C. D. McCaig, and J. M. Penninger, "Electrical signals control wound healing through phosphatidylinositol-3-OH kinase-$\gamma$ and PTEN", Nature **442**, 457–460 (2006) 10.1038/nature04925.

[173]C. D. McCaig, A. M. Rajnicek, B. Song, and M. Zhao, "Controlling Cell Behavior Electrically: Current Views and Future Potential", Physiol. Rev. **85**, 943–978 (2005) 10.1152/physrev.00020.2004.

[174]T. J. Kirby and J. Lammerding, "Emerging views of the nucleus as a cellular mechanosensor", Nat. Cell Biol. **20**, 373–381 (2018) 10.1038/s41556-018-0038-y.

[175]D. Leckband and J. De Rooij, "Cadherin Adhesion and Mechanotransduction", Annu. Rev. Cell Dev. Biol. **30**, 291–315 (2014) 10.1146/annurev-cellbio-100913-013212.

[176]M. Rocio Servin-Vences, M. Moroni, G. R. Lewin, and K. Poole, "Direct measurement of TRPV4 and PIEZO1 activity reveals multiple mechanotransduction pathways in chondrocytes", eLife **6**, e21074 (2017) 10.7554/eLife.21074.

[177]R. Syeda, J. Xu, A. E. Dubin, B. Coste, J. Mathur, T. Huynh, J. Matzen, J. Lao, D. C. Tully, I. H. Engels, H. M. Petrassi, A. M. Schumacher, M. Montal, M. Bandell, and A. Patapoutian, "Chemical activation of the mechanotransduction channel Piezo1", eLife **4**, e07369 (2015) 10.7554/eLife.07369.

[178]A. Elosegui-Artola, I. Andreu, A. E. Beedle, A. Lezamiz, M. Uroz, A. J. Kosmalska, R. Oria, J. Z. Kechagia, P. Rico-Lastres, A.-L. Le Roux, C. M. Shanahan, X. Trepat, D. Navajas, S. Garcia-Manyes, and P. Roca-Cusachs, "Force Triggers YAP Nuclear Entry by Regulating Transport across Nuclear Pores", Cell **171**, 1397–1410.e14 (2017) 10.1016/j.cell.2017.10.008.

[179]C. Guilluy, L. D. Osborne, L. Van Landeghem, L. Sharek, R. Superfine, R. Garcia-Mata, and K. Burridge, "Isolated nuclei adapt to force and reveal a mechanotransduction pathway in the nucleus", Nat. Cell Biol. **16**, 376–381 (2014) 10.1038/ncb2927.

[180]S. V. Plotnikov, A. M. Pasapera, B. Sabass, and C. M. Waterman, "Force Fluctuations within Focal Adhesions Mediate ECM-Rigidity Sensing to Guide Directed Cell Migration", Cell **151**, 1513–1527 (2012) 10.1016/j.cell.2012.11.034.

[181]C.-P. Heisenberg and Y. Bellaïche, "Forces in Tissue Morphogenesis and Patterning", Cell **153**, 948–962 (2013) 10.1016/j.cell.2013.05.008.

[182]S. S. Ranade, R. Syeda, and A. Patapoutian, "Mechanically Activated Ion Channels", Neuron **87**, 1162–1179 (2015) 10.1016/j.neuron.2015.08.032.

[183]S. Dupont, L. Morsut, M. Aragona, E. Enzo, S. Giulitti, M. Cordenonsi, F. Zanconato, J. Le Digabel, M. Forcato, S. Bicciato, N. Elvassore, and S. Piccolo, "Role of YAP/TAZ in mechanotransduction", Nature **474**, 179–183 (2011) 10.1038/nature10137.

[184]M. Aragona, T. Panciera, A. Manfrin, S. Giulitti, F. Michielin, N. Elvassore, S. Dupont, and S. Piccolo, "A Mechanical Checkpoint Controls Multicellular Growth through YAP/TAZ Regulation by Actin-Processing Factors", Cell **154**, 1047–1059 (2013) 10.1016/j.cell.2013.07.042.

[185]J. Plummer, "Understanding a way to fly high", Nat. Mater. **15**, 819–820 (2016) 10.1038/nmat4699.

[186]K. Dey, E. Roca, G. Ramorino, and L. Sartore, "Progress in the mechanical modulation of cell functions in tissue engineering", Biomater. Sci. **8**, 7033–7081 (2020) 10.1039/D0BM01255F.

[187]M. A. Brady, S. D. Waldman, and C. R. Ethier, "The Application of Multiple Biophysical Cues to Engineer Functional Neocartilage for Treatment of Osteoarthritis. Part I: Cellular Response", Tissue Eng. Part B Rev. **21**, 1–19 (2015) 10.1089/ten.teb.2013.0757.

[188]T. Hodgkinson, I. N. Amado, F. J. O'Brien, and O. D. Kennedy, "The role of mechanobiology in bone and cartilage model systems in characterizing initiation and progression of osteoarthritis", APL Bioeng. **6**, 011501 (2022) 10.1063/5.0068277.

[189]S. J. Gilbert and E. J. Blain, "Cartilage mechanobiology: How chondrocytes respond to mechanical load", in *Mechanobiology in Health and Disease* (Elsevier, 2018), pp. 99–126, 10.1016/B978-0-12-812952-4.00004-0.

[190]L. Sharma and F. Berenbaum, eds., *Osteoarthritis: a companion to Rheumatology* (Mosby, Philadelphia, 2007), 279 pp.

[191]X. L. Lu and V. C. Mow, "Biomechanics of Articular Cartilage and Determination of Material Properties", Med. Sci. Sports Exerc. **40**, 193–199 (2008) 10.1249/mss.0b013e31815cb1fc.

[192]G. A. Ateshian, "The role of interstitial fluid pressurization in articular cartilage lubrication", J. Biomech. **42**, 1163–1176 (2009) 10.1016/j.jbiomech.2009.04.040.

[193]F. E. Freeman, "Mechanobiology in Osteochondral Tissue", in *Osteochondral Tissue Engineering*, edited by J. M. Oliveira, S. Pina, and R. L. Reis (Springer Nature Switzerland, Cham, 2026), pp. 1–29, 10.1007/978-3-031-80976-7_55-1.

[194]L. Baumgartner, K. Wuertz-Kozak, C. L. Le Maitre, F. Wignall, S. M. Richardson, J. Hoyland, C. Ruiz Wills, M. A. González Ballester, M. Neidlin, L. G. Alexopoulos, and J. Noailly, "Multiscale Regulation of the Intervertebral Disc: Achievements in Experimental, In Silico, and Regenerative Research", Int. J. Mol. Sci. **22**, 703 (2021) 10.3390/ijms22020703.

[195]M. Zhang, N. Meng, X. Wang, W. Chen, and Q. Zhang, "TRPV4 and PIEZO Channels Mediate the Mechanosensing of Chondrocytes to the Biomechanical Microenvironment", Membranes **12**, 237 (2022) 10.3390/membranes12020237.

[196]S. Uddin, B. Richbourgh, Y. Ding, A. Hettinghouse, D. Komatsu, Y.-X. Qin, and C.-J. Liu, "Chondro-protective effects of low intensity pulsed ultrasound", Osteoarthritis Cartilage **24**, 1989–1998 (2016) 10.1016/j.joca.2016.06.014.

[197]X.-Y. Zhou, X.-X. Zhang, G.-Y. Yu, Z.-C. Zhang, F. Wang, Y.-L. Yang, M. Li, and X.-Z. Wei, "Effects of Low-Intensity Pulsed Ultrasound on Knee Osteoarthritis: A Meta-Analysis of Randomized Clinical Trials", BioMed Res. Int. **2018**, 1–7 (2018) 10.1155/2018/7469197.

[198]T. Nakamura, S. Fujihara, K. Yamamoto-Nagata, T. Katsura, T. Inubushi, and E. Tanaka, "Low-Intensity Pulsed Ultrasound Reduces the Inflammatory Activity of Synovitis", Ann. Biomed. Eng. **39**, 2964–2971 (2011) 10.1007/s10439-011-0408-0.

[199]J. Zhu, Q. Luo, G. Yang, and L. Xiao, "Biofabrication of Tissue-Engineered Cartilage Constructs Through Faraday Wave Bioassembly of Cell-Laden Gelatin Microcarriers", Adv. Healthc. Mater. **13**, 2304541 (2024) 10.1002/adhm.202304541.

[200]T. Nishino, T. Ishii, F. Chang, T. Yanai, A. Watanabe, T. Ogawa, H. Mishima, K. Nakai, and N. Ochiai, "Effect of gradual weight-bearing on regenerated articular cartilage after joint distraction and motion in a rabbit model", J. Orthop. Res. **28**, 600–606 (2010) 10.1002/jor.21016.

[201]K.-H. Koo, J. S. Lee, Y. J. Lee, K.-J. Kim, J. J. Yoo, and H. J. Kim, "Endothelial nitric oxide synthase gene polymorphisms in patients with nontraumatic femoral head osteonecrosis", J. Orthop. Res. **24**, 1722–1728 (2006) 10.1002/jor.20164.

[202]M. Papandony, L. Chou, M. Seneviwickrama, F. Cicuttini, K. Lasserre, A. Teichtahl, Y. Wang, A. Briggs, and A. Wluka, "Patients' perceived health service needs for osteoarthritis (OA) care: a scoping systematic review", Osteoarthritis Cartilage **25**, 1010–1025 (2017) 10.1016/j.joca.2017.02.799.

[203]L. A. Ambattu and L. Y. Yeo, "Sonomechanobiology: Vibrational stimulation of cells and its therapeutic implications", Biophys. Rev. **4**, 021301 (2023) 10.1063/5.0127122.

[204]S. V. Gudkov, V. I. Pustovoy, R. M. Sarimov, D. A. Serov, A. V. Simakin, and I. A. Shcherbakov, “Diversity of Effects of Mechanical Influences on Living Systems and Aqueous Solutions”, Int. J. Mol. Sci. **26**, 5556 (2025) 10.3390/ijms26125556.

[205]K.-J. Bathe, ed., *Finite element procedures*, 2nd edition (K.J. Bathe, Watertown, MA, 2014), 1043 pp.

[206]A. ak, *A Finite Element Approach for Wave Propagation in Elastic Solids*, Lecture Notes on Numerical Methods in Engineering and Sciences (Springer Nature Switzerland, Cham, 2024), 10.1007/978-3-031-56836-7.

[207]R. J. LeVeque, *Finite Difference Methods for Ordinary and Partial Differential Equations: Steady-State and Time-Dependent Problems* (Society for Industrial and Applied Mathematics, Jan. 2007), 10.1137/1.9780898717839.

[208]S. A. Sauter and C. Schwab, *Boundary Element Methods*, Vol. 39, Springer Series in Computational Mathematics (Springer Berlin Heidelberg, Berlin, Heidelberg, 2011), 10.1007/978-3-540-68093-2.

[209]S. Weißer, “Boundary Integral Equations and Their Approximations”, in *BEM-based Finite Element Approaches on Polytopal Meshes*, Vol. 130 (Springer International Publishing, Cham, 2019), pp. 107–140, 10.1007/978-3-030-20961-2_4.

[210]G. Cohen and S. Pernet, *Finite Element and Discontinuous Galerkin Methods for Transient Wave Equations*, Scientific Computation (Springer Netherlands, Dordrecht, 2017), 10.1007/978-94-017-7761-2.

[211]T. M. Atanacković, S. Pilipović, B. Stanković, and D. Zorica, *Fractional Calculus With Applications in Mechanics: Wave Propagation, Impact and Variational Principles*, 1st ed. (Wiley, Jan. 21, 2014), 10.1002/9781118909065.

[212]W. Cai, W. Chen, J. Fang, and S. Holm, “A Survey on Fractional Derivative Modeling of Power-Law Frequency-Dependent Viscous Dissipative and Scattering Attenuation in Acoustic Wave Propagation”, Appl. Mech. Rev. **70**, 030802 (2018) 10.1115/1.4040402.

[213]L. Tourrette and L. Halpern, eds., *Absorbing boundaries and layers, domain decomposition methods: applications to large scale computers* (Nova Science Publ, Huntington, NY, 2001), 382 pp.

[214]Comsol, *Comsol - Acoustics Module* ().

[215]Ansys, *Ansys - Mechanical APDL - 2026 R1* (Ansys Inc., 2026).

[216]Ansys, *Ansys - Mechanical Application - 2026 R1* (Ansys Inc., 2026).

[217]B. E. Treeby and B. T. Cox, "K-Wave: MATLAB toolbox for the simulation and reconstruction of photoacoustic wave fields", J. Biomed. Opt. **15**, 021314 (2010) 10.1117/1.3360308.

[218]Dassault Systèmes SIMULIA Corp, *Abaqus Analysis User's Manual* (Dassault Systèmes SIMULIA Corp, 2016).

[219]A. Logg, K.-A. Mardal, and G. Wells, eds., *Automated Solution of Differential Equations by the Finite Element Method: The FEniCS Book*, Vol. 84, Lecture Notes in Computational Science and Engineering (Springer Berlin Heidelberg, Berlin, Heidelberg, 2012), 10.1007/978-3-642-23099-8.

[220]M. Alnæs, J. Blechta, J. Hake, A. Johansson, B. Kehlet, A. Logg, C. Richardson, J. Ring, M. E. Rognes, and G. N. Wells, "The FEniCS Project Version 1.5", version 1.0.0, Arch. Numer. Softw. **Vol 3**, edited by Archive Of Numerical Software, Starting Point and Frequency: Year: 2013 (2015) 10.11588/ANS.2015.100.20553.

[221]M. W. Scroggs, I. A. Baratta, C. N. Richardson, and G. N. Wells, "Basix: a runtime finite element basis evaluationlibrary", J. Open Source Softw. **7**, 3982 (2022) 10.21105/joss.03982.

[222]M. W. Scroggs, J. S. Dokken, C. N. Richardson, and G. N. Wells, "Construction of Arbitrary Order Finite Element Degree-of-Freedom Maps on Polygonal and Polyhedral Cell Meshes", ACM Trans. Math. Softw. **48**, 1–23 (2022) 10.1145/3524456.

[223]I. A. Baratta, J. P. Dean, J. S. Dokken, M. Habera, J. S. Hale, C. N. Richardson, M. E. Rognes, M. W. Scroggs, N. Sime, and G. N. Wells, *DOLFINx: The next generation FEniCS problem solving environment*, (Dec. 31, 2023) 10.5281/ZENODO.10447666, https://zenodo.org/doi/10.5281/zenodo.10447666 (visited on 04/02/2026), pre-published.

[224]M. S. Alnæs, A. Logg, K. B. Ølgaard, M. E. Rognes, and G. N. Wells, "Unified form language: A domain-specific language for weak formulations of partial differential equations", ACM Trans. Math. Softw. **40**, 1–37 (2014) 10.1145/2566630.

[225]D. Arndt, W. Bangerth, D. Davydov, T. Heister, L. Heltai, M. Kronbichler, M. Maier, J.-P. Pelteret, B. Turcksin, and D. Wells, "The deal.II finite element library: Design, features, and insights", Comput. Math. Appl. **81**, 407–422 (2021) 10.1016/j.camwa.2020.02.022.

[226]D. Arndt, W. Bangerth, M. Bergbauer, B. Blais, M. Fehling, R. Gassmöller, T. Heister, L. Heltai, M. Kronbichler, M. Maier, P. Munch, S. Scheuerman, B. Turcksin, S. Uzunbajakau, D. Wells, and M. Wichrowski, "The deal.II library, version 9.7", J. Numer. Math. **33**, 403–415 (2025) 10.1515/jnma-2025-0115.

[227]T. Kolev and V. Dobrev, *Modular Finite Element Methods (MFEM)*, Lawrence Livermore National Laboratory (LLNL), Livermore, CA (United States), 2010, 10.11578/DC.20171025.1248.

[228]R. Anderson, J. Andrej, A. Barker, J. Bramwell, J.-S. Camier, J. Cerveny, V. Dobrev, Y. Dudouit, A. Fisher, T. Kolev, W. Pazner, M. Stowell, V. Tomov, I. Akkerman, J. Dahm, D. Medina, and S. Zampini, "MFEM: A modular finite element methods library", Comput. Math. Appl. **81**, 42–74 (2021) 10.1016/j.camwa.2020.06.009.

[229]J. Andrej, N. Atallah, J.-P. Bäcker, J.-S. Camier, D. Copeland, V. Dobrev, Y. Dudouit, T. Duswald, B. Keith, D. Kim, T. Kolev, B. Lazarov, K. Mittal, W. Pazner, S. Petrides, S. Shiraiwa, M. Stowell, and V. Tomov, "High-performance finite elements with MFEM", Int. J. High Perform. Comput. Appl., 10943420241261981 (2024) 10.1177/10943420241261981.

[230]M. Mencarelli, L. Puggelli, A. Virga, R. Furferi, and Y. Volpe, "Characterization of soft tissue-mimicking materials for ultrasound training phantoms", J. Mater. Sci. Mater. Med. **37**, 44 (2026) 10.1007/s10856-026-07020-7.

[231]A. Jawli, W. Aldehani, G. Nabi, and Z. Huang, "Tissue-Mimicking Material Fabrication and Properties for Multiparametric Ultrasound Phantoms: A Systematic Review", Bioengineering **11**, 620 (2024) 10.3390/bioengineering11060620.

[232]D. Phani, R. K. V., A. Thomas, R. Paramu, M. S. Singh, S. V. S., V. Muraleedharan, and R. K. Nair, *Acoustic and Ultrasonographic Characterization of Neoprene, Beeswax, and Carbomer-Gel to Mimic Soft-tissue for Ultrasound*, version 1, (2020) 10.48550/ARXIV.2004.05355, https://arxiv.org/abs/2004.05355 (visited on 03/24/2026), pre-published.

[233]International Electrotechnical Commission, *IEC 60601-2-5:2009 Medical electrical equipment - Part 2-5: Particular requirements for the basic safety and essential performance of ultrasonic physiotherapy equipment*, 2009.

[234]International Electrotechnical Commission, *IEC 60601-2-37:2024 Medical electrical equipment - Part 2-37: Particular requirements for the basic safety and essential performance of ultrasonic medical diagnostic and monitoring equipment*, 2024.

[235]International Electrotechnical Commission, *IEC TS 62791:2022 Ultrasonics - Pulse-echo scanners - Low-echo sphere phantoms and method for performance testing of grey-scale medical ultrasound scanners applicable to a broad range of transducer types*, 2022.

[236]C. Sun, S. D. Pye, J. E. Browne, A. Janeczko, B. Ellis, M. B. Butler, V. Sboros, A. J. Thomson, M. P. Brewin, C. H. Earnshaw, and C. M. Moran, "The Speed of Sound and Attenuation of an IEC Agar-Based Tissue-Mimicking Material for High Frequency Ultrasound Applications", Ultrasound Med. Biol. **38**, 1262–1270 (2012) 10.1016/j.ultrasmedbio.2012.02.030.

[237]P. Chen, A. M. Pollet, A. Panfilova, M. Zhou, S. Turco, J. M. Den Toonder, and M. Mischi, "Acoustic characterization of tissue-mimicking materials for ultrasound perfusion imaging research", Ultrasound Med. Biol. **48**, 124–142 (2022) 10.1016/j.ultrasmedbio.2021.09.004.

[238]J. Browne, K. Ramnarine, A. Watson, and P. Hoskins, "Assessment of the acoustic properties of common tissue-mimicking test phantoms", Ultrasound Med. Biol. **29**, 1053–1060 (2003) 10.1016/S0301-5629(03)00053-X.

[239]S. R. Bisht, B. P. Marri, J. Karmakar, and K. P. Mercado Shekhar, "Viscoelastic Characterization of Phantoms for Ultrasound Elastography Created Using Low- and High-Viscosity Poly(vinyl alcohol) with Ethylene Glycol as the Cryoprotectant", ACS Omega, acsomega.3c09224 (2024) 10.1021/acsomega.3c09224.

[240]A. Kumar and D. Sheet, "Method for Developing Tissue-mimicking Ultrasound Imaging Phantoms of Organs using Polyvinyl Alcohol and 3-D Printed Moulds", Ultrasound Med. Biol. **52**, 401–410 (2026) 10.1016/j.ultrasmedbio.2025.10.006.

[241]G. Menikou and C. Damianou, "Acoustic and thermal characterization of agar based phantoms used for evaluating focused ultrasound exposures", J. Ther. Ultrasound **5**, 14 (2017) 10.1186/s40349-017-0093-z.

[242]M. Mencarelli, L. Puggelli, A. Virga, R. Furferi, and Y. Volpe, "Acoustic velocity and stability of tissue-mimicking echogenic materials for ultrasound training phantoms", J. Mater. Sci. **59**, 6509–6524 (2024) 10.1007/s10853-024-09610-8.

[243]S. A. Armstrong, R. Jafary, J. S. Forsythe, and S. D. Gregory, "Tissue-Mimicking Materials for Ultrasound-Guided Needle Intervention Phantoms: A Comprehensive Review", Ultrasound Med. Biol. **49**, 18–30 (2023) 10.1016/j.ultrasmedbio.2022.07.016.

[244]A. Hariri, J. Palma-Chavez, K. A. Wear, T. J. Pfefer, J. V. Jokerst, and W. C. Vogt, "Polyacrylamide hydrogel phantoms for performance evaluation of multispectral photoacoustic imaging systems", Photoacoustics **22**, 100245 (2021) 10.1016/j.pacs.2021.100245.

[245]K. Zell, J. I. Sperl, M. W. Vogel, R. Niessner, and C. Haisch, "Acoustical properties of selected tissue phantom materials for ultrasound imaging", Phys. Med. Biol. **52**, N475–N484 (2007) 10.1088/0031-9155/52/20/N02.

[246]E. Villa, N. Arteaga-Marrero, J. González-Fernández, and J. Ruiz-Alzola, "Bimodal microwave and ultrasound phantoms for non-invasive clinical imaging", Sci. Rep. **10**, 20401 (2020) 10.1038/s41598-020-77368-5.

[247]M. Ahmad, N. Suardi, A. Shukri, H. Mohammad, A. Oglat, A. Alarab, and O. Makhamrah, "Chemical characteristics, motivation and strategies in choice of materials used as liver phantom: A literature review", J. Med. Ultrasound **28**, 7 (2020) 10.4103/JMU.JMU_4_19.

[248]A. J. Cloonan, D. Shahmirzadi, R. X. Li, B. J. Doyle, E. E. Konofagou, and T. M. McGloughlin, "3D-Printed Tissue-Mimicking Phantoms for Medical Imaging and Computational Validation Applications", 3D Print. Addit. Manuf. **1**, 14–23 (2014) 10.1089/3dp.2013.0010.

[249]L. Zalka, J. Köhrer, C. Songsaeng, P. Homolka, C. Kollmann, J. Hummel, and M. Figl, "Application of additive manufacturing for the adaptive design of ultrasound phantoms", Front. Phys. **12**, 1461255 (2025) 10.3389/fphy.2024.1461255.

[250]K. J. M. Surry, H. J. B. Austin, A. Fenster, and T. M. Peters, "Poly(vinyl alcohol) cryogel phantoms for use in ultrasound and MR imaging", Phys. Med. Biol. **49**, 5529–5546 (2004) 10.1088/0031-9155/49/24/009.

[251]S. Chatelin, E. Breton, A. Arulrajah, C. Giraudeau, B. Wach, L. Meylheuc, and J. Vappou, *Investigation of PVC plastisol tissue-mimicking phantoms for MR-and ultrasound-elastography*, version 1, (2020) 10.48550/ARXIV.2012.04365, https://arxiv.org/abs/2012.04365 (visited on 03/24/2026), pre-published.

[252]N. Bush and C. Hill, "Gelatine-alginate complex gel: A new acoustically tissue-equivalent material", Ultrasound Med. Biol. **9**, 479–484 (1983) 10.1016/0301-5629(83)90020-0.

[253]K. Chen, C. Yu, J. Pan, Y. Xu, Y. Luo, T. Yang, X. Yang, L. Xie, J. Zhang, and R. Zhuo, "Prediction of the Nottingham prognostic index and molecular subtypes of breast cancer through multimodal magnetic resonance imaging", Magn. Reson. Imaging **108**, 168–175 (2024) 10.1016/j.mri.2024.02.012.

[254]N. A. T. C. Fernandes, D. I. Alves, D. P. Ferreira, M. Monteiro, A. Arieira, F. Silva, B. Hinckel, A. Leal, and Ó. Carvalho, "Sustainable Tunable Anisotropic Ultrasound Medical Phantoms for Skin, Skeletal Muscle, and Other Fibrous Biological Tissues Using Natural Fibers and a Bio-Elastomeric Matrix", J. Compos. Sci. **9**, 370 (2025) 10.3390/jcs9070370.

[255]A. I. Chen, M. L. Balter, M. I. Chen, D. Gross, S. K. Alam, T. J. Maguire, and M. L. Yarmush, "Multilayered tissue mimicking skin and vessel phantoms with tunable mechanical, optical, and acoustic properties", Med. Phys. **43**, 3117–3131 (2016) 10.1118/1.4951729.

[256]K. Andr□kut□, I. Subotinait□, S. Valiukevičien□, and R. Raišutis, "Development and investigation of skin melanoma phantoms for ultrasonic examination", Acta Medica Litu. **20**, 85–92 (2013) 10.6001/actamedica.v20i2.2697.

[257]R. Patel, A. Khan, D. Wirth, M. Kamionek, D. Kandil, R. Quinlan, and A. N. Yaroslavsky, "Multimodal optical imaging for detecting breast cancer", J. Biomed. Opt. **17**, 066008 (2012) 10.1117/1.JBO.17.6.066008.

[258]N. Hungr, J.-A. Long, V. Beix, and J. Troccaz, "A realistic deformable prostate phantom for multimodal imaging and needle-insertion procedures", Med. Phys. **39**, 2031–2041 (2012) 10.1118/1.3692179.

[259]S. V. Fernandez, J.-H. Kim, D. Sadat, C. Marcus, E. Suh, R. McIntosh, A. Shah, and C. Dagdeviren, "A Dynamic Ultrasound Phantom with Tissue-Mimicking Mechanical and Acoustic Properties", Adv. Sci. **11**, 2400271 (2024) 10.1002/advs.202400271.

[260]S. I. Lee, C. Hong, C. Lee, and H.-M. Cho, "Demonstration of Fat Properties in Diagnostic Ultrasound Images through the Development of a Modular Phantom", Appl. Sci. **13**, 432 (2022) 10.3390/app13010432.

[261]A. Suzuki, Y. Tsubota, W. Wu, K. Yamanaka, T. Terada, Y. Otake, and K. Kawabata, "Oil Gel-Based Phantom for Evaluating Quantitative Accuracy of Speed of Sound Measured in Ultrasound Computed Tomography", Ultrasound Med. Biol. **45**, 2554–2567 (2019) 10.1016/j.ultrasmedbio.2019.05.011.

[262]J. R. Cook, R. R. Bouchard, and S. Y. Emelianov, "Tissue-mimicking phantoms for photoacoustic and ultrasonic imaging", Biomed. Opt. Express **2**, 3193 (2011) 10.1364/BOE.2.003193.

[263]F. Dong, E. L. Madsen, M. C. MacDonald, and J. A. Zagzebski, "Nonlinearity parameter for tissue-mimicking materials", Ultrasound Med. Biol. **25**, 831–838 (1999) 10.1016/S0301-5629(99)00016-2.

[264]M. S. Kim, J. Y. Kim, H. D. Jung, J. Y. Kim, and H. H. Choi, "A Fat-Tissue Mimic Phantom for Therapeutic Ultrasound", IEIE Trans. Smart Process. Comput. **3**, 153–159 (2014) 10.5573/IEIESPC.2014.3.3.153.

[265]J. Ormachea and K. J. Parker, *A preliminary study of liver fat quantification using reported longitudinal ultrasound speed of sound and attenuation parameters*, version 1, (2021) 10.48550/ARXIV.2109.04419, https://arxiv.org/abs/2109.04419 (visited on 03/25/2026), pre-published.

[266]T. Yang, Y. Jin, and A. Neogi, "Acoustic Attenuation and Dispersion in Fatty Tissues and Tissue Phantoms Influencing Ultrasound Biomedical Imaging", ACS Omega **8**, 1319–1330 (2023) 10.1021/acsomega.2c06750.

[267]C. Gaudette, H. Cho, M. J. Saikia, and B. J. Ranger, "Mimicry of skeletal muscle tissue with layered phantom for ultrasound imaging", in 2022 IEEE MIT Undergrad. Res. Technol. Conf. URTC (Sept. 30, 2022), pp. 1–6, 10.1109/URTC56832.2022.10002212.

[268]N. Gun, B. Karaboce, and S. U. Yurdalan, "Characterization of Muscle Phantom Used in Calibration of Physiotherapy Ultrasound: Measurement of Acoustic Parameters of Phantom (2020)", in 2021 IEEE Int. Symp. Med. Meas. Appl. MeMeA (June 23, 2021), pp. 1–6, 10.1109/MeMeA52024.2021.9478685.

[269]A. Filippou, I. Louca, and C. Damianou, "Characterization of a fat tissue mimicking material for high intensity focused ultrasound applications", J. Ultrasound **26**, 505–515 (2022) 10.1007/s40477-022-00746-4.

[270]A. Wydra and R. G. Maev, "A novel composite material specifically developed for ultrasound bone phantoms: cortical, trabecular and skull", Phys. Med. Biol. **58**, N303–N319 (2013) 10.1088/0031-9155/58/22/N303.

[271]A. Chaboty, V.-H. Nguyen, G. Haiat, and P. Bélanger, "Estimating the properties of bone phantom cylinders through the inversion of axially transmitted low-frequency ultrasonic guided waves", Ultrasonics **155**, 107694 (2025) 10.1016/j.ultras.2025.107694.

[272]F. Vogl, B. Bernet, D. Bolognesi, and W. R. Taylor, "Towards assessing cortical bone porosity using low-frequency quantitative acoustics: A phantom-based study", PLOS ONE **12**, edited by J. L. Williams, e0182617 (2017) 10.1371/journal.pone.0182617.

[273]T. Falardeau and P. Belanger, "Ultrasound tomography in bone mimicking phantoms: Simulations and experiments", J. Acoust. Soc. Am. **144**, 2937–2946 (2018) 10.1121/1.5079533.

[274]N. Bochud, Q. Vallet, J.-G. Minonzio, and P. Laugier, "Predicting bone strength with ultrasonic guided waves", Sci. Rep. **7**, 43628 (2017) 10.1038/srep43628.

[275]A. Safari and E. K. Akdoğan, eds., *Piezoelectric and Acoustic Materials for Transducer Applications* (Springer US, Boston, MA, 2008), 10.1007/978-0-387-76540-2.

[276]K. Uchino, "Piezoelectric ceramics for transducers", in *Ultrasonic Transducers* (Elsevier, 2012), pp. 70–116, 10.1533/9780857096302.1.70.

[277]X. Meng and S. Lin, "Analysis of a Cascaded Piezoelectric Ultrasonic Transducer with Three Sets of Piezoelectric Ceramic Stacks", Sensors **19**, 580 (2019) 10.3390/s19030580.

[278]J. Liu, H. Chen, Y. Luo, and Q. Chen, "Analytical and experimental study on bilayer membrane-type Capacitive Micromechanical Ultrasonic Transducer", Sens. Actuators Phys. **376**, 115639 (2024) 10.1016/j.sna.2024.115639.

[279]R. Boubenia, P. Le Moal, G. Bourbon, E. Ramasso, and E. Joseph, "CMUT-Based Sensor for Acoustic Emission Application: Experimental and Theoretical Contributions to Sensitivity Optimization", Sensors **21**, 2042 (2021) 10.3390/s21062042.

[280]S. Luo, "Advances In Ultrasound Transducer Technologies for Portable Medical Imaging: A Comparative Review of Piezoelectric, CMUT, And Optical Approaches", Acad. J. Sci. Technol. **18**, 656–664 (2025) 10.54097/vnaby125.

[281]X. Cao, H. Yang, and B.-B. Li, *Ultrasound sensing with optical microcavities*, version 2, (2023) 10.48550/ARXIV.2303.11814, https://arxiv.org/abs/2303.11814 (visited on 04/03/2026), pre-published.

[282]J. Wang, X. Wu, Y. Song, and L. Sun, "Study of the Influence of the Backplate Position on EMAT Thickness-Measurement Signals", Sensors **22**, 8741 (2022) 10.3390/s22228741.

[283]S. V. Joshi, S. Sadeghpour, N. Kuznetsova, C. Wang, and M. Kraft, "Flexible micromachined ultrasound transducers (MUTs) for biomedical applications", Microsyst. Nanoeng. **11**, 9 (2025) 10.1038/s41378-024-00783-5.

[284]J. Cannata, T. Ritter, Wo-Hsing Chen, and K. Shung, "Design of focused single element (50-100 MHz) transducers using lithium niobate", in 2000 IEEE Ultrason. Symp. Proc. Int. Symp. Cat No00CH37121, Vol. 2 (2000), pp. 1129–1133, 10.1109/ULTSYM.2000.921524.

[285]H. Kim, A. Chiu, S. Park, and S.-S. Yoo, "Image-guided navigation of single-element focused ultrasound transducer", Int. J. Imaging Syst. Technol. **22**, 177–184 (2012) 10.1002/ima.22020.

[286]S. J. Ilham, Z. Kashani, and M. Kiani, "Design and Optimization of Ultrasound Phased Arrays for Large-Scale Ultrasound Neuromodulation", IEEE Trans. Biomed. Circuits Syst. **15**, 1454–1466 (2021) 10.1109/TBCAS.2021.3133133.

[287]X.-Y. Cui, X.-Z. Liu, P. Wu, J. Yang, Z.-B. Zhang, Y.-G. Peng, S.-C. Bao, and X.-F. Zhu, "Steerable High-Resolution Ultrasound Focusing via Phase-Array-Activated Acoustic Meta-Lenses", Adv. Phys. Res. **4**, e00147 (2025) 10.1002/apxr.202500147.

[288]F. Rossano, S. M. Aglioti, F. Apollonio, G. Ruocco, and M. Liberti, "Probing phased-array focused ultrasound transducers using realistic 3D in-silico trabecular skull models: A numerical study", Ultrasonics **154**, 107692 (2025) 10.1016/j.ultras.2025.107692.

[289]H. Kannajosyula, C. J. Lissenden, and J. L. Rose, "Analysis of annular phased array transducers for ultrasonic guided wave mode control", Smart Mater. Struct. **22**, 085019 (2013) 10.1088/0964-1726/22/8/085019.

[290]J. Ketterling, O. Aristizabal, D. Turnbull, and F. Lizzi, "Design and fabrication of a 40-MHz annular array transducer", IEEE Trans. Ultrason. Ferroelectr. Freq. Control **52**, 672–681 (2005) 10.1109/TUFFC.2005.1428050.

[291]Z. Chen, X. Qian, X. Song, Q. Jiang, R. Huang, Y. Yang, R. Li, K. Shung, Y. Chen, and Q. Zhou, "Three-Dimensional Printed Piezoelectric Array for Improving Acoustic Field and Spatial Resolution in Medical Ultrasonic Imaging", Micromachines **10**, 170 (2019) 10.3390/mi10030170.

[292]F. Suñol, D. A. Ochoa, L. R. Suñé, and J. E. García, "Design and characterization of immersion ultrasonic transducers for pulsed regime applications", Instrum. Sci. Technol. **47**, 213–232 (2019) 10.1080/10739149.2018.1518876.

[293]V. T. Rathod, "A Review of Acoustic Impedance Matching Techniques for Piezoelectric Sensors and Transducers", Sensors **20**, 4051 (2020) 10.3390/s20144051.

[294]K. Zhu, J. Ma, X. Qi, B. Shen, Y. Liu, E. Sun, and R. Zhang, "Enhancement of Ultrasonic Transducer Bandwidth by Acoustic Impedance Gradient Matching Layer", Sensors **22**, 8025 (2022) 10.3390/s22208025.

[295]V. M. Do Nascimento, V. L. D. S. Nantes Button, J. M. Maia, E. T. Costa, and E. J. V. Oliveira, "Influence of backing and matching layers in ultrasound transducer performance", in , edited by W. F. Walker and M. F. Insana (May 23, 2003), p. 86, 10.1117/12.479924.

[296]W. N. Bodé and H. Bruus, "Numerical study of the coupling layer between transducer and chip in acoustofluidic devices", J. Acoust. Soc. Am. **149**, 3096–3105 (2021) 10.1121/10.0004871.

[297]C. Wang, C. Wang, Y. Lana, and W. Caod, *Dependence of functional mechanism of matching layer on excitation signal type for ultrasonic transducers-2*, version 1, (2020) 10.48550/ARXIV.2012.00342, https://arxiv.org/abs/2012.00342 (visited on 04/03/2026), pre-published.

[298]S. Callegari, M. Ricci, S. Caporale, M. Monticelli, M. Eroli, L. Senni, R. Rovatti, G. Setti, and P. Burrascano, "From Chirps to Random-FM Excitations in Pulse Compression Ultrasound Systems", version 1, (2013) 10.48550/ARXIV.1310.6593.

[299]Y. Je, M. Sim, Y. Cho, S.-G. Lee, and H.-S. Seo, "Theoretical and Experimental Studies on Sensitivity and Bandwidth of Thickness-Mode Driving Hydrophone Utilizing A 2-2 Piezoelectric Single Crystal Composite", Sensors **23**, 3445 (2023) 10.3390/s23073445.

[300]Z. Piao, T. Hou, Y. Wang, J. Tong, H. Panhwar, Y. Lv, and Y. Xin, "Low-Frequency Piezoelectric Hydrophone with High Sensitivity Based on a Piston Structure", Acoustics **8**, 15 (2026) 10.3390/acoustics8010015.

[301]C. Chen and M. A. P. Pertijs, "Integrated Transceivers for Emerging Medical Ultrasound Imaging Devices: A Review", IEEE Open J. Solid-State Circuits Soc. **1**, 104–114 (2021) 10.1109/OJSSCS.2021.3115398.

[302]Y. Lin, M. A. O'Reilly, and K. Hynynen, "A PVDF Receiver for Acoustic Monitoring of Microbubble-Mediated Ultrasound Brain Therapy", Sensors **23**, 1369 (2023) 10.3390/s23031369.

[303]R. C. Gessner, C. B. Frederick, F. S. Foster, and P. A. Dayton, "Acoustic Angiography: A New Imaging Modality for Assessing Microvasculature Architecture", Int. J. Biomed. Imaging **2013**, 1–9 (2013) 10.1155/2013/936593.

[304]A. Bezugly, "High frequency ultrasound study of skin tumors in dermatological and aesthetic practice", Med. Ultrason. **17** (2015) 10.11152/mu.2013.2066.174.hfy.

[305]S. E. Shelton, B. D. Lindsey, J. K. Tsuruta, F. S. Foster, and P. A. Dayton, "Molecular Acoustic Angiography: A New Technique for High-resolution Superharmonic Ultrasound Molecular Imaging", Ultrasound Med. Biol. **42**, 769–781 (2016) 10.1016/j.ultrasmedbio.2015.10.015.

[306]N. Wagner, Y. C. Eldar, and Z. Friedman, "Compressed Beamforming in Ultrasound Imaging", IEEE Trans. Signal Process. **60**, 4643–4657 (2012) 10.1109/TSP.2012.2200891.

[307]Z. Jiang, K. Sujarittam, B. I. Yildiz, R. J. Dickinson, and J. J. Choi, "Passive Cavitation Detection With a Needle Hydrophone Array", IEEE Trans. Ultrason. Ferroelectr. Freq. Control **69**, 233–240 (2022) 10.1109/TUFFC.2021.3120263.

[308]K. A. Wear, "Considerations for Choosing Sensitive Element Size for Needle and Fiber-Optic Hydrophones—Part I: Spatiotemporal Transfer Function and Graphical Guide", IEEE Trans. Ultrason. Ferroelectr. Freq. Control **66**, 318–339 (2019) 10.1109/TUFFC.2018.2886067.

[309]G. R. Harris, S. M. Howard, A. M. Hurrell, P. A. Lewin, M. E. Schafer, K. A. Wear, V. Wilkens, and B. Zeqiri, "Hydrophone Measurements for Biomedical Ultrasound Applications: A Review", IEEE Trans. Ultrason. Ferroelectr. Freq. Control **70**, 85–100 (2023) 10.1109/TUFFC.2022.3213185.

[310]C. Koch and K.-V. Jenderka, "Measurement of sound field in cavitating media by an optical fibre-tip hydrophone", Ultrason. Sonochem. **15**, 502–509 (2008) 10.1016/j.ultsonch.2007.05.007.

[311]P. Lutzmann, B. Göhler, C. A. Hill, and F. V. Putten, "Laser vibration sensing at Fraunhofer IOSB: review and applications", Opt. Eng. **56**, 031215 (2016) 10.1117/1.OE.56.3.031215.

[312]M. S. Canney, M. R. Bailey, L. A. Crum, V. A. Khokhlova, and O. A. Sapozhnikov, "Acoustic characterization of high intensity focused ultrasound fields: A combined measurement and modeling approach", J. Acoust. Soc. Am. **124**, 2406–2420 (2008) 10.1121/1.2967836.

[313]H. Lu, G. Xing, P. Yang, F. Qian, K. Wang, L. He, and J. Hu, "Determination of acoustic field parameters for high-frequency focusing ultrasonic transducers up to 100 MHz", Acta Acust. **9**, 67 (2025) 10.1051/aacus/2025052.

[314]Y. Xu, H. Liu, Y. Ma, X. Bai, Q. Hu, Y. Cai, H. Zhang, T. Huang, M. Liu, J. Li, M. Ding, and M. Yuchi, "Laser Deflection Acoustic Field Quantification: A Non-Invasive Measurement Technique for Focused Ultrasound Field Characterization", Bioengineering **13**, 22 (2025) 10.3390/bioengineering13010022.

[315]S. Ichihara, M. Yamagishi, Y. Kurashina, M. Ota, and Y. Tagawa, "High-resolution pressure imaging via background-oriented schlieren tomography: A spatiotemporal measurement for MHz ultrasound fields and hydrophone calibration", Ultrasonics **152**, 107614 (2025) 10.1016/j.ultras.2025.107614.

[316]T. Marhenke, S. J. Sanabria, B. R. Chintada, R. Furrer, J. Neuenschwander, and O. Goksel, "Acoustic Field Characterization of Medical Array Transducers Based on Unfocused Transmits and Single-Plane Hydrophone Measurements", Sensors **19**, 863 (2019) 10.3390/s19040863.

[317]Department of Food Product Development, IIFPT, MoFPI, Thanjavur-613005 Tamil Nadu, India, S. Janghu, Department of Food Engineering and Technology, SLIET, Longowal-148106 Sangrur, Punjab, India, M. B. Bera, Department of Food Engineering and Technology, SLIET, Longowal-148106 Sangrur, Punjab, India, V. Nanda, Department of Food Engineering and Technology, SLIET, Longowal-148106 Sangrur, Punjab, India, A. Rawson, and Department of Food Safety and Quality Testing, IIFPT, MoFPI, Thanjavur-613005 Tamil Nadu, India, "Studies on Power Ultrasound Process Optimization and Its Comparative Analysis with Conventional Thermal Processing for Treatment of Raw Honey", Food Technol. Biotechnol. **55** (2017) 10.17113/ftb.55.04.17.5263.

[318]R. Mayworm, E. Webster, S. Davidson, A. Alvarenga, and R. Costa-Felix, "Ultrasonic power measurement by Kibble balance", Measurement **203**, 111788 (2022) 10.1016/j.measurement.2022.111788.

[319]International Electrotechnical Commission, *IEC 62127-1:2022 Ultrasonics - Hydrophones - Part 1: Measurement and characterization of medical ultrasonic fields*, Mar. 25, 2022.

[320]International Electrotechnical Commission, *IEC 60565-1:2020 Underwater acoustics - Hydrophones - Calibration of hydrophones - Part 1: Procedures for free-field calibration of hydrophones*, Apr. 24, 2020.

# Chapter 3

# Conceptual Solution

## 3.1 The fundamental paradox of articular cartilage regeneration

Knee OA is widely recognized as one of the most prevalent and disabling musculoskeletal disorders worldwide, affecting hundreds of millions of individuals and representing a major contributor to pain and functional limitation in aging populations[1,2]. Its progression is intrinsically linked to the degeneration of articular cartilage, a highly specialized tissue responsible for load distribution and near-frictionless joint motion. However, the structural characteristics of cartilage limit early diagnosis. As an aneural tissue, it isn't connected to the nervous system, meaning that damage can accumulate silently without triggering pain in the patient. Consequently, patients often remain asymptomatic until degeneration has reached advanced stages when two bones start contacting each other, at which point therapeutic options become significantly more limited[3].

From a biological perspective, the regenerative capacity of cartilage is severely constrained. Articular cartilage is avascular and hypocellular, relying primarily on diffusion from synovial fluid for nutrient supply, which results in a slow metabolic turnover and a limited intrinsic healing potential[3]. Even minor defects tend not to repair effectively and may progressively worsen over time, frequently evolving into osteoarthritic degeneration. This intrinsic limitation explains why current clinical strategies struggle to achieve true regeneration, typically leading instead to the formation of mechanically inferior repair tissue rather than restoring native cartilage structure[2], as illustrated in figure 46.

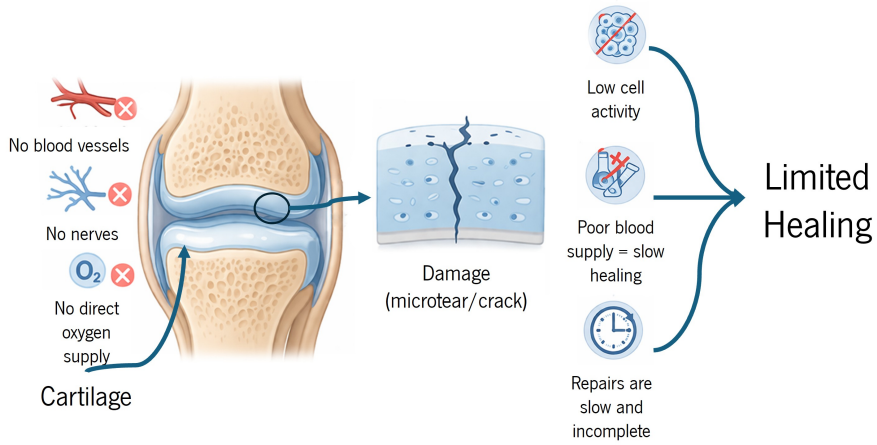



Figure 46: Articular cartilage structure and its limited regenerative capacity, highlighting its avascular and aneural nature, the occurrence of microdamage, and the resulting low cellular activity and slow, incomplete healing response.

Mechanical stimulation has been consistently identified as a key regulator of cartilage homeostasis. Chondrocytes, the resident cells of cartilage, are highly mechanosensitive and respond to dynamic loading by modulating matrix synthesis and degradation processes. Cyclic mechanical loading enhances

fluid flow, promotes nutrient transport, and activates mechanotransduction pathways that are essential for maintaining tissue integrity[4]. In this sense, controlled physical activity is one of the primary natural mechanisms through which cartilage health is preserved.

However, a fundamental paradox emerges in the context of osteoarthritis. While mechanical stimulation is necessary to sustain cartilage function, patients with OA frequently experience pain, inflammation, and reduced mobility, which severely limit their ability to engage in physical activity. As a result, the essential stimulus required for cartilage maintenance becomes inaccessible. Reduced joint use leads to diminished mechanical stimulation, impairing chondrocyte activity and accelerating tissue degeneration, thereby reinforcing a self-perpetuating cycle of decline.

In light of this contradiction, the present work proposes a conceptual shift: instead of relying on whole-joint mechanical loading through exercise, it seeks to induce mechanically localized cyclic loading stimuli directly at the cellular level through controlled acoustic excitation. Therapeutic ultrasound has been shown to modulate chondrocyte behavior, influencing pathways associated with matrix synthesis, inflammation, and cell survival[5]. By delivering carefully tuned acoustic waves through the layered structure of the knee, it becomes possible to generate localized mechanical fields within cartilage, effectively stimulating chondrocytes without requiring macroscopic joint loading. In this sense, the proposed approach aims to replicate the beneficial effects of physical activity at the microscale, enabling a form of “cellular exercise” that bypasses the functional limitations imposed by osteoarthritis.

## 3.2 Proposed Conceptual Design

Mechanotransduction is the fundamental process by which cells convert mechanical stimuli into biochemical responses, enabling them to regulate functions such as proliferation, matrix synthesis, and differentiation. In articular cartilage, chondrocytes are continuously subjected to mechanical forces transmitted through the extracellular matrix, including compression, shear, and hydrostatic pressure. These forces are conveyed through the cytoskeleton and associated mechanosensitive structures toward the nucleus, where deformation plays a critical role in regulating gene expression. As such, nuclear strain is the central mediator of mechanotransduction, with deformation of the nuclear envelope influencing chromatin organization and transcriptional activity[6,7]. The importance of nuclear strain is further emphasized in ultrasound-based stimulation, where it has been shown that acoustic pressure can concentrate within the nucleus, leading to enhanced gene expression when excitation occurs near resonant conditions of the cell[7]. This establishes a direct link between externally applied mechanical fields and intracellular biological responses, positioning nuclear strain as the key target for therapeutic stimulation (figure 47).

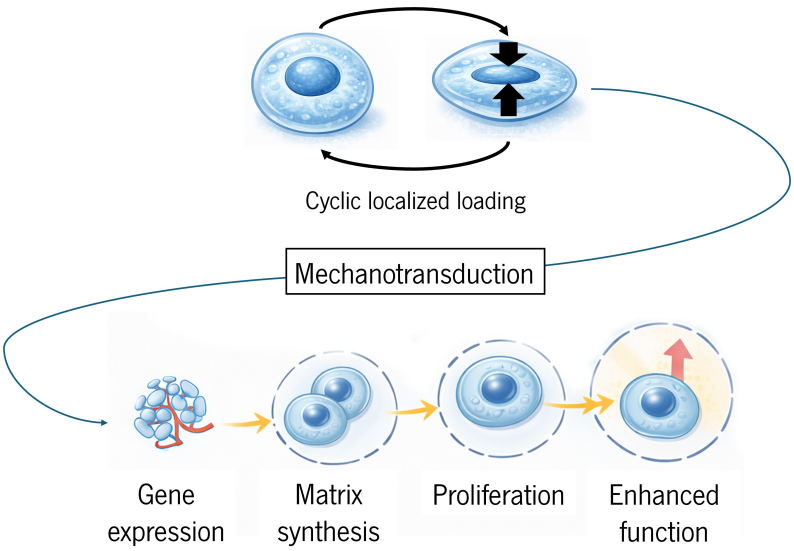



Figure 47: Chondrocyte mechanotransduction, where mechanical deformation (particularly nuclear strain) triggers intracellular signalling pathways that promote gene expression, extracellular matrix synthesis, cell proliferation, and enhanced cellular function.

Acoustic waves provide a particularly attractive mechanism to induce such mechanical deformation stimuli in a controlled and non-invasive manner. When propagating within a confined or partially bounded medium, acoustic waves can interfere constructively and destructively, giving rise to standing wave patterns characterized by spatially distributed nodes and antinodes (figure 48). These regions correspond to minima and maxima of dynamic pressure and particle displacement, respectively, generating localized oscillatory loading conditions within the medium. At sufficiently small scales, such

pressure gradients are capable of exerting forces on cells and subcellular structures, a phenomenon widely exploited in acoustics and increasingly investigated in tissue engineering applications. In particular, acoustic stimulation has been shown to generate tuneable biomechanical forces capable of influencing chondrocyte behavior and promoting cartilage tissue formation, highlighting its potential as a mechanobiological tool[8].

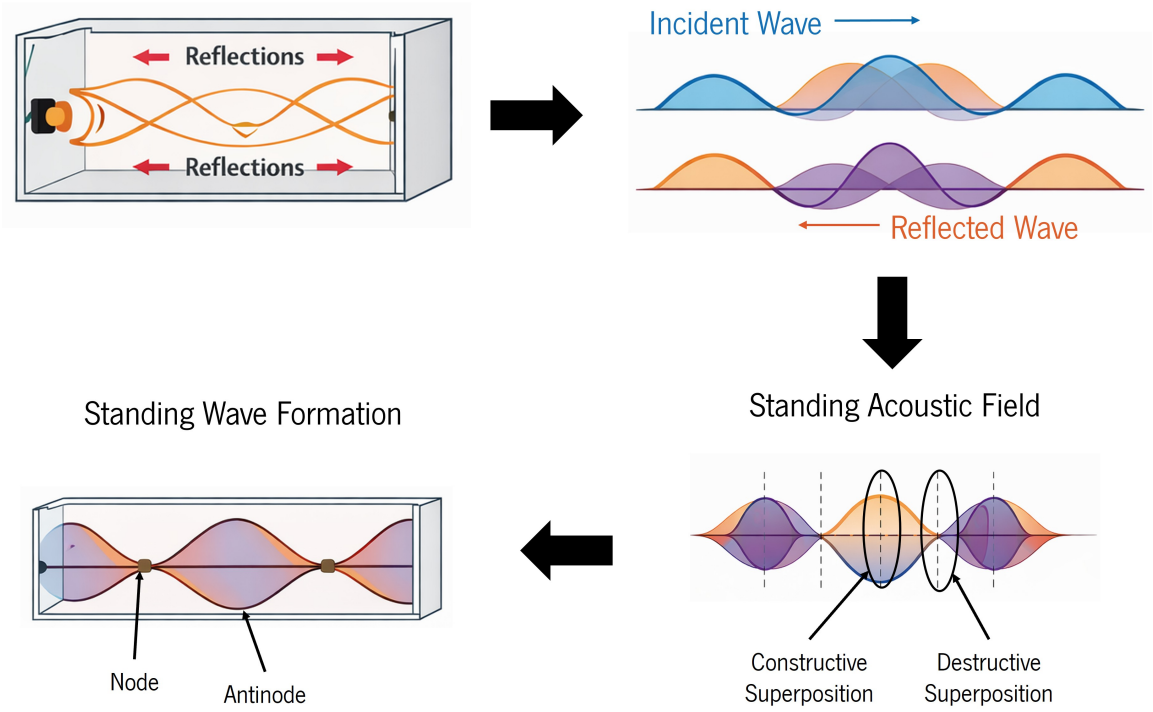



Figure 48: Standing wave formation in a confined domain, showing the superposition of incident and reflected waves, leading to the emergence of nodes and antinodes and the establishment of a stationary acoustic field.

The operation of the proposed device is fundamentally governed by the controlled delivery of an acoustic field from an external transducer into the knee joint, where wave propagation through heterogeneous biological tissues, determining the mechanical strain experienced at the cellular level. The transducer is positioned externally, in direct contact with the skin and coupled through an appropriate medium to minimize reflection losses at the interface. From this point, the generated acoustic waves propagate sequentially through the anatomical layers of the knee, following a transmission path that typically includes skin, subcutaneous adipose tissue, skeletal muscle, and finally the articular cartilage (figure 49). Each of these layers exhibits distinct acoustic properties which collectively shape the evolution of the wave as it travels through the medium. Experimental and numerical studies have consistently shown that biological tissues introduce frequency-dependent attenuation and dispersion, with adipose tissue in particular contributing significantly to energy loss and wave distortion due to its strong dissipative behavior[9]. Additionally, variations in acoustic impedance

between layers lead to partial reflections and transmissions at interfaces, further modifying the spatial distribution of the pressure field.

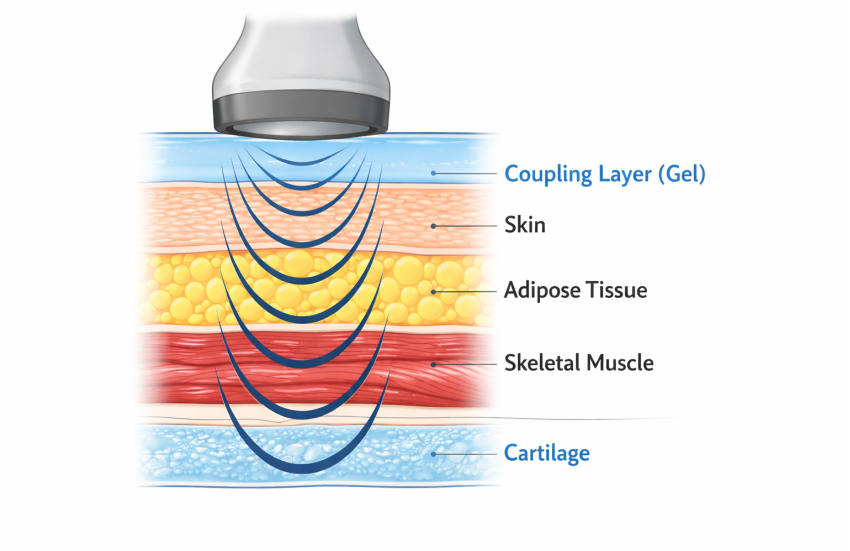



Figure 49: Ultrasound wave propagation from a surface transducer through a coupling gel and layered biological tissues (skin, adipose tissue, skeletal muscle), illustrating transmission toward the cartilage target region.

As a result of these interactions, the acoustic field that reaches the cartilage is not a simple replica of the emitted signal, but a transformed field that reflects the cumulative influence of tissue heterogeneity. This transformation includes amplitude reduction, phase shifts, and potential spatial focusing or unfocusing effects depending on geometry and boundary conditions. Numerical simulations and imaging studies of the knee have demonstrated that the layered structure (skin, fat, muscle, and cartilage) can be resolved acoustically and that each layer contributes distinctly to the final pressure distribution within the joint[10]. Within the cartilage, the transmitted acoustic field manifests as a dynamic pressure field that induces oscillatory mechanical loading at the tissue scale. These oscillations generate cyclic strains within the extracellular matrix, which are subsequently transmitted to embedded chondrocytes through solid–fluid interactions and local deformation mechanisms.

Building upon these principles, the central premise of this thesis is that acoustic fields can be engineered to create spatially and temporally controlled antinodes that interact with cellular structures at relevant length scales (figure 50). The proposed conceptual design seeks to develop a device capable of generating standing acoustic fields whose characteristic wavelengths and pressure distributions are compatible with the dimensions of chondrocytes and, more critically, their nuclei. By tuning the excitation frequency and boundary conditions, it becomes possible to manipulate the spatial arrangement of nodes and antinodes such that localized oscillatory pressures induce cyclic deformation at the nuclear level. In this framework, the objective is not simply to stimulate tissue globally, but to achieve resonance-informed mechanical coupling between the acoustic field and the cell, thereby

maximizing mechanotransductive efficiency. Such an approach represents a shift from empirical ultrasound application toward a physics-driven design paradigm, where the interaction between wave phenomena and cellular architecture is explicitly considered as the basis for therapeutic intervention.

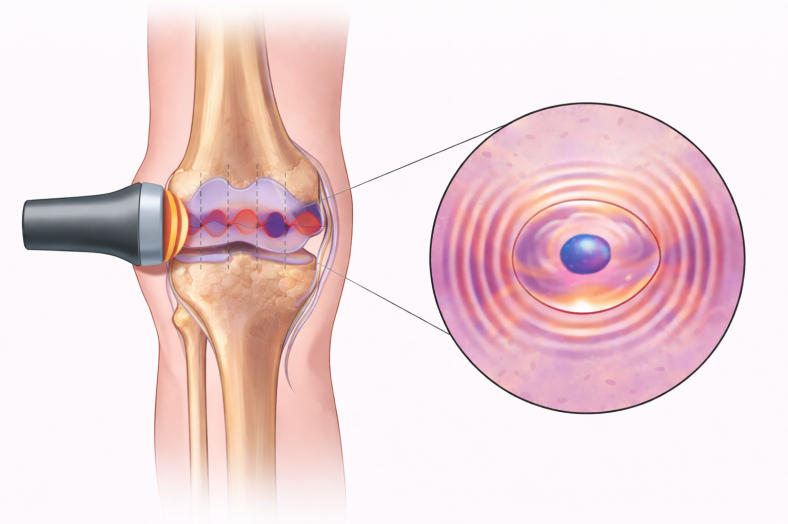


Figure 50: Ultrasound wave propagating to the knee joint, showing the generation of a localized standing acoustic field within the cartilage and the resulting microscale mechanical stimulation of chondrocytes, with emphasis on induced nuclear deformation associated with mechanotransduction.

An acoustic study, as is depicted in figure 51, typically follows a sequential workflow that bridges experimental characterization, computational modelling, and validation in a closed-loop engineering framework. The process begins with material characterization, where experimental setups are defined to extract relevant physical properties under controlled test conditions. These parameters serve as the foundation for the subsequent computational study, in which numerical models are calibrated, structural designs are developed, and optimization procedures are conducted to refine system performance. The workflow then transitions into structural assembly, where the designed system is physically implemented, incorporating experimental testing setups and realistic boundary conditions to ensure fidelity between simulation and real-world behavior. Finally, experimental validation closes the loop by assessing the underlying hypothesis, comparing predicted and measured responses, and confirming whether the system performs as intended. This progression reflects a rigorous integration of physics-based modelling and empirical verification, ensuring both predictive accuracy and practical applicability.

### 3.2.1 Material Characterization

Material characterization constitutes the foundational step upon which all subsequent computational and experimental investigations are constructed. A controlled ultrasonic excitation setup needs to be

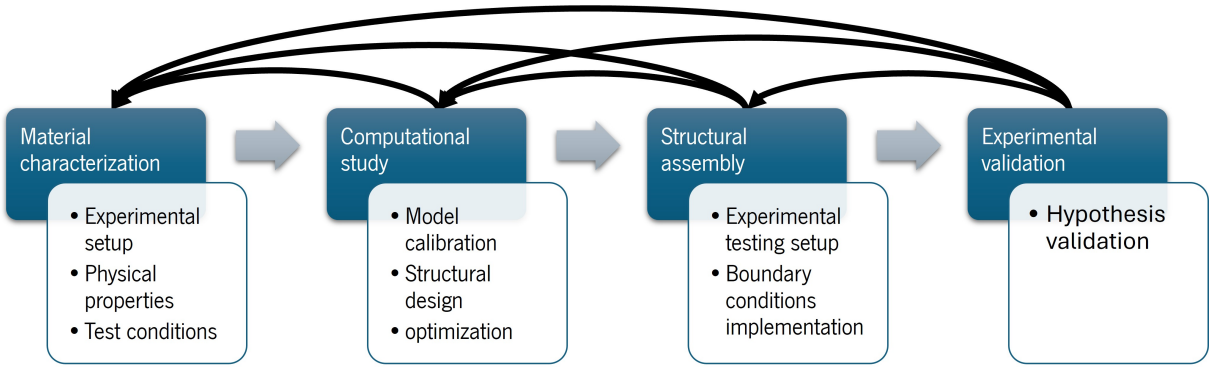



Figure 51: Integrated workflow depicting how an acoustic study typically links material characterization, computational modelling, structural implementation, and experimental validation for system development and verification.

designed to transmit acoustic energy through a central sample. The interaction of the waves within the material induces a periodic mechanical field, allowing the acquisition of the propagated wave (figure 52). This wave reflects the harmonic nature of the excitation, where pressure oscillates in a predictable and continuous manner, enabling the study of material response under well-defined cyclic loading. The accurate determination of intrinsic material properties (such as density, speed of sound and frequency-dependent attenuation) is essential to ensure that any modelled system reflects physical reality rather than an abstract approximation. In the context of wave propagation through heterogeneous biological media even small deviations in parameters such as speed of sound or attenuation coefficients can lead to significant errors in predicted pressure fields, propagating behavior, and energy dissipation.

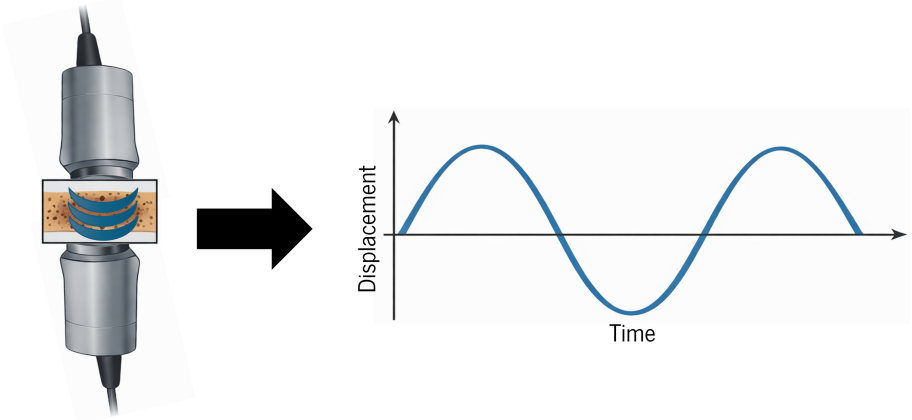



Figure 52: A dual-transducer ultrasonic setup inducing harmonic wave propagation through a sample, alongside its cosine waveform representation.

These experimentally derived properties directly inform the computational study, where they are embedded into governing equations and constitutive models. The fidelity of numerical simulations depends strongly on the accuracy of these inputs, especially when dealing with multiphysics interactions such as acoustic–structure coupling or nonlinear wave propagation, since they will define the fidelity of the measured signal and the boundary conditions. For instance, frequency-dependent attenuation laws

and viscoelastic behavior must be properly parameterized to capture realistic damping and dispersion effects, which in turn influence resonance phenomena and energy transmission across interfaces. Without robust material characterization, model calibration becomes ill-posed, often leading to non-unique or physically inconsistent solutions.

During the structural assembly phase, the selection of materials and the implementation of boundary conditions rely on previously identified properties to ensure that the constructed system behaves as intended. This continuity enables meaningful comparisons during experimental validation, where discrepancies between predicted and measured responses can be attributed to model assumptions rather than uncertainties in material behavior. In this sense, material characterization acts as a grounding layer allowing the entire workflow to transition from theoretical formulation to validated physical performance with confidence.

### 3.2.2 Computational Studies

The computational study constitutes the central predictive framework of the workflow, where the physical reality established during material characterization is translated into a controllable and analyzable virtual environment. At this stage, the experimentally derived material properties are embedded into governing equations that describe wave propagation, structural response, and their coupling across heterogeneous domains. Given the layered and multiphysics nature of the system under investigation, the computational model must simultaneously account for acoustic propagation in soft tissues, elastic deformation in solid structures, and the interaction between these domains. This requires the adoption of numerical formulations capable of resolving complex interface phenomena, impedance mismatches, and frequency-dependent attenuation, ensuring that energy transmission and dissipation are captured with high fidelity.

In general the structured computational strategy is built in three sequential steps (figure 53). First, acoustic wave propagation is characterized in isolated material layers, where each tissue analog is studied independently to capture its intrinsic response, including attenuation and transmission behavior. Second, the experimental observations obtained experimentally are compared with the computational results and both are iteratively calibrated until the simulated pressure fields match the measured responses. This stage serves as the validation bridge between physical behavior and numerical representation. Finally, the calibrated layers are assembled into a comprehensive, multilayer knee model, preserving the anatomical arrangement and interface interactions between tissues. This progression (from reductionist characterization to integrated simulation) ensures that the full-scale model

is not assumed, but constructed upon physically grounded and numerically validated building blocks, enabling reliable prediction of wave propagation and targeted mechanical stimulation within the joint.

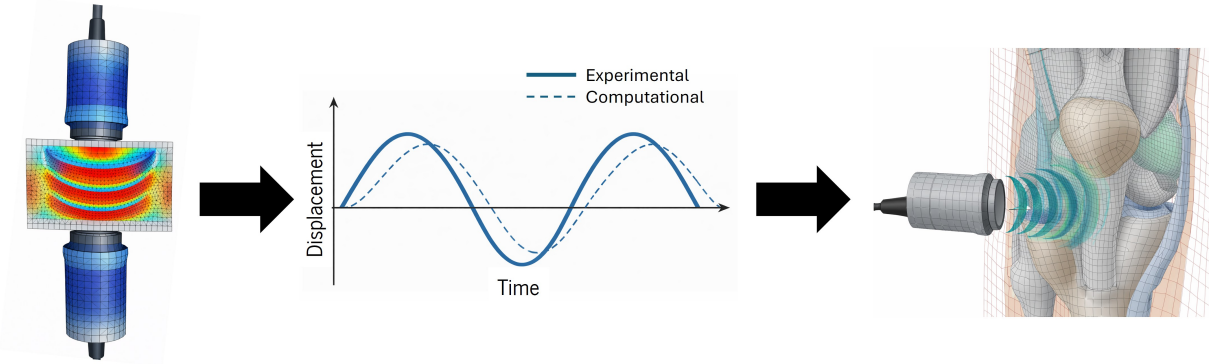



Figure 53: Three-stage computational framework: propagation in individual layers, numerical replication of experimental data for calibration, and assembly into a full-scale finite element model of the knee.

Model calibration is a critical component of this stage, acting as the bridge between experimental observations and numerical representation. Calibration involves adjusting uncertain or indirectly measured parameters so that the model reproduces known experimental responses. This process is both corrective and interpretative, as it reveals the sensitivity of the system to different physical mechanisms and helps identify dominant factors governing wave behavior. In highly attenuating and dispersive media, such as biological tissues, this step is particularly important to ensure that simulated pressure fields and frequency responses remain physically meaningful.

Once calibrated, the computational framework enables structural design and optimization in a manner that would be impractical or prohibitively expensive through experimentation alone. Parametric studies can be conducted to explore the influence of geometric configurations, transducer placement, excitation frequency, and boundary conditions on the resulting mechanical fields. Optimization strategies can then be employed to identify configurations that maximize desired outcomes while minimizing undesired effects like excessive attenuation or off-target energy deposition. This transforms the computational model into a design tool, capable of guiding decisions before physical prototypes are constructed.

Beyond design, the computational study also provides access to quantities that are difficult or impossible to measure experimentally. Internal pressure distributions, localized strain fields, and energy flux within layered media can be resolved with high spatial and temporal resolution, offering insight into the underlying mechanisms of wave–tissue interaction. In the context of biological stimulation, this allows the quantification of mechanical stimuli at specific sites, such as the extracellular matrix or cellular structures, thereby linking macroscopic excitation conditions to microscopic responses.

### 3.2.3 Structural Assembly

The structural assembly stage represents the transition from the abstract, predictive space of computation to the tangible domain of physical implementation, where the designed system is realized under controlled yet realistic conditions. At this stage, the optimized configurations derived from the computational study are translated into an equivalent physical setup that preserves, as closely as possible, the assumptions embedded in the numerical model. This requires careful consideration of manufacturability, material interfaces, and alignment, as even minor deviations in geometry or contact conditions can introduce significant discrepancies in wave propagation, particularly in systems governed by impedance mismatches and strong attenuation. In the case of this thesis, since it is not yet possible to build a human knee exactly like the one it is simulated and guarantee all boundary conditions, a UTMP will be manufactured to closely replicate the conditions in the computational study (figure 54).

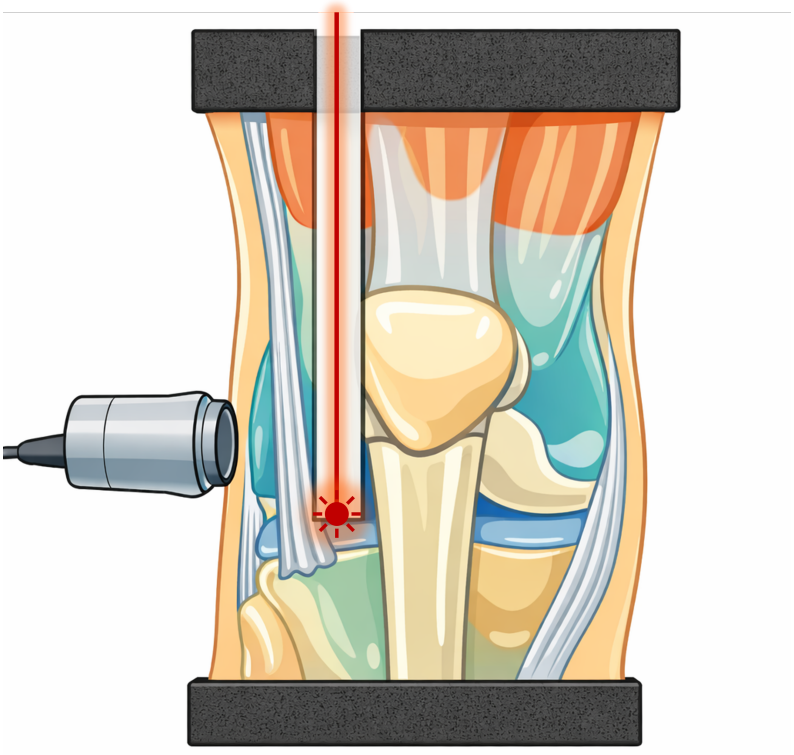


Figure 54: Schematic representation of the assembled knee phantom, showing the layered structure (silicone skin, gelatin-based soft tissues, and resin bones) confined within foam supports. A laser vibrometer is aligned through a dedicated optical path to enable non-contact measurement of structural response at the target region.

A central aspect of the structural assembly lies in the implementation of boundary conditions that faithfully reproduce those assumed in the computational domain. In practice, this involves recreating mechanical constraints, coupling conditions, and loading scenarios in a way that minimizes unwanted effects such as reflections or unintended damping. For acoustic systems, particular attention must be given to the coupling between the transducer and the medium, often requiring the use of intermediary

layers to ensure efficient energy transmission and to avoid impedance discontinuities at the interface. The positioning and fixation of the transducer relative to the layered structure must also be controlled with high precision, as spatial misalignment can alter focusing patterns and reduce the effectiveness of the intended stimulation.

The experimental testing setup is then constructed to enable reproducible and quantifiable measurements of the system's response. This includes the integration of sensing technologies (hydrophones, vibrometers, or embedded sensors) capable of capturing relevant physical quantities, including pressure fields, displacement, or strain. The selection and placement of these measurement devices must be informed by the computational predictions, targeting regions of interest where significant physical phenomena are expected to occur. Additionally, the setup must ensure stability and repeatability across tests, controlling environmental variables and minimizing external disturbances that could obscure the interpretation of results.

### 3.2.4 Experimental Validation

The experimental validation stage constitutes the final and decisive step of the workflow, where the predictive capability of the computational model and the fidelity of the structural assembly are rigorously assessed against measured physical responses. At this stage, the system is subjected to controlled excitation conditions that replicate those defined in the computational study, ensuring consistency between simulated and experimental scenarios. The objective is not only to verify whether the system behaves as expected, but to quantify the degree of agreement between predicted and observed responses, thereby establishing confidence in the underlying modelling assumptions and material representations.

Measurements are acquired using appropriately selected sensing techniques capable of capturing the relevant physical quantities with sufficient spatial and temporal resolution. Depending on the nature of the problem, this may include pressure field mapping, displacement measurements, or strain evaluation at critical locations within the structure. The placement of sensors is strategically guided by prior computational results, focusing on regions where significant gradients, focal zones, or peak responses are anticipated. Care is taken to account for measurement limitations, including spatial averaging effects, sensor bandwidth, and potential perturbations introduced by the measurement itself, ensuring that the acquired data accurately reflects the system's intrinsic behavior.

The comparison between experimental and numerical results is then performed through quantitative metrics, such as amplitude differences, frequency response alignment, and spatial distribution of fields.

Discrepancies are analyzed systematically to identify their origin, which may stem from uncertainties in material properties, simplifications in the computational model, or imperfections in the physical assembly. Rather than representing a failure, such deviations provide critical insight into the sensitivity of the system and highlight areas where the model can be refined. This iterative feedback loop allows for the progressive improvement of both the numerical framework and the experimental setup (figure 55).

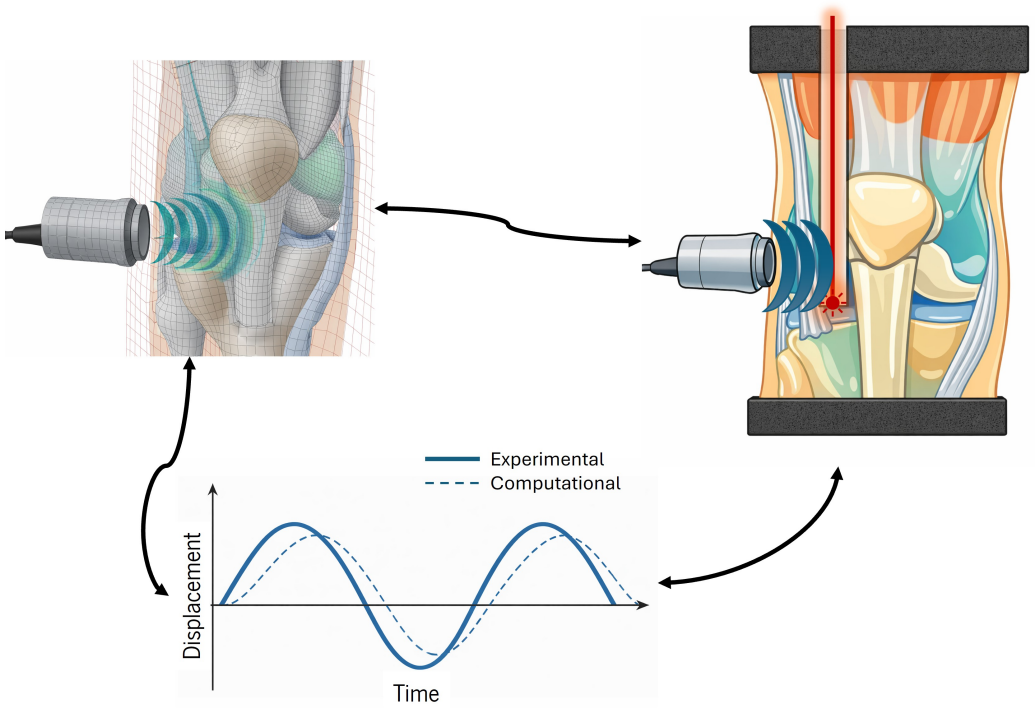



Figure 55: Iterative validation workflow illustrating the feedback loop between experimental measurements and computational modelling, where measured responses are used to calibrate and refine the numerical model, and updated simulations guide subsequent experimental adjustments.

Experimental validation has to transform the computational model from a theoretical construct into a validated predictive tool, capable of guiding design decisions and extrapolating system behavior beyond tested conditions. In this sense, validation is not merely a confirmation step, but a process of reconciliation, aligning simulation, material characterization, and physical implementation into a coherent and trustworthy representation of the system under investigation.

## 3.3 Development of medical devices

The development of a medical device follows a structured and highly regulated pathway that ensures safety, performance, and clinical relevance prior to market introduction (figure 56).

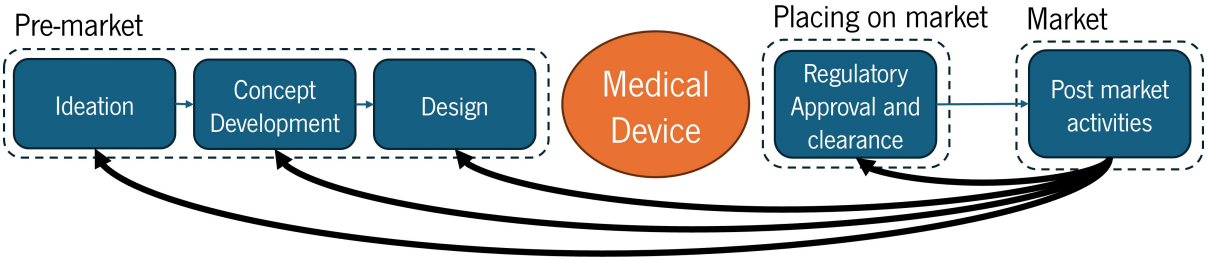



Figure 56: Medical device development pathway, illustrating the progression from ideation through concept development and design, culminating in regulatory approval and post-market activities, with iterative feedback loops linking later-stage insights to early-stage refinement, adapted[11].

This process conventionally begins with ideation, where an unmet clinical need is identified and translated into a preliminary concept. This stage is inherently exploratory, combining clinical insight with engineering feasibility to define the intended use, target population, and underlying mechanism of action. Subsequently, concept development refines this initial idea into a technically viable solution through iterative modelling, feasibility studies, and early-stage prototyping. At this stage, key design parameters are established, and fundamental hypotheses regarding device functionality are formulated and preliminarily validated. The design phase represents a critical transition toward formalization, where the device architecture is defined in accordance with engineering standards and regulatory expectations. This includes detailed design specifications, risk analysis, and verification planning. Computational modelling and experimental validation are typically integrated within this stage to ensure that the device performs as intended under controlled conditions. In parallel, considerations related to manufacturability, reproducibility, and material selection are incorporated to align the design with practical implementation constraints.

Following design finalization, the device enters the regulatory approval and clearance phase, which requires comprehensive demonstration of safety and efficacy. This involves preclinical testing, which may include in vitro studies, laboratory validation, and, where necessary, animal models, followed by clinical evaluation depending on the device classification and regulatory framework. Documentation generated throughout the development process is compiled to support regulatory submissions.

The work developed in this thesis is positioned at the terminal stage of pre-market activities, bridging the gap between conceptual design and regulatory readiness. Specifically, it contributes to the rigorous characterization, modelling, and validation of the proposed system, which are essential components of design verification and preclinical assessment. By integrating multiphysics simulation with

experimentally informed parameters and controlled validation strategies, the research establishes a predictive and reproducible framework for understanding device performance within biologically relevant conditions.

This positioning implies that the outcomes of this work are expected to inform subsequent regulatory steps by providing quantitative evidence of functional behavior, identifying optimal operational regimes, and supporting safety considerations, particularly in terms of bioacoustic exposure limits. While not constituting a complete regulatory submission, the developed framework significantly reduces uncertainty in device behavior and reduces risks in future translational efforts.

## 3.4 Bibliography

[1]S. Gubert, H. Moon, N. Oliva, and R. Texidó, "The osteochondral regeneration paradox: why biomimetic scaffolds are biologically superior but injectable systems dominate the clinic", RSC Adv. **16**, 11370–11390 (2026) 10.1039/D5RA09529H.

[2]H.-Y. Xue, X.-L. Shen, Z.-H. Wang, H.-C. Bi, H.-G. Xu, J. Wu, R.-M. Cui, and M.-W. Liu, "Research progress on mesenchymal stem cell-derived exosomes in the treatment of osteoporosis induced by knee osteoarthritis (Review)", Int. J. Mol. Med. **56**, 1–32 (2025) 10.3892/ijmm.2025.5601.

[3]C. A. Baumann, B. B. Hinckel, C. C. Bozynski, and J. Farr, "Articular Cartilage: Structure and Restoration", in *Joint Preservation of the Knee*, edited by A. B. Yanke and B. J. Cole (Springer International Publishing, Cham, 2019), pp. 3–24, 10.1007/978-3-030-01491-9_1.

[4]D. Martínez-Moreno, G. Jiménez, P. Gálvez-Martín, G. Rus, and J. Marchal, "Cartilage biomechanics: A key factor for osteoarthritis regenerative medicine", Biochim. Biophys. Acta BBA - Mol. Basis Dis. **1865**, 1067–1075 (2019) 10.1016/j.bbadis.2019.03.011.

[5]S. Oliveira, R. Andrade, F. Silva, J. Espregueira-Mendes, B. Hinckel, A. Leal, and Ó. Carvalho, "Effects and mechanotransduction pathways of therapeutic ultrasound on healthy and osteoarthritic chondrocytes: a systematic review of in vitro studies", Osteoarthritis Cartilage **31**, 317–339 (2023) 10.1016/j.joca.2022.07.014.

[6]N. Wang, Y. Lu, B. B. Rothrauff, A. Zheng, A. Lamb, Y. Yan, K. E. Lipa, G. Lei, and H. Lin, "Mechanotransduction pathways in articular chondrocytes and the emerging role of estrogen receptor-$\alpha$", Bone Res. **11**, 13 (2023) 10.1038/s41413-023-00248-x.

[7]A. D. Miller, A. Chama, T. M. Louw, A. Subramanian, and H. J. Viljoen, "Frequency sensitive mechanism in low-intensity ultrasound enhanced bioeffects", PLOS ONE **12**, edited by J. W. Ramos, e0181717 (2017) 10.1371/journal.pone.0181717.

[8]R. Rasouli, K. M. Villegas, and M. Tabrizian, "Acoustofluidics – changing paradigm in tissue engineering, therapeutics development, and biosensing", Lab. Chip **23**, 1300–1338 (2023) 10.1039/D2LC00439A.

[9]T. Yang, Y. Jin, and A. Neogi, "Acoustic Attenuation and Dispersion in Fatty Tissues and Tissue Phantoms Influencing Ultrasound Biomedical Imaging", ACS Omega **8**, 1319–1330 (2023) 10.1021/acsomega.2c06750.

[10]J. Wiskin, B. Malik, D. Borup, N. Pirshafiey, and J. Klock, "Full wave 3D inverse scattering transmission ultrasound tomography in the presence of high contrast", Sci. Rep. **10**, 20166 (2020) 10.1038/s41598-020-76754-3.

[11]I. C. T. Santos, "Product development methodologies: the case of medical devices" ().

[12]N. Jiménez, F. Camarena, J. Redondo, V. Sánchez-Morcillo, Y. Hou, and E. E. Konofagou, "Time-domain simulation of ultrasound propagation in a tissue-like medium based on the resolution of the nonlinear acoustic constitutive relations", version 1, Acta Acust. United Acust. (2016) 10.48550/ARXIV.1507.00319.

# Chapter 4

# Biological tissue characterization

# 4.1 Introduction

This section presents the experimental and computational framework used to characterize the acoustic behavior of biological tissues. It focuses on the measurement of key physical and acoustic properties, including density, speed of sound, attenuation, and nonlinearity, and on their integration into numerical models for wave propagation. Particular emphasis is placed on deriving and validating sound diffusivity as a unifying parameter for frequency-dependent attenuation. Through this combined approach, the section establishes the methodological basis for linking experimental observations with predictive simulations of ultrasound–tissue interaction.

Ultrasound has emerged as a cornerstone of modern biomedical technology, largely due to its non-invasive character and well-established safety profile[1,2]. By relying on high-frequency acoustic waves rather than ionizing radiation, it enables real-time visualization of soft tissues, vascular flow, and fetal development with minimal biological risk. Beyond imaging, ultrasound-based techniques are designed to be well tolerated, efficient, and clinically accessible, offering tangible benefits in pain management and functional recovery without the need for pharmacological or invasive interventions[3,4]. Technological advancements have further expanded its capabilities, including the development of three-dimensional shear wave elastography[5,6] and high-resolution imaging of blood flow and microcirculation[7,8]. More recently, artificial intelligence has been integrated into ultrasound systems to improve diagnostic performance, particularly in applications such as prenatal assessment, where accuracy and speed are critical[9,10]. Combined with its relatively low cost and portability, these features have driven widespread adoption, positioning ultrasound as one of the most widely used imaging modalities worldwide, with handheld and point-of-care devices increasingly enabling bedside diagnostics[11].

In parallel with its diagnostic role, ultrasound is rapidly gaining relevance in therapeutic applications. Techniques such as High Intensity Focused Ultrasound(HIFU) enable non-invasive ablation of pathological tissues and have already been approved for clinical use in conditions such as uterine fibroids and prostate disease[12]. At lower intensities, ultrasound is being investigated for neuromodulation and for transiently increasing the permeability of the blood–brain barrier to facilitate targeted drug delivery[13]. Additionally, LIPUS has demonstrated the ability to promote cellular activity, enhance stem cell proliferation, and accelerate tissue repair processes, particularly in bone and soft tissues[6,14]. These developments highlight the growing potential of ultrasound as both a diagnostic and therapeutic tool. In contexts where conventional interventions, such as orthotic devices, lack objective evaluation metrics[15,16], ultrasound-based approaches are increasingly being explored as complementary or alternative solutions, especially in degenerative conditions such as osteoarthritis[17,18].

Despite these advantages, the reliability of ultrasound-based technologies is strongly dependent on the accuracy of the underlying computational models used to describe wave propagation in biological tissues. Inadequate parameter estimation can lead to significant clinical and operational consequences. For instance, inaccuracies in elastography models may increase false-negative rates in tumor detection, while errors in thermal or acoustic simulations can compromise treatment efficacy in therapeutic applications[19]. From a computational standpoint, inefficient algorithms can substantially increase processing time, energy consumption, and system cost[20,21], while also contributing to delays in regulatory approval and product development[21,22]. These challenges underscore the importance of developing robust, validated modeling frameworks capable of accurately capturing the complex behavior of ultrasound in biological media.

Modeling wave propagation in such tissues remains inherently difficult due to their viscoelastic, anisotropic, and nonlinear nature. Biological materials exhibit frequency-dependent attenuation and dispersion, requiring models that account for both elastic and viscous responses[23,24]. Fractional viscoelastic formulations, such as the Kelvin–Voigt fractional derivative and fractional Zener models, have been proposed as effective approaches to capture this behavior, as they inherently describe the distributed relaxation mechanisms observed in soft tissues and reproduce experimentally observed power-law attenuation trends[25–28]. These formulations have also been linked to widely used fractional wave equations, which can be interpreted as simplified representations of more general constitutive models[29]. Experimental studies have shown that such approaches often outperform traditional integer-order models in representing biological materials[30,31]. At the same time, structural anisotropy, particularly in tissues such as muscle and tendon, necessitates modeling approaches that move beyond isotropic assumptions, as directional dependence significantly influences wave propagation[32,33].

Attenuation itself, typically described through power-law relationships, remains challenging to incorporate accurately into propagation models, particularly when nonlinear effects such as harmonic generation and waveform distortion are considered[24,34–36]. Although experimental attenuation data are widely available, many simulation frameworks still rely on simplified assumptions that fail to capture the full complexity of heterogeneous and lossy biological tissues[23,37,38] . Multiphysics simulation environments, such as COMSOL Multiphysics, offer the capability to model coupled acoustic, thermal, and mechanical phenomena with high fidelity, making them suitable for the design of advanced therapeutic systems[39–41]. However, their predictive capability is fundamentally limited by the availability of accurate, experimentally validated input parameters.

Within this context, sound diffusivity ($\delta$) emerges as a particularly relevant parameter, as it provides

a unified description of acoustic wave dispersion and attenuation in nonlinear wave propagation models, including formulations such as the Westervelt equation[42]. Despite its importance, direct experimental quantification of $\delta$ in biological tissues remains largely absent from the literature. Existing studies have focused on related quantities, such as attenuation coefficients or thermal diffusivity, without extending the analysis to derive sound diffusivity for use in acoustic simulations[43]. This lack of experimental data represents a critical limitation, as many computational tools require $\delta$ to accurately describe frequency-dependent losses in nonlinear media. To the best of current knowledge, systematic experimental determination of sound diffusivity across biological tissues has not been previously reported, highlighting a significant gap in the field.

Addressing this limitation requires an integrated experimental–computational approach, in which key acoustic properties are not only measured but also directly incorporated into validated simulation frameworks. In this work, a time-domain, time-explicit numerical strategy is adopted, solving the full nonlinear acoustic wave equations using an explicit Runge–Kutta scheme. This approach captures the temporal evolution of the acoustic field, including phase information and broadband attenuation effects, and is validated through direct comparison with experimentally measured waveforms. A comprehensive experimental campaign is conducted to determine density, speed of sound, attenuation coefficient, and nonlinearity parameter B/A across a range of ex vivo tissues. While parameters such as density and sound speed are well established[44], accurate measurement of attenuation and especially nonlinear parameters remains less standardized[45]. These experimentally derived values are then implemented within a multiphysics simulation environment to estimate the frequency-dependent sound diffusivity $\delta(f)$, which is subsequently validated through regression analysis.

By combining experimental characterization with advanced numerical modeling, this chapter aims to establish a physically grounded framework for describing ultrasound propagation in biological tissues. This approach not only improves the reliability of computational predictions but also supports the development of more accurate diagnostic tools and targeted therapeutic technologies, contributing to the broader goal of advancing ultrasound-based biomedical applications.

The work developed within this research led to the publication of a peer-reviewed scientific article, in which both sound diffusivity and viscous attenuation models were investigated as complementary approaches to describe acoustic energy dissipation in biological tissues. However, for the purpose of this thesis, the discussion is intentionally focused on sound diffusivity, as it provides a more direct and computationally efficient framework for capturing frequency-dependent attenuation across a wide range of tissues. The viscous attenuation analysis, including the estimation of bulk and dynamic viscosity

parameters, is therefore not explored in detail here, although it remains fully documented and accessible in the published article for readers seeking a more comprehensive treatment of the underlying dissipation mechanisms[46], and a software tool used to characterize biological tissues[47], which is further discussed in section 6.3.2.3.

## 4.2 Materials and Methods

This section describes the integrated experimental and computational methodology adopted to characterize and model acoustic wave propagation in biological tissues. The approach combines controlled laboratory measurements with advanced signal processing, regression analysis, and multiphysics simulation to extract physically meaningful parameters governing ultrasound–tissue interactions. This combined methodology provides a robust and systematic pathway for linking experimental observations to predictive acoustic models in complex biological media.

### 4.2.1 Overview of Methodological Framework

The methodological framework developed in this section is conceived as a unified and hierarchical experimental–computational pipeline, specifically designed to bridge the gap between measurable acoustic responses in biological tissues and their accurate representation within predictive multiphysics models. At its core, the approach is structured around a sequential set of stages that collectively transform raw physical observations into validated simulation inputs (figure 57).

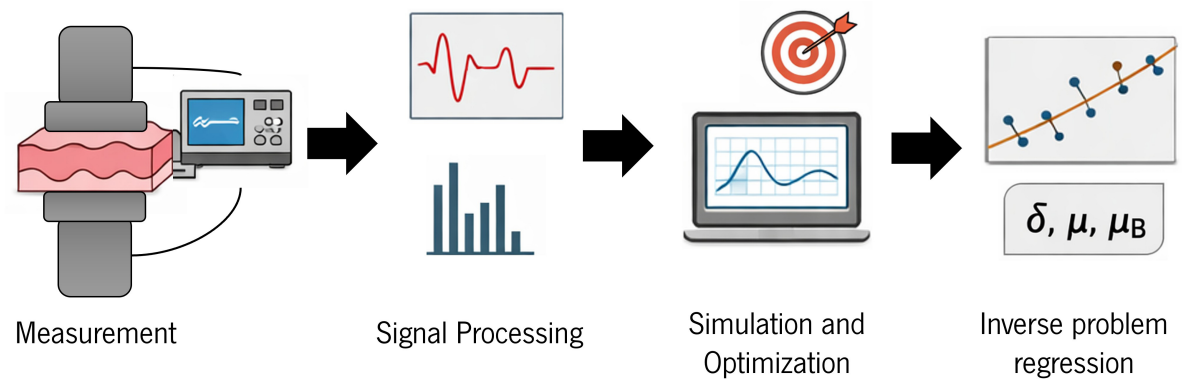



Figure 57: Integrated experimental–computational framework for acoustic characterization of biological tissues, illustrating the workflow from experimental measurement and signal processing to regression-based parameterization and inverse multiphysics modelling, enabling the extraction and validation of frequency-dependent acoustic properties.

The first stage consists of a rigorous experimental characterization, in which key acoustic and physical parameters (density, speed of sound, frequency-dependent attenuation, and the nonlinearity parameter B/A) are measured across a range of biological tissues (skin, adipose tissue, skeletal muscle, tendon, ligament, cartilage, cortical and trabecular bone) under tightly controlled environmental conditions. Particular attention is given to preserving tissue hydration, structural integrity, and geometrical consistency, ensuring that the measured responses reflect intrinsic material behavior rather than experimental artifacts. These measurements establish a physically grounded dataset that captures both linear and nonlinear aspects of ultrasonic wave propagation in heterogeneous media.

Building upon this foundation, the second stage focuses on signal processing and spectral analysis, where the experimentally acquired waveforms are transformed from the time domain into the frequency domain using filtering, windowing, and Fourier-based techniques. This transformation enables the isolation of fundamental and harmonic components, facilitating the quantification of attenuation mechanisms and nonlinear interactions that are otherwise obscured in raw signals.

The third stage introduces a regression-based modelling strategy, in which the extracted acoustic parameters are fitted using multiple functional forms, with particular emphasis on power-law relationships. This step is critical, as it reveals the inherent scale-dependent behavior of biological tissues and provides a compact mathematical representation of frequency-dependent phenomena, enabling interpolation across unmeasured frequency ranges and enhancing the generalizability of the results.

The final stage of the framework consists of a computational modelling and inverse problem formulation, in which the experimentally derived parameters are integrated into a multiphysics simulation environment to reconstruct wave propagation behavior. Within this context, advanced numerical methods are employed to solve nonlinear acoustic equations, and parameter estimation techniques are applied to iteratively adjust model variables until the simulated responses converge with experimental observations in both time and frequency domains. This closed-loop strategy ensures that the resulting models are not only mathematically consistent but also physically validated, effectively anchoring simulation outputs to empirical evidence. By systematically linking experimental measurement, signal interpretation, mathematical abstraction, and numerical reconstruction, the proposed framework establishes a robust and scalable methodology for characterizing and modelling ultrasound propagation in complex biological media.

### 4.2.2 Biological Materials and Sample Preparation

The biological materials considered in this study were selected to represent a targeted subset of tissues directly relevant to the knee's musculoskeletal structure and ultrasound propagation in the context of joint biomechanics. The investigated samples comprised skin, adipose tissue, skeletal muscle, tendon, ligament, cartilage, and both cortical and trabecular bone, primarily of porcine and bovine origin, as summarized in table 9.

Table 9: Summary of biological tissue samples used in this study.

| Biological Tissue | Origin | Number of Samples |
|---|---|---|
| Skin (thigh) | Porcine | 5 |

| | | |
|---|---|---|
| Adipose Tissue (thigh) | Porcine | 5 |
| Skeletal Muscle (*biceps femoris*) | Porcine | 10 |
| Trabecular Bone (femur) | Bovine | 5 |
| Cortical Bone (femur) | Bovine | 5 |
| Tendon (*flexor digitorum medialis*) | Bovine | 5 |
| Ligament (anterior cruciate ligament) | Bovine | 5 |
| Cartilage (femorotibial joint) | Bovine | 5 |

This selection is aligned with the anatomical layers relevant for ultrasound transmission in musculoskeletal applications, including the propagation path from superficial tissues to deeper load-bearing structures.

To ensure reproducibility and consistency in acoustic measurements, all soft tissues were prepared with standardized geometrical dimensions, consisting of circular specimens with a diameter of 24 mm and an approximate thickness of 2 mm (figure 58). These samples were obtained using a sterile hollow punch applied in a controlled, single-motion rotation, minimizing shear-induced deformation and ensuring smooth, well-defined edges. For hard tissues, a dedicated preparation protocol was implemented to account for their higher stiffness and structural complexity, as has been previously reported in other studies[48,49]. Bone samples were initially sectioned into manageable blocks using a low-speed saw under continuous saline irrigation to prevent thermal and mechanical damage. Subsequently, cylindrical specimens with a diameter of $24$ mm were produced using a hole saw drill bit operated at low rotational speeds and under cooling conditions, preserving both cortical density and trabecular architecture, once again based on procedures previously performed in the literature[50,51].

Given the sensitivity of biological tissues to environmental conditions, strict handling and preservation protocols were followed throughout the preparation and testing procedures. All samples were maintained at low temperatures (approximately $4$°C) prior to experimentation to reduce enzymatic activity and delay *post-mortem* degradation. During testing, tissues were kept fully hydrated using a physiological saline solution (phosphate-buffered saline), preventing dehydration, which could otherwise lead to artificial stiffening, volumetric shrinkage, and consequent alterations in acoustic properties. In addition, exposure to ambient conditions was minimized, and measurements were conducted as promptly as possible following sample preparation to ensure that the recorded responses reflected the

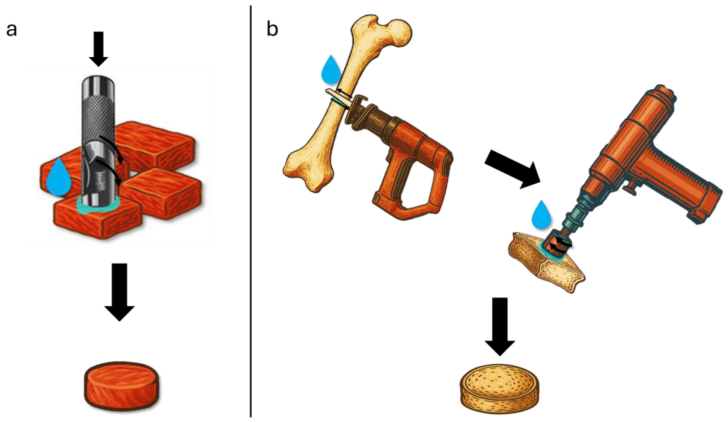



Figure 58: Specimen preparation. (a) Soft tissues were cut into 24 mm discs using a handheld hollow punch in a single rotation to minimize deformation. (b) Bone was first sectioned with a low-speed reciprocating saw under saline irrigation, then machined into 24 mm cylinders using a hole saw at low speed with cooling to preserve structural integrity[46].

closest approximation to the native physiological state.

The adopted preparation methodology serves a dual purpose: to standardize the geometry required for controlled acoustic measurements and to preserve the intrinsic mechanical and structural integrity of the tissues. Maintaining hydration and minimizing post-mortem changes are particularly critical for ensuring acoustic consistency, as variations in water content, microstructure, or internal stress states can significantly influence wave speed, attenuation, and nonlinear behavior.

### 4.2.3 Experimental methods

The experimental characterization of acoustic properties constitutes the foundational step in the proposed methodological framework, enabling the direct measurement of parameters that govern ultrasonic wave propagation in biological tissues. The adopted approach is designed to capture both linear and nonlinear acoustic behavior across a physiologically relevant frequency range, while ensuring that the extracted quantities are suitable for direct integration into computational models.

#### 4.2.3.1 Density Measurement

The density of each biological sample was determined through a direct geometric–gravimetric approach, in which the volume was calculated from measured dimensions and the mass was obtained using a precision balance. Specifically, the radius and thickness of each specimen were measured using a high-precision digital calliper, allowing the computation of volume under the assumption of cylindrical geometry. Density ($\rho$) was then obtained according to equation 206.

$$\rho = \frac{m}{l \cdot 2\pi r^2} \tag{206}$$

where $m$ is the mass, $l$ is the sample thickness and $r$ is sample radius

Although straightforward, this parameter plays a fundamental role in acoustic modelling, as it directly influences acoustic impedance and wave propagation characteristics. In particular, the acoustic impedance governs the transmission and reflection of waves at interfaces between different tissues. Accurate density measurements are therefore essential to ensure correct representation of impedance mismatches and energy transfer in subsequent simulations.

#### 4.2.3.2 Ultrasound Transmission Setup

The experimental setup for ultrasound transmission was specifically designed to overcome the limitations of conventional measurement techniques when applied to soft, deformable biological tissues and as an alternative to water transmission setups[52]. Classical transmission methods in solids typically rely on direct mechanical contact between transducers and samples, which can introduce uncontrolled compression, leading to alterations in thickness, density, and internal structure. Such deformation is particularly problematic for highly compliant tissues, including adipose tissue, cartilage, and muscle, where even small mechanical loads can significantly distort acoustic measurements.

To address this limitation, a modified transmission system inspired by the impedance tube (Kundt's tube) concept was developed. In this configuration, the biological sample is positioned between two aligned ultrasonic transducers, while its thickness is constrained using rigid spacer rings with a fixed dimension. This arrangement ensures a non-compressive boundary condition, maintaining constant sample geometry throughout the measurement process and eliminating variability associated with mechanical deformation. By decoupling mechanical loading from acoustic transmission, the setup preserves the intrinsic properties of the tissue and enables more reliable and reproducible measurements(figure 59). The technical drawing and assembly can be found in chapter A.

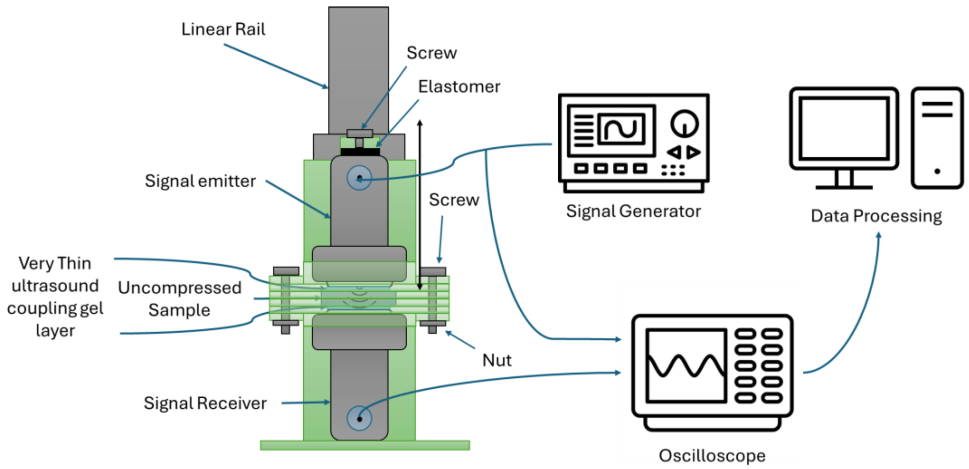



Figure 59: Schematic of the customized ultrasound transmission setup, illustrating the non-compressive measurement configuration with spacer-constrained sample positioning, signal generation and acquisition chain, and coupling strategy for accurate characterization of acoustic wave propagation in biological tissues[46].

Ultrasonic excitation was performed using piezoelectric transducers (Mitech ultrasonic, China) with a diameter of 24 mm, operating across a frequency range of 0.5 to 5 MHz. This range was selected to encompass both diagnostic and therapeutic ultrasound regimes, allowing the investigation of frequency-dependent phenomena. The transducers were driven by a function generator capable of producing controlled sinusoidal signals at specified amplitudes and frequencies. The transmitted signals were captured using a receiving transducer aligned coaxially with the source, and the resulting waveforms were recorded using a digital oscilloscope.

The signal generation and acquisition chain was designed to ensure high fidelity in both time and frequency domains. Low-amplitude excitations were used to characterize linear acoustic properties, while higher amplitudes were employed to induce nonlinear effects. This dual-regime approach enables the simultaneous investigation of attenuation, propagation speed, and harmonic generation within the same experimental framework.

#### 4.2.3.3 Speed of Sound Measurement

The speed of sound in each biological sample was determined using a time-of-flight methodology, based on the measurement of the propagation time of an ultrasonic pulse through a known thickness. In this approach, a signal is transmitted without the sample and through the sample, and the time delay difference between emission and reception of both conditions is recorded. The speed of sound ($c$) is then calculated as the ratio between the sample thickness and the measured transit time(equation 207).

$$c = \frac{l}{t_{sample} - t_{withoutsample}} \tag{207}$$

where $l$ is the sample thickness and $t_{sample}$ is the time of flight between the transmitting and receiving transducers with the sample and $t_{withoutsample}$ without the sample.

From a physical perspective, the speed of sound represents the propagation velocity of longitudinal waves within a medium and is directly related to its elastic and inertial properties. In biological tissues, this parameter is influenced by factors such as composition, hydration, and structural organization.

#### 4.2.3.4 Attenuation Characterization

The acoustic attenuation coefficient ($\alpha$) was quantified using an amplitude decay method, in which the reduction in signal amplitude after propagation through the sample was compared to a reference signal obtained in the absence of the sample. By measuring the ratio between the incident and transmitted amplitudes and normalizing by the sample thickness, the attenuation coefficient was calculated for each

frequency, as is demonstrated in equation 208,

$$\alpha(f) = \frac{20 \log_{10}\left(\frac{A_1}{A_2}\right)}{l} \tag{208}$$

where $f$ is the frequency of the acoustic wave, $l$ is the sample thickness, $A_1$ is the amplitude of the reference signal (baseline, no sample) and $A_2$ is the amplitude of the transmitted signal through the sample.

The frequency dependence of attenuation was subsequently analysed using a power-law formulation, reflecting the well-established relationship between acoustic losses and frequency in biological tissues. This step is particularly significant, as it introduces frequency as a governing variable in the characterization of wave propagation. Unlike density and speed of sound, which are often treated as constant parameters in linear propagation, attenuation exhibits a strong and nonlinear dependence on frequency, capturing the combined effects of viscous dissipation, scattering, and microstructural interactions.

#### 4.2.3.5 Nonlinearity Parameter B/A

The nonlinearity parameter B/A was determined through a harmonic generation approach, based on the analysis of waveform distortion under high-amplitude excitation. In this method, ultrasonic waves are propagated through the sample at elevated amplitudes, leading to the generation of higher-order harmonics due to nonlinear interactions within the medium. By quantifying the relative amplitudes of the fundamental frequency and its second harmonic in the frequency spectrum, the B/A parameter can be computed. Equation 209 was utilized,

$$\frac{B}{A} = \frac{8\rho c^3}{2\pi f} \frac{A_2^{measured}}{A_1^2} 10^{\left(\frac{(\alpha(2f) - 2\alpha(f))l}{20}\right)} \tag{209}$$

where $\rho$ is the density, $c$ is the speed of sound, $A_1^2$ is the amplitude of the fundamental frequency in the spectrum, and $A_2^{measured}$ is the amplitude of the second harmonic in the spectrum, $\alpha$ is the acoustic attenuation coefficient and $f$ is the frequency in MHz. A correction factor was included to compensate for the fact that attenuation is frequency-dependent, and thus the second harmonic undergoes greater attenuation than the fundamental. This adjustment ensures a more accurate estimation of the nonlinearity parameter.

This parameter provides a direct measure of the nonlinear compressibility of the medium and plays a central role in describing finite-amplitude wave propagation. In contrast to linear acoustic parameters, B/A captures the asymmetry between compression and rarefaction phases, which leads to waveform distortion, harmonic generation, and, in extreme cases, shock formation.

### 4.2.4 Signal Processing

The signal processing stage constitutes a critical intermediary layer between experimental measurement and parameter identification, enabling the transformation of raw ultrasonic waveforms into physically interpretable features suitable for quantitative analysis. Given the sensitivity of acoustic measurements to noise, boundary reflections, and instrumentation artifacts, a structured processing pipeline was implemented to ensure that the extracted information accurately represents the intrinsic response of the biological tissues. This stage is particularly important in the present framework, as it governs the transition from time-domain observations to frequency-domain representations, where key phenomena such as attenuation, dispersion, and nonlinear harmonic generation can be rigorously quantified.

The acquired signals, recorded in the time domain using a digital oscilloscope, were first subjected to a filtering process to remove high-frequency noise and unwanted signal components outside the bandwidth of interest. A low pass $5^{th}$ order Butterworth filter was employed, with a cutoff frequency of $3 \cdot f_{fundamental}$ and a roll-off of $6$ dB/octave (figure 60).

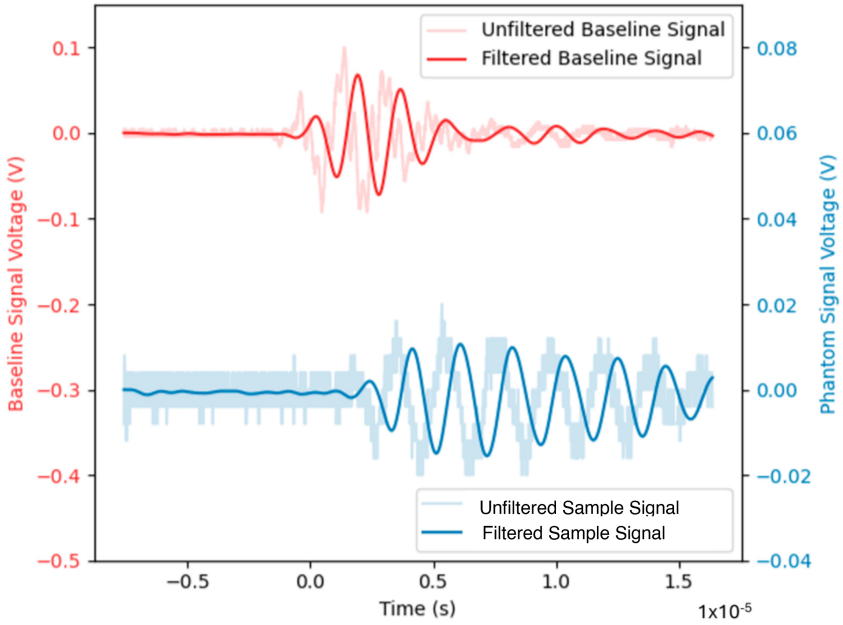



Figure 60: Comparison of unfiltered and Butterworth-filtered ultrasonic signals for baseline and sample measurements, illustrating noise reduction and preservation of waveform features for subsequent spectral analysis and feature extraction[53].

Following filtering, the signals were processed using a windowing technique prior to spectral analysis. A Hanning window was applied to each time-domain signal segment to reduce spectral leakage associated with the finite duration of the recorded waveform. By smoothly tapering the signal at its boundaries, the windowing function mitigates discontinuities that would otherwise introduce spurious frequency components in the Fourier domain.

The frequency-domain representation of the signals was obtained through the Fast Fourier Transform (FFT), enabling the decomposition of the waveform into its constituent frequency components. The FFT provides a direct means of identifying the fundamental excitation frequency and any higher-order harmonics generated during propagation through the tissue.

Feature extraction was subsequently performed through peak detection algorithms applied to the amplitude spectrum. The fundamental frequency peak and its corresponding harmonics were identified, and their amplitudes were quantified for each measurement condition.

### 4.2.5 Regression and Parameter Identification

Following the extraction of frequency-domain features, the next stage of the methodology focuses on the abstraction of experimental observations into compact mathematical models capable of describing and generalizing the acoustic behavior of biological tissues in function of frequency. In this context, regression techniques are employed to identify the most appropriate analytical forms that capture the underlying physics governing attenuation and wave propagation in heterogeneous media.

#### 4.2.5.1 Attenuation Modelling

The attenuation behaviour of biological tissues was modelled using a power-law formulation, which has been widely reported as an appropriate representation of frequency-dependent acoustic losses in soft and complex media. In this formulation, the attenuation coefficient is expressed as a function of frequency through a scaling relationship, where the exponent $n$ characterizes the frequency sensitivity of the medium. This approach captures the combined effects of viscous dissipation, scattering, and structural heterogeneity, all of which contribute to energy loss during wave propagation.

To estimate the parameters of the power-law model, the experimentally obtained attenuation data were transformed into a logarithmic space, enabling linearization of the nonlinear relationship (equation 210). Specifically, by taking the logarithm of both attenuation and frequency, the power-law expression is recast into a linear form, allowing the use of least-squares regression to determine the slope and intercept of the resulting line. The slope corresponds directly to the exponent n, while the intercept provides the attenuation coefficient at a reference frequency. This log–log regression approach offers numerical stability and facilitates the identification of scaling behavior across the investigated frequency range.

$$\log_{10}(\alpha(f)) = \log_{10}(\alpha_0) + n \cdot \log_{10}(f) \tag{210}$$

The use of a power-law model is particularly advantageous in the context of biological tissues, as it enables interpolation and extrapolation beyond the measured frequency points, thereby supporting its integration into computational frameworks where continuous parameter definitions are required.

#### 4.2.5.2 Model Comparison

In order to assess the suitability of the power-law formulation, alternative regression models were also evaluated, including linear (equation 211), exponential (equation 212), and logarithmic (equation 213) relationships between attenuation and frequency.

$$\alpha(f) = A \cdot f + B \tag{211}$$

$$\alpha(f) = A \cdot e^{Bf} \tag{212}$$

$$\alpha(f) = A \cdot \log(f) + B \tag{213}$$

Each model was fitted to the experimental data, and their performance was compared based on goodness-of-fit metrics, such as the coefficient of determination observed in equation 214,

$$R^2 = 1 - \frac{\sum_i \left(y_i - \hat{y}_i\right)^2}{\sum_i \left(y_i - \overline{y}\right)^2} \tag{214}$$

where $R^2$ is the goodness of fit coefficient, $y_i$ is the experimental value, $\overline{y_i}$ is the average value of $y$, and $\hat{y}_i$ is the predicted value for $i$.

The linear model assumes a direct proportionality between attenuation and frequency, which may be adequate over narrow frequency ranges but fails to capture the nonlinear scaling observed in most biological tissues. The exponential model introduces a rapidly increasing attenuation behavior, which can overestimate losses at higher frequencies and lacks a clear physical interpretation in the context of wave propagation. The logarithmic model, while capable of representing sublinear growth, does not adequately reflect the multiplicative nature of frequency-dependent attenuation mechanisms.

In contrast, the power-law formulation consistently provides a superior fit to the experimental data, capturing both the curvature and scaling behavior observed across different tissue types. More importantly, it aligns with the physical understanding of acoustic attenuation in complex media, where multiple interacting mechanisms operate across scales. This observation reinforces a key principle underpinning the present work: biological tissues do not exhibit simple linear acoustic behavior, but rather follow scale-invariant laws that reflect their hierarchical and heterogeneous structure.

### 4.2.6 Computational Modelling Framework

The computational modelling framework constitutes the stage at which experimentally derived parameters are integrated into a predictive numerical environment, enabling the reconstruction of acoustic wave propagation in biological tissues. This stage closes the methodological loop by linking measured physical quantities to their governing equations and validating their consistency through simulation.

#### 4.2.6.1 Governing Equations

Wave propagation in biological tissues was modelled using a nonlinear acoustic formulation based on the Westervelt equation (equation 53), which extends the classical linear wave equation by incorporating attenuation and finite-amplitude effects. This formulation is particularly suited for biological media, where both dissipative mechanisms and nonlinear interactions play a significant role in shaping the propagating waveform. In COMSOL Multiphysics, this equation is slightly modified, taking the form in equation 215

$$\frac{1}{\rho c^2}\frac{\partial^2 p_t}{\partial t^2} + \nabla\Big( -\frac{1}{\rho}(\nabla p_t - \mathbf{q}_d) - \frac{\delta}{\rho c^2}\frac{\partial p_t}{\partial_t}\Big) = \frac{\beta}{\rho^2 c^4}\frac{\partial^2 p_t^2}{\partial t^2} + \mathbf{Q}_m \tag{215}$$

where $p_t$ is the total pressure, and $mathbfq_d$ and $mathbfQ_m$ are dipole and monopole sources, respectively, that might be inserted in the medium[54].

Within this framework, three key parameters govern the acoustic response. The sound diffusivity ($\delta$) represents the cumulative effect of energy dissipation mechanisms, including viscous and thermal losses, and directly controls the attenuation and spatial smoothing of the wave field. The nonlinearity parameter characterizes the deviation from linear compressibility, governing the generation of higher-order harmonics and waveform distortion during propagation. Finally, viscosity introduces an additional mechanism of energy dissipation, particularly relevant at higher frequencies and in highly hydrated tissues, where internal friction contributes to amplitude decay and phase shifts.

These parameters are directly connected to the theoretical developments presented in the preceding chapters, where the derivation of nonlinear acoustic equations establishes the physical basis for their inclusion. By adopting the Westervelt formulation, the model captures the essential physics required to describe ultrasound propagation in complex, heterogeneous, and dissipative biological media.

#### 4.2.6.2 Numerical Implementation (COMSOL)

The governing equations were implemented within a finite element framework using COMSOL Multiphysics. A time-explicit integration scheme using the Runge–Kutta method (RK34) with a fixed time

step to ensure numerical stability was employed to resolve transient wave propagation, enabling accurate tracking of waveform evolution, including harmonic generation and attenuation effects.

To ensure numerical stability and accuracy in the presence of strong material contrasts and high-frequency content, a DGM formulation was adopted. This approach allows for local discontinuities between elements, improving the handling of wave transmission across interfaces with differing acoustic impedances and reducing numerical dispersion. The DGM method is particularly advantageous in wave propagation problems involving heterogeneous media, where conventional continuous formulations may suffer from spurious reflections or instability.

An axisymmetric simplification was introduced to reduce computational cost while preserving the essential physics of the problem. Given the circular geometry of the transducers and samples, the assumption of rotational symmetry enables the reduction of a three-dimensional problem to a two-dimensional domain without significant loss of accuracy.

#### 4.2.6.3 Geometry and Boundary Conditions

The computational domain was defined as a two-dimensional axisymmetric representation of the experimental setup, including the transmitting and receiving transducers, the biological sample, and the surrounding medium (figure 61). The geometry was constructed to replicate the spatial configuration of the experimental apparatus, ensuring consistency between measured and simulated conditions.

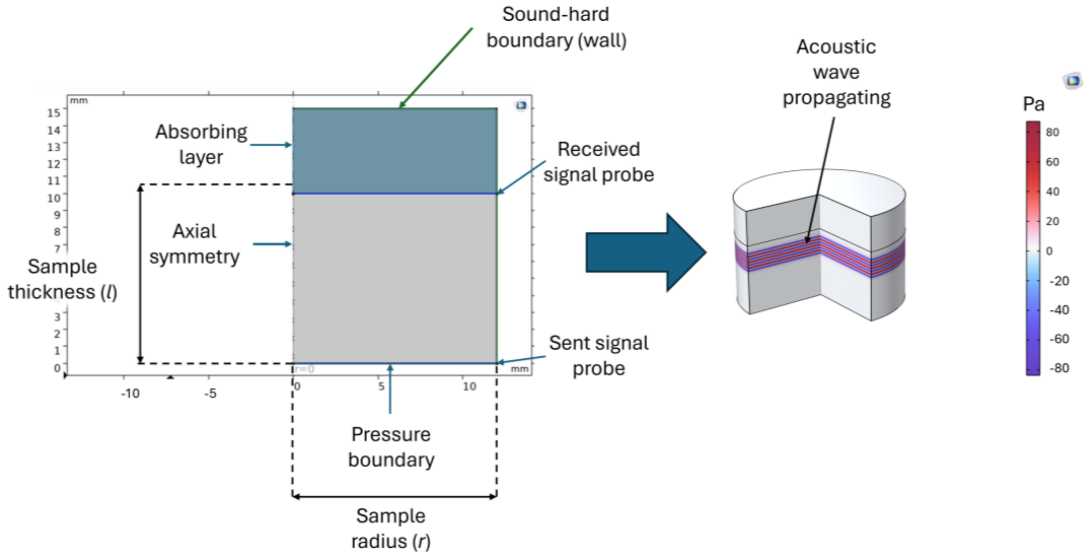



Figure 61: Axisymmetric computational domain and boundary conditions used for acoustic wave propagation, including absorbing layer, pressure excitation, probe locations, and resulting pressure field distribution[46].

To prevent artificial reflections at the boundaries of the computational domain, absorbing layers were implemented, effectively mimicking an infinite medium. These layers attenuate outgoing waves, reducing boundary-induced artifacts that could otherwise contaminate the simulated signal. The accurate

representation of boundary conditions is critical in wave propagation problems, as even minor reflections can significantly alter the amplitude and phase of the transmitted signal.

Probe locations were defined within the domain to extract time-domain signals corresponding to the positions of the experimental receivers. These virtual probes enable direct comparison between simulated and measured waveforms, forming the basis for parameter identification and model validation.

#### 4.2.6.4 Mesh and Stability Criteria

The accuracy of the numerical solution is strongly dependent on the spatial and temporal discretization of the domain. To adequately resolve the propagating wave field, the mesh was designed according to the principle of elements per wavelength, ensuring that each wavelength is discretized with a sufficient number of elements to capture its spatial variation. This criterion is particularly important at higher frequencies, where shorter wavelengths demand finer meshes to avoid numerical dispersion and amplitude errors.

In addition to spatial resolution, temporal stability was enforced through compliance with the CFL condition, which governs the relationship between time step, wave speed, and element size. The domain was discretized utilizing triangular mesh elements. The mesh was designed to satisfy a CFL condition of 0.2, ensuring numerical stability for most biological tissues. However, for materials exhibiting high acoustic attenuation, such as trabecular and cortical bone, a denser mesh was required to accurately capture wave behavior. In these cases, the number of elements per wavelength was doubled, yielding a more stringent CFL condition of 0.1. A summary of the number of element utilized is displayed in table 10.

Table 10: Number of mesh elements used in the simulation domain for each biological tissue sample.

| | **Number of Domain Elements** | | | | |
|---|---|---|---|---|---|
| **Sample** | **0.5 MHz** | **1 MHz** | **2 MHz** | **4 MHz** | **5 MHz** |
| Skin | 4,484 | 17,668 | 70,188 | 286,734 | 454,478 |
| Adipose Tissue | 3,410 | 13,436 | 53,188 | 211,874 | 336,434 |
| Skeletal Muscle (⊥ fibres) | 4,746 | 18,524 | 73,650 | 302,692 | 478,522 |
| Skeletal Muscle (‖ fibres) | 7,502 | 29,298 | 117,240 | 500,168 | 782,262 |

| | | | | | |
|---|---|---|---|---|---|
| Tendon | 3,658 | 14,500 | 57,632 | 235,336 | 375,674 |
| Ligament | 2,500 | 9,766 | 39,208 | 155,366 | 243,538 |
| Cartilage | 1,720 | 6,786 | 26,426 | 104,988 | 165,692 |
| Trabecular Bone | 8,484 | 33,556 | 133,310 | 567,116 | 904,214 |
| Cortical Bone | 4,560 | 17,746 | 70,728 | 291,248 | 462,560 |

### 4.2.7 Inverse Problem and Parameter Estimation

The final stage of the methodological framework addresses the inverse problem associated with acoustic wave propagation in biological tissues, wherein the objective is to infer intrinsic material parameters from observed wave behavior. In contrast to the forward problem, where the governing equations are solved for known material properties, the inverse formulation seeks to determine the set of parameters that best reproduce experimentally measured signals when embedded within the computational model. This approach is fundamental to the present work, as several key parameters governing attenuation and nonlinear propagation, such as sound diffusivity and viscous contributions, cannot be measured directly with sufficient accuracy and must instead be estimated through model-based inference.

Formally, the inverse problem can be expressed as an optimization problem in which a set of unknown parameters $\theta$ is identified such that the discrepancy between experimental observations and numerical predictions is minimized. The objective is to determine the optimal parameter vector $\theta*$ through equation 216

$$\theta* = \arg\min_{theta} \mathbf{J}(\theta) \tag{216}$$

where $\mathbf{J}(\theta)$ is a cost function quantifying the mismatch between experimental and simulated signals.

In this work, a least-squares formulation was adopted, defining the objective function as equation 217

$$min_{\delta} J(\delta) = \sum_{i,j} \left[ p^{simulation}(x_i, t : j, \delta) - p^{observed}(x_i, t_j) \right]^2 \tag{217}$$

This formulation penalizes deviations in the time domain, ensuring that both amplitude and phase information are captured during the optimization process.

In this work, the Bound Optimization BY Quadratic Approximation (BOBYQA) algorithm was employed. BOBYQA is a trust-region method that constructs a local quadratic approximation of the objective function based on a set of interpolation points, iteratively refining this approximation to converge toward a minimum.

At each iteration, BOBYQA evaluates the objective function at strategically selected points, updating the quadratic model and adjusting the trust-region radius based on the quality of the approximation. This approach is particularly well-suited for problems where function evaluations are computationally expensive, as is the case for time-dependent multiphysics simulations.

The algorithm operates within a bounded parameter space, allowing the incorporation of physically meaningful constraints on the variables, such as positivity of diffusivity and viscosity. The defined boundary conditions are in table 11.

Table 11: Overview of the parameter estimation limits.

| **Parameters** | **Initial Value** | **Scale** | **Upper Bound** | **Lower Bound** |
|---|---|---|---|---|
| Sound Diffusivity ($m^2/s$) | 0 | $1 \cdot 10^{-3}$ | 0 | 0.2 |
| Dynamic Viscosity ($Pa \cdot s$) | 0 | $1 \cdot 10^{-3}$ | 0 | 0.2 |
| Bulk Viscosity ($Pa \cdot s$) | 0 | 0.1 | 0 | 100 |

### 4.2.8 Sound Diffusivity-Based Modelling Approaches

The accurate representation of acoustic attenuation in biological tissues requires the incorporation of dissipative mechanisms within the governing equations. In the present work, two complementary modelling approaches are considered to account for energy losses during wave propagation: a sound diffusivity-based formulation and a viscosity-based formulation. Although both approaches aim to reproduce the observed attenuation behavior, they differ fundamentally in their physical interpretation and mathematical representation. The former adopts a phenomenological perspective, capturing the emergent macroscopic effects of dissipation, while the latter is grounded in constitutive physics, explicitly modelling the mechanisms responsible for energy loss at the material level.

The sound diffusivity model introduces attenuation through an effective diffusion term embedded within the Westervelt equation (equation 53). From a physical standpoint, the diffusivity parameter does not correspond to a single identifiable mechanism, but rather encapsulates the cumulative effects of multiple dissipative processes, including viscous losses, thermal conduction, and scattering due to microstructural heterogeneity. The diffusivity model treats attenuation as an emergent phenomenon, capturing the macroscopic outcome of multiple interacting mechanisms without resolving them

individually.

## 4.3 Results

The results presented in this chapter synthesize the outcomes of the experimental and computational framework, progressively transitioning from raw signal observations to the extraction of physically meaningful acoustic parameters and their validation within a predictive modelling environment. Given the extensive dataset acquired across multiple tissues, frequencies, and excitation conditions, the presentation of results is structured to emphasize representative behaviours, dominant trends, and physically relevant insights, rather than exhaustive data repetition. Accordingly, selected key metrics are discussed in the main text to illustrate the underlying phenomena, while the complete set of processed measurements is provided in the Appendix to ensure transparency and reproducibility. This approach enables a clear and concise interpretation of the results while preserving full access to the experimental dataset.

### 4.3.1 Experimental Signal Characterization

The initial stage of the results focuses on the characterization of the acquired ultrasonic signals in the time domain, providing a direct assessment of the measurement quality and the influence of biological tissues on wave propagation. Due to the large number of measurements performed (a total of 225 processed signals) a representative example will be demonstrated in this section, since the complete dataset was batch processed and all parameters were extracted.

The time-domain signals for both calibration and sample measurements are presented in figure 62. The calibration signal (figure 62 A) corresponds to the wave propagating from one transducer to another, while the sample signal (figure 62 B) represents propagation through the biological tissue under study. In both cases, the raw acquired signals were subjected to filtering to reduce high-frequency noise and spurious fluctuations. The filtered signals preserve the main wave packet structure, including the primary oscillation and its decaying tail, while effectively suppressing background noise and isolated spikes. This filtering step is essential to ensure reliable identification of waveform features such as peak amplitude and arrival time. A clear reduction in amplitude is observed in the sample signal compared to the calibration case, reflecting energy dissipation due to absorption and scattering within the tissue.

To quantify wave propagation characteristics, the time-of-flight and peak amplitude were extracted from the processed signals, as illustrated in figure 63. The temporal position of the maximum amplitude was used to determine the arrival time of the wave, enabling the calculation of the speed of sound based on the known propagation distance. Simultaneously, the difference in peak amplitudes between calibration

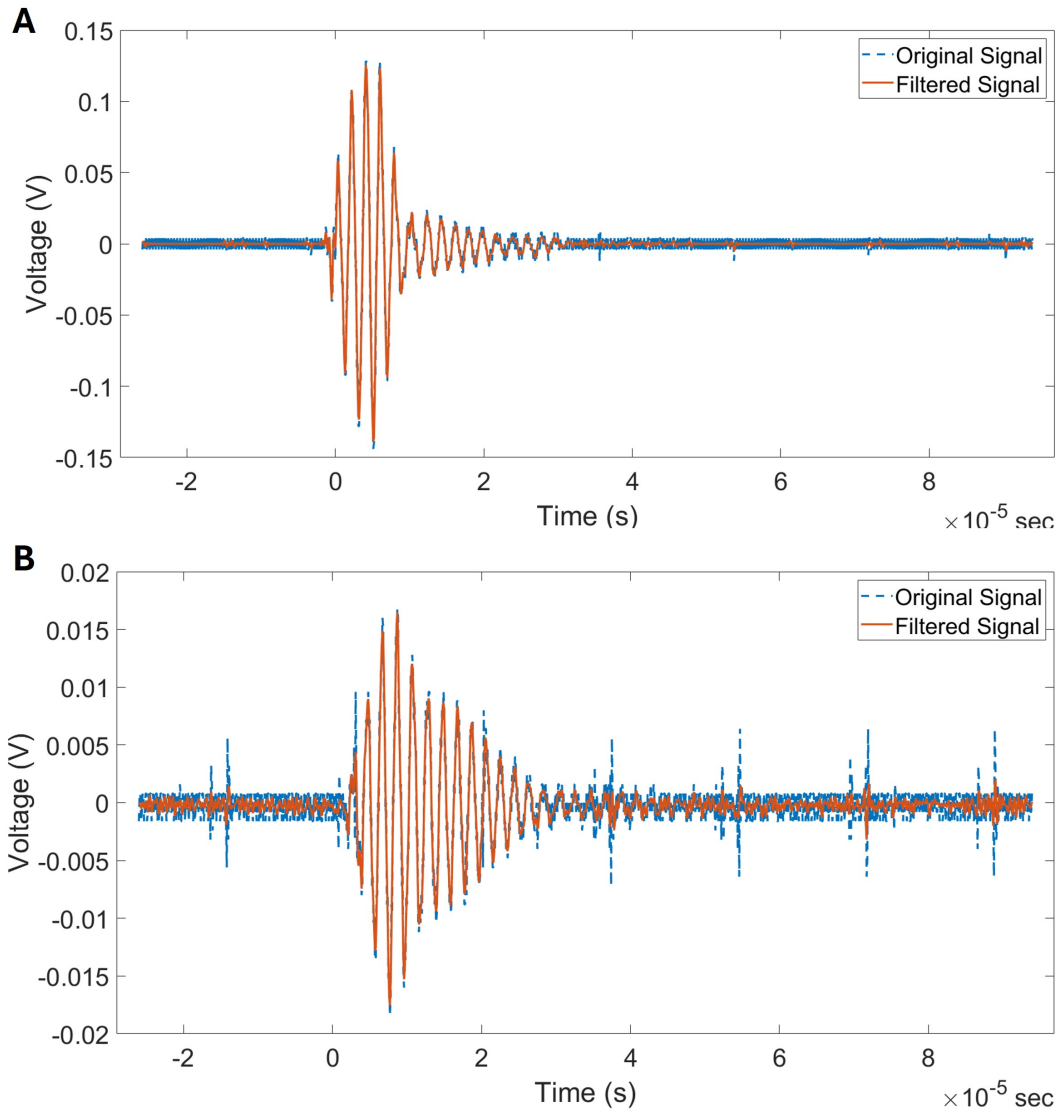



Figure 62: Time-domain ultrasonic signals: (A) calibration signal and (B) signal transmitted through the sample. Both original and filtered signals are shown, highlighting noise reduction and preservation of the main wave packet.

and sample signals provides a direct measure of attenuation. The use of clearly identifiable maxima ensures robustness in the presence of residual noise and waveform distortion. The comparison between calibration and sample signals highlights both a temporal shift, associated with changes in propagation velocity, and a reduction in amplitude, indicative of energy losses within the medium.

The frequency-domain representation of the signals is shown in figure 64, obtained via FFT. The spectrum reveals a dominant fundamental frequency component, accompanied by higher-order harmonics. These harmonic components arise from nonlinear propagation effects and are essential for the estimation of the acoustic nonlinearity parameter B/A. In particular, the relative amplitudes of the fundamental and second harmonic components were used to quantify nonlinear behavior within the medium. The presence of well-defined harmonic peaks confirms that the excitation signal and measurement system are capable of capturing nonlinear acoustic phenomena. The decay of spectral

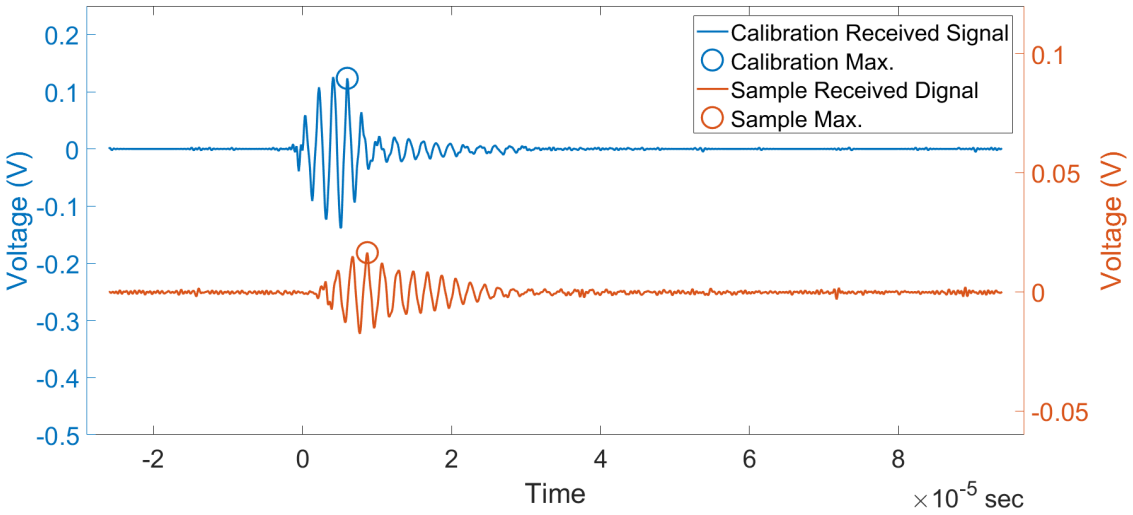



Figure 63: Time-of-flight and peak amplitude identification for calibration and sample signals, used to determine speed of sound and attenuation.

amplitude at higher frequencies further reflects the combined effects of attenuation and bandwidth limitations.

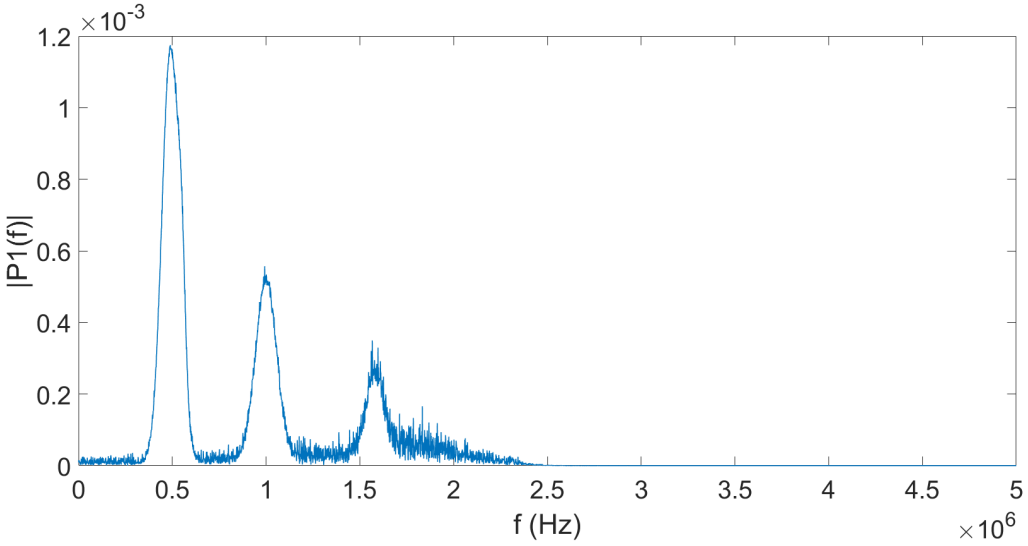



Figure 64: Frequency spectrum of the received signal obtained via FFT, showing the fundamental frequency and higher-order harmonics used for the estimation of the acoustic nonlinearity parameter B/A.

The presented signals illustrate the typical response observed during transmission experiments, highlighting the transition from unfiltered to filtered waveforms following the application of the signal processing pipeline described previously. In general, the raw signals exhibit a combination of the transmitted waveform, environmental noise, and potential reflections arising from boundary interactions. After filtering, the signals display a clearer oscillatory structure, with improved signal-to-noise ratio and well-defined amplitude envelopes, enabling reliable identification of key features such as peak amplitudes and temporal delays.

### 4.3.2 Experimental Acoustic Parameters Extraction

Building upon the signal processing framework described previously, this stage focuses on quantifying the fundamental parameters governing acoustic propagation, namely density, speed of sound, attenuation, and nonlinearity. These parameters are not directly observed in the time-domain signals, but are instead inferred through systematic analysis in both time and frequency domains, linking measurable features such as time delays, amplitude decay, and harmonic content to intrinsic material properties. Given the extensive dataset obtained across multiple tissues and excitation conditions, the results presented in this section emphasize representative trends and statistically consistent behaviours.

#### 4.3.2.1 Density

The density of the investigated biological tissues was determined using the geometric–gravimetric, with the results, summarized in figure 65, reveal a clear distinction between soft and hard tissues, reflecting their intrinsic structural composition and water content.

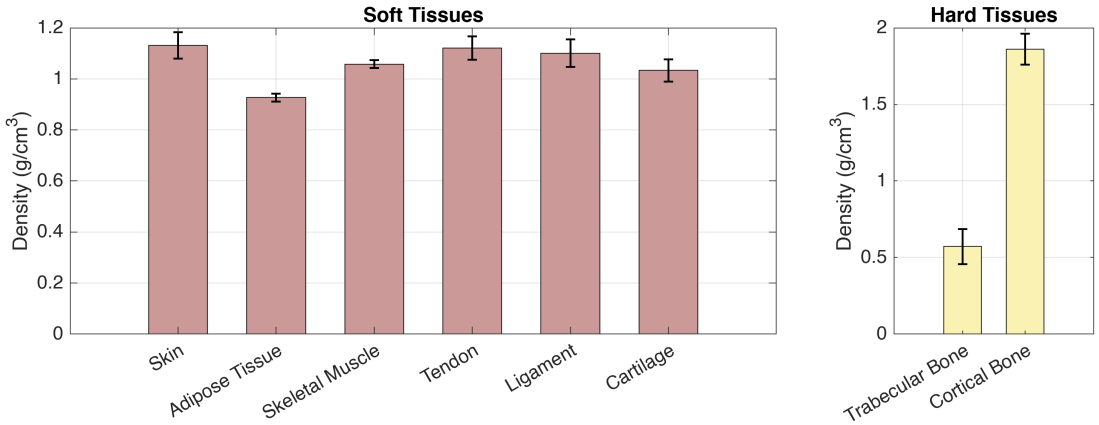



Figure 65: Measured density of soft and hard biological tissues, highlighting the relatively narrow range of soft tissue densities compared to the higher variability and increased values observed in hard tissue.

Soft tissues, including skin, adipose tissue, skeletal muscle, tendon, ligament, and cartilage, exhibited densities within a relatively narrow range, typically close to that of water. Measured values ranged approximately from 0.92 g/cm$^3$ for adipose tissue to $1.13 g/cm^3$ for tendon and skin, with most tissues clustering around 1.00–1.10 g/cm$^3$. This consistency is expected, as soft biological tissues are predominantly composed of water and organic matrix components, resulting in similar bulk densities despite differences in microstructure and mechanical behavior. Adipose tissue, characterized by its high lipid content, exhibited the lowest density among the soft tissues, reflecting the lower density of fat compared to aqueous media. In contrast, fibrous tissues such as tendon and ligament showed slightly higher densities, consistent with their dense collagen architecture.

On the other hand, hard tissues displayed significantly greater variability and higher absolute density values. Trabecular bone exhibited a comparatively low density, around 0.55–0.60 g/cm$^3$, due to its porous, lattice-like structure, which includes substantial void space filled with marrow. Cortical bone, on the other hand, presented the highest density values, approaching approximately 1.80–1.90 g/cm$^3$, reflecting its compact and highly mineralized composition.

#### 4.3.2.2 Speed of Sound

The speed of sound in the investigated biological tissues was determined using the time-of-flight methodology and the results are presented in figure 66, reveal distinct propagation characteristics across soft and hard tissues, reflecting differences in mechanical stiffness, structural organization, and composition.

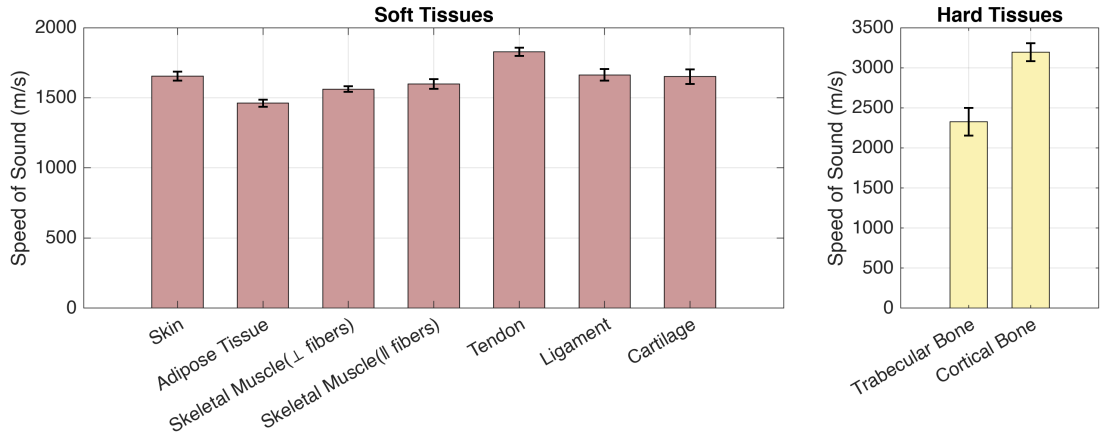



Figure 66: Measured speed of sound in soft and hard biological tissues, highlighting anisotropic behavior in skeletal muscle and significantly higher propagation velocities in cortical bone compared to hard tissues

Soft tissues exhibited speeds of sound within a relatively constrained range, typically between approximately 1450 m/s and 1850 m/s. Adipose tissue presented the lowest propagation velocity, around 1450 m/s, which is consistent with its high lipid content and reduced stiffness compared to other soft tissues. Skeletal muscle showed anisotropic behavior, with measured values differing depending on fibre orientation, highlighting the influence of microstructural alignment on wave propagation. Specifically, propagation perpendicular to muscle fibres resulted in lower velocities compared to parallel orientations, reflecting the directional dependence of mechanical stiffness. Fibrous tissues such as tendon and ligament exhibited higher propagation speeds, with tendon reaching values near 1800 m/s, consistent with its dense collagen structure and high elastic modulus. Cartilage and skin presented intermediate values, reflecting their composite and hydrated nature.

On the other hand, hard tissues demonstrated significantly higher speeds of sound, with trabecular bone exhibiting values around 2300 m/s and cortical bone reaching approximately 3200 m/s. This

substantial increase is directly related to the higher stiffness and mineral content of bone tissue, which facilitate faster transmission of compressional waves. The difference between trabecular and cortical bone is particularly notable, as it reflects the influence of porosity and internal architecture on effective wave propagation. While trabecular bone contains a network of voids and marrow that reduce its effective stiffness, cortical bone is dense and compact, enabling much higher wave speeds.

#### 4.3.2.3 Attenuation

The frequency-dependent attenuation of ultrasonic waves in biological tissues results are presented in figure 67. The attenuation coefficient was evaluated over a frequency range of 0.5 to 5 MHz, enabling the identification of scaling behavior across both soft and hard tissues.

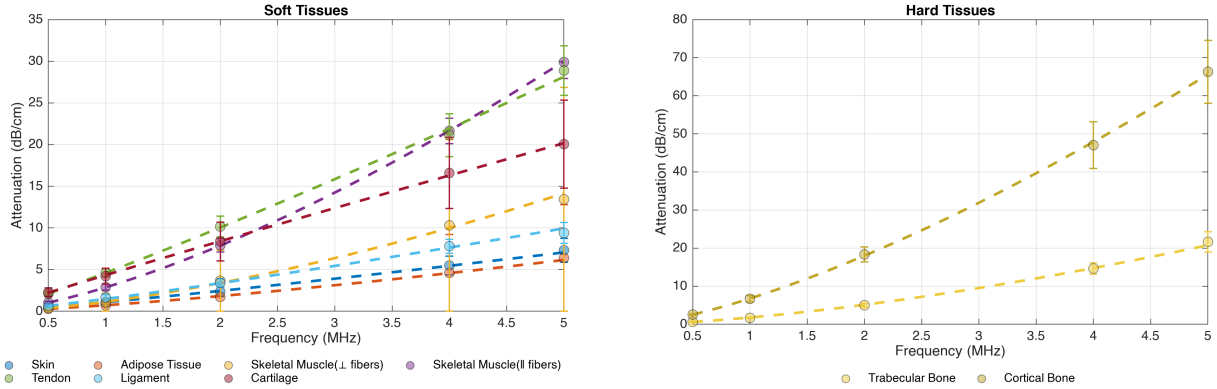



Figure 67: Measured attenuation as a function of frequency for soft and hard biological tissues, showing strong frequency dependence and excellent agreement with power-law fits across all tissue types.

For soft tissues, attenuation values increase progressively with frequency, with distinct differences observed between tissue types. Skeletal muscle, particularly when measured parallel to fibre orientation, exhibited the highest attenuation among soft tissues, reaching values close to 30 dB/cm at 5 MHz. This behavior reflects the anisotropic and fibrous structure of muscle, which enhances scattering and internal friction mechanisms. Tendon and cartilage also showed relatively high attenuation, consistent with their dense collagen networks and viscoelastic nature. In contrast, skin and adipose tissue exhibited lower attenuation values, remaining below approximately 10 dB/cm at the highest frequency, indicating reduced energy dissipation during propagation. Ligament displayed intermediate behavior, reflecting its structural similarity to tendon but with slightly lower density and stiffness.

Hard tissues exhibited markedly higher attenuation compared to soft tissues, with cortical bone showing the most pronounced frequency dependence. Attenuation in cortical bone reached values exceeding 60 dB/cm at 5 MHz, reflecting strong energy dissipation due to its highly mineralized and stiff structure. Trabecular bone, while less dense, also exhibited significant attenuation, although at lower levels compared to cortical bone. The difference between these two bone types highlights the influence

of microstructure, where porosity and internal interfaces in trabecular bone contribute to scattering, while the compact structure of cortical bone leads to stronger intrinsic absorption.

The extracted parameters, summarized in table 12, further reinforce the scale-dependent nature of attenuation.

Table 12: Fitted power-law attenuation parameters ($\alpha_0$, $n$) and corresponding coefficients of determination ($R^2$) for each biological tissue, demonstrating strong agreement between experimental data and scaling behavior.

| **Sample** | $\alpha_0$ **(dB/cm)** | **n** | $\mathbf{R}^2$ |
|---|---|---|---|
| Skin | 1.096 | 1.157 | 0.9979 |
| Adipose Tissue | 0.7264 | 1.328 | 0.9989 |
| Skeletal Muscle ($\perp$ fibers) | 1.150 | 1.560 | 0.9983 |
| Skeletal Muscle ($\parallel$ fibers) | 2.870 | 1.458 | 0.9930 |
| Tendon | 4.617 | 1.123 | 0.9995 |
| Ligament | 1.489 | 1.180 | 0.9960 |
| Cartilage | 4.336 | 0.9553 | 0.9995 |
| Trabecular Bone | 1.784 | 1.525 | 0.9989 |
| Cortical Bone | 6.779 | 1.410 | 0.9999 |

The extracted parameters further reinforce the scale-dependent nature of attenuation. The exponent $n$ varies between approximately 0.95 and 1.56 across tissues, indicating that attenuation does not follow a simple linear relationship with frequency, but instead reflects a more complex scaling behavior. Soft tissues generally exhibit exponents close to unity, while fibrous and structured tissues, such as muscle, tend to show higher values, indicating stronger frequency sensitivity. Similarly, bone tissues exhibit elevated exponents, consistent with their complex interaction mechanisms involving both absorption and scattering. The high coefficients of determination ($R \approx 0.99$) confirm the suitability of the power-law model in describing attenuation behavior in biological media.

#### 4.3.2.4 Nonlinearity Parameter B/A

The nonlinearity parameter B/A of the investigated biological tissues was estimated using the harmonic generation methodology and the results are presented in figure 68.




Figure 68: Measured nonlinearity parameter B/A for soft and hard biological tissues, highlighting moderate nonlinear behavior in soft tissues and significantly elevated values in trabecular bone due to its porous structure.

For soft tissues, the measured B/A values fall within a relatively moderate range, typically between approximately 6 and 11. Adipose tissue exhibited the highest nonlinearity among the soft tissues, with values exceeding 10, indicating a pronounced tendency for waveform distortion and harmonic generation. This behavior is consistent with its heterogeneous composition, where lipid inclusions and structural irregularities contribute to nonlinear interactions. In contrast, skeletal muscle displayed anisotropic behavior, with lower B/A values observed when the wave propagated perpendicular to the fibre direction compared to parallel propagation. This highlights the influence of microstructural alignment on nonlinear acoustic response, similarly to what was observed for the speed of sound. Other soft tissues, including skin, tendon, ligament, and cartilage, exhibited intermediate values, generally between 7 and 8, suggesting a relatively consistent nonlinear behavior across these hydrated, collagen-based structures.

A markedly different trend was observed for hard tissues. Trabecular bone exhibited exceptionally high B/A values, approaching approximately 80, indicating strong nonlinear behavior and significant waveform distortion during propagation. This can be attributed to its complex porous architecture, where multiple scattering, reflections, and local stress concentrations enhance nonlinear effects. In contrast, cortical bone showed substantially lower B/A values, around 20, despite its higher density and stiffness. This suggests that structural homogeneity and reduced internal interfaces in cortical bone limit the development of nonlinear interactions compared to trabecular bone.

### 4.3.3 Computational Model Validation

The detailed validation of the computational model, including extended comparisons between experimental and simulated signals, is provided in section B.1. This supplementary material contains the complete set of validation results across all tested conditions, ensuring full transparency and

reproducibility of the modelling framework, while allowing the main text to focus on the most representative and physically relevant outcomes.

### 4.3.4 Inverse Parameter Estimation

In this section, the problem is formulated as an optimization task, in which model parameters are iteratively adjusted until the simulated acoustic response reproduces the measured signals in both time and frequency domains. This approach effectively transforms the computational model into an identification tool, allowing the extraction of physically meaningful parameters from complex wave–tissue interactions.

#### 4.3.4.1 Sound Diffusivity

Unlike directly measurable quantities such as density or speed of sound, $\delta$ represents an emergent parameter that encapsulates the cumulative effects of multiple attenuation mechanisms, including viscous losses, thermal diffusion, and microstructural scattering. As such, its estimation relies on enforcing consistency between experimentally observed waveforms and their numerical reconstruction. The obtained values are presented in figure 69 for soft tissues and figure 70 for hard tissues.

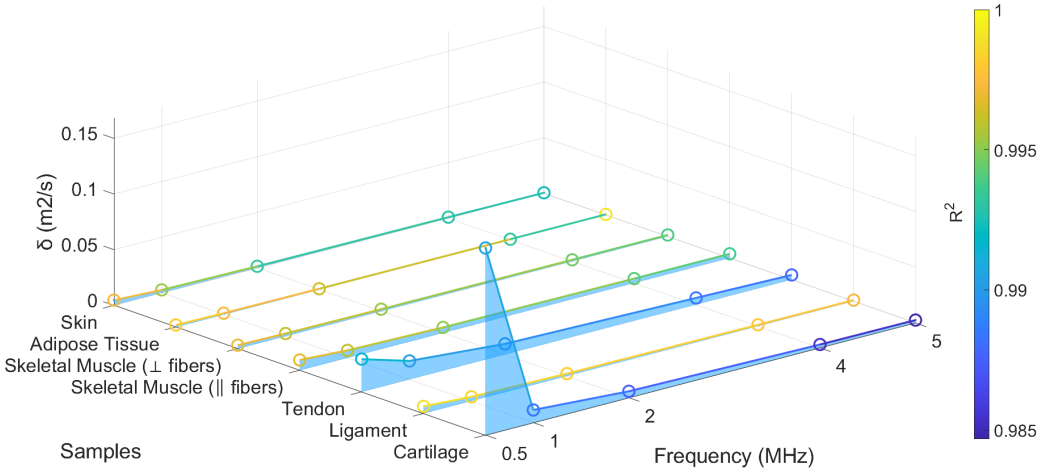



Figure 69: Estimated sound diffusivity ($\delta$) as a function of frequency for soft tissues, showing strong agreement between experimental data and model predictions, as indicated by high $R^2$ values.

The estimated sound diffusivity values demonstrated a consistently strong agreement between the experimental observations and the computational model across all investigated tissues and frequency ranges. The fitted curves closely follow the measured attenuation trends, with minimal deviation throughout the spectrum. This is further supported by the high coefficients of determination ($R^2$), which remain consistently close to unity for all cases, indicating an excellent quality of fit.

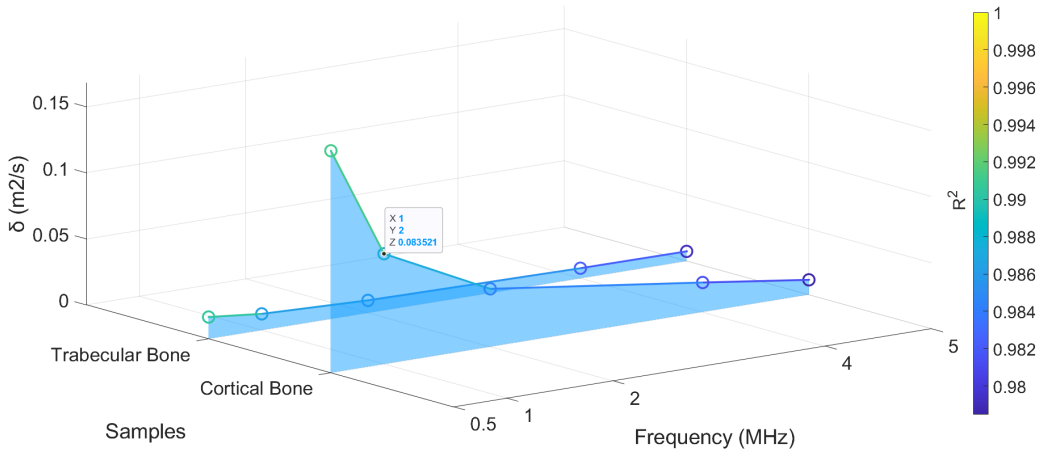



Figure 70: Estimated sound diffusivity ($\delta$) as a function of frequency for hard tissues, showing strong agreement between experimental data and model predictions, as indicated by high $R^2$ values.

To further evaluate the suitability of different analytical descriptions for frequency-dependent attenuation, multiple regression models were applied to the experimental data. The equations and curves fitting for all the models are available in section B.2. The results are of the goodness of fit coefficient are presented in figure 71.

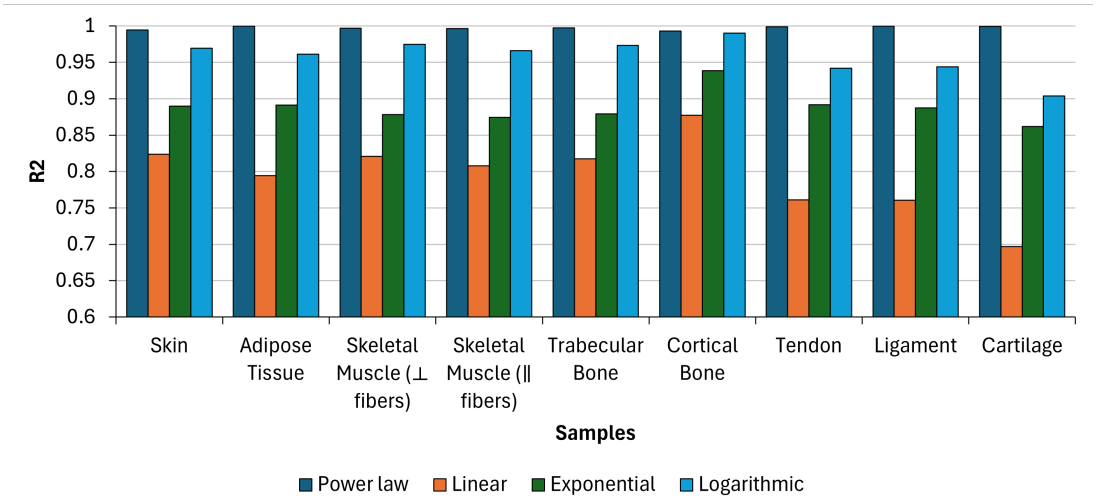



Figure 71: Comparison of regression model performance ($R^2$) for power-law, linear, exponential, and logarithmic fits across different biological tissues, highlighting the superior agreement of the power-law formulation.[46].

The results clearly indicate that the power-law model provides the best overall fit to the experimental attenuation data across all investigated tissues, consistently achieving $R^2$ values approaching unity. This confirms its ability to accurately capture the frequency-dependent behavior of acoustic attenuation in both soft and hard tissues. In contrast, linear models systematically exhibit lower $R^2$ values, reflecting their inability to represent the nonlinear scaling observed in the data, particularly at higher frequencies. Exponential and logarithmic models show intermediate performance, with reasonable fits in certain cases but lacking consistency across all tissue types. The discrepancy between models is more

pronounced in structurally complex tissues, such as bone and anisotropic muscle, where attenuation mechanisms are governed by multiscale interactions.

As such, the $\delta$ of biological tissues can be explained by a power-law formulation, according to equation 218

$$\delta(f) = \delta_0 f^n \tag{218}$$

where $\delta(f)$ is the sound diffusivity at frequency $f$, $\delta_0$ is the reference diffusivity constant at $f = 1$ MHz, and $n$ is the frequency exponent. The suggested parameters for each sample can be found in table 13.

Table 13: Power-law regression parameters for sound diffusivity $\delta(f) = \delta_0 f^n$ in biological tissues.

| **Sample** | $\delta_0$ **(**$m^2/s$**)** | **n** | $\mathbf{R}^2$ |
|---|---|---|---|
| Skin | 0.0026 | −0.934 | 0.9908 |
| Adipose Tissue | 0.0012 | −0.608 | 1 |
| Skeletal Muscle (⊥ fibers) | 0.0024 | −0.349 | 0.9980 |
| Skeletal Muscle (∥ fibers) | 0.0068 | −0.379 | 0.9862 |
| Tendon | 0.0168 | −0.801 | 0.999 |
| Ligament | 0.0038 | −0.758 | 0.999 |
| Cartilage | 0.0261 | −1.654 | 0.941 |
| Trabecular Bone | 0.0126 | −0.364 | 0.9955 |
| Cortical Bone | 0.0837 | −1.094 | 0.9965 |

## 4.4 Discussion

The discussion presented in this section aims to interpret the experimental and computational findings within a unified physical framework, linking measured acoustic properties to the underlying mechanisms governing ultrasound propagation in biological tissues. Rather than treating each parameter in isolation, the analysis integrates density, speed of sound, attenuation, nonlinearity, and sound diffusivity to provide a coherent understanding of how tissue composition, structure, and heterogeneity influence wave behaviour. Particular emphasis is placed on assessing the validity and limitations of the proposed modeling approaches, especially the use of power-law formulations and diffusivity-based representations, in capturing frequency-dependent attenuation and energy dissipation. By critically comparing the obtained results with established literature and theoretical expectations, this section seeks to identify both consistent trends and deviations, highlighting the role of anisotropy, poroelasticity, and microstructural complexity.

### 4.4.1 Experimental Acoustic Parameters Discussion

The experimental characterization of density, speed of sound, acoustic attenuation coefficient, and nonlinearity parameter B/A served to understand if the signals being measured are consistent with the literature, validating the reliability of the adopted measurement methodology. These parameters, although often treated independently in the literature, are intrinsically coupled through the governing equations of acoustic wave propagation, collectively defining impedance, energy transmission, dissipation, and nonlinear distortion. Their joint interpretation therefore enables a more complete description of wave–tissue interaction.

The measured density values exhibit a clear separation between soft and hard tissues, reflecting their fundamental compositional differences. The generally low standard deviation values observed across most tissues suggest good repeatability and reliability in both sample preparation and measurement procedures. In contrast, the greater variability identified in trabecular and cortical bone is most plausibly associated with their inherent microstructural heterogeneity, as well as variations in porosity and marrow distribution.

The experimentally obtained densities for hydrated ex vivo tissues were benchmarked against recently reported values for human, porcine, and bovine samples. Overall, a strong agreement was observed between the measured results and those documented in the literature for hydrated biological media. For instance, the density measured for skin (1.07 g/cm$^3$) is slightly lower than the reference value of 1.10 g/cm$^3$[55]. Adipose tissue, which is characteristically low in density due to its lipid-rich composition, yielded

a value of approximately 0.92 g/cm$^3$, closely matching the commonly reported 0.90 g/cm$^3$[56]. Similarly, skeletal muscle (1.05 g/cm$^3$) aligns well with typical literature values around 1.06 g/cm$^3$[57,58]. Collagen-rich connective tissues such as tendon and ligament showed relatively high densities (1.22 and 1.19 g/cm$^3$, respectively), which are consistent with reported tendon values around 1.12 g/cm$^3$[59], although ligament-specific data are less frequently reported. Cartilage density (1.17 g/cm$^3$) is also in line with previously published values (1.15 g/cm$^3$)[60]. Cortical bone exhibited high density (1.93 g/cm$^3$), consistent with the reported range of 1.9–2.0 g/cm$^3$ for human bone[61]. In contrast, trabecular bone presented a substantially lower apparent density (0.72 g/cm$^3$), which can be attributed to its porous structure. However, this value is higher than the 0.09–0.35 g/cm$^3$ range often reported for vertebral trabecular bone[62], suggesting that the analysed samples may have had reduced porosity or retained marrow content.

Taken together, the measured densities fall within approximately 5–10% of literature values, indicating a high degree of consistency and supporting the reliability of the experimental methodology.

Cortical bone presented the highest speed of sound, with an average value of (3193.95 $\pm$ 113.28 m/s), followed by trabecular bone at (2325.38 $\pm$ 172.80 m/s). These elevated values are consistent with the high stiffness and density characteristic of osseous tissues, while the larger variability observed in trabecular bone reflects its porous structure and microstructural heterogeneity. In contrast, soft tissues exhibited speeds of sound within a narrower range, approximately between 1460 and 1660 m/s. Higher values were recorded for skin (1654.93 $\pm$ 32.82 m/s), tendon (1827.43 $\pm$ 29.43 m/s), and ligament (1663.68 $\pm$ 42.29 m/s), whereas adipose tissue showed the lowest value (1461.77 $\pm$ 26.11 m/s), consistent with its lower stiffness and higher lipid content. Skeletal muscle demonstrated clear anisotropic behavior, with wave propagation occurring faster along the fibre direction (1598.68 $\pm$ 34.34 m/s) than perpendicular to it (1562.18 $\pm$ 20.76 m/s). Cartilage showed moderately elevated values (1650.80 $\pm$ 51.95 m/s).

A comparison with previously reported data indicates strong agreement between the measured values and established references. Skin exhibited a speed of sound close to 1655 m/s, consistent with reported values for dermal layers[63]. Adipose tissue measurements (1460 m/s) closely matched typical values around 1450 m/s[64]. Skeletal muscle results ($\perp$=1560 m/s and $\parallel$=1600 m/s) align with literature ranges, although many references do not explicitly account for anisotropy and report broader intervals (1430–1579 m/s)[64]. Tendon and ligament exhibited relatively high propagation speeds (1830 m/s and 1660 m/s), consistent with their collagen-rich structure, although ligament data remain less well documented[65]. Cartilage (1650 m/s) showed a slight increase compared to previously reported values (1627 m/s)[66]. Bone tissues displayed the greatest variability, with cortical bone (3200 m/s)

consistent with reported values near 3400 m/s, while trabecular bone (2325 m/s) fell within the wide range described in the literature (approximately 1500–2900 m/s), depending on porosity and density[65].

The acoustic attenuation coefficient results reveal a strong and predictable dependence on frequency, well described by a power-law relationship across all tissue types. This behavior confirms that attenuation mechanisms in biological tissues are inherently governed by distributed relaxation processes rather than discrete phenomena. Soft tissues exhibit relatively low attenuation and near-linear frequency dependence, reflecting their highly hydrated and viscoelastic nature, whereas fibrous and mineralized tissues show significantly higher attenuation due to increased scattering and internal friction. The anisotropic attenuation observed in skeletal muscle further emphasizes the role of microstructural alignment in modulating energy dissipation. Importantly, the high coefficient of determination obtained for the power-law fits indicates that attenuation can be reliably parameterized across the investigated frequency range, providing a robust basis for both analytical modelling and numerical simulation. This reinforces the concept that, despite biological complexity, acoustic attenuation follows a structured and predictable behavior that can be exploited for both diagnostic and therapeutic applications.

Soft tissues, including skin, adipose tissue and ligament exhibited relatively low attenuation coefficients at 1 MHz ($\alpha_0$ typically below 1.5 dB/cm), with frequency exponents generally ranging between 1.0 and 1.3. This behavior is consistent with previously reported data and reflects the highly hydrated and viscoelastic nature of these tissues, where attenuation tends to scale approximately linearly with frequency. In contrast, skeletal muscle showed pronounced anisotropic behavior. When acoustic waves propagated along the fibre direction, both $\alpha_0$ and the frequency exponent $n$ were higher ($\alpha_0$=2.87 dB/cm, $n$=1.46) compared to propagation perpendicular to the fibres ($\alpha_0$=1.15 dB/cm, $n$=1.56). These elevated $n$ values in both orientations suggest a more complex viscoelastic response, while the directional differences emphasize the influence of structural anisotropy on attenuation.

Higher attenuation levels were observed in cortical bone, tendon and cartilage. Cartilage displayed a relatively strong baseline attenuation ($\alpha_0$=4.34 dB/cm) combined with a modest frequency dependence ($n$=0.96), consistent with its semi-rigid, load-bearing matrix. Cortical bone and tendon, on the other hand, exhibited both elevated $\alpha_0$ values (4.62 and 6.78 dB/cm, respectively) and more pronounced frequency dependence ($n$=1.12 and 1.41), indicating that attenuation in these tissues is strongly influenced by their dense, fibrous structures and collagen organization. Trabecular bone, although less dense than cortical bone, also showed significant attenuation ($\alpha_0$=1.78 dB/cm, $n$=1.52), accompanied by higher variability, which can be attributed to its porous and heterogeneous architecture.

The high coefficients of determination ($R^2$>0.996 in nearly all cases) confirm that the fitted power-law

parameters provide a reliable representation of the attenuation behavior across tissues. Slightly lower $R^2$ values observed ligament (0.9960) may be attributed to biological variability or experimental noise but remain well within acceptable limits for modeling purposes.

Comparison with existing literature further supports the validity of the obtained results. Most soft tissues are known to follow an approximately linear frequency dependence ($n \approx 1$), with $\alpha_0$ values typically between 0.5 and 1 dB/cm[67,68], which is consistent with the present measurements for tissues such as muscle and kidney. Skeletal muscle, in particular, has been reported to exhibit anisotropic attenuation, with lower values perpendicular to fibres (1.1 dB/cm/MHz) and higher values parallel to fibres (2.9 dB/cm/MHz)[69], closely matching the experimental observations ($\perp$= 1.15 dB/cm, $\|$=2.87 dB/cm).

In contrast, connective tissues exhibit substantially higher attenuation. Tendon and ligament, which are rich in collagen[70], typically show $\alpha_0$ values on the order of 4–5 dB/cm/MHz, significantly exceeding those of softer tissues[67,68]. Cartilage has also been reported to present relatively high attenuation ($\alpha_0 \approx$ 4.0 dB/cm/MHz)[71], consistent with the experimental results. Bone tissues display the most extreme behavior, with reported broadband attenuation values ranging widely for trabecular bone (1–61 dB/cm/MHz) and reaching approximately 5–12 dB/cm/MHz for cortical bone[72]. These values are substantially higher than the Food and Drug Administration reference of 0.3 dB/cm/MHz and reflect the strong influence of scattering and absorption mechanisms in mineralized structures[73].

Overall, the measured attenuation characteristics are in close agreement with literature data. Soft tissues such as skin and adipose tissue, around $\alpha_0 \approx$ 0.5–1.0 dB/cm with $n \approx 1$, while collagen-rich tissues and bone exhibit significantly higher attenuation levels. The observed deviations can be primarily attributed to anisotropy, as in muscle, and to structural heterogeneity, particularly in trabecular bone. Nevertheless, no significant systematic discrepancies were identified.

The nonlinearity parameter B/A introduces an additional dimension to the characterization by capturing the deviation from linear acoustic behavior. Soft tissues, including skin, tendon and ligament, exhibited B/A values generally clustered between 7.0 and 7.5, with relatively low standard deviations, indicating stable and reproducible measurements. Adipose tissue deviated from this trend, presenting a higher value ($10.75 \pm 1.46$), which can be attributed to its lipid-rich and highly compressible structure, known to enhance nonlinear acoustic behavior. Slightly elevated B/A values were also observed in cartilage and skeletal muscle along the fibre direction (8.12 and 7.61, respectively), reflecting the influence of fibrous architecture and anisotropic mechanical properties. In contrast, trabecular bone showed a significantly higher nonlinearity parameter ($80.58 \pm 21.03$), consistent with its porous

structure and pronounced nonlinear elastic response under acoustic excitation. Cortical bone, while still exhibiting greater nonlinearity than soft tissues, presented a comparatively lower B/A value (12.95 $\pm$ 1.90), which is likely associated with its denser and more uniform structure. The larger variability observed in trabecular bone is indicative of its inherent microstructural heterogeneity.

A comparison with published data reveals strong agreement with established trends. Most soft tissues, including muscle tendon and ligament typically exhibit B/A values in the range of approximately 6.5 to 7.5, consistent with widely reported values around 7 for non-fatty biological tissues[74,75]. The higher value measured for adipose tissue aligns with literature reports indicating B/A values between approximately 9.6 and 11, making it one of the most nonlinear soft tissues[45,75]. In skeletal muscle, the measured anisotropy ($\|$=7.61 and $\perp$=6.63) contrasts with many literature sources that report a single isotropic value near 7[75]; however, this discrepancy is plausible given the known mechanical anisotropy of muscle tissue[53,76]. The slightly higher value along the fibre direction may be associated with structural alignment effects, although such directional distinctions are rarely explored in previous studies.

Bone tissues exhibited substantially higher nonlinearity parameters compared to soft tissues. While direct literature values for B/A in bone are scarce, the elevated values measured for both trabecular and cortical bone are consistent with expectations based on their high stiffness and complex hierarchical structure[61,77,78]. The particularly high value observed in trabecular bone, along with its large standard deviation, likely reflects the influence of porosity and marrow content, which introduce significant variability in local mechanical response[79]. Cartilage showed a moderate increase in B/A (8.12) relative to soft tissues, consistent with its collagen–proteoglycan matrix and semi-rigid behavior[80], although direct literature comparisons remain limited. Tendon and ligament, despite their dense collagen composition[81], exhibited B/A values similar to other soft tissues, likely due to their low lipid content and more uniform structural organization[82].

Overall, the distribution of B/A values across tissues reflects their structural composition and mechanical behavior, demonstrating good agreement with existing literature and reinforcing the reliability of the experimental approach. These findings highlight the importance of incorporating nonlinear parameters in acoustic modeling, particularly for applications involving high-intensity ultrasound, where effects such as harmonic generation, waveform distortion, and nonlinear energy deposition play a critical role in accurately predicting tissue response.

The observed trends highlight the importance of accounting for tissue-specific properties, including anisotropy, heterogeneity, and composition, when modelling ultrasound propagation. Simplified assumptions, such as isotropy or linearity, may be sufficient for preliminary analyses but fail to capture

the full complexity of wave–tissue interactions, particularly in applications requiring high accuracy. Ultimately, this comprehensive characterization establishes a robust experimental basis for linking measurable acoustic properties to underlying physical mechanisms, enabling more accurate and predictive modelling of ultrasound propagation in biological systems.

### 4.4.2 Sound Diffusivity Regression Discussion

The present results address a critical gap in biomedical acoustics, namely the absence of experimentally informed diffusivity parameters, by establishing a consistent relationship between measured attenuation and inferred diffusivity.

The obtained results confirm a clear decrease in sound diffusivity ($\delta$) with increasing frequency, in agreement with theoretical expectations for frequency-dependent attenuation mechanisms. Soft tissues such as skin and adipose tissue consistently exhibited low diffusivity values, generally below 0.005 $m^2/s$, alongside excellent regression performance ($R^2$>0.995). This behavior supports the validity of the power-law formulation for these media and suggests a predominantly homogeneous acoustic response, where viscoelastic damping governs attenuation and scattering effects remain limited. Skeletal muscle follows a comparable trend, although slight variations in $\delta$ are observed depending on fibre orientation. Both parallel and perpendicular propagation directions display well-defined frequency-dependent behavior with high fitting accuracy ($R^2$>0.99), indicating that despite its anisotropic structure, muscle can still be effectively described within a power-law framework. Tissues with more complex internal organization, such as tendon, and ligament, show moderately higher diffusivity values, particularly at lower frequencies. This increase can be attributed to their fibrous composition and structural heterogeneity, which introduce additional dissipation mechanisms, including microstructural interactions and scattering. Nevertheless, the power-law model continues to provide an accurate representation of their behavior, with regression coefficients remaining above 0.99. In contrast, cartilage demonstrates elevated diffusivity at lower frequencies (The highest value for soft tissues) and slightly reduced fitting accuracy compared to other soft tissues. This behavior is likely linked to its biphasic composition, where fluid–solid interactions and nonlinear viscoelastic effects introduce deviations from idealized power-law behavior. Despite this, the model maintains acceptable predictive capability ($R^2$>0.98), confirming its robustness as an approximation.

In contrast, bone tissues exhibit significantly higher diffusivity, especially at lower frequencies, as observed in trabecular and cortical bone. This reflects the combined influence of mineral content, porosity, and complex wave interactions within their hierarchical structure. A slight reduction in fitting accuracy is

observed at higher frequencies (4–5 MHz), indicating increased difficulty in capturing steep attenuation gradients in highly dissipative media. These discrepancies are not solely physical but also numerical in nature. Standard simulation settings, including typical CFL conditions, proved insufficient in some cases, leading to instability in the form of non-physical pressure amplification. Improved stability was achieved by refining time-stepping conditions and employing higher-order integration schemes, highlighting the importance of solver selection and discretization strategy when modeling wave propagation in highly attenuating materials.

From a physical standpoint, the variation of $\delta$ across tissue types reveals distinct propagation regimes depending on the microstructure of the medium. Adipose tissue, a fluid-rich and structurally homogeneous tissues, such exhibits low diffusivity values and highly stable regression behavior, indicating that acoustic attenuation is predominantly governed by viscoelastic damping with minimal contribution from scattering effects. In contrast, structurally organized soft tissues, including skeletal muscle and ligament display moderately increased diffusivity values, reflecting the combined influence of viscoelastic dissipation, anisotropic architecture, and microstructural heterogeneity. Although diffusivity is treated as a scalar parameter in the present formulation, these results suggest that it implicitly captures directional dependencies, raising important questions regarding its potential tensorial nature in anisotropic media. At the upper end of the spectrum, highly heterogeneous and mineralized tissues such as trabecular and cortical bone, as well as cartilage, exhibit significantly elevated diffusivity values, particularly at lower frequencies. This behavior is consistent with the presence of strong scattering phenomena, impedance mismatches, and complex internal interfaces, which enhance energy redistribution and loss. However, a slight reduction in regression quality at higher frequencies in these tissues highlights both the increased complexity of their attenuation mechanisms and the numerical challenges associated with resolving steep dissipation gradients in highly lossy media.

The observed decrease of diffusivity with frequency provides further insight into the underlying physics of wave–tissue interaction. As frequency increases and wavelength decreases, acoustic waves become more sensitive to local microstructural features, leading to rapid energy absorption and scattering before significant spatial diffusion can occur. In this sense, diffusivity can be interpreted as a measure of the wave's ability to spatially redistribute energy, which diminishes at higher frequencies as dissipation becomes increasingly localized. This interpretation reinforces the suitability of power-law models for describing biological attenuation, as they inherently capture the multiscale and distributed nature of tissue relaxation processes. The stability of parameter estimation across all cases, with $R^2$ values consistently exceeding $0.98$, further confirms the robustness of the inverse modelling approach

used to derive diffusivity from experimental attenuation data. This consistency reinforces the reliability of the proposed computational framework. From a modelling perspective, the sound diffusivity approach offers a significant advantage by providing an effective parameter that encapsulates multiple attenuation mechanisms without requiring explicit decomposition into viscous, thermal, and scattering contributions. As demonstrated, diffusivity-based models achieve superior agreement with experimental data compared to linear formulations, particularly in reproducing both time-domain waveforms and frequency-domain spectral decay, while maintaining a more favourable computational cost relative to fully viscous models.

Despite these strengths, several limitations must be acknowledged. The estimation of $\delta$ relies on inverse modeling techniques, introducing a degree of dependency on the chosen simulation framework and optimization strategy. Furthermore, while the power-law formulation provides an excellent approximation for most tissues, deviations observed in cartilage and brain suggest that additional mechanisms, such as poroelasticity, fluid–solid coupling, or frequency-dependent anisotropy, may need to be incorporated for a more comprehensive description. The scalar nature of diffusivity also limits its ability to explicitly represent anisotropic propagation, particularly in fibrous tissues such as muscle and tendon. Finally, numerical considerations, including mesh resolution and stability constraints, play a critical role in accurately capturing wave behavior in highly attenuating media, emphasizing that the fidelity of the model is intrinsically linked to both physical and computational factors.

From an applied perspective, the characterization of sound diffusivity has direct implications for the design and optimization of ultrasound-based therapeutic systems. By providing a quantitative measure of how acoustic energy disperses within biological tissues, $\delta$ enables the prediction of penetration depth, spatial pressure distribution, and frequency-dependent energy deposition. This is particularly relevant in the context of mechanobiological stimulation, where controlled delivery of acoustic energy at the cellular level is required. In this sense, frequency selection becomes a tool not only for modulating attenuation, but for shaping the spatial distribution of mechanical stimuli through the manipulation of diffusivity. Ultimately, sound diffusivity emerges as a unifying parameter that bridges experimental observation and computational modelling, offering a robust and physically meaningful framework for describing acoustic wave propagation in complex biological media and supporting the development of more precise, predictable, and physiologically relevant therapeutic ultrasound applications.

Finally, it is important to note that, to the best of current knowledge, direct experimental characterization of sound diffusivity in biological tissues remains largely unexplored. While attenuation and wave speed have been extensively studied, the explicit quantification of diffusivity and its frequency dependence has not been previously reported in a comprehensive manner. As such, the present results

contribute a novel perspective to the field, providing new parameters that can support more accurate modeling of acoustic wave propagation and inform the development of advanced diagnostic and therapeutic ultrasound technologies.

### 4.4.3 General Discussion

The suggested modelling approaches demonstrated high predictive accuracy ($R^2$>0.99) when compared to conventional linear formulations, providing a significantly improved representation of experimental waveforms in both time and frequency domains. Although the inclusion of nonlinear effects and frequency-dependent losses increases computational cost, this is offset by a clear gain in model fidelity.

Sound diffusivity offers a macroscopic description of energy spreading, effectively capturing the cumulative effects of absorption and scattering, particularly in structurally complex or heterogeneous tissues. Cortical bone exhibited markedly distinct behavior compared to other tissues, reflecting its dense, highly mineralized structure and low porosity. These features result in elevated acoustic impedance, higher propagation speeds, and increased resistance to deformation. Unlike soft tissues, where attenuation is largely governed by viscous and fluid-mediated mechanisms, energy dissipation in bone is dominated by scattering at mineral interfaces and intrinsic absorption within the rigid matrix. Its organized microstructure and reduced fluid content further limit relaxation processes, explaining why its acoustic properties fall well outside the range observed in softer, hydrated tissues.

Future work should extend the analysis beyond the current frequency range (0.5–5 MHz) to improve model generality and physical insight. Higher frequencies would allow investigation of microstructural interactions and localized scattering phenomena, while intermediate ranges could help identify transitions between dominant attenuation mechanisms. Expanding the spectral domain would enhance parameter robustness and improve the predictive capability of the models across different biomedical contexts.

This work establishes a comprehensive framework for characterizing acoustic attenuation by integrating phenomenological and mechanistic approaches. The results emphasize the importance of adopting tissue-specific models that account for structural, viscoelastic, and nonlinear properties. By combining diffusivity-based descriptions with viscous modeling, a more complete understanding of ultrasound–tissue interaction is achieved, providing a solid foundation for the development of accurate simulation tools and advanced therapeutic technologies.

## 4.5 Conclusion

This work presents a computational framework for analysing ultrasonic attenuation in biological tissues by combining experimental characterization with model-based parameter estimation. The measured acoustic properties, including speed of sound, attenuation, and nonlinearity, showed good agreement with literature values, supporting the reliability of the experimental methodology. The results demonstrate that power-law formulations provide an accurate representation of frequency-dependent behavior, with strong predictive performance across most tissues. The sound diffusivity model demonstrated great agreement with experimental data ($R^2$>0.99 for most tissues) in the frequency domain, and although it outperformed linear formulations, it severely increased computational cost. Future developments should focus on extending the frequency range of analysis and incorporating additional mechanisms, such as anisotropy and poroelastic effects, to improve model fidelity. Validation under in vivo conditions remains a key step toward practical application, along with the integration of these models into clinical ultrasound systems for real-time parameter estimation. Overall, this work establishes a robust basis for more accurate and physiologically relevant acoustic modeling, with direct implications for the design and optimization of ultrasound-based therapeutic technologies.

## 4.6 Bibliography

[1]D. L. Miller, A. Abo, J. S. Abramowicz, T. A. Bigelow, D. Dalecki, E. Dickman, J. Donlon, G. Harris, and J. Nomura, "Diagnostic Ultrasound Safety Review for Point-of-Care Ultrasound Practitioners", J. Ultrasound Med. **39**, 1069–1084 (2020) 10.1002/jum.15202.

[2]R. A. Phillips, M. E. Stratmeyer, and G. R. Harris, "Safety and U.S. Regulatory Considerations in the Nonclinical Use of Medical Ultrasound Devices", Ultrasound Med. Biol. **36**, 1224–1228 (2010) 10.1016/j.ultrasmedbio.2010.03.020.

[3]R. A. Ungur, V. M. Ciortea, L. Irsay, A. D. Ciubean, B. A. N□sui, R. A. Codea, V. E. Singurean, O. B. Groza, S. C□inap, G. S. Marti□ (Petru□), C. Borda, and I. M. Borda, "Can Ultrasound Therapy Be an Environmental-Friendly Alternative to Non-Steroidal Anti-Inflammatory Drugs in Knee Osteoarthritis Treatment?", Materials **14**, 2715 (2021) 10.3390/ma14112715.

[4]X. Li, Y. Lin, P. He, and Q. Wang, "Efficacy and safety of low-intensity ultrasound therapy for myofascial pain syndrome: a systematic review and meta-analysis", BMC Musculoskelet. Disord. **25** (2024) 10.1186/s12891-024-08174-7.

[5]C. Papadacci, E. A. Bunting, and E. E. Konofagou, "3D Quasi-Static Ultrasound Elastography With Plane Wave In Vivo", IEEE Trans. Med. Imaging **36**, 357–365 (2017) 10.1109/tmi.2016.2596706.

[6]H. Qin, L. Du, Z. Luo, Z. He, Q. Wang, S. Chen, and Y.-L. Zhu, "The therapeutic effects of low-intensity pulsed ultrasound in musculoskeletal soft tissue injuries: Focusing on the molecular mechanism", Front. Bioeng. Biotechnol. **10**, 1080430 (2022) 10.3389/fbioe.2022.1080430.

[7]J.-y. Gao and C. Hou, "Progresses and clinical application of super-resolution ultrasound imaging: a narrative review", Ultrasound J. **17**, 29 (2025) 10.1186/s13089-025-00432-6.

[8]R. Seddiki, T. Mirault, J. Sitruk, N. Mohamedi, E. Messas, M. Pernot, J. Baranger, and G. Goudot, "Advancements in Noncontrast Ultrasound Imaging for Low-Velocity Flow: A Technical Review and Clinical Applications in Vascular Medicine", Ultrasound Med. Biol. **51**, 1035–1042 (2025) 10.1016/j.ultrasmedbio.2025.03.001.

[9]G. Mushtaq and K. Veningston, "A comprehensive review on fetal health surveillance using ultrasound imagery", Discov. Appl. Sci. **7**, 478 (2025) 10.1007/s42452-025-06644-8.

[10]H. Boumeridja, M. Ammar, M. Alzubaidi, S. Mahmoudi, L. N. Benamer, M. Agus, M. Househ, K. Lekadir, and M. El Habib Daho, "Enhancing fetal ultrasound image quality and anatomical plane recognition in low-resource settings using super-resolution models", Sci. Rep. **15**, 8376 (2025) 10.1038/s41598-025-91808-0.

[11]P. S. Sidhu, C. Ewertsen, M. Piskunowicz, M. Secil, P. Ricci, T. Fischer, D. Gaitini, V. Mitkov, A. K. P. Lim, Q. Lu, W. K. Chong, and D. A. Clevert, "Diversity of current ultrasound practice within and outside radiology departments with a vision for 20 years into the future: a position paper of the ESR ultrasound subcommittee", Insights Imaging **14**, 202 (2023) 10.1186/s13244-023-01548-w.

[12]M. A. O'Reilly, "Exploiting the mechanical effects of ultrasound for noninvasive therapy", Science **385**, eadp7206 (2024) 10.1126/science.adp7206.

[13]A. Singh and J. N. J. Reynolds, "Therapeutic ultrasound: an innovative approach for targeting neurological disorders affecting the basal ganglia", Front. Neuroanat. **18**, 1469250 (2024) 10.3389/fnana.2024.1469250.

[14]Z. Lin, L. Gao, N. Hou, X. Zhi, Y. Zhang, Z. Che, and A. Deng, "Application of low-intensity pulsed ultrasound on tissue resident stem cells: Potential for ophthalmic diseases", Front. Endocrinol. **14**, 1153793 (2023) 10.3389/fendo.2023.1153793.

[15]N. Fernandes, F. S. Silva, Ó. Carvalho, and A. Leal, "Effect of lower limb orthoses on cartilage in patients with knee osteoarthritis: A narrative review", **47** (2022).

[16]N. A. T. C. Fernandes, A. Arieira, B. Hinckel, F. S. Silva, Ó. Carvalho, and A. Leal, "Unlocking the Secrets of Knee Joint Unloading: A Systematic Review and Biomechanical Study of the Invasive and Non-Invasive Methods and Their Influence on Knee Joint Loading", Rheumato **5**, 8 (2025) 10.3390/rheumato5030008.

[17]S. Oliveira, R. Andrade, C. Valente, J. Espregueira-Mendes, F. Silva, B. B. Hinckel, Ó. Carvalho, and A. Leal, "Mechanical-based therapies may reduce pain and disability in some patients with knee osteoarthritis: A systematic review with meta-analysis", The Knee **37**, 28–46 (2022) 10.1016/j.knee.2022.05.005.

[18]S. Oliveira, R. Andrade, F. Silva, J. Espregueira-Mendes, B. Hinckel, A. Leal, and Ó. Carvalho, "Effects and mechanotransduction pathways of therapeutic ultrasound on healthy and osteoarthritic chondrocytes: a systematic review of in vitro studies", Osteoarthritis Cartilage **31**, 317–339 (2023) 10.1016/j.joca.2022.07.014.

[19]M. Beeckmans, P. Huycke, T. Verguts, and P. Verbeke, "How much data do we need to estimate computational models of decision-making? The COMPASS toolbox", Behav. Res. Methods **56**, 2537–2548 (2023) 10.3758/s13428-023-02165-7.

[20]A.-A. Arifin, B. B. S M, and K. M. Asif Ashrafi, "Development of Less Computational Costly Ultrasound Imaging Using the Finite Element Method", Int. J. Eng. Trends Technol. **72**, 299–312 (2024) 10.14445/22315381/ijett-v72i5p131.

[21]R. L. Winslow, N. Trayanova, D. Geman, and M. I. Miller, "Computational Medicine: Translating Models to Clinical Care", Sci. Transl. Med. **4** (2012) 10.1126/scitranslmed.3003528.

[22]R. Luqmani, E. Lee, and S. Singh, "The Role of Ultrasound Compared to Biopsy of Temporal Arteries in the Diagnosis and Treatment of Giant Cell Arteritis (TABUL): a diagnostic accuracy and cost-effectiveness study.", in *Cost-effectiveness analysis* (NIHR Journals Library, Southampton (UK), Nov. 2016), Chapter 7.

[23]B. R. Chintada, R. Rau, and O. Goksel, "Nonlinear Characterization of Tissue Viscoelasticity with Acoustoelastic Attenuation of Shear-Waves", version 1, IEEE Trans. Ultrason. Ferroelectr. Freq. Control (2021) 10.48550/ARXIV.2002.12908.

[24]N. Jiménez, F. Camarena, J. Redondo, V. Sánchez-Morcillo, Y. Hou, and E. E. Konofagou, "Time-domain simulation of ultrasound propagation in a tissue-like medium based on the resolution of the nonlinear acoustic constitutive relations", version 1, Acta Acust. United Acust. (2016) 10.48550/ARXIV.1507.00319.

[25]S. Acosta, J. Chan, R. Johnson, and B. Palacios, *Pseudodifferential Models for Ultrasound Waves with Fractional Attenuation*, version 2, (2023) 10.48550/ARXIV.2312.09080, https://arxiv.org/abs/2312.09080 (visited on 08/10/2025), pre-published.

[26]F. C. Meral, T. J. Royston, and R. L. Magin, "Fractional Order Models for Viscoelasticity of Soft Biological Tissues", in Vol. 2 Biomed. Biotechnol. Eng. (Jan. 1, 2008), pp. 721–722, 10.1115/IMECE2008-68137.

[27]A. Gomez, G. Rus, and N. Saffari, "Wave Propagation in a Fractional Viscoelastic Tissue Model: Application to Transluminal Procedures", Sensors **21**, 2778 (2021) 10.3390/s21082778.

[28]A. Gomez, A. Callejas, G. Rus, and N. Saffari, "Experimental evidence of shear waves in fractional viscoelastic rheological models", Sci. Rep. **12**, 7448 (2022) 10.1038/s41598-022-11490-4.

[29]S. Holm and S. P. Näsholm, "Comparison of Fractional Wave Equations for Power Law Attenuation in Ultrasound and Elastography", Ultrasound Med. Biol. **40**, 695–703 (2014) 10.1016/j.ultrasmedbio.2013.09.033.

[30]F. Meral, T. Royston, and R. Magin, "Fractional calculus in viscoelasticity: An experimental study", Commun. Nonlinear Sci. Numer. Simul. **15**, 939–945 (2010) 10.1016/j.cnsns.2009.05.004.

[31]Y. Kobayashi, N. Okamura, M. Tsukune, M. G. Fujie, and M. Tanaka, "Non-minimum phase viscoelastic properties of soft biological tissues", version 2, (2018) 10.48550/ARXIV.1804.00979.

[32]B. Qiang, J. C. Brigham, S. Aristizabal, J. F. Greenleaf, X. Zhang, and M. W. Urban, "Modeling transversely isotropic, viscoelastic, incompressible tissue-like materials with application in ultrasound shear wave elastography", Phys. Med. Biol. **60**, 1289–1306 (2015) 10.1088/0031-9155/60/3/1289.

[33]S. F. Levinson, "Ultrasound propagation in anisotropic soft tissues: The application of linear elastic theory", J. Biomech. **20**, 251–260 (1987) 10.1016/0021-9290(87)90292-2.

[34]K. J. Parker, "Power laws prevail in medical ultrasound", version 1, (2022) 10.48550/ARXIV.2203.04239.

[35]M. Valdez and B. Balachandran, "Longitudinal nonlinear wave propagation through soft tissue", J. Mech. Behav. Biomed. Mater. **20**, 192–208 (2013) 10.1016/j.jmbbm.2013.01.002.

[36]M. Shishlenin, A. Kozelkov, and N. Novikov, "Nonlinear Medical Ultrasound Tomography: 3D Modeling of Sound Wave Propagation in Human Tissues", Mathematics **12**, 212 (2024) 10.3390/math12020212.

[37]X. Chen, X. Li, S. Turco, R. J. G. Van Sloun, and M. Mischi, "Ultrasound Viscoelastography by Acoustic Radiation Force: A State-of-the-Art Review", IEEE Trans. Ultrason. Ferroelectr. Freq. Control **71**, 536–557 (2024) 10.1109/tuffc.2024.3381529.

[38]B. R. Chintada, R. Rau, and O. Goksel, "Spectral Ultrasound Imaging of Speed-of-Sound and Attenuation Using an Acoustic Mirror", Front. Phys. **10** (2022) 10.3389/fphy.2022.860725.

[39]M. Moghimnezhad, "Multiphysics Analysis of Ultrasonic Shock Wave Lithotripsy and Side Effects on Surrounding Tissues", J. Biomed. Phys. Eng. **11** (2021) 10.31661/jbpe.v0i0.1182.

[40]Z. Gharehnazifam, R. Dolatabadi, M. Baniassadi, H. Shahsavari, A.-M. Kajbafzadeh, K. Abrinia, K. Gharehnazifam, and M. Baghani, "Multiphysics modeling and experiments on ultrasound-triggered drug delivery from silk fibroin hydrogel for Wilms tumor", Int. J. Pharm. **621**, 121787 (2022) 10.1016/j.ijpharm.2022.121787.

[41]H. Song, P. Qi, D. Peng, X. Zhang, and L. Zhu, "Propagation of ultrasound-modulated scattered light in biological tissue by using COMSOL multiphysics", in Adv. Opt. Imaging Technol. II, edited by P. S. Carney, X.-C. Yuan, K. Shi, and M. G. Somekh (Nov. 19, 2019), p. 37, 10.1117/12.2537447.

[42]V. Nikolić and B. Said-Houari, "The Westervelt–Pennes model of nonlinear thermoacoustics: Global solvability and asymptotic behavior", J. Differ. Equ. **336**, 628–653 (2022) 10.1016/j.jde.2022.07.031.

[43]M. A. El-Brawany, D. K. Nassiri, G. Terhaar, A. Shaw, I. Rivens, and K. Lozhken, "Measurement of thermal and ultrasonic properties of some biological tissues", J. Med. Eng. Technol. **33**, 249–256 (2009) 10.1080/03091900802451265.

[44]A. Benjamin, R. E. Zubajlo, M. Dhyani, A. E. Samir, K. E. Thomenius, J. R. Grajo, and B. W. Anthony, "Surgery for Obesity and Related Diseases: I. A Novel Approach to the Quantification of the Longitudinal Speed of Sound and Its Potential for Tissue Characterization", Ultrasound Med. Biol. **44**, 2739–2748 (2018) 10.1016/j.ultrasmedbio.2018.07.021.

[45]A. Panfilova, R. J. G. Van Sloun, H. Wijkstra, O. A. Sapozhnikov, and M. Mischi, "A review on *B/A* measurement methods with a clinical perspective", J. Acoust. Soc. Am. **149**, 2200–2237 (2021) 10.1121/10.0003627.

[46]N. A. T. C. Fernandes, S. Sharma, A. Arieira, B. Hinckel, F. Silva, A. Leal, and Ó. Carvalho, "Experimental Validation of Time-Explicit Ultrasound Propagation Models with Sound Diffusivity or Viscous Attenuation in Biological Tissues Using COMSOL Multiphysics", Bioengineering **12**, 946 (2025) 10.3390/bioengineering12090946.

[47]N. A. T. C. Fernandes, *Nnunofernandes/Ultrasound-Wave-Material-Characterization: First Release*, version 1.0.1, Zenodo, May 21, 2026, 10.5281/ZENODO.20334339.

[48]C. F. Njeh and C. M. Langton, "The effect of cortical endplates on ultrasound velocity through the calcaneus: an in vitro study.", Br. J. Radiol. **70**, 504–510 (1997) 10.1259/bjr.70.833.9227233.

[49]M. Eskner and R. Sandström, "Mechanical Property Evaluation Using the Small Punch Test", J. Test. Eval. **32**, 282–289 (2004) 10.1520/jte11504.

[50]T. B. Lannin, M. P. Kelly, and T. P. James, "Reciprocating Bone Saw: Effect of Blade Speed on Cutting Rate", in Vol. 3 Des. Manuf. (Jan. 1, 2011), pp. 767–771, 10.1115/imece2011-62457.

[51]E. Shakouri, P. Ghorbani, P. Pourheidari, and S. Fotuhi, "Resection of bone by sagittal saw: Investigation of effects of blade speed, feed rate, and irrigation on temperature rise", Proc. Inst. Mech. Eng. [H] **235**, 625–635 (2021) 10.1177/0954411921999482.

[52]G. R. Harris, S. M. Howard, A. M. Hurrell, P. A. Lewin, M. E. Schafer, K. A. Wear, V. Wilkens, and B. Zeqiri, "Hydrophone Measurements for Biomedical Ultrasound Applications: A Review", IEEE Trans. Ultrason. Ferroelectr. Freq. Control **70**, 85–100 (2023) 10.1109/TUFFC.2022.3213185.

[53]N. A. T. C. Fernandes, D. I. Alves, D. P. Ferreira, M. Monteiro, A. Arieira, F. Silva, B. Hinckel, A. Leal, and Ó. Carvalho, "Sustainable Tunable Anisotropic Ultrasound Medical Phantoms for Skin, Skeletal Muscle, and Other Fibrous Biological Tissues Using Natural Fibers and a Bio-Elastomeric Matrix", J. Compos. Sci. **9**, 370 (2025) 10.3390/jcs9070370.

[54]Comsol, *Comsol - Acoustics Module* ().

[55]S. Seltzer, *Stopping-Powers and Range Tables for Electrons, Protons, and Helium Ions, NIST Standard Reference Database 124* (National Institute of Standards and Technology, 1993), 10.18434/T4NC7P.

[56]T. A. M. Harrington, E. L. Thomas, G. Frost, N. Modi, and J. D. Bell, "Distribution of Adipose Tissue in the Newborn", Pediatr. Res. **55**, 437–441 (2004) 10.1203/01.pdr.0000111202.29433.2d.

[57]S. R. Ward and R. L. Lieber, "Density and hydration of fresh and fixed human skeletal muscle", J. Biomech. **38**, 2317–2320 (2005) 10.1016/j.jbiomech.2004.10.001.

[58]K. C. Leonard, N. Worden, M. L. Boettcher, E. Dickinson, K. M. Omstead, A. M. Burrows, and A. Hartstone-Rose, "Anatomical and ontogenetic influences on muscle density", Sci. Rep. **11** (2021) 10.1038/s41598-021-81489-w.

[59]E. P. Snelling, A. A. Biewener, Q. Hu, D. A. Taggart, A. Fuller, D. Mitchell, S. K. Maloney, and R. S. Seymour, "Scaling of the ankle extensor muscle-tendon units and the biomechanical implications for bipedal hopping locomotion in the post-pouch kangaroo *Macropus fuliginosus*", J. Anat. **231**, 921–930 (2017) 10.1111/joa.12715.

[60]S. Kar, D. W. Smith, B. S. Gardiner, and A. J. Grodzinsky, "Systems Based Study of the Therapeutic Potential of Small Charged Molecules for the Inhibition of IL-1 Mediated Cartilage Degradation", PLOS ONE **11**, edited by D. Heymann, e0168047 (2016) 10.1371/journal.pone.0168047.

[61]E. F. Morgan, G. U. Unnikrisnan, and A. I. Hussein, "Bone Mechanical Properties in Healthy and Diseased States", Annu. Rev. Biomed. Eng. **20**, 119–143 (2018) 10.1146/annurev-bioeng-062117-121139.

[62]C. Öhman-Mägi, O. Holub, D. Wu, R. M. Hall, and C. Persson, "Density and mechanical properties of vertebral trabecular bone—A review", JOR SPINE **4** (2021) 10.1002/jsp2.1176.

[63]C. Moran, N. Bush, and J. Bamber, "Ultrasonic propagation properties of excised human skin", Ultrasound Med. Biol. **21**, 1177–1190 (1995) 10.1016/0301-5629(95)00049-6.

[64]N. Korta Martiartu, D. Nakhostin, L. Ruby, T. Frauenfelder, M. B. Rominger, and S. J. Sanabria, "Speed of sound and shear wave speed for calf soft tissue composition and nonlinearity assessment", Quant. Imaging Med. Surg. **11**, 4149–4161 (2021) 10.21037/qims-20-1321.

[65]S. C. Wearing, S. L. Hooper, C. M. Langton, M. Keiner, T. Horstmann, N. Crevier-Denoix, and P. Pourcelot, "The Biomechanics of Musculoskeletal Tissues during Activities of Daily Living: Dynamic Assessment Using Quantitative Transmission-Mode Ultrasound Techniques", Healthcare **12**, 1254 (2024) 10.3390/healthcare12131254.

[66]J. Töyräs, M. S. Laasanen, S. Saarakkala, M. J. Lammi, J. Rieppo, J. Kurkijärvi, R. Lappalainen, and J. S. Jurvelin, "Speed of sound in normal and degenerated bovine articular cartilage", Ultrasound Med. Biol. **29**, 447–454 (2003) 10.1016/s0301-5629(02)00708-1.

[67]E. Hysi, J. Baek, A. Koven, X. He, L. Ulloa Severino, Y. Wu, K. Kek, S. Huang, A. Krizova, M. Farcas, M. Ordon, K.-H. Fok, R. Stewart, K. T. Pace, M. C. Kolios, K. J. Parker, and D. A. Yuen, "A first-in-human study of quantitative ultrasound to assess transplant kidney fibrosis", Nat. Med. **31**, 970–978 (2025) 10.1038/s41591-024-03417-5.

[68]S. L. Baldwin, K. R. Marutyan, M. Yang, K. D. Wallace, M. R. Holland, and J. G. Miller, "Estimating myocardial attenuation from M-mode ultrasonic backscatter", Ultrasound Med. Biol. **31**, 477–484 (2005) 10.1016/j.ultrasmedbio.2004.12.024.

[69]D. Nassiri, D. Nicholas, and C. Hill, "Attenuation of ultrasound in skeletal muscle", Ultrasonics **17**, 230–232 (1979) 10.1016/0041-624x(79)90054-4.

[70]M. R. Buckley, E. B. Evans, P. E. Matuszewski, Y.-L. Chen, L. N. Satchel, D. M. Elliott, L. J. Soslowsky, and G. R. Dodge, "Distributions of types I, II and III collagen by region in the human supraspinatus tendon", Connect. Tissue Res. **54**, 374–379 (2013) 10.3109/03008207.2013.847096.

[71]H. J. Nieminen, S. Saarakkala, M. S. Laasanen, J. Hirvonen, J. S. Jurvelin, and J. Töyräs, "Ultrasound attenuation in normal and spontaneously degenerated articular cartilage", Ultrasound Med. Biol. **30**, 493–500 (2004) 10.1016/j.ultrasmedbio.2003.12.007.

[72]X. Han, B. Yang, F. Zou, and J. Sun, "Clinical therapeutic efficacy of mesenchymal stem cells derived from adipose or bone marrow for knee osteoarthritis: a meta-analysis of randomized controlled trials", J. Comp. Eff. Res. **9**, 361–374 (2020) 10.2217/cer-2019-0187.

[73]*Marketing Clearance of Diagnostic Ultrasound Systems and Transducers*, Feb. 2023.

[74]C. Sehgal, G. Brown, R. Bahn, and J. Greenleaf, "Measurement and use of acoustic nonlinearity and sound speed to estimate composition of excised livers", Ultrasound Med. Biol. **12**, 865–874 (1986) 10.1016/0301-5629(86)90004-9.

[75]W. Law, L. Frizzell, and F. Dunn, "Determination of the nonlinearity parameter B/A of biological media", Ultrasound Med. Biol. **11**, 307–318 (1985) 10.1016/0301-5629(85)90130-9.

[76]N. A. Fernandes, S. Schmitt, and O. Martynenko, "Modelling and Validation of the 3D Muscle-Tendon Unit with Solid Finite Elements in LS-DYNA for Active Human Body Model Applications", in S1-8 Comput. Model. Hum. Body Models (Sept. 2019).

[77]H.-S. N. Musthafa and J. Walker, "Design of Trabecular Bone Mimicking Voronoi Lattice-Based Scaffolds and CFD Modelling of Non-Newtonian Power Law Blood Flow Behaviour", Computation **12**, 241 (2024) 10.3390/computation12120241.

[78]K. D. Hunt, V. D. O'Loughlin, D. W. Fitting, and L. Adler, "Ultrasonic determination of the elastic modulus of human cortical bone", Med. Biol. Eng. Comput. **36**, 51–56 (1998) 10.1007/bf02522857.

[79]S. Tadano and B. Giri, "X-ray diffraction as a promising tool to characterize bone nanocomposites", Sci. Technol. Adv. Mater. **12**, 064708 (2011) 10.1088/1468-6996/12/6/064708.

[80]W. J. McCarty, A. L. Pallante, R. J. Rone, W. D. Bugbee, and R. L. Sah, "The Proteoglycan Metabolism of Articular Cartilage in Joint-Scale Culture", Tissue Eng. Part A **16**, 1717–1727 (2010) 10.1089/ten.tea.2009.0663.

[81]D. M. Hudson, M. Archer, J. Rai, M. Weis, R. J. Fernandes, and D. R. Eyre, "Age-related type I collagen modifications reveal tissue-defining differences between ligament and tendon", Matrix Biol. Plus **12**, 100070 (2021) 10.1016/j.mbplus.2021.100070.

[82]A. P. Rumian, A. L. Wallace, and H. L. Birch, "Tendons and ligaments are anatomically distinct but overlap in molecular and morphological features—a comparative study in an ovine model", J. Orthop. Res. **25**, 458–464 (2007) 10.1002/jor.20218.

# Chapter 5

# Simulation of Acoustic Wave Propagation Through the Human Body

# 5.1 Introduction to Acoustic Wave Simulation in Biological Systems

The accurate simulation of acoustic wave propagation through the human body constitutes a fundamental step toward the rational design of ultrasound-based therapeutic systems. Within the present work, this problem was addressed through a hierarchical modelling strategy grounded on two complementary computational approaches, first a reduced-order 1D model enabling rapid assessment of wave transmission across layered biological media, which reseulted in a scientific publication[1,2], and after it a multiscale, patient-specific framework coupling macroscopic wave propagation in the knee joint with microscopic mechanotransductive responses at the cellular level, which is currently under peer review.

## 5.1.1 Motivation and Role in Ultrasound-Based Therapies

Acoustic wave simulation in biological systems plays a critical role in ultrasound-based therapies by enabling precise, personalized, and safe treatment planning. It allows for the prediction of how sound waves propagate, focus, and scatter through complex, heterogeneous tissues, which is essential for maximizing therapeutic outcomes while minimizing unintended damage to healthy surrounding tissue[3,4].

The increasing demand for non-invasive, targeted, and patient-specific therapeutic strategies has positioned ultrasound as one of the most promising modalities in modern biomedical engineering. Unlike conventional treatments that rely on pharmacological or surgical interventions, ultrasound offers the unique capability to mechanically stimulate deep within biological tissues in a non-invasive, controlled and spatially localized manner, without the use of ionizing radiation. This intrinsic safety profile, combined with its versatility, has driven a rapid expansion of ultrasound from a purely diagnostic tool into a multifunctional therapeutic platform applied across musculoskeletal, neurological, oncological, and regenerative medicine domains[5]. However, ultrasound as a non-invasive therapeutic modality is inseparable from a fundamental limitation: the human body is not acoustically transparent. It is a labyrinth of impedance mismatches, anisotropies, and frequency-dependent attenuation mechanisms that distort, scatter, and dissipate the applied wave before it reaches its intended target[6]. In this context, without predictive modelling, ultrasound therapy remains an illusory science, and thus simulation becomes a necessary tool to predict and engineer the intended acoustic behaviour.

Unlike homogeneous engineering materials, biological tissues exhibit strong heterogeneity across spatial scales, from layered anatomical structures (skin, fat, muscle, bone) to microstructural variations

within tissues themselves. These features lead to nonlinear interactions such as reflection, refraction, mode conversion, and frequency-dependent attenuation, which cannot be intuitively predicted or experimentally isolated in vivo. Numerical simulation provides a controlled environment in which these mechanisms can be explicitly resolved, enabling the prediction of pressure fields, energy distribution, and wave–tissue interactions under physiologically realistic conditions. Recent advances in computational acoustics highlight that full-wave and multiphysics simulations are now essential tools for capturing these complex interactions with sufficient fidelity, particularly in heterogeneous biological environments[7,8].

Simulation plays a central role in bridging the gap between externally applied acoustic energy and internal biological response. In ultrasound-based therapies, the clinically relevant quantity is not the emitted pressure at the transducer, but the effective mechanical stimulus at the target tissue and at the cellular level. However, this stimulus cannot be directly measured in vivo with sufficient spatial resolution. Computational models therefore act as a "virtual measurement system", reconstructing internal pressure fields and enabling the estimation of quantities such as local stress, strain, and energy density. This capability is particularly important in applications such as cartilage stimulation, where therapeutic efficacy depends on precise targeting and controlled mechanical stimulation[8].

From a clinical perspective, simulation is indispensable for treatment planning and personalization. The variability in human anatomy (differences in tissue thickness, composition, and geometry) can significantly alter acoustic propagation wave propagation. As a result, identical ultrasound inputs may produce substantially different internal responses across patients. Simulation-based planning allows these variations to be explicitly accounted for, enabling patient-specific optimization of parameters such as frequency, intensity, transducer position, and focusing strategy. In transcranial and neuromodulation therapies, for instance, computational models are routinely used to predict how ultrasound waves propagate through complex structures like the skull, ensuring accurate targeting while minimizing unintended exposure to surrounding tissues. This predictive capability is essential for ensuring both safety and efficacy in clinical applications[9].

Beyond planning, simulation also serves as a powerful tool for design and optimization of therapeutic devices. The development of ultrasound systems involves a high-dimensional parameter space, including transducer geometry, excitation signals, and coupling conditions. Experimental exploration of this space is often impractical due to cost, time, and ethical constraints. Numerical models enable rapid parametric studies, allowing researchers to explore different configurations, identify optimal operating conditions, and evaluate trade-offs between penetration depth, spatial resolution, and energy delivery. In this sense,

simulation hastens design, reducing reliance on trial-and-error experimentation and enabling more systematic development of ultrasound technologies[10,11].

At a deeper level, simulation is the only viable approach for addressing the inherently multiscale nature of ultrasound therapies. Acoustic waves are applied at the macroscopic scale, propagate through tissues at the mesoscale, and ultimately induce biological effects at the cellular and subcellular scales. These scales are governed by different physical laws—fluid acoustics, solid mechanics, and mechanobiology—yet are tightly coupled through wave–matter interactions. Modern simulation frameworks, particularly those based on multiphysics and multiscale modelling, allow these interactions to be captured within a unified computational environment. This enables the quantification of how macroscopic pressure fields translate into microscopic deformation and mechanotransductive stimuli, providing a mechanistic foundation for therapy design rather than relying on empirical correlations[12,13].

Simulation becomes a necessity imposed by the physics of the problem in biological systems. Direct experimental measurement of internal acoustic fields in living tissues is severely limited, particularly at the spatial and temporal scales relevant for mechanotransduction. Ethical constraints, measurement invasiveness, and instrumentation limitations all restrict the ability to probe these phenomena directly[6]. Simulation therefore becomes the only viable means of interrogating the internal dynamics of ultrasound–tissue interaction in a comprehensive and non-invasive manner.

The role of simulation in ultrasound-based therapies can be understood along three fundamental areas: prediction, optimization, and understanding. It predicts how waves propagate through complex anatomical structures, optimizes therapy parameters for safety and efficacy, and provides mechanistic insight into how acoustic energy is converted into biological response. Without simulation, ultrasound therapy operates without a clear understanding, guided by empirical rules and limited observations. With simulation, it becomes a precisely tuneable system, capable of delivering targeted mechanical stimuli with scientific rigour.

### 5.1.2 Challenges in Modelling Heterogeneous Biological Media

The numerical modelling of acoustic wave propagation in biological media is fundamentally constrained by the intrinsic complexity of living tissues, which deviate significantly from the idealized assumptions underlying classical wave theory. Unlike homogeneous and isotropic engineering materials, biological tissues are heterogeneous, anisotropic, viscoelastic, and often exhibit nonlinear behaviour, creating a multi-physics problem that is inherently difficult to represent with high fidelity.

One of the primary challenges arises from spatial heterogeneity and impedance contrast. Biological

tissues are composed of multiple layers (skin, adipose tissue, muscle, cartilage, and bone) each characterized by distinct acoustic properties. These discontinuities lead to strong reflections and partial transmissions at interfaces, significantly altering the propagation of the acoustic field. In particular, interfaces between soft tissues and bone introduce extreme impedance mismatches that can reflect a substantial portion of the incident energy and generate complex interference patterns. Accurately resolving these effects requires high-resolution spatial discretization and careful numerical treatment of boundary conditions, particularly in coupled acoustic–elastic domains, easily creating highly demandable computational models[14].

A second major difficulty lies in the frequency-dependent attenuation and dispersion of biological tissues. Acoustic energy is not conserved during propagation; instead, it is progressively dissipated through absorption and scattering mechanisms. These losses are strongly dependent on frequency and tissue composition, typically following a power-law relationship rather than a simple linear model. This behaviour originates from complex microscopic processes, including viscous damping, thermal conduction, and structural relaxation. Capturing such phenomena requires advanced constitutive models (often based on fractional calculus) that significantly increase the mathematical and computational complexity of the problem. Moreover, the lack of standardized experimental data for parameters such as sound diffusivity further limits the predictive accuracy of these models[15,16]

Another critical challenge is the viscoelastic and anisotropic nature of biological tissues. Soft tissues behave as anisotropic media, whose wave propagation profile on both time and frequency, exhibiting memory effects and directional dependence. For example, skeletal muscle demonstrates anisotropic wave propagation due to fibre orientation, while cartilage exhibits depth-dependent mechanical properties[15]. These characteristics require coupling acoustic wave equations with formulations that usually disregard anisotropy and assume isotropic wave propagation (for example, Westervelt equation), often leading to fully coupled fluid–structure interaction problems. Such multiphysics coupling increases the dimensionality of the problem and imposes strict numerical stability constraints, particularly in time-domain simulations[17].

The multiscale nature of biological systems introduces an additional layer of complexity. Acoustic waves propagate at the macroscopic level (centimetres), interact with tissue microstructure at the mesoscale level (millimetres to micrometres), and ultimately induce biological responses at the cellular and subcellular scales (micrometres to nanometres). Each of these scales is governed by different physical mechanisms, yet they are tightly coupled. Resolving all relevant scales within a single computational framework is often infeasible due to prohibitive computational cost, necessitating the development of reduced-order or multiscale modelling strategies that introduce additional

approximations and potential sources of error[18,19].

Closely related to this is the issue of computational cost and numerical stability. High-frequency ultrasound requires extremely fine spatial and temporal discretization to satisfy the CFL condition, particularly in explicit time-domain solvers. As frequency increases, the wavelength decreases, leading to a rapid growth in the number of elements required to accurately resolve the acoustic field. In 3D simulations of anatomically realistic domains, this can result in computational models containing hundreds of millions of degrees of freedom, making simulations resource-intensive and time-consuming. Consequently, trade-offs between accuracy and computational feasibility are often unavoidable[20].

Another important limitation stems from the uncertainty and variability of material properties. Biological tissues exhibit significant inter-patient variability, as well as intra-tissue variability due to factors such as hydration, age, pathology, and loading conditions. Furthermore, many acoustic and mechanical properties are not well characterized in the literature. This uncertainty propagates through numerical models, affecting the reliability of predictions. Even small variations in parameters such as attenuation coefficients or elastic moduli can lead to substantial differences in predicted pressure fields and energy transmission.

Finally, the limited availability of experimental validation remains a persistent challenge. Direct measurement of internal acoustic fields within living tissues is extremely difficult due to invasiveness and instrumentation constraints. As a result, many models rely on indirect validation using phantoms or simplified experimental setups, which may not fully capture the complexity of in vivo conditions. This creates a gap between simulation and reality, reinforcing the need for robust validation frameworks and experimentally grounded parameter identification[21].

Given these challenges, modelling acoustic wave propagation in complex heterogeneous biological media becomes a convergence of uncertainties, scale disparities, and coupled physical phenomena. Each layer of complexity, from tissue heterogeneity to cellular mechanics, acts as both a barrier and a signal: a barrier to straightforward modelling, and a signal that simplified assumptions must be treated with caution. The challenge, therefore, is not to eliminate this complexity, but to navigate it, constructing models that are sufficiently detailed to capture the governing physics, yet sufficiently efficient to remain tractable.

## 5.2 Reduced-Order Modelling of Wave Propagation

Finite-difference time-domain (FDTD) are an implementation of FDM that are widely used for modelling acoustic wave propagation in complex heterogeneous media due to their ability to directly resolve transient pressure and particle velocity fields in time and space[22–24]. Their explicit formulation makes them particularly suitable for pulsed ultrasound applications, where steady-state assumptions are not valid. In biological tissues, this is especially relevant, as wave propagation is strongly influenced by spatial heterogeneity and frequency-dependent attenuation mechanisms[25,26].

Despite the maturity of numerical methods, existing simulation tools present limitations when applied to transient bioacoustic problems. Frequency-domain formulations commonly used in commercial solvers inherently assume steady-state conditions and are therefore not well suited for time-domain pulsed excitation. Conversely, many simplified implementations lack accurate representations of frequency-dependent attenuation, which is a critical parameter for predicting how much acoustic energy reaches a target region.

To address this, a reduced-order modelling strategy based on a 1D approximation was adopted. In layered biological media under near-normal incidence, wave propagation is dominated by longitudinal pressure waves along the main propagation axis. Under these conditions, a 1D formulation captures the primary physical mechanisms while neglecting secondary effects such as diffraction and beam spreading. This reduction significantly lowers computational cost while preserving the key factors governing energy transmission. The work discussed in this section is based on the algorithm described in previously published work by the author[1], and the code is available online[2].

### 5.2.1 Governing Equations and Physical Assumptions

In a one-dimensional framework, the propagation of longitudinal acoustic waves can be described through a pair of coupled first-order partial differential equations. The first corresponds to the conservation of momentum, derived from Newton's laws, and is expressed in equation 219,

$$\frac{\partial c}{\partial t} = \frac{\partial p}{\rho \cdot \partial x} \tag{219}$$

where the temporal variation of particle velocity $\frac{\partial c}{\partial t}$ is governed by the spatial gradient of pressure, scaled by the inverse of the material density $\rho$. The second equation arises from mass conservation and is given by the continuity relation in equation 220,

$$\frac{\partial p}{\partial t} = \frac{-K \cdot \partial c}{\partial x} \tag{220}$$

in which the rate of pressure variation $\frac{\partial p}{\partial t}$ is controlled by the spatial variation of particle velocity and the bulk modulus $K$ of the medium[27].

These two equations form a coupled linear system that supports the propagation of acoustic waves. The assumption of linearity implies that oscillations are of sufficiently small amplitude such that nonlinear, thermal, and viscous effects can be neglected. This approximation is appropriate for ultrasound applications operating under moderate intensity conditions.

At interfaces between materials with different properties, acoustic waves undergo partial reflection and transmission. These phenomena are governed by the acoustic impedance $Z$, defined in equation 221,

$$Z = \rho \cdot c \tag{221}$$

which, for planar wave propagation, depends on the density $\rho$ and the speed of sound $c$ of the medium. Discontinuities in impedance determine the proportion of energy reflected and transmitted, which can be quantified using the reflection and transmission coefficients given in equation 222 and equation 223, respectively,

$$R = \frac{Z_2 - Z_1}{Z_2 + Z_1} \tag{222}$$

$$T = \frac{2 \cdot Z_2}{Z_2 + Z_1} \tag{223}$$

### 5.2.2 Numerical Implementation Using Finite-Difference Time-Domain

A first-order acoustic FDTD solver was developed in Python, employing an explicit time integration scheme on a staggered spatial grid. In this formulation, particle velocity and pressure are evaluated at alternating spatial locations, forming an interleaved computational arrangement that enhances numerical stability and mitigates dispersion errors (figure 72).

The discretized form of the governing equations is obtained using finite differences in both space and time. For each spatial node $i$, the particle velocity $c$ and pressure $p$ are updated at each time increment $\Delta t$ over a spatial step $\Delta x$, as described in equation 224 and equation 225.

$$c_i^{n+\frac{1}{2}} = c_i^{n-\frac{1}{2}} - (p_{i+1}^n - p_i^n) \cdot \frac{\Delta t}{\rho_i \cdot \Delta x} \tag{224}$$

$$p_i^{n+\frac{1}{2}} = c_i^n - (c_{i+1}^{n+\frac{1}{2}} - c_i^{n+\frac{1}{2}}) \cdot \frac{\Delta t \cdot K_i}{\Delta x} \tag{225}$$

This discretization naturally captures wave interactions at material boundaries, as local variations in density and bulk modulus govern reflection and transmission phenomena without requiring additional interface conditions.

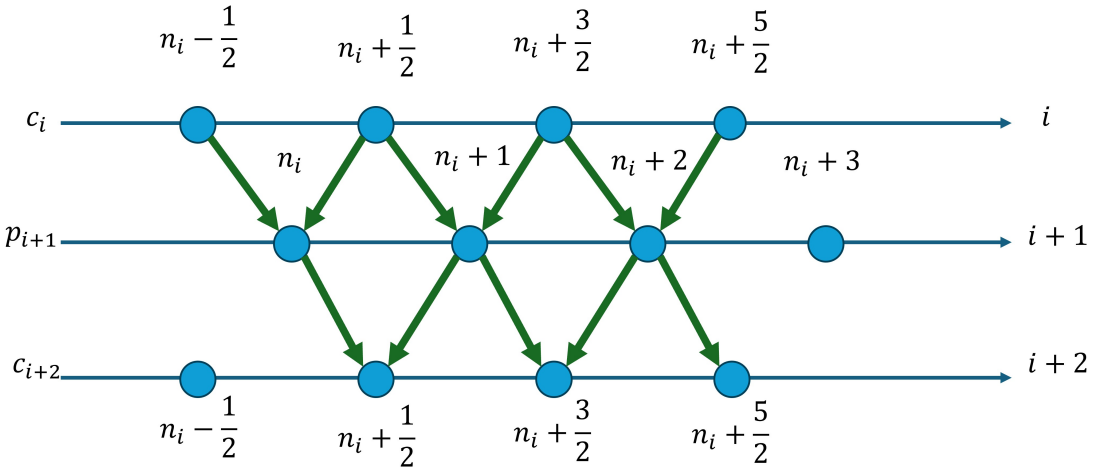



Figure 72: FDTD scheme illustrating the staggered grid formulation, where pressure and particle velocity are computed at interleaved spatial and temporal locations.

In biological media, acoustic attenuation is frequency-dependent and typically expressed in dB/MHz/cm ($\alpha_{dB}$). To incorporate attenuation into the time-domain framework, these values are converted into Np/m using equation 226,

$$\alpha = \left(\frac{\alpha_{dB}}{20 \cdot \log_{10} e}\right) \cdot \frac{f}{10^6} \cdot 100 \tag{226}$$

where $f$ denotes the excitation frequency.

The resulting attenuation coefficient is then scaled by the local speed of sound and the temporal discretization. Attenuation is implemented as an exponential decay factor applied at each time step, as defined in equation 227,

$$\gamma = \alpha \cdot c \cdot \Delta t \tag{227}$$

which is subsequently applied to the pressure field according to equation 228.

$$p_i^n = p_i^n \cdot \gamma \tag{228}$$

Material properties were spatially assigned based on experimentally determined values presented in the previous chapter, as well as the characteristics of the transducers available in the laboratory (table 14).

Table 14: Material parameters used for the simulation in 1D FDTD wave propagation.

| **Sample** | **Speed of Sound (m/s)** | **Density (g/cm$^3$)** | **$\alpha$ (dB/MHz/cm)** |
|---|---|---|---|
| Skin | 1654.93 | 1.131 | 1.096 |
| Adipose Tissue | 1461.77 | 0.927 | 0.7264 |
| Cartilage | 1650.80 | 1.033 | 4.336 |

| | | | |
|---|---|---|---|
| Transducer (PZT) | 4.200 | 7700 | 0 |
| Matching Layer | 2700 | 1.500 | 0 |

The one-dimensional computational domain was configured to represent a simplified propagation pathway from the external transducer to the knee articular cartilage. This domain included a PZT source layer, an acoustic matching layer, and sequential biological layers corresponding to skin, subcutaneous adipose tissue, and cartilage (figure 73).

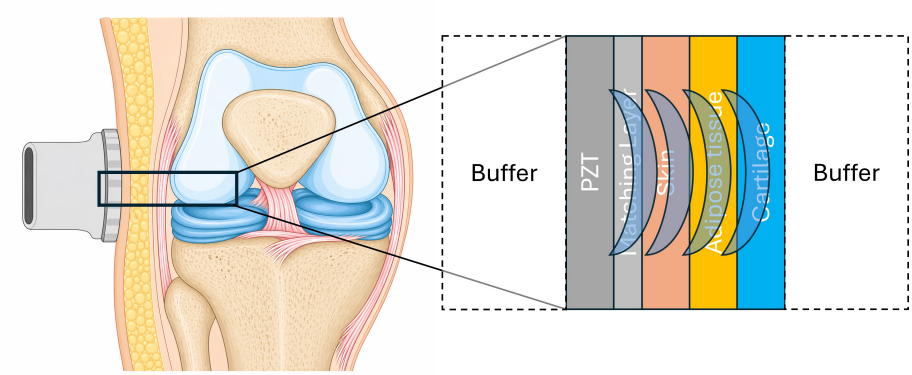



Figure 73: Representation of the simplified one-dimensional acoustic propagation model for knee stimulation.

The thicknesses of the PZT and matching layers were defined based on the excitation frequency, adopting half-wavelength and quarter-wavelength criteria, respectively, to approximate optimal transducer operation and impedance matching[28]. The biological layers were assigned representative thicknesses of approximately 2 mm for skin, 10 mm for subcutaneous adipose tissue, and 2.5 mm for cartilage[29–31]. To minimize artificial reflections at the domain boundaries, buffer regions of 6 cm on the cartilage side and 9 cm on the transducer side were included, resulting in a total biological propagation path of approximately 14.5 mm.

The excitation signal consisted of a single-cycle sinusoidal burst modulated by a Hann window to reduce spectral leakage. This signal was introduced into the particle velocity field to enhance numerical stability. The amplitude was scaled according to the transducer impedance to achieve a prescribed pressure level. Simulations were conducted across a range of excitation frequencies: 0.02, 0.04, 0.05, 0.1, 0.2, 0.4, 0.5, 1, 2, 4, and 5 MHz.

To ensure numerical stability and accuracy, the spatial discretization $\Delta x$ was selected based on the minimum wavelength in the system, satisfying $\Delta x \leq \frac{\lambda_{min}}{10}$. The temporal step $\Delta t$ was defined according to the CFL stability condition, $\Delta t \leq \frac{CFL \cdot \Delta x}{c_{\max}}$, with $CFL = 0.1$.

Pressure signals in the time domain were recorded at multiple locations along the propagation path, including the transducer–skin interface, the skin–adipose interface, the adipose–cartilage interface, and

at a depth of 1.25 mm within the cartilage. To improve signal clarity and reduce numerical noise, pressure values below $10^{-7}$ Pa were truncated, as such amplitudes fall below typical experimental detection limits. The results were presented using Sound Transmission Loss in equation 229,

$$\text{STL} = 20 \cdot \log_{10}\left(\frac{p_{source}}{p_{cartilage}}\right) \tag{229}$$

where $p_{source}$ is the pressure amplitude input in the system by transducer and $p_{cartilage}$ is the pressure amplitude measured in the probe inserted in the cartilage domain.

### 5.2.3 Results

The results in figure 74 demonstrate a clear frequency-dependent attenuation of acoustic wave transmission through the layered medium.

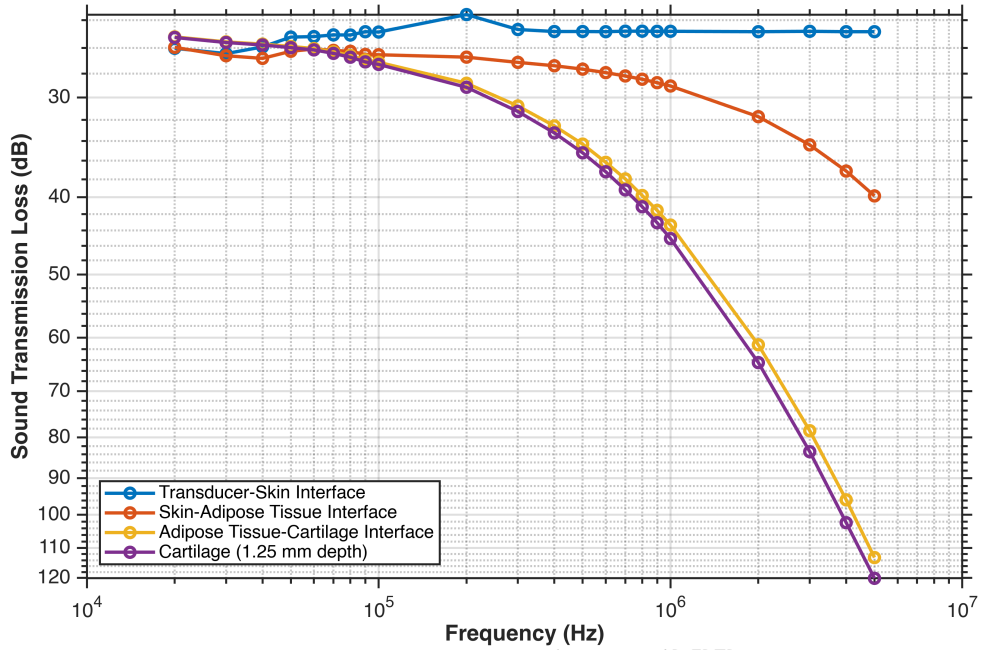



Figure 74: Frequency-dependent sound transmission loss across tissue interfaces in the 1D FDTD model.

At the transducer–skin interface, STL remain relatively low and nearly constant across the investigated frequency range, indicating minimal energy dissipation at the source boundary. However, as the wave propagates through successive tissue layers, attenuation increases significantly, particularly beyond approximately 0.5–1 MHz. At the skin–adipose interface, a gradual increase in STL is observed with frequency, reflecting moderate attenuation within superficial tissues. This effect becomes substantially more pronounced at deeper interfaces. At the adipose–cartilage boundary and within the cartilage layer (1.25 mm depth), transmission loss exhibits a sharp nonlinear increase with frequency, reaching values exceeding 100 dB at the highest frequencies considered.

### 5.2.4 Discussion

The obtained results indicate that higher-frequency acoustic waves experience severe attenuation and are unlikely to deliver sufficient energy to the cartilage. In contrast, lower frequencies (<100 kHz) exhibit comparatively low transmission losses across all interfaces, suggesting a significantly higher potential for effective energy delivery to deep tissue regions.

These findings contrast with the frequency ranges commonly employed in therapeutic ultrasound applications. Clinical and experimental studies typically operate within the range of approximately 0.2–3 MHz, with most knee osteoarthritis treatments using frequencies around 1 MHz[32,33]. While such frequencies are traditionally selected as a compromise between penetration and localized energy deposition, the present results suggest that even within this range, significant attenuation may occur before the wave reaches cartilage. Moreover, some theoretical studies have proposed optimal frequencies in the MHz range for cartilage stimulation based on cellular resonance considerations[34]. However, the current propagation analysis indicates that such frequencies may be strongly attenuated before reaching the target site, highlighting a potential mismatch between propagation efficiency and cellular response.

It is important to note that these findings are derived under the assumption of planar wave propagation, which does not account for spatial effects such as focusing, diffraction, or interference. In practical applications, the formation of standing wave patterns (if harmonic excitation is used) can locally amplify or reduce the acoustic energy delivered to the target. Such phenomena may partially compensate for propagation losses or, conversely, lead to spatially heterogeneous stimulation. This reduced-order domain was not intended to reproduce the full anatomical complexity of the knee, but rather to provide an initial estimate of acoustic transmission through the dominant superficial soft-tissue layers before reaching cartilage. Therefore, while the present results clearly demonstrate that high-frequency propagation alone is associated with substantial energy loss, the actual energy distribution in vivo may differ depending on the acoustic field configuration.

Several further limitations should be acknowledged. First, The skin thickness was selected as a representative value within the range reported for adult skin using high-frequency ultrasound, acknowledging that skin thickness varies with anatomical site, sex, age, and body composition. The adipose layer was assigned a nominal thickness of 10 mm to represent a moderate soft-tissue path around the knee; however, this value is expected to vary substantially between individuals. MRI-based studies of the knee have shown that subcutaneous fat thickness around the patellofemoral region is strongly patient-dependent and associated with body composition, with reported clinically relevant

thresholds of approximately 5.8 mm for prepatellar subcutaneous fat and 25.6 mm for medial subcutaneous fat[35]. The cartilage layer was assigned a representative thickness of 2.5 mm, consistent with MRI measurements of healthy adult knee cartilage, where mean regional cartilage thicknesses commonly fall between approximately 1.5 and 3.2 mm, with local values reaching up to about 5 mm depending on the compartment[31]. Second, the model assumes homogeneous, layer-wise material properties, whereas biological tissues exhibit spatial variability and anisotropy. Third, nonlinear acoustic effects, although expected to be limited at moderate intensities, were not explicitly considered. Finally, the simplified anatomical pathway excludes structures such as muscle, bone, and synovial fluid, which may significantly influence wave propagation in the knee joint.

Future work should focus on expanding this FDTD model toward higher-dimensional patient-specific simulations that incorporate realistic knee anatomy, including muscle, bone, synovial fluid, menisci, and cartilage geometry. This would enable evaluation of focusing, diffraction, reflection, and standing-wave formation, which may substantially alter the local energy delivered to cartilage.

### 5.2.5 Conclusion

This reduced-order model provided an efficient first approximation of acoustic wave propagation from an external transducer toward knee articular cartilage. By representing the propagation path as a layered one-dimensional medium, the model captured the main transmission mechanisms associated with impedance mismatch, reflection, and frequency-dependent attenuation. The results showed that acoustic energy can reach the cartilage region, but that transmission is strongly dependent on excitation frequency. Lower frequencies exhibited markedly lower losses, whereas frequencies in the MHz range underwent substantial attenuation before and within the cartilage layer.

Although the model is limited to planar pulse propagation and does not account for focusing, diffraction, anatomical curvature, or standing-wave formation, it establishes an important preliminary constraint for ultrasound-based cartilage stimulation. Specifically, it demonstrates that frequency selection cannot be based solely on cellular response or transducer availability, but must also consider the ability of the acoustic wave to traverse the intervening tissues. This analysis therefore supports the need for subsequent higher-dimensional, patient-specific simulations capable of resolving spatial field patterns and linking transmitted pressure to mechanotransductive stimulation at the cartilage and cellular scales.

## 5.3 Multi-Scale Patient-Specific Simulation Framework

This section presents a multiscale computational framework to quantify how externally applied acoustic waves propagate through the knee joint and induce mechanotransduction through chondrocyte nucleus strain. Patient-specific knee geometries ($n$=8) were used to simulate acoustic wave transmission through layered tissues, while a representative volume element modelled the coupled solid–shell–acoustic behavior of the chondrocyte, pericellular matrix, and extracellular matrix. Modal and frequency-response analyzes identified the spheroidal $s_1$ mode as the dominant contributor to nuclear deformation. Strain amplification was found to occur within defined frequency bands rather than at a single frequency, with healthy chondrocytes exhibiting a broader mid-frequency amplification region (70–85 kHz) and osteoarthritic cells showing a shifted low-frequency (20–30 kHz) dominance due to hypertrophy and altered stiffness. Macro-to-micro coupling demonstrated that, despite anatomical variability, consistent transmissibility trends were preserved across patients, with ideal frequencies for healthy and OA patients. Time-explicit simulations comparing linear and nonlinear acoustic formulations revealed negligible harmonic generation at the applied pressure levels, indicating that linear acoustics adequately describe propagation within the mechanotransduction sensitive strain considered. Overall, the results demonstrate that cartilage stimulation is frequency-band dependent and disease-sensitive, and they provide a mechanistically grounded basis for optimizing ultrasound excitation parameters based on cellular-scale mechanics rather than empirical frequency selection. The work presented in this section has been submitted as a scientific article.

### 5.3.1 Overview of the Multi-Scale Modelling Strategy

The simulation of acoustic wave propagation in biological systems inherently requires a multiscale formulation, as the relevant physical phenomena span several orders of magnitude, from macroscopic tissue-level transmission to microscopic cellular deformation. In this work, a hierarchical modelling strategy was adopted to bridge these scales, integrating simplified wave propagation models with anatomically realistic simulations and cellular-level mechanical analyzes (figure 75).

At the microscale, the mechanical response of cartilage was investigated through a RVE comprising the extracellular matrix, pericellular matrix, and embedded chondrocytes. This model includes as a coupled fluid–structure system, allowing acoustic pressure waves to induce elastic deformation within the cell and its nucleus. Modal and harmonic analyses were performed to characterize the intrinsic vibrational behavior of chondrocytes and to identify the frequency-dependent relationship between applied pressure

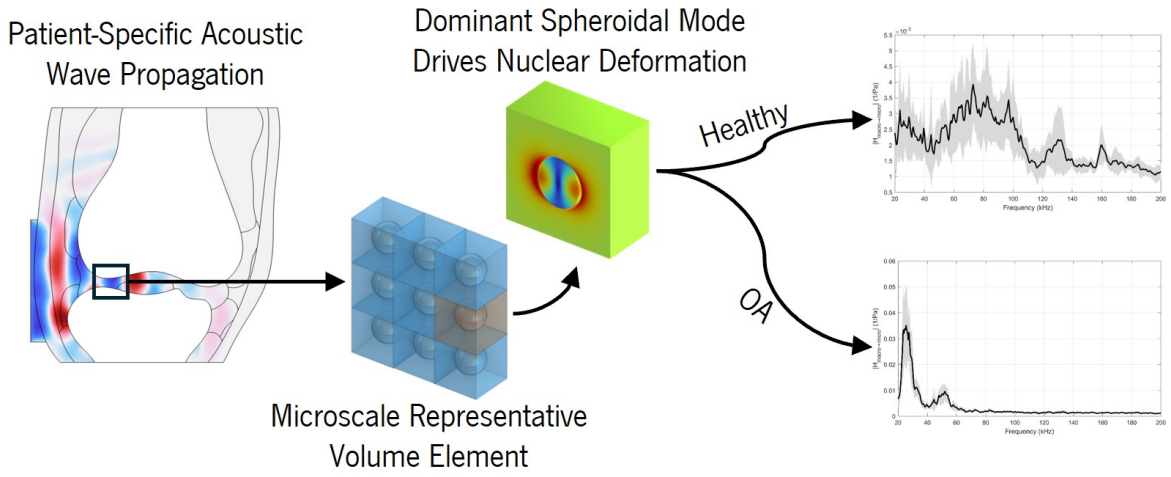



Figure 75: Multiscale modelling strategy, where acoustic wave propagation is simulated at the patient-specific knee level, followed by localization of the pressure field within cartilage. This field is transferred to a microscale representative volume element, where chondrocyte dynamics are analyzed to identify dominant resonance modes governing nuclear deformation in both healthy and osteoarthritic conditions.

and resulting nuclear strain.

At the macroscale, acoustic wave propagation was modelled within patient-specific geometries of the knee joint, reconstructed from medical imaging data. This level captures the interaction of ultrasound waves with heterogeneous biological tissues, including skin, adipose tissue, muscle, bone, and cartilage. The governing physics are dominated by acoustic impedance mismatches, attenuation, and wave reflections at tissue interfaces, which collectively determine the pressure field distribution reaching the cartilage.

The coupling between macro and microscales constitutes the central component of the modelling strategy. The pressure field computed at the tissue level serves as the input boundary condition for the microscale model, enabling the evaluation of how externally applied acoustic waves translate into intracellular mechanical stimuli. This coupling is achieved through frequency-domain transfer functions, which relate macroscopic pressure amplitudes to nuclear strain within the chondrocyte.

### 5.3.2 Computational MultiScale Modelling

A computational multiscale framework was developed to link macroscopic acoustic wave propagation within the knee joint to the microscopic mechanical response of chondrocytes in articular cartilage. By coupling micro and macroscale through a RVE approach, the model enables the evaluation of pressure-to-strain transmissibility and the identification of frequency ranges that maximize biologically relevant stimulation, providing a physically grounded basis for the optimization of ultrasound-based therapies in both healthy and osteoarthritic conditions.

#### 5.3.2.1 Articular Cartilage Geometry

To represent hyaline cartilage, a parametric homogenized RVE was adopted, as illustrated in Figure 76. Within this framework, the size and spatial distribution of the constituent phases were varied parametrically to account for the intrinsic heterogeneity of cartilage tissue. This approach enables the representation of the underlying mechanical and structural variability while maintaining a computationally tractable model.

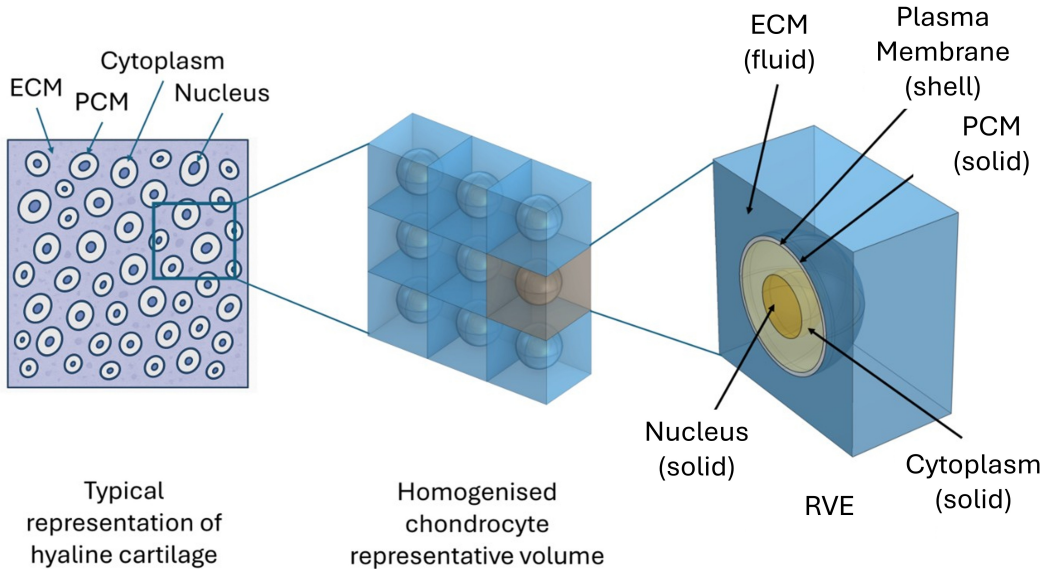



Figure 76: Schematic illustration of hyaline cartilage structure, showing ECM, PCM, and embedded chondrocytes. A representative chondrocyte volume is isolated and expanded to highlight nucleus, cytoplasm, plasma membrane, and surrounding PCM, creating the basis of the homogenized representative volume element used in the simulations.

The geometrical parameters used to define the RVE, including the dimensions of individual chondrocytes and their surrounding structures, are summarized in Table 15.

Table 15: Morphological parameters of chondrocytes and their pericellular environment in healthy and OA cartilage, including cell radius, nuclear radius, membrane and PCM thicknesses, and intercellular spacing, with corresponding literature references.

| **Parameter** | **Values** | | **References** |
|---|---|---|---|
| | **Healthy** | **OA** | |
| Chondrocite radius ($r_c$ - $\mu$m) | 5-10 | 10-20 | 36,37 |
| Nucleus radius ($r_n$ - $\mu$m) | $\frac{r_c}{2}$ | | 36,38 |
| Plasma membrane thickness ($t_{pcm}$ - $\mu$m) | 2-4 | 1-3 | 39 |
| PCM thickness ($t_{pm}$ - $\mu$m) | 0.005-0.01 | | 40 |

| | | | |
|---|---|---|---|
| Distance between chondrocytes ($d_c$ - $\mu$m) | 40-80 | 50-100 | [36,41,42] |

In osteoarthritic tissue, the chondrocyte radius was assumed to increase due to hypertrophic changes[37]. The nucleus was considered to occupy approximately half of the cell volume[38], a proportional relationship reported for healthy cartilage and assumed to remain valid under hypertrophic conditions[37]. Due to the absence of reliable measurements for the plasma membrane thickness, particularly in OA conditions, a standard reference value for mammalian cells was adopted[39]. In contrast, the thickness of the PCM was assumed to decrease in osteoarthritis, reflecting the well-documented degradation of this matrix[40]. Regarding cellular distribution, healthy adult hyaline cartilage typically exhibits intercellular spacing on the order of tens of micrometers, commonly ranging between 40 and 80 μm depending on the depth zone[36]. In OA tissue, this spacing becomes more heterogeneous, with regions of increased separation due to cell loss coexisting with clustered arrangements (chondrons), resulting in an estimated range of 50-100 μm[41,42].

Cell dispersion and spatial periodicity were incorporated into the model, with their implementation described in Section 5.3.4.

#### 5.3.2.2 Patients' data for anatomic knee models

A cohort comprising eight subjects from the OpenKnee project database was utilized in this study[43,44]. The corresponding demographic and anthropometric characteristics are summarized in Table 16.

Table 16: Demographic and anthropometric characteristics of the subjects included in the study. These parameters were incorporated into the computational workflow to ensure physiologically representative joint geometry.

| Patient | Knee | Age | Gender | Height (m) | Weight (kg) | BMI |
|---|---|---|---|---|---|---|
| A | Right Knee | 71 | Male | 1.83 | 77.1 | 23.1 |
| B | Right Knee | 67 | Female | 1.55 | 45.3 | 18.9 |
| C | Left Knee | 25 | Female | 1.73 | 68 | 22.8 |
| D | Right Knee | 46 | Female | 1.575 | 54.43 | 21.9 |
| E | Right Knee | 71 | Female | 1.524 | 49.4 | 21.3 |
| F | Right Knee | 71 | Male | 1.8 | 65.77 | 22.7 |
| G | Right Knee | 40 | Male | 1.778 | 63.5 | 20.09 |

| | | | | | | |
|---|---|---|---|---|---|---|
| H | Left Knee | 34 | Male | 1.8 | 68.3 | 20.0 |

For each subject, coronal-plane MRI data of the knee were employed to reconstruct two-dimensional macroscale geometries for simulation, as is displayed in figure 77. The full images of the extracted geometries are provided in the Supplemental Data (section C.1). The segmentation process involved the delineation of individual tissue classes, including skin, adipose tissue, skeletal muscle, bone, cartilage, and tendons. These segmented regions were subsequently reconstructed into computational geometries suitable for acoustic simulation in COMSOL Multiphysics. The incorporation of subject-specific anatomical

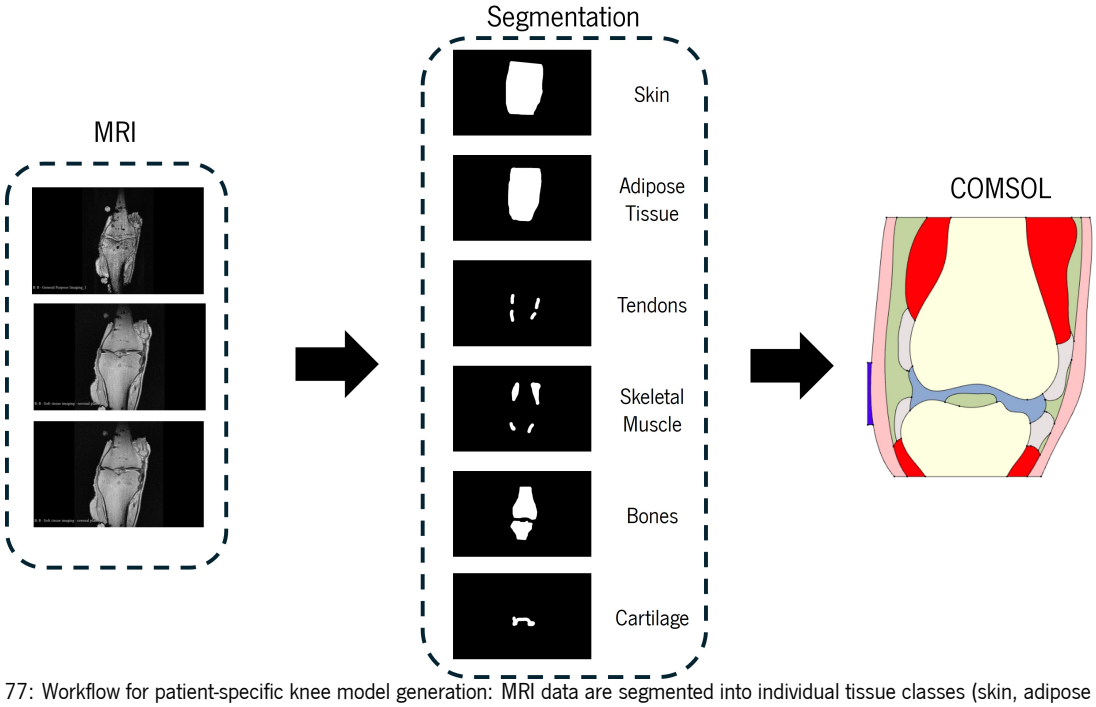



Figure 77: Workflow for patient-specific knee model generation: MRI data are segmented into individual tissue classes (skin, adipose tissue, tendons, skeletal muscle, bone, and cartilage), which are subsequently reconstructed into a computational geometry for acoustic simulation in COMSOL Multiphysics.

features enables a more accurate representation of acoustic wave propagation within the joint, particularly with respect to cartilage thickness, limb alignment, and soft-tissue distribution. This approach ensures that both acoustic transmission and mechanical transmissibility analyses are grounded in physiologically realistic conditions, capturing inter-patient variability within the computational framework.

### 5.3.3 Material Properties

The accurate representation of acoustic wave propagation and mechanotransduction response requires the consistent definition of material properties across both cellular and tissue scales. Particular attention was given to the incorporation of frequency-dependent attenuation and disease-specific

variations, ensuring that both wave propagation and mechanical coupling are represented in a physiologically meaningful manner across scales.

#### 5.3.3.1 Articular Cartilage Material properties

The mechanical and acoustic properties assigned to the chondrocyte, nucleus, plasma membrane, PCM, and ECM under both healthy and OA conditions are summarized in Table 17.

Table 17: Mechanical and acoustic material properties used for the healthy and OA chondrocyte microenvironment.

| **Parameter** | **Values** | | **References** |
|---|---|---|---|
| | **Healthy** | **OA** | |
| **Chondrocyte (cytoplasm)** | | | |
| Density ($\rho_{cytoplasm}$ - g/cm$^3$) | 1.03 | | [45] |
| Young's Modulus ($E_{Cytoplasm}$ - kPa) | 8.9 | 6.3 | [46] |
| Poisson's Ratio ($\nu_{Cytoplasm}$) | 0.37 | | [46] |
| Sound Diffusivity ($\delta_{cytoplasm}$ -m$^2$/s) | $0.0261 \cdot f^{-1.654}$ | | [15] |
| **Nucleus** | | | |
| Density ($\rho_{nucleus}$ - g/cm$^3$) | 1.1 | | [47] |
| Young's Modulus ($E_{nucleus}$ - kPa) | 3 | 5 | [42,47] |
| Poisson's Ratio ($\nu_{nucleus}$) | 0.46 | | [47] |
| Sound Diffusivity ($\delta_{nucleus}$ - m$^2$/s) | $0.0261 \cdot f^{-1.654}$ | | [15] |
| **Plasma Membrane** | | | |

| | | | |
|---|---|---|---|
| Density ($\rho_{plasmamembrane}$ - g/cm$^3$) | 1.1 | | [48] |
| Young's Modulus ($E_{plasmamembrane}$ - kPa) | 3 | 5 | [49] |
| Poisson's Ratio ($\nu_{plasmamembrane}$) | 0.46 | | [47,50] |
| **PCM** | | | |
| Density ($\rho_{PCM}$ - g/cm$^3$) | 1.03 | | [45] |
| Young's Modulus ($E_{PCM}$ - kPa) | 27.7 | 5.3 | [46,51] |
| Poisson's Ratio ($\nu_{PCM}$) | 0.47 | | [42] |
| Sound Diffusivity ($\delta_{PCM}$ - m$^2$/s) | $0.0261 \cdot f^{-1.654}$ | | [15] |
| **ECM** | | | |
| Density ($\rho_{ECM}$ - g/cm$^3$) | 1.03 | | [45] |
| Speed of Sound ($c_{ECM}$ - m/s) | 1650.8 | | [15] |
| Sound Diffusivity ($\delta_{ECM}$ - m$^2$/s) | $0.0261 \cdot f^{-1.654}$ | | [15] |

The material parameters of the cellular domains were defined based on current evidence regarding osteoarthritic alterations. In accordance with previous studies[47,52], the nucleus was initially assumed to exhibit approximately twice the viscosity of the cytoplasm. However, due to the lack of experimental data describing nuclear and cytoplasmic viscosity at the high-frequency (kHz) range relevant for acoustic stimulation, the direct use of viscoelastic parameters resulted in excessive damping during preliminary simulations. To mitigate this limitation and avoid non-physical behavior, viscous effects were instead

represented through an equivalent acoustic attenuation coefficient, which provides a more appropriate description of frequency-dependent energy dissipation in biological media.

Variations in elastic properties were incorporated to reflect disease-specific changes. In particular, an increase in the Young's modulus of the nucleus was considered for osteoarthritic conditions, consistent with reported stiffening behavior[42]. Conversely, density and Poisson's ratio were assumed to remain unchanged, as their reported variations between healthy and OA chondrocytes are minimal[42,52].

The ECM surrounding the chondrocyte–PCM assembly was modelled as a continuous and homogeneous medium. Its acoustic properties were defined to match those of bulk cartilage tissue, ensuring that wave propagation, attenuation, and energy transmission are representative of physiological in situ conditions.

#### 5.3.3.2 Biological Tissues Material properties

Table 18 presents the acoustic properties assigned to the soft and hard tissues included in the macroscale knee model, namely skin, adipose tissue, skeletal muscle, bone, cartilage, and tendon.

Table 18: Acoustic and mechanical properties of the biological tissues included in the macro-scale knee model.

| Parameter | Value | References |
|---|---|---|
| **Skin** | | |
| Density ($\rho_{skin}$ - g/cm$^3$) | $1.13124$ | [15] |
| Speed of Sound ($c_{skin}$ - m/s) | $1654.93$ | [15] |
| B/A Nonlinearity Parameter | $7.237$ | [15] |
| Sound Diffusivity ($\delta_{skin}$ - m$^2$/s) | $0.0026 \cdot f^{-0.934}$ | [15] |
| **Adipose Tissue** | | |
| Density ($\rho_{adiposetissue}$ - g/cm$^3$) | $0.927091$ | [15] |
| Speed of Sound ($c_{adiposetissue}$ - m/s) | $1461.77$ | [15] |
| B/A Nonlinearity Parameter | $10.574$ | [15] |
| Sound Diffusivity ($\delta_{adiposetissue}$ - m$^2$/s) | $0.0012 \cdot f^{-0.608}$ | [15] |
| **Muscle** | | |

| | | |
|---|---|---|
| Density ($\rho_{skeletalmuscle}$ - g/cm$^3$) | $1.05775$ | [15] |
| Speed of Sound ($c_{skeletalmuscle}$ - m/s) | $1562.18$ | [15] |
| B/A Nonlinearity Parameter | $6.632$ | [15] |
| Sound Diffusivity ($\delta_{skeletalmuscle}$ - m$^2$/s) | $0.0024 \cdot f^{-0.349}$ | [15] |
| **Tendon** | | |
| Density ($\rho_{tendon}$ - g/cm$^3$) | $1.12106$ | [15] |
| Speed of Sound ($c_{tendon}$ - m/s) | $1827.43$ | [15] |
| B/A Nonlinearity Parameter | $7.047$ | [15] |
| Sound Diffusivity ($\delta_{tendon}$ - m$^2$/s) | $0.0168 \cdot f^{-0.801}$ | [15] |
| **Cartilage** | | |
| Density ($\rho_{cartilage}$ - g/cm$^3$) | $1.03345$ | [45] |
| Speed of Sound ($c_{cartilage}$ - m/s) | $1650.80$ | [15] |
| B/A Nonlinearity Parameter | $8.118$ | [15] |
| Sound Diffusivity ($\delta_{cartilage}$ - m$^2$/s) | $0.0261 \cdot f^{-0.1654}$ | [15] |
| **Bone** | | |
| Density ($\rho_{bone}$ - g/cm$^3$) | $1.86170$ | [45] |
| Longitudinal Wave Speed ($c_{l,bone}$ - m/s) | $3193.95$ | [15] |
| Shear Wave Speed ($c_{s,bone}$ - m/s) | $1500.00$ | [53] |
| Sound Diffusivity ($\delta_{bone}$ - m$^2$/s) | $0.0024 \cdot f^{-0.349}$ | [15] |

Wave propagation in soft biological tissues was modelled assuming fluid-like behavior, characterized by density, speed of sound, nonlinearity parameter (B/A), and a frequency-dependent sound diffusivity to account for viscous and thermal dissipation mechanisms. In contrast, bone was represented as a linear

elastic solid, requiring the definition of both longitudinal and shear wave velocities instead of a single acoustic wave speed. This distinction reflects the capability of solid media to withstand both compressional and transverse wave modes, which are not present in fluid-like tissues.

### 5.3.4 Mesh and Boundary Conditions

The definition of the computational mesh and boundary conditions is critical to accurately resolve wave propagation across both cellular and tissue scales while maintaining numerical stability and physical consistency. In the present work, discretization strategies were selected to adequately capture the spatial and temporal characteristics of high-frequency acoustic waves, ensuring sufficient resolution of short wavelengths and strong gradients arising at material interfaces. Particular emphasis was placed on the correct representation of coupling between fluid and solid domains, as well as on the mitigation of non-physical reflections at computational boundaries.

#### 5.3.4.1 Representative volume element meshing

The RVE was formulated to represent the coupled acoustic and mechanical response of a single chondrocyte embedded within its immediate extracellular environment, while ensuring that the computational domain reflects the behavior of a periodically repeating tissue. Within this framework, the nucleus, cytoplasm, and PCM were modelled as linear elastic solids, enabling the propagation of both compressional and shear waves across intracellular and pericellular regions. The plasma membrane, which separates the cytoplasm from the ECM, was represented as a thin structural shell. Its mechanical interaction with the cytoplasm was enforced through a structure–shell interface condition, ensuring continuity of both displacement and traction fields across the interface. The surrounding ECM was treated as an acoustic pressure domain, supporting only longitudinal wave propagation and coupled to the solid regions via acoustic–structure boundary conditions that impose continuity of normal acceleration and equilibrium of normal stresses.

To reproduce the periodic organization of chondrocytes within cartilage and to avoid edge effects associated with isolated domains, Floquet periodic boundary conditions were applied to all faces of the cubic RVE. These conditions enforce a phase-consistent relationship between opposing boundaries, allowing the domain to emulate an infinite periodic lattice of identical units. Mathematically, this is expressed as equation 230,

$$u(\mathbf{r} + \mathbf{R}) = e^{i\mathbf{k}\cdot\mathbf{R}}\, u(\mathbf{r}) \tag{230}$$

where $u(\mathbf{r})$ represents the displacement or acoustic pressure field, **R** is the lattice translation vector between corresponding points on opposite faces of the RVE, and **k** denotes the wave vector associated with the harmonic excitation. This formulation ensures that the fields on opposite boundaries differ only by a phase shift determined by the imposed wave.

The wave vector is defined as equation 231,

$$k_i = \frac{\pi}{l} \tag{231}$$

where $l$ corresponds to the characteristic spacing between adjacent chondrocytes. This definition establishes the periodicity of the excitation and ensures consistency with the spatial arrangement of the cellular lattice.

#### 5.3.4.2 Macroscale modelling

Figure 78 presents the computational domain and the associated acoustic interactions within the knee joint considered for cartilage stimulation analysis.

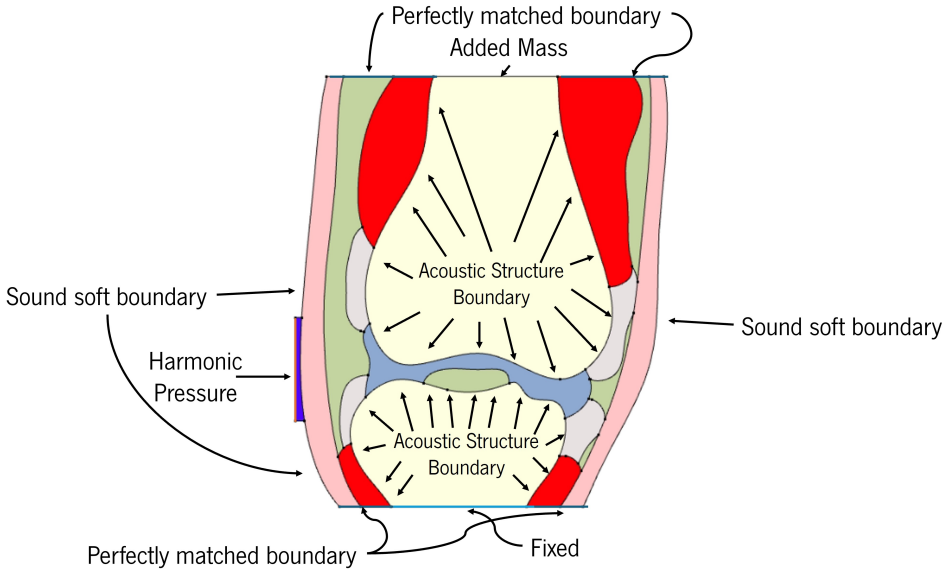



Figure 78: Schematic cross-sectional representation of the human knee joint used in the simulations, indicating domain boundaries and the applied harmonic acoustic excitation.

The femoral and tibial structures, separated by the articular cartilage and meniscus, create a geometrically and acoustically heterogeneous system. Wave propagation within this domain is strongly influenced by impedance mismatches across tissue interfaces, which act as acoustic–structure boundaries. At these locations, reflection, transmission, and scattering phenomena govern the redistribution of acoustic energy and, consequently, the mechanical stimulus delivered to the cartilage.

The acoustic source was modelled as a harmonic pressure field applied within a coupling gel layer, representing the incident wave generated by an ultrasonic transducer. This intermediate layer ensures efficient energy transfer between the transducer and the biological tissues while maintaining realistic wavefront characteristics at the interface. The transducer aperture was varied parametrically between 30 and 70 mm to assess the influence of source geometry on wave focusing, spatial pressure distribution, and energy delivery to the cartilage.

Spatial discretization for frequency-domain simulations was selected to satisfy stability and accuracy requirements, enforcing a CFL condition of 0.2. For time-explicit analysis, a DGM formulation was employed, with a corresponding CFL condition of 2/3. In both cases, the mesh was refined according to the local wavelength and excitation frequency to ensure adequate resolution of the propagating acoustic field, particularly within the cartilage region.

Boundary conditions were defined to approximate physiological and open-domain behavior. Soft sound boundary conditions were applied at external tissue interfaces to reduce artificial reflections and emulate free-field radiation. At the outer limits of the computational domain, absorbing boundaries were implemented to represent an unbounded medium and prevent spurious wave reflections. Additionally, a distributed load equivalent to 55 kg was applied to account for the average body weight above the knee, excluding the mass of the lower limb, following established modelling approaches[54].

Cartilage stimulation was quantified by performing a surface integration of the acoustic pressure field over the cartilage domain, yielding an averaged pressure value representative of the effective mechanical stimulus transmitted to the tissue.

### 5.3.5 Simulation Setup

The simulation framework was designed to systematically investigate acoustic wave propagation and its associated mechanical effects across multiple spatial scales using complementary numerical approaches. Three distinct analyses were employed: modal analysis to identify the intrinsic vibrational characteristics of the cellular system, harmonic analysis to evaluate frequency-dependent pressure–strain transmissibility between tissue and cellular levels, and time-explicit simulations to resolve transient wave propagation and assess the influence of nonlinear acoustic effects. This combined strategy enables a comprehensive characterization of both steady-state and transient responses, ensuring that the underlying physical mechanisms governing wave–structure interaction, energy transmission, and mechanotransduction stimulation are consistently captured.

#### 5.3.5.1 Modal analysis Setup

Modal analysis at the cellular scale was carried out in COMSOL Multiphysics using a fully coupled multiphysics framework integrating solid mechanics, shell mechanics, and acoustic pressure domains representative of the chondrocyte microenvironment. The nucleus, cytoplasm, and PCM were modelled as linear elastic solids governed by the Navier–Cauchy equation, thereby allowing the propagation of both compressional and shear wave modes within the intracellular and pericellular regions. The plasma membrane was represented as a thin structural shell, mechanically coupled to the cytoplasm through a structure–shell interface enforcing continuity of displacements and tractions. The surrounding ECM was treated as an acoustic medium using the Pressure Acoustics, Frequency Domain interface, in which wave propagation is governed by the Helmholtz equation.

Coupling between the fluid and solid domains was established through acoustic–structure boundary conditions applied at each interface, ensuring continuity of normal accelerations and equilibrium of normal stresses. This formulation enables bidirectional interaction, whereby acoustic pressure fluctuations in the ECM induce deformation in the solid regions, while structural vibrations generate secondary pressure fields within the fluid domain. The shell mechanics interface was likewise coupled to the adjacent solid domains to maintain mechanical consistency across the plasma membrane.

A modal analysis study was subsequently performed on the fully coupled system to determine the natural frequencies and corresponding eigenmodes of the composite cell–PCM–ECM structure.

#### 5.3.5.2 Harmonic Analysis Setup

Harmonic analysis was performed using a two-stage multiscale approach. Initially, simulations were conducted at the microscale using a RVE representing a single chondrocyte embedded within its PCM and ECM. Subsequently, the microscale response was coupled with a macroscale tissue-level acoustic model to evaluate pressure–strain transmissibility across spatial scales.

At the cellular level, harmonic excitation was applied within the ECM domain using the Pressure Acoustics, Frequency Domain interface in COMSOL. A harmonic acoustic pressure $p(f)$ of prescribed amplitude was imposed on one boundary of the periodic RVE, while Floquet periodic boundary conditions ensured that the domain represented an infinite periodic array of chondrocytes. The resulting acoustic field was coupled to the solid mechanics domain through acoustic–structure interfaces, enabling the transmission of pressure waves into elastic deformation of the cytoplasm, nucleus, PCM, and plasma membrane shell. The computed displacement field $u(\mathbf{x}, f)$ was used to evaluate the nuclear strain $\varepsilon(f)$ through surface-averaged strain measures at the nuclear boundary. By sweeping the excitation frequency,

the microscale frequency response function was defined as equation 232,

$$|H_{\varepsilon p}(f)| = \frac{\varepsilon(f)}{p(f)} \tag{232}$$

where $\varepsilon(f)$ denotes the induced nuclear strain and $p(f)$ the applied harmonic pressure amplitude. This formulation provides a direct measure of the efficiency with which an incident acoustic wave induces deformation at the nuclear level.

At the macroscale, harmonic simulations were carried out on a continuum representation of the knee joint using an equivalent pressure-acoustics formulation that accounts for anatomical geometry and relevant boundary conditions associated with ultrasound excitation. The corresponding transfer function was defined as equation 233,

$$|H_{pp}(f)| = \frac{p_{\text{cartilage}}(f)}{p_{\text{transducer}}(f)} \tag{233}$$

where $p_{\text{cartilage}}(f)$ represents the spatially averaged pressure within the cartilage region and $p_{\text{transducer}}(f)$ is the applied pressure amplitude at the transducer interface.

The coupling between scales was achieved by using the macroscale pressure field as input to the microscale response. Specifically, the local ECM pressure amplitude obtained from the macroscale model was mapped onto the corresponding RVE response function $H_{\varepsilon p}(f)$, enabling the evaluation of nuclear strain without explicitly resolving each individual cell. The overall multiscale transmissibility was therefore expressed as equation 234.

$$|H_{\text{macro}\rightarrow\text{micro}}(f)| = H_{\varepsilon p}(f) \cdot H_{pp}(f) \tag{234}$$

This two-level harmonic framework enables the quantification of pressure-to-strain transmission from the joint scale to the intracellular level, providing insight into how externally applied acoustic excitation propagates through cartilage and induces nuclear deformation through mechanotransduction in both healthy and osteoarthritic chondrocytes.

#### 5.3.5.3 Time-Explicit Simulations Setup

Time-domain simulations were carried out using an explicit DGM time-integration scheme to resolve the transient propagation of acoustic and elastodynamic waves within the coupled fluid–structure system. This formulation was selected due to its stability for high-frequency problems, its capacity to accurately resolve short-wavelength phenomena, and its suitability for handling strongly coupled interfaces between acoustic media and deformable solids.

Both linear and nonlinear acoustic formulations with dissipative effects were considered. In the linear regime, wave propagation in fluid domains was described by the classical acoustic wave equation

(equation 27), while solid regions, including cells, cartilage, and bone where applicable, were governed by linear elastodynamics. To assess the potential relevance of finite-amplitude effects, a nonlinear formulation based on the Westervelt equation (Equation 53) was also implemented in the fluid domains, incorporating quadratic pressure nonlinearity and frequency-dependent attenuation. A direct comparison between linear and nonlinear responses under identical excitation conditions enabled evaluation of whether nonlinear effects significantly influence the system response at the pressure levels of interest.

To minimize spurious reflections at the domain boundaries, perfectly matched layers were replaced by absorbing regions in the time-explicit framework. These layers were defined with progressively increasing attenuation to emulate an unbounded medium and ensure stable dissipation of outgoing waves across the full frequency range. This strategy is particularly effective for transient simulations, where broadband excitation and multiple reflections can otherwise compromise the solution.

The excitation was introduced as a transient pressure input, allowing full characterization of the temporal response. The resulting pressure, displacement, and strain fields were evaluated within the ECM, as well as at the cellular and nuclear scales. To excite a controlled frequency band while maintaining temporal localization, the input signal was defined as a Gaussian-modulated sinusoidal pulse in equation 235,

$$p(t) = p_0 \sin(2\pi f_0 t) e^{-\frac{(t-t_0)^2}{2\sigma^2}} \tag{235}$$

where $p_0$ is the peak pressure amplitude, $f_0$ the central excitation frequency, $t_0$ the temporal center of the pulse, and $\sigma$ controls both pulse duration and spectral bandwidth. This formulation allows selective excitation of the dominant vibrational modes while avoiding the unrealistic infinite bandwidth associated with impulsive loading, making it well suited for transient analyses of wave propagation and mechanotransduction response.

The adopted time-explicit framework enables a direct comparison between linear and nonlinear propagation regimes, providing a quantitative basis to assess the influence of nonlinear acoustic effects on stress transmission and nuclear strain under physiologically relevant excitation conditions.

## 5.3.6 Results

### 5.3.6.1 Microscale Modal Analysis

The modal response of the chondrocyte in the absence of the surrounding ECM is presented in Figure 79.

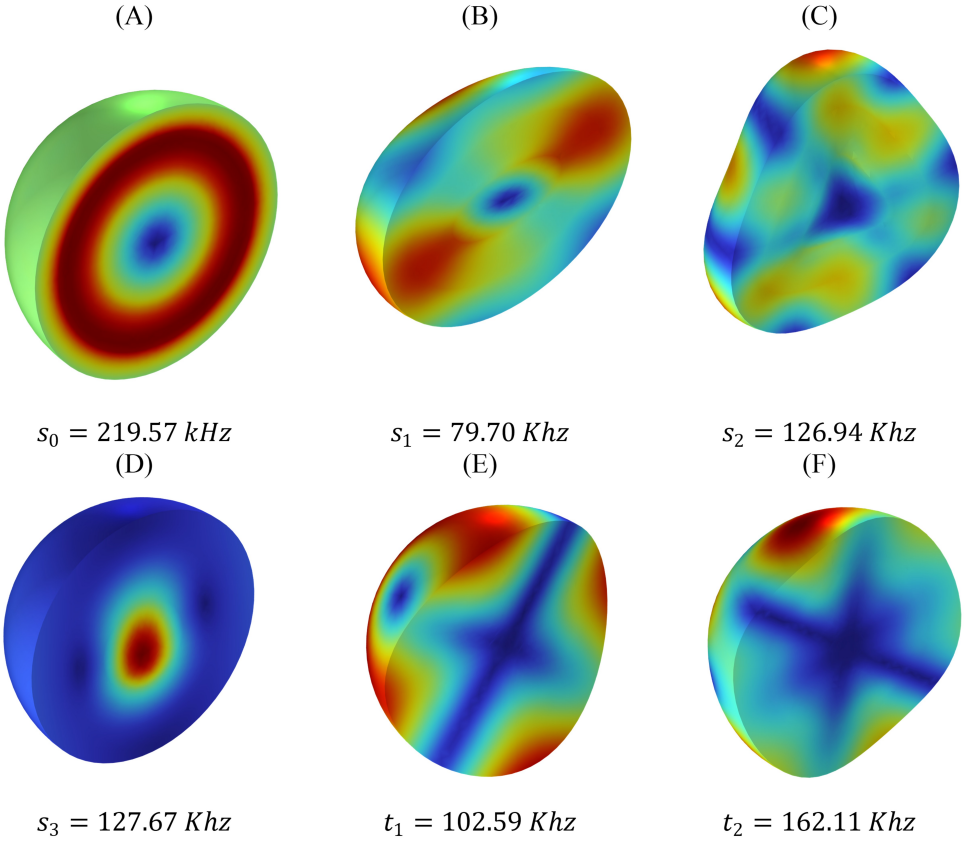



Figure 79: Fundamental vibration modes of healthy chondrocytes, without ASI, considering $r_c = 15$ μm, $r_n = 7.5$ μm, $t_{PCM} = 3$ μm and $t_{PM} = 7.5$ nm, where (A) is the breathing mode, (B) the first spherical mode, (C) the second spherical mode, (D) the third spherical mode, (E) the first torsion mode and (F) the second torsion mode.

The first six dominant vibration modes exhibit strong agreement with classical solutions for free elastic spheres[55], comprising spheroidal ($s_n$) and torsional ($t_n$) modes. Spheroidal modes involve coupled radial and tangential motion, whereas torsional modes are characterized by purely shear deformation without volumetric change. Among these, the $s_0$ mode corresponds to the breathing mode, defined by uniform radial expansion and contraction. However, the $s_3$ mode demonstrates the most significant mechanical interaction with the nucleus, producing pronounced deformation within this region and therefore representing the most relevant mode for potential mechanotransduction stimulation.

The inclusion of the ECM as a surrounding fluid medium modifies the modal characteristics of the system, as shown in Figure 80.

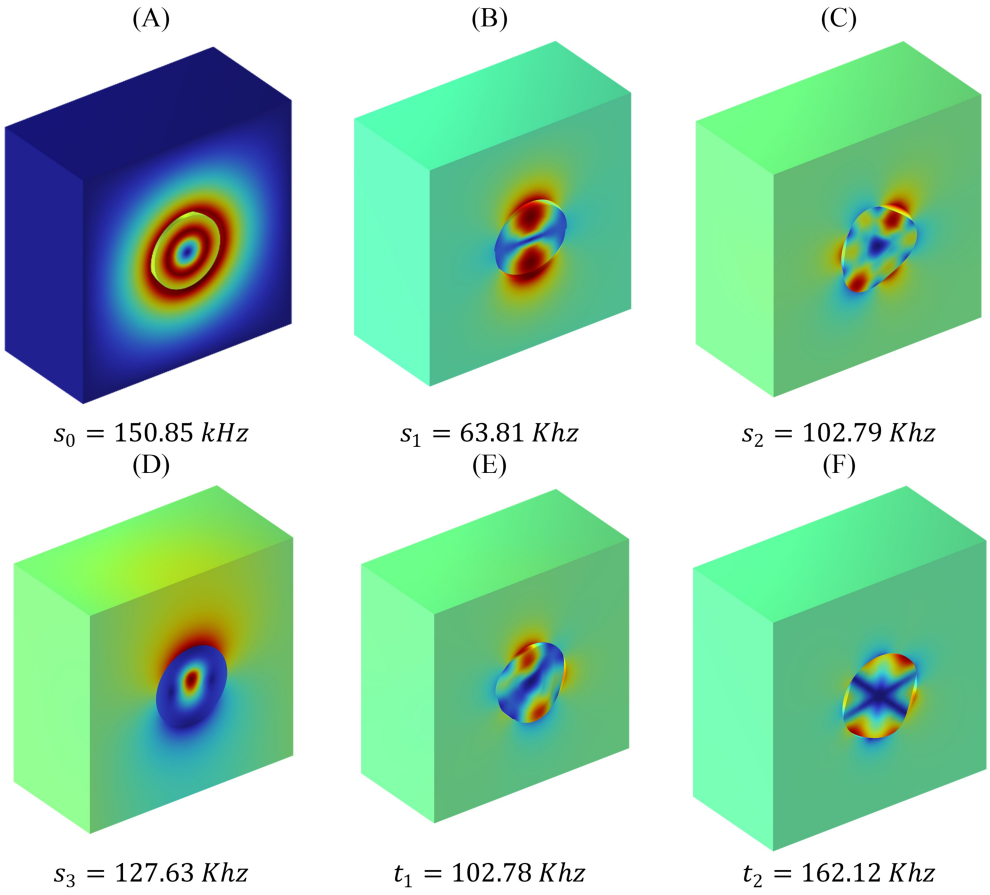



Figure 80: Fundamental vibration modes of healthy chondrocytes, with ASI, considering $r_c = 15$ µm, $r_n = 7.5$ µm, $t_{PCM} = 3$ µm, $t_PM = 7.5$ nm and $d_c = 60$ µm where (A) is the breathing mode, (B) the first spherical mode, (C) the second spherical mode, (D) the third spherical mode, (E) the first torsion mode and (F) the second torsion mode.

The introduction of acoustic–structure interaction leads to fluid loading and increased damping, which attenuate the discrete nature of the resonance spectrum. In this configuration, the system exhibits broadened, highly damped responses rather than well-defined eigenmodes. This effect is particularly evident for the lower-order spheroidal modes ($s_0$, $s_1$, and $s_2$), whose predominantly radial motion results in strong coupling with the fluid domain. In contrast, higher-order and shear-dominated modes, including $s_3$, $t_1$, and $t_2$, remain comparatively unaffected, as their deformation fields are more localized and exhibit weaker interaction with the surrounding medium. Notably, the $s_3$ mode shows minimal variation in both frequency and damping, reinforcing its relevance as the dominant nuclear-coupled mode.

The modal behavior of osteoarthritic chondrocytes, illustrated in Figure 81, follows a similar pattern.

All eigenfrequencies shifted toward lower values relative to the healthy case. This reduction is consistent with the combined effects of cellular hypertrophy, which increases the effective mass, and mechanical softening associated with cytoskeletal degradation, which reduces stiffness. Despite this shift, the $s_3$ mode remains the most significant contributor to nuclear deformation, maintaining its role as the primary mechanotransduction mode.

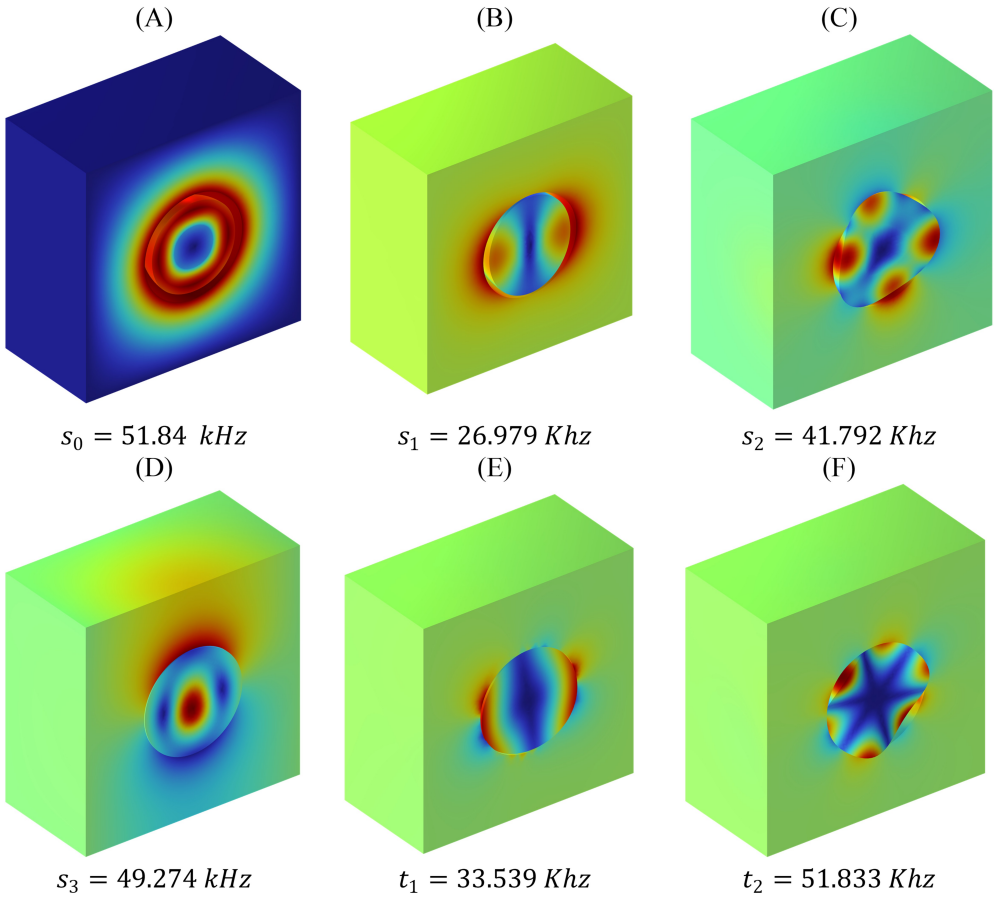



Figure 81: Fundamental vibration modes of OA chondrocytes, with ASI, considering $r_c = 15$ µm, $r_n = 7.5$ µm, $t_{PCM} = 3$ µm, $t_PM = 7.5$ nm and $d_c = 75$ µm, where (A) is the breathing mode, (B) the first spherical mode, (C) the second spherical mode, (D) the third spherical mode, (E) the first torsion mode and (F) the second torsion mode.

While previous studies have focused on ultrasound stimulation in the MHz range (typically around $5$ MHz for suspended cells)[56,57], the present results indicate that the dominant nuclear-coupled mode occurs at substantially lower frequencies within the kHz range (healthy: 63.81-162.12 kHz; OA: 26.979-51.84 kHz). This discrepancy arises from the inclusion of the PCM and ECM, which introduce additional loading and damping effects. Consequently, although higher frequencies may excite alternative vibrational modes, they are unlikely to efficiently induce nuclear strain under in situ conditions. These findings suggest that excitation strategies targeting the kHz frequency range may be more effective for achieving nucleus-driven mechanotransduction responses in cartilage.

#### 5.3.6.2 Microscale Frequency Response

The harmonic response of the RVE representing a healthy chondrocyte is shown in Figure 82.

The resulting FRF reveals a clear hierarchy in terms of nuclear strain amplification across the identified vibrational modes. The $s_0$ (breathing) mode exhibits the largest response, followed by $s_1$ and $t_2$, whereas

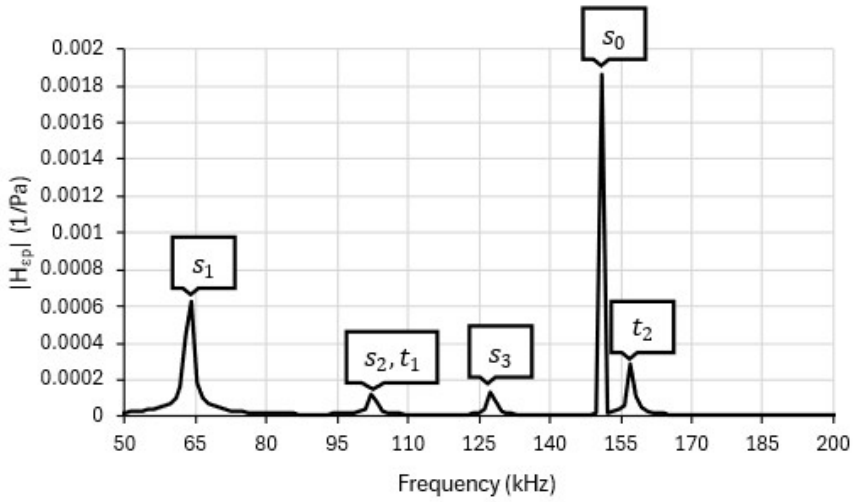



Figure 82: Frequency response of a healthy chondrocyte, considering $r_c = 7.5$ μm, $r_n = 3.75$ μm, $t_{PCM} = 3$ μm, $t_PM = 7.5$ nm and $d_c = 60$ μm.

the $s_3$ mode, despite being identified in the modal analysis as the most strongly coupled to the nucleus, produces a comparatively lower peak. The $s_2$ and $t_1$ modes display similar amplitudes and are therefore considered together. These results indicate that, under harmonic excitation, the overall magnitude of nuclear deformation is dominated by the breathing mode, while modes such as $s_3$ remain structurally relevant due to their localized deformation patterns.

A parametric analysis was conducted to evaluate the influence of geometrical variations on the FRF, as presented in Figure 84.

The parametric FRF maps reveal how each geometric parameter subtly or dramatically bends the acoustic identity of a healthy chondrocyte. When the chondrocyte radius increases (figure 84 A), the resonance bands slide unmistakably toward lower frequencies, carving diagonal streaks across the map. This happens because enlarging the cell boosts its effective acoustic mass and lengthens the wave-propagation path, lowering the natural frequencies in a way that mirrors a classic mass–spring oscillator. These size-driven shifts are substantial, tens of kilohertz for just a few microns, and demonstrate that radius is the dominant tuner of the cell's vibroacoustic behavior.

In contrast, altering the plasma membrane thickness (figure 84 B) from $5$ to $10$ nm barely budges the modal frequencies: the resonance lines stay almost perfectly vertical, revealing that the ultra-thin membrane has minimal influence on global mechanical impedance. It may tweak amplitude or damping slightly, but it cannot change the frequencies at which modes $s_1$, $s_2/t_1$, $s_3$, $s_0$ or $t_2$ emerge.

The PCM thickness (figure 84 C) plays a more nuanced role: increasing it from 2 to 4 μm leads to modest frequency shifts (gentler slopes compared to figure 84 A) because the PCM adds both mass and compliance around the cell. Modes that involve strong interaction at the cell–PCM boundary (such as $s_1$ or

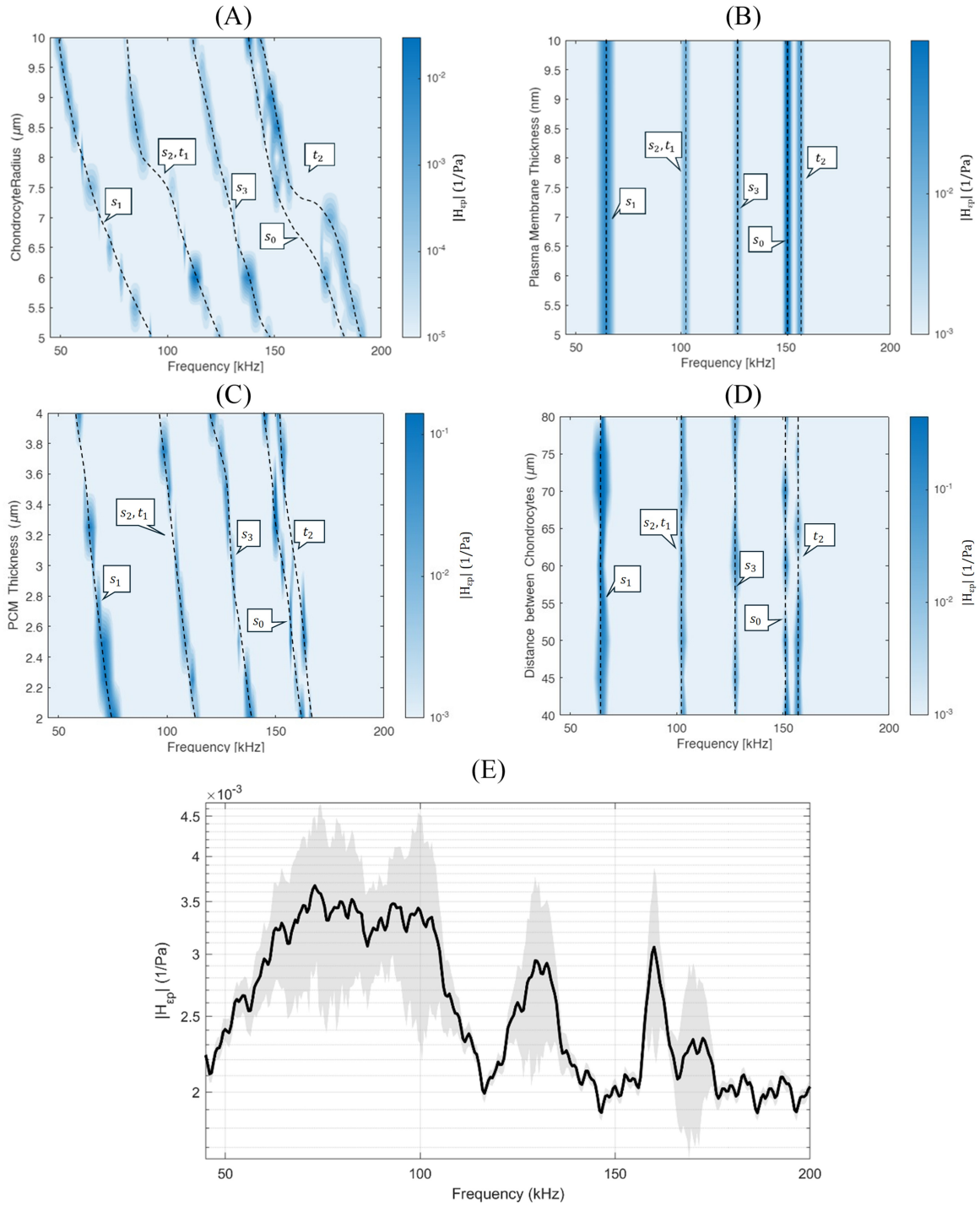



Figure 83: Parametric FRF of healthy chondrocytes where (A) $r_c[5;10]$ μm, (B) $t_{PM}[5;10]$ nm, (C) $t_{PCM}[2;4]$ μm, (D) $d_c[40;80]$ μm and (E) the average FRF plot of all the results, including standard deviation.

$s_2/t_1$) feel this effect more strongly, while others remain comparatively stable. PCM thickness therefore acts as a secondary fine-tuning parameter, modifying not only frequency but also the intensification or suppression of specific modes.

Finally, varying the distance between chondrocytes (figure 84 D) does not alter the modal frequencies at all, the resonance bands remain vertical, signalling that each chondrocyte's natural modes are intrinsic

and not dictated by neighbor proximity. What changes instead is the amplitude of the response: shorter inter-cell distances strengthen near-field acoustic coupling and multiple scattering, producing more intense peaks, while larger spacing reduces collective amplification.

In figure 84 E the main resonance bands remain within stable frequency ranges, confirming that the spectral structure of the healthy chondrocyte is preserved despite parameter changes. Greater dispersion is observed in the lower-frequency band, consistent with the strong sensitivity of the first structural mode to variations in cell radius and PCM thickness. Higher-frequency modes show comparatively limited spread, indicating reduced sensitivity to geometric perturbations. The FRF analysis indicate that chondrocyte radius and PCM thickness predominantly determine the location of the resonant modes, whereas plasma membrane thickness and intercellular spacing primarily modulate the amplitude and collective reinforcement of those modes.

The harmonic response of OA chondrocytes, shown in Figure 84, exhibits a significant redistribution of modal contributions.

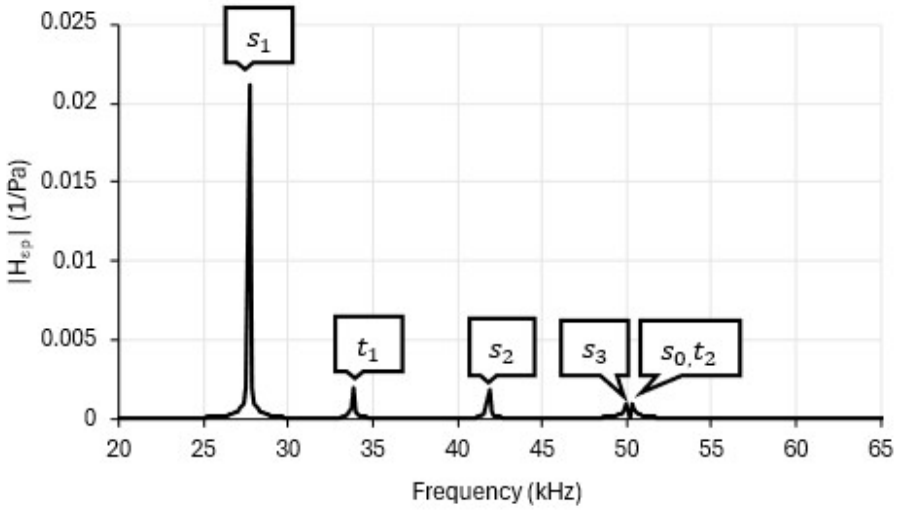



Figure 84: Frequency response of a OA chondrocyte, considering $r_c = 15$ μm, $r_n = 7.5$ μm, $t_{PCM} = 2$ μm, $t_{PM} = 7.5$ nm and $d_c = 75$ μm.

For OA chondrocytes, the FRF analysis revealed a clear reorganization of the modal hierarchy when compared with healthy cells. The $s_1$ mode became the dominant contributor, with a much higher response of 0.0212 $Pa^{-1}$, over an order of magnitude larger than any mode in the healthy configuration. This was followed, at a much lower level, by $t_1$ (0.00197 $Pa^{-1}$) and $s_2$ (0.00191 $Pa^{-1}$), while $s_3$ and the coupled $s_0$. $t_2$ responses were comparatively small and very similar (0.000982 $Pa^{-1}$ and 0.000958 $Pa^{-1}$). Thus, whereas in healthy cells the breathing mode $s_0$ drove the largest dynamic nuclear response under harmonic pressure excitation, in OA cells this role is effectively taken over by the $s_1$ mode, with the $s_1$ nucleus compressing mode remaining dynamically subdominant in both conditions. This shift in

modal dominance with disease state suggests that osteoarthritic hypertrophy and softening not only lower the natural frequencies but also redistribute how external acoustic energy is partitioned among vibrational modes, potentially altering which patterns of deformation are most efficiently excited in the nuclear region.

The corresponding parametric analysis for OA conditions, presented in Figure 85.

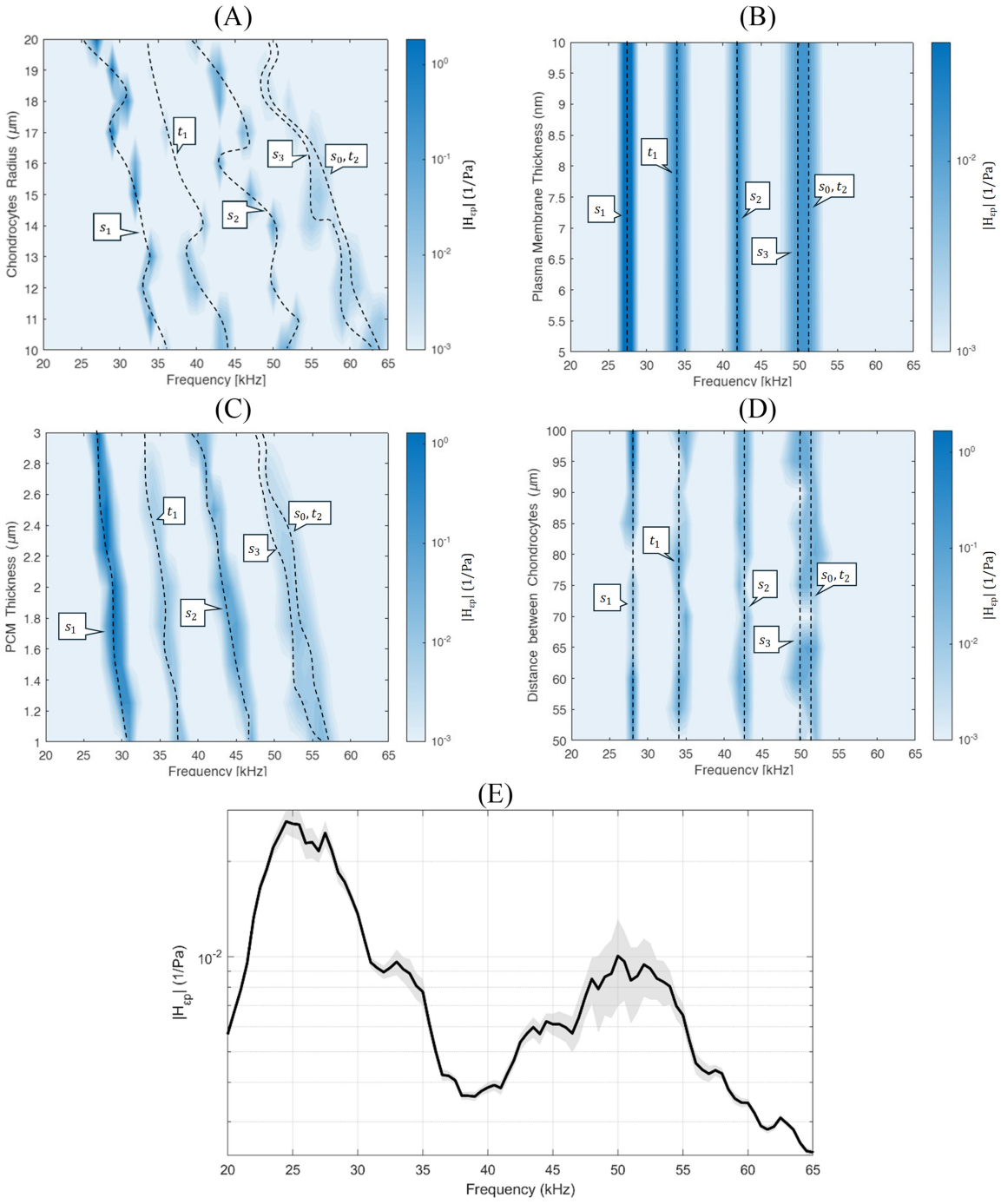



Figure 85: Parametric FRF of OA chondrocytes where (A) $r_c[10;20]$ μm, (B) $t_P M[5;10]$ nm , (C)$t_P CM[1;3]$ μm, (D) $d_c[50;100]$ μm and (E) the average FRF plot of all the results, including standard deviation.

When comparing the parametric frequency-response maps of OAchondrocytes with those obtained

for healthy cells, several systematic mechanical shifts become evident. First, variations in chondrocyte radius (figure 85 A) produce the same characteristic diagonal modal trajectories observed in healthy tissue; however, all modal branches ($s_1$,$t_1$, $s_2$, $s_3$, $s_0/t_2$) are displaced toward substantially lower frequencies, consistent with the well-documented reductions in intracellular stiffness and altered cytoskeletal organization associated with OA[58]. These downshifts, together with the visibly broader and less sharply defined amplification zones, indicate increased damping and mechanical heterogeneity.

Similar to the healthy case, variations in plasma membrane thickness (figure 85 B) produce nearly vertical modal lines, confirming that the membrane remains mechanically insignificant in determining the eigenfrequency structure.

Differences in PCM thickness (figure 85 C) again exert a secondary tuning effect, but in OA tissue this influence becomes more pronounced: modal frequencies shift more noticeably as PCM thickness increases, and amplitude patterns are more sensitive, indicating a heightened reliance on PCM mechanical properties due to reduced intrinsic stiffness of the cell body.

Finally, changes in inter-chondrocyte distance (figure 85 D) continue to leave modal frequencies largely invariant, demonstrating that resonance is an intrinsic single-cell property in both healthy and OA tissue. However, OA samples display more irregular amplitude distributions and weaker intercellular coupling signatures, consistent with the disrupted ECM organization and impaired mechanical connectivity characteristic of OA cartilage.

Comparison between healthy and OA conditions confirms a global shift of the resonance spectrum toward lower frequencies, accompanied by increased damping and reduced modal sharpness. While the qualitative role of each geometric parameter remains consistent, osteoarthritic chondrocytes exhibit greater sensitivity to structural variations and a stronger dependence on PCM mechanics. These findings are consistent with the biomechanical alterations associated with OA, including cytoskeletal degradation, matrix disruption, and increased cellular heterogeneity[36,37,58].

#### 5.3.6.3 Macroscale Frequency Response

The transfer function magnitude $H_{pp}$ from the transducer to the cartilage for Patient A (figure 86) exhibits a consistent frequency-dependent behavior across transducer diameters ranging from 30-75 mm.

For smaller diameters (30–55 mm), moderate amplitude variations are observed, particularly within the low-frequency range (20–60 kHz), where peak values show some sensitivity to source–tissue separation. However, for diameters exceeding approximately 60 mm, the response curves converge, and

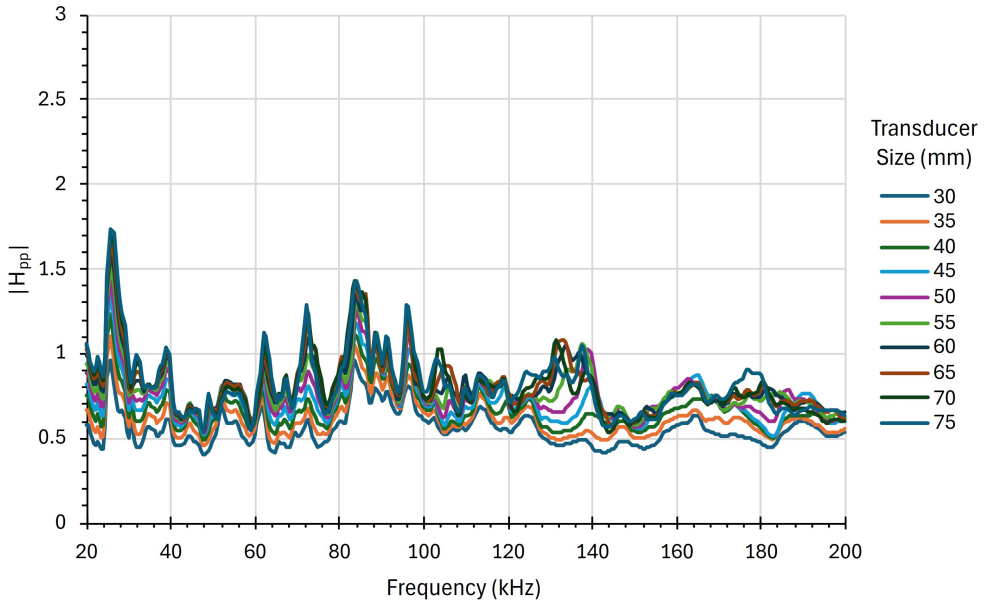



Figure 86: Transfer function magnitude $|H_{pp}|$ from transducer to cartilage for Patient A as a function of frequency for varying transducer diameters ($30$–$75$ mm).

differences attributable to transducer size become negligible across the full frequency spectrum. In this regime, both the magnitude and location of dominant peaks remain largely unchanged, indicating that once a sufficient propagation distance is achieved, further increases in transducer separation do not significantly affect acoustic transmissibility to the cartilage.

A comparable trend was observed across all patients (section C.2). While variations in absolute amplitude and minor peak shifts were present due to anatomical differences, the overall frequency-dependent profile and convergence behavior at larger transducer distances remained consistent. In all cases, the primary amplification regions occurred within similar frequency bands, and distance-related effects diminished beyond approximately 60 mm. These findings suggest that, within the investigated range, transducer positioning beyond this threshold has limited influence on the frequency-domain transmission characteristics, supporting the robustness of the observed acoustic response across patient-specific geometries.

The spatial distribution of the acoustic field, represented by the RMS pressure maps for Patient A (figure 87), provides further insight into wave propagation within the knee joint.

At lower excitation conditions, the acoustic field is relatively diffuse, with moderate pressure levels distributed across soft tissues and progressively attenuating toward the cartilage interfaces. This behavior indicates that wave propagation is primarily governed by bulk tissue properties, including impedance and attenuation.

With increasing excitation, localized regions of higher pressure become apparent, particularly near

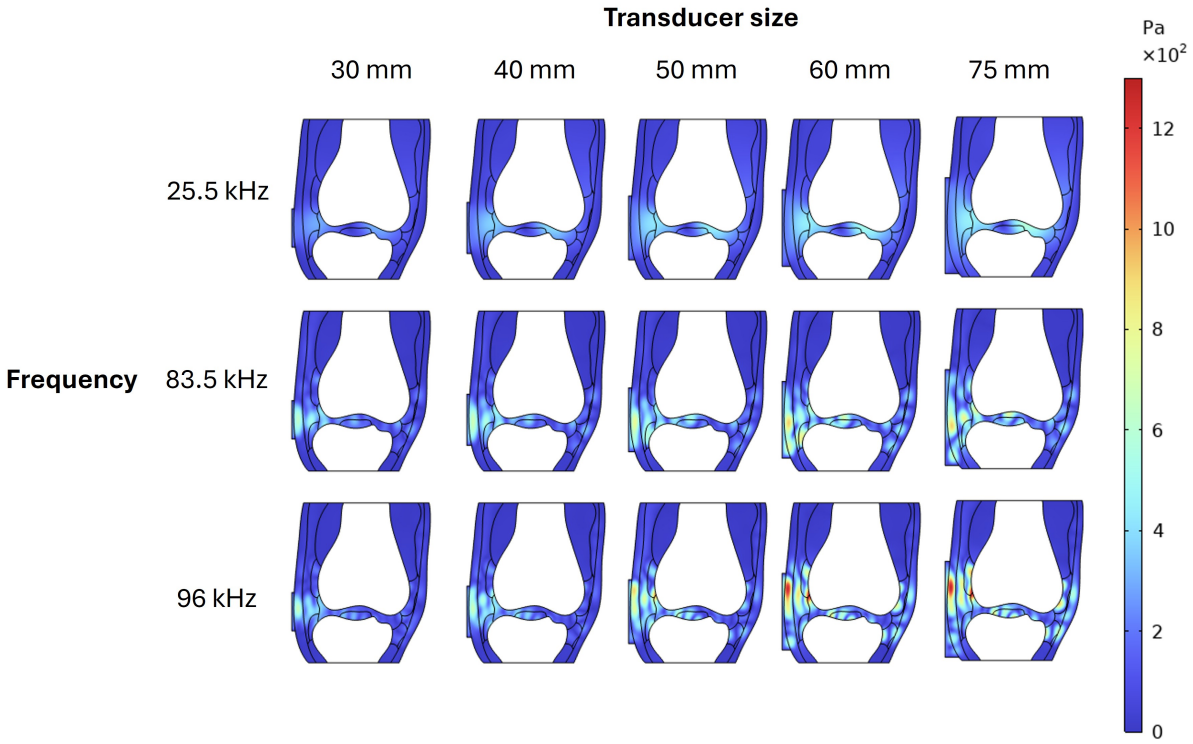



Figure 87: RMS acoustic pressure distribution for Patient A under varying excitation conditions. The color scale represents pressure amplitude (Pa $\times 10^2$).

tissue interfaces and adjacent to cartilage surfaces. These localized amplifications are indicative of constructive interference and reflection phenomena arising from impedance discontinuities, especially at transitions between soft tissues and bone. The concentration of acoustic energy within the joint space highlights the influence of anatomical geometry in guiding wave propagation toward the cartilage. Although the general propagation pattern remains consistent, variations in excitation parameters lead to changes in the magnitude and spatial localization of peak pressures, suggesting that specific conditions can enhance energy focusing within the joint cavity. Nevertheless, the overall transmission pathway remains structurally stable, indicating that the underlying propagation mechanism is relatively insensitive to moderate variations in excitation.

The RMS pressure distributions consistently demonstrate that acoustic energy reaches the cartilage region with a spatially heterogeneous profile influenced by both tissue interfaces and geometric confinement. This behavior was observed across all patients (section C.3) and is in agreement with the trends identified in the frequency-domain analysis, confirming that macroscale propagation effectively delivers acoustic energy to the cartilage while exhibiting localized amplification effects governed by anatomical structure.

The average transfer function across all patients (figure 88) reveals a clear frequency-dependent decay in transmissibility.

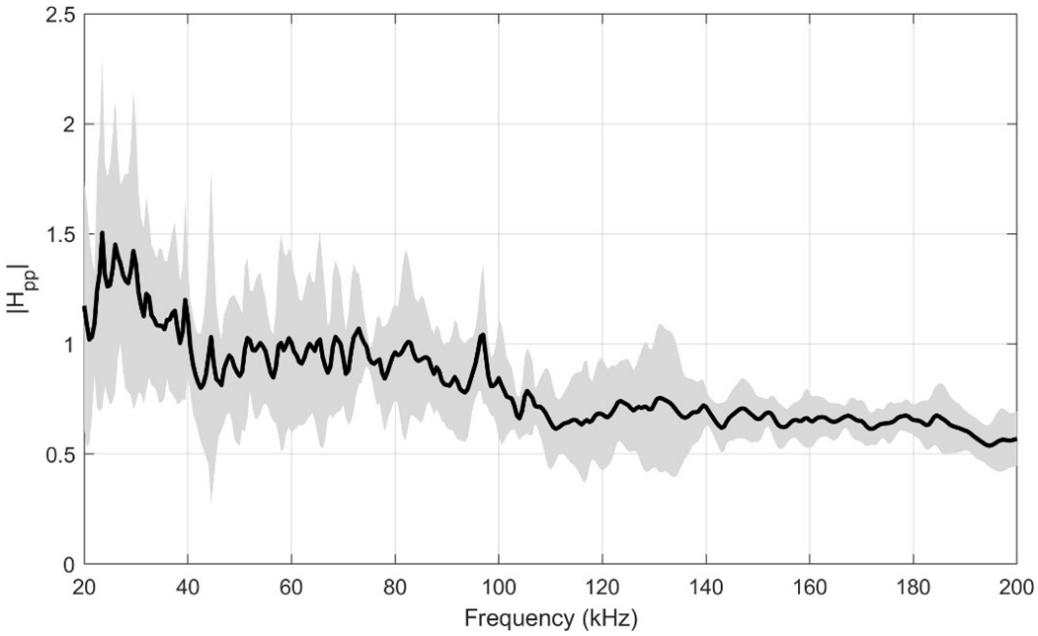



Figure 88: Average transfer function magnitude $H_{pp}$ to cartilage across all patients as a function of frequency. The solid line represents the mean response, and the shaded region indicates inter-patient variability.

The highest values occur in the low-frequency range (approximately 20–40 kHz), where peak magnitudes approach 1.4–1.5, indicating strong transmission of acoustic pressure to the cartilage. This region also exhibits the greatest inter-patient variability, reflecting increased sensitivity to anatomical differences at lower frequencies. Between approximately 40 and 100 kHz, the response stabilizes near unity, with reduced dispersion and moderate fluctuations. A secondary amplification is observed around 90–100 kHz, although less pronounced than in the low-frequency regime. At higher frequencies (above approximately 110–120 kHz), the transfer function gradually decreases, approaching values between 0.55 and 0.7, accompanied by reduced variability. This trend indicates increasing attenuation and diminished sensitivity to anatomical variability at higher frequencies.

Overall, the averaged response demonstrates that acoustic transmissibility to cartilage is more efficient at lower frequencies, while higher frequencies are progressively attenuated and exhibit reduced dependence on patient-specific anatomical features.

#### 5.3.6.4 Multiscale Coupled Frequency Response

The multiscale coupled transfer function $H_{macro \rightarrow micro}$ demonstrates a clear dependence on both frequency and cellular condition (figure 89), illustrating how microstructural alterations influence the transmission of acoustic pressure from the joint level to nuclear deformation.

For healthy chondrocytes (Figure 89A), the response is characterized by a broad amplification region spanning approximately 50 to 100 kHz, with a well-defined maximum in the range of 70–85 kHz. Within

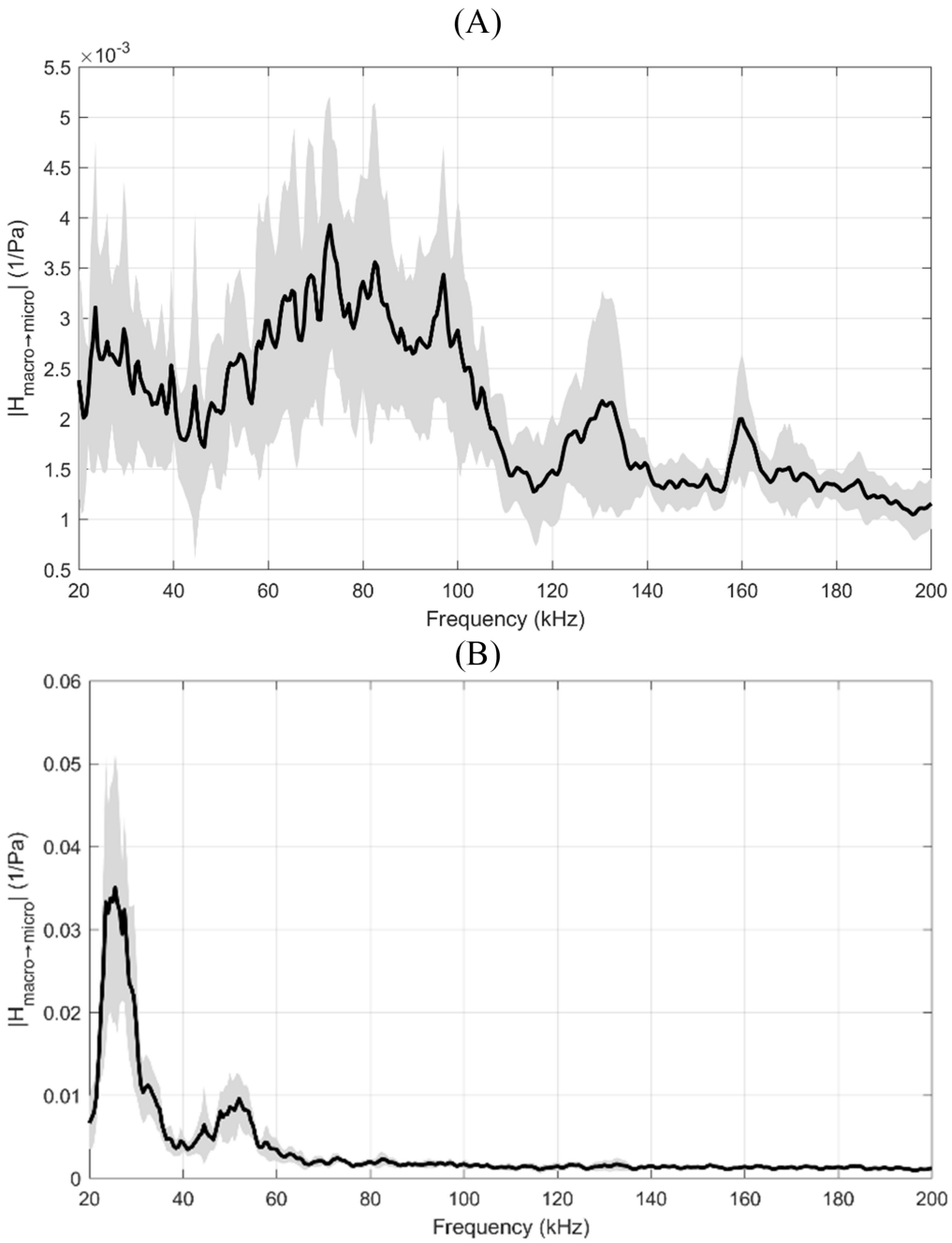



Figure 89: Multi-scale coupled transfer function $H_{macro \rightarrow micro}$ as a function of frequency where (A) is for healthy chondrocytes and (B) OA chondrocytes. The solid line represents the mean response across patients, and the shaded region indicates inter-patient variability.

this band, the transfer function attains magnitudes on the order of $10^{-3}$ $Pa^{-1}$, indicating effective conversion of macroscopic pressure fluctuations into nuclear strain. Although some inter-patient variability is observed, particularly between 60 and 90 kHz, the overall response profile remains consistent, suggesting that this amplification region is relatively insensitive to anatomical differences. At higher frequencies (above approximately 110 kHz), the transmissibility decreases progressively and approaches a low-amplitude regime, reflecting increased attenuation and reduced modal interaction.

In contrast, osteoarthritic chondrocytes (Figure 89B) exhibit a markedly different behavior. The response is dominated by a narrow peak located in the low-frequency range, approximately between 20 and 30 kHz, with amplitudes reaching 0.03–0.05 $Pa^{-1}$. Beyond 40 kHz, the transfer function decreases rapidly and remains close to baseline across the remaining frequency range. This indicates that, under osteoarthritic conditions, the efficiency of pressure-to-strain transmission is concentrated on a limited low-frequency window, while higher-frequency excitation contributes minimally to nuclear deformation.

These differences are consistent with disease-related modifications in cellular morphology and mechanical properties. In healthy chondrocytes, the broader amplification band reflects a more distributed modal response, particularly within the mid-frequency range associated with spheroidal deformation modes. In osteoarthritic cells, hypertrophy and reduced stiffness shift the dynamic behavior toward lower frequencies, resulting in a more localized and dominant low-frequency response while suppressing higher-frequency contributions.

Overall, the multiscale analysis indicates that the frequency at which acoustic energy is most effectively converted into nuclear strain is strongly dependent on the physiological state of the tissue. Healthy cartilage exhibits optimal responsiveness in the mid-frequency range, whereas osteoarthritic tissue shows enhanced sensitivity at lower frequencies. These findings suggest that optimal excitation parameters for ultrasound-based stimulation should be adapted to the mechanical condition of the target tissue.

#### 5.3.6.5 Multiscale Coupled Time-explicit Response

Time-explicit simulations were performed to evaluate whether finite-amplitude nonlinear propagation significantly influences the acoustic response under the excitation conditions identified as optimal from the frequency-domain analysis (figure 90). For each configuration, three closely spaced excitation frequencies ($0.9f_0$, $f_0$, and $1.1f_0$) were considered to assess sensitivity in the vicinity of the operating point, and the resulting spectra were compared for linear and nonlinear acoustic formulations.

In both the healthy case (Figure 90A, $f_0$ ≈73 kHz) and the osteoarthritic case (Figure 90B, $f_0$ ≈25.5 kHz), the spectral response is dominated by the fundamental excitation frequency, with

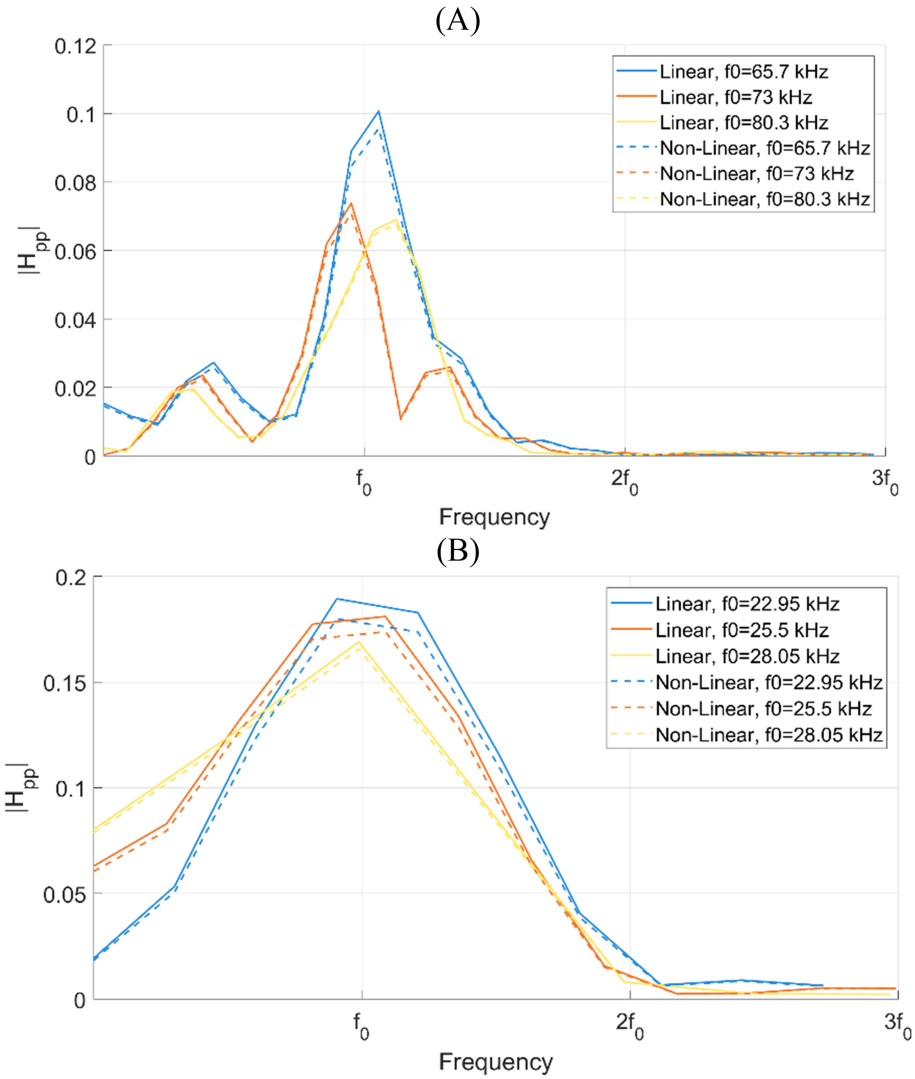



Figure 90: Time-explicit spectral response under linear and nonlinear acoustic propagation for excitation frequencies $0.9f_0$, $f_0$, and $1.1f_0$ for (A) healthy patient A and (B) patient A with OA.

negligible energy observed at higher harmonics. The nonlinear simulations do not exhibit significant harmonic generation at frequencies near $2f_0$ or $3f_0$, and the spectral profiles closely match those obtained under linear assumptions for all excitation conditions. These results indicate that, within the investigated pressure amplitudes and propagation distances, nonlinear effects such as waveform distortion and harmonic generation are minimal. Consequently, linear acoustic modelling provides an adequate description of the system response for the conditions relevant to mechanotransduction stimulation.

The simulations also highlight sensitivity to excitation frequency in a narrow region around $f_0$. This effect is more pronounced in the healthy configuration, where the response exhibits a sharp peak at the fundamental frequency and decreases rapidly for $0.9f_0$ and $1.1f_0$, consistent with a resonance-driven amplification mechanism previously identified in the harmonic analysis. In contrast, the osteoarthritic

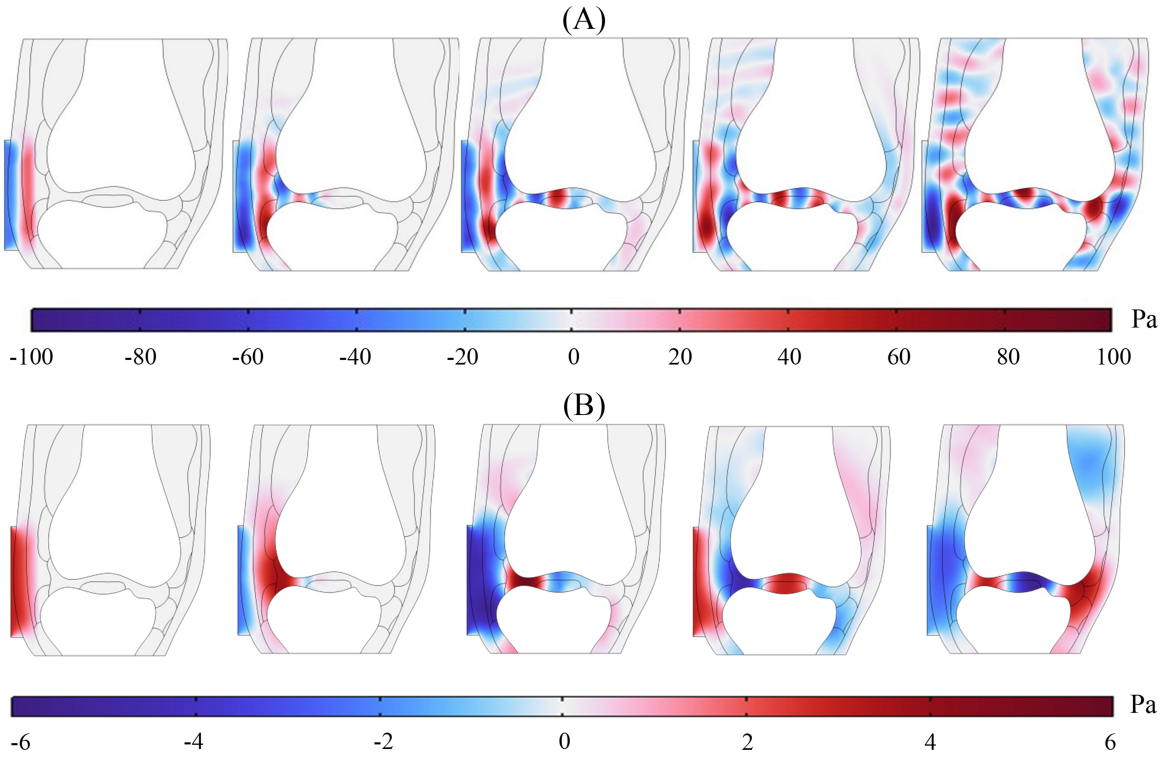



Figure 91: Time-explicit acoustic pressure field showing wave propagation across the knee joint for patient A using ideal $f_0$ for (A) Healthy Patients and (B) OA Patients. The color scale represents instantaneous pressure (Pa).

configuration displays a broader response around the fundamental frequency, indicating reduced frequency selectivity. This behavior is consistent with increased damping and structural heterogeneity associated with osteoarthritic tissue. In both cases, the close agreement between linear and nonlinear results confirms that the dominant factor governing the response is frequency-dependent transmissibility rather than nonlinear propagation.

The transient pressure fields shown in figure 91 illustrate the spatial evolution of the acoustic wave as it propagates through the layered structures of the knee.

In both configurations, the wave originates at the soft-tissue boundary and travels toward the joint cavity, interacting with multiple interfaces characterized by impedance contrasts.

In the healthy configuration (figure 91A), higher pressure amplitudes are observed, along with well-defined oscillatory patterns as the wave traverses muscle, adipose tissue, and cartilage. Within the joint space, alternating compressive and rarefaction regions indicate strong reflections and interference between cartilage and adjacent bone structures. This results in partial confinement of acoustic energy within the joint cavity and localized amplification along cartilage interfaces. The increasing spatial regularity of these patterns with depth is consistent with resonance-driven transmission mechanisms identified in the frequency-domain analysis.

In contrast, the osteoarthritic configuration (figure 91B) exhibits reduced pressure amplitudes and a

more diffuse propagation pattern. Oscillatory features within the joint space are less pronounced, and the wave attenuates more rapidly as it propagates. This behavior reflects diminished constructive interference and weaker confinement of acoustic energy within the cartilage region. The smoother spatial gradients and lower amplitudes are consistent with the altered mechanical properties and increased damping associated with osteoarthritic tissue, which shift the response toward lower frequencies and reduce high-frequency amplification.

In both cases, acoustic energy is transmitted through superficial tissues and reaches the joint cavity, confirming the feasibility of delivering mechanical stimuli to cartilage at the macroscale. However, the spatial distribution and intensity of the pressure field are strongly influenced by tissue properties. The healthy knee supports more structured, standing-wave-like patterns, whereas the osteoarthritic knee exhibits a more attenuated and less resonant response. These observations are consistent with the multiscale transfer function results, demonstrating that disease-related changes affect not only frequency-domain behavior but also the spatial organization of acoustic energy within the joint.

### 5.3.7 Discussion

The results of this study demonstrate that acoustic stimulation of cartilage is strongly dependent on frequency, sensitive to disease-induced alterations in cellular mechanics[36,37], and predominantly governed by linear wave propagation under clinically relevant pressure levels. At the cellular scale, modal analysis showed that chondrocytes exhibit spheroidal and torsional vibration modes consistent with elastic sphere behavior. Among these, the ($s_1$) spheroidal mode was identified as the most effective in inducing nuclear deformation, and thus represents the primary candidate for mechanotransduction stimulation. Parametric investigations further indicated that chondrocyte radius is the dominant factor controlling modal frequency, while PCM thickness provides secondary modulation, and plasma membrane thickness and intercellular spacing have negligible influence on the resonance structure. In osteoarthritic cells, modal frequencies shift toward lower values due to hypertrophy and reduced stiffness, confirming a disease-dependent dynamic response. Frequency-response analysis revealed that nuclear strain amplification occurs over finite frequency bands rather than at isolated frequencies, with healthy cells exhibiting a broader mid-frequency amplification region and osteoarthritic cells showing a dominant low-frequency peak with diminished sensitivity at higher frequencies.

At the macroscale, simulations of acoustic propagation through layered knee tissues showed that energy reaches the cartilage with a spatially heterogeneous distribution governed by impedance contrasts and anatomical geometry. Beyond a critical transducer distance, transmissibility stabilizes,

indicating reduced sensitivity to source positioning. When coupled across scales, the results confirmed that disease state significantly modifies pressure-to-strain transmission: healthy cartilage supports broader amplification in the 70–85 kHz range, whereas osteoarthritic tissue concentrates the response within a narrower low-frequency band (20–30 kHz). Time-explicit simulations further demonstrated that nonlinear acoustic effects are negligible under the considered excitation conditions, with minimal harmonic generation observed. This confirms that linear acoustic formulations are sufficient to describe wave propagation and mechanotransduction response within the investigated regime.

The frequency ranges identified in this study differ substantially from those typically employed in cartilage and osteoarthritis research. Conventional therapeutic ultrasound protocols generally operate within the MHz range, commonly between 1 and 3 MHz[5]. Randomized controlled trials frequently utilize continuous ultrasound at approximately 1 MHz with intensities of 1–2 $W/cm^2$ and treatment durations of 5–10 minutes[32], while extended treatments may employ 3 MHz at lower intensities over longer durations[59]. LIPUS protocols are also predominantly based on empirically selected frequencies between 1.0 and 1.5 MHz[57,60], with similar values used in experimental studies[61]. More recent cartilage-targeted approaches have explored lower frequencies, such as 0.6 MHz, to improve penetration and direct stimulation[62].

However, these conventional frequency choices are not aligned with the mechanistic findings of the present study. Higher-frequency ultrasound is known to attenuate more rapidly and is typically associated with superficial effects, whereas lower frequencies enable deeper penetration[5]. Clinical evidence reflects this limitation: systematic reviews report only modest improvements in pain with conventional ultrasound, with low overall certainty of evidence[32], and large controlled trials using LIPUS devices have not demonstrated significant clinical benefits[63]. Furthermore, current clinical guidelines often conclude that there is insufficient evidence to support therapeutic ultrasound as a primary intervention compared to exercise or weight management strategies[64]. These outcomes may be partly explained by the mismatch between applied frequencies and the intrinsic resonant behavior of chondrocytes, as well as the reliance on thermal or diathermic mechanisms rather than targeted mechanical stimulation.

In contrast, vibration-based approaches for cartilage stimulation typically operate at much lower frequencies, ranging from 5–20 Hz in whole-body vibration studies[65,66] to a few hundred hertz in direct cellular stimulation experiments[67]. While these approaches have demonstrated some biological effects, they remain significantly below the kilohertz frequency range identified in the present model. The predicted optimal bands of 20–30 kHz (OA) and 70–85 kHz (healthy) therefore occupy an intermediate and largely unexplored region between low-frequency mechanical loading and conventional MHz

ultrasound. This suggests that resonance-based stimulation within this range may offer improved efficiency in inducing mechanotransduction responses.

Notably, similar frequency ranges are already employed in other biomedical applications, such as transdermal ultrasound and sonophoresis, where 20–200 kHz is commonly defined as low-frequency ultrasound[68]. Clinical prototypes operating within 20–100 kHz have been developed for applications such as chronic wound treatment, aiming to deliver non-thermal and non-cavitational stimulation under controlled conditions[69]. These examples support the feasibility of implementing ultrasound systems within the frequency ranges identified in this study.

A key contribution of this work is the development of a unified multiscale computational framework that directly links macroscale acoustic propagation within a patient-specific knee geometry to mechanotransduction strain at the level of the chondrocyte nucleus. While previous studies have investigated either cellular-scale dynamics[13] or tissue-scale wave propagation[1,70], the integration of modal analysis, frequency-response characterization, and macro-to-micro coupling within a single framework represents a significant methodological advancement. This approach provides a mechanistically grounded basis for selecting stimulation parameters and highlights the importance of disease-specific tuning. Additionally, the comparison between linear and nonlinear formulations strengthens the modelling assumptions by demonstrating that nonlinear effects are negligible under the relevant conditions.

Despite these contributions, several limitations should be acknowledged. The study is based entirely on computational modelling, and experimental validation of the predicted nuclear strain levels and optimal frequency ranges is required. Material properties, particularly at high frequencies and at the cellular scale, are derived from literature and may not fully capture in vivo behavior. The use of engineered phantoms with controlled acoustic and mechanical properties may provide a suitable platform for preliminary validation of wave propagation and energy transmission[71–73]. Furthermore, the present model focuses on mechanical interactions and does not account for biochemical pathways involved in mechanotransduction. Future work should therefore incorporate experimental validation at multiple scales and explore the coupling between mechanical stimuli and cellular signalling processes.

Countless open questions remain for future investigation. The relationship between predicted nuclear strain and specific biological responses, such as gene expression or matrix synthesis, has not yet been established experimentally. The influence of tissue heterogeneity and anisotropy, which are known to affect cartilage mechanics, is also not explicitly represented. More advanced cellular models, such as those incorporating cytoskeletal networks through discrete structural elements[12], could improve the fidelity

of the microscale representation. Additionally, the long-term effects of repeated acoustic stimulation and potential adaptive responses remain unexplored. Addressing these aspects will be essential for translating the proposed framework into clinically applicable ultrasound therapies.

### 5.3.8 Conclusions

This study sought to establish a mechanistic framework linking externally applied acoustic excitation to biologically relevant deformation at the level of the chondrocyte nucleus. Existing ultrasound-based cartilage stimulation strategies are predominantly empirical and do not explicitly incorporate the multiscale transmission of mechanical energy from the joint to the cellular domain. To address this limitation, a patient-specific multiscale computational approach was developed, integrating macroscale acoustic wave propagation within the knee joint with microscale cellular mechanics through a representative volume element formulation. The results indicate that nuclear strain amplification occurs over finite frequency bands rather than at a single discrete frequency, with spheroidal modes, particularly the ($s_1$) mode—contributing significantly to nuclear deformation. Osteoarthritic conditions were found to shift the effective frequency range toward lower values and to reduce sensitivity at higher frequencies (healthy: 70–85 kHz; OA: 20–30 kHz). Although anatomical variability introduced differences in absolute response, consistent transmissibility patterns were observed across patients. Furthermore, time-explicit simulations confirmed that nonlinear acoustic effects are negligible under the considered pressure levels, indicating that linear formulations are sufficient for capturing the relevant mechanotransduction behavior. These findings suggest that effective cartilage stimulation should be designed within specific frequency bands and adapted to the mechanical state of the tissue. The proposed framework provides a quantitative basis for the rational selection of ultrasound parameters, grounded in cellular-scale mechanics rather than empirical optimization.

## 5.4 Concluding Remarks on Simulation Framework

The computational framework developed in this work integrates reduced-order modelling, patient-specific macro-scale simulations, and microscale cellular analyses into a unified multiscale approach for investigating acoustic wave propagation and mechanotransduction response in cartilage. By systematically linking wave transmission across heterogeneous tissues to nuclear-scale deformation within chondrocytes, the framework enables a coherent interpretation of how externally applied acoustic fields translate into biologically relevant mechanical stimuli. This section synthesizes the principal outcomes of the modelling strategy, discusses their implications for therapeutic ultrasound design, and outlines future directions for advancing multiscale acoustic modelling toward improved predictive capability and clinical applicability.

### 5.4.1 Summary of Key Findings

The reduced-order modelling framework provided a clear and computationally efficient description of acoustic wave propagation through layered biological media, enabling systematic evaluation of frequency-dependent transmission behavior. The results demonstrated that wave attenuation increases markedly with frequency, leading to significant energy loss as the acoustic wave traverses successive tissue layers. The presence of impedance mismatches at tissue interfaces was shown to cause partial reflections, further reducing the transmitted energy and contributing to the observed frequency-dependent attenuation.

The multiscale computational framework extended these findings by linking macroscopic acoustic propagation within the knee joint to microscopic mechanotransduction responses at the chondrocyte level. At the tissue scale, acoustic transmission to cartilage exhibited consistent frequency-dependent behavior across patient-specific geometries, with dominant amplification occurring in the low-frequency regime and diminishing at higher frequencies due to increased attenuation and reduced impedance-driven coupling. The influence of transducer size was found to be secondary beyond a characteristic threshold, with transmissibility stabilizing for larger opening.

At the cellular scale, both modal and harmonic analyses revealed that nuclear strain amplification occurs within specific frequency bands rather than at discrete frequencies. The dominant deformation modes were shown to depend on both cellular geometry and mechanical properties, with chondrocyte radius and pericellular matrix thickness acting as primary tuning parameters. OA alterations were observed to shift the resonant response toward lower frequencies and to reduce modal sharpness, reflecting increased damping and structural heterogeneity.

The coupled macro-to-micro analysis demonstrated that these cellular-scale dynamics directly

influence the efficiency of pressure-to-strain transmission. Healthy cartilage exhibited a broader mid-frequency amplification band, whereas osteoarthritic tissue showed a concentrated low-frequency response, indicating that optimal stimulation conditions are disease-dependent. Time-domain simulations further confirmed that, within the investigated pressure ranges, nonlinear acoustic effects are negligible, and the system response is predominantly governed by linear wave propagation.

### 5.4.2 Implications for Device Design and Optimization

The results obtained from both the reduced-order and multiscale modelling frameworks provide direct guidance for the rational design and optimization of ultrasound-based devices for cartilage stimulation. A primary implication is that excitation frequency should not be selected arbitrarily or based solely on conventional therapeutic ranges, but instead tuned to frequency bands that maximize pressure transmission at the joint scale and strain amplification at the cellular level. The identification of distinct optimal bands for healthy and osteoarthritic tissue indicates that device operation should be adaptable, enabling disease-specific targeting rather than relying on a single fixed frequency.

From a transducer design perspective, the findings indicate that increasing aperture size improves energy delivery only up to a threshold, beyond which transmissibility becomes largely insensitive to further geometric changes. This suggests that excessively large transducers may not yield proportional performance gains and could be replaced by more compact configurations without compromising effectiveness. Consequently, device optimization should balance aperture size, ergonomics, and coupling efficiency, rather than prioritizing maximum size.

The observed spatial distribution of acoustic pressure further highlights the importance of accounting for anatomical geometry and impedance mismatches. Localized amplification near cartilage interfaces suggests that device positioning and orientation can be optimized to exploit constructive interference and geometric confinement within the joint. This supports the development of patient-specific or anatomically guided placement strategies to enhance targeting accuracy and energy focusing.

At the microscale, the dependence of nuclear strain amplification on cellular geometry and pericellular properties underscores the need to design excitation protocols that align with the intrinsic mechanical response of chondrocytes. The shift in resonant behavior under osteoarthritic conditions implies that effective stimulation requires not only frequency tuning but also consideration of altered tissue mechanics. Devices incorporating frequency sweeping or adaptive control strategies may therefore offer improved performance by dynamically identifying and maintaining operation within optimal bands.

Finally, the confirmation that nonlinear acoustic effects are negligible under the investigated

conditions simplifies device design requirements, as linear acoustic models are sufficient to predict system behavior within the relevant pressure ranges. This reduces modelling complexity and supports more efficient optimization workflows.

### 5.4.3 Future Directions in Multi-Scale Acoustic Modelling

The present framework establishes a foundation for linking joint-level acoustics to intracellular mechanics; however, several avenues remain to further improve predictive capability and physiological relevance. A key direction involves the integration of more detailed tissue representations. The current assumption of homogeneous and isotropic properties can be extended to incorporate depth-dependent structure, anisotropy, and viscoelastic heterogeneity, particularly in cartilage and skeletal muscle, where collagen architecture and fiber orientation influence wave propagation and energy distribution.

At the cellular scale, future models should aim to refine the representation of chondrocyte mechanics by explicitly incorporating subcellular structures such as the cytoskeleton. Discrete or network-based formulations, for example using truss or beam elements, could capture the mechanical contribution of filamentous structures and improve the accuracy of predicted deformation patterns. Such developments would enable more realistic coupling between external acoustic fields and intracellular stress transmission pathways.

Another important extension concerns the coupling between mechanical and biological responses. While the current approach quantifies nuclear strain as a proxy for mechanotransduction, the downstream biochemical processes governing gene expression, matrix synthesis, and inflammatory signalling are not explicitly represented. Future work should therefore aim to integrate mechanobiological models with the mechanical framework, allowing direct prediction of biological outcomes from acoustic stimulation.

Experimental validation remains essential to support model development. The use of tissue-mimicking phantoms with controlled acoustic and mechanical properties offers a practical intermediate step for validating wave propagation and pressure-to-strain transmission. In parallel, in vitro and ex vivo studies should be conducted to quantify cellular responses under controlled excitation conditions, enabling calibration of model parameters and validation of predicted frequency-dependent behavior.

From a computational perspective, advances in numerical methods and high-performance computing may enable the resolution of larger and more complex multiscale systems. Adaptive coupling strategies, reduced-order surrogates, and machine learning-assisted parameter identification could facilitate efficient exploration of large design spaces while preserving physical fidelity.

Finally, the extension of the framework to patient-specific and time-dependent conditions represents a critical step toward clinical translation. Incorporating subject-specific imaging data, disease progression, and loading conditions would allow dynamic assessment of treatment efficacy and support personalized optimization of acoustic stimulation protocols.

## 5.5 Bibliography

[1]N. A. T. C. Fernandes, A. Arieira, B. Hinckel, F. Silva, A. Leal, and Ó. Carvalho, "A Python FDTD Method Algorithm for 1D Planar Acoustic Wave Propagation: Simulating High-Frequency Ultrasound in the Brain and Beyond", in *Proceedings of ICOVP and WMVC 2025*, Vol. 197, edited by Z. Dimitrovová, P. Biswas, and T. A. N. Silva (Springer Nature Switzerland, Cham, 2026), pp. 391–401, 10.1007/978-3-032-13225-3_39.

[2]N. A. T. C. Fernandes, *Nnunofernandes/1D-FDTD-Multilayer-Acoustic-Wave-Planar-Propagation: 1.0.1*, version 1.0.1, Zenodo, May 29, 2026, 10.5281/ZENODO.20445080.

[3]T. D. Mast, "Acoustic field modeling in therapeutic ultrasound", in AIP Conf. Proc. Vol. 838 (2006), pp. 209–216, 10.1063/1.2210348.

[4]M. Liebler, T. Dreyer, and R. E. Riedlinger, "Modeling of interaction between therapeutic ultrasound propagation and cavitation bubbles", Ultrasonics **44**, e319–e324 (2006) 10.1016/j.ultras.2006.07.006.

[5]M. Matthews and M. Stretanski, *Ultrasound Therapy [Updated 2023 Jul 31]*, StatPearls [Internet], (2025) https://www.ncbi.nlm.nih.gov/books/NBK547717/ (visited on 02/24/2026).

[6]A. Pereira, V. Cardoso, M. Martins, and N. A. T. C. Fernandes, "Development of a hydrophone for measuring the propagation of acoustic waves in biological tissues", in *Proceedings of ICOVP & WMVC 2025. ICOVP & WMVC 2025*, Lecture Notes in Mechanical Engineering (Springer, Cham, 2025), 10.1007/978-3-032-11549-2_63.

[7]A. Krokhmal, I. C. Simcock, B. E. Treeby, and E. Martin, "A comparative study of experimental and simulated ultrasound beam propagation through cranial bones", Phys. Med. Biol. **70**, 025007 (2025) 10.1088/1361-6560/ada19d.

[8]J. Zhu, G. Lin, T. Hu, Y. Gao, S. Wang, S. Li, and L. Zhang, "Recent development in numerical simulation of ultrasonic process enhancement", Chem. Eng. Sci. **319**, 122302 (2026) 10.1016/j.ces.2025.122302.

[9]C. Angla, B. Larrat, J.-L. Gennisson, and S. Chatillon, "Transcranial ultrasound simulations: A review", Med. Phys. **50**, 1051–1072 (2023) 10.1002/mp.15955.

[10]S. Agrawal, T. Suresh, A. Garikipati, A. Dangi, and S.-R. Kothapalli, "Modeling combined ultrasound and photoacoustic imaging: Simulations aiding device development and artificial intelligence", Photoacoustics **24**, 100304 (2021) 10.1016/j.pacs.2021.100304.

[11]A. Chetioui, T. Masia, P.-G. Claret, T. Markarian, L. Muller, J. Y. Lefrant, J. E. De La Coussaye, C. Roger, and X. Bobbia, "Pocket-sized ultrasound device for internal jugular puncture: A randomized study of performance on a simulation model", J. Vasc. Access **20**, 404–408 (2019) 10.1177/1129729818812733.

[12]J. Gómez Girón and J. M. Rodríguez Lelis, "A FEM modal and harmonic approach to the natural frequencies of cancer and healthy cells", J. Braz. Soc. Mech. Sci. Eng. **47**, 147 (2025) 10.1007/s40430-025-05472-6.

[13]A. Ahmed Mubeen, S. Chaudhary, A. Barathwaj R, and C. C V, "Dynamic analysis of MCF-10A and MCF-7: A simulation approach", Vibroengineering Procedia **30**, 126–132 (2020) 10.21595/vp.2020.21392.

[14]P. Marty, C. Boehm, C. Paverd, M. Rominger, and A. Fichtner, *Full-Waveform Ultrasound Modeling of Soft Tissue-Bone Interactions using Conforming Hexahedral Meshes*, edited by W. Zhao and L. Yu, (2022) 10.3929/ETHZ-C-000569826, https://www.research-collection.ethz.ch/handle/20.500.11850/569826 (visited on 04/22/2026), pre-published.

[15]N. A. T. C. Fernandes, S. Sharma, A. Arieira, B. Hinckel, F. Silva, A. Leal, and Ó. Carvalho, "Experimental Validation of Time-Explicit Ultrasound Propagation Models with Sound Diffusivity or Viscous Attenuation in Biological Tissues Using COMSOL Multiphysics", Bioengineering **12**, 946 (2025) 10.3390/bioengineering12090946.

[16]W. Cai, W. Chen, J. Fang, and S. Holm, "A Survey on Fractional Derivative Modeling of Power-Law Frequency-Dependent Viscous Dissipative and Scattering Attenuation in Acoustic Wave Propagation", Appl. Mech. Rev. **70**, 030802 (2018) 10.1115/1.4040402.

[17]M. Osika and P. Kijanka, "Ultrasound Shear Wave Propagation Modeling in General Tissue–Like Viscoelastic Materials", Ultrasound Med. Biol. **50**, 627–638 (2024) 10.1016/j.ultrasmedbio.2024.01.008.

[18]A. B. Naveed, A. Mubashar, M. K. A. Khan, A. Tariq, and K. A. Khan, "High-Fidelity Versus Reduced-Order Numerical Models for Sound Transmission Loss Prediction of Acoustic Metamaterials", in ICAME 2025 (Oct. 21, 2025), p. 17, 10.3390/engproc2025111017.

[19]V. C. Meesala, S. Ragab, M. R. Hajj, and S. Shahab, "Acoustic-electroelastic interactions in ultrasound energy transfer systems: Reduced-order modeling and experiment", J. Sound Vib. **475**, 115255 (2020) 10.1016/j.jsv.2020.115255.

[20]G. Pinton, *Ultrasound imaging of the human body with three dimensional full-wave nonlinear acoustics. Part 1: simulations methods*, version 1, (2020) 10.48550/ARXIV.2003.06934, https://arxiv.org/abs/2003.06934 (visited on 04/22/2026), pre-published.

[21]Y. Jin, T. Yang, and Y. Qi, "Acoustic Wave Propagation Behaviors and Energy Loss Mechanisms in Agar Gels with Small Particles", Polymers **17**, 2226 (2025) 10.3390/polym17162226.

[22]G. Petris, M. Cianferra, and V. Armenio, "A numerical method for the solution of the three-dimensional acoustic wave equation in a marine environment considering complex sources", Ocean Eng. **256**, 111459 (2022) 10.1016/j.oceaneng.2022.111459.

[23]G. V. Norton and J. C. Novarini, "Finite-difference time-domain simulation of acoustic propagation in dispersive medium: An application to bubble clouds in the ocean", Comput. Phys. Commun. **174**, 961–965 (2006) 10.1016/j.cpc.2006.01.003.

[24]M. Saeki, L. Bustamante, T. Misaki, K. Chiba, I. Mano, Y. Nagatani, and M. Matsukawa, "FDTD simulation study of ultrasonic wave propagation in human radius model generated from 3D HR-pQCT images", Phys. Med. **10**, 100029 (2020) 10.1016/j.phmed.2020.100029.

[25]M. Hirsekorn, P. Delsanto, N. Batra, and P. Matic, "Modelling and simulation of acoustic wave propagation in locally resonant sonic materials", Ultrasonics **42**, 231–235 (2004) 10.1016/j.ultras.2004.01.014.

[26]X. Wang, X. Gong, C. Qin, D. Zhang, H. Wu, and D. Zhang, "Finite-difference time-domain scheme for nonlinear acoustic waves in solids", Mech. Syst. Signal Process. **130**, 790–799 (2019) 10.1016/j.ymssp.2018.06.057.

[27]L. E. Kinsler, ed., *Fundamentals of acoustics*, 4th ed (Wiley, New York, 2000), 548 pp.

[28]V. T. Rathod, "A Review of Acoustic Impedance Matching Techniques for Piezoelectric Sensors and Transducers", Sensors **20**, 4051 (2020) 10.3390/s20144051.

[29]S. Wang, R.-X. Yu, W. Fan, C.-X. Li, W.-M. Fei, S. Li, J. Zhou, R. Hu, M. Liu, F. Xu, J. Xu, and Y. Cui, "Detection of skin thickness and density in healthy Chinese people by using high-frequency ultrasound", Skin Res. Technol. **29**, e13219 (2023) 10.1111/srt.13219.

[30]V. Kızılgöz, M. Kantarci, and S. Aydın, "Association between the subcutaneous fat thickness of the knee and chondromalacia patella: a magnetic resonance imaging-based study", J. Int. Med. Res. **51**, 03000605231183581 (2023) 10.1177/03000605231183581.

[31]M. Debnath and V. Patel, "T2 Mapping of Articular Cartilage of the Adult Knee Joint: Changes in the Relaxation Time and Thickness of Knee Cartilage with Age among Normal Adult Patients in 3 Tesla MRI", J. Health Allied Sci. NU **15**, 238–246 (2024) 10.1055/s-0044-1801295.

[32]L. O. Dantas, M. C. Osani, and R. R. Bannuru, "Therapeutic ultrasound for knee osteoarthritis: A systematic review and meta-analysis with grade quality assessment", Braz. J. Phys. Ther. **25**, 688–697 (2021) 10.1016/j.bjpt.2021.07.003.

[33]Y. Liu, Y. Wang, Y. Wang, and X. Jia, "A Meta-Analysis of Analgesic Effect of Ultrasound Therapy for Patients With Knee Osteoarthritis", J. Ultrasound Med. **41**, 1861–1872 (2022) 10.1002/jum.15866.

[34]A. D. Miller, A. Subramanian, and H. J. Viljoen, "Theoretically proposed optimal frequency for ultrasound induced cartilage restoration", Theor. Biol. Med. Model. **14**, 21 (2017) 10.1186/s12976-017-0067-4.

[35]T. A. M. Harrington, E. L. Thomas, G. Frost, N. Modi, and J. D. Bell, "Distribution of Adipose Tissue in the Newborn", Pediatr. Res. **55**, 437–441 (2004) 10.1203/01.pdr.0000111202.29433.2d.

[36]A. Nahian and A. Sapra, "Histology, Chondrocytes", in *StatPearls [Internet]* (StatPearls Publishing, Treasure Island (FL), Jan. 2025).

[37]S. Chawla, A. Mainardi, N. Majumder, L. Dönges, B. Kumar, P. Occhetta, I. Martin, C. Egloff, S. Ghosh, A. Bandyopadhyay, and A. Barbero, "Chondrocyte Hypertrophy in Osteoarthritis: Mechanistic Studies and Models for the Identification of New Therapeutic Strategies", Cells **11**, 4034 (2022) 10.3390/cells11244034.

[38]Y.-H. M. Chan and W. F. Marshall, "Scaling properties of cell and organelle size", Organogenesis **6**, 88–96 (2010) 10.4161/org.6.2.11464.

[39]C. Campos Muñiz and F. J. Fernández Perrino, "Evolution of the Concepts of Architecture and Supramolecular Dynamics of the Plasma Membrane", Membranes **13**, 547 (2023) 10.3390/membranes13060547.

[40]F. Guilak, R. J. Nims, A. Dicks, C.-L. Wu, and I. Meulenbelt, "Osteoarthritis as a disease of the cartilage pericellular matrix", Matrix Biol. **71–72**, 40–50 (2018) 10.1016/j.matbio.2018.05.008.

[41]L. J. Sandell and T. Aigner, "Articular cartilage and changes in Arthritis: Cell biology of osteoarthritis", Arthritis Res. Ther. **3**, 107 (2001) 10.1186/ar148.

[42]S. Pettenuzzo, A. Arduino, E. Belluzzi, A. Pozzuoli, C. G. Fontanella, P. Ruggieri, V. Salomoni, C. Majorana, and A. Berardo, "Biomechanics of Chondrocytes and Chondrons in Healthy Conditions and Osteoarthritis: A Review of the Mechanical Characterisations at the Microscale", Biomedicines **11**, 1942 (2023) 10.3390/biomedicines11071942.

[43]S. Chokhandre, E. E. Neumann, T. F. Nagle, R. W. Colbrunn, C. A. Flask, C. Colak, J. Halloran, and A. Erdemir, "Specimen specific imaging and joint mechanical testing data for next generation virtual knees", Data Brief **35**, 106824 (2021) 10.1016/j.dib.2021.106824.

[44]S. Chokhandre, A. Schwartz, E. Klonowski, B. Landis, and A. Erdemir, "Open Knee(s): A Free and Open Source Library of Specimen-Specific Models and Related Digital Assets for Finite Element Analysis of the Knee Joint", Ann. Biomed. Eng. **51**, 10–23 (2023) 10.1007/s10439-022-03074-0.

[45]U. Moran, R. Phillips, and R. Milo, "SnapShot: Key Numbers in Biology", Cell **141**, 1262–1262.e1 (2010) 10.1016/j.cell.2010.06.019.

[46]C. Chen, D. T. Tambe, L. Deng, and L. Yang, "Biomechanical properties and mechanobiology of the articular chondrocyte", Am. J. Physiol.-Cell Physiol. **305**, C1202–C1208 (2013) 10.1152/ajpcell.00242.2013.

[47]K. N. Dahl, A. J. Ribeiro, and J. Lammerding, "Nuclear Shape, Mechanics, and Mechanotransduction", Circ. Res. **102**, 1307–1318 (2008) 10.1161/CIRCRESAHA.108.173989.

[48]D. W. McKeel and L. Jarett, "PREPARATION AND CHARACTERIZATION OF A PLASMA MEMBRANE FRACTION FROM ISOLATED FAT CELLS", J. Cell Biol. **44**, 417–432 (1970) 10.1083/jcb.44.2.417.

[49]M. Doktorova, M. V. LeVine, G. Khelashvili, and H. Weinstein, "A New Computational Method for Membrane Compressibility: Bilayer Mechanical Thickness Revisited", Biophys. J. **116**, 487–502 (2019) 10.1016/j.bpj.2018.12.016.

[50]W. R. Trickey, F. P. Baaijens, T. A. Laursen, L. G. Alexopoulos, and F. Guilak, "Determination of the Poisson's ratio of the cell: recovery properties of chondrocytes after release from complete micropipette aspiration", J. Biomech. **39**, 78–87 (2006) 10.1016/j.jbiomech.2004.11.006.

[51]L. G. Alexopoulos, M. A. Haider, T. P. Vail, and F. Guilak, "Alterations in the Mechanical Properties of the Human Chondrocyte Pericellular Matrix With Osteoarthritis", J. Biomech. Eng. **125**, 323–333 (2003) 10.1115/1.1579047.

[52]E. Darling, S. Zauscher, and F. Guilak, "Viscoelastic properties of zonal articular chondrocytes measured by atomic force microscopy", Osteoarthritis Cartilage **14**, 571–579 (2006) 10.1016/j.joca.2005.12.003.

[53]P. White, G. Clement, and K. Hynynen, "Longitudinal and shear mode ultrasound propagation in human skull bone", Ultrasound Med. Biol. **32**, 1085–1096 (2006) 10.1016/j.ultrasmedbio.2006.03.015.

[54]N. A. T. C. Fernandes, A. Arieira, B. Hinckel, F. S. Silva, Ó. Carvalho, and A. Leal, "Unlocking the Secrets of Knee Joint Unloading: A Systematic Review and Biomechanical Study of the Invasive and Non-Invasive Methods and Their Influence on Knee Joint Loading", Rheumato **5**, 8 (2025) 10.3390/rheumato5030008.

[55]S. Hosseini-Hashemi and J. Anderson, "Orthogonality and normalization of torsional modes of vibration of solid elastic spheres", J. Sound Vib. **121**, 511–524 (1988) 10.1016/S0022-460X(88)80373-0.

[56]T. M. Louw, G. Budhiraja, H. J. Viljoen, and A. Subramanian, "Mechanotransduction of Ultrasound is Frequency Dependent Below the Cavitation Threshold", Ultrasound Med. Biol. **39**, 1303–1319 (2013) 10.1016/j.ultrasmedbio.2013.01.015.

[57]A. D. Miller, A. Chama, T. M. Louw, A. Subramanian, and H. J. Viljoen, "Frequency sensitive mechanism in low-intensity ultrasound enhanced bioeffects", PLOS ONE **12**, edited by J. W. Ramos, e0181717 (2017) 10.1371/journal.pone.0181717.

[58]N. Pascarelli, G. Collodel, E. Moretti, S. Cheleschi, and A. Fioravanti, "Changes in Ultrastructure and Cytoskeletal Aspects of Human Normal and Osteoarthritic Chondrocytes Exposed to Interleukin-1$\beta$ and Cyclical Hydrostatic Pressure", Int. J. Mol. Sci. **16**, 26019–26034 (2015) 10.3390/ijms161125936.

[59]S. L. Winkler, A. E. Urbisci, and T. M. Best, "Sustained acoustic medicine for the treatment of musculoskeletal injuries: a systematic review and meta-analysis", BMC Sports Sci. Med. Rehabil. **13**, 159 (2021) 10.1186/s13102-021-00383-0.

[60]J. Zhou, E. Ning, L. Lu, H. Zhang, X. Yang, and Y. Hao, "Effectiveness of low-intensity pulsed ultrasound on osteoarthritis: molecular mechanism and tissue engineering", Front. Med. **11**, 1292473 (2024) 10.3389/fmed.2024.1292473.

[61]J. Sekino, M. Nagao, S. Kato, M. Sakai, K. Abe, E. Nakayama, M. Sato, Y. Nagashima, H. Hino, N. Tanabe, T. Kawato, M. Maeno, N. Suzuki, and K. Ueda, "Low-intensity pulsed ultrasound induces cartilage matrix synthesis and reduced MMP13 expression in chondrocytes", Biochem. Biophys. Res. Commun. **506**, 290–297 (2018) 10.1016/j.bbrc.2018.10.063.

[62]L. Jia, Y. Wang, J. Chen, and W. Chen, "Efficacy of focused low-intensity pulsed ultrasound therapy for the management of knee osteoarthritis: a randomized, double blind, placebo-controlled trial", Sci. Rep. **6**, 35453 (2016) 10.1038/srep35453.

[63]A. D. Sawitzke, C. G. Jackson, K. Carlson, M. D. Bizien, M. Leiner, D. J. Reda, T. Sindowski, C. Hanrahan, R. G. Spencer, C. K. Kwoh, S. J. Lee, K. Hose, L. Robin, D. W. Cain, M. D. Taylor, N. Bangerter, M. Finco, and D. O. Clegg, "Effect of Pulsed Low-Intensity Ultrasonography on Symptom Relief and Tibiofemoral Articular Cartilage Thickness Among Veterans Affairs Enrollees With Knee Osteoarthritis: A Randomized Clinical Trial", JAMA Netw. Open **5**, e220632 (2022) 10.1001/jamanetworkopen.2022.0632.

[64]C. Overton, A. E. Nelson, and T. Neogi, "Osteoarthritis Treatment Guidelines from Six Professional Societies", Rheum. Dis. Clin. N. Am. **48**, 637–657 (2022) 10.1016/j.rdc.2022.03.009.

[65]R. Lützenberg, M. Wehland, K. Solano, M. Z. Nassef, C. Buken, D. Melnik, J. Bauer, S. Kopp, M. Krüger, S. Riwaldt, R. Hemmersbach, H. Schulz, M. Infanger, and D. Grimm, "Beneficial Effects of Low Frequency Vibration on Human Chondrocytes in Vitro", Cell. Physiol. Biochem. **53**, 623–637 (2019) 10.33594/000000161.

[66]H. Wang, C. Zhang, S. Zhu, C. Gao, Q. Gao, R. Huang, S. Liu, X. Wei, H. Zhang, Q. Wei, and C. He, "Low-frequency whole-body vibration can enhance cartilage degradation with slight changes in subchondral bone in mice with knee osteoarthritis and does not have any morphologic effect on normal joints", PLOS ONE **18**, edited by L. Han, e0270074 (2023) 10.1371/journal.pone.0270074.

[67]J. A. Kaupp and S. D. Waldman, "Mechanical vibrations increase the proliferation of articular chondrocytes in high-density culture", Proc. Inst. Mech. Eng. [H] **222**, 695–703 (2008) 10.1243/09544119JEIM376.

[68]D. Marathe, V. S. Bhuvanashree, C. H. Mehta, A. T., and U. Y. Nayak, "Low-Frequency Sonophoresis: A Promising Strategy for Enhanced Transdermal Delivery", Adv. Pharmacol. Pharm. Sci. **2024**, edited by M. Oliveira, 1247450 (2024) 10.1155/2024/1247450.

[69]O. Ngo, E. Niemann, V. Gunasekaran, P. Sankar, M. Putterman, A. Lafontant, S. Nadkarni, R. A. DiMaria-Ghalili, M. Neidrauer, L. Zubkov, M. Weingarten, D. J. Margolis, and P. A. Lewin, "Development of Low

Frequency (20–100 kHz) Clinically Viable Ultrasound Applicator for Chronic Wound Treatment", IEEE Trans. Ultrason. Ferroelectr. Freq. Control **66**, 572–580 (2019) 10.1109/TUFFC.2018.2836311.

[70]S. Sharma, N. A. T. C. Fernandes, and Ó. Carvalho, "A Frequency-Dependent and Nonlinear, Time-Explicit Five-Layer Human Head Numerical Model for Realistic Estimation of Focused Acoustic Transmission Through the Human Skull for Noninvasive High-Intensity and High-Frequency Transcranial Ultrasound Stimulation: An Application to Neurological and Psychiatric Disorders", Bioengineering **12**, 1161 (2025) 10.3390/bioengineering12111161.

[71]A. Z. Santos, S. Rocha, B. Carneiro, N. A. Fernandes, J. Padrão, and Ó. Carvalho, "Current state of elastography research in multiple anatomical structures and respective phantoms", Phys. Med. **138**, 105192 (2025) 10.1016/j.ejmp.2025.105192.

[72]A. Z. Santos, S. Rocha, N. A. T. C. Fernandes, D. I. Alves, D. P. Ferreira, S. M. Costa, J. Padrão, and Ó. Carvalho, "Sustainable Shear Wave Elastography Medical Phantoms: Waste-Based Fibrous Structures for Medical Applications", Textiles **6**, 6 (2026) 10.3390/textiles6010006.

[73]N. A. T. C. Fernandes, D. I. Alves, D. P. Ferreira, M. Monteiro, A. Arieira, F. Silva, B. Hinckel, A. Leal, and Ó. Carvalho, "Sustainable Tunable Anisotropic Ultrasound Medical Phantoms for Skin, Skeletal Muscle, and Other Fibrous Biological Tissues Using Natural Fibers and a Bio-Elastomeric Matrix", J. Compos. Sci. **9**, 370 (2025) 10.3390/jcs9070370.

# Chapter 6

# Experimental Validation Through Acoustic Medical Phantoms

## 6.1 The Physical Role of Anatomical Phantoms in Ultrasound-based Therapies

The work presented in this chapter is supported by two first-author publications[1,2], one accepted manuscript, and two collaborative studies addressing shear-wave elastography and hydrophone-based acoustic characterization[3,4]. This research stage also involved the development of computational tools for the design of tissue-mimicking phantoms and the characterization of acoustic properties[5], together with software for tensile-test post-processing and Cauchy stress tensor estimation[6].

UTMPs play a central role in ultrasound-based therapies because they provide a controlled, repeatable, and ethically acceptable platform for translating acoustic concepts into experimentally testable therapeutic systems. In therapeutic ultrasound, the biological target is rarely accessed through a homogeneous medium, instead, the acoustic field must propagate through layered, curved, attenuating, and mechanically heterogeneous tissues, where reflections, refraction, scattering, absorption, standing-wave formation, and local heating may substantially alter the delivered dose. TMM should reproduce not only ultrasound image appearance, but also relevant physical properties such as speed of sound, acoustic attenuation, density, mechanical stiffness, and, when required, thermal response, making them essential for calibration, quality assurance, device development, and preclinical validation[7–9]. This is particularly important for therapeutic modalities such as HIFU, low-intensity focused ultrasound neuromodulation, ultrasound-assisted tissue engineering, and mechanically mediated regenerative therapies, where treatment efficacy depends on accurately controlling the spatial distribution of acoustic pressure, mechanical stress, and thermal dose within the target region[10,11]. In this context, anatomical phantoms act as an intermediate validation stage between numerical simulation and biological testing, allowing the predicted pressure fields, attenuation losses, temperature elevations, and target-region energy deposition to be experimentally assessed under reproducible conditions. Compared with simplified planar samples, anatomically representative phantoms are especially valuable because they preserve the geometry and interface distribution that govern real ultrasound delivery, thereby enabling optimization of transducer frequency, aperture, positioning, coupling strategy, exposure amplitude, and safety margins before progressing to ex vivo, in vivo, or clinical studies. For the present thesis, the development of an anatomical knee phantom is therefore not merely a methodological accessory, but a necessary engineering step to verify whether an external ultrasound-based therapeutic device can deliver controlled mechanical stimulation to cartilage while minimizing undesired exposure of surrounding soft tissues and bone.

Simplified and homogeneous UTMP are useful for preliminary calibration and controlled material characterization, but they are intrinsically limited for evaluating ultrasound-based therapies because they do not reproduce the anatomical, acoustic, mechanical, and thermal complexity that determines the real therapeutic dose delivered to biological targets. In homogeneous phantoms, the acoustic path is usually idealized, with uniform speed of sound, attenuation, density, and impedance. As such, they cannot adequately capture wave reflection and transmission at tissue interfaces, refraction through curved geometries, scattering from heterogeneous structures, local standing-wave formation, or frequency-dependent energy loss across multilayered tissues. High-fidelity ultrasound phantoms require simultaneous control of acoustic attenuation, speed of sound, stiffness, stability, and tissue-specific structure, rather than only bulk acoustic similarity[7–9]. This limitation is particularly relevant in therapeutic ultrasound, where treatment efficacy and safety depend on spatially accurate pressure delivery, thermal deposition, and mechanical stimulation. A phantom that is geometrically and materially oversimplified may therefore overestimate target exposure, underestimate losses at interfaces, and fail to reveal undesired hot spots in surrounding tissues. Patient anatomy, tissue heterogeneity, acoustic aberration, attenuation, and monitoring uncertainty remain major constraints in reliable treatment planning and delivery[11,12]. For this reason, while simplified phantoms remain valuable for isolated parameter measurements and repeatability studies, they should not be considered sufficient for validating therapeutic ultrasound devices intended to operate in anatomically complex regions such as the knee joint, where cartilage targeting is strongly affected by layered soft tissues, bone boundaries, joint curvature, and transducer positioning.

In this section, an anatomical knee phantom is developed to provide a controlled experimental platform for evaluating ultrasound therapy delivery. The phantom is used for two main purposes: first, to study the influence of transducer positioning on the acoustic waves transmitted toward the condylar region; and second, to validate the acoustic field generated by the adapted transducer configuration. By combining anatomically inspired geometry with tissue-mimicking materials, this framework enables assessment of how coupling conditions, propagation path, and local tissue interfaces affect ultrasound transmission within the knee joint.

## 6.2 Development of specialized measuring equipment

Accurate characterization of ultrasound acoustic fields in medical phantoms is essential for the development, calibration, and validation of therapeutic ultrasound systems. This requirement is particularly relevant when high spatial resolution, broadband sensitivity, and controlled directional response are needed to evaluate wave propagation through complex anatomical structures. In this context, the present work resulted in a publication describing a physically based framework for the design and validation of an acoustic horn needle attachment compatible with commercially available ultrasound transducers. This approach avoids the need to develop fully customized hydrophone systems while providing a reproducible strategy for broadband field characterization in medical phantom environments.

Numerical simulations were performed in COMSOL Multiphysics to investigate guided longitudinal wave propagation through the horn needle and to optimize the main geometric parameters, including needle length and horn base transition geometry. Frequency-domain parametric studies were conducted over the 1–5 MHz range. Cylindrical, conical, and exponential horn configurations were evaluated in terms of geometric optimization, directivity, and receiver sensitivity. Experimental validation was then performed by mechanically coupling the optimized horn needle to a commercial piezoelectric transducer (Mitech, 1 MHz, 24 mm diameter) using epoxy adhesive bonding.

The assembled system was experimentally characterized in water and in a generic medical phantom. The measured receiver sensitivity ranged from $-53.34$ to $-33.6$ dB re 1 V/$\mu$Pa over a bandwidth of 0.1–9 MHz. In the cranial phantom, sound transmission loss values between 63.4 and 139.2 dB were obtained within the 0.5–5 MHz range at a depth of 15 mm in the brain-mimicking region, remaining consistent with values reported in the literature. Overall, the results demonstrated that wavelength-scaled horn needle attachments can provide performance comparable to custom hydrophone configurations, offering a versatile and reproducible solution for ultrasound field characterization in medical phantom studies.

### 6.2.1 Physics, Materials and Methods

#### 6.2.1.1 Needle Hydrophone Physical Principles

Needle hydrophones operate as passive acoustic waveguides, transferring pressure information from the measurement location to a piezoelectric sensing element[13]. The theoretical basis for their frequency-dependent behaviour can be described using the rigid-cylinder diffraction model proposed by Wear et

al.[14,15]. According to this model, the frequency at which diffraction effects become most pronounced is governed by the cylinder diameter and the sound speed in the surrounding medium, as expressed in equation 236,

$$f_{\text{max}} = \frac{2.4c}{\pi d} \tag{236}$$

where $c$ is the speed of sound in the surrounding fluid and $d$ is the needle diameter. For a 3 mm aluminium needle immersed in tissue, assuming $c = 1562$ m/s[16], this characteristic frequency becomes equation 237.

$$f_{\text{max}} = \frac{2.4 \times 1562}{\pi \times 3} \approx 398 \text{ kHz} \tag{237}$$

Since the frequency range considered in this work is 0.5–5 MHz, which lies above $f_{\text{max}}$, the hydrophone response is expected to remain relatively stable, although local modulation may occur due to mechanical resonances[15].

The performance of a needle hydrophone is strongly influenced by acoustic transmissibility along the tissue–needle–piezoelectric pathway. For normal incidence, the pressure transmission coefficient between two media can be approximated by equation 238,

$$T = \frac{4Z_1 Z_2}{(Z_1 + Z_2)^2} \tag{238}$$

where $Z_1$ and $Z_2$ are the acoustic impedances of the two adjacent media. In the present application, soft tissue can be approximated by an acoustic impedance as described in equation 239,

$$Z_{\text{brain}} = \rho c \approx 1047 \text{ kg/m}^3 \times 1562 \text{ m/s} \approx 1.6 \text{ MRayl} \tag{239}$$

whereas typical PZT ceramics present substantially higher acoustic impedances, commonly around $33$ MRayl[17]. This large impedance mismatch makes direct analytical prediction of the overall pressure transfer from tissue to the piezoelectric element difficult, particularly when intermediate structural components are introduced. In addition, most candidate needle materials exhibit structural or viscoelastic damping, meaning that attenuation increases with propagation distance and with the wavelength-dependent behaviour of the guided wave. This can substantially reduce the pressure amplitude reaching the piezoelectric receiver.

Beyond material selection and impedance matching, the geometry of the needle is a critical determinant of hydrophone performance. Although the needle primarily functions as a guided-wave conduit, a purely collimated wave would concentrate the acoustic field over only a limited portion of the piezoelectric surface, reducing the effective use of the active sensing area. Therefore, the needle geometry should promote controlled diffraction and lateral wave expansion near the piezoelectric

interface, acting as an acoustic horn[18]. This progressive expansion distributes the transmitted pressure over a larger region of the transducer surface and can improve electromechanical coupling efficiency. Common horn geometries include cylindrical, conical, and exponential profiles[19], which are evaluated in this work. Thus, the needle geometry must balance two requirements: minimizing propagation losses while promoting sufficient spatial spreading of the acoustic field to improve interaction with the piezoelectric receiver and preserve signal fidelity.

The numerical models used in this work were implemented in COMSOL Multiphysics 5.3 using a fully coupled acoustic–structure interaction framework. In the fluid domain, longitudinal acoustic propagation was described by the pressure acoustics wave equation 240:

$$\nabla \cdot \left( \frac{1}{\rho_f} \nabla p \right) - \frac{1}{\rho_f c_f^2} \frac{\partial^2 p}{\partial t^2} = 0 \tag{240}$$

where $p$ is the acoustic pressure, $\rho_f$ is the fluid density, and $c_f$ is the sound speed in the fluid[20].

Elastic wave propagation in the solid domains was governed by the momentum balance equation 241:

$$\nabla \cdot \boldsymbol{\sigma} = \rho_s \frac{\partial^2 \mathbf{u}}{\partial t^2} \tag{241}$$

where $\boldsymbol{\sigma}$ is the Cauchy stress tensor, $\mathbf{u}$ is the displacement field, and $\rho_s$ is the solid density.[21]. At acoustic–structure interfaces, the acoustic pressure was applied as a normal traction on the solid boundary, originating the coupling condition expressed in equation 242,

$$\boldsymbol{\sigma} \cdot \mathbf{n} = -p\mathbf{n} \tag{242}$$

while continuity of normal acceleration was imposed as equation 243,

$$\mathbf{n} \cdot \frac{\partial^2 \mathbf{u}}{\partial t^2} = -\mathbf{n} \cdot \left( \frac{1}{\rho_f} \nabla p \right) \tag{243}$$

following the acoustic–structure interaction formulation[20].

In the piezoelectric region, the mechanical response was coupled to the quasi-static electric field through Gauss's law in equation 244,

$$\nabla \cdot \mathbf{D} = 0 \tag{244}$$

and the linear piezoelectric constitutive equations 245,

$$\boldsymbol{\sigma} = \mathbf{C}^E : \varepsilon - \mathbf{e}^T \mathbf{E}, \qquad \mathbf{D} = \mathbf{e} : \varepsilon + \varepsilon^S \mathbf{E} \tag{245}$$

where $\varepsilon$ is the strain tensor, $\mathbf{E} = -\nabla V$ is the electric field, $\mathbf{C}^E$ is the stiffness tensor at constant electric field, $\mathbf{e}$ is the piezoelectric coupling tensor, and $\varepsilon^S$ is the permittivity tensor at constant strain.

Mechanical continuity of displacement and stress was imposed at solid–solid interfaces, while open-circuit electrical boundary conditions were prescribed at the piezoelectric electrodes to reproduce measurement conditions[22]. This coupled formulation enables acoustic excitation, elastic wave transmission, and piezoelectric signal generation to be represented within a single multiphysics model.

#### 6.2.1.2 Material Screening via Numerical Simulation

An initial numerical screening was conducted to assess the acoustic transmission performance of candidate needle materials placed between a soft biological medium and a piezoelectric sensing element. The relationship between the relevant material properties and the desired design requirements is summarized in the Ashby-style map shown in figure 92.

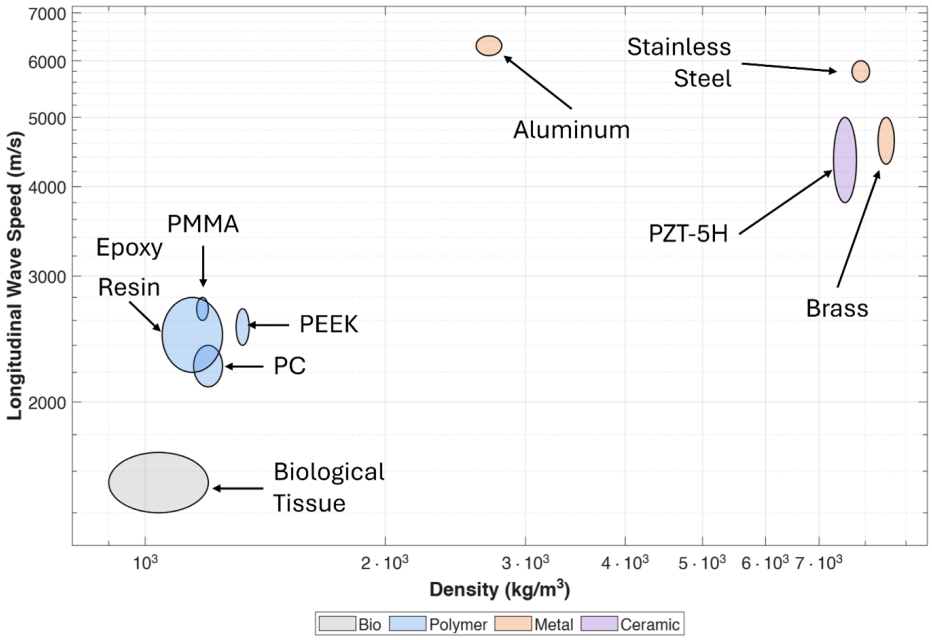



Figure 92: Ashby-style map showing the relationship between density and longitudinal wave speed for biological tissues, polymers, metals, and ceramics relevant to the acoustic horn needle design.

Finite element simulations were performed to evaluate wave propagation through needle structures manufactured from representative materials. The models incorporated material-specific density, elastic wave speeds, and damping parameters obtained from the literature and manufacturer datasheets. The properties used in the initial screening are summarized in table 19.

Table 19: Material properties used in the initial material screening simulations.

| Material | Parameter | Value | Reference |
|---|---|---|---|
| Soft Tissues | Density (kg/m$^3$) | 1046.92 | 16 |

| | | | |
|---|---|---|---|
| | Longitudinal wave speed (m/s) | 1562.09 | |
| | B/A non-linearity coefficient | 7.216 | |
| | Sound diffusivity ($m^2/s$) | 0.0017210 | |
| Polycarbonate | Density ($kg/m^3$) | 1250 | [23] |
| | Longitudinal wave speed (m/s) | 2300 | |
| | Shear wave speed (m/s) | 1100 | |
| | Damping ratio ($\zeta$) | 0.07 | [24] |
| PMMA | Density ($kg/m^3$) | 1180 | [25] |
| | Longitudinal wave speed (m/s) | 2730 | |
| | Shear wave speed (m/s) | 1400 | |
| | Damping ratio ($\zeta$) | 0.0016 | [26] |
| Epoxy Resin | Density ($kg/m^3$) | 1350 | [27] |
| | Longitudinal wave speed (m/s) | 2500 | |
| | Shear wave speed (m/s) | 1200 | |
| | Loss Factor ($\zeta$) | 0.0088 | [28] |
| PEEK | Density ($kg/m^3$) | 1340 | [29] |
| | Longitudinal wave speed (m/s) | 2600 | |
| | Shear wave speed (m/s) | 1200 | |
| | Loss Factor ($\zeta$) | 0.06 | [30] |
| Aluminum | Density ($kg/m^3$) | 3600 | [31] |

| | | | |
|---|---|---|---|
| | Longitudinal wave speed (m/s) | 6350 | |
| | Shear wave speed (m/s) | 3130 | |
| | Loss Factor ($\zeta$) | 0.0029 | [32] |
| Brass | Density (kg/m$^3$) | 8510 | [33] |
| | Longitudinal wave speed (m/s) | 4500 | |
| | Shear wave speed (m/s) | 2150 | |
| Stainless Steel | Density (kg/m$^3$) | 7790 | [34] |
| | Longitudinal wave speed (m/s) | 5800 | |
| | Shear wave speed (m/s) | 3150 | |
| Matching Layer | Density (kg/m$^3$) | 2280 | [35] |
| | Longitudinal wave speed (m/s) | 3400 | |
| | Shear wave speed (m/s) | 1920 | |
| Backing Layer | Density (kg/m$^3$) | 6580 | [35] |
| | Longitudinal wave speed (m/s) | 1500 | |
| | Shear wave speed (m/s) | 775 | |
| PZT-5H | Density (kg/m$^3$) | 7700 | [35,36] |
| | Longitudinal wave speed (m/s) | 4620 | |
| | Shear wave speed (m/s) | 1750 | |

When longitudinal or shear wave speeds were not directly available, they were estimated from the

elastic properties of the material. The longitudinal wave speed was calculated according to equation 246,

$$c_l = \sqrt{\frac{E}{\rho}} \tag{246}$$

where $c_l$ is the longitudinal wave speed, $E$ is Young's modulus, and $\rho$ is the material density. The shear wave speed was estimated as equation 247,

$$c_s = \sqrt{\frac{E}{\rho(1+\nu)}} \tag{247}$$

where $c_s$ is the shear wave speed and $\nu$ is Poisson's ratio.

The material parameters were implemented in COMSOL Multiphysics to simulate elastic wave propagation through the needle element, acoustic horn, backing layer, piezoelectric transducer, and matching layer. The piezoelectric domain was modelled using a fully coupled piezoelectric interface, while nonlinear ultrasound physics was included to describe the incident acoustic field. A pressure excitation was applied at the input boundary and guided along the axisymmetric needle geometry toward the sensing region. To reduce artificial reflections and approximate an unbounded acoustic medium, an absorbing layer was introduced near the excitation boundary, while sound-soft and low-reflecting boundary conditions were applied to control lateral and distal reflections.

The elongated geometry of the needle, with a length of 200 mm, was designed to promote guided wave propagation and to progressively direct acoustic energy toward the piezoelectric element located near the needle tip. Acoustic–structure interaction was implemented using a discontinuous Galerkin finite element formulation, providing numerical stability across interfaces with large impedance contrasts. A localized region of the computational domain was assigned brain-like acoustic properties and surrounded by absorbing layers to avoid non-physical propagation artifacts. The excitation consisted of a pressure pulse with a spatial extent equal to one acoustic wavelength and a peak amplitude of 1 MPa.

The transducer dimensions were scaled relative to the acoustic wavelength, $\lambda$, to promote gradual impedance transition[37] and controlled diffraction as the wave expanded before reaching the piezoelectric surface. This design strategy was intended to improve pressure transfer efficiency and frequency-dependent receiver sensitivity, forming the physical basis of the proposed needle hydrophone concept, as illustrated in figure 93.

All domains were discretized using tetrahedral elements, with a minimum resolution of 1.5 elements per wavelength. Mesh smoothing was applied during post-processing while preserving the accuracy of the numerical solution, following previously validated COMSOL modelling procedures. To reduce computational demand while maintaining the relevant physical behaviour, the simulations were

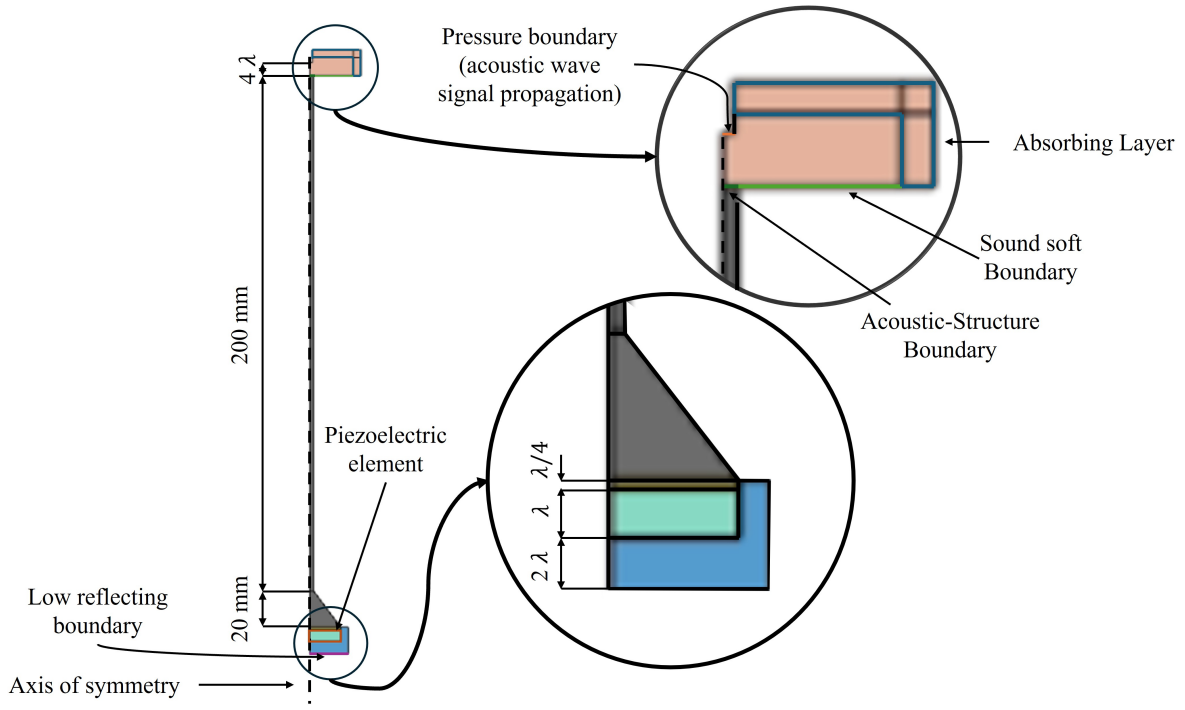



Figure 93: Schematic representation of the axisymmetric needle hydrophone with an integrated acoustic horn, showing the computational domain, boundary conditions, and wavelength-scaled geometry used to guide and concentrate the incident acoustic wave onto the piezoelectric sensing element.

performed using a two-dimensional axisymmetric formulation. This approach enabled efficient comparison of material transmissibility under equivalent excitation and boundary conditions.

The results of this preliminary screening were used to support the selection of the most appropriate needle material. The objective was to identify a material capable of providing efficient acoustic guidance, favourable impedance transition, reduced transmission losses, and improved receiver sensitivity for the proposed horn needle hydrophone.

#### 6.2.1.3 Experimental Evaluation of Material Properties

Based on the preliminary numerical results, aluminium was selected as the most appropriate material for the needle structure, as it provided a suitable compromise between acoustic impedance compatibility with soft tissue, coupling efficiency with the PZT element, low intrinsic damping, mechanical stability, and manufacturing feasibility. To support reproducible fabrication of long needle geometries, casting was identified as the preferred production method.

Two aluminium alloys commonly used in precision casting, AlSi and AlMg, were selected for experimental assessment. To validate the numerical predictions, 5 cm long specimens were prepared from welding electrodes with external diameters of 2.5 mm and 3.2 mm. These samples were used to determine longitudinal wave speed and acoustic attenuation following the experimental procedure previously described by Fernandes et al. (2025)[1,16], based on pulse transmission, time-of-flight analysis,

and amplitude decay along the propagation path.

The experimentally measured attenuation coefficient, $\alpha(\omega)$, was converted into an equivalent Rayleigh damping formulation to allow direct implementation in the numerical model. Under the Rayleigh damping assumption, the damping matrix is defined as equation 248:

$$\mathbf{C} = \alpha_R \mathbf{M} + \beta_R \mathbf{K} \tag{248}$$

where **C**, **M**, and **K** are the damping, mass, and stiffness matrices, respectively. The relationship between frequency-dependent attenuation and the Rayleigh coefficients is given byequation 249[38]:

$$\alpha(\omega) = \frac{1}{2c_l}\left(\alpha_R + \beta_R \omega^2\right) \tag{249}$$

where $\alpha_R$ is the mass-proportional damping coefficient, $\beta_R$ is the stiffness-proportional damping coefficient, $c_l$ is the longitudinal wave speed, and $\omega$ is the angular frequency.

This procedure enabled the experimentally observed acoustic losses to be represented through mass- and stiffness-proportional damping terms. The resulting coefficients were then used to calibrate the aluminium material models, allowing more realistic simulation of guided wave propagation within the acoustic horn needle hydrophone.

#### 6.2.1.4 Numerical Optimization and evaluation of Needle Elements

**Horn Needle Geometric Size Optimization**

A systematic geometric optimization study was performed in COMSOL Multiphysics 5.3 to identify the needle length and base-transition geometry most suitable for guiding longitudinal acoustic waves toward the sensing region, as shown in Figure 94. The needle geometry was defined through a parametric sweep and comparative numerical assessment rather than through an automated optimization algorithm. Therefore, in this work, the term optimization refers to the systematic evaluation of predefined geometric configurations and the selection of the most suitable design based on acoustic response, rather than the minimization or maximization of an objective function by a dedicated numerical optimizer.

The parametric study focused on three geometric variables: total needle length, cone height for linear horn transitions, and exponential height for smoothly varying horn profiles. All dimensions were scaled with respect to the longitudinal wavelength, $\lambda$, propagating in the aluminium needle. This wavelength-based scaling was used to ensure gradual impedance transitions over distances ranging from sub-wavelength scales, $\lambda/8$, to wavelength-scale dimensions, with the objective of reducing internal reflections and improving pressure transmission toward the piezoelectric interface. The investigated

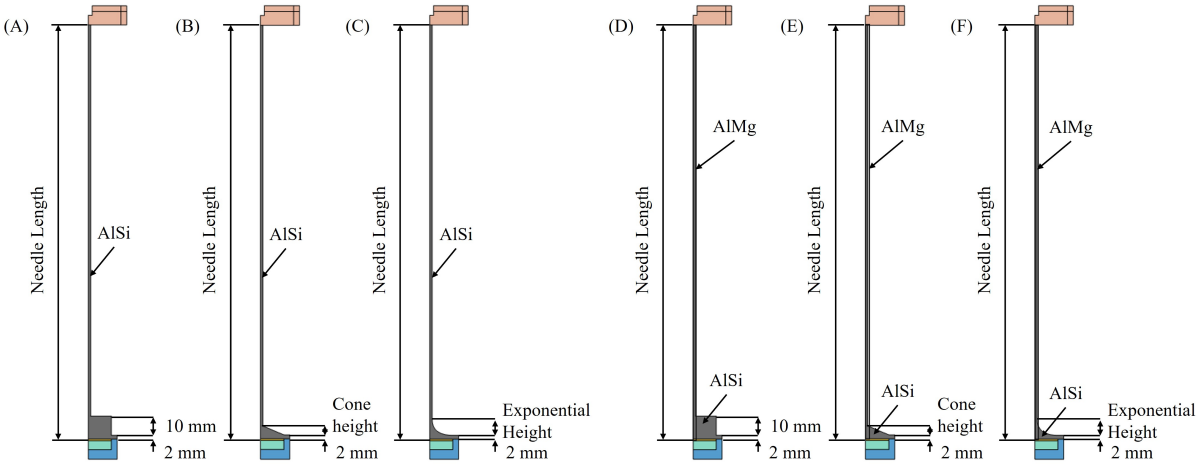



Figure 94: Geometric configurations investigated in the numerical size optimization study, with dimensions scaled relative to the longitudinal acoustic wavelength: (A) cylindrical AlSi needle and horn, (B) conical AlSi needle and horn, (C) exponential AlSi needle and horn, (D) cylindrical AlMg needle and AlSi horn, (E) conical AlMg needle and AlSi horn, and (F) exponential AlMg needle and AlSi horn.

parameter ranges are summarized in Table 20. Since the needle was required to have a minimum length of 200 mm, the first evaluated configuration corresponded to $45\lambda$. For the cylindrical base configuration, the transition height was fixed at 1 cm to simplify fabrication and provide a practical reference geometry against which the conical and exponential horn profiles could be compared.

Table 20: Parameters evaluated in the numerical geometric optimization studies.

| **Shape** | **Needle material** | **Needle diameter (mm)** | **Optimized parameters** |
|---|---|---|---|
| Cylindrical | AlSi | 2.5 | Needle length: |
| | | 3.2 | $[45\lambda–47\lambda]$ |
| | AlMg | 2.5 | |
| | | 3.2 | |
| Conical | AlSi | 2.5 | Needle length: |
| | | | $45\lambda–47\lambda$ |
| | | 3.2 | $[45\lambda–47\lambda]$ |
| | AlMg | 2.5 | cone height: $\lambda/8–8\lambda$ |
| | | 3.2 | |
| Exponential | AlSi | 2.5 | Needle length: |
| | | | $45\lambda–47\lambda$ |
| | | 3.2 | $[45\lambda–47\lambda]$ |
| | AlMg | 2.5 | cone height: $\lambda/8–8\lambda$ |

Apart from the geometric parameters under investigation, all simulations used the same numerical formulation, material properties, excitation conditions, and boundary settings described in Section 2.2. This ensured that differences in acoustic response could be attributed to the evaluated geometry rather than to changes in the numerical setup. In total, 4096 batch simulations were performed across the different combinations of material, diameter, needle length, and horn-transition geometry, allowing a consistent comparison of their acoustic guidance and transmission performance.

**Horn Needle Directivity Numerical methods**

To evaluate the angular directivity of the proposed horn needle attachments, the numerical configuration was modified as shown in Figure 95. This revised model enabled the acoustic response to be assessed as a function of incidence angle relative to the needle axis.

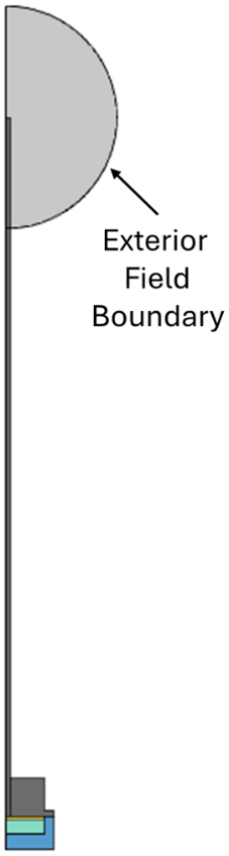



Figure 95: Numerical model used to evaluate the angular directivity of the proposed needle hydrophone attachment with a cylindrical base, showing the exterior field boundary used for far-field pressure sampling.

The axisymmetric model was extended into the surrounding acoustic medium and bounded by an exterior field boundary. This formulation allowed the radiated and scattered pressure fields to be sampled over a full angular range of $360°$, with an angular resolution of $1°$, while minimizing artificial

reflections from the computational boundaries. In the directivity study, $0^\circ$ was defined as normal incidence, corresponding to a wave propagating perpendicular to the needle surface. Conversely, $90^\circ$ represented propagation parallel to the needle axis. Due to the axisymmetric formulation, the $-90^\circ$ direction corresponds to the mirrored counterpart of the positive angular domain.

Because directivity is intrinsically frequency-dependent, the analysis was performed in the frequency domain, resulting in a total of 12 simulations. In this stage, the Solid Mechanics interface was used instead of the Elastic Waves module, which prevented the use of the discontinuous Galerkin formulation adopted in the previous simulations. Consequently, more restrictive mesh requirements were imposed, and the minimum spatial resolution was increased to five finite elements per wavelength to ensure numerical stability and accuracy.

This configuration enabled the computation of angle-dependent pressure responses relative to the needle axis, providing a quantitative assessment of hydrophone directivity. For each horn geometry, namely cylindrical, conical, and exponential bases, only the best-performing configurations from the previous sensitivity and wave-guiding optimization studies were selected. This ensured that the directivity comparison was conducted using geometries already optimized for acoustic performance, allowing the influence of horn shape on angular response to be evaluated independently from the effects of suboptimal designs.

**Numerical Frequency Dependent Sensitivity Calibration**

As in the previous analysis, the best-performing horn needle configurations were selected for further evaluation. The numerical model was then reformulated to reproduce the calibration procedure described by Oliveira et al.[39], as illustrated in Figure 96.

The calibration analysis was performed entirely in the frequency domain over a range from 100 kHz to 10 MHz, using a logarithmic frequency sweep with 30 points per decade. The prescribed harmonic pressure reproduced the experimental calibration condition in which solid NDT transducers generate a known acoustic field incident on the hydrophone assembly. Since the excitation was transmitted through a solid waveguide rather than through a fluid domain, the inclusion of an acoustic fluid region was not required in this model.

This formulation enabled direct comparison with experimental calibration data while isolating the mechanical–acoustic response of the horn needle hydrophone. By avoiding additional fluid–structure interaction effects, the model focused on the transmission of guided elastic waves through the waveguide and their subsequent coupling into the hydrophone structure. A total of 12 frequency-domain simulation studies were performed, corresponding to the selected optimized configurations.

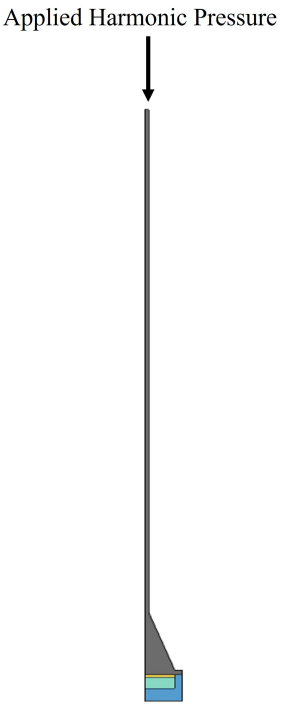



Figure 96: Schematic representation of the boundary condition used in the frequency-domain calibration simulation. A harmonic pressure excitation is applied to the upper surface of a rigid waveguide structure, allowing acoustic energy to be transmitted toward the hydrophone model positioned at its base. This configuration reproduces the calibration approach based on solid NDT transducers.

#### 6.2.1.5 Fabrication of Optimized Needle Designs

The aluminium horn needles corresponding to the optimized geometries were produced using a reproducible sand-casting procedure followed by post-machining, as schematically represented in figure 97. Initially, a stainless-steel external mould was filled with fine red clay-bonded moulding sand and compacted to provide adequate thermal resistance and dimensional stability during casting. A PLA 3D-printed counter-mould, containing the negative geometry of the acoustic horn, was then inserted into the compacted sand to define the horn cavity and the central needle channel with controlled taper and alignment.

After removal of the counter-mould, the AlSi alloy was melted in a crucible furnace at temperatures between 660 and $720\ ^{\circ}\mathrm{C}$. This temperature range was selected to remain above the eutectic melting temperature of the alloy, approximately $577\ ^{\circ}\mathrm{C}$, ensuring sufficient fluidity to fill the slender horn geometry. The molten aluminium was then poured into the prepared sand mould and allowed to solidify under ambient conditions. After cooling, the cast component was extracted by breaking the mould, producing a rough horn–needle preform.

The cast preform was subsequently machined using a precision turning lathe to remove excess material, improve surface quality, and define the final horn profile, shaft diameter, and total length. The resulting aluminium horn needles presented smooth surfaces, consistent geometry, and dimensional

tolerances suitable for acoustic waveguiding. After machining, the samples were ready for integration into the piezoelectric transducer assembly.

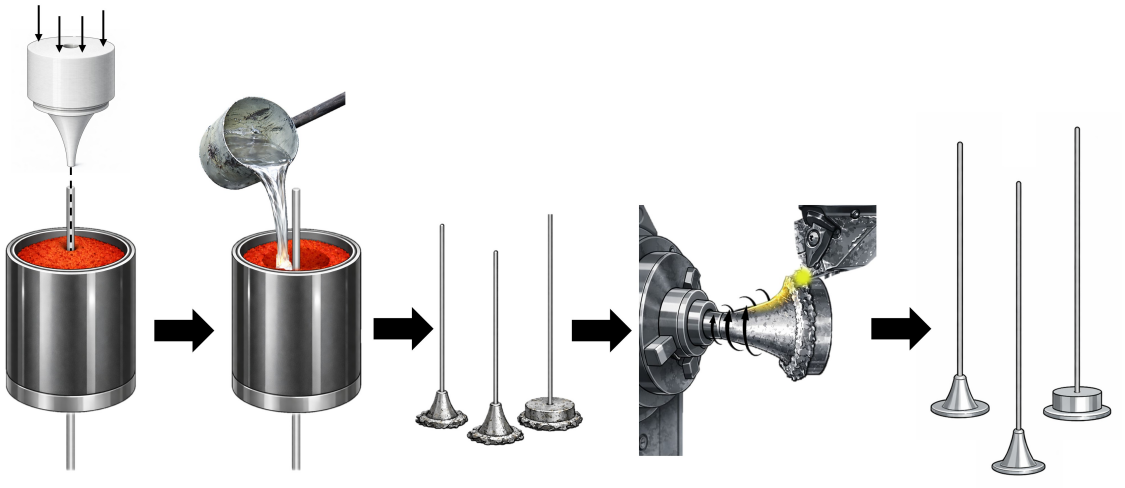


Figure 97: Schematic representation of the manufacturing route used to produce the aluminium horn needle elements, including sand mould preparation, alloy casting, post-machining, and the final needle geometries.

A total of nine aluminium horn needle samples were fabricated using this procedure, as summarized in Table 21. For all cast components, AlSi was used as the casting alloy due to its lower melting temperature, narrower solidification interval, and improved process control, particularly for thin and elongated geometries. The needle sections were produced using either AlSi or AlMg alloys to experimentally evaluate the influence of material composition on guided wave propagation. Two nominal external diameters were considered, namely 2.5 and 3.2 mm.

Table 21: Identification of the manufactured aluminium horn needle samples.

| **Sample Name** | **Base Shape** | **Needle alloy** | **Diameter (mm)** |
|---|---|---|---|
| CylAlSi3_2 | Cylinder | AlSi | 3.2 |
| ConAlSi2_5 | Conical | AlSi | 2.5 |
| ConAlSi3_2 | | | 3.2 |
| ConAlMg2_5 | | AlMg | 2.5 |
| ConAlMg3_2 | | | 3.2 |
| ExpAlSi2_5 | Exponential | AlSi | 2.5 |
| ExpAlSi3_2 | | | 3.2 |
| ExpAlMg2_5 | | AlMg | 2.5 |
| ExpAlMg3_2 | | | 3.2 |

The sample set included one cylindrical base configuration with a 3.2 mm diameter, two conical base

configurations with diameters of 2.5 and 3.2 mm, and two exponential base configurations with the same diameter values. The cylindrical geometry was included as a reference design because of its simpler mould architecture, easier fabrication, and higher expected reproducibility. This reference configuration enabled the acoustic performance of the more complex conical and exponential horn geometries to be assessed against a manufacturable baseline.

#### 6.2.1.6 Experimental Validation and Testing Methods

**Pressure Calibration** The horn needle hydrophone was calibrated in a water tank using a broadband frequency-domain sweep. During calibration, the needle was aligned vertically with the acoustic source and maintained at a fixed distance to ensure repeatable measurement conditions, following the procedure described by Oliveira et al.[39]. The experimental arrangement is shown in Figure 98.

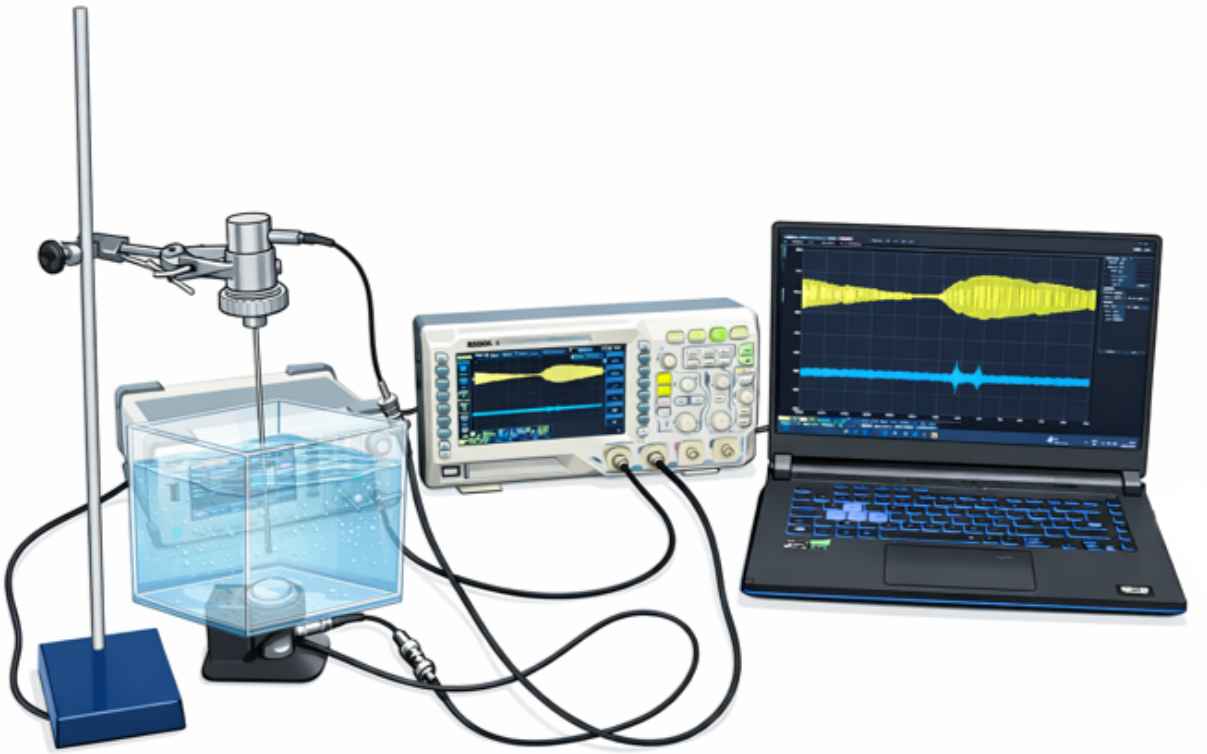


Figure 98: Calibration setup used for the horn needle hydrophone, showing the needle mounted on a precision positioning system and immersed in a water tank above the transmitting transducer. The electrical response was monitored using an oscilloscope and recorded on a computer for subsequent post-processing.

A harmonic frequency sweep was applied from 100 kHz to 10 MHz, covering the intended operating bandwidth of the hydrophone. The sweep was performed using logarithmic frequency increments, with sufficient dwell time at each frequency to reach steady-state conditions. Including signal averaging to improve the signal-to-noise ratio, each sweep required approximately 2–3 min of acquisition time.

The electrical response of the horn needle was recorded using a digital oscilloscope and stored for offline analysis. Signal post-processing was performed in MATLAB R2024b, where the measured voltage

spectra were converted into frequency-dependent sensitivity values by normalizing the hydrophone response against the known excitation conditions[1,4,16]. This procedure enabled consistent comparison of receiver sensitivity across frequency and between different horn needle configurations.

## 6.2.2 Results

### 6.2.2.1 Needle Horn Material Screening

The results of the preliminary horn needle material selection study are presented in Figure 99.

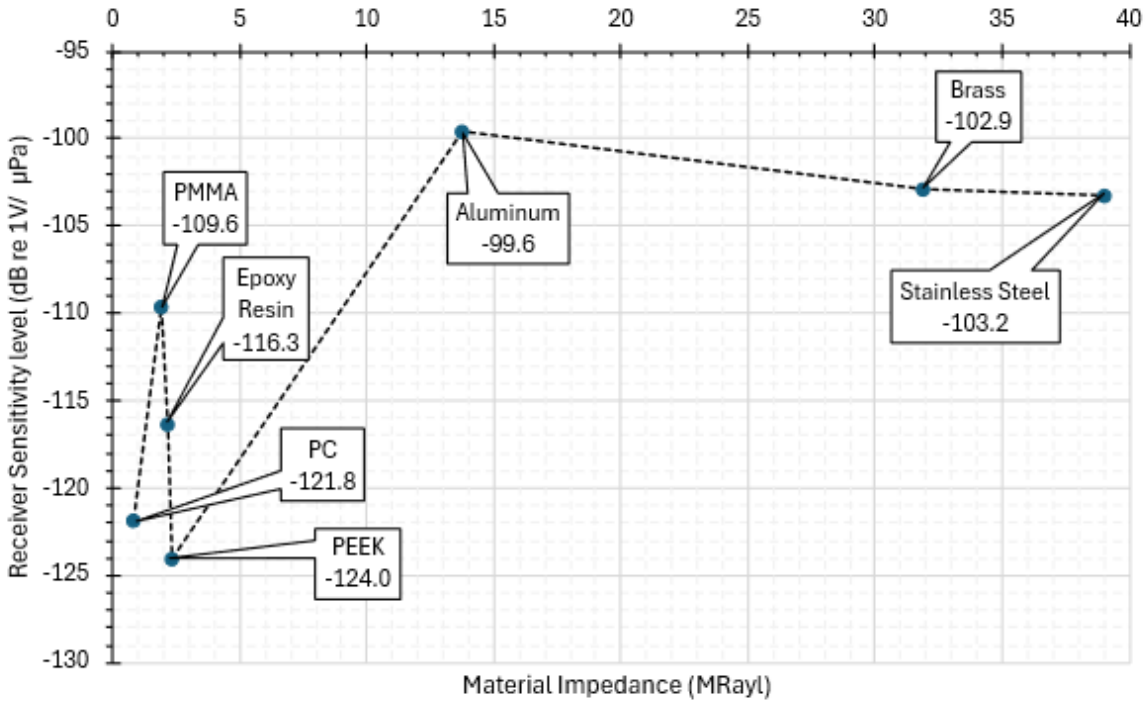



Figure 99: Receiver sensitivity of the proposed needle hydrophone as a function of the acoustic impedance of the horn material, expressed in dB re 1 V/$\mu$Pa for the optimized geometries.

The results indicate a clear dependence of receiver sensitivity on the acoustic impedance of the horn needle material. Among the evaluated materials, aluminium produced the highest sensitivity, with a value of $-99.6$ dB re 1 V/$\mu$Pa, indicating the most efficient transfer of acoustic energy from the surrounding medium to the piezoelectric sensing element. This performance is attributed to the favourable combination of moderate acoustic impedance, effective coupling with the PZT element, low intrinsic damping, and efficient longitudinal wave propagation.

Materials with higher acoustic impedance, such as stainless steel and brass, showed reduced sensitivity, most likely due to increased reflection losses at the material interfaces. Conversely, polymeric materials, including PMMA, resin, polycarbonate, and PEEK, exhibited substantially lower sensitivities. Although these materials provide closer impedance matching with soft tissues, their higher intrinsic

attenuation limited the pressure transmitted to the piezoelectric element. These findings suggest that polymer-based horn needles may become viable if acoustic damping is sufficiently reduced. However, under the simulated conditions, aluminium provided the most suitable compromise between acoustic transmission, impedance transition, damping, and manufacturability, and was therefore selected as the preferred material for the horn needle design.

#### 6.2.2.2 Aluminium Alloys Characterization

The experimentally measured longitudinal wave speed and acoustic attenuation coefficient, described in Section 2.3, are presented in Figure 100.

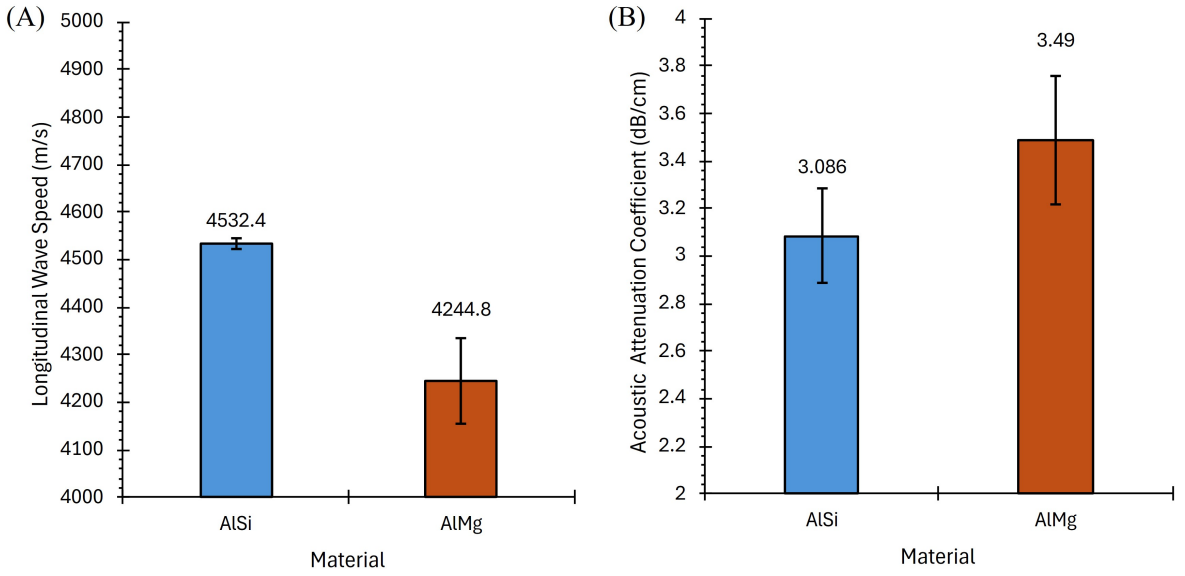



Figure 100: Experimentally measured (A) longitudinal wave speed and (B) acoustic attenuation coefficient for the AlSi and AlMg needle samples.

The experimentally determined acoustic properties of the aluminium alloys are directly relevant to the horn needle design, since the needle operates as a guided longitudinal waveguide and its geometry must be scaled according to the wavelength within the material. AlSi exhibited a higher longitudinal wave speed, $4532.4 \pm 11.2$ m/s, resulting in a longer internal wavelength for a given excitation frequency. This facilitates the definition of horn transition lengths, cone heights, and exponential profiles as controlled fractions of the wavelength, supporting gradual impedance transition and reducing internal reflections.

In contrast, AlMg presented a lower longitudinal wave speed, $4244.8 \pm 91.3$ m/s, which reduces the internal wavelength and modifies the phase accumulation along the needle. As a result, geometries optimized for AlSi may experience shifted resonance and anti-resonance conditions when manufactured from AlMg. This difference highlights the importance of using experimentally measured wave speeds rather than nominal material values during wavelength-scaled design.

The attenuation measurements also support the selection of AlSi for the horn needle structure. AlMg showed a higher attenuation coefficient, $3.49 \pm 0.269$ dB/cm, compared with $3.086 \pm 0.198$ dB/cm for AlSi. This increased attenuation implies greater acoustic energy loss along the propagation path, which becomes particularly relevant in long and slender waveguides where efficient energy transfer toward the piezoelectric element is required.

Consequently, horn needles fabricated from AlMg would require shorter effective propagation lengths and smoother transition geometries to reduce cumulative losses and internal reflection. Conversely, the lower attenuation and higher longitudinal wave speed of AlSi allow longer needle designs and more pronounced horn profiles while preserving acoustic sensitivity. Overall, the combination of higher wave speed and reduced intrinsic attenuation makes AlSi the more suitable alloy for the proposed horn needle hydrophone, enabling wavelength-based geometric scaling, improved pressure transmission, and enhanced frequency-dependent response.

#### 6.2.2.3 Numerical Results

**Geometry Size Optimization results**

The variation in receiver sensitivity as a function of needle length, normalized by the longitudinal wavelength, $\lambda$, for the investigated aluminium alloy configurations is presented in figure 101. This analysis was used to determine the wavelength-dependent length conditions that maximize acoustic transmission toward the piezoelectric sensing region.

For the AlSi needle with a diameter of 2.5 mm, shown in figure 101A, the receiver sensitivity exhibited a periodic dependence on needle length. Local sensitivity maxima of $-95.75$ and $-96.58$ dB re 1 V/$\mu$Pa were observed, with maxima and minima separated by approximately one wavelength after $(45 + 1/8)\lambda$. This behaviour indicates the presence of constructive and destructive interference of guided longitudinal waves within the needle. Maximum sensitivity therefore occurs at specific length conditions where reflected wave components reinforce pressure transfer toward the piezoelectric element.

For the AlSi needle with a diameter of 3.2 mm, shown in figure 101B, a similar periodic response was observed, although the sensitivity variations were less pronounced. The oscillations followed a more regular spacing of approximately $\lambda/2$, with local maxima of $-93.78$, $-94.61$, $-94.66$, and $-96.09$ dB re 1 V/$\mu$Pa. This suggests that the larger diameter improves wave confinement and reduces sensitivity to small changes in needle length after $(45 + 1/8)\lambda$, resulting in a more stable and slightly higher average response than the 2.5 mm AlSi configuration.

The AlMg needle with a diameter of 2.5 mm, presented in figure 101C, showed lower overall sensitivity

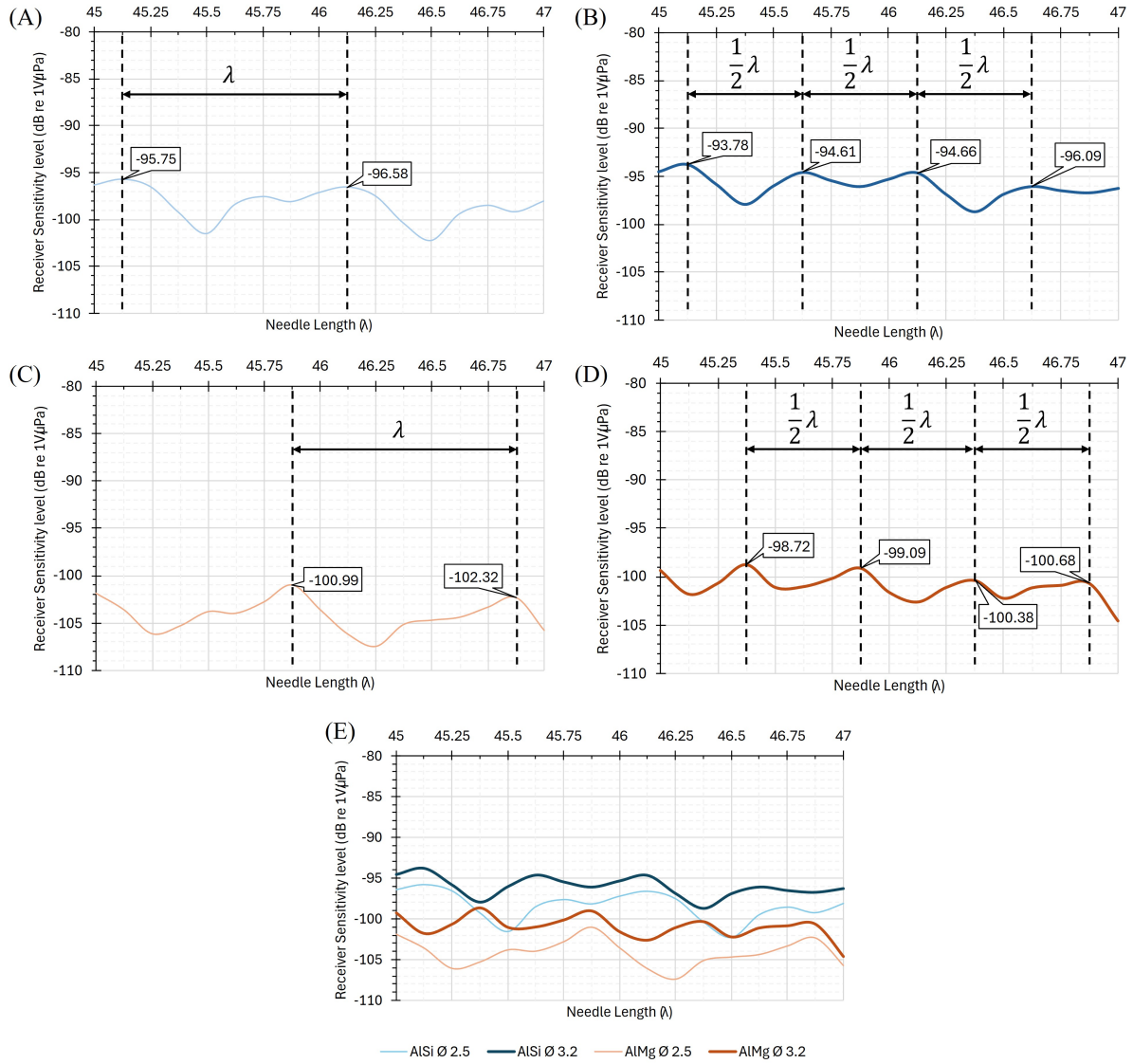



Figure 101: Influence of needle length, expressed as multiples of the longitudinal wavelength, $\lambda$, on the receiver sensitivity of the horn needle hydrophone for different material and diameter configurations: (A) AlSi, 2.5 mm diameter; (B) AlSi, 3.2 mm diameter; (C) AlMg, 2.5 mm diameter; (D) AlMg, 3.2 mm diameter; and (E) comparative overview of all configurations.

and stronger attenuation effects. Although wavelength-dependent oscillations remained evident, with local maxima of $-100.99$ and $-102.32$ dB re 1 V/$\mu$Pa, the peak sensitivities were lower and the minima were more pronounced than those observed for AlSi. This response is consistent with the lower longitudinal wave speed and higher intrinsic damping of the AlMg alloy. For the 3.2 mm AlMg needle, shown in figure 101D, the larger cross-section partially reduced attenuation effects and produced smoother sensitivity variations, with local maxima of $-98.72$, $-99.09$, $-100.38$, and $-100.68$ dB re 1 V/$\mu$Pa. Nevertheless, the sensitivity remained lower than that obtained for the corresponding AlSi configuration.

The comparison of all configurations in figure 101E confirms that AlSi needles consistently provided higher sensitivity over the evaluated length range. Among the tested cases, the AlSi needle with a 3.2 mm diameter showed the most stable and highest overall response. In contrast, AlMg configurations exhibited

systematically reduced sensitivity, particularly for the smaller diameter. These results demonstrate the combined influence of material damping, longitudinal wave speed, and geometric scaling on the acoustic performance of the horn needle hydrophone. The corresponding optimal needle lengths are summarized in table 22.

Table 22: Summary of wavelength-dependent sensitivity behaviour and resulting optimal horn needle lengths for AlSi and AlMg configurations.

| **Material** | **Diameter (mm)** | **Spacing between local maxima** | **Ideal horn needle length** |
|---|---|---|---|
| AlSi | 2.5 | $\lambda$ | $(45 + 1/8)\lambda$ |
| AlSi | 3.2 | $\lambda/2$ | $(45 + 1/8)\lambda$ |
| AlMg | 2.5 | $\lambda$ | $(45 + 7/8)\lambda$ |
| AlMg | 3.2 | $\lambda/2$ | $(45 + 3/8)\lambda$ |

After defining the optimal needle length for each material and diameter, the effect of conical horn height was evaluated, as shown in figure 102. In this study, the needle length was fixed at the previously identified optimal value, allowing the influence of cone height on diffraction behaviour and impedance transition at the horn–needle interface to be isolated.

For the AlSi needle with a diameter of 2.5 mm, figure 102A shows that sensitivity increased when the cone height approached integer multiples of the wavelength. Local maxima of $-85.84$, $-85.97$, and $-86.36$ dB re 1 V/$\mu$Pa were identified, separated by approximately $\lambda$ after a cone height of $(5 + 1/4)\lambda$. These peaks indicate that cone heights commensurate with the internal wavelength promote constructive diffraction and improve coupling of longitudinal waves toward the piezoelectric element. For the 3.2 mm AlSi configuration, shown in figure 102B, the response was smoother and more stable, with local maxima of $-86.19$, $-85.34$, $-85.88$, and $-86.35$ dB re 1 V/$\mu$Pa occurring at approximately wavelength-spaced intervals after $(4 + 1/8)\lambda$. This configuration provided slightly higher and more consistent sensitivity, suggesting improved wave confinement and reduced sensitivity to geometric perturbations.

The AlMg configurations showed lower sensitivity than their AlSi counterparts. For the 2.5 mm AlMg needle, shown in figure 102C, wavelength-dependent maxima of $-92.90$, $-92.55$, $-93.00$, and $-93.33$ dB re 1 V/$\mu$Pa were observed after a cone height of $(4 + 7/8)\lambda$. However, the sensitivity gains remained limited by the higher intrinsic damping of the alloy. The 3.2 mm AlMg needle, shown in figure 102D, produced more distinct peaks, with local maxima of $-90.85$, $-91.09$, $-91.12$, and $-91.67$ dB re 1 V/$\mu$Pa, also separated by approximately one wavelength after $(4 + 7/8)\lambda$. Although the larger diameter reduced attenuation effects, the absolute sensitivity remained below the equivalent

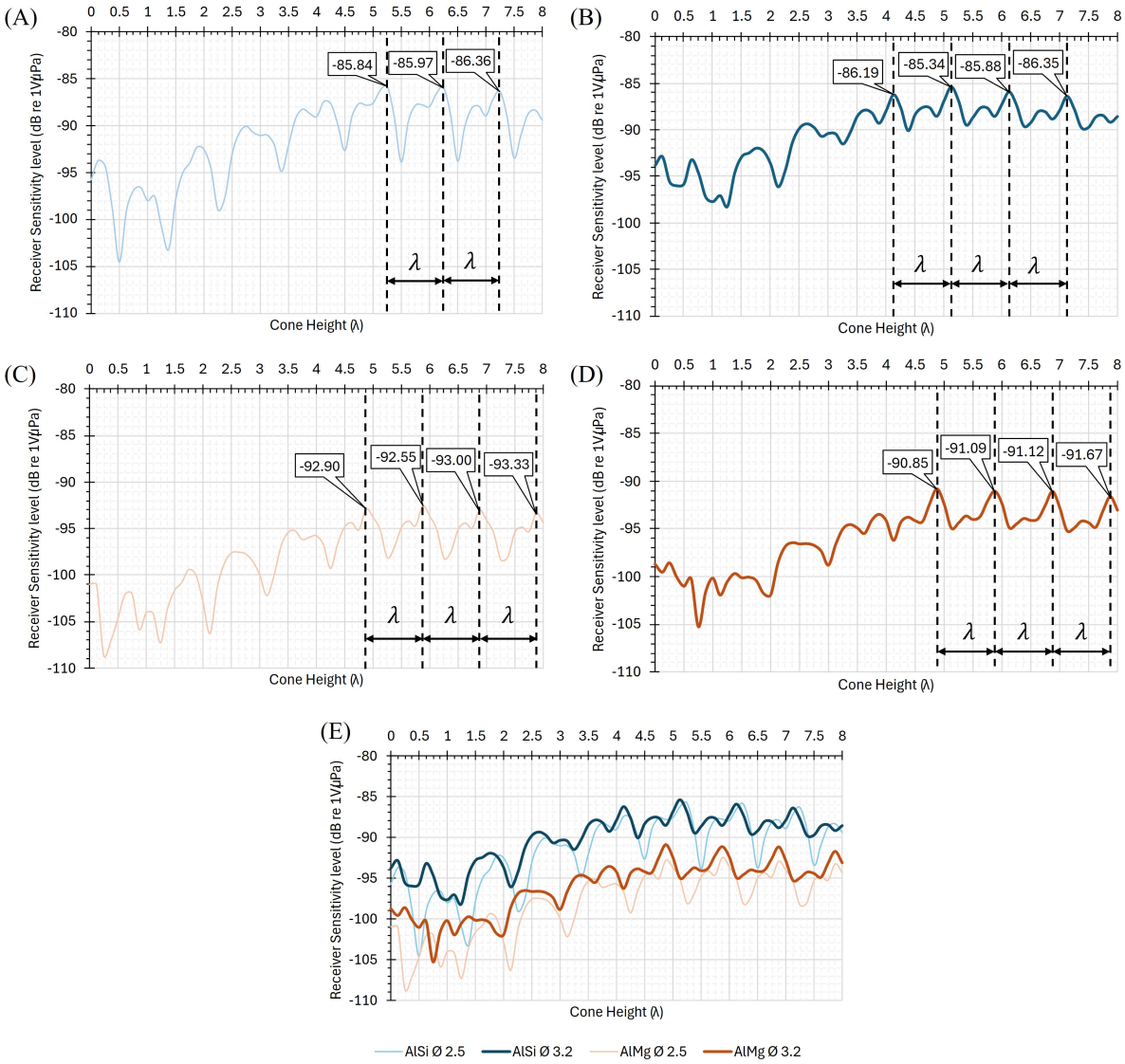



Figure 102: Effect of cone height, expressed as multiples of the longitudinal wavelength, $\lambda$, on the receiver sensitivity of the horn needle hydrophone for fixed optimized needle lengths: (A) AlSi, 2.5 mm diameter; (B) AlSi, 3.2 mm diameter; (C) AlMg, 2.5 mm diameter; (D) AlMg, 3.2 mm diameter; and (E) comparative overview of all configurations.

AlSi geometry.

The comparative analysis in figure 102E demonstrates that AlSi-based conical horn needles outperformed AlMg configurations across the investigated cone height range. The AlSi 3.2 mm needle provided the highest and most stable sensitivity, confirming that both material selection and horn transition geometry are critical for maximizing diffraction efficiency and hydrophone response. The derived optimal cone heights are presented in table 23.

Table 23: Optimized conical horn heights for AlSi and AlMg needle configurations, determined from the wavelength-scaled spacing of local sensitivity maxima.

| **Material** | **Diameter (mm)** | **Spacing between local maxima** | **Ideal horn needle length** |
|---|---|---|---|

| | | | |
|---|---|---|---|
| AlSi | 2.5 | $\lambda$ | $(5 + 1/4)\lambda$ |
| AlSi | 3.2 | $\lambda$ | $(4 + 1/8)\lambda$ |
| AlMg | 2.5 | $\lambda$ | $(4 + 7/8)\lambda$ |
| AlMg | 3.2 | $\lambda$ | $(4 + 7/8)\lambda$ |

A detailed view of the simulated wave propagation through the conical horn is shown in figure 103 for the AlSi 3.2 mm configuration.

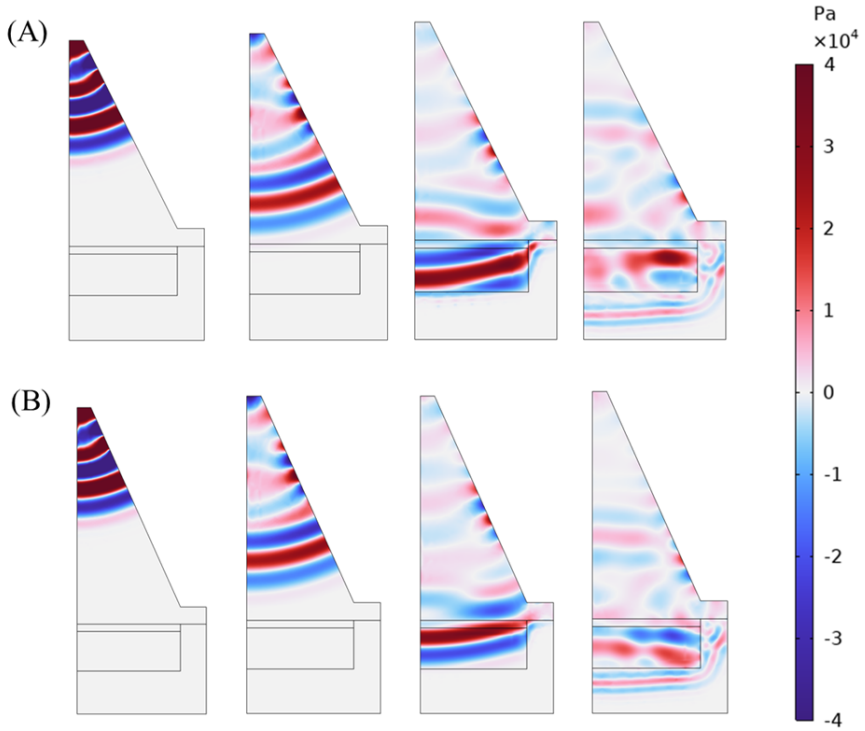



Figure 103: Numerically simulated pressure field distribution within the horn needle for AlSi with a diameter of 3.2 mm, illustrating longitudinal wave propagation and diffraction for two horn heights: (A) $(4 + 5/8)\lambda$ and (B) $(5 + 1/8)\lambda$. The colour scale represents instantaneous acoustic pressure amplitude.

The pressurefield maps show that the two conical horn geometries produced distinct wave propagation patterns. In figure 103A, the more abrupt transition generated stronger wavefront curvature, localized pressure gradients, and increased interference near the horn–needle junction. These effects indicate stronger internal reflection and mode conversion, reducing the efficiency of energy transfer toward the sensing region. In contrast, figure 103B shows a smoother pressure evolution, with more uniform wavefronts and fewer pressure discontinuities along the horn walls. The more gradual transition therefore improved impedance matching and allowed longitudinal waves to couple into the needle with reduced reflection. As a result, this geometry concentrated acoustic energy more effectively at the piezoelectric interface, increasing sensitivity and reducing transmission losses.

The receiver sensitivity as a function of exponential horn height is shown in figure 104. As in the conical study, the needle length was fixed at the optimized value for each configuration, allowing the effect of the exponential transition on wave diffraction and impedance matching to be evaluated independently.

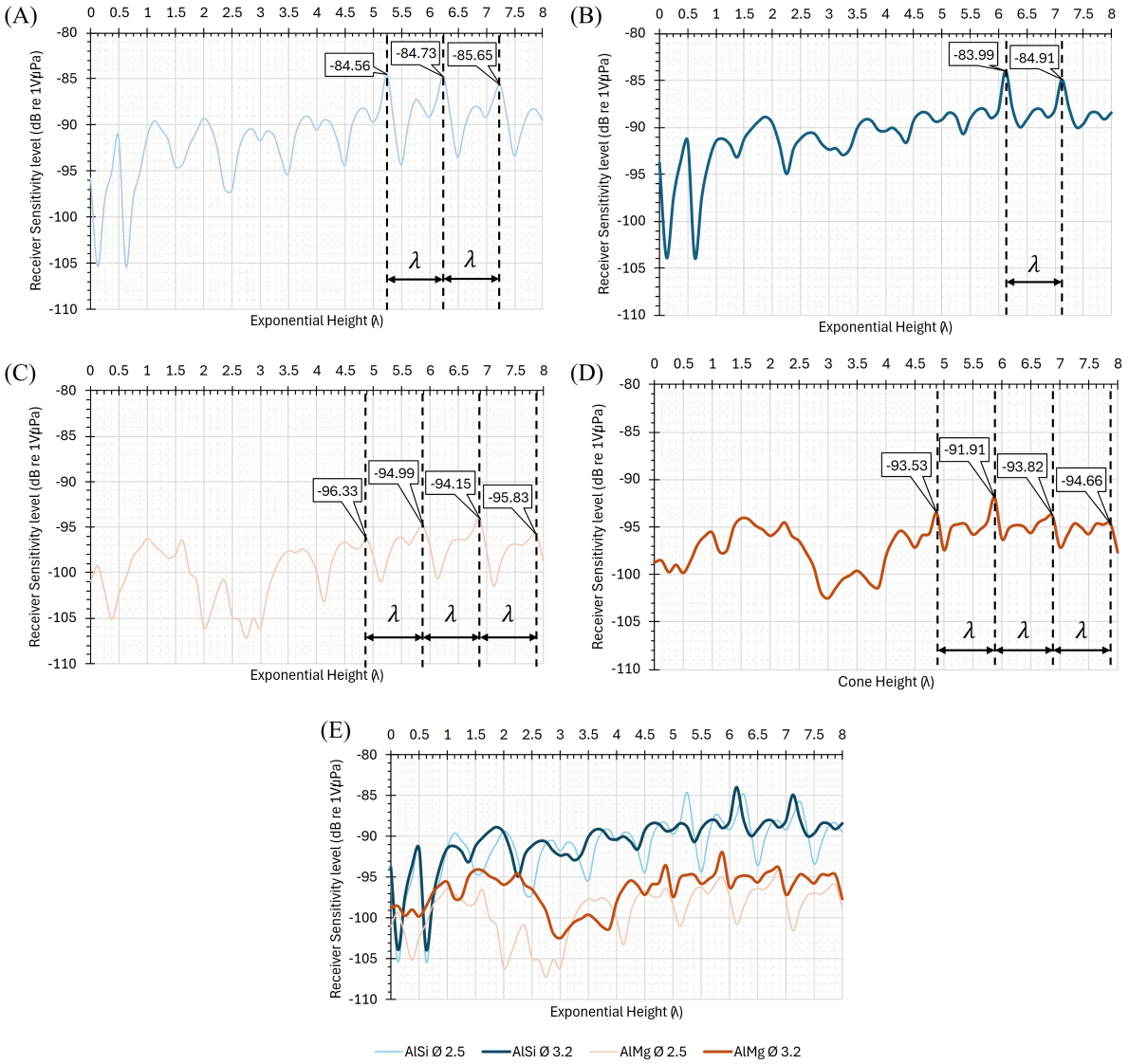



Figure 104: Effect of exponential horn height, expressed as multiples of the longitudinal wavelength, $\lambda$, on the receiver sensitivity of the horn needle hydrophone for fixed optimized needle lengths: (A) AlSi, 2.5 mm diameter; (B) AlSi, 3.2 mm diameter; (C) AlMg, 2.5 mm diameter; (D) AlMg, 3.2 mm diameter; and (E) comparative overview of all configurations.

For the AlSi needle with a diameter of 2.5 mm, shown in figure 104A, receiver sensitivity increased with exponential height and exhibited periodic maxima of $-84.56$, $-84.73$, and $-85.65$ dB re 1 V/$\mu$Pa. These peaks appeared at intervals of approximately one wavelength after $(5 + 1/4)\lambda$, indicating that exponential horn lengths aligned with the internal wavelength enhance constructive diffraction and longitudinal wave transfer. Compared with the conical horn, this configuration produced slightly higher peak sensitivity. For the AlSi needle with a diameter of 3.2 mm, shown in figure 104B, the response was smoother, with local maxima of $-83.99$ and $-84.91$ dB re 1 V/$\mu$Pa occurring at

wavelength-spaced intervals after $(6 + 1/8)\lambda$. This configuration achieved the highest overall sensitivity and the lowest sensitivity fluctuation, demonstrating the benefit of combining a larger diameter with a smoothly varying exponential transition.

The AlMg needle with a diameter of 2.5 mm, shown in figure 104C, again showed lower sensitivity and stronger attenuation effects. Although wavelength-dependent maxima were observed, with values of $-96.33$, $-94.99$, $-94.15$, and $-95.83$ dB re 1 V/$\mu$Pa after $(4 + 7/8)\lambda$, the attainable sensitivity remained below the AlSi configurations. For the AlMg needle with a diameter of 3.2 mm, shown in figure 104D, the exponential horn partially compensated for material losses and produced more stable sensitivity peaks of $-93.53$, $-91.91$, $-93.82$, and $-94.66$ dB re 1 V/$\mu$Pa. Nevertheless, the absolute sensitivity remained lower than that of the corresponding AlSi horn.

The comparison of all configurations in figure 104E shows that exponential horn profiles generally produced smoother sensitivity trends and slightly higher peak values than conical geometries when the same optimized needle lengths were used. Overall, AlSi-based exponential horns provided the most robust performance, confirming that smooth wavelength-scaled transitions improve diffraction control and acoustic energy transfer in horn needle hydrophones. The optimal exponential horn heights are summarized in table 24.

Table 24: Optimized exponential horn heights for AlSi and AlMg needle configurations, determined from the wavelength-scaled spacing of local sensitivity maxima.

| **Material** | **Diameter (mm)** | **Spacing between local maxima** | **Ideal horn needle length** |
|---|---|---|---|
| AlSi | 2.5 | $\lambda$ | $(5 + 1/4)\lambda$ |
| AlSi | 3.2 | $\lambda$ | $(6 + 1/8)\lambda$ |
| AlMg | 2.5 | $\lambda$ | $(4 + 7/8)\lambda$ |
| AlMg | 3.2 | $\lambda$ | $(4 + 7/8)\lambda$ |

A detailed view of the acoustic field within the exponential horn is presented in figure 105.

The simulated pressure fields reveal that the exponential transition strongly influences guided wave propagation. In figure 105A, although the profile is smoother than cylindrical or conical transitions, pressure localization and distorted wavefronts remain visible near the horn–needle junction. These features indicate incomplete impedance matching and residual internal reflections, which may produce mode conversion and reduce the efficiency of energy transfer into the needle section. In figure 105B, the more gradual exponential profile produced smoother wavefront progression and a more uniform pressure distribution along the horn walls. This improved transition reduced scattering and reflection,

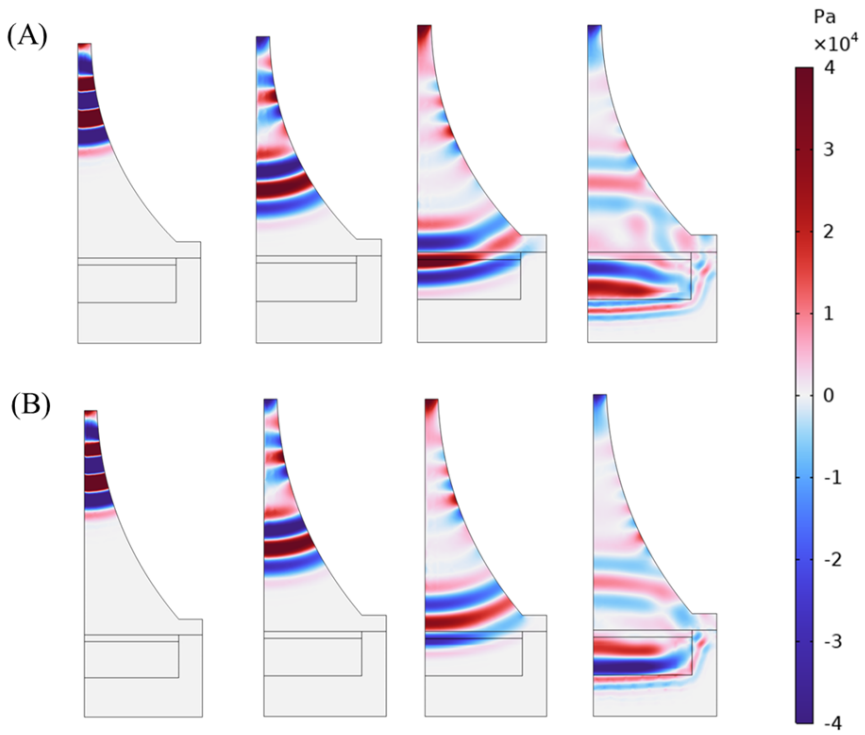



Figure 105: Numerically simulated acoustic pressure field within an exponential horn needle for AlSi with a diameter of 3.2 mm, showing longitudinal wave propagation and diffraction for two exponential profiles: (A) $(5+3/8)\lambda$ and (B) $(5+7/8)\lambda$. The colour scale represents instantaneous acoustic pressure amplitude.

allowing the longitudinal wave to couple more efficiently into the needle. Consequently, the latter configuration generated a stronger and more coherent pressure field at the sensing region, resulting in higher sensitivity, lower transmission loss, and improved broadband stability.

**Directivity Analysis of Optimized Horn Needle Hydrophone Configurations**

The numerically computed directivity sensitivity of the optimized horn needle hydrophone configurations is presented in figure 106. The polar plots show the angular dependence of the received sound pressure level as a function of the incident wave angle relative to the needle axis. This representation enables direct comparison of angular selectivity, forward sensitivity, and side-lobe behaviour for the different materials, diameters, and horn base geometries.

For the cylindrical horn configuration, shown in figure 106A, the directivity patterns presented broad main lobes and pronounced side-lobe structures, indicating limited angular selectivity. The highest sensitivity occurred near normal incidence, $0°$, and decreased rapidly at oblique angles. The oscillatory response observed away from the main lobe is likely associated with internal reflections and modal interference within the straight cylindrical transition.

The conical horn geometry, shown in figure 106B, produced a more focused main lobe and reduced side-lobe amplitudes when compared with the cylindrical case. This effect was particularly evident for the

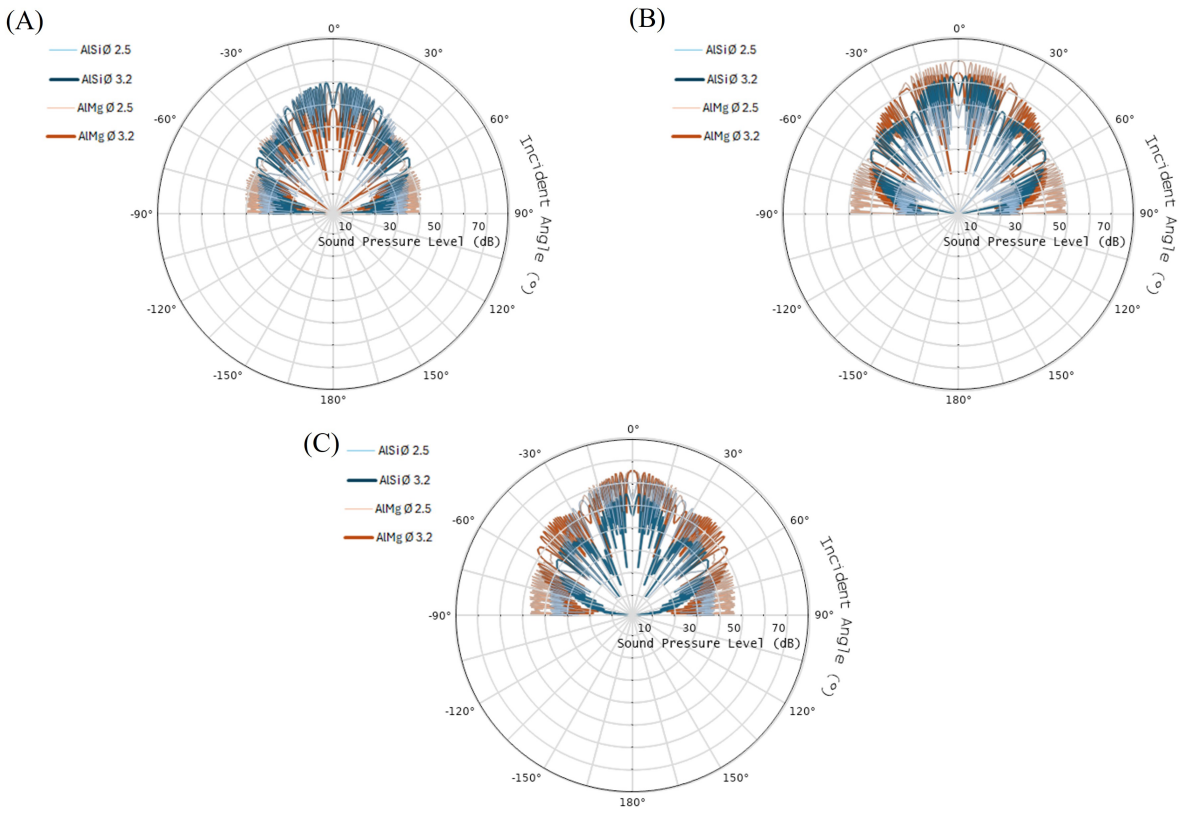



Figure 106: Simulated angular directivity patterns of the optimized horn needle hydrophone for different horn base geometries: (A) cylindrical horn, (B) conical horn, and (C) exponential horn. Results are shown for AlSi and AlMg needles with diameters of 2.5 and 3.2 mm.

3.2 mm diameter needles. The improved angular response suggests that the conical transition enhanced impedance matching and promoted more controlled diffraction at the horn base, resulting in greater forward sensitivity and a more stable directional response.

The exponential horn configuration, presented in figure 106C, exhibited the most regular and well-defined directivity patterns. The main lobe was narrower and more symmetric, while side-lobe amplitudes were further reduced and the angular decay was smoother. This behaviour was most evident for the AlSi needle with a diameter of 3.2 mm, which combined favourable material properties with a smooth wavelength-scaled transition. Across all geometries, AlSi configurations consistently produced higher received sound pressure levels than the corresponding AlMg needles. In addition, the larger 3.2 mm diameter generally improved forward sensitivity and directivity control, confirming the combined influence of material selection, diameter, and horn profile on the angular performance of the hydrophone.

**Horn Needle Sensitivity Numerical Study**

Figure 107 compares the simulated broadband receiver sensitivity of the optimized horn needle hydrophone configurations. The geometries correspond to the optimal dimensions previously identified

in Tables 4–6. The three panels show the influence of horn-base geometry, needle material, and needle diameter on the frequency-dependent response, while figure 107D summarizes the root-mean-square (RMS) sensitivity calculated over the 1–5 MHz band.

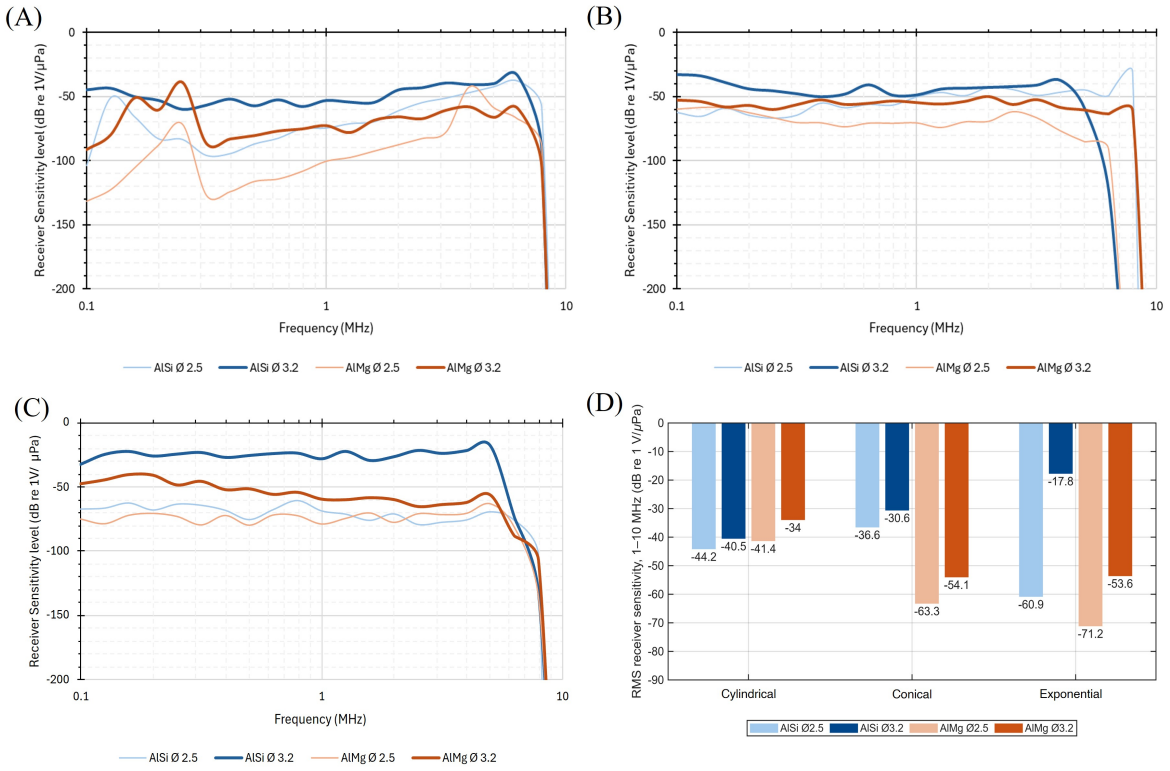



Figure 107: Simulated frequency-dependent receiver sensitivity of the optimized horn needle hydrophone for different horn-base geometries: (A) cylindrical, (B) conical, and (C) exponential. For each geometry, results are shown for AlSi and AlMg needles with diameters of 2.5 and 3.2 mm over the 0.1–10 MHz range. (D) Root-mean-square receiver sensitivity calculated over the 1–5 MHz frequency band for the 12 simulated configurations.

All configurations exhibited the expected behaviour of a guided-wave receiver, with a relatively stable mid-band response superimposed with moderate oscillations caused by wave interference along the needle. At higher frequencies, a pronounced sensitivity reduction was observed, indicating that guided-wave propagation and coupling to the sensing element become less efficient near the upper limit of the analysed bandwidth. Across the three horn designs, AlSi generally produced higher sensitivity than AlMg, which is consistent with its higher longitudinal wave speed and lower measured attenuation. These properties allow acoustic energy to be transmitted more efficiently toward the piezoelectric element. In addition, the 3.2 mm diameter needles generally produced more stable responses than the 2.5 mm configurations, suggesting improved wave confinement and reduced sensitivity to small geometric deviations.

For the cylindrical geometry, shown in figure 107A, the sensitivity spectra presented the greatest variability across the frequency range, with more pronounced oscillations at lower frequencies. This

behaviour is consistent with the abrupt transition at the cylindrical base, where impedance discontinuities and mode conversion can generate internal reflections. These reflections produce local sensitivity maxima and minima, particularly for the smaller-diameter needles. Despite this variability, the AlSi 3.2 mm configuration maintained the highest sensitivity across most of the usable band, whereas the AlMg 2.5 mm needle produced the weakest response, especially at low frequencies where attenuation and inefficient coupling are more influential.

The conical horn configuration, presented in figure 107B, produced a smoother broadband response than the cylindrical case. The gradual conical transition reduced abrupt impedance changes and promoted more controlled diffraction toward the sensing region. As a result, the sensitivity curves were more closely grouped in the mid-frequency range, with shallower minima and a more uniform plateau-like response. This indicates that, when cone height and needle length are selected using wavelength-scaled criteria, the conical horn provides a more repeatable transfer function and lower sensitivity to minor geometric variations. The AlSi 3.2 mm configuration again provided the highest sustained sensitivity, while the AlMg needles remained consistently less sensitive.

The exponential horn, shown in figure 107C, provided the most stable broadband response. This geometry produced higher sensitivity levels and a more consistent separation between materials and diameters. The smooth exponential expansion distributes the impedance transition over a longer effective distance, reducing internal reflection and limiting mode conversion. This is reflected in the reduced ripple amplitude and more uniform mid-band sensitivity. Although the same performance hierarchy was maintained, with AlSi outperforming AlMg and 3.2 mm diameters generally exceeding 2.5 mm configurations, the exponential profile reduced the performance penalty associated with less favourable material properties and coupling conditions. Therefore, the exponential AlSi 3.2 mm horn represents the most robust configuration among the analysed designs.

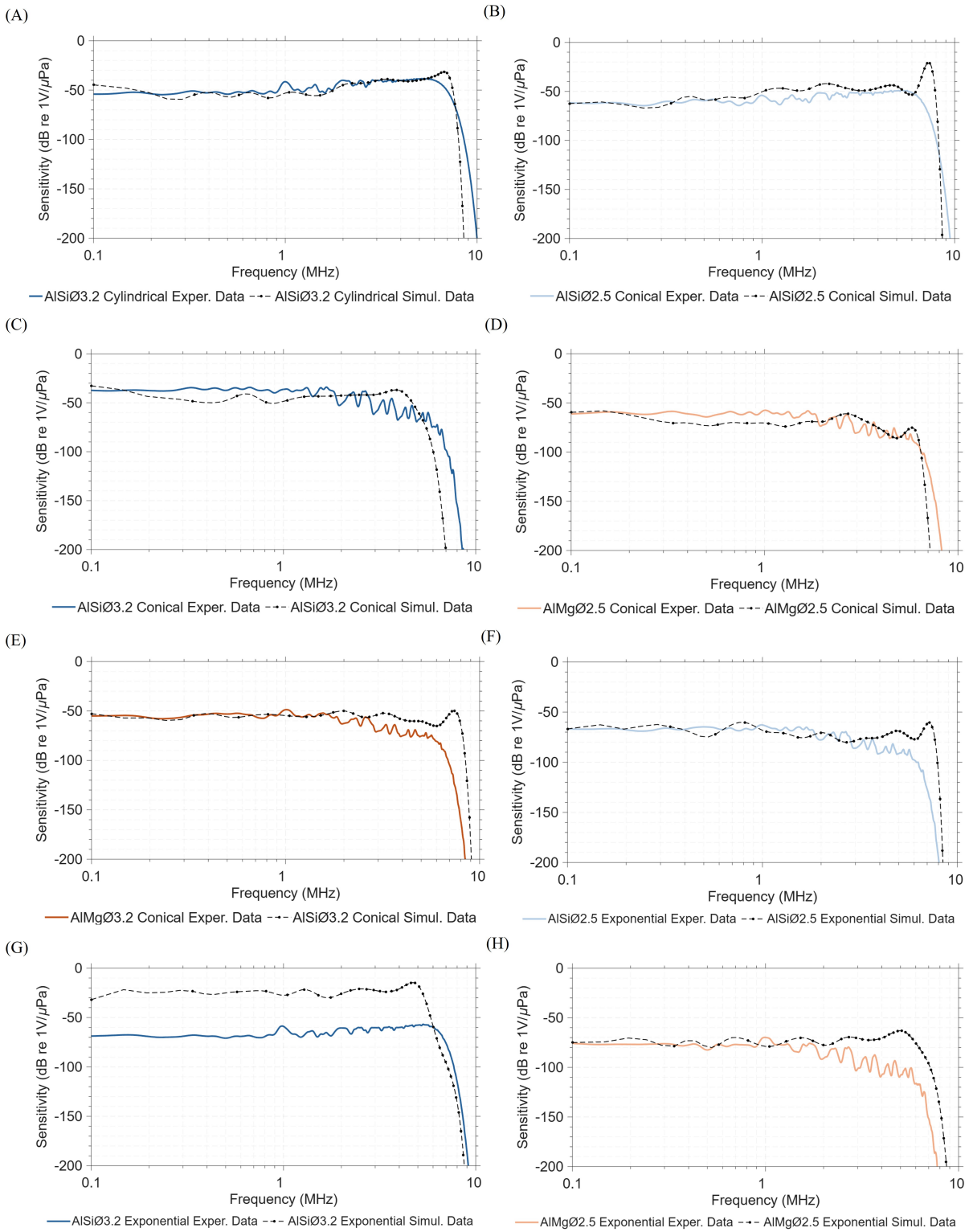
#### 6.2.2.4 Experimental results

**Horn Needle Sensitivity Calibration**

Figure 108 compares the experimentally measured receiver sensitivity spectra with the corresponding numerical predictions for nine horn needle configurations. The evaluated samples include cylindrical, conical, and exponential horn geometries produced using AlSi and AlMg alloys with two nominal diameters. In all panels, the continuous curves correspond to experimental measurements, whereas the dashed curves represent the simulated response obtained from the previously described numerical model.

For the cylindrical AlSi ∅2.5 mm horn needle, shown in figure 108A, the experimental and numerical

responses showed good agreement in the mid-frequency region. Both curves reproduced the general sensitivity level and the progressive increase toward higher frequencies. The simulated sensitivity ranged from $-59.2$ to $-31.9$ dB re 1 V/$\mu$Pa, while the experimental values ranged from $-53.9$ to $-40.9$ dB re 1 V/$\mu$Pa. The differences observed at lower frequencies may be associated with experimental alignment tolerances and simplified boundary conditions in the numerical model. The high-frequency roll-off was



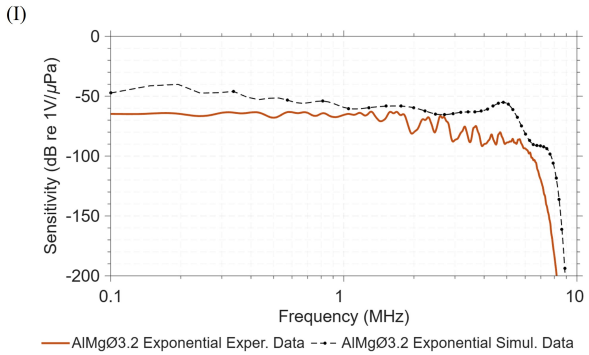



Figure 108: Comparison between experimentally measured and numerically simulated receiver sensitivity spectra for the horn needle hydrophone across different horn geometries, materials, and diameters: (A) cylindrical horn, AlSi ∅2.5 mm; (B–C) conical horn, AlSi ∅2.5 mm and ∅3.2 mm; (D–E) conical horn, AlMg ∅2.5 mm and ∅3.2 mm; (F–G) exponential horn, AlSi ∅2.5 mm and ∅3.2 mm; and (H–I) exponential horn, AlMg ∅2.5 mm and ∅3.2 mm.

consistently reproduced, indicating that the model captured the main bandwidth limitation of the cylindrical configuration.

Figures 108B and 108C present the results for the AlSi conical horn needles with diameters of 2.5 and 3.2 mm, respectively. For the 2.5 mm configuration, the simulated sensitivity varied from $-62.2$ to $-50.6$ dB re 1 V/$\mu$Pa, whereas the experimental response ranged from $-66.6$ to $-21.3$ dB re 1 V/$\mu$Pa. For the 3.2 mm configuration, the simulated and experimental ranges were $-50.4$ to $-32.8$ dB re 1 V/$\mu$Pa and $-53.34$ to $-33.6$ dB re 1 V/$\mu$Pa, respectively. In both cases, the numerical model reproduced the broadband behaviour and the reduced ripple structure relative to the cylindrical geometry. The 3.2 mm conical AlSi sample showed particularly strong agreement across the frequency band, suggesting greater robustness to fabrication tolerances and alignment variability.

The AlMg conical horn needles are shown in figures 108D and 108E. For the 2.5 mm configuration, the simulated sensitivity ranged from $-74.9$ to $-58.8$ dB re 1 V/$\mu$Pa, compared with experimental values between $-80.7$ and $-60.8$ dB re 1 V/$\mu$Pa. For the 3.2 mm configuration, the simulated range was $-59.9$ to $-48.8$ dB re 1 V/$\mu$Pa, while the experimental range was $-57.6$ to $-49.7$ dB re 1 V/$\mu$Pa. Although the main spectral trends were captured, the deviations were larger than those observed for the AlSi conical samples, particularly at higher frequencies. This behaviour is consistent with the higher attenuation and damping of AlMg, which may amplify the influence of microstructural variability, surface finish, and manufacturing imperfections not fully represented in the model.

Figures 108F and 108G show the AlSi exponential horn needles with diameters of 2.5 and 3.2 mm. These configurations presented the largest discrepancy between simulation and experiment. For the 2.5 mm needle, the simulated sensitivity ranged from $-76.9$ to $-60.7$ dB re 1 V/$\mu$Pa, while the experimental response remained between $-71.4$ and $-69.1$ dB re 1 V/$\mu$Pa. For the 3.2 mm needle, the numerical model predicted substantially higher sensitivity, ranging from $-32.7$ to $-15.5$ dB re

1 V/$\mu$Pa, whereas the experimental measurements ranged from $-71.7$ to $-58.8$ dB re 1 V/$\mu$Pa. Although the frequency-dependent trend was partially preserved, the absolute sensitivity level was not accurately reproduced. This suggests that exponential geometries are more sensitive to experimental factors such as machining tolerances, coupling quality, surface roughness, bonding conditions, and mounting alignment.

The AlMg exponential horn results are presented in figures 108H and 108I. For the 2.5 mm configuration, the simulated sensitivity ranged from $-79.8$ to $-69.2$ dB re 1 V/$\mu$Pa, while the experimental response varied between $-82.5$ and $-63.4$ dB re 1 V/$\mu$Pa. For the 3.2 mm configuration, the simulated range was $-65.5$ to $-38.3$ dB re 1 V/$\mu$Pa, compared with experimental values between $-86.7$ and $-68.2$ dB re 1 V/$\mu$Pa. Although the AlMg exponential samples showed lower sensitivity than the corresponding AlSi configurations, the simulations captured the main spectral features and the high-frequency roll-off. The larger deviation observed for the 3.2 mm AlMg exponential horn indicates that this configuration may be particularly sensitive to material losses or to deviations between the manufactured and nominal geometry.

Overall, the comparison between experimental measurements and numerical predictions supports the validity of the modelling strategy. Although exact agreement was not obtained for every geometry, the simulations reproduced the dominant spectral trends, sensitivity envelopes, and bandwidth limitations across the nine fabricated samples. The conical geometries showed the closest correspondence with the numerical predictions, indicating superior robustness and manufacturability when compared with the exponential profiles. Among the evaluated designs, the conical AlSi configurations provided the most reliable agreement between simulation and experiment, supporting their suitability for reproducible horn needle hydrophone fabrication and calibration.

### 6.2.3 Discussion

This study examined the development of an acoustic horn needle attachment compatible with commercially available ultrasound transducers for the characterization of acoustic wave propagation in medical phantom studies. Although previous investigations have reported custom hydrophone designs[4,40,41], fewer studies have focused on adapting existing commercial transducers. This strategy avoids the need to design and manufacture both the transducer and the needle-based sensing structure from first principles.

The numerical simulations indicated that the exponential horn provided the best overall performance, followed by the conical and cylindrical geometries. This configuration produced strong

sensitivity in the perpendicular direction and maintained a stable response up to approximately 9 MHz. However, the experimental measurements showed a different ranking, with the conical horn achieving the highest sensitivity, followed by the cylindrical and exponential designs. Across both numerical and experimental analyses, AlSi consistently performed better than AlMg, and larger needle diameters increased sensitivity. These results are consistent with established hydrophone literature, where sensitivity and directivity are strongly influenced by guided wave propagation, attenuation, diffraction near the sensing region, and material losses at MHz frequencies[42,43]. Previous studies on needle and membrane hydrophones have also shown that smoother impedance transitions can reduce internal reflections and improve broadband stability, whereas higher attenuation decreases sensitivity and increases frequency-dependent variability[42,44].

In this context, the numerical prediction that exponential geometries should outperform conical and cylindrical designs agrees with classical acoustic waveguide theory. Nevertheless, experimental hydrophone calibration studies have shown that fabrication tolerances, surface roughness, adhesive bonding, and coupling conditions can substantially affect measured performance[45]. These factors may explain why the conical design provided the best experimental response, despite the numerical advantage predicted for the exponential geometry. The improved performance of AlSi relative to AlMg, together with the sensitivity increase observed for larger diameters, further supports the interpretation that reduced intrinsic attenuation and improved wave confinement enhance hydrophone sensitivity. Overall, the observed trends are physically consistent with the literature, while also emphasizing the importance of manufacturability and coupling conditions when translating numerically optimized designs into functional experimental devices.

The results also suggest that, although sound transmission loss is intrinsically dependent on material properties and geometry, the experimental configuration used to measure it can strongly influence the obtained values. The sound transmission loss measured with the conical acoustic horn needle in the 0.5–5 MHz range, between 63.4 and 139.2 dB at a brain-mimicking depth of 15 mm, agreed well with values reported by Fernandes et al.[46] and Sharma et al.[47] over the same frequency range. Comparable measurements obtained using the AlSi 3.2 mm conical horn needle and the hydrophone developed by Pereira et al.[4] yielded sound transmission loss values between 64.6 and 126.3 dB at 15 mm depth in the 0.5–5 MHz range. These results are consistent with trends reported in transcranial ultrasound studies, where transmission or insertion loss increases strongly with frequency due to reflection at tissue–bone interfaces, absorption, and scattering within cranial structures[48,49].

Previous experimental and numerical studies generally report lower losses below approximately

0.5–1 MHz, followed by a marked increase at higher frequencies, which is consistent with the monotonic frequency-dependent increase observed in the present work [67]. However, many literature values refer to skull-only insertion loss measured in water–skull–water configurations. In contrast, the present measurements include propagation to a defined depth within a brain-mimicking region, which naturally produces higher absolute sound transmission loss while preserving comparable frequency-dependent behaviour [67]. The literature also indicates that sound transmission loss is highly sensitive to measurement conditions, including boundary constraints, incidence angle, and experimental setup, reinforcing the need for frequency-specific characterization when comparing transcranial ultrasound transmission results across different studies[50,51].

Several limitations should be considered. First, the adhesive used to bond the horn needle to the transducer was restricted to a single epoxy formulation and was not optimized for acoustic impedance matching or reduced damping. Variations in adhesive properties and bond-layer thickness may therefore have introduced additional attenuation and sensitivity variability. Second, the manufacturing process was constrained by casting and machining tolerances. More precise manufacturing methods could reduce geometric deviations, surface roughness, and alignment errors, potentially improving repeatability and absolute sensitivity. Third, the validation was performed in medical phantom conditions and cannot be directly generalized to in vivo use, where perfusion, temperature regulation, tissue hydration, and mechanical properties may alter acoustic propagation. Finally, although the horn needle attachment can, in principle, be adapted to other propagation media, its response remains medium-dependent and would require recalibration and potentially geometric or material re-optimization for accurate measurements in different acoustic environments.

Future work should focus on improving the robustness and applicability of the proposed horn needle system. Temperature-dependent calibration should be performed to account for changes in material properties and wave speed under realistic experimental or physiological conditions. The nonlinear response should also be characterized at higher pressure levels to quantify harmonic generation and potential sensitivity deviations outside the linear regime. Alternative coupling and bonding materials should be investigated to improve acoustic impedance matching and reduce intrinsic damping at the needle–transducer interface. Finally, miniaturized integrated electronics for in situ signal conditioning could improve the signal-to-noise ratio and enable more reliable measurements in practical experimental settings.

Overall, the findings demonstrate that a hydrophone does not necessarily need to be developed entirely from first principles. The proposed horn needle attachment can adapt commercial ultrasound transducers

and achieve performance comparable to custom hydrophone systems, while offering a more accessible and reproducible approach for ultrasound field characterization in medical phantom studies.

### 6.2.4 Conclusion

This work addressed the design of an acoustic horn needle attachment compatible with commercially available ultrasound transducers, with the objective of improving sensitivity, broadband response, and directional control through wavelength-scaled geometric design and informed material selection. The numerical results indicated that the response of the attachment is mainly governed by guided longitudinal wave propagation within the horn needle. Accordingly, scaling the geometry relative to the acoustic wavelength provided a systematic strategy to reduce transmission losses and improve acoustic coupling toward the sensing element. Among the evaluated materials, aluminium, particularly AlSi, was identified as the most suitable option due to its combination of high longitudinal wave speed, reduced intrinsic attenuation, mechanical robustness, and favourable manufacturability. These properties enabled improved sensitivity and a more stable broadband response. Three horn geometries were investigated numerically, namely cylindrical, conical, and exponential configurations. The exponential horn presented the best predicted performance, followed by the conical and cylindrical geometries, suggesting that smooth wavelength-scaled transitions are advantageous for reducing internal reflections and improving acoustic energy transfer. Experimental validation showed good agreement with the main numerical trends across the nine fabricated samples, although differences were observed in the absolute sensitivity levels. In practice, the exponential geometry underperformed relative to the numerical prediction, while the conical horn provided the highest experimental sensitivity, ranging from $-53.34$ to $-33.6$ dB re 1 V/$\mu$Pa. This difference highlights the influence of manufacturing tolerances, bonding conditions, surface finish, and coupling quality on the final hydrophone response. Therefore, although the exponential horn remains theoretically favourable, the conical geometry demonstrated superior experimental robustness and repeatability. Although the horn needle attachment was not ultimately used in the final experimental workflow due to a change in the expected frequency range of the study, its development remains relevant for the broader hydrophone literature. The results provide a physically grounded and reproducible framework for adapting commercial ultrasound transducers into broadband sensing devices, avoiding the need to develop fully custom hydrophone systems from first principles. Overall, this work demonstrates that wavelength-scaled horn needle attachments can improve sensitivity, bandwidth, and calibration robustness, while offering a practical route for acoustic field characterization in medical phantom and ultrasound propagation studies.

## 6.3 Biological Tissues Tissue Mimicking Materials

The development of TMMs for skin, soft tissue, and bone applications is crucial for advancing ultrasound imaging and therapy techniques. These materials serve as phantoms that replicate the acoustic properties of biological tissues, allowing for the testing and optimization of ultrasound devices and procedures in a controlled environment. The following sections provide an overview of the theoretical background, materials and methods used for the fabrication and characterization of TMMs, as well as the results and discussion of their performance in mimicking the acoustic properties of their biological counterparts.

### 6.3.1 Theoretical Background

This section encompasses the theoretical background related to the development and characterization of TMMs for skin, soft tissue, and bone applications, and the hypothetical performance of these materials in replicating the acoustic properties of their biological counterparts.

#### 6.3.1.1 Skin-Mimicking Materials

Skin is a multilayered organ composed mainly of the epidermis, dermis, and hypodermis, each presenting distinct structural, mechanical, and acoustic characteristics[52]. The epidermis forms the external protective barrier, whereas the dermis contains collagen-rich connective tissue that largely governs the tensile strength, elasticity, and anisotropic response of skin. The hypodermis, composed predominantly of adipose tissue, contributes to cushioning and thermal insulation. Therefore, skin-mimicking TMMs intended for ultrasound applications should reproduce not only the global acoustic response of skin, but also the directional mechanical behavior associated with collagen organization in the dermal layer[53,54].

In simplified skin phantom designs, the epidermis and superficial homogeneous regions are commonly represented by an isotropic matrix, while the dermis may be approximated using a fiber-reinforced composite to account for anisotropy[55,56]. Accordingly, the material developed in this work was designed as a layered structure inspired by native skin, consisting of a homogeneous silicone-based layer and a fiber-reinforced layer, where the fibers were aligned to emulate the preferential orientation of collagen bundles in the dermis, as shown in Figure 109.

Since this material constitutes the external contact layer with the ultrasound transducer, adequate compliance is also required to promote acoustic coupling and reduce signal losses caused by poor contact

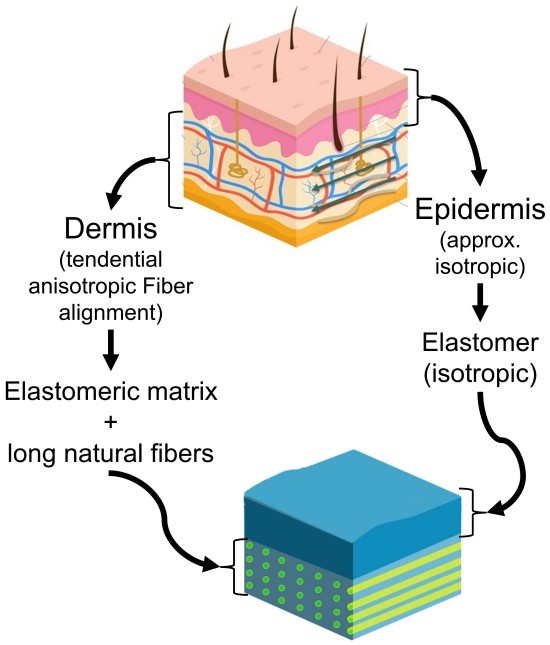



Figure 109: Representation of the structure of the skin-mimicking material, inspired by the natural skin structure. The material consists of a homogeneous layer representing the epidermis and a fiber-reinforced layer representing the dermis, where the fibers are aligned to mimic the orientation of collagen fibers in human skin.

or impedance mismatch. For this reason, the selected matrix should combine low stiffness, high elasticity, processing capacity, and compatibility with fiber reinforcement. Silicone elastomers are therefore suitable candidates for skin-mimicking TMMs, as they provide flexible and stable matrices that can be structurally modified to approximate the mechanical behavior of fibrous biological tissues.

#### 6.3.1.2 Soft Tissue-Mimicking Materials

Due to their biphasic composition, characterized by a solid extracellular matrix saturated with interstitial fluid, biological soft tissues are commonly replicated using hydrogel-based TMMs. Hydrogels consist of water-rich polymer networks whose composition can be adjusted to control mechanical stiffness, density, speed of sound, attenuation, and acoustic impedance[57]. Among these systems, agar–gelatin formulations are widely used because they are simple to process and allow the production of stable tissue-like matrices. The incorporation of glycerol provides an additional means of tuning the acoustic response, particularly by modifying the speed of sound and attenuation. Therefore, agar–gelatin hydrogels supplemented with glycerol were selected in this work to develop soft tissue-mimicking materials with adjustable properties suitable for ultrasound-based phantom applications.

#### 6.3.1.3 Bone-Mimicking Materials

Bone is a highly heterogeneous and anisotropic tissue, characterized by a mineralized matrix and a porous architecture that together define its mechanical stiffness, strength, and acoustic response[58]. From an anatomical perspective, bone is commonly divided into cortical bone, a dense external layer with high density and stiffness, and trabecular bone, a porous internal structure with lower apparent density[59,60]. Reproducing the full acoustic behavior of bone is therefore challenging, particularly due to its high impedance, strong attenuation, and structural complexity.

Since the present work is primarily focused on acoustic wave propagation through soft tissues and interaction with the bone boundary, the bone-mimicking material was designed to approximate the acoustic response of the cortical bone interface rather than the complete through-transmission behavior of native bone. Replicating the latter would require a more complex architecture capable of representing both cortical and trabecular regions. For this purpose, PLA was selected as a practical bone-mimicking material due to its higher acoustic impedance relative to soft tissue TMMs, low cost, accessibility, and compatibility with 3D printing. Additive manufacturing also enables the control of infill density, internal architecture, and surface geometry, allowing the acoustic response of the printed structure to be partially tailored toward that of natural bone.

As previously described, acoustic impedance is defined as the ratio between acoustic pressure and particle velocity. Although it is often simplified as the product of density and speed of sound, this expression is valid for plane wave propagation under normal incidence. In a more general formulation, the relevant quantity at an interface is the normal specific acoustic impedance, defined as the ratio between the acoustic pressure and the normal component of particle velocity[61]. For an obliquely incident wave, this can be written as equation 250,

$$Z = \frac{p}{v_{normal}} = \frac{p}{v\cos(\theta)} = \frac{Z}{\cos(\theta)} \tag{250}$$

where $p$ is the acoustic pressure, $v_{\text{normal}}$ is the normal component of particle velocity, $v$ is the particle velocity magnitude, $\theta$ is the incidence angle, and $Z(f)$ is the characteristic acoustic impedance of the material. This relationship shows that the apparent impedance experienced at the interface increases with the angle of incidence, as illustrated in Figure 110.

Although PLA presents a higher acoustic impedance than soft tissue TMMs, its impedance remains lower than that of cortical bone. Therefore, an angled lattice structure was introduced at the interface as a metamaterial-inspired strategy to increase the effective impedance by modifying the local angle of wave interaction. By promoting oblique reflection at the structured surface, the apparent impedance of

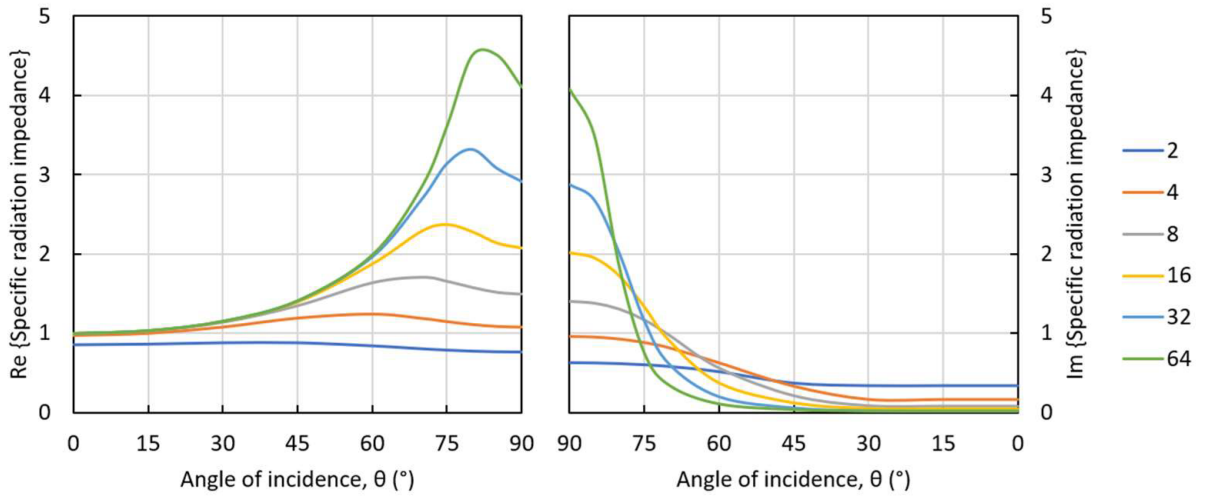



Figure 110: Representation of the acoustic impedance of different materials as a function of the angle of incidence of the acoustic wave[62].

the interface may be increased toward values closer to cortical bone, while preserving the advantages of PLA-based 3D printing as an accessible and cost-effective approach for bone phantom fabrication. This concept is schematically represented in Figure 111.

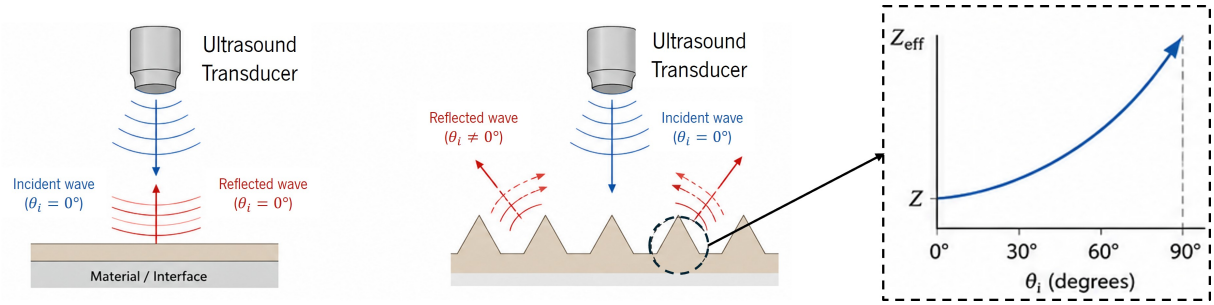



Figure 111: Metamaterial structure designed to mimic the acoustic properties of cortical bone, where the angled lattice pattern is exemplified to demonstrate how it can increase the effective impedance.

Based on this approximation, the ideal incidence angle required to match the effective impedance of the PLA interface to that of cortical bone can be estimated as equation 251,

$$\theta = \arccos\left(\frac{Z_{PLA}}{Z_{bone}}\right) \tag{251}$$

where $Z_{\text{PLA}}$ is the characteristic acoustic impedance of the printed PLA material and $Z_{\text{bone}}$ is the target acoustic impedance of cortical bone.

### 6.3.2 Materials and Methods

This section describes the materials and methods used for the fabrication and characterization of the tissue-mimicking materials for skin, soft tissue, and bone applications. The procedures were designed to ensure reproducibility and consistency across samples, while also allowing for the control of their structural and acoustic properties.

#### 6.3.2.1 Material Selection

The materials selected for the fabrication of the tissue-mimicking materials were chosen based on their ability to replicate the mechanical and acoustic properties of the target biological tissues, as well as their ease of processing and availability. The selection process involved a comprehensive review of existing literature on tissue-mimicking materials, as well as preliminary experiments to evaluate the suitability of different material combinations for skin, soft tissue, and bone applications.

**Skin Tissue-Mimicking Material**

The samples were fabricated using a biocompatible silicone elastomer (SG587, EcoArte, Porto, Portugal; with an approximate Shore A hardness of 30) and Natural fibers from *Cordyline Australis* were used as reinforcement. The silicone elastomer was selected for its flexibility, and ease of processing, making it suitable for mimicking the mechanical properties of skin. The natural fibers were chosen for their ability to provide reinforcement and enhance the mechanical strength of the composite material, while also contributing to the anisotropic properties that are characteristic of biological tissues. The combination of these materials allows for the creation of a skin-mimicking material with tunable mechanical properties and structural characteristics that closely resemble those of natural skin.

**Soft Tissues Tissue-Mimicking Material**

Soft tissue-mimicking materials were developed using gelatin-based formulations supplemented with glycerol, following approaches commonly reported in the literature for ultrasound phantom fabrication. Agar-based gelatin was selected as hydrogel-forming components due to their ability to produce water-rich matrices with tunable mechanical consistency and acoustic behavior, while glycerol was incorporated to adjust the density, speed of sound, and acoustic impedance of the final material. This formulation strategy enables the production of soft tissue analogs with controlled composition and reproducible properties, suitable for evaluating ultrasound propagation under conditions representative of biological soft tissues. Several mix ratios were experimentally characterized, presented in table 25.

Table 25: Composition and materials used in the soft tissue TMM samples.

| Sample | Water (wt%) | Gelatin (wt%) | Glycerol (wt%) |
|---|---|---|---|
| 5Gel | 95% | 5% | 0% |
| 10Gel | 90% | 10% | 0% |
| 15Gel | 85% | 15% | 0% |

| | | | |
|---|---|---|---|
| 10Gel5Gly | 85% | 10% | 5% |
| 10Gel10Gly | 80% | 10% | 10% |
| 10Gel15Gly | 75% | 10% | 15% |

**Bone Tissue-Mimicking Material**

PLA was selected as the material for bone-mimicking samples due to its widespread availability, ease of processing using 3D printing techniques, and its relatively high stiffness compared to soft tissues. PLA is a biodegradable thermoplastic polymer that can be easily fabricated into complex geometries, making it suitable for creating bone-mimicking structures with varying densities and internal architectures. By adjusting the infill density and pattern during the 3D printing process, it is possible to tailor the acoustic properties of the PLA samples to better match those of natural bone, while also providing a cost-effective and accessible option for bone phantom fabrication in ultrasound applications.

#### 6.3.2.2 Manufacture Process

The manufacturing process for the tissue-mimicking materials of skin, soft tissue, and bone is described in the following sections. The process for each type of material was designed to ensure the reproducibility and consistency of the samples, while also allowing for the control of their structural and acoustic properties.

**Skin Tissue-Mimicking Material Manufacturing**

The silicone elastomer was prepared by combining the base and curing agent in a 1:1 ratio, according to the manufacturer's instructions. Both components were weighed with a high-precision milligram scale and mechanically homogenized to obtain a uniform mixture. Natural fibers, with diameters ranging from 48 to 184 $\mu$m, were also weighed to ensure a controlled fiber-to-matrix ratio. Prior to incorporation, the fibers were manually brushed to remove loose impurities and improve alignment. As continuous reinforcements, the fibers extended along the full length of each specimen and were positioned inside the mold according to the intended orientation, reproducing the dominant fiber direction of the target biological tissue.

The silicone mixture was then carefully poured into the mold to fully impregnate the fiber network while minimizing fiber displacement. The filled mold was placed in a vacuum chamber, with an ultimate vacuum of 0.8 Pa, for 20 min to remove entrapped air and reduce void formation. A custom 3D-printed mold with adjustable height was used to enable the fabrication of multilayered architectures. After degassing, the samples were compressed under a 3 kPa load for 3 h at room temperature to promote

matrix consolidation and fiber integration. When multilayered specimens were required, the procedure was repeated sequentially for each layer, with the mold height adjusted accordingly, until the desired structure was obtained. The complete manufacturing procedure is illustrated in figure 112.

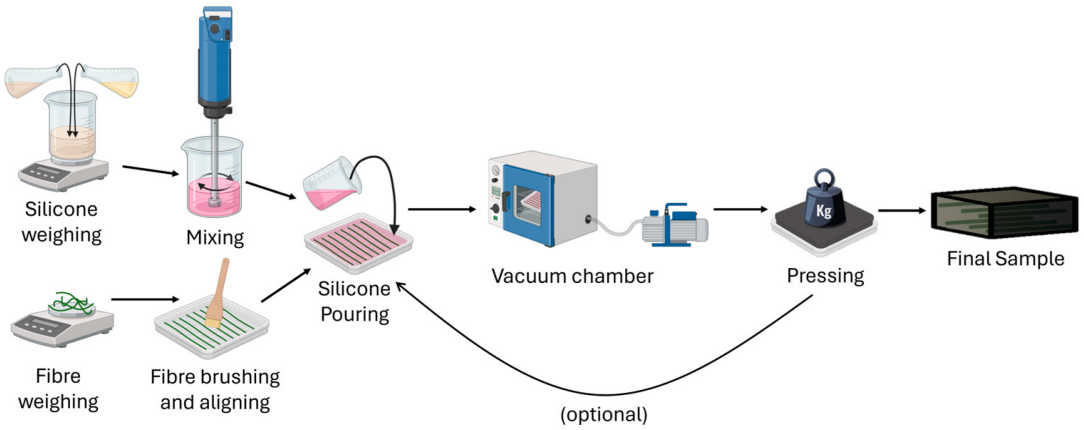



Figure 112: Manufacturing process used to produce skin-mimicking materials. The silicone elastomer was mixed in a 1:1 ratio of base to curing agent, and the natural fibers were weighed and prepared. The fibers were arranged in the mold, and the silicone mixture was poured to encapsulate the fibers. The filled mold was degassed in a vacuum chamber for 20 min, followed by compression under a load of 3 kPa for 3 h at room temperature to ensure fiber integration and matrix consolidation. This process could be repeated for additional layers if needed.

Two sample configurations were produced to evaluate the proposed material concept. All specimens were fabricated with identical in-plane dimensions of 120 mm $\times$ 150 mm and a total thickness of 2 mm, allowing direct comparison of their mechanical and acoustic responses under equivalent testing conditions. In fiber-reinforced samples, the fibers were oriented parallel to the specimen width, corresponding to the 120 mm direction, to ensure consistent directional testing. After fabrication, the specimens were sectioned into smaller samples according to the requirements of each characterization procedure (figure 113).

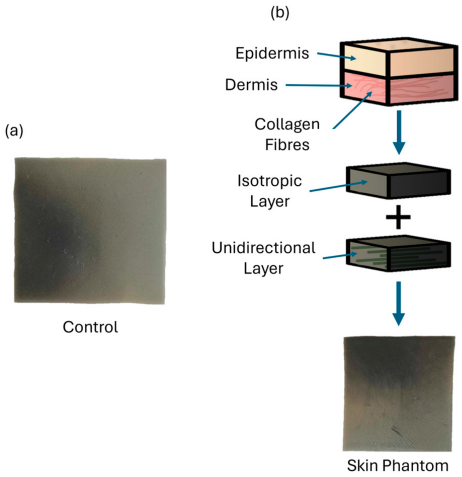



Figure 113: Photographs of the two sample configurations produced for skin-mimicking materials: (a) unreinforced silicone elastomer and (b) bilayer composite with a pure silicone layer and a unidirectional long-fiber-reinforced silicone layer. Both configurations have identical in-plane dimensions of 120 mm $\times$ 150 mm and a total thickness of 2 mm.

The first configuration consisted of an unreinforced silicone elastomer sample, produced entirely from the SG587 matrix and used as a control material for comparison with both composite specimens

and commercially available phantom materials (figure 113a). The second configuration was a bilayer composite composed of a pure silicone layer and a unidirectional long-fiber-reinforced silicone layer, each with a thickness of 1 mm, resulting in the same total thickness of 2 mm (figure 113b). This layered architecture was designed to approximate the structure of human skin, with the homogeneous silicone layer representing the non-directional epidermal region and the fiber-reinforced layer representing the dermis, where aligned collagen fibers contribute to the anisotropic mechanical behavior associated with Langer's lines[63].

### Soft Tissue Tissue-Mimicking Material Manufacturing

Three cylindrical specimens (∅ 30 mm, height 30 mm) were produced for each formulation to ensure reproducibility and enable statistical analysis of the measured properties. The samples were fabricated by casting the hydrogel mixtures into open-ended PVC tube molds, which allowed direct height measurement with a high-precision caliper and facilitated subsequent ultrasound characterization. Two thin layers of plastic film were placed at the base of each mold to assist demolding. Each formulation was prepared by mixing the required proportions of distilled water, agar powder, gelatin, and glycerol in a beaker under magnetic stirring. The mixture was heated on a hotplate set to 150 °C until reaching 90-100 °C, ensuring complete dissolution of the hydrogel components. The heat source was then turned off, while stirring was maintained for an additional 3 min to promote homogeneity. During cooling, the agar-based mixture progressively formed a gel network, with gelatin occurring near 40-45 °C. Once the temperature decreased to approximately 40 °C, the solution was poured into the corresponding molds. The specimens were left to cool and solidify at room temperature for 24 h before demolding and acoustic characterization. The process is schematically represented in figure 114.

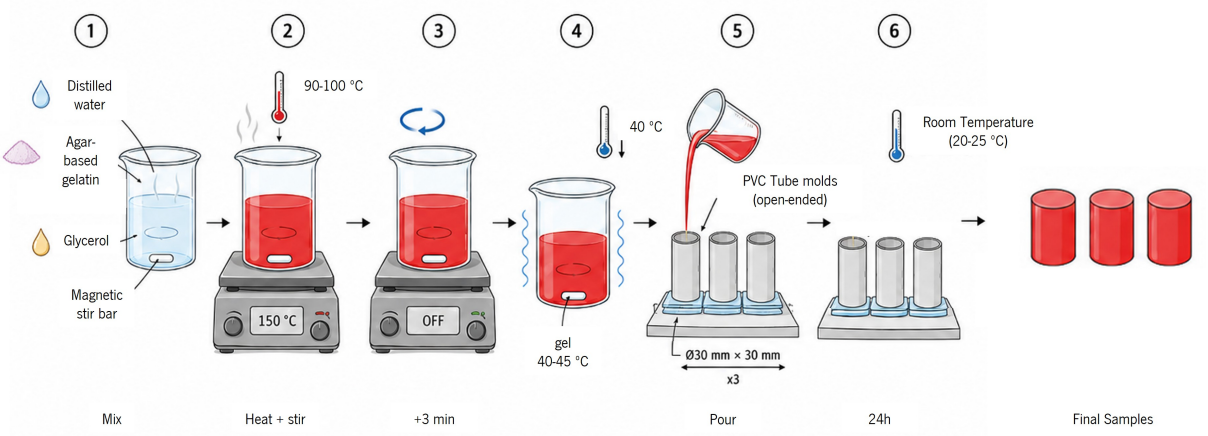



Figure 114: Schematic representation of the manufacturing process used to produce agar-gelatin-based soft tissue-mimicking materials. Distilled water, agar-based gelatin, and glycerol were mixed under magnetic stirring, heated to 90-100 °C on a hotplate set to 150 °C, stirred for an additional 3 min after heating, cooled to approximately 40 °C, and poured into open-ended PVC molds (∅ 30 mm × 30 mm). The specimens were then left to solidify at room temperature for 24 h before demolding.

**Bone Tissue-Mimicking Material Manufacturing**

Three cylindrical PLA specimens (∅ 30 mm) were fabricated by fused filament fabrication using a Creality Ender 3 V3 SE printer. Samples were produced with heights of 10, 20, and 30 mm to evaluate the influence of propagation length on the measured acoustic response. The printing parameters were kept constant, with a layer height of 0.2 mm and a print speed of 50 mm/s, while the infill density was varied between 75 and 100% in 5% increments using a gyroid infill pattern. These conditions were selected to ensure adequate dimensional accuracy, structural integrity, and repeatability across the printed specimens. After printing, the samples were allowed to cool, removed from the build plate, and stored for subsequent acoustic characterization.

To further tailor the acoustic response of the PLA interface, structured surface patterns were introduced. The triangular pattern is shown in Figure 115. Its characteristic height was selected to remain smaller than the acoustic wavelength within the frequency range of interest, thereby reducing diffraction effects and promoting a dominant interaction through oblique reflection rather than scattering.

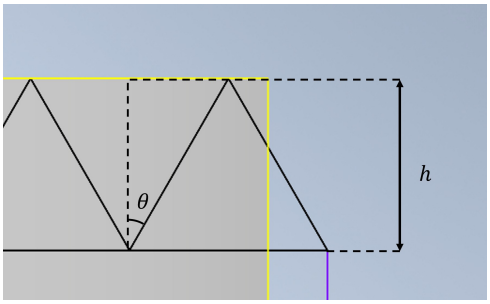



Figure 115: Triangular pattern applied at the PLA surface, demonstrating the design for minimizing diffraction effects and enhancing oblique reflection for acoustic characterization, which can be controlled by adjusting the height $h$ and the angle $\theta$.

In addition to the triangular geometry, a sinusoidal surface pattern was designed according to equation 252,

$$z = h \cdot \left( \sin\left(\frac{x}{f}\right) + \sin\left(\frac{y}{f}\right) \right) \tag{252}$$

where $h$ defines the pattern amplitude and $f$ controls the spatial periodicity of the surface. By adjusting $f$, the local surface inclination can be modified, thereby influencing the effective acoustic interaction at the interface. The sinusoidal surface was generated in Blender and subsequently imported into Inventor, where Boolean operations were used to create the final specimen geometry.

A dome-like surface pattern was also produced using equation 253,

$$z = h \cdot \left( \sin\left(\frac{x}{f}\right) \cdot \sin\left(\frac{y}{f}\right) \right) \tag{253}$$

where $h$ represents the dome height and $f$ defines the spatial periodicity of the pattern. As with the sinusoidal geometry, the dome surface was created in Blender and imported into Inventor for integration into the final PLA model using Boolean operations.

The resulting surface geometries are presented in figure 116.

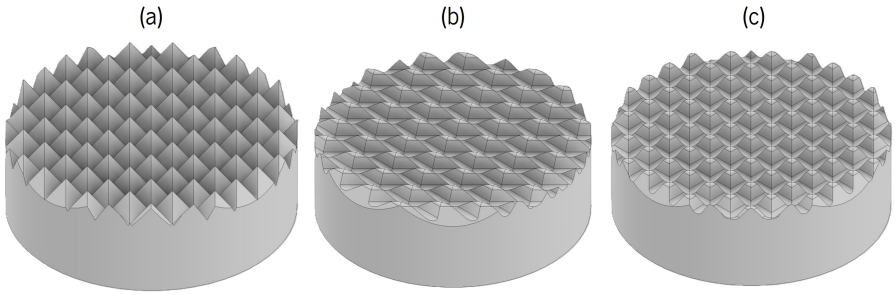



Figure 116: Different surface patterns applied to the PLA samples: (a) triangular pattern, (b) sinusoidal pattern, and (c) dome pattern. These patterns were designed to enhance the effective acoustic impedance of the PLA material by promoting oblique reflection and minimizing diffraction effects.

#### 6.3.2.3 Experimental characterization Manufacturing

The parameters necessary for acoustic characterization of the tissue-mimicking materials are described in this section. Further characterizations was done and are available in section D.1.

**Density Measurement**

Density was measured using a standard measuring method, where the mass of the sample was measured using a precision balance, and the volume was determined by calculating the volume as a cylinder. The density was then calculated using the formula in equation 254

$$\rho = \frac{m}{V} \tag{254}$$

where $m$ is the mass and $V$ is the volume of the sample.

**Acoustic Measurement Setup**

The acoustic properties of the tissue-mimicking materials were characterized using a through-transmission ultrasound setup. The setup consisted of a pair of broadband ultrasonic transducers (one transmitter and one receiver) aligned coaxially with the sample placed in between. The transducers were connected to a signal generation unit that generated the necessary signals. The transmitted signal was a short pulse, and the received signal was recorded using an oscilloscope for further analysis. Five frequencies were tested: 0.5 MHz, 1 MHz, 2 MHz, 4 MHz, and 5 MHz. The setup is demonstrated in figure 117.

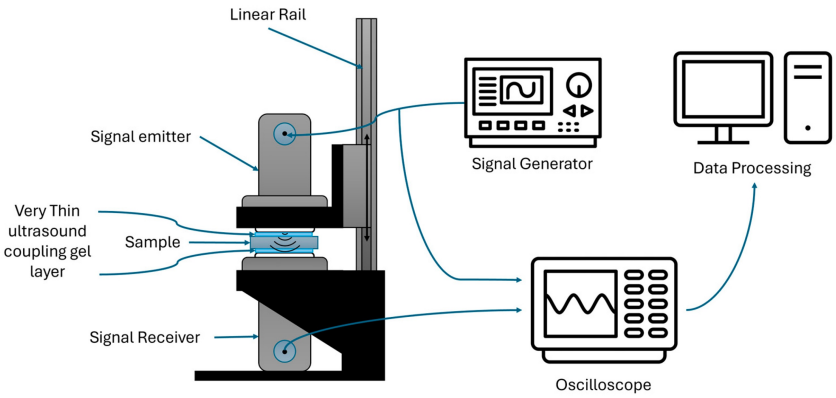



Figure 117: Representation of the through-transmission ultrasound setup used for acoustic characterization of the tissue-mimicking materials. The setup consists of a pair of broadband ultrasonic transducers (one transmitter and one receiver) aligned coaxially with the sample placed in between. The transducers are connected to a signal generation unit that generates short pulse signals, and the received signal is recorded using an oscilloscope for further analysis.

A low pass filter was applied to the received signals to reduce noise and improve the accuracy of the measurements with a cutoff frequency of double the desired frequency. The filtered signals were then analyzed to extract the relevant acoustic parameters, such as speed of sound, attenuation, and acoustic impedance, which were calculated using the formulas described in the following sections.

An app was designed in Matlab to extract the desired features for the speed of sound and attenuation from the recorded signals. The app allows for the selection of the desired frequency and the corresponding signal, and it applies the necessary processing steps to calculate the acoustic parameters based on the formulas provided. The app also provides a user-friendly interface for visualizing the results and comparing them across different samples and frequencies (figure 118).

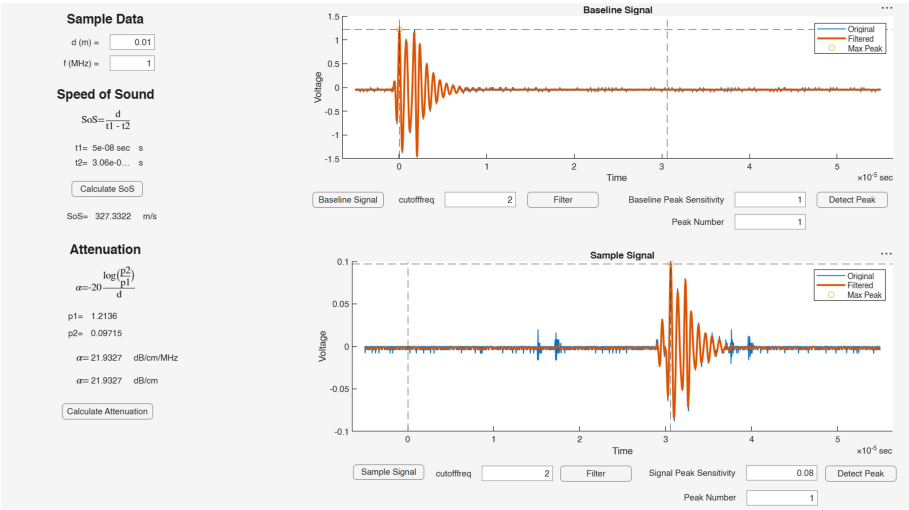



Figure 118: User-friendly interface of the Matlab app designed for extracting acoustic parameters from the recorded ultrasound signals. The app allows for the selection of the desired frequency and the corresponding signal, and it applies the necessary processing steps to calculate the acoustic parameters based on the formulas provided.

This app allowed to severely speed up the process of extracting the desired features from the recorded

signals, as it automates the necessary calculations and provides a streamlined workflow for analyzing the acoustic properties of the tissue-mimicking materials, and is available in matlab central file exchange[5].

In it, the signal-processing routine uses a baseline measurement and a sample-transmitted signal as the two main inputs. Both signals are first passed through a low-pass filter to reduce high-frequency noise and improve the reliability of subsequent time- and amplitude-based calculations. This filtering step is important because noise can affect both peak detection and the identification of the arrival time of the transmitted wave. After filtering, the code follows two parallel analysis paths. In the first path, the time delay between the baseline and sample signals is determined using a time-of-flight approach. Since the sample thickness is known, this delay is used to calculate the speed of sound through the material. In the second path, the peak amplitudes of the filtered baseline and transmitted signals are extracted and compared. The reduction in amplitude after propagation through the sample is then used to estimate the attenuation coefficient, as is described in figure 119.

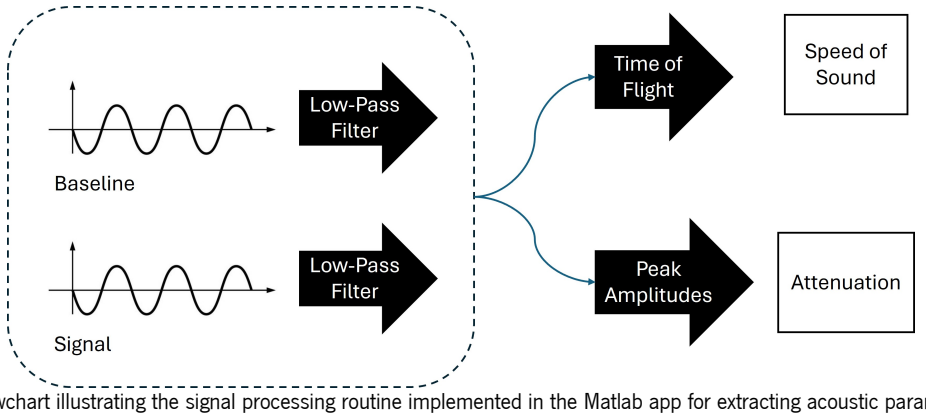



Figure 119: Flowchart illustrating the signal processing routine implemented in the Matlab app for extracting acoustic parameters from the recorded ultrasound signals. The routine includes a low-pass filtering step to reduce noise, followed by parallel analysis paths for calculating speed of sound using time-of-flight and attenuation using amplitude comparison.

### Speed of Sound Measurement

The speed of sound in the samples was calculated using the time-of-flight method, where the time taken for the ultrasound pulse to travel through the sample was measured when compared to the time of flight between solely the transmitted and received transducers. The speed of sound was then calculated using the formula in equation 255

$$c = \frac{L}{t_s - t_0} \tag{255}$$

where $L$ is the distance traveled by the ultrasound pulse and $t_0$ and $t_s$ are the times of flight for signals between the transducers without and with the sample, respectively.

### Attenuation Measurement

The attenuation of the TMM was measured by analyzing the amplitude of the received ultrasound signals as they traveled through the sample in comparison with the reference signal. The attenuation coefficient was then calculated using as the slope of linear regression of the logarithmic amplitude decay, as described in the formula in equation 256

$$\alpha = \frac{d}{df}\frac{1}{L}\log_{10}\left(\frac{A_0}{A_s}\right) \tag{256}$$

where $L$ is the distance traveled by the ultrasound pulse, $A_0$ is the amplitude of the transmitted signal, and $A_s$ is the amplitude of the received signal through the sample. This approach assumes that there is an offset in the amplitude due to the impedance mismatch between the transducers and the sample, which can be accounted for by considering only the slope of the logarithmic amplitude decay rather than the absolute values of the amplitudes.

When samples of different thicknesses are available, the attenuation coefficient can be calculated without including distance, as the slope of the logarithmic amplitude decay with respect to distance, as described in the formula in equation 257

$$\alpha = \frac{d}{dx}\log_{10}\left(\frac{A_0}{A_s}\right) \tag{257}$$

where $x$ is the distance traveled by the ultrasound pulse. This method allows for a more accurate estimation of the attenuation coefficient, as it accounts for any potential variations in the amplitude due to factors other than attenuation, such as impedance mismatch or scattering. However, it requires the availability of samples with varying thicknesses, which may not always be feasible in practice.

### Acoustic Impedance Calculation

The acoustic impedance of the samples was calculated using the relationship between the speed of sound and density, as given in equation 258

$$Z = \rho c \tag{258}$$

where $Z$ is the acoustic impedance, $\rho$ is the density, and $c$ is the speed of sound.

Unfortunately, to calculate the effective acoustic impedance is not so direct. According to Snell's law, the effective acoustic impedance can be determined by considering the effective transmitted pressure and the properties of the materials involved. As such, the effective acoustic impedance can be calculated using the formula in equation 259,

$$T_{eff} = \frac{2Z_{eff}}{Z_{softtissues} + Z_{eff}} \Leftrightarrow Z_{eff} = Z_{softtissues} \cdot \frac{T_{eff}}{2 - T_{eff}} \tag{259}$$

where $Z_{eff}$ is the effective acoustic impedance, and $Z_{softtissues}$ is the acoustic impedance of the soft tissues.

Taking into account that the received wave has been attenuated, it is needed to compensate this in order to calculate transmittance, according to equation 260,

$$T_{eff} = 10^{\Delta\alpha(f)/20} \cdot \frac{2 \cdot Z_{eff}}{Z_{softtissues} + Z_{eff}} \tag{260}$$

where $T_{eff}$ is the effective transmittance, $\Delta\alpha(f)$ is the attenuation difference between the reference and the sample at frequency $f$, and $Z_{softtissues}$ is the acoustic impedance of the soft tissues.

Substituting the expression for $T_{eff}$ from equation 260 into equation 259, the effective acoustic impedance can be calculated as shown in equation 261,

$$Z_{eff} = Z_{softtissues} \cdot \frac{10^{\Delta\alpha(f)/20} \cdot \frac{2 \cdot Z_{eff}}{Z_{softtissues} + Z_{eff}}}{2 - 10^{\Delta\alpha(f)/20} \cdot \frac{2 \cdot Z_{eff}}{Z_{softtissues} + Z_{eff}}} \tag{261}$$

## 6.3.3 Results and discussion

### 6.3.3.1 Density

The silicone samples for skin-mimicking materials were measured, and the results are presented in figure 120.

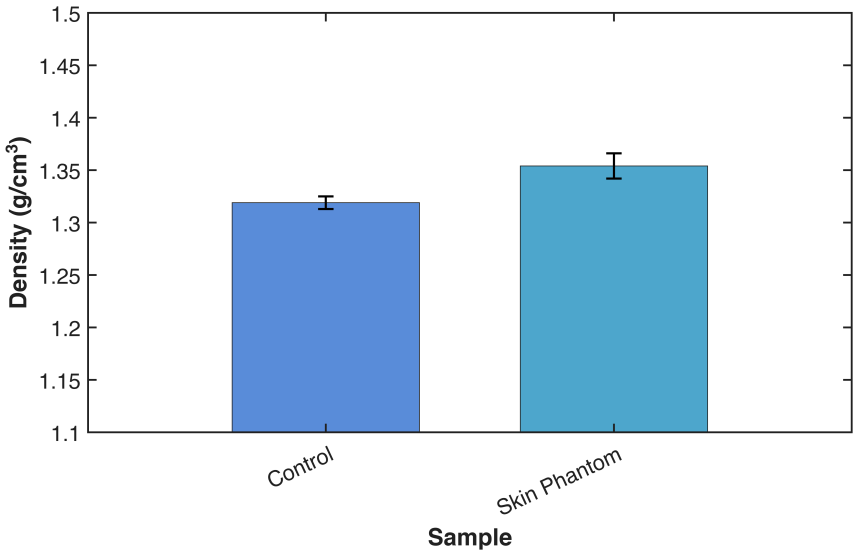



Figure 120: Density measurements for the skin-mimicking materials, including the unreinforced silicone elastomer and the bilayer composite with fiber reinforcement.

The measured density of the developed skin phantom was approximately 1.354 g/cm$^3$, slightly higher than the unreinforced silicone control, which presented a density of approximately 1.319 g/cm$^3$. This increase of about 2.7% suggests that the incorporation of the fibrous reinforcement produced a modest identification of the silicone matrix. However, both materials were denser than reported values

for native skin. In ultrasound phantom literature, human skin density is commonly reported in the range of 1.10–1.13 g/cm$^3$ [16, 55]. Therefore, the present skin phantom density is approximately 20–23% higher than the expected density of biological skin. This deviation indicates that, although the silicone–fiber architecture may be suitable for reproducing the layered and anisotropic structure of skin, its density is above the biological target range. Since acoustic impedance depends directly on density and speed of sound, this increased density may lead to an overestimation of impedance if the speed of sound is not proportionally lower. Consequently, the material should be interpreted as a mechanically and structurally inspired skin-mimicking layer rather than a fully density-matched acoustic analog of human skin.

The results for the density measurements of the soft tissue TMMs are presented in figure 121.

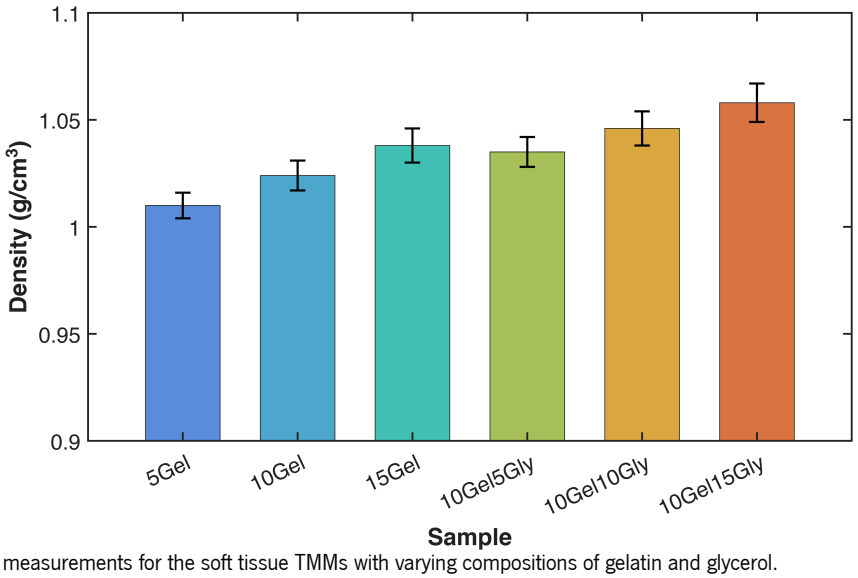



Figure 121: Density measurements for the soft tissue TMMs with varying compositions of gelatin and glycerol.

The density of the generalized soft-tissue phantoms ranged from approximately 1.010 to 1.058 g/cm$^3$, increasing with gelatin and glycerol content. The 5Gel formulation presented the lowest density, around 1.010 g/cm$^3$, while 10Gel and 15Gel increased to approximately 1.024 and 1.038 g/cm$^3$, respectively. The addition of glycerol further increased density, with 10Gel5Gly, 10Gel10Gly, and 10Gel15Gly reaching approximately 1.035, 1.046, and 1.058 g/cm$^3$. This trend is expected, since glycerol has a higher density than water and therefore increases the bulk density of hydrogel-based tissue-mimicking materials.

These values are in good agreement with reference data used in ultrasound phantom studies. The ICRU Report 61 is commonly used as a benchmark for tissue substitutes in medical ultrasound, and soft-tissue-mimicking materials are often evaluated against a target density close to 1.043 g/cm$^3$[64]. Studies using this benchmark reported an acceptance density of 1.043 ± 0.021 g/cm$^3$, for soft-tissue equivalence[57]. In that context, the formulations between approximately 1.020 and 1.060 g/cm$^3$ fall

within or very close to the expected soft-tissue range, while the 5Gel sample is slightly below the central target but still reasonably close for a water-rich hydrogel phantom.

Among the tested formulations, 15Gel, 10Gel5Gly, and 10Gel10Gly appear to provide the closest density match to generalized soft tissue, with values near 1.04–1.05 g/cm$^3$[16,57]. The 10Gel15Gly formulation remains within the upper part of the reported acceptance interval but may slightly overestimate the density of average soft tissue. This may be useful if the objective is to mimic denser soft tissues, such as muscle-like tissues, but less appropriate for more water-rich or adipose-like tissues. Conversely, the 5Gel formulation is closer to water-like tissue-mimicking media and may be less suitable as a generalized soft-tissue analog if density matching is the main criterion.

For the PLA Samples, the density measured is presented in table 26.

Table 26: Density of the PLA material used in the bone-mimicking samples.

| **Material** | **Density (g/cm³)** |
|---|---|
| PLA | $1.188 \pm 0.0229$ |

The measured density of the PLA bone-mimicking material was 1.188±0.0229 g/cm$^3$, which is substantially lower than values typically reported for cortical bone. In therapeutic ultrasound studies, cortical bone is commonly represented with a density of approximately 1.4-2.0 g/cm$^3$[16,65]. Compared with the commonly used reference value the PLA specimens present a density deficit of approximately 34% lower density than cortical bone. Even when compared with the lower bound of the reported cortical bone range, 1.4 g/cm$^3$, the PLA remains approximately 15% lower. This indicates that, from a density perspective alone, the printed PLA does not fully reproduce the material density of cortical bone.

#### 6.3.3.2 Speed of Sound

The skinTMMs were measured for speed of sound, and the results are presented in figure 122.

The measured speed of sound of the skin phantom was approximately 1090 m/s, very close to the silicone control, which was 1086 m/s. The incorporation of the fiber-reinforced layer therefore produced only a small change in longitudinal wave speed, indicating that the acoustic velocity remained dominated by the silicone matrix rather than by the fibrous architecture.

These values are substantially lower than those reported for human skin in ultrasound studies. Previous studies have reported a generalized skin value of 1654.93 m/s[16], with more specific studies reporting mean speeds of sound of 1645 m/s for the epidermis and 1595 m/s for the dermis[66].

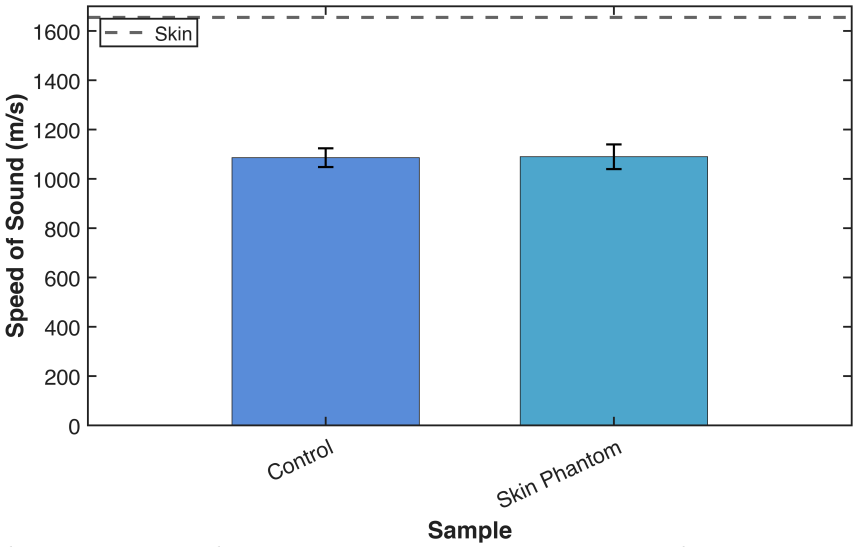



Figure 122: Speed of sound measurements for the skin-mimicking materials, including the unreinforced silicone elastomer and the bilayer composite with fiber reinforcement.

Compared with the reference values, the present skin phantom underestimates the speed of sound by approximately 32%.

This deviation is acoustically relevant because speed of sound directly affects time-of-flight, wavelength, refraction, and acoustic impedance. Although the developed material may reproduce aspects of the layered and fiber-reinforced structure of skin, its measured wave speed is closer to low-velocity elastomeric phantom materials than to native skin. Therefore, this formulation should be interpreted primarily as a mechanically inspired skin-mimicking layer rather than an acoustically matched skin analog.

The results for the speed of sound measurements of the soft tissue TMMs are presented in figure 123.

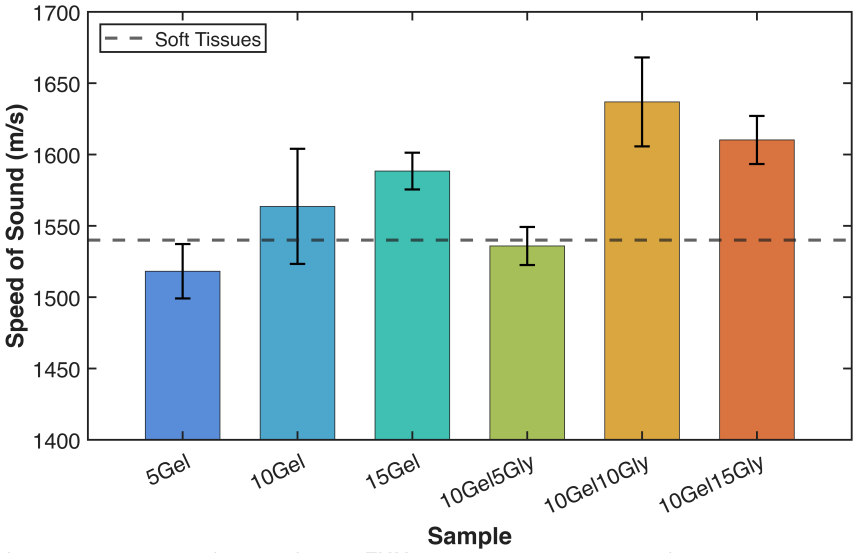



Figure 123: Speed of sound measurements for the soft tissue TMMs with varying compositions of gelatin and glycerol.

The measured speed of sound of the generalized soft-tissue phantoms ranged from approximately 1518 to 1636 m/s. The 5Gel formulation presented the lowest value, 1517 m/s, while 10Gel and 15Gel increased to 1563 and 1588 m/s, respectively. The glycerol-containing formulations showed a further increase, with 10Gel5Gly 1535 m/s, 10Gel10Gly 1636 m/s, and 10Gel15Gly around 1610 m/s. Overall, the results indicate that increasing gelatin concentration and glycerol content generally increased the speed of sound, although the 10Gel5Gly formulation remained very close to the soft-tissue reference value.

The reference value most commonly adopted for generalized soft tissue in diagnostic ultrasound is approximately 1540 m/s. This value is widely used in ultrasound phantom literature as the average speed of sound in soft tissue, while broader biological soft tissues typically occupy a range around this value depending on composition, hydration, and temperature[57]. Compared with the conventional 1540 m/s reference, the 10Gel5Gly formulation provides the closest match, with a deviation close to zero.

For the PLA Samples, the speed of sound measured is presented in table 27.

Table 27: Speed of Sound in the PLA material used in the bone-mimicking samples.

| **Material** | **Speed of Sound (m/s)** |
|---|---|
| PLA | $1989.25 \pm 29.55$ |

The measured speed of sound of the PLA bone phantom was 1989.25±29.55 m/s. In acoustic studies, cortical bone typically presents longitudinal wave speeds in the range of approximately 3000–4500 m/s, depending on anatomical direction, porosity, hydration, and measurement configuration[16,67]. Compared with the human cortical bone the PLA phantom underestimates the speed of sound by a reduction of about 45%. The difference becomes larger when compared with longitudinal propagation along the main bone axis. In equine cortical bone, ultrasound velocities of 4125 m/s in the longitudinal direction and approximately 3428–3442 m/s in radial or transverse directions have been reported, demonstrating the strong anisotropy of cortical bone[68]. Similarly, literature on human cortical bone reports bulk velocities commonly ranging from 3400 to 4000 m/s, depending on direction and microstructure. Relative to 4000 m/s, the PLA phantom reaches only about 50% of the cortical bone wave speed[69].

Therefore, the PLA specimen should not be interpreted as a fully acoustically matched cortical bone analog in terms of speed of sound. Instead, it represents an intermediate material with a wave velocity higher than soft tissue but substantially lower than cortical bone.

#### 6.3.3.3 Attenuation

The attenuation of the skinTMMs was measured, and the results are presented in figure 124.

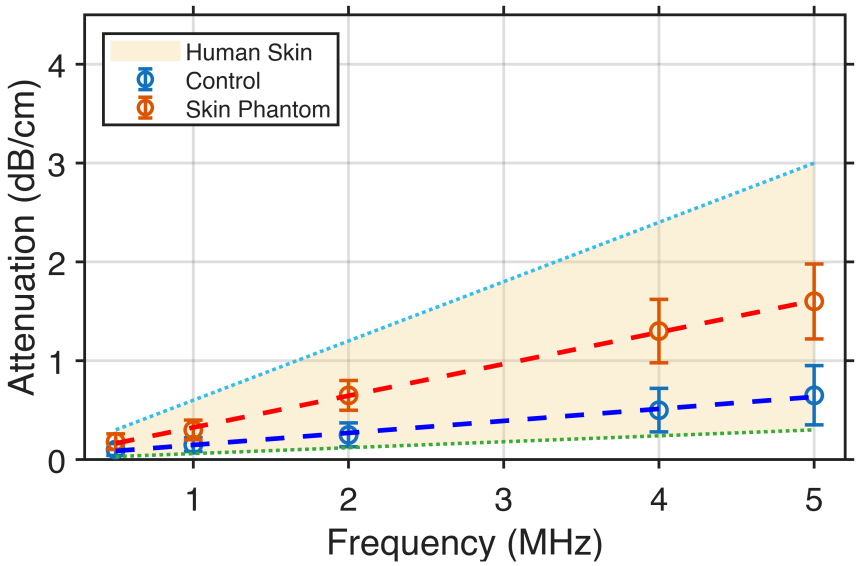



Figure 124: Attenuation measurements for the skin-mimicking materials, including the unreinforced silicone elastomer and the bilayer composite with fiber reinforcement.

The control sample showed low attenuation, 0.13 dB/cm/MHz, which is consistent with the expected behavior of a homogeneous silicone matrix, where limited internal heterogeneity reduces acoustic scattering and dissipative losses. In contrast, the skin phantom presented a higher attenuation coefficient of 0.32±0.07 dB/cm/MHz, indicating that the incorporation of structural modifications increased acoustic energy loss within the material. This value falls within the physiological range reported for human skin, approximately 0.094–0.70 dB/cm/MHz[66], suggesting that the developed skin-mimicking material provides a more representative attenuation response than the unmodified silicone control.

The measured attenuation is also comparable to values reported for other ultrasound tissue-mimicking materials. Rubert and Varghese reported attenuation coefficients between 0.4 and 0.5 dB/cm/MHz for soft-tissue-mimicking phantoms[70], while O'Neill et al. developed a regulatory-compliant tissue-mimicking material with an attenuation coefficient of approximately 0.3 dB/cm/MHz[71], closely matching the value obtained for the present skin phantom. Similarly, Aoyagi et al. reported a mean attenuation of 0.54±0.18 dB/cm/MHz for calcium alginate phantoms[72], although hydrogel-based systems may be more susceptible to dehydration, fragility, and thermal instability. Overall, the increased attenuation observed in the skin phantom reflects the greater acoustic heterogeneity of the modified matrix, likely associated with enhanced viscoelastic dissipation and microstructural scattering.

The results for the attenuation measurements of the soft tissue TMMs are presented in figure 125.

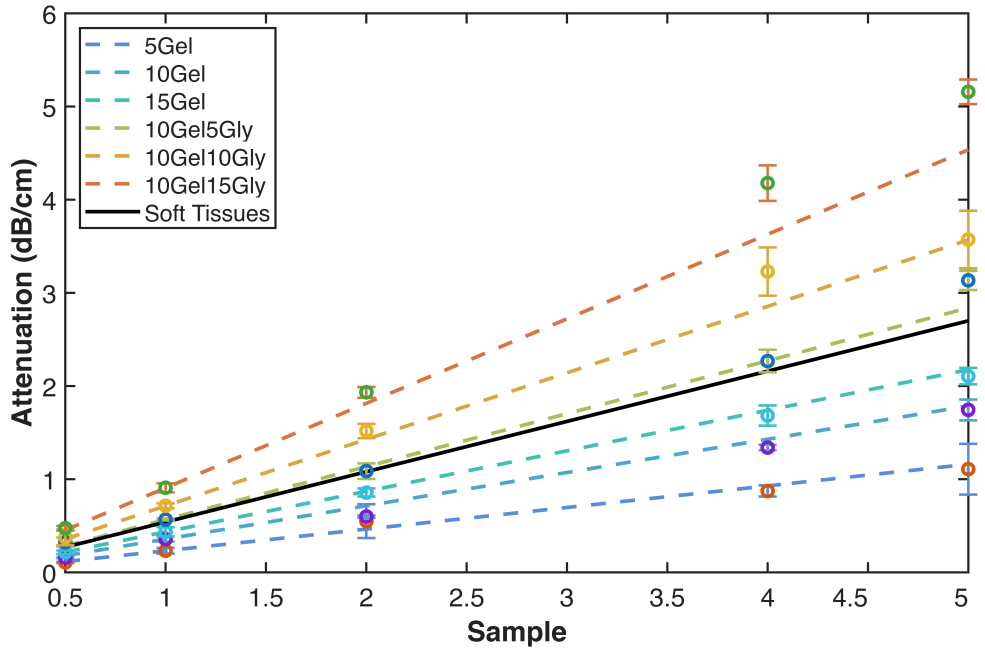



Figure 125: Attenuation measurements for the soft tissue TMMs with varying compositions of gelatin and glycerol.

The attenuation of the soft tissue TMMs increased approximately linearly with frequency for all formulations, which is consistent with the expected behavior of ultrasound attenuation in soft biological tissues. The gelatin-only formulations presented the lowest attenuation. The 5Gel sample remained below the soft-tissue reference line across the tested range, reaching only 1.1 dB/cm/MHz at 5 MHz. The 10Gel and 15Gel samples showed progressively higher attenuation, with values of 1.8 and 2.1 dB/cm/MHz at 5 MHz, respectively. This suggests that increasing gelatin concentration increased acoustic energy dissipation, most likely due to a denser polymer network and increased viscoelastic losses, and the low purity of the used gelatin (62%). The addition of glycerol produced a clear increase in attenuation. The 10Gel5Gly formulation closely followed the reference soft-tissue trend, reaching 3.1 dB/cm/MHz at 5 MHz, close to the plotted soft-tissue reference value of 3.0 dB/cm/MHz. In contrast, 10Gel10Gly and 10Gel15Gly showed higher attenuation, reaching 3.8 and 5.2 dB/cm/MHz at 5 MHz, respectively. These values indicate that higher glycerol contents may overestimate the attenuation of generalized soft tissue, although they may be useful for mimicking more attenuating tissues or for compensating low-loss paths in simplified phantoms.

In the literature, soft-tissue attenuation is commonly reported within a broad range. Cook's tissue-mimicking phantoms for ultrasonic and photoacoustic imaging reports soft-tissue attenuation coefficients from approximately 0.5 to 3.3 dB/cm/MHz, with blood as low as 0.18 dB/cm/MHz[73]. A benchmark frequently used for generalized ultrasound soft-tissue substitutes is around 0.5–0.7 dB/cm/MHz, derived from ICRU-based phantom criteria; one acoustic characterization study used 0.5–0.7 dB/cm/MHz as the acceptable attenuation range and reported a carbomer-gel phantom with 0.6 dB/cm/MHz[74]. Recent

gelatin-based ultrasound phantom work reported attenuation coefficients from 0.21 to 1.10 dB/cm, with a soft-tissue benchmark of 0.54 dB/cm/MHz, indicating that gelatin systems can be tuned across a biologically relevant attenuation range[57].

Compared with these references, the 10Gel5Gly formulation provides the closest overall match to generalized soft tissue, because its frequency-dependent attenuation follows the reference trend without the stronger overestimation observed for 10Gel10Gly and 10Gel15Gly. The 5Gel, 10Gel, and 15Gel formulations are less attenuating and may be better suited for low-loss or water-rich tissues, while the higher-glycerol formulations are more appropriate when higher acoustic damping is required.

Regarding PLA, the values obtained for 0.5 MHZ and 1 MHz are presented in figure 126 for the different heights, while for the remaining frequencies, the attenuation was too high to be accurately measured with the current setup, as the received signal was below the noise floor of the system.

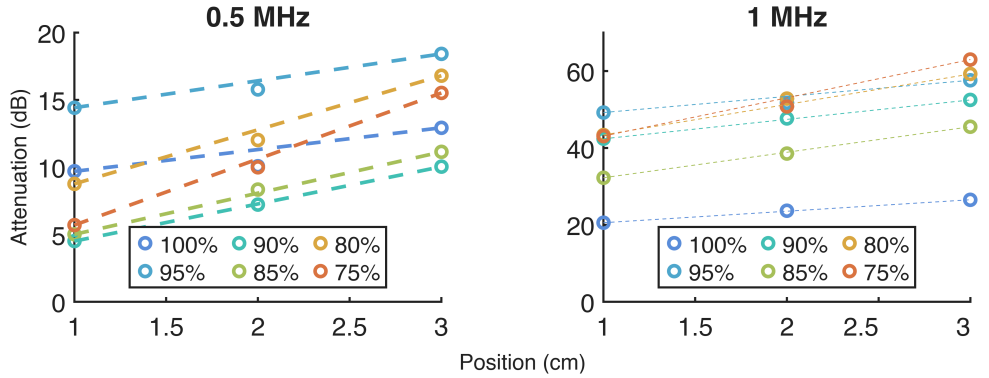



Figure 126: Attenuation measurements for the PLA bone-mimicking material at 0.5 MHz and 1 MHz for different heights.

The PLA samples showed a clear increase in attenuation with propagation distance at both frequencies, confirming that acoustic energy loss accumulated with sample thickness. At 0.5 MHz, attenuation values increased from 4.5–14.5 dB at 1 cm to 10–18.5 dB at 3 cm, depending on infill density. At 1 MHz, the losses were substantially higher, increasing from 20–50 dB at 1 cm to 27–63 dB at 3 cm. Therefore, attenuation was strongly frequency-dependent, with the 1 MHz measurements showing roughly three to four times higher total attenuation than the 0.5 MHz measurements.

At 0.5 MHz, the 90% and 85% infill samples showed the lowest attenuation, increasing from 4.5–5.0 dB at 1 cm to 10–11 dB at 3 cm. The 100% infill sample presented intermediate values, from 9.5 dB at 1 cm to 13 dB at 3 cm. The 95% infill sample showed the highest attenuation, reaching 18.5 dB at 3 cm, while the 80% and 75% samples also showed relatively high losses, around 16.5 and 15.5 dB at 3 cm, respectively. This indicates that attenuation did not vary monotonically with infill density, suggesting that internal architecture, pore connectivity, printing defects, and local scattering may be more influential than nominal infill percentage alone.

At 1 MHz, attenuation increased substantially for all samples. The 100% infill sample showed the lowest attenuation, rising from about 20 dB at 1 cm to 27 dB at 3 cm. In contrast, the 95%, 80%, and 75% infill samples presented the highest losses, reaching 57–63 dB at 3 cm. The 90% sample also showed high attenuation, around 52 dB at 3 cm, while the 85% sample remained lower, near 45 dB. These results suggest that, at higher frequency, the internal printed structure produces stronger scattering and dissipative losses, particularly in partially filled specimens where the acoustic wavelength becomes more sensitive to internal voids and periodic features.

A linear regression was performed to obtain the attenuation coefficient for the PLA samples at 0.5 MHz and 1 MHz, and the slope was considered, with the results presented in figure 127.

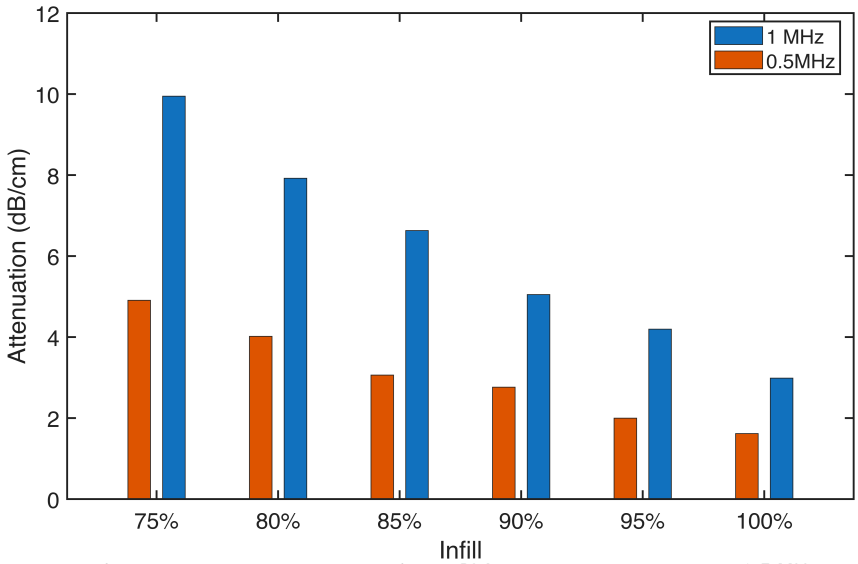



Figure 127: Linear regression of the logarithmic amplitude decay for the PLA bone-mimicking material at 0.5 MHz and 1 MHz to obtain the attenuation coefficient.

The PLA attenuation increased clearly with frequency for all infill densities. At 0.5 MHz, attenuation ranged from approximately 1.6 to 4.9 dB/cm, while at 1 MHz it increased to approximately 3.0 to 9.9 dB/cm. The increase was close to twofold for most infill levels: 75% infill increased from 4.9 to 9.9 dB/cm, 80% from 4.0 to 7.9 dB/cm, 85% from 3.1 to 6.6 dB/cm, 90% from 2.8 to 5.1 dB/cm, 95% from 2.0 to 4.2 dB/cm, and 100% from 1.6 to 3.0 dB/cm. The results show that PLA attenuation is strongly frequency-dependent and decreases with increasing infill density. Lower infill structures therefore promote higher acoustic losses, likely due to increased internal scattering and reflections at air–PLA interfaces.

Finally, the attenuation coefficient for the PLA samples at 0.5 MHz and 1 MHz was calculated using the slope of the linear in function of frequency, with the results presented in figure 128.

The PLA specimens showed attenuation coefficients that increased both with frequency and with decreasing infill density. At 0.5 MHz, attenuation ranged from 1.6 dB/cm for 100% infill to 4.9 dB/cm for 75% infill. At 1 MHz, the same samples increased to 3.0 and 9.9 dB/cm, respectively. This indicates

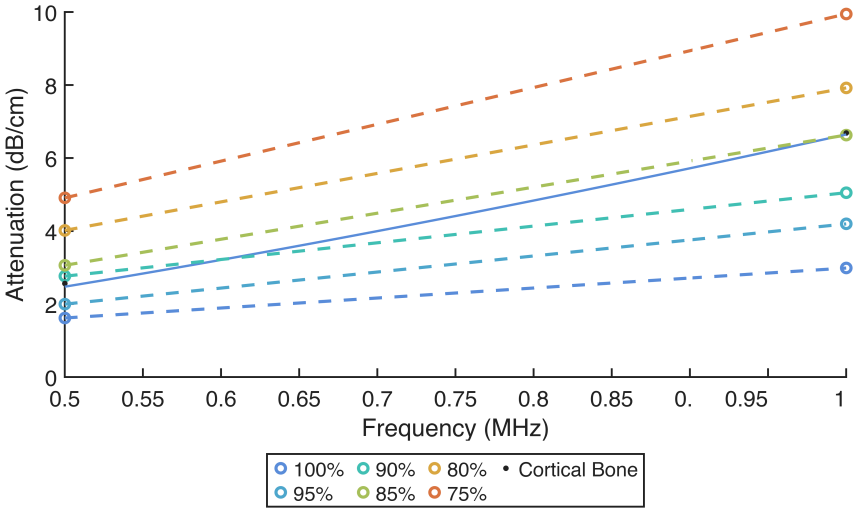



Figure 128: Attenuation coefficient for the PLA bone-mimicking material at 0.5 MHz and 1 MHz.

that the internal porosity introduced by lower infill densities substantially increased acoustic losses, most likely through internal scattering, multiple reflections, and mode conversion at PLA–air interfaces. When compared with cortical bone, the PLA samples reproduce part of the expected attenuation range, depending on infill density. However, this agreement is only partial, since cortical bone typically exhibits frequency-dependent attenuation that is better described by a power-law relationship, whereas the attenuation measured in the PLA specimens followed an approximately linear trend over the tested frequency range.

Based on the change between 0.5 and 1 MHz, the estimated frequency-dependent attenuation slope of the PLA samples ranged from 2.8 dB/MHz/cm for 100% infill to 10 dB/MHz/cm for 75% infill. Therefore, the 100% infill PLA sample is slightly below the typical cortical bone range, while the 95% and 90% infill samples, with slopes around 4.4 dB/MHz/cm, fall within the lower cortical bone range. The 85% and 80% infill samples, with slopes near 7.2–7.8 dB/MHz/cm, are close to the central-to-upper cortical bone range. The 75% infill sample, with a slope near 10 dB/MHz/cm, approaches the higher attenuation values reported for cortical specimens.

When compared with the review by Krech et al., these results support the use of PLA as a practical 3D-printed material for ultrasound-visible, bone-like structures, but not as a complete cortical bone analog. The PLA samples reproduced part of the cortical-bone attenuation range, particularly at lower infill densities, with attenuation increasing from 1.6–4.9 dB/cm at 0.5 MHz to 3.0–9.9 dB/cm at 1 MHz. However, this agreement is limited because cortical bone attenuation is typically better described by a power-law frequency dependence, whereas the PLA samples showed an approximately linear trend over the tested range. Therefore, PLA can be used to tune attenuation and echogenicity through infill density, but additional material or structural modifications are required to more accurately reproduce

cortical bone acoustic behavior[75].

Among the tested configurations, the 85–80% infill range appears to provide the closest attenuation match to cortical bone, whereas 100% infill is under-attenuating and 75% infill may overestimate cortical bone losses. This confirms that infill architecture is a useful parameter for tuning the acoustic attenuation of PLA-based bone phantoms.

#### 6.3.3.4 Acoustic Impedance

The skin TMMs were measured for acoustic impedance, and the results are presented in figure 129.

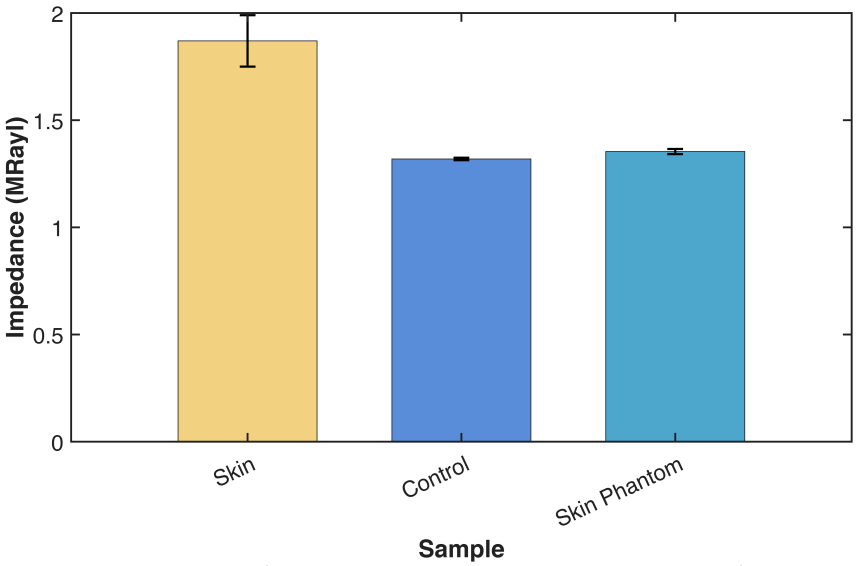



Figure 129: Acoustic impedance measurements for the skin-mimicking materials, including the unreinforced silicone elastomer and the bilayer composite with fiber reinforcement.

The measured acoustic impedance of the skin phantom was about 1.35 MRayl, only slightly higher than the silicone control, around 1.31 MRayl, but clearly lower than the reference value for human skin shown in the figure, around 1.85 MRayl. This indicates that the fiber-reinforced skin phantom modestly increased the impedance relative to the neat silicone matrix, but did not fully reproduce the acoustic impedance of native skin.

Literature values for skin and skin-like ultrasound phantoms are generally higher than the values obtained here. Moran et al. reported impedance values commonly near 1.7–1.9 MRayl[66]. Similarly, multilayered skin-vessel phantom studies aim to reproduce skin-like acoustic behavior close to soft biological tissues, where impedance is typically around 1.5–1.7 MRayl depending on formulation and layer composition[56]. Compared with general ultrasound tissue-mimicking materials, the present skin phantom is closer to low-impedance soft phantoms than to human skin. For example, Phani et al. reported a carbomer-gel soft-tissue phantom with acoustic impedance 1.61 MRayl[74]. Other gelatin-based

tissue-mimicking materials have reported impedance values from 1.373 to 1.707 MRayl, while liver and blood mimicking materials were reported at 1.693 and 1.624 MRayl, respectively[76].

The results for the acoustic impedance measurements of the soft tissue TMMs are presented in figure 130.

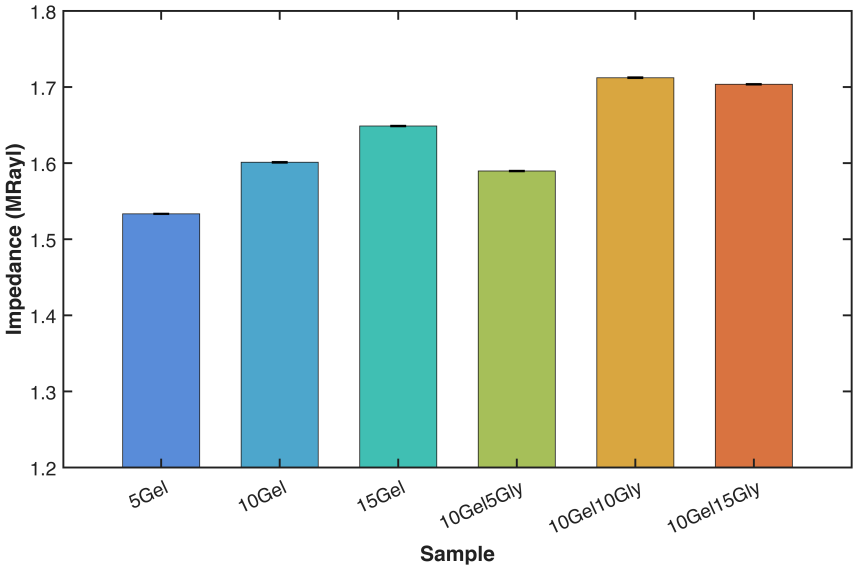



Figure 130: Acoustic impedance measurements for the soft tissue TMMs with varying compositions of gelatin and glycerol.

The measured acoustic impedance of the soft-tissue TMMs ranged from 1.53 to 1.71 MRayl. The 5Gel formulation presented the lowest value, 1.53 MRayl, while 10Gel and 15Gel increased to 1.60 and 1.65 MRayl, respectively. The glycerol-containing formulations remained within a similar soft-tissue-relevant range, with 10Gel5Gly at 1.59 MRayl and the highest values obtained for 10Gel10Gly and 10Gel15Gly, at 1.71 and 1.70 MRayl. This confirms that increasing gelatin and glycerol content generally increased acoustic impedance, mainly through the combined increase in density and speed of sound.

These values compare well with reference values used in ultrasound soft-tissue phantom studies. Phani et al. used ICRU Report 61 as a benchmark and defined a soft-tissue acoustic impedance target of 1.63 MRayl, together with a density of 1.043 g/cm$^3$ and a speed of sound of 1561 m/s. In that context, the 15Gel formulation, at 1.65 MRayl, is the closest match, differing by only 0.02 MRayl. The 10Gel formulation, at 1.60 MRayl, and 10Gel5Gly, at 1.59 MRayl, are also close to the reference, differing by 0.03–0.04 MRayl[74]. The measured values are also consistent with reported acoustic impedances for gelatin-based soft-tissue-mimicking materials. Altun et al. reported acoustic impedance values between 1.328 and 1.707 MRayl for oil-in-gelatin breast soft-tissue TMMs measured using scanning acoustic microscopy. The present formulations fall almost entirely within this range, with 10Gel10Gly at 1.71 MRayl lying at the upper boundary[76]. Compared with agar-based and multiparametric ultrasound phantoms, the results are also within the expected range. A recent systematic review reported that IEC

agar-based soft-tissue phantoms can present acoustic impedance values around 1.66–1.71 MRayl depending on the inclusion of scattering additives such as Al$_2$O$_3$. The 15Gel, 10Gel10Gly, and 10Gel15Gly formulations therefore approach the impedance of these established soft-tissue phantom systems[7].

The results for acoustic impedance (including effective impedance) of the bone TMMs are presented in figure 131.

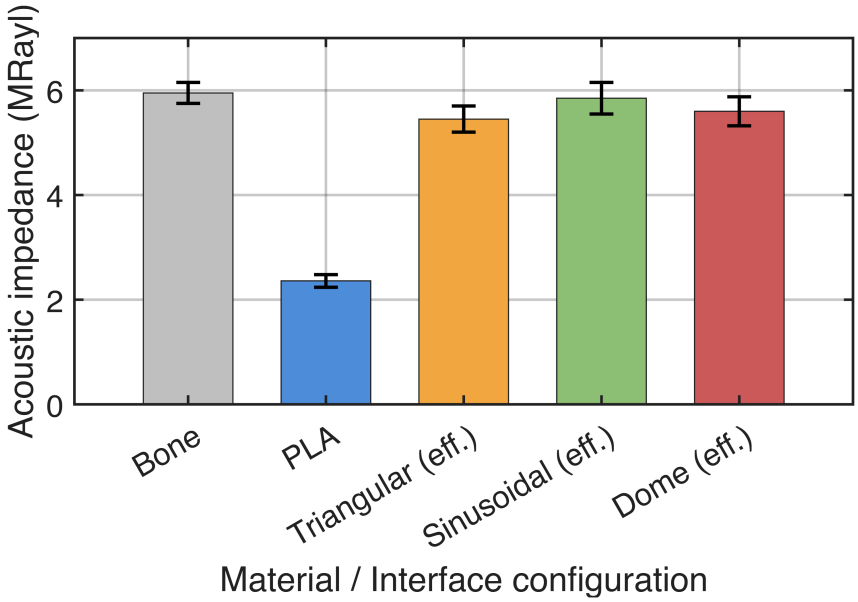



Figure 131: Acoustic impedance measurements for the PLA bone-mimicking material at 0.5 MHz and 1 MHz for different infill densities.

The measured acoustic impedance of bulk PLA was about 2.36 MRayl, which is clearly below the cortical bone reference of 5.95 MRayl[16]. This corresponds to a deficit of about 60%, confirming that PLA alone does not reproduce the impedance contrast expected at a cortical bone interface. The structured PLA interfaces substantially increased the effective impedance. The triangular pattern reached 5.45 MRayl, the dome pattern 5.60 MRayl, and the sinusoidal pattern 5.85 MRayl. Relative to the 5.95 MRayl cortical bone target used in the study, the sinusoidal interface provided the closest match, differing by only about 1.7%, followed by the dome pattern at about 5.9% below the target and the triangular pattern at about 8.4% below the target. This indicates that interface structuring can compensate for the low intrinsic impedance of PLA by increasing the apparent impedance experienced by the incident wave.

Compared with other ultrasound bone-phantom materials, the bulk PLA impedance obtained in this work, 2.36 MRayl, is very close to previously reported 3D-printed polymer bone substitutes. Menikou and Damianou used ABS-M30 as a bone-mimicking material for focused ultrasound phantoms and reported an acoustic impedance of 2.13±0.08 MRayl, clearly below typical cortical bone, which they cited as 7.38 MRayl[77]. A related MRI-compatible bone phantom study also reported ABS impedance between 2.31 and 2.36 MRayl[78]. Yoshizawa et al. developed calcium-loaded oil-jelly bone-mimicking phantoms and

reported impedances of 2.0, 2.2, and 2.6 MRayl for calcium contents of 50, 55, and 59 wt.%, respectively, measured at 3.5 MHz[79]. This suggests that solid PLA can match some low-impedance bone-mimicking phantom materials, particularly those intended to represent reduced-density or osteoporosis-related bone substitutes, but not dense cortical bone.

The proposed geometries should be interpreted as effective bone-interface mimics, and among the tested configurations, the sinusoidal surface produced the most suitable impedance response, suggesting that smooth periodic surface modulation may be more effective than triangular or dome geometries for increasing the apparent acoustic impedance of PLA-based bone phantoms.

#### 6.3.3.5 Limitations and Future Improvements

The tissue-mimicking materials developed in this work demonstrated acoustic properties within biologically relevant ranges for several target tissues, particularly for generalized soft tissues and for the effective impedance response of structured PLA bone interfaces. Nevertheless, some limitations must be acknowledged. First, the skin-mimicking material reproduced the layered and fiber-reinforced architecture of skin, but its acoustic properties were not fully matched to native tissue. In particular, the measured speed of sound and acoustic impedance remained below the values typically reported for human skin, indicating that the silicone matrix dominated the acoustic response despite the incorporation of fibrous reinforcement. Therefore, this material should be interpreted primarily as a structurally and mechanically inspired skin layer rather than as a fully acoustically equivalent skin TMM.

For the generalized soft-tissue TMMs, the agar–gelatin–glycerol formulations provided tunable density, speed of sound, attenuation, and acoustic impedance. However, the formulations did not reproduce all soft tissues equally. Lower gelatin concentrations produced more water-like materials with reduced attenuation, whereas higher glycerol concentrations increased both speed of sound and attenuation, in some cases exceeding the values expected for average soft tissue. This indicates that the developed formulations are suitable for controlled acoustic tuning, but that each formulation should be selected according to the specific target tissue rather than treated as a universal soft-tissue analogue. Future work should therefore expand the formulation matrix to include tissue-specific targets, such as adipose tissue, skeletal muscle, tendon, ligament, and cartilage, while also accounting for anisotropy, hydration stability, and long-term degradation.

The PLA-based bone-mimicking materials also presented important limitations. Bulk PLA showed density, speed of sound, and acoustic impedance values below those of cortical bone, confirming that unmodified PLA is not a fully material-matched substitute for native bone. The use of structured

interfaces, including triangular, sinusoidal, and dome-like geometries, substantially increased the effective acoustic impedance and improved the agreement with cortical bone interface values. However, this agreement is based on an apparent impedance effect generated by oblique reflection rather than on intrinsic material equivalence. Therefore, this geometry is suitable for studies focused on acoustic propagation through soft tissues and interaction with a bone-like boundary, as considered in the present work, but it remains unsuitable for applications requiring a material response equivalent to native cortical bone. Moreover, cortical bone exhibits complex anisotropic and frequency-dependent attenuation behavior, commonly better represented by a power-law relationship, whereas the PLA specimens showed a more linear attenuation response over the tested frequency range. Future work should investigate mineral-filled PLA composites, calcium phosphate-loaded polymers, ceramic–polymer composites, and multi-material printing strategies to improve the intrinsic density, stiffness, speed of sound, and attenuation of the bone-mimicking region. In addition, further numerical simulations should be performed to characterize the acoustic field generated by the structured PLA interfaces in greater detail. These simulations should evaluate how surface geometry, incidence angle, wavelength, and frequency influence reflection, scattering, and effective impedance. This would allow identification of the wavelength range over which the metamaterial-inspired surface remains effective and clarify whether its response is governed primarily by oblique reflection, diffraction, local resonances, or scattering from the patterned geometry.

Another limitation concerns the experimental measurement setup. The acoustic characterization was performed using the available transducers, signal generation, and acquisition equipment, which constrained the usable frequency range, excitation voltage, and signal-to-noise ratio. These constraints are particularly relevant for attenuation measurements, where low received amplitudes, transducer bandwidth limitations, coupling variability, and electronic noise can affect the calculated attenuation coefficient. Future work should therefore include the acquisition of improved instrumentation, including a signal generator or pulse/receiver capable of higher-frequency excitation, higher-voltage output for improved transmission through highly attenuating samples, and a lower-noise oscilloscope with higher bandwidth and sampling resolution. These improvements would increase measurement reliability, particularly for highly attenuating materials such as PLA-based bone phantoms and for frequency-dependent attenuation analysis.

A further development should involve the fabrication and use of dedicated calibration blocks with well-characterized acoustic properties. For soft-tissue measurements, a water-based calibration block or controlled water-path reference should be implemented, since water has well-established acoustic

properties and provides a reproducible baseline for time-of-flight, amplitude transmission, and attenuation correction. For bone-mimicking measurements, a second calibration block should be produced using acrylic, or another stable solid material with known density, speed of sound, attenuation, and acoustic impedance. Such reference blocks would allow correction of system-dependent losses, including transducer response, coupling variability, diffraction effects, electronic gain, and interface transmission losses. This would improve the separation between true material attenuation and attenuation introduced by the measurement system.

Future work should also improve the reproducibility and validation of the developed TMMs. This includes increasing the number of replicates, controlling sample hydration and storage conditions, measuring temperature during acoustic testing, and evaluating the stability of acoustic properties over time. For hydrogel-based materials, dehydration and microbial degradation should be minimized through sealed storage, preservatives, or alternative polymer systems. For silicone- and PLA-based materials, additional microstructural characterization should be performed to relate acoustic behavior to fiber distribution, internal porosity, infill architecture, and surface roughness. Finally, the developed materials should be validated not only as isolated samples, but also after integration into multilayer anatomical phantoms, where interfacial reflections, coupling conditions, standing wave formation, and geometry-dependent propagation may significantly affect the acoustic field.

## 6.4 Transducer characterization and optimization

This section presents the experimental and numerical characterization of the ultrasonic transducer used in the present work. First, the transducer surface response was measured experimentally using a Polytec LDV, allowing non-contact quantification of the out-of-plane vibration velocity under operating conditions. The experimental setup was designed to ensure repeatable boundary conditions, correct optical alignment, and minimal mechanical loading of the radiating surface. The measured response was then used to calibrate and validate an axisymmetric numerical model of the piezoelectric transducer, in which the experimentally measured voltage was applied as the electrical input. After validation, acrylic tape layers were introduced as an attenuation interface to reduce the transmitted vibration amplitude and improve thermal safety during tissue exposure. The calibrated model was subsequently used to evaluate the acoustic pressure field, temperature rise, and predicted tissue damage for different tape configurations, enabling the selection of a final configuration that reduced acoustic energy deposition while preserving controlled ultrasound transmission.

### 6.4.1 Materials and methods

#### 6.4.1.1 Ultrasound Transducer Selection and Description

The ultrasonic excitation was generated using a piezoelectric ultrasonic cleaning transducer assembly composed of a 28 kHz, 100 W transducer coupled to a 220 $V_{ac}$ driver board. The selected transducer was a commercial low-frequency ultrasonic transducer, consisting of a piezoelectric ceramic stack bonded to a metallic radiating body. According to the supplier specifications, the nominal operating frequency was 28 kHz and the maximum electrical power was 100 W. Comparable 28 kHz ultrasonic transducers report resonant frequencies close to $28 \pm 1$ kHz, resonant impedance values below approximately 15 $\Omega$, and capacitance values in the order of several nF, which are consistent with high-power Langevin-type cleaning transducers (figure 132).

This transducer was selected as a low-cost and high-power excitation source for preliminary acoustic characterization and phantom testing. Its relatively low operating frequency allows efficient generation of mechanical vibration and acoustic pressure in fluid-coupled systems, while the 100 W nominal power rating provides sufficient excitation amplitude for transmission measurements through attenuating materials. However, since the device was designed for ultrasonic cleaning rather than calibrated biomedical ultrasound measurements, its output pressure, bandwidth, electroacoustic efficiency, and spatial pressure distribution were not assumed from the manufacturer specifications. Therefore, all



Figure 132: 28 kHz ultrasonic transducer used for acoustic excitation in this study. The transducer consists of a piezoelectric ceramic stack (visible as the central cylindrical component) bonded to a metallic radiating body (the larger cylindrical housing).

acoustic measurements were interpreted relative to the experimental calibration procedure and reference measurements, rather than from the nominal electrical power of the transducer alone.

#### 6.4.1.2 Experimental Characterization

The surface velocity of the ultrasonic transducer was experimentally measured using a Polytec laser Doppler vibrometer (LDV) (Polytec OFV-551-2A). The LDV was directed normal to the radiating surface of the transducer in order to measure the out-of-plane vibration velocity. To ensure correct alignment between the laser beam and the vibrating surface, the LDV was mounted on a support with tri-axial adjustment, allowing fine calibration of the position and orientation of the optical head. This configuration enabled the laser beam to be aligned as close as possible to the normal direction of the transducer surface, minimizing angular measurement errors. The LDV head was positioned at a distance of 237 mm from the measurement point, corresponding to a recommended measurement distance defined in the equipment manual as a multiple of the laser wavelength. A small piece of reflective tape was applied to the measurement point to improve laser backscatter and increase the quality of the optical signal. This procedure allowed non-contact measurement of the transducer vibration without adding significant mechanical loading to the surface.

The velocity signal acquired by the LDV was recorded using a Siemens SCADAS data acquisition system. The acquisition frequency was set to 50 kHz, which was selected to capture the dynamic response of the transducer within the frequency range of interest while satisfying the sampling requirements for the excitation frequency. Data acquisition and signal recording were performed using LMS Test.Xpress 8 software. The measured signal was stored as a time-domain velocity response, allowing the determination of the peak velocity, root-mean-square velocity, and frequency-domain response of the transducer surface.

To ensure repeatable boundary conditions during the measurement, a dedicated support structure was

designed and manufactured specifically for the transducer. The support held the transducer in a stable position while avoiding mechanical pre-tension or compression of the radiating surface. This was important because any imposed preload could alter the dynamic response of the piezoelectric assembly, shift its resonance behavior, or modify the measured surface velocity. Therefore, the transducer was constrained only as required for positional stability, while the active vibrating surface remained mechanically unloaded (Figure 133). The technical drawing of the support structure can be found in chapter A.

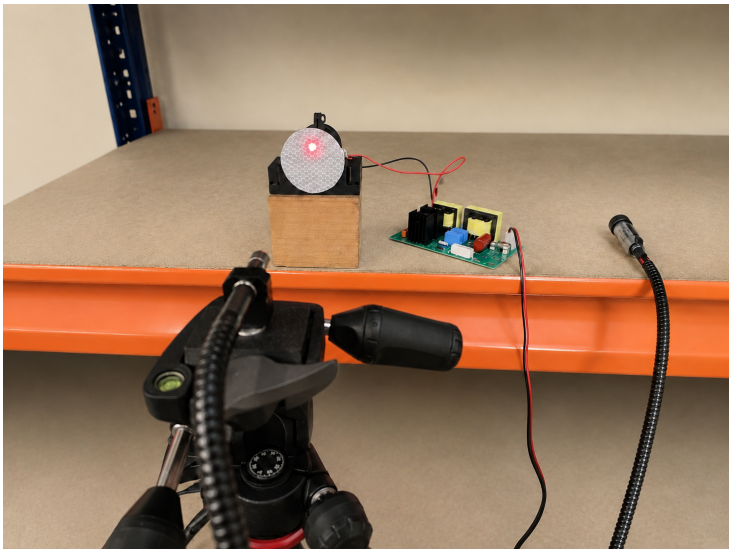


Figure 133: Custom-designed support structure for the ultrasonic transducer. The support holds the transducer in a stable position while allowing the radiating surface to vibrate freely without mechanical loading.

Several points were chosen across the surface, and three readings were performed in each of them. This experimental configuration enabled direct quantification of the transducer surface velocity under operating conditions. Since the measurement was performed using a non-contact optical method, the obtained velocity response was not affected by the mass loading that would occur with contact sensors such as accelerometers.

After the initial calibration of the LDV measurement and acquisition chain, an acrylic tape layer was applied to the radiating surface of the transducer. This layer was introduced as an acoustic attenuator, since the transducer was expected to generate high-amplitude surface vibrations under the selected excitation conditions. The use of acrylic tape reduced the transmitted vibration amplitude and helped maintain the measured response within a suitable acquisition range, preventing signal saturation and improving the reliability of the velocity measurements. This attenuation layer was only added after calibration to ensure that the calibration procedure characterized the measurement system independently of the additional damping introduced by the tape.

#### 6.4.1.3 Numerical Characterization

A numerical characterization framework was developed to support the experimental analysis of the ultrasonic transducer and to evaluate its interaction with the developed tissue-mimicking materials. The simulations were performed using an axisymmetric formulation, which reduced the computational cost while preserving the radial symmetry of the transducer geometry and the dominant through-thickness propagation path. This approach was considered suitable because the transducer and the main propagation domain were approximately rotationally symmetric around the central acoustic axis. Four separate numerical studies were performed, each addressing a specific aspect of the transducer–material interaction.

**Free Transducer Vibration and Vibrometer-Based Validation**

The first simulation considered the ultrasonic transducer operating without contact with tissue-mimicking materials. The objective was to validate the material parameters and boundary conditions used to describe the electromechanical response of the piezoelectric assembly. A coupled piezoelectric multiphysics interface was implemented between the piezoelectric ceramic elements and the metallic transducer body, allowing conversion between the applied electrical excitation and the resulting mechanical vibration (figure 134).

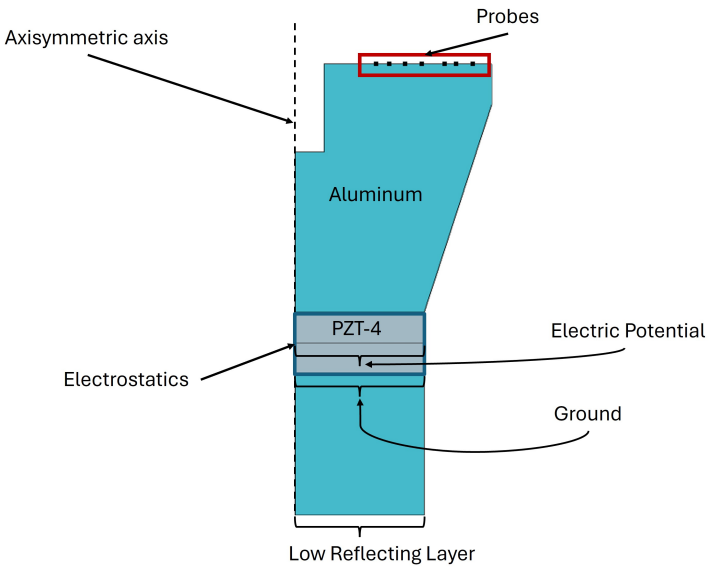



Figure 134: Schematic of the transducer model used for numerical simulations.

The input excitation was a voltage signal corresponding to the experimental conditions, ensuring consistency between the numerical and experimental setups, applying a signal described by equation 262,

$$V(t) = 168 \cdot \sin(2 \cdot \pi \cdot 26000 \cdot t) \tag{262}$$

where the frequency (26 kHz) and amplitude (168 V) were measured experimentally beforehand.

The default library material properties for aluminum and PZT-4 were adopted, as they provided sufficient accuracy for the intended numerical characterization. The solid mechanics module was used for the aluminum and PZT-4 materials, while the Electrostatics was used for the PZT-4, where the input voltage was declared. Acoustic attenuation in the aluminum body was included to account for internal energy dissipation during vibration, using an isotropic loss factor of 0.02 as commonly defined in the literature[80].

The model was built using triangular elements, ensuring that the CFL condition was below 0.2. This resulted in a total of 3310 elements. The numerical surface velocity was extracted at seven points (2.8, 5.3, 7, 10.4, 12.8, 15.2 and 17.15 mm from the center) distributed across the radiating surface of the transducer and compared with the corresponding laser Doppler vibrometer (LDV) measurements. This comparison was used to assess whether the selected piezoelectric, elastic, damping, and boundary parameters reproduced the experimentally observed vibration field. Agreement between the simulated and measured surface velocities was used as the main validation criterion before coupling the transducer to the tissue-mimicking domains.

### Direct Coupling to Soft Tissue-Mimicking Materials and Thermal Analysis

The second numerical study investigated the direct coupling between the ultrasonic transducer and a soft-tissue domain. In this configuration, the radiating surface of the transducer was acoustically coupled to the tissue-mimicking material through a thin gel layer, reproducing the experimental condition required to minimize air gaps and enhance acoustic transmission, as shown in Figure 135.

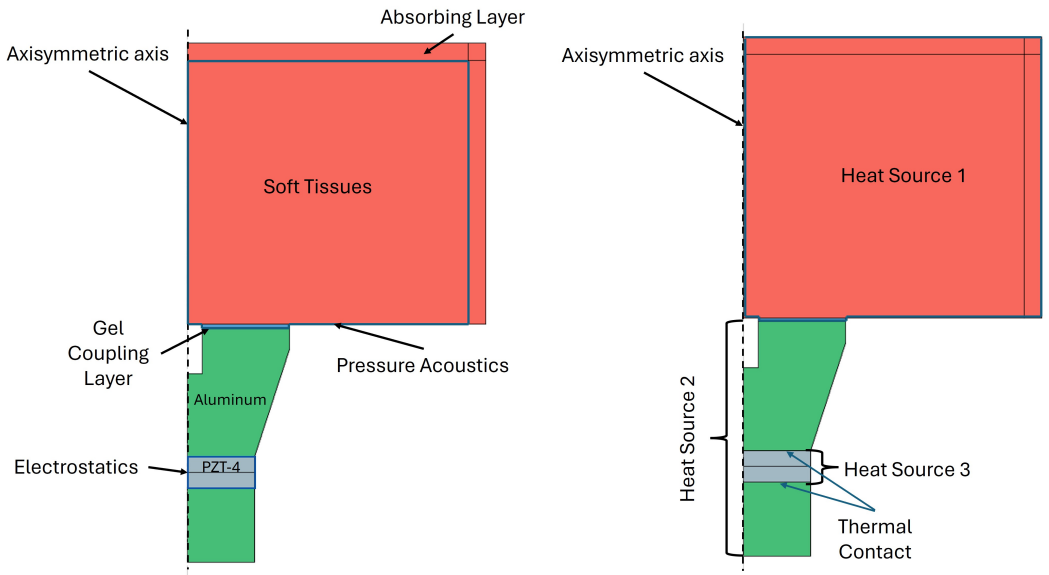



Figure 135: Schematic representation of the transducer–tissue coupling model used in the numerical simulations. The radiating surface of the transducer was coupled to the soft-tissue domain through a thin acoustic coupling gel layer.

The model included four coupled physics interfaces: pressure acoustics, solid mechanics, and electrostatics in the frequency domain, followed by bioheat transfer in the time domain. The analysis was divided into sequential study steps. In the first step, the acoustic and electromechanical response of the system was solved in the frequency domain using the voltage amplitude and central frequency defined in the previous transducer calibration simulation. The resulting dissipated acoustic power in the soft-tissue and solid domains was determined by integrating the local power density over the respective volumes. This procedure provided an estimate of the acoustic energy absorbed by the tissue, which is directly associated with thermal deposition and potential tissue injury.

The dissipated acoustic power obtained from the frequency-domain solution was then used as an input for the thermal analysis. In the following study step, an inverse Fourier transform was applied to convert the frequency-domain response into the time domain over a duration corresponding to 50 periods. Two heat sources were defined from the acoustic dissipation calculated in the tissue and solid domains. A third heat source was assigned to the piezoelectric transducer, representing the power dissipated within the piezoelectric domain. This contribution was calculated by integrating the local power density in the piezoelectric material, assuming a transducer efficiency of 60%, as commonly reported for Langevin-type ultrasonic transducers[81]. This heat source accounted for thermal energy generated within the transducer, which may contribute to heating of the adjacent tissue through conduction and radiation.

The soft-tissue domain was defined using acoustic and thermal properties representative of generalized biological soft tissue. The selected values followed commonly adopted ultrasound tissue-substitute guidelines and phantom literature, remaining consistent with the reference ranges described in ICRU Report 61 and widely used in ultrasound phantom studies[64].

The thermal response was evaluated by solving the heat transfer problem over the prescribed exposure duration. This enabled assessment of whether the acoustic excitation could generate excessive temperature elevations within the tissue-mimicking domain. For each study, two meshes were generated, using triangular elements and satisfying a CFL condition below 0.2. The meshes contained 10840 and 8405 elements, respectively. The resulting temperature distribution was subsequently used to estimate the risk of thermally induced tissue damage, following the principle that ultrasound safety must account for both acoustic exposure and heat generation. This approach is consistent with ultrasound safety standards, and both the soft tissue material properties and the contact conditions were extracted from them, in which soft-tissue heating is represented through the soft tissue thermal index[64].

For this purpose, the maximum temperature within the soft-tissue domain and the corresponding damaged tissue fraction were evaluated. Tissue injury was estimated using the Arrhenius damage model,

with parameters representative of soft-tissue thermal damage[82]. This provided a quantitative estimate of the potential thermal injury produced by the simulated exposure conditions and allowed the safety of the transducer operation in direct contact with soft tissue to be assessed.

**Influence of Acrylic Tape Layers on Soft Tissue Heating**

The third simulation used the same transducer–gel–soft tissue configuration as the previous, and the same multiple study steps, but included several layers of acrylic tape applied between the transducer and the coupling interface. These layers were introduced to represent the experimental attenuation strategy used to reduce the high-amplitude vibration transmitted by the transducer, and the high temperature rise. Different tape configurations were simulated by varying the number, position, and arrangement of the acrylic layers, with thermal contacts being modelled between each layer (figure 136). The objective was to determine whether the additional attenuation introduced by the tape could reduce the acoustic power delivered to the tissue and thereby increase the allowable exposure time before reaching critical thermal or damage thresholds.

Different acrylic tape configurations were numerically evaluated to assess how the attenuation layer influenced acoustic energy delivery to the soft tissue domain. First, the number of continuous tape layers placed over the transducer surface was varied to determine the effect of increasing attenuation-layer thickness on transmitted acoustic power and tissue heating. Additional configurations were then created by introducing gaps in the tape layer. These gaps were varied in both number and position to investigate how localized acoustic windows influenced the spatial distribution of the pressure field, the resulting heat generation, and the predicted exposure time before reaching relevant thermal limits. In configurations where more than one gap was present, the gap length was calculated as the sum of all gap lengths. This parametric strategy allowed comparison between uniform attenuation, partial transmission, and spatially redistributed acoustic excitation.

For each configuration, the acoustic field, dissipated power, temperature rise, and predicted tissue damage were compared with the direct-coupling case. This enabled evaluation of the acrylic tape not only as a practical experimental attenuator, but also as a controllable interface layer capable of modifying the delivered acoustic energy. The simulation therefore provided a numerical basis for selecting tape configurations that reduce excessive heating while maintaining sufficient acoustic transmission for tissue stimulation.

**Transducer Calibration with Acrylic Tape**

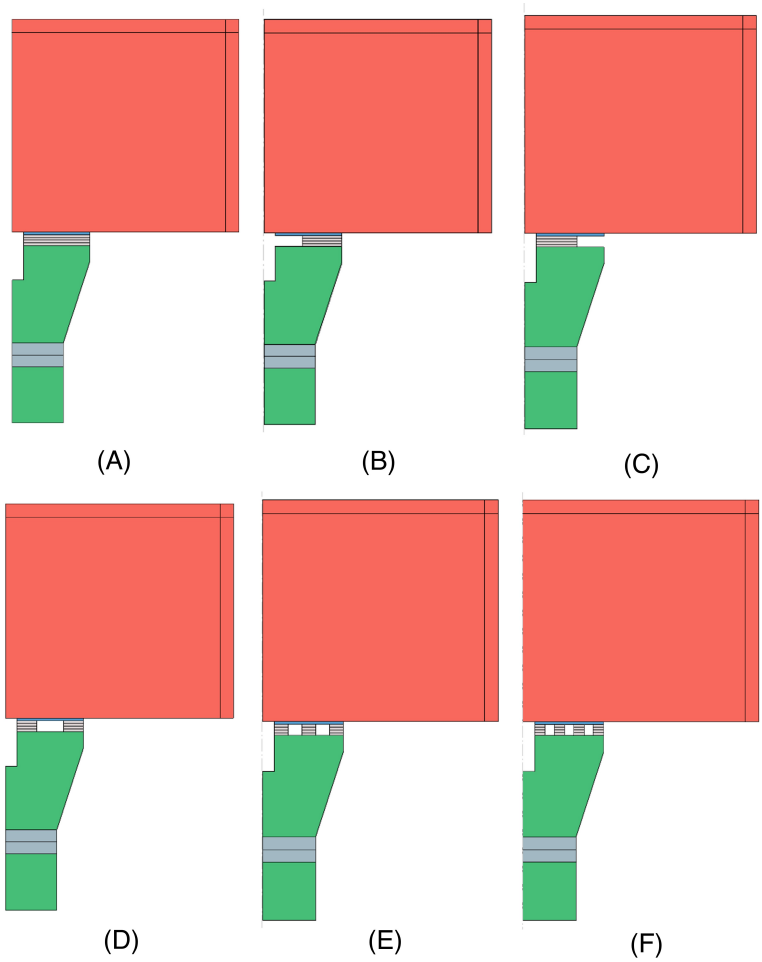



Figure 136: Axisymmetric models of the acrylic tape configurations used to evaluate the influence of attenuation-layer thickness and spatial distribution on acoustic transmission and soft tissue heating. Configurations (A–C) represent continuous acrylic tape layers with different thicknesses, used to assess the effect of increasing the number of layers. Configurations (D–F) include discontinuous tape arrangements with different numbers and positions of gaps, allowing localized acoustic transmission through partial coupling windows.

The fourth simulation reproduced the free-transducer validation model but included the best acrylic tape layer on the radiating surface. This study was performed to verify whether the numerical model remained consistent with the experimental calibration after the attenuation layer was added. The tape-modified transducer response was compared with the measured LDV velocity field, using the same voltage input and the same surface evaluation strategy as in the initial validation simulation.

This final calibration step was necessary because the acrylic tape modifies the boundary condition at the transducer surface by adding mass, damping, and an additional compliant layer. Consequently, the tape can alter both the surface velocity amplitude and the spatial distribution of vibration. Once again, four points were chosen (6.16, 10.3, 12 and 21.6 mm distance from the center) to cross-reference with the experimental data. By validating the tape-coupled model independently, the subsequent heating simulations could be interpreted with greater confidence. Overall, the four-step numerical framework allowed progressive validation of the transducer model, evaluation of direct soft tissue heating, assessment

of acrylic tape as an attenuation layer, and verification of the modified transducer response after tape application.

## 6.4.2 Results

### 6.4.2.1 Initial Transducer Calibration and Validation

The results of the initial calibration of the ultrasonic transducer cross-referenced with the simulation are shown in figure 137. The individual time-domain and FFTs for the seven points can be found in section D.2.

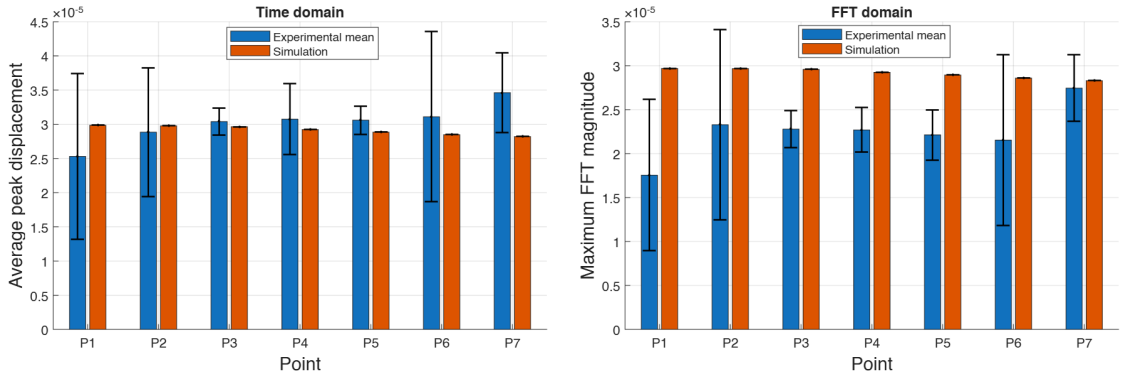



Figure 137: Comparison between experimental LDV measurements and numerical predictions at seven points across the transducer surface.

The calibration results show a reasonable agreement between the numerical model and the experimental LDV measurements, particularly in the time-domain peak displacement. Experimentally, the average peak displacement remained within the order of $2.5\times10^{-5}$ to $3.5\times10^{-5}$ m across the seven measurement points, while the simulated values were close to $2.8\times10^{-5}$ to $3.0\times10^{-5}$ m. The best agreement was observed near the central points, especially P3–P5, where the simulation remained within the experimental variability. Larger deviations appeared at P1, P6, and P7, but the standard deviations were also wider at these locations, suggesting higher spatial variability in the measured vibration response near the outer regions of the transducer surface.

In the frequency domain, the simulation predicted a relatively uniform maximum FFT magnitude, decreasing slightly from approximately $3.0\times10^{-5}$ to $2.8\times10^{-5}$ across P1–P7. The experimental FFT magnitudes were generally lower, ranging from approximately $1.8\times10^{-5}$ at P1 to $2.8\times10^{-5}$ at P7. This indicates that the model slightly overestimated the harmonic response amplitude, particularly at P1–P6. However, the simulated values remained within or near the upper experimental variability for several points, and the agreement improved at P7, where the experimental and numerical responses were close.

The results indicate that the axisymmetric numerical model reproduces the order of magnitude and spatial trend of the transducer vibration response. The time-domain comparison supports the selected material and damping parameters, while the FFT comparison suggests that additional refinement of damping, boundary conditions, or piezoelectric coupling may be required to improve the predicted frequency-domain amplitude.

#### 6.4.2.2 Thermal Simulation of Transducer Coupling to Soft Tissue

The acoustic field generated by the transducer in direct contact with the soft tissue is shown in figure 138. The simulated acoustic field shows the pressure distribution generated by the transducer

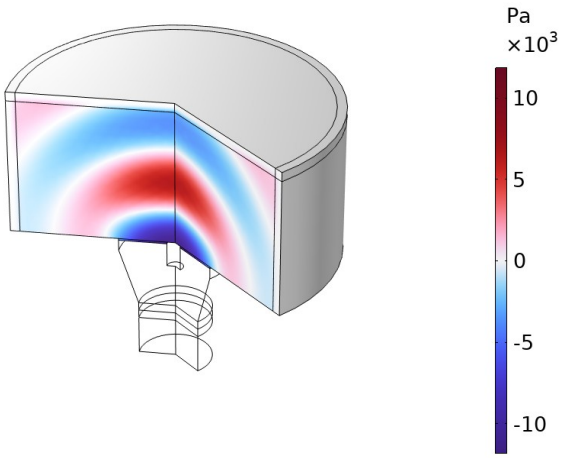



Figure 138: Acoustic field generated by the transducer in direct contact with the soft tissue.

when coupled to the soft-tissue domain. The pressure field is not spatially uniform, presenting alternating positive and negative pressure regions with amplitudes in the order of $\pm 10 \times 10^3$ Pa. The highest pressure amplitudes are concentrated near the transducer–tissue interface and along the central propagation region, where the acoustic energy is first delivered into the medium. Away from this region, the pressure field becomes redistributed, showing regions of constructive and destructive interference. This behavior suggests that local pressure amplification may occur even when the global excitation level is moderate.

The temperature field shows a progressive increase during ultrasonic excitation (figure 139).

At $t = 0$ s, the model remains close to the initial thermal condition, with no relevant localized heating. After 90 s, temperature elevation becomes visible near the transducer and coupling interface, indicating that heat generation is concentrated in the region where acoustic dissipation and piezoelectric losses are highest. As the exposure time increases to 180 and 270 s, the heated region expands and the maximum temperature rises, while the soft-tissue domain remains comparatively cooler due to heat diffusion and

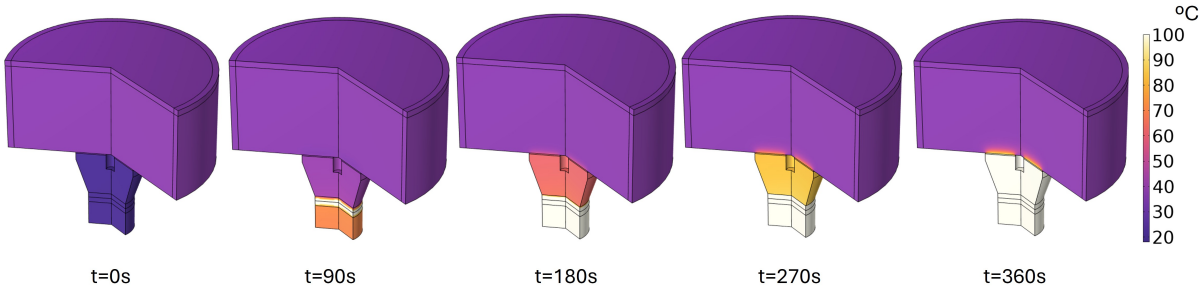



Figure 139: Transient temperature distribution in the coupled transducer–soft tissue model at $t = 0$, 90, 180, 270, and 360 s. The temperature rise is initially localized near the transducer and coupling region, where acoustic and piezoelectric losses are highest, and progressively spreads into the surrounding structure with increasing exposure time.

lower local energy deposition. At 360 s, the highest temperatures are concentrated at the transducer–tissue interface, approaching the upper range of the plotted scale. This confirms that the thermal response is strongly time-dependent and that prolonged excitation can lead to localized heating near the acoustic source.

The tissue damage field in figure 140 shows a strongly localized and time-dependent response.

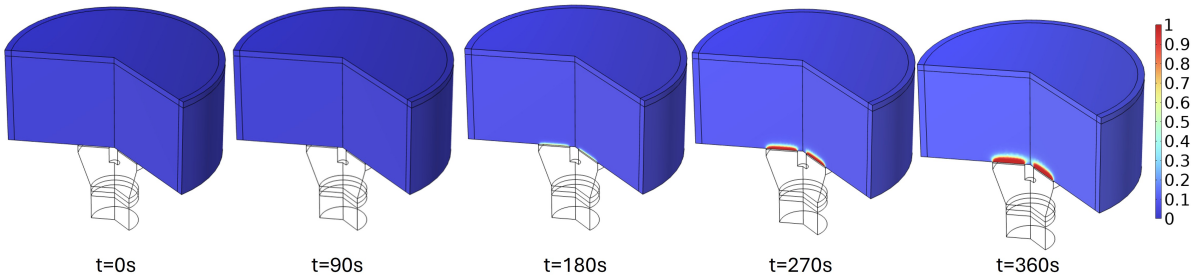



Figure 140: Transient tissue damage distribution in the coupled transducer–soft tissue model at $t = 0$, 90, 180, 270, and 360 s. The damage variable ranges from 0, indicating no damage, to 1, indicating complete local tissue damage. Damage initiation occurs near the transducer–tissue interface and progressively increases with exposure time due to localized thermal accumulation.

At $t = 0$ and 90 s, the damage variable remains close to zero throughout the soft-tissue domain, indicating that the exposure duration is insufficient to induce relevant thermal injury. At 180 s, damage initiation becomes visible near the transducer–tissue interface, corresponding to the region of highest temperature rise. As the exposure time increases to 270 and 360 s, the damaged region expands laterally along the interface and reaches values close to 1, indicating severe local tissue damage. The results show that tissue injury is not uniformly distributed across the domain, but is concentrated near the acoustic source where thermal accumulation is highest. This confirms that exposure time is a critical parameter in the safety assessment of the proposed ultrasonic excitation configuration.

Figure 141 shows how the maximum temperature and damage evolve over the simulated time. For a thermally safe operating condition, the tissue temperature should ideally remain close to physiological values ($\sim$ 37 °C) and, for prolonged exposures, below approximately 43 °C, which is commonly

associated with the onset of thermal injury. Likewise, the fraction of damage should ideally remain close to $0$, indicating negligible tissue injury.

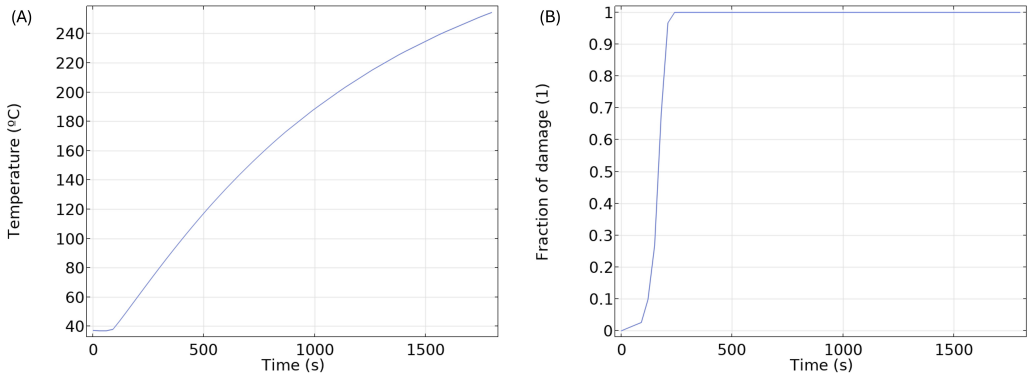



Figure 141: Numerical prediction of thermal response and tissue damage during direct transducer excitation without an attenuation layer. (A) Maximum tissue temperature as a function of exposure time; (B) Corresponding fraction of tissue damage.

Figure 141(A) shows that the tissue temperature rises continuously from an initial value close to physiological conditions (37$^o$C) to more than 250$^o$C at the end of the simulation. From a thermal safety perspective, the ideal situation is to keep tissue temperature close to baseline and, in most cases, below about 43$^o$C, since this limit is commonly associated with the onset of thermal injury during prolonged exposure. In this case, that threshold is exceeded very early, at 125 s. The curve then reaches 50$^o$C at 160 s and 60$^o$C at 210 s. These temperatures are well above the range generally considered safe and are consistent with rapid protein denaturation and coagulative damage.

Figure 141(B) confirms this behavior through the damage metric. Ideally, the fraction of damage should remain close to 0, indicating negligible tissue injury. In contrast, the present response shows a rapid increase in damage after the first 100 s. The fraction of damage reaches 0.1 at 120 s, indicating the onset of relevant injury, exceeds 0.5 at 180 s, and approaches 1 between at 220 s, corresponding to essentially complete tissue damage. Therefore, both the temperature and damage curves indicate that the applied condition is far from a safe operating regime, with the critical thermal and biological thresholds being reached within the first few minutes of exposure.

Figure 142 shows how the maximum temperature and damage evolve over the simulated time

Figure 142(A) shows that increasing the number of acrylic tape layers delays the temperature rise and reduces the heating rate. However, all configurations eventually exceed the $43$ °C threshold within the simulated time window. This threshold is reached at $250$ s, $400$–$450$ s, $500$ s, $700$ s, $850$ s, and $950$ s for 1, 2, 3, 4, 5, and 6 layers, respectively. A temperature of $50$ °C, which is already associated with rapid thermal injury, is reached at approximately $430$ s, $620$ s, $800$ s, $980$ s, $1200$ s, and $1400$ s, respectively. By the end of the simulation, the maximum temperature is about $134$ °C for 1 layer,

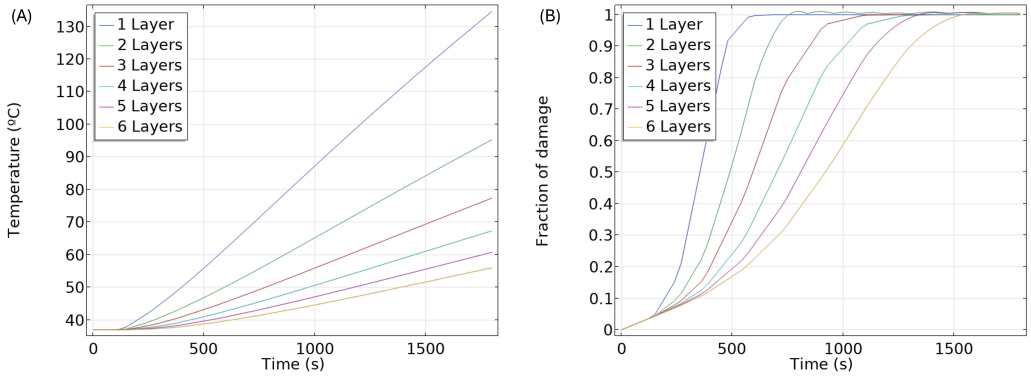



Figure 142: Numerical prediction of (A) maximum tissue temperature and (B) fraction of tissue damage for transducer configurations with 1 to 6 acrylic tape layers.

decreasing progressively to about $56$ °C for 6 layers.

Figure 142(B) confirms the same trend in terms of cumulative tissue injury. Ideally, the damage fraction should remain near zero throughout the exposure. Instead, all cases exhibit progressive damage accumulation, although at markedly different rates. The onset of relevant damage, taken here as a damage fraction of approximately $0.1$, occurs at about $220$ s, $300$ s, $330$ s, $350$ s, $360$ s, and $380$ s for 1 to 6 layers, respectively. More severe injury, corresponding to a damage fraction of approximately $0.5$, is reached at roughly $380$ s, $500$ s, $620$ s, $760$ s, $860$ s, and $950$ s. Complete tissue damage, represented by a damage fraction approaching $1$, occurs at approximately $600$ s, $800$ s, $1100$ s, $1300$ s, $1400$ s, and $1500$–$1600$ s for 1, 2, 3, 4, 5, and 6 layers, respectively. Therefore, the addition of acrylic tape is effective in delaying both excessive heating and irreversible tissue damage, although even the 6-layer configuration does not fully prevent critical injury over long exposure durations.

The acoustic pressure field changed markedly after the introduction of the six acrylic tape layers, has is shown in figure 143.

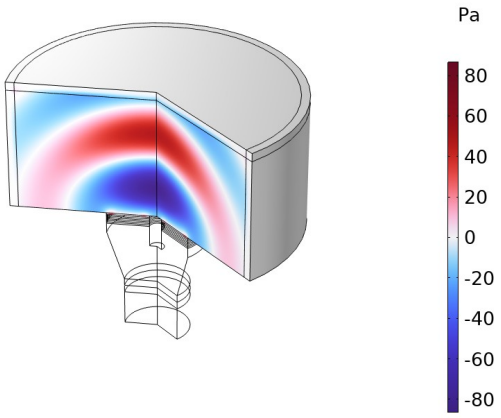



Figure 143: Numerical acoustic pressure field generated by the ultrasonic transducer after coupling with six acrylic tape layers placed at the transducer surface.

When six acrylic tape layers were introduced, the spatial distribution of the acoustic field remained

qualitatively similar, preserving the main wavefront structure and alternating positive and negative pressure regions. However, the pressure amplitude was substantially reduced, with the colour scale decreasing to $-80$ to $80$ Pa. This corresponds to a reduction of more than two orders of magnitude compared with the direct-coupling case. The tape layers therefore acted as an effective acoustic attenuation barrier, reducing the pressure transmitted into the tissue domain while maintaining the overall wave propagation pattern. This reduction in pressure amplitude is consistent with the thermal results, where the addition of tape layers delayed the temperature increase and postponed the onset of tissue damage. The acrylic layers reduced the acoustic energy delivered to the tissue, thereby decreasing acoustic dissipation and subsequent heat generation. Nevertheless, the persistence of a structured pressure field indicates that the tape did not fully block acoustic transmission, but instead attenuated the wave to a lower-amplitude regime.

When the tape layer was modified to include gaps, the temperature was further decreased, as shown in figure 144.

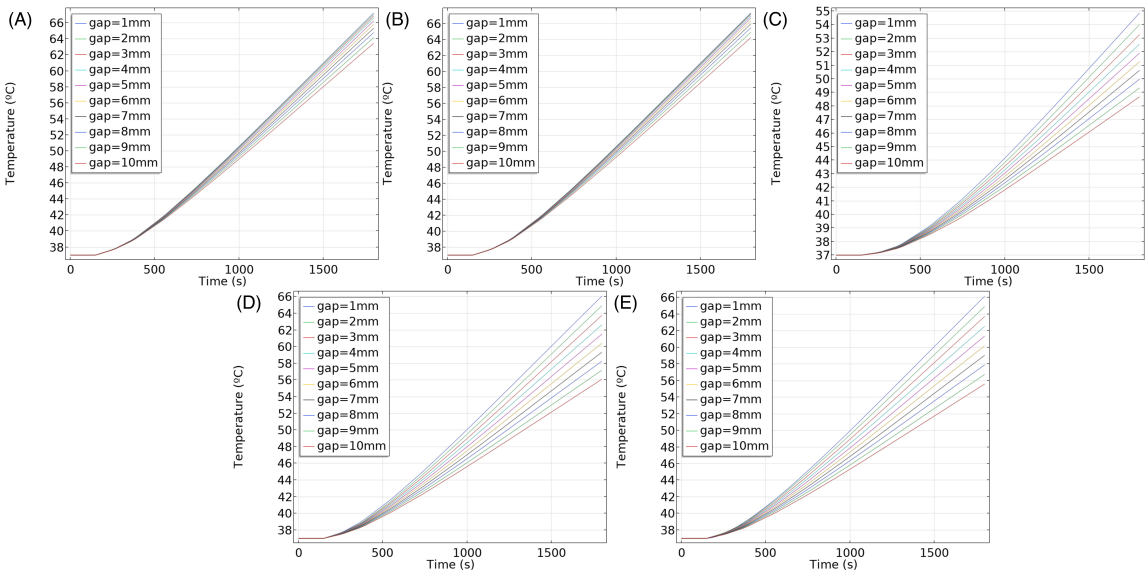



Figure 144: Numerical temperature evolution for the six-layer acrylic tape configuration modified by different internal gap arrangements: (A) inner gap, (B) outer gap, (C) single middle gap, (D) two middle gaps, and (E) three middle gaps.

Configurations **A** (inner gap) and **B** (outer gap) produced the highest temperatures. At $1800$ s, the final temperature remained in the range of $63$ to $67\,^{\circ}$C for gaps between $1$ and $10$ mm, which is consistently $7$ to $11\,^{\circ}$C above the reference six-layer case. The effect of increasing the gap slightly reduced the final temperature, but the reduction was modest. Since these temperatures are well above the reference value, these two configurations would be expected to accelerate damage accumulation and reach $\Omega = 1$ earlier than the $1500$ s observed for the standard six-layer arrangement.

Configuration **C** (single middle gap) showed the strongest attenuation effect. The final temperature at $1800$ s ranged from $55\,^{\circ}$C for a $1$ mm gap to $48$–$49\,^{\circ}$C for a $10$ mm gap. Therefore, this configuration

reduced the peak temperature by up to $7$–$8\,^{\circ}$C relative to the reference six-layer case. For smaller gaps, the thermal response remained close to the reference; however, for larger gaps, the temperature stayed well below $56\,^{\circ}$C, indicating a slower thermal dose accumulation and, consequently, delayed tissue damage.

Configuration **D** (two middle gaps) produced an intermediate response. At $1800$ s, the final temperature varied from $66\,^{\circ}$C for a $1$ mm gap to $56\,^{\circ}$C for a $10$ mm gap. Thus, small gaps led to substantially higher temperatures than the reference, whereas large gaps made the response approach the original six-layer case. In thermal terms, this means that small and intermediate gaps would likely produce faster damage than the reference, while gaps near $9$–$10$ mm would give a response close to the original configuration.

Configuration **E** (three middle gaps) followed a similar trend to configuration D. Final temperatures ranged from $66\,^{\circ}$C for a $1$ mm gap to $55$–$56\,^{\circ}$C for a $10$ mm gap. This indicates that the introduction of multiple middle gaps can progressively reduce thermal delivery as the gap size increases, although the attenuation is less pronounced than in configuration C. Consequently, large gaps in this configuration yield a damage response comparable to, or slightly slower than, the reference six-layer case, whereas small gaps still promote faster damage accumulation.

Simillarly, the results for the predicted tissue damage, shown in figure 145, confirm the trends observed in the temperature analysis.

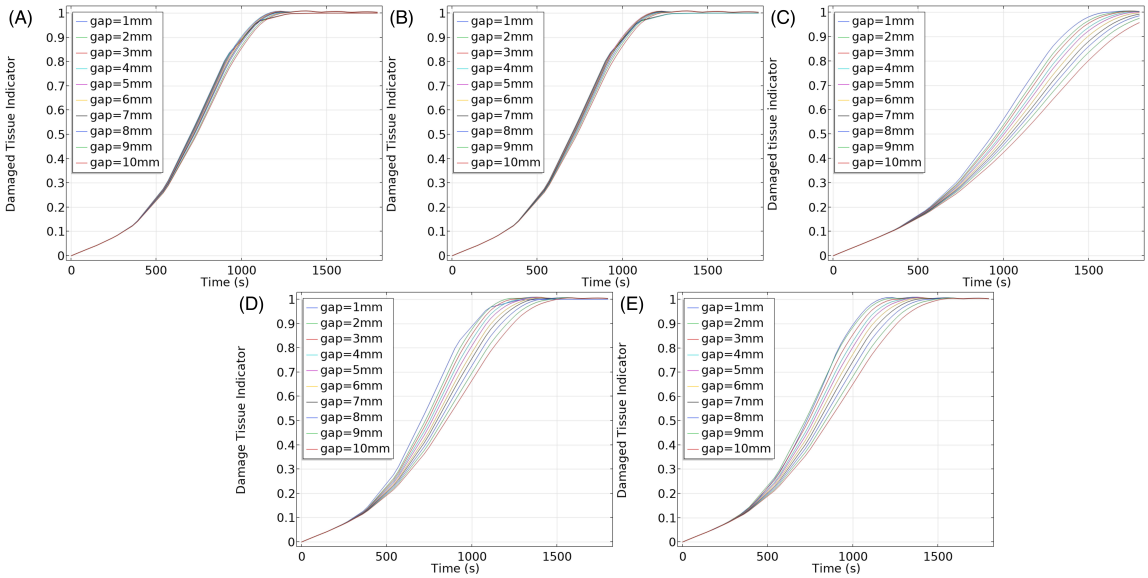



Figure 145: Predicted damaged tissue indicator for six-layer acrylic tape configurations with different gap arrangements: (A) inner gap, (B) outer gap, (C) single middle gap, (D) two middle gaps, and (E) three middle gaps.

Configurations **A** (inner gap) and **B** (outer gap) showed limited sensitivity to gap size. In both cases, all curves followed a similar evolution, with the damaged tissue indicator reaching $\Omega = 0.5$ at $750$–$800$ s and approaching $\Omega = 1$ at $1100$–$1200$ s. Therefore, these configurations produced complete tissue

damage earlier than the six-layer reference case, indicating that inner and outer gap arrangements reduce the protective effect of the acrylic tape stack.

Configuration **C** (single middle gap) produced the slowest damage accumulation. The damaged tissue indicator reached $\Omega = 0.5$ between $950$ and $1150$ s, depending on gap size, and approached $\Omega = 1$ only near the end of the simulation. Larger gaps delayed damage more effectively, with the $10$ mm gap remaining below complete damage for most of the simulated duration. This indicates that a single middle gap provides the most effective configuration for delaying irreversible thermal injury.

Configurations **D** (two middle gaps) and **E** (three middle gaps) showed intermediate behaviour. In both cases, $\Omega = 0.5$ was reached at $800$–$1000$ s, while complete damage occurred between $1300$ and $1500$ s, depending on the gap size. Larger gaps delayed damage accumulation, but the improvement was less pronounced than in configuration C. Thus, multiple middle gaps can improve performance relative to inner or outer gaps, but they do not outperform the single middle-gap configuration.

Based on the thermal and damage analyses, the six-layer acrylic tape configuration with a single middle gap of 10 mm was selected as the final attenuation strategy. This configuration provided the most favorable compromise between acoustic transmission and thermal safety, since it produced the lowest temperature increase and delayed tissue damage more effectively than the other gap arrangements. The final acoustic pressure distribution shows that the selected middle-gap configuration is shown in figure 146.

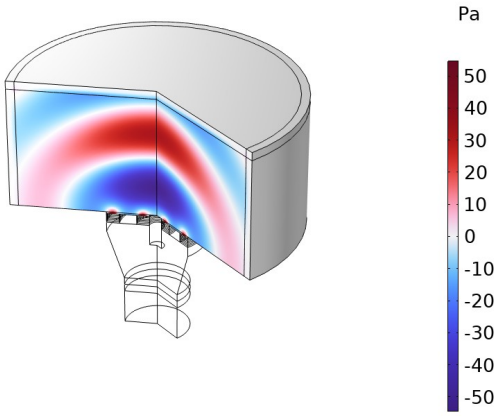



Figure 146: Numerical acoustic pressure distribution obtained for the selected six-layer acrylic tape configuration with a single 10 mm middle gap.

The final acoustic pressure distribution shows that the selected middle-gap configuration preserved the general spatial structure of the wave field observed for the six-layer tape case, with alternating positive and negative pressure regions propagating from the transducer into the tissue domain. However, the pressure amplitude was further reduced. In the six-layer tape configuration without the middle gap, the pressure field reached values of approximately $\pm 80$ Pa, whereas the final 10 mm middle-gap configuration reduced

the pressure range to approximately $\pm 50$ Pa. This corresponds to a reduction of approximately 37.5% in peak pressure amplitude relative to the continuous six-layer tape configuration.

This reduction indicates that introducing a 10 mm middle gap within the acrylic tape stack modifies the acoustic coupling between the transducer and the tissue domain, decreasing the transmitted pressure while maintaining a coherent wavefront. The lower pressure amplitude is consistent with the previously observed reduction in temperature rise and delayed damage accumulation. Therefore, the middle-gap configuration acts not only as an attenuating interface, but also as a practical strategy to reduce acoustic energy deposition in the tissue while preserving controlled ultrasound transmission.

#### 6.4.2.3 Transducer Calibration with Acrylic Tape

The final calibration results for the tape-modified transducer model are shown in figure 147.

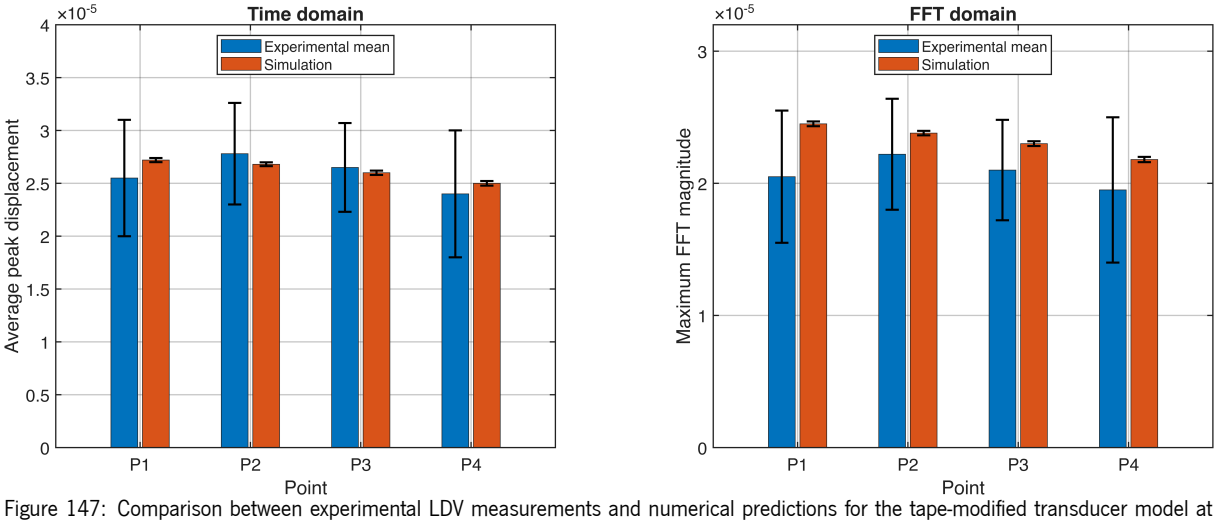



Figure 147: Comparison between experimental LDV measurements and numerical predictions for the tape-modified transducer model at seven points across the transducer surface.

The final calibration performed with the acrylic tape shows good agreement between the experimental measurements and the numerical simulation. In the time domain, the simulated average peak displacement remained close to the experimental mean at all four evaluated points. The simulated values were approximately $2.7 \times 10^{-5}$, $2.7 \times 10^{-5}$, $2.6 \times 10^{-5}$, and $2.5 \times 10^{-5}$ m for P1–P4, respectively, while the experimental means ranged from approximately $2.4 \times 10^{-5}$ to $2.8 \times 10^{-5}$ m. All simulated values fell within the experimental variability, indicating that the model reproduced the measured displacement amplitude of the tape-coupled transducer with acceptable accuracy.

In the frequency domain, the same trend was observed. The simulated maximum FFT magnitudes were slightly higher than the experimental mean values, particularly at P1 and P4, but remained within or close to the experimental standard deviation range. The experimental FFT magnitude decreased from

approximately $2.1 \times 10^{-5}$ at P1 to $2.0 \times 10^{-5}$ at P4, while the simulation ranged from approximately $2.45 \times 10^{-5}$ to $2.2 \times 10^{-5}$. This indicates that the numerical model slightly overestimated the spectral response but preserved the spatial trend across the transducer surface.

The recalibration confirms that the acrylic tape-modified transducer model provides a reasonable representation of the experimental response. The agreement in both peak displacement and FFT magnitude supports the use of this calibrated model for subsequent acoustic and thermal simulations involving the tape attenuation layer. The remaining differences are likely associated with uncertainties in tape thickness, adhesion conditions, local damping, and experimental variability in the LDV measurements.

The numerical analysis was performed under a conservative worst-case operating condition, in which the PZT transducer was assumed to operate under continuous harmonic excitation. This condition represents the maximum thermal loading scenario, since acoustic and electrical energy are delivered without interruption during the full exposure time. Consequently, the predicted temperature rise and tissue damage provide a conservative estimate of the safety limits associated with continuous operation. In practical use, the excitation signal could be divided into shorter bursts or applied with a reduced duty cycle, allowing partial thermal relaxation between pulses. Such pulsed operation would decrease the average deposited power, reduce cumulative heating, and potentially enable substantially longer treatment durations while maintaining the same peak excitation amplitude.

## 6.5 Anatomical tissue phantom for ultrasound therapy delivery to the knee joint

This section presents the development, characterization, and experimental evaluation of the anatomical knee phantom designed for ultrasound therapy delivery. The work integrates the previously developed tissue-mimicking materials into a multimaterial knee model, combining a fiber-reinforced silicone skin layer, a gelatin-based soft-tissue surrogate, and structured PLA bone-mimicking components. The phantom was used to assess acoustic transmission toward the condylar region, evaluate the influence of transducer positioning, and determine the conditions under which the adapted ultrasonic excitation system could be applied safely.

### 6.5.1 Materials and methods

In order to assess ultrasound therapy delivery to the knee joint under anatomically representative conditions, an anatomical UTMP was designed and fabricated. The phantom was developed to reproduce the main acoustic characteristics of the principal tissues involved in knee ultrasound propagation, namely skin, soft tissue, and bone. The final structure consisted of a fiber-reinforced silicone composite skin layer, a gelatin-based soft-tissue surrogate, and embedded sinusoidal PLA bone structures, as illustrated in figure 148.

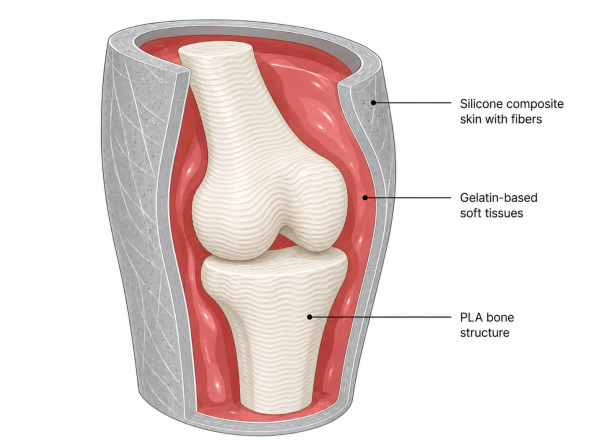



Figure 148: Scientific illustration of the anatomical knee phantom, showing a fiber-reinforced silicone composite skin, gelatin-based soft-tissue surrogate, and sinusoidal PLA bone structures embedded within the phantom.

The anatomical UTMP was produced through a sequential fabrication procedure. First, the bone structures were manufactured by fused filament fabrication using PLA filament. This material was selected because its acoustic response, although not fully equivalent to cortical bone, provides a practical bone-like interface for ultrasound phantom applications. The bone geometries were derived from the MRI dataset

previously used for Patient A. Sinusoidal surface patterns were then applied in Blender to increase the effective acoustic impedance of the bone-mimicking structures, following the approach described earlier in this chapter (Figure 149). A hole was introduced in alignment with the left femoral condyle to allow laser access during LDV-based acoustic measurements.

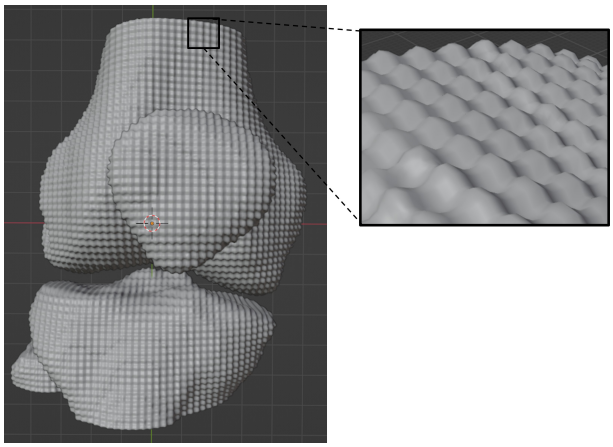


Figure 149: Scientific illustration of the sinusoidal pattern applied to the bone structures, designed to enhance their effective impedance and better mimic the acoustic properties of human bone.

Two moulds were designed to define the inner and outer geometry of the skin layer. These moulds were used to cast the fiber-reinforced silicone composite, which was left to cure until a stable skin-like shell was obtained. After curing, the moulds were removed, resulting in a hollow structure suitable for subsequent filling with the soft-tissue surrogate. The design of the moulds and the resulting skin layer are shown in figure 150.

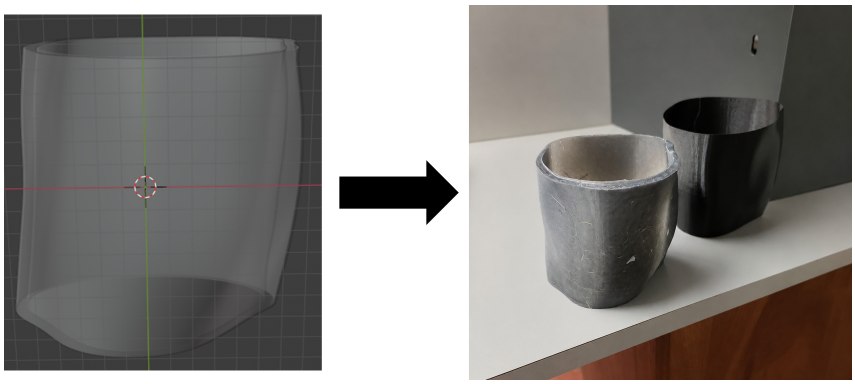


Figure 150: Design of the skin moulds, which were used to create the fiber-reinforced silicone composite skin layer of the anatomical knee phantom, adn the resulting structure.

The outer skin layer was then positioned inside the mould, and the bottom region was sealed using three thin layers of plastic wrapping film to prevent leakage during casting. The tibia and fibula were placed in their corresponding anatomical positions, while the femur and patella were suspended within the mould using duct tape. The mould was partially filled with the 10Gel5Gly formulation to embed the

bone structures and ensure adequate positioning of the femur and tibia within the soft-tissue surrogate. The gelatin-based material was allowed to set for 24 h. After this first gelation period, the duct tape support was removed and the remaining mould volume was filled with the same soft-tissue surrogate. The phantom was then left to set for an additional 24 h. During this process, the femoral hole was preserved to maintain optical access for later LDV measurements, as shown in figure 151.

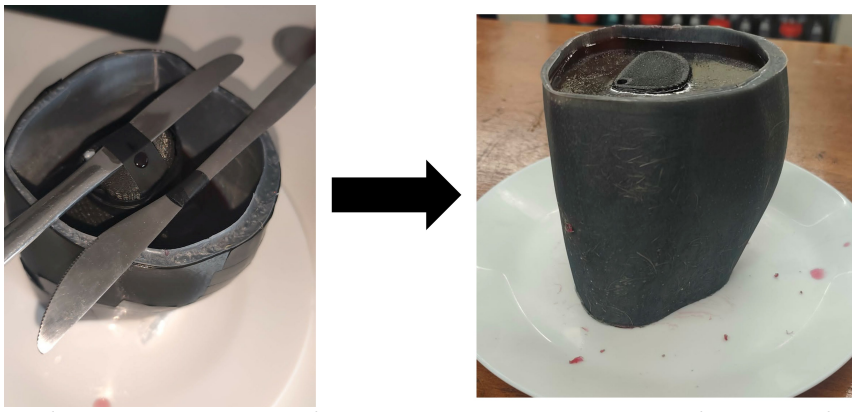


Figure 151: Embedding of the bone structures in the soft-tissue surrogate, showing the placement of the tibia and fibula in their respective positions, and the femur and patella suspended in the middle of the mould, supported by duct tape.

Following completion of the soft-tissue casting stage, the anatomical knee phantom was left to stabilize for an additional 24 h to promote structural integrity between the different components before acoustic testing. The phantom was mounted in the experimental configuration shown in figure 152. During testing, the knee phantom was rotated in increments of $15^{\circ}$ to the left and right to evaluate the influence of transducer placement angle on the measured acoustic response. The orientation shown in figure 152 was defined as the $0^{\circ}$ position, while clockwise and counter-clockwise rotations were assigned negative and positive angular values, respectively.

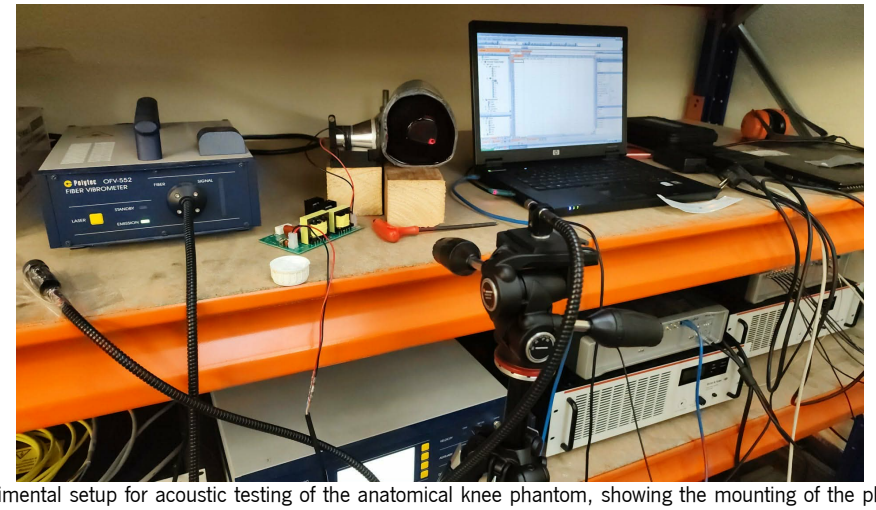


Figure 152: Experimental setup for acoustic testing of the anatomical knee phantom, showing the mounting of the phantom to evaluate acoustic measurements at different angles of transducer placement.

The phantom was mounted such that the femoral hole remained aligned with the LDV laser beam, allowing vibration measurements to be obtained at the left femoral condyle for different transducer positions. A reflective marker was placed at the bottom of the femoral hole to improve laser backscatter and increase the reliability of the optical measurement. The distance between the reflective marker and the laser source was measured to ensure compatibility with the recommended LDV measurement distance specified in the equipment manual.

### 6.5.2 Results

Figure 153 shows the variation of the vibration velocity measured at the left condyle as a function of transducer angular position around the knee.

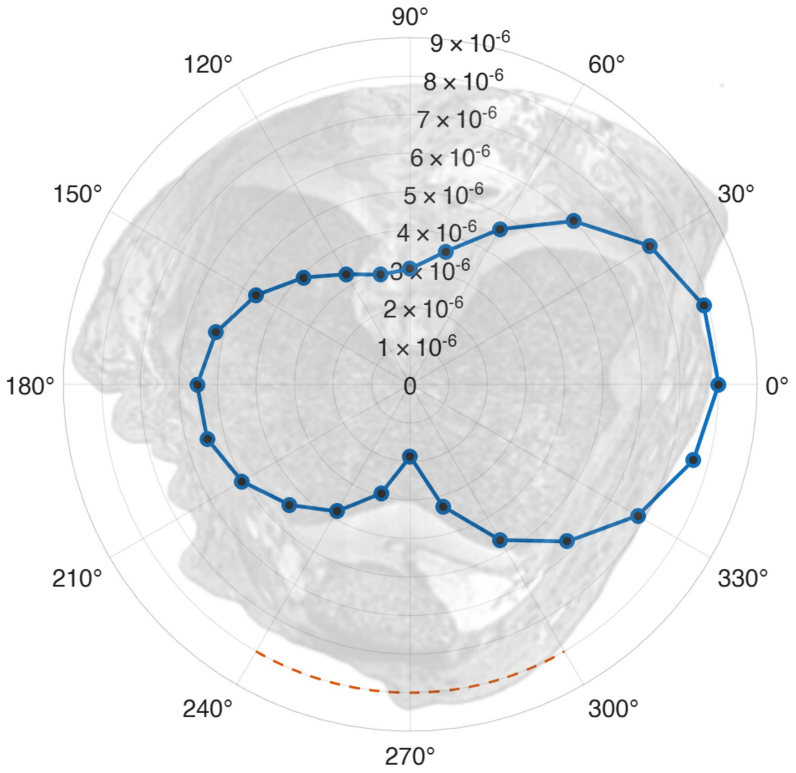



Figure 153: Polar representation of the vibration velocity measured by LDV at the left condyle as a function of transducer angular position around the knee.

The measured response was highly dependent on transducer placement, with the highest velocity amplitudes observed near the anterior–lateral region, particularly between $330°$ and $30°$, where the measured velocity approached $8 \times 10^{-6}$ m/s. This suggests that positions where the transducer achieved a larger and more stable contact area with the skin promoted greater acoustic transmissibility

toward the condylar region. In these configurations, improved mechanical coupling likely reduced local reflection and energy loss at the skin–transducer interface.

A marked reduction in transmitted velocity was observed near $270^\circ$, where the signal decreased to approximately $1.5\times10^{-6}$ m/s. This pronounced dip is consistent with the anatomical obstruction imposed by the patella and surrounding anterior structures, which limit direct acoustic propagation toward the left condyle. The response partially recovered between $150^\circ$ and $210^\circ$, reaching values close to $5\times10^{-6}$ m/s, indicating that posterior or posterolateral transducer positions may still provide moderate transmission, although with lower efficiency than the anterior–lateral placements.

The spatial variation appears to be governed by a combination of contact area, tissue thickness, local curvature, and anatomical barriers. In particular, regions that allowed better surface contact between the skin and transducer increased transmissibility, whereas the patella acted as a clear propagation-limiting structure. These findings indicate that optimal transducer placement should consider not only geometric proximity to the target, but also the quality of coupling and the anatomical pathway between the excitation site and the intended region of stimulation.

A further limitation of the developed anatomical phantom concerns the absence of direct thermal sensorization during ultrasound exposure. Ideally, the phantom should incorporate embedded temperature sensors, such as thermocouples or fiber-optic probes, at critical locations within the soft tissue, cartilage, and bone-mimicking regions. This would allow direct experimental validation of the predicted temperature fields and provide a quantitative comparison between numerical heating simulations and measured thermal response. In particular, thermal validation would be important near impedance-mismatched interfaces, where local absorption and reflection may produce spatially non-uniform heating. The incorporation of distributed thermal monitoring would therefore strengthen the use of the phantom as a platform for evaluating ultrasound therapy safety.

Nevertheless, the present phantom was developed using material properties selected according to established ultrasound tissue-substitute guidelines, with the acoustic parameters evaluated experimentally and compared with values reported for biological tissues. Furthermore, the transducer model was experimentally calibrated using LDV and subsequently validated in silico before being coupled to the phantom domains. Therefore, although direct thermal measurements were not performed at this stage, the combination of guideline-based material selection, experimental acoustic characterization, and validated numerical transducer modelling provides a consistent framework for estimating acoustic delivery and thermal risk. The current model can therefore be considered sufficiently validated for preliminary design assessment and comparative evaluation of attenuation strategies.

Another relevant limitation is that the phantom represents the knee as a simplified multilayer structure rather than as a fully tissue-specific anatomical replica. The present framework distinguishes between skin, generalized soft tissue, and bone-like regions, which is appropriate for evaluating the dominant acoustic transmission path and the effect of high-impedance interfaces. However, the knee contains several tissues with distinct acoustic and mechanical properties, including adipose tissue, skeletal muscle, tendon, ligament, cartilage, meniscus, synovial fluid, cortical bone, and trabecular bone. These tissues differ not only in density, speed of sound, attenuation, and impedance, but also in anisotropy, viscoelasticity, hydration, and thermal response.

Now that a multimaterial phantom framework has been established, future versions may divide the anatomical model into additional subregions representing specific tissues. For example, the generalized soft tissue layer could be separated into adipose tissue and skeletal muscle, while the joint region could incorporate cartilage, tendon, ligament, meniscus, and synovial-fluid-mimicking compartments. This would allow a more realistic representation of acoustic propagation through the knee, particularly because thin tissues such as cartilage and tendon may strongly affect local reflection, refraction, and energy deposition. However, each added material should be independently characterized and validated before integration, since increasing anatomical complexity without sufficient validation may reduce the interpretability of the phantom response.

Future developments should also address the long-term stability and repeatability of the developed TMMs. Hydrogel-based materials may be affected by dehydration, microbial degradation, and changes in mechanical or acoustic properties over time. Silicone-based and 3D-printed materials are generally more stable, but their acoustic response may still depend on manufacturing parameters, surface roughness, internal porosity, adhesion between layers, and curing conditions. Therefore, future work should include ageing studies, repeated acoustic measurements, and controlled storage protocols to determine whether the phantom properties remain stable over clinically relevant testing periods. It could also be intersting explore the creation of a digital twin of the anatomical knee phantom and ultrasound delivery system. By combining the experimentally validated numerical model with machine learning algorithms, it would be possible to progressively improve prediction accuracy, optimize transducer placement, estimate safe exposure windows, and identify material or geometric configurations that enhance acoustic delivery while minimizing thermal risk. Such an approach would allow the phantom to evolve from a static validation platform into an adaptive optimization framework for patient-specific ultrasound therapy planning.

Finally, future validation should move from isolated material characterization toward full-system validation. This should include acoustic field mapping within the assembled phantom, comparison with

hydrophone or vibrometer measurements, thermal validation under controlled exposure, and evaluation of repeatability between phantom replicas. Such validation would allow the anatomical phantom to evolve from a material demonstration platform into a reliable preclinical tool for optimizing ultrasound therapy delivery to the knee joint.

### 6.5.3 Conclusion

This section demonstrated the feasibility of developing a multimaterial anatomical platform for evaluating ultrasound therapy delivery to the knee joint. The final phantom integrated a fiber-reinforced silicone skin layer, a gelatin-based soft-tissue surrogate, and structured PLA bone-mimicking components, allowing the main acoustic interfaces of the knee to be represented within a controlled experimental system. The use of LDV-based measurements further enabled non-contact evaluation of vibration transmission toward the condylar region, providing a practical method to assess how transducer position influences local acoustic delivery.

The transducer was experimentally characterized and numerically validated before being applied to the phantom. The initial direct-coupling configuration produced excessive thermal accumulation and rapid tissue damage, indicating that the unmodified excitation condition was not suitable for prolonged exposure. However, after the introduction of acrylic tape as an attenuation interface and subsequent optimization of the tape arrangement, the transmitted acoustic field was substantially reduced while maintaining controlled wave delivery. Among the tested configurations, the six-layer acrylic tape arrangement with a single 10 mm middle gap provided the most favorable balance between reduced heating, delayed tissue damage, and preserved acoustic transmission.

Based on the thermal and damage simulations, the adapted transducer configuration can be considered suitable for use under the tested conditions, provided that the exposure duration remains below 1150 s. This limit provides a conservative operating window before the onset of critical thermal damage predicted by the model. Therefore, the transducer should not be interpreted as intrinsically safe in its original configuration, but rather as conditionally safe after acoustic attenuation and numerical validation. Its use requires control of exposure time, coupling conditions, and excitation parameters.

Overall, the developed phantom and adapted transducer configuration provide a reproducible framework for studying ultrasound delivery to the knee joint. The results also show that anatomical geometry, tissue-mimicking material selection, transducer position, and attenuation strategy strongly influence the acoustic and thermal response. Future work should incorporate direct thermal sensorization, additional tissue-specific compartments, and further experimental validation of acoustic

and thermal fields to improve the predictive reliability of the phantom for ultrasound therapy optimization.

## 6.6 Bibliography

[1]N. A. T. C. Fernandes, D. I. Alves, D. P. Ferreira, M. Monteiro, A. Arieira, F. Silva, B. Hinckel, A. Leal, and Ó. Carvalho, "Sustainable Tunable Anisotropic Ultrasound Medical Phantoms for Skin, Skeletal Muscle, and Other Fibrous Biological Tissues Using Natural Fibers and a Bio-Elastomeric Matrix", J. Compos. Sci. **9**, 370 (2025) 10.3390/jcs9070370.

[2]N. A. T. C. Fernandes, D. I. Alves, D. P. Ferreira, A. Arieira, F. Silva, B. Hinckel, A. Leal, and Ó. Carvalho, "MICRO AND MACROMECHANICAL MODELLING AND SIMULATION OF BIO ELASTOMERIC COMPOSITES REINFORCED WITH NATURAL FIBRES FOR CRANIAL SKIN ULTRASOUND MEDICAL PHANTOMS", (2025) 10.13140/RG.2.2.17942.05440.

[3]A. Z. Santos, S. Rocha, N. A. T. C. Fernandes, D. I. Alves, D. P. Ferreira, S. M. Costa, J. Padrão, and Ó. Carvalho, "Sustainable Shear Wave Elastography Medical Phantoms: Waste-Based Fibrous Structures for Medical Applications", Textiles **6**, 6 (2026) 10.3390/textiles6010006.

[4]A. Pereira, V. Cardoso, M. Martins, and N. A. T. C. Fernandes, "Development of a hydrophone for measuring the propagation of acoustic waves in biological tissues", in *Proceedings of ICOVP & WMVC 2025. ICOVP & WMVC 2025*, Lecture Notes in Mechanical Engineering (Springer, Cham, 2025), 10.1007/978-3-032-11549-2_63.

[5]N. A. T. C. Fernandes, *Nnunofernandes/Ultrasound-Wave-Material-Characterization: First Release*, version 1.0.1, Zenodo, May 21, 2026, 10.5281/ZENODO.20334339.

[6]N. A. T. C. Fernandes, *Nnunofernandes/Cauchy-Stress-Tensile-Test-Post-Processing: First Release*, version 1.0.0, Zenodo, May 24, 2026, 10.5281/ZENODO.20369750.

[7]A. Jawli, W. Aldehani, G. Nabi, and Z. Huang, "Tissue-Mimicking Material Fabrication and Properties for Multiparametric Ultrasound Phantoms: A Systematic Review", Bioengineering **11**, 620 (2024) 10.3390/bioengineering11060620.

[8]C. K. McGarry, L. J. Grattan, A. M. Ivory, F. Leek, G. P. Liney, Y. Liu, P. Miloro, R. Rai, A. Robinson, A. J. Shih, B. Zeqiri, and C. H. Clark, "Tissue mimicking materials for imaging and therapy phantoms: a review", Phys. Med. Biol. (2020) 10.1088/1361-6560/abbd17.

[9]A. Z. Santos, S. Rocha, B. Carneiro, N. A. Fernandes, J. Padrão, and Ó. Carvalho, "Current state of elastography research in multiple anatomical structures and respective phantoms", Phys. Med. **138**, 105192 (2025) 10.1016/j.ejmp.2025.105192.

[10]K. Melde, A. G. Athanassiadis, D. Missirlis, M. Shi, S. Seneca, and P. Fischer, "Ultrasound-assisted tissue engineering", Nat. Rev. Bioeng. **2**, 486–500 (2024) 10.1038/s44222-024-00166-5.

[11]W. Legon and A. Strohman, "Low-intensity focused ultrasound for human neuromodulation", Nat. Rev. Methods Primer **4**, 91 (2024) 10.1038/s43586-024-00368-6.

[12]M. Lafond, A. Payne, and C. Lafon, "Therapeutic ultrasound transducer technology and monitoring techniques: a review with clinical examples", Int. J. Hyperthermia **41**, 2389288 (2024) 10.1080/02656736.2024.2389288.

[13]L. Crum, "Acoustic cavitation series: part five rectified diffusion", Ultrasonics **22**, 215–223 (1984) 10.1016/0041-624X(84)90016-7.

[14]K. A. Wear, "Mechanisms of Interaction of Ultrasound With Cancellous Bone: A Review", IEEE Trans. Ultrason. Ferroelectr. Freq. Control **67**, 454–482 (2020) 10.1109/TUFFC.2019.2947755.

[15]K. A. Wear, Y. Liu, and G. R. Harris, "Pressure Pulse Distortion by Needle and Fiber-Optic Hydrophones due to Nonuniform Sensitivity", IEEE Trans. Ultrason. Ferroelectr. Freq. Control **65**, 137–148 (2018) 10.1109/TUFFC.2017.2778566.

[16]N. A. T. C. Fernandes, S. Sharma, A. Arieira, B. Hinckel, F. Silva, A. Leal, and Ó. Carvalho, "Experimental Validation of Time-Explicit Ultrasound Propagation Models with Sound Diffusivity or Viscous Attenuation in Biological Tissues Using COMSOL Multiphysics", Bioengineering **12**, 946 (2025) 10.3390/bioengineering12090946.

[17]D. Callens, C. Bruneel, and J. Assaad, "Matching ultrasonic transducer using two matching layers where one of them is glue", NDT E Int. **37**, 591–596 (2004) 10.1016/j.ndteint.2004.03.005.

[18]H. Dong, H. Gao, X. Feng, and Y. Shen, "Shape optimization of acoustic horns for improved directivity control and radiation efficiency based on the multimodal method", J. Acoust. Soc. Am. **149**, 1411–1424 (2021) 10.1121/10.0003568.

[19]K. M. Shu, W. H. Hsieh, and H. S. Yen, "Design and Analysis of Acoustic Horns for Ultrasonic Machining", Appl. Mech. Mater. **284–287**, 662–666 (2013) 10.4028/www.scientific.net/AMM.284-287.662.

[20]*Acoustics Module - User's Guide*, Comsol Multiphysics 5.3 (COMSOL AB, 2018).

[21]*Structural Mechanics Module - User's Guide*, Comsol Multiphysics 5.3 (COMSOL AB, 2018).

[22]*AC/DC Module - User's Guide*, Comsol Multiphysics 5.3 (COMSOL AB, 2018).

[23] *Overview of materials for Polycarbonate, Molded*, MatWeb - Material Property Data, https://www.matweb.com/search/DataSheet.aspx?MatGUID=84b257896b674f93a39596d00d999d77&ckck=1 (visited on 10/15/2025).

[24] M. Afzali and Y. Rostamiyan, "Study the damping and vibrational properties of polycarbonate reinforced ZrO2", Int. J. Multiphysics (2022) 10.21152/1750-9548.16.1.31.

[25] *Mocom (ALBIS) ALCOM® LDDC PMMA 1000 UV 18124 BK1074-11 PMMA*, MatWeb - Material Property Data, https://www.matweb.com/search/DataSheet.aspx?MatGUID=28916247af454eca905039c24bfea571 (visited on 10/15/2025).

[26] K. Ono, "Review on Structural Health Evaluation with Acoustic Emission", Appl. Sci. **8**, 958 (2018) 10.3390/app8060958.

[27] *Overview of materials for Epoxy Cure Resin*, MatWeb - Material Property Data, https://www.matweb.com/search/datasheet.aspx?matguid=956da5edc80f4c62a72c15ca2b923494&ckck=1 (visited on 10/15/2025).

[28] R. Li, G. Fan, X. Ouyang, G. Wang, and H. Wei, "Dynamic mechanical behaviors of epoxy resin/hollow polymeric microsphere composite foams under forced non-resonance and forced resonance", Compos. Adv. Mater. **30**, 26349833211008195 (2021) 10.1177/26349833211008195.

[29] *Overview of materials for Polyetheretherketone, Unreinforced*, MatWeb - Material Property Data, https://www.matweb.com/search/DataSheet.aspx?MatGUID=2164cacabcde4391a596640d553b2ebe (visited on 10/15/2025).

[30] S. Berretta, Y. Wang, R. Davies, and O. R. Ghita, "Polymer viscosity, particle coalescence and mechanical performance in high-temperature laser sintering", J. Mater. Sci. **51**, 4778–4794 (2016) 10.1007/s10853-016-9761-6.

[31] *Overview - Alumina, 98%, Al2O3*, MatWeb - Material Property Data, https://www.matweb.com/search/DataSheet.aspx?MatGUID=38cd8590a98f457a8f4bea462fe91cfa (visited on 10/15/2025).

[32] N. Srikanth, V. Ganesh, and M. Gupta, "Damping characterisation of aluminium containing interconnected wire reinforcement using a novel frequency domain based method", Mater. Sci. Technol. **19**, 48–54 (2003) 10.1179/026708303225008699.

[33] *Overview of materials for Brass*, MatWeb - Material Property Data, https://www.matweb.com/search/DataSheet.aspx?MatGUID=d3bd4617903543ada92f4c101c2a20e5 (visited on 10/15/2025).

[34] *Overview of materials for Stainless Steel*, MatWeb - Material Property Data, https://www.matweb.com/search/DataSheet.aspx?MatGUID=71396e57ff5940b791ece120e4d563e0 (visited on 10/15/2025).

[35] R. Ren, H. Wang, X. Sun, and H. Quan, "Design and Implementation of an Ultrasonic Flowmeter Based on the Cross-Correlation Method", Sensors **22**, 7470 (2022) 10.3390/s22197470.

[36] *Morgan Advanced Ceramics High Performance Piezo PZT-5H Piezoelectric Material*, MatWeb - Material Property Data, https://www.matweb.com/search/DataSheet.aspx?MatGUID=0dbf53f43867476e8c336294e2f078ae (visited on 10/15/2025).

[37] V. T. Rathod, "A Review of Acoustic Impedance Matching Techniques for Piezoelectric Sensors and Transducers", Sensors **20**, 4051 (2020) 10.3390/s20144051.

[38] C. Ramadas, K. Balasubramaniam, A. Hood, M. Joshi, and C. Krishnamurthy, "Modelling of attenuation of Lamb waves using Rayleigh damping: Numerical and experimental studies", Compos. Struct. **93**, 2020–2025 (2011) 10.1016/j.compstruct.2011.02.021.

[39] E. G. Oliveira, A. V. Alvarenga, and R. P. B. Costa-Felix, "Ensuring the validity of results of hydrophone calibration by a mutual comparison calibration method", J. Phys. Conf. Ser. **1826**, 012010 (2021) 10.1088/1742-6596/1826/1/012010.

[40] Y. Shi, G. Cai, and W. Wu, "A panoramic review of transcranial focused ultrasound neuromodulation: from basic research to clinical applications", J. NeuroEngineering Rehabil. **22**, 227 (2025) 10.1186/s12984-025-01753-2.

[41] G. R. Harris, S. M. Howard, A. M. Hurrell, P. A. Lewin, M. E. Schafer, K. A. Wear, V. Wilkens, and B. Zeqiri, "Hydrophone Measurements for Biomedical Ultrasound Applications: A Review", IEEE Trans. Ultrason. Ferroelectr. Freq. Control **70**, 85–100 (2023) 10.1109/TUFFC.2022.3213185.

[42] K. A. Wear, "Considerations for Choosing Sensitive Element Size for Needle and Fiber-Optic Hydrophones—Part I: Spatiotemporal Transfer Function and Graphical Guide", IEEE Trans. Ultrason. Ferroelectr. Freq. Control **66**, 318–339 (2019) 10.1109/TUFFC.2018.2886067.

[43]K. A. Wear, C. Baker, and P. Miloro, "Directivity and Frequency-Dependent Effective Sensitive Element Size of Membrane Hydrophones: Theory Versus Experiment", IEEE Trans. Ultrason. Ferroelectr. Freq. Control **66**, 1723–1730 (2019) 10.1109/TUFFC.2019.2930042.

[44]G. R. Harris and P. M. Gammell, "Sensitivity measurements of piezoelectric polymer hydrophones from 0.2–2 MHz using a broadband-pulse technique", J. Acoust. Soc. Am. **105**, 725–731 (1999) 10.1121/1.426263.

[45]L. Qin, Y. Lu, Y. Xu, and W. He, "The calibration methods of hydrophones for underwater environmental sound measurements or biomedical ultrasound measurements: A review", Measurement **242**, 115700 (2025) 10.1016/j.measurement.2024.115700.

[46]N. A. T. C. Fernandes, A. Arieira, B. Hinckel, F. Silva, A. Leal, and Ó. Carvalho, "A Python FDTD Method Algorithm for 1D Planar Acoustic Wave Propagation: Simulating High-Frequency Ultrasound in the Brain and Beyond", in *Proceedings of ICOVP and WMVC 2025*, Vol. 197, edited by Z. Dimitrovová, P. Biswas, and T. A. N. Silva (Springer Nature Switzerland, Cham, 2026), pp. 391–401, 10.1007/978-3-032-13225-3_39.

[47]S. Sharma, N. A. T. C. Fernandes, and Ó. Carvalho, "A Frequency-Dependent and Nonlinear, Time-Explicit Five-Layer Human Head Numerical Model for Realistic Estimation of Focused Acoustic Transmission Through the Human Skull for Noninvasive High-Intensity and High-Frequency Transcranial Ultrasound Stimulation: An Application to Neurological and Psychiatric Disorders", Bioengineering **12**, 1161 (2025) 10.3390/bioengineering12111161.

[48]F. Acquaticci, S. E. Lew, and S. N. Gwirc, "Ultrasound Axicon: Systematic Approach to Optimize Focusing Resolution through Human Skull Bone", Materials **12**, 3433 (2019) 10.3390/ma12203433.

[49]F. J. Fry and J. E. Barger, "Acoustical properties of the human skull", J. Acoust. Soc. Am. **63**, 1576–1590 (1978) 10.1121/1.381852.

[50]P. J. White, G. T. Clement, and K. Hynynen, "Local frequency dependence in transcranial ultrasound transmission", Phys. Med. Biol. **51**, 2293–2305 (2006) 10.1088/0031-9155/51/9/013.

[51]M. S. Kilinc, C. Arvanitis, and F. L. Degertekin, "A figure of merit for transcranial ultrasound transmission based on coupled elastic-thermal analysis", Phys. Med. Biol. **70**, 235013 (2025) 10.1088/1361-6560/ae1ee3.

[52]Z. Lotfollahi, "The anatomy, physiology and function of all skin layers and the impact of ageing on the skin", Wound Pract. Res. **32** (2024) 10.33235/wpr.32.1.6-10.

[53]A. Ní Annaidh, K. Bruyère, M. Destrade, M. D. Gilchrist, and M. Otténio, "Characterization of the anisotropic mechanical properties of excised human skin", J. Mech. Behav. Biomed. Mater. **5**, 139–148 (2012) 10.1016/j.jmbbm.2011.08.016.

[54]M. Pawlaczyk, M. Lelonkiewicz, and M. Wieczorowski, "Age-dependent biomechanical properties of the skin", Adv. Dermatol. Allergol. **5**, 302–306 (2013) 10.5114/pdia.2013.38359.

[55]S. V. Fernandez, J.-H. Kim, D. Sadat, C. Marcus, E. Suh, R. McIntosh, A. Shah, and C. Dagdeviren, "A Dynamic Ultrasound Phantom with Tissue-Mimicking Mechanical and Acoustic Properties", Adv. Sci. **11**, 2400271 (2024) 10.1002/advs.202400271.

[56]A. I. Chen, M. L. Balter, M. I. Chen, D. Gross, S. K. Alam, T. J. Maguire, and M. L. Yarmush, "Multilayered tissue mimicking skin and vessel phantoms with tunable mechanical, optical, and acoustic properties", Med. Phys. **43**, 3117–3131 (2016) 10.1118/1.4951729.

[57]M. Mencarelli, L. Puggelli, A. Virga, R. Furferi, and Y. Volpe, "Characterization of soft tissue-mimicking materials for ultrasound training phantoms", J. Mater. Sci. Mater. Med. **37**, 44 (2026) 10.1007/s10856-026-07020-7.

[58]M. Asgari, J. Abi-Rafeh, G. N. Hendy, and D. Pasini, "Material anisotropy and elasticity of cortical and trabecular bone in the adult mouse femur via AFM indentation", J. Mech. Behav. Biomed. Mater. **93**, 81–92 (2019) 10.1016/j.jmbbm.2019.01.024.

[59]M. Georgiadis, R. Müller, and P. Schneider, "Techniques to assess bone ultrastructure organization: orientation and arrangement of mineralized collagen fibrils", J. R. Soc. Interface **13**, 20160088 (2016) 10.1098/rsif.2016.0088.

[60]M. Bittner-Frank, A. G. Reisinger, O. G. Andriotis, D. H. Pahr, and P. J. Thurner, "Cortical and trabecular mechanical properties in the femoral neck vary differently with changes in bone mineral density", JBMR Plus **8**, ziae049 (2024) 10.1093/jbmrpl/ziae049.

[61]L. E. Kinsler, ed., *Fundamentals of acoustics*, 4th ed (Wiley, New York, 2000), 548 pp.

[62]J. H. Rindel, "An Impedance Model for Angle-Dependent Sound Reflection and Absorption with Diffraction Effects", Acoustics **7**, 53 (2025) 10.3390/acoustics7030053.

[63]A. Elouneg, J. Chambert, A. Lejeune, Q. Lucot, E. Jacquet, and S. Bordas, "Anisotropic mechanical characterization of human skin by in vivo multi-axial ring suction test", J. Mech. Behav. Biomed. Mater. **141**, 105779 (2023) 10.1016/j.jmbbm.2023.105779.

[64]IRCU, *ICRU Report 61, Tissues Substitutes, Phantoms and Computation Modelling in Medical Ultrasound*, 61 (IRCU, USA).

[65]G. Sellani, D. Fernandes, A. Nahari, M. F. De Oliveira, C. Valois, W. C. A. Pereira, and C. B. Machado, "Assessing heating distribution by therapeutic ultrasound on bone phantoms and in vitro human samples using infrared thermography", J. Ther. Ultrasound **4**, 13 (2016) 10.1186/s40349-016-0058-7.

[66]C. Moran, N. Bush, and J. Bamber, "Ultrasonic propagation properties of excised human skin", Ultrasound Med. Biol. **21**, 1177–1190 (1995) 10.1016/0301-5629(95)00049-6.

[67]H. Nguyen Minh, M. Muller, and K. Raum, "Estimation of Thickness and Speed of Sound for Transverse Cortical Bone Imaging Using Phase Aberration Correction Methods: An In Silico and Ex Vivo Validation Study", Appl. Sci. **12**, 5283 (2022) 10.3390/app12105283.

[68]R. McCarthy, L. Jeffcott, and R. McCartney, "Ultrasound speed in equine cortical bone: Effects of orientation, density, porosity and temperature", J. Biomech. **23**, 1139–1143 (1990) 10.1016/0021-9290(90)90006-O.

[69]S. Bensamoun, J.-M. Gherbezza, J.-F. De Belleval, and M.-C. Ho Ba Tho, "Transmission scanning acoustic imaging of human cortical bone and relation with the microstructure", Clin. Biomech. **19**, 639–647 (2004) 10.1016/j.clinbiomech.2004.02.009.

[70]N. Rubert and T. Varghese, "The effect of low scatterer number density on ultrasound attenuation estimation", in 2014 IEEE Int. Ultrason. Symp. (Sept. 2014), pp. 2418–2421, 10.1109/ULTSYM.2014.0603.

[71]T. P. O'Neill, A. J. Winkler, and J. Wu, "Ultrasound heating in a tissue-bone phantom", Ultrasound Med. Biol. **20**, 579–588 (1994) 10.1016/0301-5629(94)90094-9.

[72]M. Aoyagi and T. Hiraguri, "Ultrasound Phantom Using Sodium Alginate as a Gelling Agent", J. Ultrasound Med. **36**, 2345–2353 (2017) 10.1002/jum.14252.

[73]J. R. Cook, R. R. Bouchard, and S. Y. Emelianov, "Tissue-mimicking phantoms for photoacoustic and ultrasonic imaging", Biomed. Opt. Express **2**, 3193 (2011) 10.1364/BOE.2.003193.

[74]D. Phani, R. K. V., A. Thomas, R. Paramu, M. S. Singh, S. V. S., V. Muraleedharan, and R. K. Nair, *Acoustic and Ultrasonographic Characterization of Neoprene, Beeswax, and Carbomer-Gel to Mimic Soft-tissue for Ultrasound*, version 1, (2020) 10.48550/ARXIV.2004.05355, https://arxiv.org/abs/2004.05355 (visited on 03/24/2026), pre-published.

[75]J. D. Krech, T. Wyatt, and D. J. Harmon, "Systematic Review of 3D -Printed Ultrasound-able Models in Graduate Medical Education", J. Ultrasound Med. **44**, 595–603 (2025) 10.1002/jum.16624.

[76]B. Altun, I. Demirkan, E. O. Isik, O. Kocaturk, M. B. Unlu, and B. Garipcan, "Acoustic impedance measurement of tissue mimicking materials by using scanning acoustic microscopy", Ultrasonics **110**, 106274 (2021) 10.1016/j.ultras.2020.106274.

[77]G. Menikou and C. Damianou, "Acoustic and thermal characterization of agar based phantoms used for evaluating focused ultrasound exposures", J. Ther. Ultrasound **5**, 14 (2017) 10.1186/s40349-017-0093-z.

[78]G. Menikou, M. Yiannakou, C. Yiallouras, C. Ioannides, and C. Damianou, "MRI-compatible bone phantom for evaluating ultrasonic thermal exposures", Ultrasonics **71**, 12–19 (2016) 10.1016/j.ultras.2016.05.020.

[79]M. Yoshizawa, H. Ushioda, and T. Moriya, "Development of a bone-mimicking phantom and measurement of its acoustic impedance by the interference method", in IEEE Ultrason. Symp. 2004, Vol. 3 (2004), pp. 1769–1772, 10.1109/ULTSYM.2004.1418169.

[80]A. Mejdi, N. Atalla, and S. Ghinet, "Wave spectral finite element model for the prediction of sound transmission loss and damping of sandwich panels", Comput. Struct. **158**, 251–258 (2015) 10.1016/j.compstruc.2015.06.014.

[81]V. N. Khmelev, A. V. Shalunov, and V. A. Nesterov, "Summation of high-frequency Langevin transducers vibrations for increasing of ultrasonic radiator power", Ultrasonics **114**, 106413 (2021) 10.1016/j.ultras.2021.106413.

[82]J. A. Pearce, "Models for Thermal Damage in Tissues: Processes and Applications", Crit. Rev. Biomed. Eng. **38**, 1–20 (2010) 10.1615/CritRevBiomedEng.v38.i1.20.

# Chapter 7

# Personalized Patient-Specific Image-Guided Acoustic Therapy Device Planning Workflow

## 7.1 Rationale for Personalized Ultrasound Stimulation

Personalized medicine is increasingly relevant in knee OA because the joint cannot be treated as a geometrically or materially uniform system. Knee morphology, cartilage thickness, subchondral bone architecture, meniscal condition, synovial inflammation, soft-tissue composition, and limb alignment vary substantially between patients, and these differences influence both disease progression and therapeutic response. Recent imaging literature emphasizes that MRI and quantitative MRI can capture patient-specific alterations in cartilage structure, biochemical composition, and joint morphology, supporting a more individualized interpretation of osteoarthritic degeneration rather than relying only on population-averaged descriptors[1,2]. This variability is particularly important for ultrasound-based stimulation, since acoustic propagation depends on tissue geometry and material properties, including density, sound speed, attenuation, stiffness, and acoustic impedance. Therefore, two patients receiving the same external ultrasound parameters may experience different pressure fields, energy deposition patterns, and mechanical stimuli at the cartilage surface or within the chondral tissue. Recent developments in ultrasound imaging and shear-wave elastography further support this rationale, as these methods allow non-invasive assessment of musculoskeletal tissue structure and spatially varying mechanical properties, which can potentially be incorporated into patient-specific computational models[3,4]. As such, the rationale for personalized ultrasound stimulation is not only clinical, but also physical: stimulation parameters should be adapted to the anatomical pathway and acoustic properties of each knee to improve targeting, reduce uncertainty, and define exposure conditions that are mechanically effective while remaining within safe therapeutic limits.

Patient-specific stimulation parameters are required because the biological and mechanical effects of ultrasound are not determined solely by the nominal settings applied at the transducer, but by the acoustic field that ultimately reaches the target tissues. In knee osteoarthritis, this distinction is particularly important because disease expression is heterogeneous, with patients presenting different structural, inflammatory, metabolic, pain-related, and mechanical phenotypes, supporting the broader need for stratified therapeutic approaches rather than uniform intervention protocols[5]. For ultrasound stimulation, parameters such as frequency, acoustic pressure, pulse duration, duty cycle, exposure time, beam geometry, and transducer position interact with patient-specific anatomical pathways and tissue properties, including cartilage thickness, soft-tissue composition, attenuation, impedance mismatch, and local stiffness. Automated MRI-based cartilage assessment studies further show that cartilage thickness varies regionally across the knee, reinforcing the need to define stimulation according to local joint morphology rather than assuming a simplified homogeneous target[6]. This is relevant because

low-intensity pulsed ultrasound acts through mechanical stimulation, converting acoustic energy into cellular responses that may influence chondrocyte activity, extracellular matrix regulation, inflammation, and cartilage degeneration pathways[6,7]. Consequently, identical external ultrasound settings may produce different intra-articular pressure distributions, mechanical strains, and energy deposition patterns between patients. A patient-specific strategy is therefore necessary to improve dose consistency at the tissue level, avoid under-stimulation or excessive exposure, and support the rational selection of stimulation conditions that are both biologically meaningful and compatible with therapeutic safety constraints.

Generic transducer placement strategies are limited because they implicitly assume that the same anatomical landmark, orientation, and coupling interface will produce comparable acoustic exposure across different knees. This assumption is difficult to justify in osteoarthritic joints, where cartilage degeneration, osteophyte formation, synovitis, meniscal extrusion, joint-space narrowing, and soft-tissue changes may alter both the acoustic propagation pathway and the accessibility of the intended target region. Recent reviews on knee osteoarthritis imaging emphasize that ultrasound can identify several of these local pathological features and may guide diagnostic or minimally invasive procedures in real time, which indirectly supports the need for image-informed positioning rather than fixed empirical placement[3]. In therapeutic ultrasound, the delivered biological stimulus depends not only on the transducer output but also on the spatial distribution of pressure, intensity, reflection, scattering, attenuation, and focal shift within tissue; therefore, small deviations in placement or incidence angle can modify the effective dose delivered to cartilage or periarticular structures. The 2024 update on therapeutic ultrasound safety further notes that tissue structures can scatter the incident therapeutic pulse and provide information on shifts in focal location due to aberration, reinforcing the importance of accounting for patient-specific propagation effects[8]. This limitation is particularly relevant for low-intensity pulsed ultrasound, for which ongoing research continues to address the definition of optimal dosage, frequency, timing, and treatment strategy in osteoarthritis applications[7]. Consequently, generic placement based only on external landmarks may lead to inconsistent stimulation, suboptimal targeting, and inter-patient variability in therapeutic response. A more robust strategy should integrate anatomical imaging, tissue-property assessment, acoustic simulation, and phantom-based validation to determine the transducer location and orientation that maximize energy delivery to the intended biological target while minimizing unintended exposure of surrounding tissues.

This chapter presents a unified strategy for patient-specific ultrasound stimulation, integrating anatomical imaging, tissue-property assessment, numerical modelling, phantom-based validation, and

device design into a coherent development workflow. Rather than proposing a definitive clinical solution, the chapter aims to establish a methodological framework through which transducer placement, stimulation parameters, and fixation geometry can be adapted to the characteristics of each knee. In this context, personalization is considered not only as a clinical objective, but also as an engineering requirement for improving acoustic targeting, reducing inter-patient variability, and supporting more reproducible therapeutic exposure. This approach therefore provides the rationale for developing ultrasound-based stimulation systems that are informed by patient anatomy, material heterogeneity, and experimentally validated acoustic behaviour.

## 7.2 Overview of the Proposed Personalized Development Workflow

The proposed workflow establishes a patient-specific strategy for the development of an ultrasound-based knee stimulation device, integrating clinical imaging, computational modelling, experimental validation, and customized orthosis design into a unified development framework. Rather than relying on generic anatomical assumptions or standardized transducer configurations, the methodology uses patient-derived information to define both the therapeutic stimulation parameters and the physical configuration of the final device. The central rationale is that anatomical morphology, tissue composition, and mechanical properties vary considerably between individuals and may influence acoustic wave propagation, energy deposition, and transducer coupling efficiency. Therefore, personalization is treated not only as a clinical objective, but also as a design constraint throughout the development process.

Figure 154 summarizes the proposed personalized development pipeline.

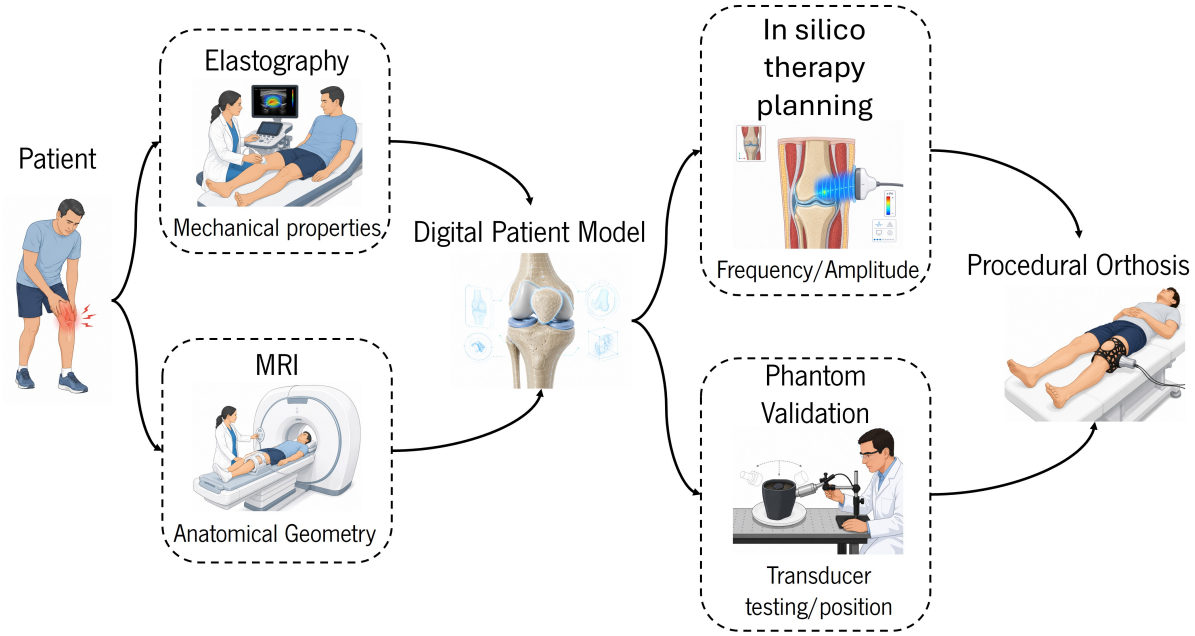



Figure 154: Overview of the proposed personalized development workflow for ultrasound-based knee stimulation. Patient-specific mechanical properties are obtained through elastography, while anatomical geometry is acquired using magnetic resonance imaging. These data are combined into a digital patient model, which supports in silico therapy planning for frequency and amplitude selection, as well as phantom-based validation of transducer positioning. The resulting information is then used to develop a procedural orthosis capable of maintaining the transducer in the prescribed position during therapy.

The workflow begins with the patient, whose knee condition motivates the acquisition of complementary clinical data. Elastography is used to estimate the mechanical properties of the relevant soft tissues, providing patient-specific information related to tissue stiffness and mechanical heterogeneity. In parallel, magnetic resonance imaging is employed to obtain the anatomical geometry

of the knee, including the spatial arrangement of bones, cartilage, and surrounding soft tissues. These two sources of information are then combined to generate a digital patient model, which serves as the computational and geometrical foundation for subsequent stages of device development.

The digital patient knee model has a dual function within the proposed methodology. First, it supports in silico therapy planning, where numerical simulations are used to evaluate ultrasound propagation through the patient-specific knee geometry. By incorporating individualized tissue properties obtained from elastography, the model enables the estimation of appropriate stimulation parameters, particularly frequency and amplitude. This step is intended to identify excitation conditions that maximize the therapeutic relevance of the acoustic field at the target region while minimizing unnecessary exposure of surrounding tissues. In this context, simulation functions as a predictive tool for treatment planning, allowing the parameter space to be explored before physical implementation.

Second, the same anatomical and mechanical information is used to guide the development of experimental phantoms for transducer testing and validation. These phantoms reproduce relevant features of the patient-specific knee geometry and tissue properties, providing a controlled platform for evaluating transducer placement, acoustic coupling, and field distribution. The phantom validation stage is therefore positioned as an intermediate link between numerical prediction and device realization. It allows the simulated acoustic field to be assessed experimentally and provides practical information regarding transducer orientation, contact conditions, and positioning constraints that may not be fully captured in computational models.

The final stage of the workflow consists of developing a procedural orthosis designed to hold the selected transducer configuration in the prescribed position. The orthosis is generated from the patient-specific anatomical data and is intended to provide stable contact between the transducer and the knee surface during stimulation. In this framework, the orthosis is not treated as a passive support element, but as an integral component of the therapeutic system. Its geometry must satisfy ergonomic, anatomical, and acoustic requirements, ensuring that the transducer remains aligned with the validated placement while maintaining appropriate skin contact and user comfort.

This strategy provides a structured route for translating individualized anatomical and mechanical data into practical design decisions, including stimulation parameters, transducer placement, and orthosis geometry. Although the approach does not eliminate the need for experimental verification, it reduces the dependence on empirical trial-and-error procedures and provides a more rational basis for the development of personalized ultrasound stimulation systems for knee joint applications.

### 7.2.1 Integration of Magnetical Resonance Imaging and Elastography

The proposed workflow is based on the integration of anatomical imaging, tissue-property assessment, numerical simulation, and experimental validation into a single patient-informed development strategy. MRI provides the geometrical basis for reconstructing the knee anatomy, including the relative position of bones, cartilage, and surrounding soft tissues. In parallel, elastography contributes complementary mechanical information by estimating spatial variations in tissue stiffness. The combination of these modalities enables the construction of a digital patient model in which geometry and material behaviour are not treated as independent assumptions, but as coupled descriptors of the same biological system. This approach is particularly relevant for ultrasound-based stimulation, since acoustic propagation is governed by both anatomical morphology and tissue-dependent material properties, including density, sound speed, attenuation, and impedance.

This integration is directly related to the biological tissue characterization work presented in chapter 4. The experimental characterization of biological tissues provides reference values for the expected range of acoustic and mechanical properties required for model definition. These data serve two complementary purposes. First, they support the assignment of realistic material parameters to the digital patient model, reducing the dependence on generic literature values. Second, they provide admissible intervals against which patient-specific elastography-derived estimates can be interpreted. In this sense, chapter 4 establishes a material-property foundation for the present workflow, while elastography introduces an individualized correction layer that accounts for inter-patient variability. The resulting model therefore combines experimentally informed baseline properties with patient-specific mechanical information.

The proposed workflow is also compatible with a non-invasive and patient-tolerable mode of assessment and treatment. MRI and ultrasound elastography allow anatomical and mechanical information to be acquired without surgical access to the joint, while therapeutic ultrasound can deliver mechanical stimulation through the skin using external transducer coupling. This reduces the need for invasive instrumentation and supports repeated evaluations during device development, treatment planning, or follow-up. The use of a patient-specific orthosis further contributes to comfort by adapting the transducer support to the external knee morphology, improving contact stability while limiting excessive compression, misalignment, or operator-dependent positioning. In this context, personalization has a practical ergonomic role: the device is designed around the patient rather than forcing the patient to adapt to a generic fixture. Recent literature on wearable and conformable ultrasound systems similarly emphasizes the potential of externally applied ultrasound devices to improve treatment accessibility,

patient compliance, and comfort during prolonged or repeated therapeutic use[7].

### 7.2.2 Computational Branch: In Silico Therapy Planning

The computational branch of the proposed workflow is intended to support patient-specific therapy planning by predicting the acoustic field generated within the knee before the physical implementation of the stimulation device. In this stage, the MRI-derived anatomical model is combined with tissue-specific acoustic and mechanical properties to simulate ultrasound propagation across the external soft tissues, joint structures, and target cartilage region. This approach allows the influence of excitation frequency, input amplitude, transducer diameter, and coupling conditions to be evaluated in a controlled numerical environment. The objective is not to define a universal stimulation protocol, but to identify a restricted set of candidate parameters that are compatible with the anatomical and material characteristics of a given patient.

This computational stage is directly related to the validation framework presented in chapter 5. The numerical studies developed in that chapter provide the methodological basis for assessing how ultrasound propagates through simplified, reduced-order, and patient-informed knee models. In particular, chapter 5 establishes the computational procedures used to evaluate acoustic transmission, frequency-dependent behaviour, pressure distribution, and the influence of anatomical variability on the delivered stimulus. These results serve to inform the expected numerical response of the personalized workflow and provide a reference against which subsequent patient-specific simulations can be interpreted. In this sense, chapter 5 functions as a computational validation stage, demonstrating the feasibility and limitations of the modelling strategy before its integration into a broader personalized device-development pipeline.

The numerical model enables the estimation of the acoustic pressure distribution, transmission efficiency, and frequency-dependent response at the target region. By analysing these outputs, it becomes possible to determine whether a given excitation condition is likely to produce a mechanically relevant stimulus at the cartilage while avoiding unnecessary exposure of superficial tissues. Similar computational principles have been applied in therapeutic ultrasound planning, where patient-specific anatomical data and heterogeneous acoustic properties are used to predict wave propagation, improve targeting, and support safer treatment design[9–12].

The computational branch also provides a rational basis for selecting the stimulation frequency and amplitude. Frequency selection is particularly relevant because biological tissues exhibit frequency-dependent attenuation, while the anatomical arrangement of the knee may promote

constructive or destructive interference depending on wavelength, interface geometry, and boundary conditions. Amplitude selection must also account for propagation losses between the transducer and the cartilage, since the externally imposed pressure is not equivalent to the local mechanical stimulus experienced by the target tissue. Consequently, the model acts as a transfer function between external actuation and the internal acoustic response. This formulation allows treatment parameters to be defined according to the predicted field at the target region rather than by the nominal output of the transducer alone.

Although the in silico stage provides a useful predictive tool, it should be interpreted as a planning and optimization step rather than as a definitive validation method. Numerical predictions remain dependent on segmentation quality, material-property assignment, boundary conditions, attenuation models, mesh resolution, and assumptions regarding tissue coupling. For this reason, the computational branch is linked to the phantom validation branch of the proposed workflow. Candidate configurations identified through simulation are subsequently assessed experimentally using anatomical or tissue-mimicking phantoms, enabling verification of the acoustic field, transducer positioning, and coupling strategy under controlled laboratory conditions. This connection between simulation and phantom testing provides a more robust development pathway, where numerical predictions guide experimental design and physical measurements are used to refine or confirm the computational assumptions.

### 7.2.3 Experimental Branch: Phantom-Based Transducer Validation

The experimental branch of the proposed workflow is designed to validate the transducer configuration under controlled laboratory conditions before its integration into the final patient-specific orthosis. While the computational branch estimates the acoustic field through numerical modelling, phantom-based validation provides a physical platform for assessing whether the selected transducer position, orientation, coupling strategy, and excitation conditions can be reproduced experimentally. This stage is particularly important because externally applied ultrasound is affected not only by tissue properties and anatomical geometry, but also by practical factors such as surface curvature, contact pressure, coupling medium thickness, transducer alignment, and fixture stability. These factors may introduce deviations between the simulated and experimentally delivered acoustic fields, making phantom testing a necessary intermediate step between in silico therapy planning and device implementation.

This experimental branch is directly related to the work presented in chapter 6, where the development

and validation of medical phantoms are addressed as a methodological foundation for ultrasound-based device assessment. The phantom validation strategy described in that chapter provides the basis for reproducing relevant anatomical and acoustic features of the knee in a controlled environment. In the context of the present workflow, chapter 6 therefore functions as the experimental validation stage that complements the computational framework developed in chapter 5. The computational model identifies candidate stimulation conditions and transducer placements, whereas the phantom model allows these configurations to be tested physically, measured experimentally, and refined before translation to the patient-specific orthosis.

The use of medical phantoms is particularly relevant for ultrasound applications because they allow acoustic propagation, transducer performance, and field distribution to be evaluated without exposing patients to repeated experimental adjustments. Tissue-mimicking materials can be formulated to approximate relevant acoustic properties, including speed of sound, attenuation coefficient, density, acoustic impedance, and scattering behaviour. These parameters determine how ultrasound waves are transmitted, reflected, and attenuated within the phantom, and therefore influence the validity of the experimental measurements. Previous studies have emphasized that ultrasound phantoms are important tools for equipment quality assurance, imaging-system evaluation, and the characterization of tissue-equivalent media[13–15].

In the proposed workflow, the phantom is not intended to represent a generic homogeneous block of material. Instead, it should reproduce the key features required to evaluate transducer placement and acoustic delivery in a knee-like configuration. This may include external morphology, relevant tissue layers, cartilage position, bone boundaries, and material regions with distinct acoustic behaviour. Anatomically informed or patient-specific phantoms are advantageous in this context because they allow the experimental setup to preserve geometrical constraints that affect wave transmission and transducer access. Additive manufacturing has expanded the feasibility of such models by enabling complex anatomical geometries to be reproduced from medical imaging data and combined with tissue-mimicking materials[16,17].

The main objective of the phantom validation stage is to determine whether the acoustic field predicted during therapy planning can be achieved experimentally with a physically realizable transducer configuration. Measurements may include transmitted pressure, frequency response, attenuation, spatial field distribution, and repeatability under different placement conditions. When appropriate, calibrated hydrophones or equivalent acoustic measurement systems can be used to quantify the pressure field and assess the relationship between the driving signal and the delivered acoustic stimulus.

Standardized hydrophone-based methods are commonly used for acoustic field characterization in medical ultrasound and provide an important reference for reproducible measurement procedures[18].

Phantom-based validation also provides design information that cannot be fully obtained from simulation alone. For example, it can reveal whether the selected transducer can maintain stable contact with the curved knee surface, whether the acoustic coupling layer introduces significant transmission losses, and whether small changes in placement produce large variations in the measured field. These observations are essential for defining the mechanical requirements of the orthosis, including transducer support, alignment control, fixation stability, and allowable contact pressure. The experimental branch therefore transforms the phantom from a passive validation object into an active design tool that informs the final device architecture.

### 7.2.4 Convergence Toward Personalized Device Generation

The final stage of the proposed workflow consists of converging the computational and experimental branches toward the generation of a personalized ultrasound stimulation device. At this stage, the information obtained from imaging, elastography, numerical simulation, and phantom validation is translated into a physical design capable of reproducing the selected therapeutic configuration on the patient. The device is therefore not conceived as a generic support for an ultrasound transducer, but as a patient-specific system in which geometry, transducer placement, coupling conditions, and stimulation parameters are defined through a structured development process.

The convergence between the computational and experimental branches is essential because each branch provides distinct but complementary information. The computational branch identifies candidate stimulation parameters and predicts the internal acoustic response within the knee. This includes the estimated pressure distribution, frequency-dependent transmission, and sensitivity of the target region to changes in transducer position and excitation amplitude. The experimental branch, developed through phantom-based validation, verifies whether these configurations can be physically reproduced under controlled conditions. In this way, the simulation stage defines the desired acoustic objective, while the phantom stage evaluates the practical feasibility of achieving that objective with a real transducer, coupling medium, and fixation strategy.

The personalized device generation process uses these outputs to define the design constraints of the orthosis. The MRI-derived anatomical model provides the external knee geometry required to adapt the support structure to the patient, while the validated transducer position determines the location, orientation, and contact interface of the acoustic element. The orthosis must preserve the spatial

configuration established during simulation and phantom testing, ensuring that the transducer remains aligned with the intended acoustic pathway during use. This requirement is particularly relevant for ultrasound-based stimulation, since small variations in positioning, inclination, or coupling thickness may alter the transmitted field and reduce the reproducibility of the treatment.

In this context, procedural or computationally assisted design methods provide a suitable route for transforming patient-specific data into manufacturable device geometries. Digital workflows based on anatomical scanning, computer-aided design, and additive manufacturing have been increasingly explored for customized orthoses and patient-specific medical devices[19–21]. These approaches are relevant to the present methodology because they allow device geometry to be generated from individual anatomical data rather than from standardized sizes. Consequently, the orthosis can be designed to improve fit, contact stability, and repeatability while also satisfying the mechanical requirements associated with transducer support.

The integration of the ultrasound transducer into the orthosis introduces additional functional constraints beyond conventional orthotic design. The device must maintain adequate acoustic coupling with the skin, limit undesired movement during stimulation, avoid excessive local compression, and allow reproducible placement across repeated sessions. These requirements are consistent with current developments in wearable ultrasound technologies, where stable body coupling, conformability, user comfort, and long-duration operation are recognized as important challenges for clinical translation[22,23]. For this reason, the personalized orthosis should be understood as both a mechanical fixture and an acoustic delivery platform.

The proposed convergence stage also provides a mechanism for reducing empirical trial-and-error during device development. Instead of manually adjusting the transducer position on the patient, the validated configuration is encoded into the orthosis geometry. This allows the therapeutic setup identified through simulation and confirmed through phantom measurements to be reproduced more consistently during use. Such an approach is especially relevant for personalized therapies, where the effectiveness of the intervention may depend on maintaining a specific relationship between the transducer, the tissue interfaces, and the target cartilage region.

## 7.3 Procedural Generation of the Personalized Orthosis

The personalized orthosis was developed through a procedural modelling workflow implemented in Blender, an open-source three-dimensional creation environment suitable for mesh modelling, scripting, surface editing, and parametric geometry generation. The objective of this workflow was not only to obtain an anatomically conformal support, but also to ensure that the therapeutic transducer remained positioned according to the placement previously identified during phantom-based validation. This approach is consistent with recent developments in patient-specific orthotic design, where digital modelling, additive manufacturing, and anatomical data are increasingly used to produce customized devices with improved comfort, reproducibility, and functional integration[24,25].

The generation process begins with the transducer pose obtained from the experimental phantom study. In this stage, the phantom provides the spatial location and orientation required to couple the Langevin transducer to the target anatomical region, as illustrated in figure 155.

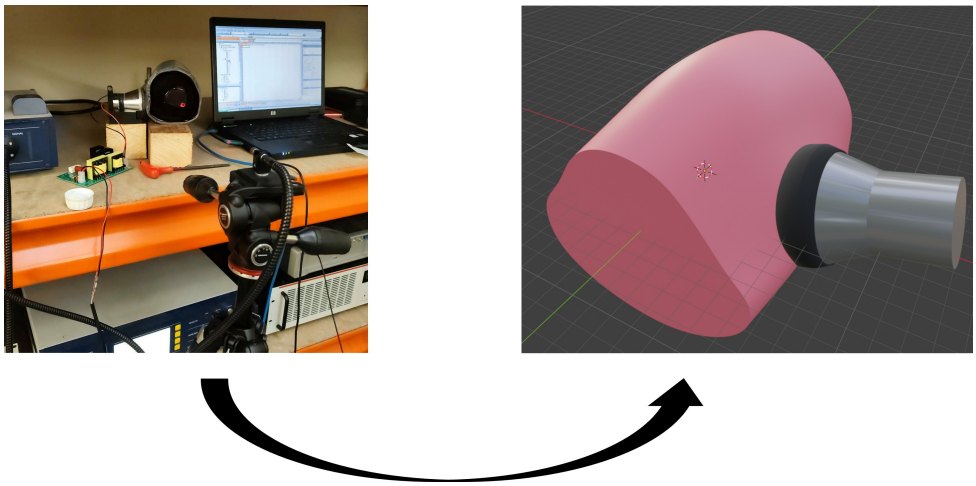


Figure 155: Phantom-informed placement of the therapeutic transducer, transferring the experimentally validated position to the digital anatomical model.

The position of the transducer can be described by a rigid transformation matrix as shown in equation 263,

$$\mathbf{T} = \begin{bmatrix} \mathbf{R}_{tr} & \mathbf{p}_{tr} \\ 0 & 1 \end{bmatrix} \tag{263}$$

where $\mathbf{R}_{tr}$ defines the orientation of the transducer axis and $\mathbf{p}_{tr}$ corresponds to its centre position relative to the patient-specific knee geometry. This transformation is transferred to the digital model so that the device is generated around a fixed therapeutic reference, rather than being designed as a generic external brace. In practical terms, the transducer is first placed against the reconstructed skin surface, and the subsequent orthosis geometry is constrained to preserve this pose during fabrication and use.

After defining the transducer location, boundary curves are introduced on the patient-specific surface to delimit the region occupied by the orthosis, as shown in figure 156.

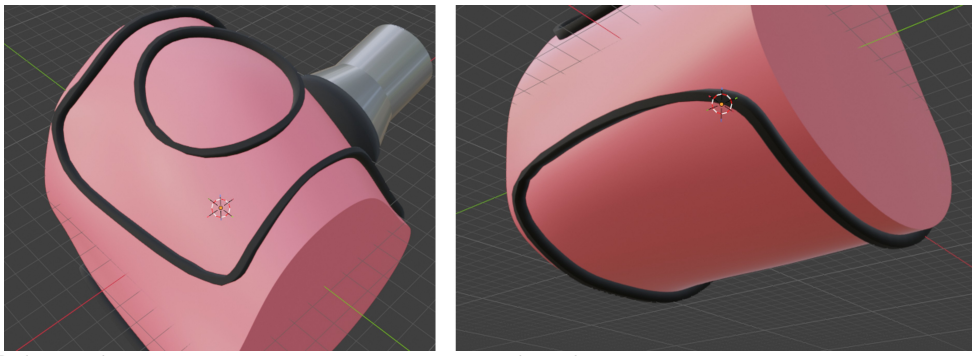


Figure 156: Definition of orthosis boundary curves on the patient-specific surface to delimit the support region and preserve transducer alignment.

These curves act as anatomical and functional constraints, preventing the device from extending into unsuitable regions while maintaining sufficient contact area for mechanical stability. If the patient skin is represented by a triangulated surface S$\mathbf{S}_p$ the orthosis domain may be defined as a bounded surface region as shown in equation 264,

$$\Omega_s = \{\mathbf{x} \in \mathbf{S}_p : g_1(\mathbf{x}) \geq 0 \wedge g_2(\mathbf{x}) \geq 0, ..., g_n(\mathbf{x}) \geq 0 \} \tag{264}$$

where $g_i(\mathbf{x})$ are implicit boundary functions associated with the manually or procedurally defined limiting curves. The final supporting shell is then obtained by offsetting the patient surface along the local outward normal direction as shown in equation 265,

$$S_0 = \{\mathbf{x}_0 = \mathbf{x} + t\mathbf{n}(\mathbf{x}) : \mathbf{x} \in \Omega_s\} \tag{265}$$

where $t$ is the prescribed orthosis thickness and $\mathbf{n}(\mathbf{x})$ is the unit normal vector of the anatomical surface. This formulation allows the device to remain conformal to the patient geometry while preserving a controlled clearance or contact condition depending on the selected offset value.

A procedural perforation pattern is subsequently generated using Voronoi noise projected onto the orthosis domain, as represented in figure 157.

Voronoi-based structures are commonly used in computational design because they allow the generation of stochastic cellular patterns that can reduce mass, improve ventilation, and create locally tunable stiffness distributions. Similar lattice and cellular design strategies have been reported in additively manufactured orthoses and thin-shell structures, where complex geometries are used to balance structural performance, material efficiency, and user comfort[26].

Mathematically, a Voronoi partition is generated from a set of seed points (equation 266),

$$P = \{\mathbf{s}_1, \mathbf{s}_2, ..., \mathbf{s}_m\} \tag{266}$$

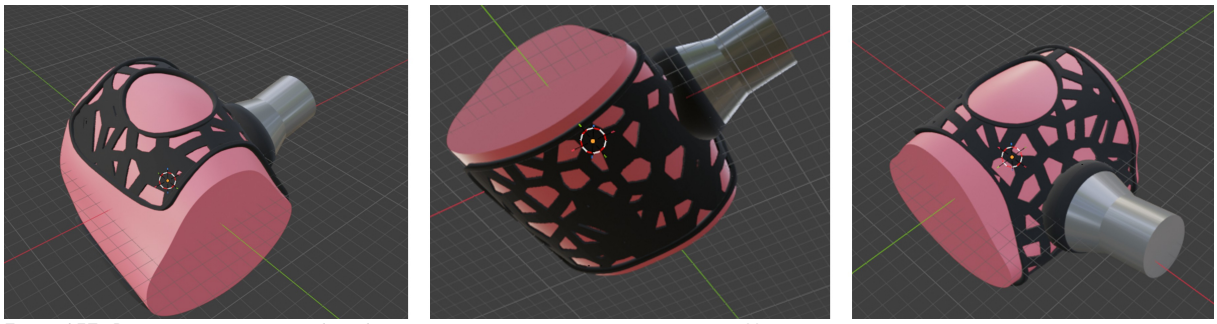


Figure 157: Procedural generation of the final personalized orthosis using a projected Voronoi pattern to obtain a lightweight, ventilated, and conformal structure.

distributed over the parameterized orthosis surface. Each Voronoi cell is defined as the region containing all points closer to one seed than to any other seed as shown in equation 267,

$$V_i = \{\mathbf{u} \in \Omega : ||\mathbf{u} - \mathbf{s}_i|| \leq ||\mathbf{u} - \mathbf{s}_j||, \forall j \neq i\} \tag{267}$$

where $\mathbf{u}$ denotes a point in the two-dimensional parametric domain associated with the surface. The generated cellular pattern is then projected back onto the three-dimensional orthosis geometry using a surface mapping function (equation 268),

$$\mathbf{x} = \phi(\mathbf{u}), \mathbf{u} \in \Omega \tag{268}$$

with $\phi$ mapping the planar procedural pattern onto $\mathbf{S}_0$. The solid regions of the orthosis correspond to the retained Voronoi edges, while the cell interiors are removed through Boolean operations. The resulting geometry forms a lightweight, ventilated, and patient-conformal support capable of maintaining the transducer in the prescribed therapeutic position.

From a design perspective, this workflow establishes a direct connection between experimental validation, anatomical personalization, and procedural device generation. The phantom study defines the functional transducer placement; the patient-specific surface provides the anatomical design space; the boundary curves impose clinical and ergonomic limits; and the Voronoi projection generates a lightweight structural pattern compatible with additive manufacturing. Consequently, the orthosis is not treated as a passive holder, but as a personalized interface that preserves the experimentally validated acoustic configuration while adapting to the patient's external morphology.

A preliminary cost estimate was performed to assess the approximate manufacturing expenditure associated with the proposed personalized orthosis. This estimate considers the main components required for the prototype, including the additively manufactured PLA structure, the therapeutic transducer and electronic driving board, and the adhesive acrylic material used for local attenuation and coupling-control strategies. The analysis does not include labour, equipment depreciation, electricity

consumption, failed prints, assembly time, software development, sterilization, packaging, quality control, regulatory certification, or clinical validation costs. Therefore, the values presented should be interpreted as a preliminary lower-bound estimate for prototype fabrication.

The generated orthosis was estimated to require approximately $90$ g of PLA filament. Considering a representative commercial PLA cost of approximately $16$–$18$ EUR/kg, the direct material cost of the printed shell may be estimated according to equation 269:

$$C_{PLA} = m_{PLA} \cdot c_{PLA} \tag{269}$$

where $C_{PLA}$ is the material cost, $m_{PLA}$ is the PLA mass in kilograms, and $c_{PLA}$ is the unit cost of the filament. For $m_{PLA} = 0.09$ kg, this results in:

$$C_{PLA} = 0.09 \times (16\text{–}18) = 1.44\text{–}1.62 \text{ EUR}. \tag{270}$$

To account for support structures, trimming, purge material, and process-related waste, a conservative material overuse factor of 10–20% may be considered. Under this assumption, the effective PLA consumption increases to approximately $99$–$108$ g, corresponding to an adjusted PLA cost of approximately $1.58$–$1.94$ EUR.

In addition to the printed structure, the active stimulation subsystem was estimated to include the therapeutic transducer and the corresponding electronic board, with an approximate combined cost of $50$ EUR. The adhesive acrylic material used in the experimental attenuation configuration was estimated at approximately $4$ EUR. The total preliminary component cost can therefore be estimated as:

$$C_{total} = C_{PLA} + C_{tr+el} + C_{adh} \tag{271}$$

where $C_{tr+el}$ is the combined cost of the transducer and electronic board, and $C_{adh}$ is the cost of the adhesive acrylic material. Using the adjusted PLA cost range, the estimated prototype cost becomes:

$$C_{total} = (1.58\text{–}1.94) + 50 + 4 = 55.58\text{–}55.94 \text{ EUR}. \tag{272}$$

This estimate suggests that the direct component cost of the proposed prototype may remain below $60$ EUR, assuming low-cost commercially available materials and electronic components. However, the complete manufacturing cost of a functional medical device would be substantially higher, since it would also include mechanical assembly, electrical integration, acoustic characterization, safety verification, reproducibility assessment, documentation, and regulatory compliance procedures. Consequently, while the personalized PLA orthotic shell represents a low-cost structural component, the final device cost would be determined primarily by the active therapeutic subsystem, validation requirements, and production quality-control processes.

## 7.4 Discussion

### 7.4.1 Advantages of the Personalized Workflow

The proposed personalized workflow provides a structured strategy for developing an ultrasound-based orthotic device that is adapted to the anatomical, mechanical, and therapeutic requirements of an individual patient. Instead of relying on a generic brace geometry or predefined transducer position, the workflow integrates patient-specific imaging, tissue characterization, numerical simulation, phantom-based validation, and procedural orthosis generation. This combination is aligned with current trends in personalized medicine, where diagnostic data and computational models are increasingly used to tailor interventions to individual variability rather than population-average assumptions. Recent reviews on digital twins and patient-specific healthcare describe this transition as a route toward safer treatment planning, improved prediction of therapeutic response, and risk-free evaluation of alternative intervention scenarios before application to the patient[27,28].

A first advantage of this approach is the explicit incorporation of patient anatomical variability. Knee geometry, soft-tissue distribution, cartilage thickness, limb alignment, and transducer access regions may vary considerably between subjects, which can influence acoustic propagation and the mechanical stability of the external device. Image-based biomechanical modelling workflows emphasize the importance of segmentation, meshing, and tissue-specific representation when constructing patient-specific finite element models from medical imaging data[29]. In the present framework, magnetic resonance imaging provides the anatomical basis for reconstructing the target region, while the orthosis is generated from the external morphology of the patient. This reduces the dependence on standardized geometries and allows the final support to conform to the actual skin surface.

A second relevant benefit is the possibility of integrating patient-specific tissue properties into the therapeutic planning stage. Ultrasound elastography and shear wave elastography can provide information on local mechanical stiffness, and recent work has highlighted their potential for generating spatially varying material properties for computational modelling of biological soft tissues[4]. This is particularly relevant for ultrasound stimulation, since wave propagation depends on density, speed of sound, attenuation, impedance, and tissue heterogeneity. The relationship between these properties show that even modest differences in tissue composition may alter acoustic transmission, especially when multiple interfaces are crossed. Therefore, the use of individualized tissue properties can improve the estimation of the excitation conditions required to deliver an adequate acoustic field to the target cartilage region.

The workflow also improves treatment planning by introducing an in silico stage before device

fabrication. Computational models are widely used in therapeutic ultrasound to assess device performance, feasibility, safety, and treatment monitoring strategies[30]. In the proposed methodology, numerical simulation allows the investigation of frequency, amplitude, transducer diameter, and placement before physical implementation. By solving this problem in a patient-informed geometry, it becomes possible to estimate whether the intended stimulation reaches the cartilage with suitable pressure amplitude and spatial distribution, while avoiding excessive exposure of non-target tissues.

Another advantage is the connection between computational predictions and experimental validation through anatomical phantoms. The phantom branch provides a controlled physical environment in which the transducer position, acoustic coupling, and emitted field can be tested before the final orthosis is produced. This reduces uncertainty in the transition from simulation to practical use, since the transducer placement is not selected only from a digital model but also verified experimentally. In the final design stage, the experimentally validated transducer pose is transferred to the Blender-based procedural model, preserving the therapeutic configuration during orthosis generation.

The use of procedural design further improves reproducibility and adaptability. Contemporary reviews of 3D-printed orthoses identify digital workflows, automated design generation, and additive manufacturing as relevant routes for accelerating orthosis production and improving clinical implementation[19,21]. In the proposed workflow, the orthosis is generated from a set of controllable operations: anatomical surface extraction, boundary definition, transducer placement, surface offset, and Voronoi-based pattern projection. This makes the design process more consistent than manual modelling alone, while still allowing patient-specific adaptation.

The projected Voronoi structure introduces additional functional advantages. Cellular and lattice-based orthotic designs have been explored for reducing mass, improving ventilation, redistributing pressure, and tuning local stiffness[26,31]. When this pattern is projected onto the patient-conformal orthosis, the resulting perforated shell can reduce material usage while maintaining a continuous mechanical frame around the transducer. This is relevant for comfort, since bulky or poorly ventilated orthoses may reduce adherence during repeated therapeutic sessions.

The personalized workflow also supports faster design iteration. Additive manufacturing and digital orthotic pipelines allow modifications to be introduced directly into the model before fabrication, reducing the need for repeated manual corrections. A parametric design-generator approach has previously been proposed for 3D-printed orthoses to simplify the production process and make customized design more accessible to users with limited CAD expertise[23]. In the present case, procedural modelling provides a similar advantage: once the rules are defined, the same workflow can be applied to different patient

geometries while preserving the validated relationship between anatomy, transducer location, and structural support.

Finally, the workflow offers a clearer route toward translational development because each stage has a distinct validation purpose. Elastography informs material parameters; MRI defines geometry; numerical modelling estimates therapeutic exposure; phantom experiments verify transducer performance; and procedural generation produces the final patient-specific interface. This modular organization improves traceability and makes the design easier to document, reproduce, and refine. Rather than treating the orthosis as a purely mechanical holder, the proposed strategy defines it as an integrated therapeutic interface that links imaging, simulation, experimental validation, and personalized fabrication.

### 7.4.2 Clinical and Translational Relevance

The proposed personalized workflow addresses a central limitation in the development of non-invasive ultrasound-based therapies for knee osteoarthritis: the difficulty of transferring a biophysical stimulus from a controlled experimental setting to a heterogeneous, patient-specific anatomical environment. Osteoarthritis management is increasingly framed as a patient-centred process, since clinical presentation, comorbidities, pain mechanisms, functional limitations, and joint morphology vary substantially between individuals. The OARSI guidelines explicitly support individualized treatment decisions for knee, hip, and polyarticular osteoarthritis, reinforcing the need for therapeutic strategies that can be adapted to patient-specific characteristics rather than applied through uniform protocols[32].

In this context, the proposed workflow contributes to clinical translation by linking imaging, tissue characterization, computational treatment planning, phantom validation, and device generation into a traceable development pipeline. The approach is compatible with the broader direction of personalized medicine and medical digital twins, where patient-specific data are used to construct computational representations that support diagnosis, treatment planning, and risk assessment. Recent reviews describe digital twins as patient-specific simulation platforms capable of integrating anatomical, physiological, and clinical data, although they also emphasize that practical implementation requires careful attention to data quality, modelling assumptions, validation, and regulatory use[33,34].

From a clinical perspective, one of the main advantages of this strategy is its non-invasive character. Ultrasound stimulation can be delivered externally without surgical implantation, intra-articular injection, or permanent alteration of the joint. This is relevant for knee osteoarthritis, where many patients are managed conservatively for long periods before arthroplasty becomes appropriate. Recent reviews indicate that low-

intensity pulsed ultrasound has been investigated as a non-pharmacological intervention for osteoarthritis, with reported effects on pain, function, inflammation, extracellular matrix metabolism, and cartilage-related pathways, although further high-quality clinical trials remain necessary before definitive therapeutic claims can be made[35–37].

The translational value of the workflow also lies in its capacity to improve dose definition. In ultrasound-based therapies, the biological response depends on several exposure parameters, including frequency, pressure amplitude, pulse duration, duty cycle, treatment duration, beam geometry, and spatial distribution of acoustic energy. Therapeutic ultrasound reviews emphasize that safety and efficacy are closely related to the control of acoustic exposure and to the avoidance of unintended bioeffects in non-target tissues[8]. By incorporating patient-specific geometry and tissue properties, the proposed methodology provides a rational basis for estimating the excitation conditions required to reach the cartilage region while limiting unnecessary exposure of surrounding tissues.

This is particularly important because the acoustic field inside the knee cannot be inferred directly from the nominal transducer output. Propagation through skin, adipose tissue, muscle, tendon, ligament, synovial structures, cartilage, and bone is affected by impedance mismatch, attenuation, scattering, reflection, and geometry-dependent focusing or shielding. A patient-specific planning stage therefore reduces dependence on empirical placement and supports a more defensible therapeutic prescription.

The workflow is also translationally relevant because it introduces experimental verification before patient application. Anatomical phantoms provide an intermediate validation platform between numerical modelling and clinical use, allowing transducer position, coupling conditions, beam direction, and acoustic field distribution to be evaluated under controlled conditions. This reduces the risk of moving directly from simulation to patient testing without confirming whether the physical system reproduces the expected field. Recent work in focused ultrasound treatment planning similarly highlights the importance of combining three-dimensional numerical prediction with phantom-based validation to support patient-specific planning[38].

The personalized orthosis further supports clinical implementation by converting the validated transducer position into a reproducible wearable interface. This is a critical translational step because ultrasound therapy depends not only on the selected stimulation parameters, but also on repeatable transducer alignment over multiple treatment sessions. A manually held transducer introduces operator dependence, variable pressure, inconsistent coupling, and uncertain beam orientation. By contrast, a patient-specific orthosis can maintain the prescribed pose relative to the knee surface, improving

repeatability and reducing the procedural burden for clinicians or trained operators.

Additive manufacturing and digital orthotic workflows are relevant in this regard because they enable individualized external devices to be produced from patient geometry. Reviews of 3D-printed orthoses report potential advantages in fit, comfort, ventilation, lightweight design, reproducibility, and clinical customization, while also noting that stronger evidence, standardized assessment, durability testing, and implementation protocols are still required[39,40]. For the present application, these advantages are not merely ergonomic; they are directly linked to therapeutic reliability because orthosis geometry determines whether the transducer remains aligned with the intended acoustic pathway.

The workflow also has relevance for regulatory and preclinical development. Patient-specific and additively manufactured medical devices require controlled design transfer, material selection, manufacturing validation, post-processing control, mechanical testing, and documentation of device performance. FDA guidance on additively manufactured medical devices outlines technical considerations for AM processes and recommends appropriate testing and characterization of finished devices, while broader reviews emphasize that personalized medical devices introduce additional challenges related to process control, repeatability, and quality assurance[41,42]. The proposed modular workflow is compatible with this logic because each stage produces verifiable outputs: anatomical geometry, tissue parameters, simulated exposure fields, phantom measurements, transducer pose, and final orthosis geometry.

Similarly, the computational component may support regulatory translation if its credibility is established through verification, validation, uncertainty quantification, and clearly defined context of use. The FDA has issued final guidance on assessing the credibility of computational modelling and simulation in medical device submissions, specifically for physics-based or mechanistic models[41]. This is relevant because the proposed framework does not rely on simulation as an isolated prediction tool; instead, computational outputs are linked to phantom experiments and device design constraints, which strengthens the evidential chain required for translational development.

Quality management is another important consideration. ISO 13485 defines internationally recognized requirements for quality management systems in the design and manufacture of medical devices, including the ability to consistently meet customer and regulatory requirements[43]. Although a thesis-stage prototype does not require full industrial certification, designing the workflow around traceability, repeatability, documented parameters, and controlled fabrication makes the system more compatible with later regulatory pathways. This is especially relevant for a personalized device, where each unit may differ geometrically while still needing to satisfy the same functional and safety

requirements.

### 7.4.3 Limitations of the Proposed Pipeline

Although the proposed pipeline provides a coherent route for patient-specific ultrasound stimulation and orthosis generation, several limitations must be considered before clinical translation. These limitations are not necessarily weaknesses of the concept, but rather constraints associated with the use of medical imaging, elastography, computational modelling, phantom validation, additive manufacturing, and personalized device regulation. Similar challenges are described in broader workflows for patient-specific medical devices, where each stage, from image acquisition to post-processing, can influence the safety, reproducibility, and performance of the final product[44,45].

A first limitation concerns the dependence on high-quality medical imaging. The proposed methodology assumes that MRI data can provide sufficient anatomical resolution to reconstruct the external knee morphology and relevant internal tissues. However, segmentation errors, partial-volume effects, motion artefacts, and variability in imaging protocols may introduce geometric inaccuracies. Since the orthosis surface, transducer position, and computational domain are derived from these data, small errors in segmentation may propagate through the design chain. This is particularly relevant near curved interfaces, thin cartilage layers, and soft-tissue boundaries, where geometric uncertainty can affect both acoustic propagation and mechanical fitting of the final device.

The use of elastography to inform tissue properties also introduces uncertainty. Although elastography can estimate tissue stiffness, the measured parameter is not directly equivalent to all mechanical and acoustic properties required for ultrasound simulation. For example, shear modulus, Young's modulus, acoustic speed, density, attenuation, and nonlinear acoustic parameters are related but not interchangeable. Therefore, additional assumptions are required to convert elastography-derived stiffness into simulation-ready material properties.

A second limitation is related to computational model simplification. The in silico branch necessarily relies on assumptions regarding tissue homogeneity, linearity, boundary conditions, coupling conditions, attenuation laws, and transducer behaviour. Even when patient geometry is included, biological tissues remain anisotropic, viscoelastic, poroelastic, heterogeneous, and frequency-dependent. This formulation is useful for treatment planning, but it may not fully represent shear conversion, nonlinear propagation, temperature-dependent effects, microscale cartilage mechanics, or patient-specific tissue anisotropy. In focused ultrasound treatment planning, recent studies emphasize that patient-specific acoustic and thermal models can improve planning, but they also require validation and careful treatment of

material-property uncertainty[46,47].

The credibility of the computational model is therefore a major translational constraint. The FDA guidance on computational modelling and simulation in medical device submissions recommends a risk-informed credibility assessment for physics-based and mechanistic models, including verification, validation, uncertainty quantification, and a clearly defined context of use[48]. In the present pipeline, the simulation results should therefore be interpreted as planning support rather than direct clinical evidence. Before the model could guide therapeutic decisions, it would require systematic comparison with experimental measurements, sensitivity analysis, and documentation of numerical convergence.

Another limitation concerns the phantom-based validation stage. Anatomical phantoms can reproduce geometry and selected acoustic properties, but they cannot fully capture the biological complexity of the living knee. Real tissues exhibit perfusion, temperature regulation, hydration changes, layered anisotropy, variable contact pressure, and time-dependent mechanical response. In contrast, phantoms usually represent a simplified and static approximation of the target anatomy. Consequently, a transducer position validated in a phantom may not fully reproduce the same acoustic field in vivo. Phantom testing is therefore valuable as an intermediate validation step, but it cannot replace animal studies, controlled human feasibility studies, or direct safety assessment.

The coupling conditions between the transducer, skin, orthosis, and soft tissues also represent a practical source of variability. The pipeline assumes that the orthosis can maintain a repeatable transducer pose and adequate acoustic coupling. However, coupling gel thickness, local skin curvature, soft-tissue compression, strap tension, patient movement, and orthosis deformation may alter the acoustic pathway. These effects are difficult to model precisely because they depend on user handling and patient-specific tissue compliance.

The procedural orthosis generation also has design limitations. Although Voronoi-based perforations can reduce mass and improve ventilation, they may introduce local stress concentrations or reduce stiffness in regions required for transducer stabilization. The relationship between pattern density, wall thickness, material properties, and mechanical performance must therefore be evaluated using mechanical simulation and experimental testing. The generated structure should satisfy both ergonomic and functional requirements, since an excessively compliant orthosis may improve comfort but compromise transducer alignment. Conversely, an overly rigid design may improve positional stability while increasing local pressure or reducing patient tolerance.

Another limitation is the absence of direct biological validation within the proposed pipeline. The workflow can estimate acoustic propagation, transducer placement, and orthosis fit, but it does not by

itself prove cartilage regeneration, symptom improvement, or disease modification. Low-intensity ultrasound has been investigated for osteoarthritis and cartilage-related applications, but clinical evidence remains heterogeneous, and treatment parameters are not yet universally standardized. Therefore, the proposed system should be presented as a platform for controlled stimulation delivery rather than as proof of therapeutic efficacy. Its clinical value would need to be demonstrated through staged validation, beginning with bench testing and safety assessment, followed by feasibility studies and controlled trials.

Finally, the proposed pipeline should be interpreted as a modular developmental framework rather than a complete clinical protocol. Its main limitation is that each module introduces uncertainty that can accumulate across the workflow. Anatomical reconstruction affects the computational model; material-property estimation influences acoustic prediction; phantom simplification affects transducer validation; fabrication tolerances affect orthosis fit; and clinical use introduces variability in coupling and alignment. A conservative translational strategy should therefore include uncertainty quantification, sensitivity analysis, repeated phantom measurements, mechanical validation of the orthosis, acoustic field verification, and prospective clinical testing. Under these conditions, the pipeline may provide a credible foundation for personalized ultrasound-based orthotic therapy, while maintaining appropriate caution regarding its current preclinical status.

### 7.4.4 Future Integration with Market Regulations

Figure 158 summarizes the main risk classes defined under the European Medical Device Regulation.

The developed orthotic ultrasound stimulation system is most likely to be classified as a Class IIa medical device, assuming that its intended purpose is the non-invasive therapeutic administration of mechanical/acoustic energy to the knee joint and that the delivered exposure remains within non-hazardous limits. Under Regulation (EU) 2017/745, active therapeutic devices intended to administer or exchange energy with the human body are generally classified as class IIa, unless the nature, density, or anatomical site of energy application introduces a potentially hazardous mode of action, in which case a higher classification may be required[49,50]. Since the proposed system is externally applied, non-invasive, and intended to deliver controlled ultrasound stimulation rather than high-intensity ablative or destructive energy, class IIa appears to be the most appropriate preliminary classification. However, this classification should be confirmed through a formal regulatory assessment based on the final intended purpose, acoustic output, exposure duration, risk analysis, and clinical

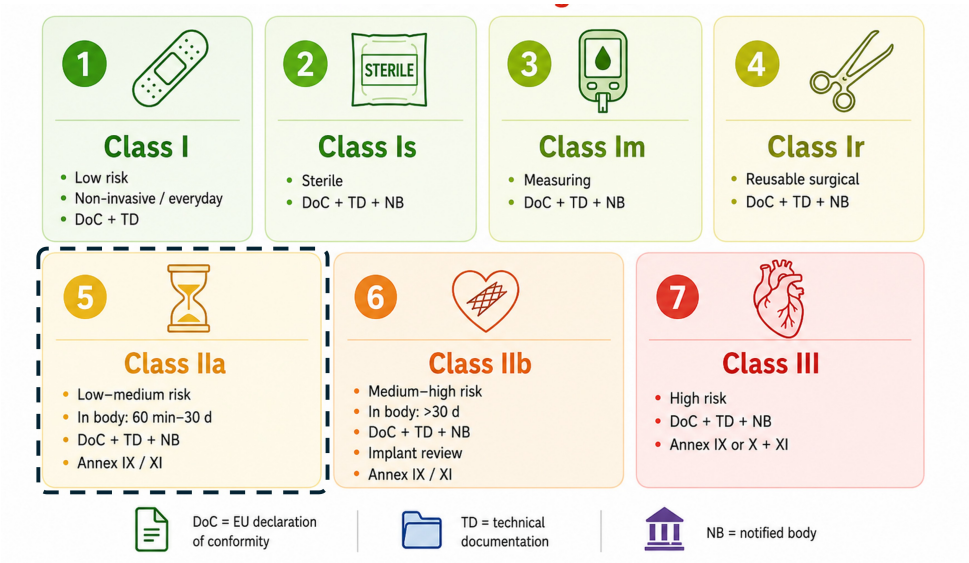



Figure 158: Preliminary regulatory classification of the developed ultrasound-based orthotic device under the European Medical Device Regulation. The system is most likely positioned within Class IIa, since it is an active therapeutic device intended to administer controlled acoustic energy to the body in a non-invasive manner. Final classification depends on the intended clinical purpose, delivered energy level, exposure conditions, anatomical site of application, and formal conformity assessment.

claims.

As a Class IIa device, the system would require technical documentation, clinical evaluation, risk management, and conformity assessment involving a notified body before being placed on the European market[49]. This distinction is relevant because the device cannot be treated as a simple Class I orthosis if the active ultrasound component is included within the intended therapeutic function. The classification therefore reflects the combined nature of the system: a patient-specific external support used to maintain transducer positioning, coupled with an active therapeutic element that delivers acoustic energy to biological tissues.

For this type of device, the validation strategy should include several complementary blocks, covering electrical safety, ultrasound performance, acoustic characterization, biological safety, software control, risk management, and clinical evidence. The specific requirements for each block would be:

1. The system should be evaluated as medical electrical equipment. Compliance with IEC 60601-1 would be central for demonstrating basic safety and essential performance, including protection against electric shock, leakage currents, insulation integrity, grounding, enclosure safety, thermal behaviour of electronic components, alarms, and relevant fault conditions. Electromagnetic compatibility should also be addressed through IEC 60601-1-2, since the device may operate in clinical or home-care environments where electromagnetic disturbances could affect performance or safety. IEC 60601-1 is generally applicable to medical electrical equipment, while particular standards should be applied when they exist for a specific device category.

2. Ultrasound-specific safety and performance requirements are particularly relevant. Since the proposed system is closer to physiotherapy ultrasound than to high-intensity focused ultrasound, IEC 60601-2-5 is a suitable reference standard. This standard addresses the basic safety and essential performance of ultrasonic physiotherapy equipment, particularly systems using unfocused treatment heads that generate beams perpendicular to the treatment surface. IEC 61689 is also relevant because it defines field specifications and measurement methods for physiotherapy ultrasound systems, including references to ultrasonic power measurement and hydrophone-based field characterization.

3. The acoustic output should be characterized using calibrated and traceable methods. Required parameters would include acoustic power, effective radiating area, beam non-uniformity ratio, spatial pressure distribution, intensity, operating frequency, duty cycle or modulation scheme, exposure repeatability, and sensitivity to coupling conditions. For the proposed knee application, this characterization should also include transmission through soft-tissue-mimicking layers, reflection at bone-like interfaces, and possible localized heating near high-impedance boundaries. These measurements are essential because the nominal electrical input does not directly define the acoustic dose delivered to the target tissues.

4. Thermal and mechanical safety should be validated experimentally. Although the in silico model provides a useful predictive framework, a device intended for clinical use would normally require physical confirmation of the underlying assumptions and safety margins. Phantom testing should therefore evaluate temperature rise under conservative worst-case conditions, including maximum driving voltage, longest intended treatment duration, reduced coupling quality, minimal contact area, and exposure near bone-equivalent interfaces. The current phantom work can be presented as an important preclinical foundation, but regulatory translation would require traceable measurements demonstrating that model predictions remain within acceptable uncertainty limits.

5. All patient-contacting components require biological safety assessment. This includes the orthosis material, coupling layers, treatment-head covers, membranes, gels, adhesives, tapes, housing interfaces, or any other material that may contact intact skin. The ISO 10993 series is the relevant framework for biological evaluation, with the specific tests determined by the nature and duration of body contact. For this system, the likely initial concern would be limited or prolonged contact with intact skin, although the final assessment would depend on the intended use scenario and material formulation.

6. Software and control functions should be validated if they influence treatment delivery. Embedded control, dose limitation, treatment timers, intensity selection, feedback loops, fault detection, and automatic shut-off functions would require software lifecycle documentation under IEC 62304. Usability engineering under IEC 62366-1 would also be relevant, particularly because incorrect placement, inappropriate parameter selection, poor coupling, or premature removal may directly affect safety and performance. IEC 62366-1 defines a process for analysing, specifying, developing, and evaluating medical device usability as it relates to safety.

7. Risk management should be treated as a central design activity rather than a late-stage documentation exercise. ISO 14971 specifies a structured process for identifying hazards, estimating and evaluating associated risks, implementing risk controls, and monitoring the effectiveness of those controls throughout the device life cycle. For the proposed system, relevant hazards include excessive tissue heating, unintended cavitation or mechanical effects, poor acoustic coupling, transducer detachment, incorrect anatomical placement, overexposure, electrical shock, burns at the skin interface, unsafe use near implants, and application in patients with impaired sensation.

8. A clinical evaluation would be required under the Medical Device Regulation. For a conventional low-risk physiotherapy ultrasound device with an established indication, literature-based evidence or equivalence may contribute to the clinical evaluation. However, for claims related to knee joint unloading, cartilage stimulation, osteoarthritis treatment, disease modification, or tissue regeneration, equivalence is likely to be difficult to justify. In that case, a clinical investigation may be necessary, particularly if the intended claim extends beyond symptomatic relief. Clinical evaluation expectations for Class IIa devices are proportional to the device's novelty, complexity, and risk profile, and the MDR framework requires appropriate clinical evidence to support safety and performance.

In practical terms, the fact that the system is not a HIFU device may avoid the highest-risk therapeutic ultrasound pathway, but it does not remove the need to demonstrate controlled energy delivery, electrical safety, acoustic performance, biological compatibility, and clinical justification. For the current concept, the most conservative preliminary route would be to treat the device as likely Class IIa under the MDR, while explicitly checking whether the intensity, exposure duration, anatomical target, or bone-interface heating could justify Class IIb classification. In Portugal, INFARMED is the competent authority for medical devices, while CE conformity assessment for Class IIa or Class IIb devices would involve a notified body.

## 7.5 Bibliography

[1]J. Martel-Pelletier, P. Paiement, and J.-P. Pelletier, "Magnetic resonance imaging assessments for knee segmentation and their use in combination with machine/deep learning as predictors of early osteoarthritis diagnosis and prognosis", Ther. Adv. Musculoskelet. Dis. **15**, 1759720X231165560 (2023) 10.1177/1759720X231165560.

[2]V. Casula and A. W. Kajabi, "Quantitative MRI methods for the assessment of structure, composition, and function of musculoskeletal tissues in basic research and preclinical applications", Magn. Reson. Mater. Phys. Biol. Med. **37**, 949–967 (2024) 10.1007/s10334-024-01174-7.

[3]V. D'Agostino, A. Sorriento, A. Cafarelli, D. Donati, N. Papalexis, A. Russo, G. Lisignoli, L. Ricotti, and P. Spinnato, "Ultrasound Imaging in Knee Osteoarthritis: Current Role, Recent Advancements, and Future Perspectives", J. Clin. Med. **13**, 4930 (2024) 10.3390/jcm13164930.

[4]B. J. Ranger, K. M. Moerman, M. Feigin, H. M. Herr, and B. W. Anthony, "3D Ultrasound Shear Wave Elastography for Musculoskeletal Tissue Assessment Under Compressive Load: A Feasibility Study", Ultrason. Imaging **46**, 251–262 (2024) 10.1177/01617346241253798.

[5]N. R. Fuggle, R. Chapurlat, A. Laslop, N. Al-Daghri, M. Alokail, J. A. Thiyagarajan, E. Balkowiec-Iskra, F. Berenbaum, A. B.-v. Bemden, J.-J. Borg, O. Bruyère, N. Burlet, E. Cavalier, M. M. Rosa, P. G. Conaghan, C. Cooper, E. M. Dennison, M. Englund, G.-i. Im, I. K. Haugen, M. Hiligsmann, A. Kurth, N. Lane, R. Lories, S. Marlovits, R. Matijevic, A. Mobasheri, S. Ormarsdóttir, M. C. P. Yerro, R. P. Radermecker, F. Rannou, B. Sepodes, S. Silverman, C. Torre, N. Veronese, R. Rizzoli, J.-Y. Reginster, and N. C. Harvey, "Novel approaches to the stratified management of knee osteoarthritis", Nat. Rev. Rheumatol. **21**, 684–695 (2025) 10.1038/s41584-025-01305-x.

[6]J. Guo, P. Yan, Y. Qin, M. Liu, Y. Ma, J. Li, R. Wang, H. Luo, and S. Lv, "Automated measurement and grading of knee cartilage thickness: a deep learning-based approach", Front. Med. **11**, 1337993 (2024) 10.3389/fmed.2024.1337993.

[7]J. Zhou, E. Ning, L. Lu, H. Zhang, X. Yang, and Y. Hao, "Effectiveness of low-intensity pulsed ultrasound on osteoarthritis: molecular mechanism and tissue engineering", Front. Med. **11**, 1292473 (2024) 10.3389/fmed.2024.1292473.

[8]K. B. Bader, F. Padilla, K. J. Haworth, N. Ellens, D. Dalecki, D. L. Miller, K. A. Wear, and Bioeffects Committee of the American Institute of Ultrasound in Medicine, "Overview of Therapeutic Ultrasound

Applications and Safety Considerations: 2024 Update", J. Ultrasound Med. **44**, 381–433 (2025) 10.1002/jum.16611.

[9]B. E. Treeby and B. T. Cox, "K-Wave: MATLAB toolbox for the simulation and reconstruction of photoacoustic wave fields", J. Biomed. Opt. **15**, 021314 (2010) 10.1117/1.3360308.

[10]B. E. Treeby, E. Z. Zhang, A. S. Thomas, and B. T. Cox, "Measurement of the Ultrasound Attenuation and Dispersion in Whole Human Blood and its Components From 0–70 MHz", Ultrasound Med. Biol. **37**, 289–300 (2011) 10.1016/j.ultrasmedbio.2010.10.020.

[11]A. Pulkkinen and K. Hynynen, "Computational aspects in high intensity ultrasonic surgery planning", Comput. Med. Imaging Graph. **34**, 69–78 (2010) 10.1016/j.compmedimag.2009.08.001.

[12]M. K. Sigona, T. J. Manuel, M. A. Phipps, K. B. Boroujeni, R. L. Treuting, T. Womelsdorf, and C. F. Caskey, "Generating Patient-Specific Acoustic Simulations for Transcranial Focused Ultrasound Procedures Based on Optical Tracking Information", IEEE Open J. Ultrason. Ferroelectr. Freq. Control **3**, 146–156 (2023) 10.1109/OJUFFC.2023.3318560.

[13]J. Browne, K. Ramnarine, A. Watson, and P. Hoskins, "Assessment of the acoustic properties of common tissue-mimicking test phantoms", Ultrasound Med. Biol. **29**, 1053–1060 (2003) 10.1016/S0301-5629(03)00053-X.

[14]A. Filippou, I. Louca, and C. Damianou, "Characterization of a fat tissue mimicking material for high intensity focused ultrasound applications", J. Ultrasound **26**, 505–515 (2022) 10.1007/s40477-022-00746-4.

[15]A. Jawli, W. Aldehani, G. Nabi, and Z. Huang, "Tissue-Mimicking Material Fabrication and Properties for Multiparametric Ultrasound Phantoms: A Systematic Review", Bioengineering **11**, 620 (2024) 10.3390/bioengineering11060620.

[16]V. Filippou and C. Tsoumpas, "Recent advances on the development of phantoms using 3D printing for imaging with CT, MRI, PET, SPECT, and ultrasound", Med. Phys. **45** (2018) 10.1002/mp.13058.

[17]J. Illi, B. Bernhard, C. Nguyen, T. Pilgrim, F. Praz, M. Gloeckler, S. Windecker, A. Haeberlin, and C. Gräni, "Translating Imaging Into 3D Printed Cardiovascular Phantoms", JACC Basic Transl. Sci. **7**, 1050–1062 (2022) 10.1016/j.jacbts.2022.01.002.

[18]K. A. Wear, "Considerations for Choosing Sensitive Element Size for Needle and Fiber-Optic Hydrophones—Part I: Spatiotemporal Transfer Function and Graphical Guide", IEEE Trans. Ultrason. Ferroelectr. Freq. Control **66**, 318–339 (2019) 10.1109/TUFFC.2018.2886067.

[19]L. Hale, E. Linley, and D. M. Kalaskar, "A digital workflow for design and fabrication of bespoke orthoses using 3D scanning and 3D printing, a patient-based case study", Sci. Rep. **10**, 7028 (2020) 10.1038/s41598-020-63937-1.

[20]T. Kermavnar, A. Shannon, K. J. O'Sullivan, C. McCarthy, C. P. Dunne, and L. W. O'Sullivan, "Three-Dimensional Printing of Medical Devices Used Directly to Treat Patients: A Systematic Review", 3D Print. Addit. Manuf. **8**, 366–408 (2021) 10.1089/3dp.2020.0324.

[21]N. H. Alrasheedi, M. Tlija, N. Elloumi, and B. Louhichi, "A critical review of 3D printed orthoses towards workflow implementation in the clinical practice", J. Eng. Res. **13**, 1038–1051 (2025) 10.1016/j.jer.2024.01.024.

[22]Y. Lei, J. Duan, Q. Qi, J. Fang, Q. Liu, S. Zhou, and Y. Wu, "The Design and Application of Wearable Ultrasound Devices for Detection and Imaging", Biosensors **15**, 561 (2025) 10.3390/bios15090561.

[23]L. Li, L. Zhao, R. Hassan, and H. Ren, "Review on Wearable System for Positioning Ultrasound Scanner", Machines **11**, 325 (2023) 10.3390/machines11030325.

[24]V. Tsiokou, A. Papatheodorou, D. Ntenekou, P. Zouboulis, and A. Karatza, "An Integrative Computational Design Workflow and Validation Methodology for 3D-Printed Personalized Orthopedic Devices: Case Study of a Wrist–Hand Orthosis (WHO)", Processes **11**, 2204 (2023) 10.3390/pr11072204.

[25]A. P Fitzpatrick, "Design of a Patient Specific, 3D printed Arm Cast", KnE Eng. **2**, 135 (2017) 10.18502/keg.v2i2.607.

[26]G. De Pasquale and D. Barra, "Voronoi lattice-based orthotics with modular stiffness for additive manufacturing", Trans. Addit. Manuf. Meets Med., 668 Pages (2022) 10.18416/AMMM.2022.2209668.

[27]S. Y. Saratkar, M. Langote, P. Kumar, P. Gote, I. N. Weerarathna, and G. V. Mishra, "Digital twin for personalized medicine development", Front. Digit. Health **7**, 1583466 (2025) 10.3389/fdgth.2025.1583466.

[28]H. Khoshfekr Rudsari, B. Tseng, H. Zhu, L. Song, C. Gu, A. Roy, E. Irajizad, J. Butner, J. Long, and K.-A. Do, "Digital twins in healthcare: a comprehensive review and future directions", Front. Digit. Health **7**, 1633539 (2025) 10.3389/fdgth.2025.1633539.

[29]F. Galbusera, A. Cina, M. Panico, D. Albano, and C. Messina, "Image-based biomechanical models of the musculoskeletal system", Eur. Radiol. Exp. **4**, 49 (2020) 10.1186/s41747-020-00172-3.

[30]P. Prakash, V. A. Salgaonkar, and C. J. Diederich, "Modelling of endoluminal and interstitial ultrasound hyperthermia and thermal ablation: Applications for device design, feedback control and treatment planning", Int. J. Hyperthermia **29**, 296–307 (2013) 10.3109/02656736.2013.800998.

[31]M. R. Amin and M. A. H. Khondoker, "Design and Characterization of Additively Manufactured Patient-Specific Wrist Hand Orthosis", in 1st Int. Conf. Ind. Manuf. Process Eng. ICIMP-2024 (Oct. 29, 2024), p. 69, 10.3390/engproc2024076069.

[32]R. Bannuru, M. Osani, E. Vaysbrot, N. Arden, K. Bennell, S. Bierma-Zeinstra, V. Kraus, L. Lohmander, J. Abbott, M. Bhandari, F. Blanco, R. Espinosa, I. Haugen, J. Lin, L. Mandl, E. Moilanen, N. Nakamura, L. Snyder-Mackler, T. Trojian, M. Underwood, and T. McAlindon, "OARSI guidelines for the non-surgical management of knee, hip, and polyarticular osteoarthritis", Osteoarthritis Cartilage **27**, 1578–1589 (2019) 10.1016/j.joca.2019.06.011.

[33]A. Silva and N. Vale, "Digital Twins in Personalized Medicine: Bridging Innovation and Clinical Reality", J. Pers. Med. **15**, 503 (2025) 10.3390/jpm15110503.

[34]S. Demuth, J. De Sèze, G. Edan, T. Ziemssen, F. Simon, and P.-A. Gourraud, "Digital Representation of Patients as Medical Digital Twins: Data-Centric Viewpoint", JMIR Med. Inform. **13**, e53542–e53542 (2025) 10.2196/53542.

[35]M. Guan, X. Zhang, X. Li, B. Liao, W. Han, J. Tan, Z. Wang, L. Wang, J. Shen, X. Han, and D. Bai, "Research Progress of Osteoarthritis Treatment by Low Intensity Pulsed Ultrasound", Smart Med. **4**, e70003 (2025) 10.1002/smmd.70003.

[36]X.-Y. Zhou, X.-X. Zhang, G.-Y. Yu, Z.-C. Zhang, F. Wang, Y.-L. Yang, M. Li, and X.-Z. Wei, "Effects of Low-Intensity Pulsed Ultrasound on Knee Osteoarthritis: A Meta-Analysis of Randomized Clinical Trials", BioMed Res. Int. **2018**, 1–7 (2018) 10.1155/2018/7469197.

[37]H. Chen, Z. Wang, X. Zhang, and M. Sun, "Effects of low-intensity pulsed ultrasound on knee osteoarthritis: A systematic review and meta-analysis of randomized controlled trials", Clin. Rehabil. **36**, 1153–1169 (2022) 10.1177/02692155221097035.

[38]F. Morelli, A. Albanesi, A. Ivanaj, S. Buratti, F. Parrotta, J. Fu, S. Tognarelli, A. Menciassi, E. De Momi, and A. Redaelli, *High-Intensity Focused Ultrasound (HIFU) Modeling:In Vitro Validation and Integration into Patient-Specific Planning Tool*, (Sept. 5, 2025) 10.21203/rs.3.rs-7427702/v1, https://www.researchsquare.com/article/rs-7427702/v1 (visited on 05/27/2026), pre-published.

[39]H. Atallah, T. Qufabz, H. R. Bakhsh, and G. Ferriero, "The current state of 3D-printed orthoses clinical outcomes: a systematic review", BMC Musculoskelet. Disord. **26**, 822 (2025) 10.1186/s12891-025-09070-4.

[40]J. D. S. Pereira, A. S. M. S. Xavier, R. D. S. Monteiro, V. V. Cruz, M. F. D. S. Pereira, A. D. Tholl, J. Felisbino, and W. C. A. Machado, "3D-printed orthoses and prostheses for people with physical disability in rehabilitation centers: a scoping review", BMC Musculoskelet. Disord. **25**, 783 (2024) 10.1186/s12891-024-07875-3.

[41]U.S. Department of Health and Human Services, *Technical Considerations for Additive Manufactured Medical Devices* (U. S. Food and Drug Administration, 2017).

[42]W. L. Ng, J. An, and C. K. Chua, "Process, Material, and Regulatory Considerations for 3D Printed Medical Devices and Tissue Constructs", Engineering **36**, 146–166 (2024) 10.1016/j.eng.2024.01.028.

[43]ISO, *ISO 13485:2016 Medical devices — Quality management systems — Requirements for regulatory purposes*, 2016.

[44]M. Salmi, "Additive Manufacturing Processes in Medical Applications", Materials **14**, 191 (2021) 10.3390/ma14010191.

[45]T. Neussl, R. Lindtner, L. Kampik, S. Pal, M. Schirmer, D. Putzer, R. Arora, and J. D. Pallua, "Quality approaches and standards of 3D printing in orthopedic and traumatological settings: a systematic review", Explor. Musculoskelet. Dis. **3**, 100794 (2025) 10.37349/emd.2025.100794.

[46]P. Gupta, T. Heffter, M. Zubair, I.-C. Hsu, E. C. Burdette, and C. J. Diederich, "Treatment Planning Strategies for Interstitial Ultrasound Ablation of Prostate Cancer", IEEE Open J. Eng. Med. Biol. **5**, 362–375 (2024) 10.1109/OJEMB.2024.3397965.

[47]S. Lari, M. Kohandel, and H. J. Kwon, "Model based deep learning method for focused ultrasound pathway scanning", Sci. Rep. **14**, 20042 (2024) 10.1038/s41598-024-70689-9.

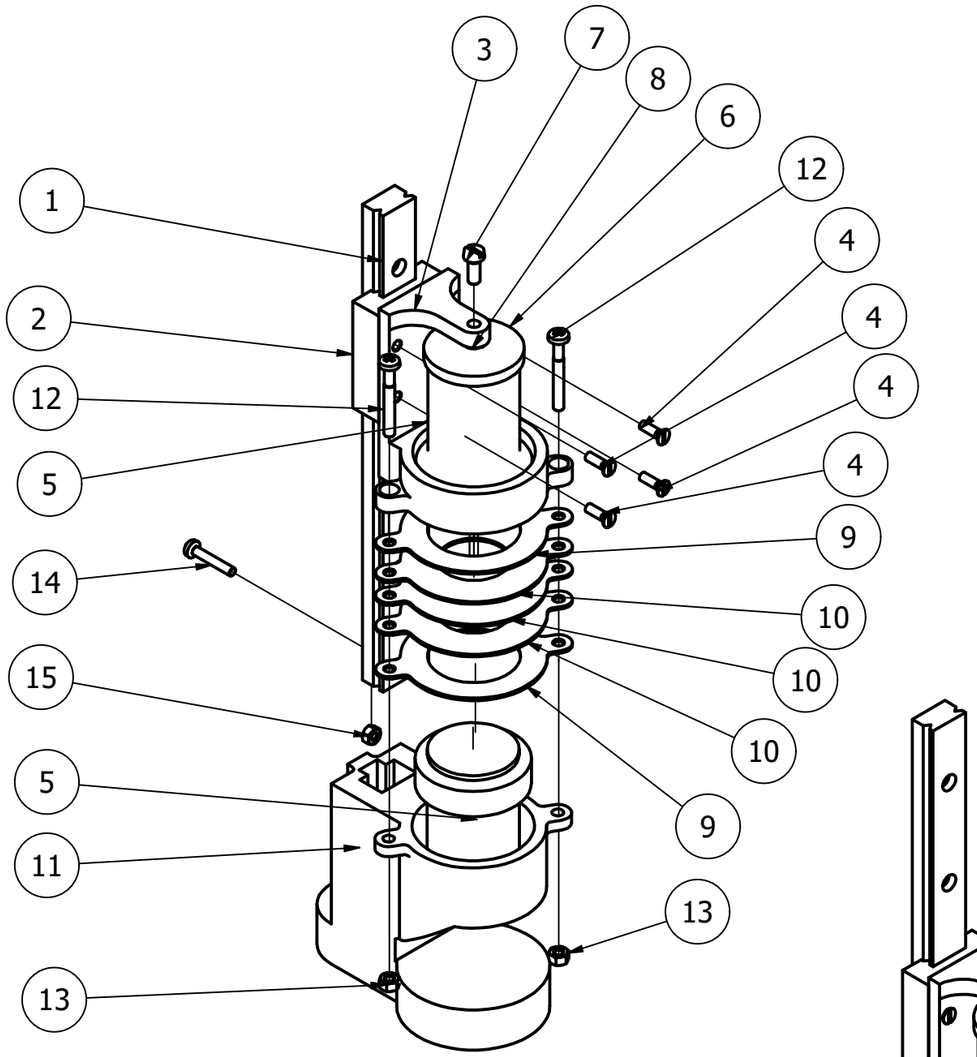
[48]U.S. Department of Health and Human Services, *Assessing the Credibility of Computational Modeling and Simulation in Medical Device Submissions* (U. S. Food and Drug Administration, 2023).

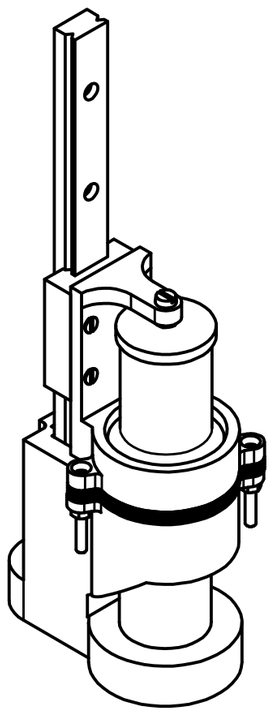
[49]European Parliament and Council of the European Union, *Regulation (EU) 2017/745 of the European Parliament and of the Council of 5 April 2017 on medical devices*, Apr. 5, 2017.

[50]Medical Device Coordination Group, *Guidance on classification of medical devices*, Oct. 2021.

# Appendix A

# Technical Drawings



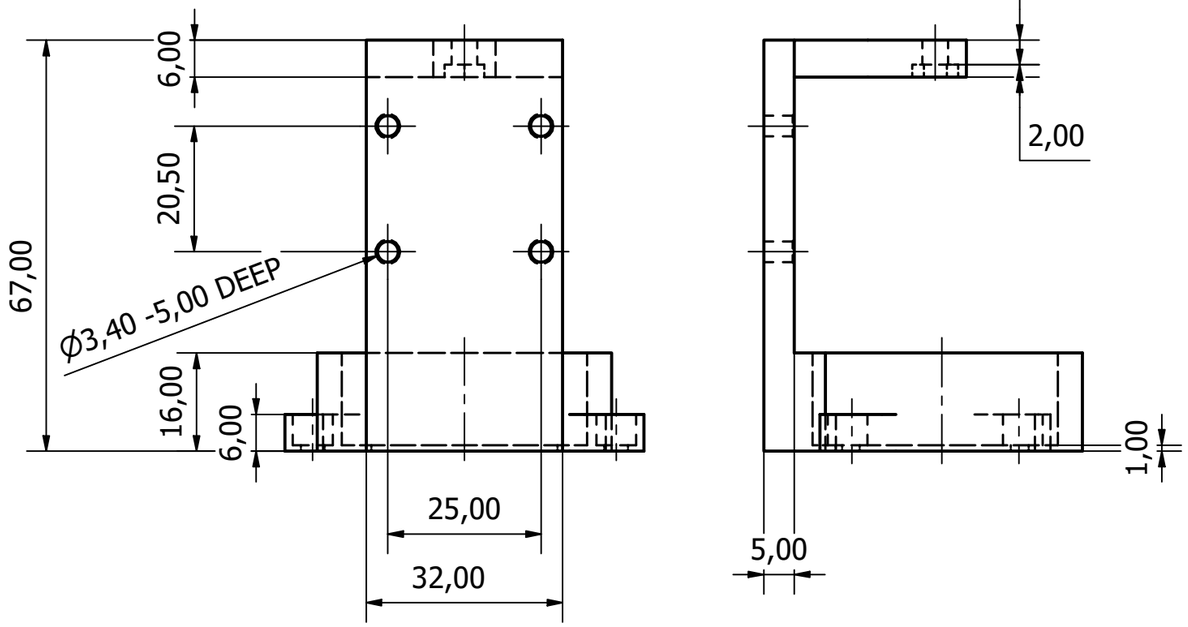
| PARTS LIST | | | |
|---|---|---|---|
| ITEM | QTY | PART NUMBER | DESCRIPTION |
| 1 | 1 | Linear Rail | |
| 2 | 1 | Linear Guide | |
| 3 | 1 | Top Support | |
| 4 | 4 | ISO 2009 - M3 x 10 | Slotted countersunk flat head screws (common head style) - Product grade A |
| 5 | 2 | Ultrasound Transducer | |
| 6 | 1 | Transducer Cover | |
| 7 | 1 | JIS B 1101 - A M4 x 10 | Slotted Cheese Head Machine Screw |
| 8 | 1 | ANSI B18.2.4.2M - M4x0.7 | Metric Hex Nuts Styles 2 |
| 9 | 2 | Transducer Ring | |
| 10 | 3 | Sample Ring | |
| 11 | 1 | Bottom Support | |
| 12 | 2 | DIN 7985 (H) - M3.5x28-H | Cross recessed raised cheese head screws - Type H |
| 13 | 2 | ANSI B18.2.4.2M - M3.5x0.6 | Metric Hex Nuts Styles 2 |
| 14 | 1 | DIN 7985 (H) - M3x18-H | Cross recessed raised cheese head screws - Type H |
| 15 | 1 | ANSI B18.2.4.2M - M3x0.5 | Metric Hex Nuts Styles 2 |

| Designed by | Checked by | Approved by | Date | | Date | |
|---|---|---|---|---|---|---|
| Nuno A. T. C. F. | | | | | 02/05/2026 | |

| | | | |
|---|---|---|---|
| Ultrasound Linear Probe Sample Holder | | | |
| Assembly | | Edition | Sheet 1 / 1 |

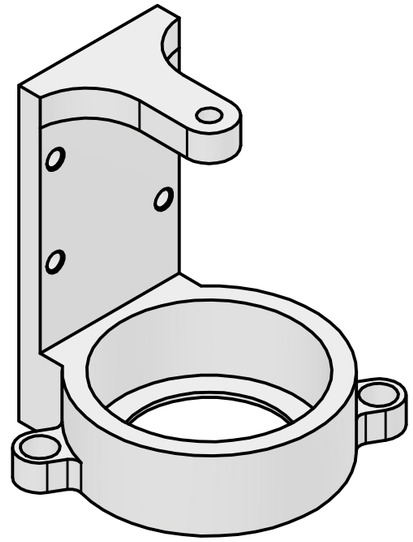
NOTES:

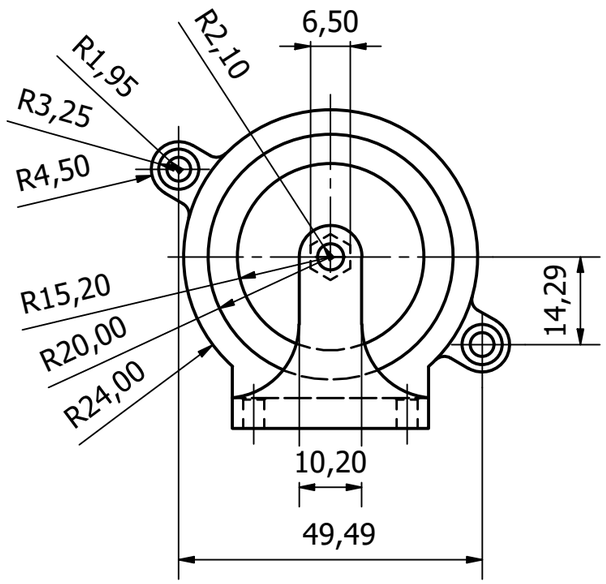
1. DEBURR ALL SHARP EDGES AND CORNERS AS NEEDED









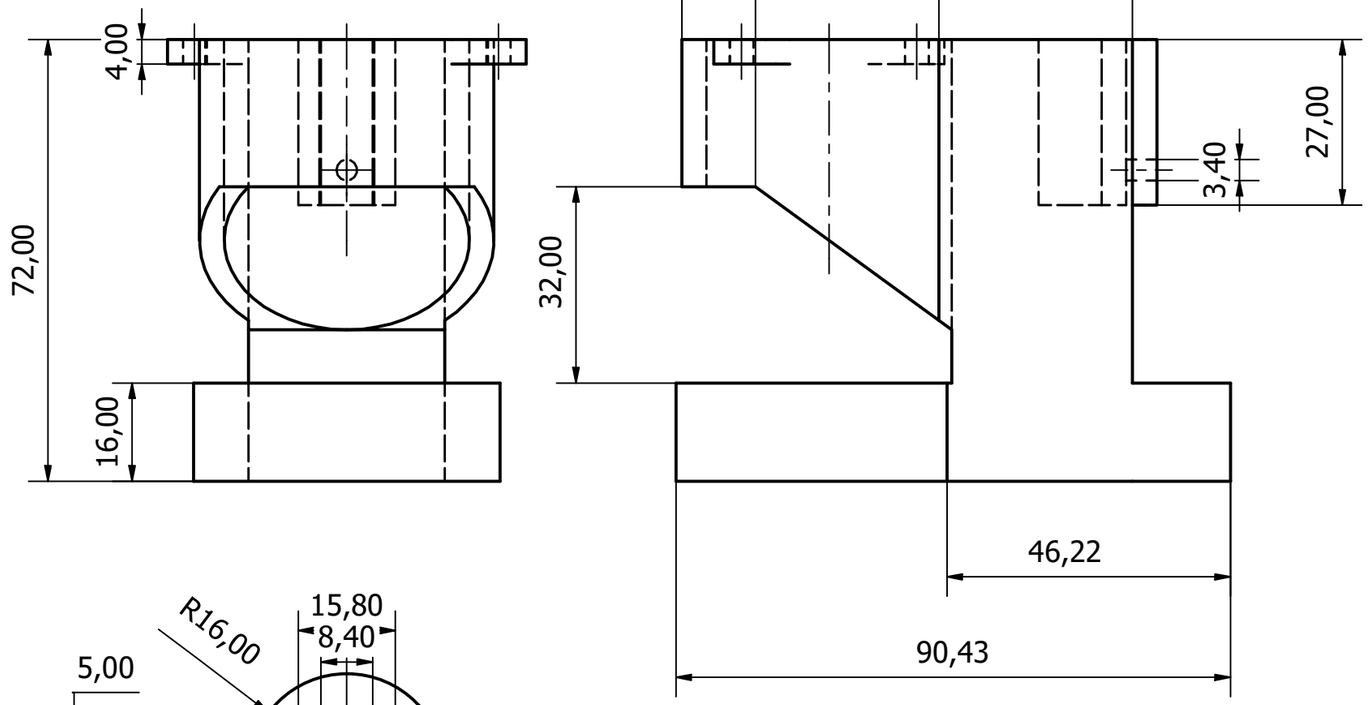


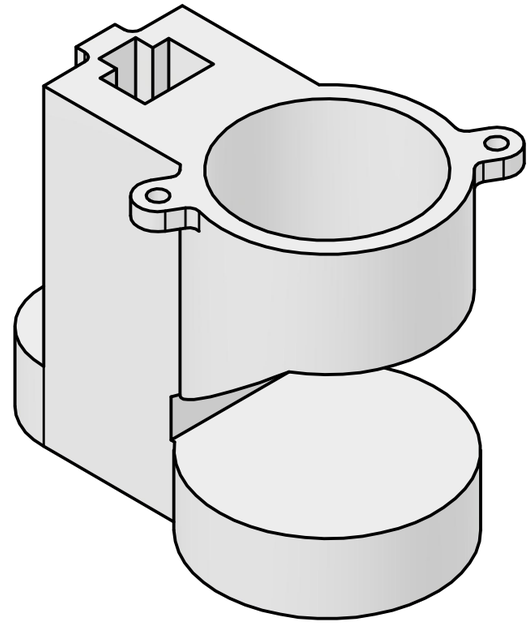

| Designed by | Checked by | Approved by | Date | | Date | |
|---|---|---|---|---|---|---|
| Nuno A. T. C. F. | | | | | 02/05/2026 | |

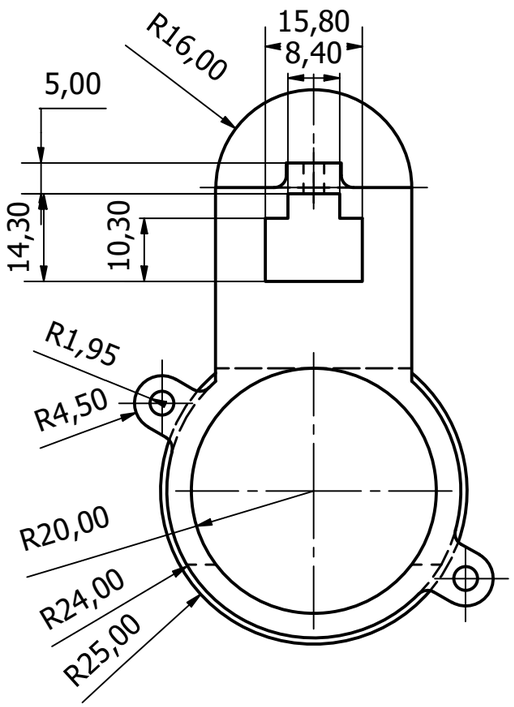
| | | | |
|---|---|---|---|
| | Top Support | | |
| 3 | | Edition | Sheet 1 / 1 |

NOTES:

1. DEBURR ALL SHARP EDGES AND CORNERS AS NEEDED

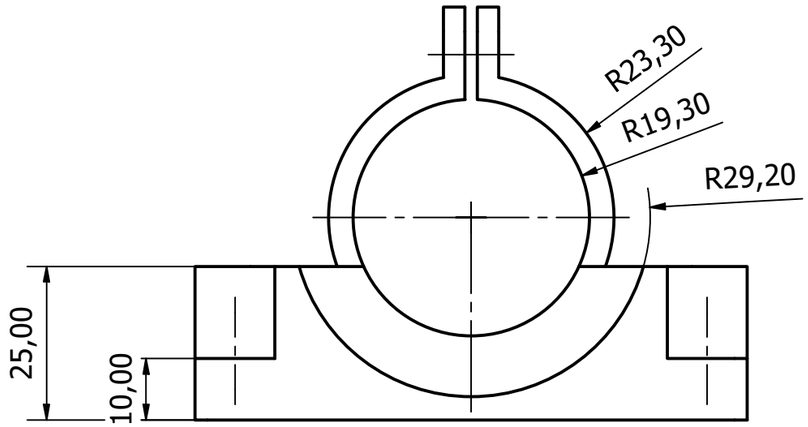


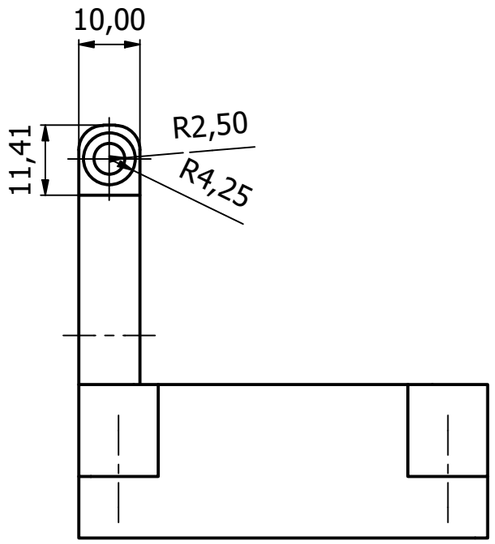



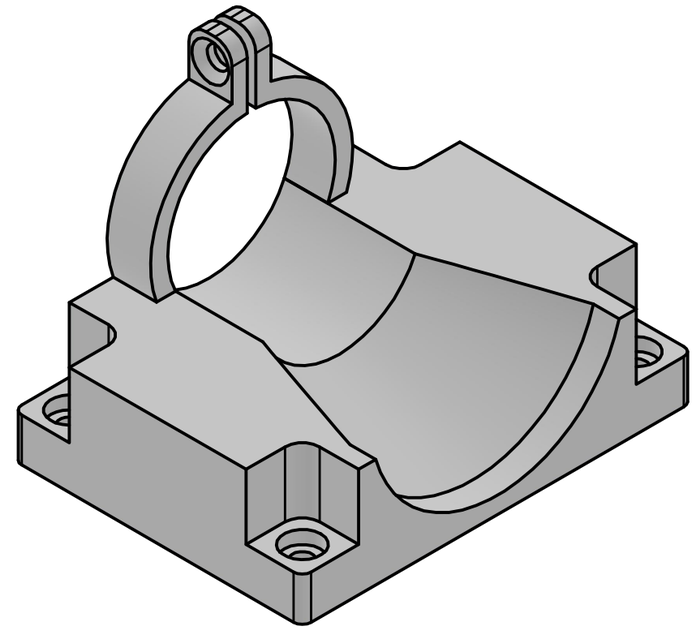


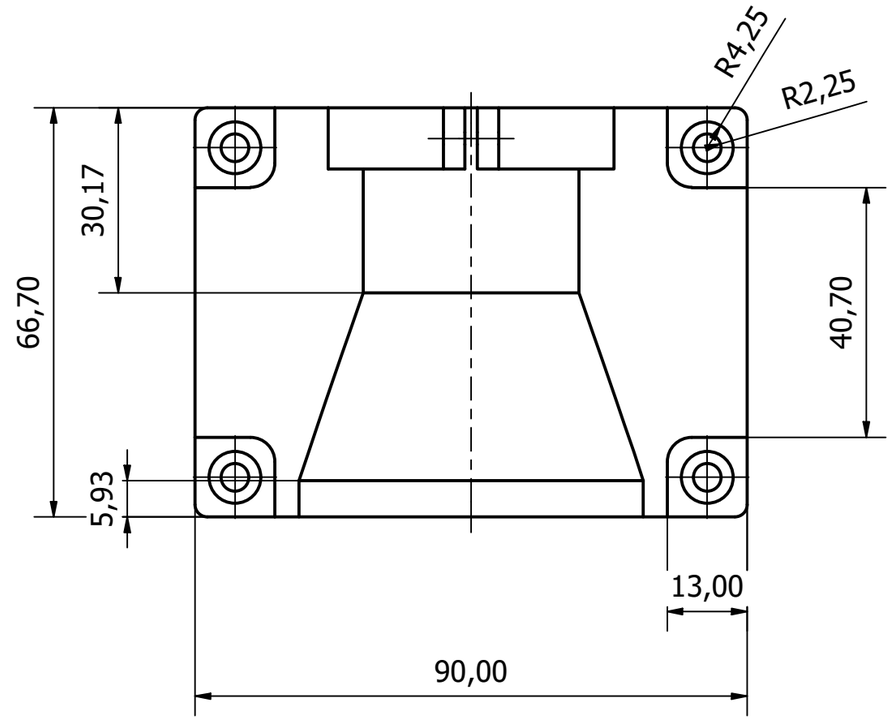

| Designed by | Checked by | Approved by | Date | | Date | |
|---|---|---|---|---|---|---|
| Nuno A. T. C. F. | | | | | 02/05/2026 | |

| | | | |
|---|---|---|---|
| | Bottom Support | | |
| 11 | | Edition | Sheet 1 / 1 |






| | | | | | |
|---|---|---|---|---|---|
| Designed by<br>Nuno A. T. C. F. | Checked by | Approved by | Date | Date<br>22/05/2026 | |
| | | Transducer Support | | | |
| | | Suporte-1 | Edition | Sheet<br>1 / 1 | |

# Appendix B

# Supplemental Biological Tissue Validation Data

# B.1 Computational Model Validation

This section examines acoustic wave propagation in biological tissues across a broad frequency range, with particular emphasis on the role of frequency-dependent attenuation and the suitability of different modeling approaches. It was omitted from the main body of the thesis to ease the findings' discussion.

## B.1.1 Skin

For acoustic wave propagation in skin at $500$ kHz (figure 159), the results indicate that linear viscous modeling is insufficient to accurately reproduce the experimental behavior, as evidenced by its overestimation of amplitude in the time domain and poorer spectral agreement. In contrast, both non-linear formulations closely match the experimental signal, capturing waveform shape and harmonic content with high fidelity, which is reflected in near-unity $R^2$ values ( $0.997$). While the non-linear viscous attenuation model achieves slightly higher accuracy, it does so at the highest computational cost, whereas the non-linear sound diffusivity model provides a comparable level of agreement with reduced computational demand.

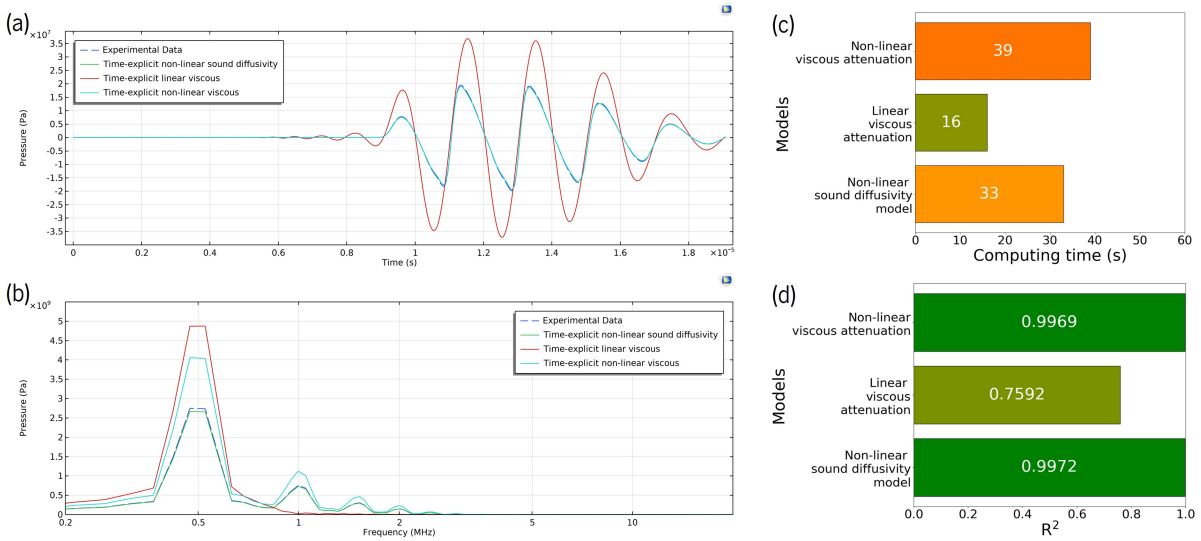



Figure 159: Experimental and simulated pressure responses for acoustic wave propagation in skin at $500$ kHz: (a) time-domain signals, (b) frequency spectra, (c) computational time, and (d) model fit ($R^2$).

At $1MHz$ (figure 160), the same qualitative behavior observed at $500$ kHz is preserved but with a more pronounced sensitivity to modeling assumptions, as expected from the increased role of attenuation and non-linear distortion at higher frequencies. The linear viscous model again fails to capture the experimental response, significantly overestimating amplitude and distorting the spectral peak, resulting in a low correlation ($R^2 \approx 0.71$), consistent with the trend at $500$ kHz but slightly more degraded. In contrast, both non-linear models maintain excellent agreement with the experimental data

($R^2 \approx 0.996$), accurately reproducing both the temporal waveform and the dominant frequency content. However, compared to $500$ kHz, the differences between the two non-linear approaches become marginally more evident in the time domain, suggesting increased sensitivity to how attenuation and diffusion are represented. Computationally, all models exhibit a substantial increase in cost due to the higher frequency resolution requirements, with non-linear models remaining significantly more expensive, though still comparable to each other.

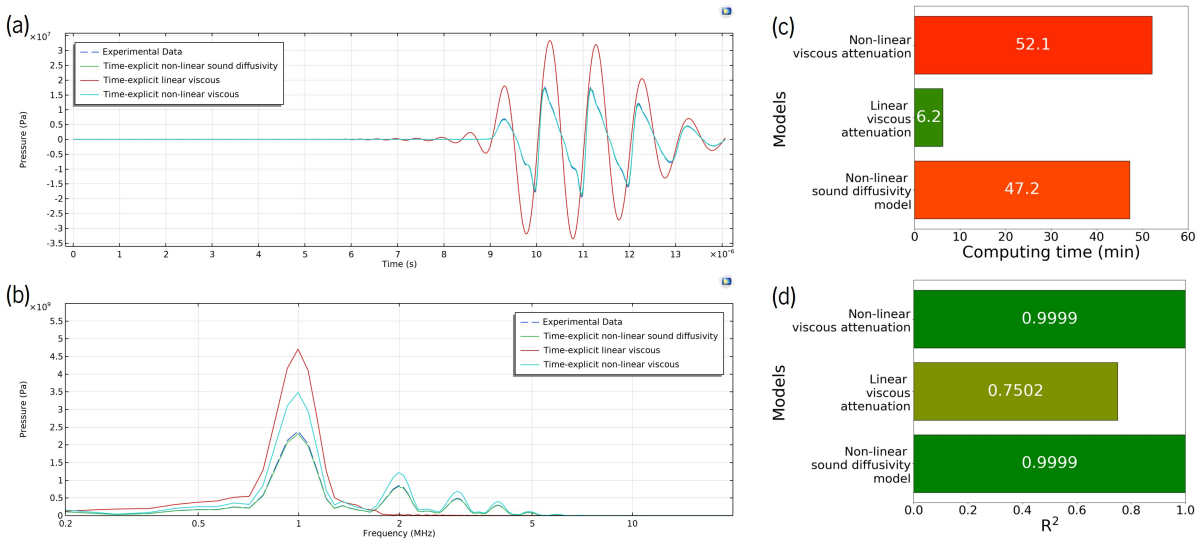



Figure 160: Experimental and simulated pressure responses for acoustic wave propagation in skin at $1$ MHz: (a) time-domain signals, (b) frequency spectra, (c) computational time, and (d) model fit ($R^2$).

At $2$ MHz (figure 161), the trends observed at $500$ kHz and $1$ MHz not only persist but become more pronounced, highlighting the increasing dominance of attenuation and non-linear propagation effects at higher frequencies. The linear viscous model continues to significantly overestimate the pressure amplitude and fails to accurately reproduce the spectral peak around the excitation frequency, resulting in poor agreement with the experimental data ($R^2 \approx 0.75$), consistent with its behavior at lower frequencies. In contrast, both non-linear models maintain a high level of accuracy, closely matching the experimental waveform and capturing the attenuated and slightly broadened spectral response, although a small reduction in correlation ($R^2 \approx 0.993$) is observed compared to $500$ kHz and $1$ MHz, suggesting increased sensitivity to modeling assumptions at this frequency. Computational cost further increases due to the higher temporal and spatial resolution required, with the non-linear viscous model remaining the most expensive, followed by the non-linear sound diffusivity model, which still provides comparable accuracy at a reduced cost.

At $4$ MHz (figure 162), the propagation regime is clearly dominated by strong attenuation and enhanced non-linear effects, further amplifying the trends observed at $2$ MHz, $1$ MHz, and $500$ kHz. The linear viscous model shows a pronounced inability to represent the experimental behavior, significantly

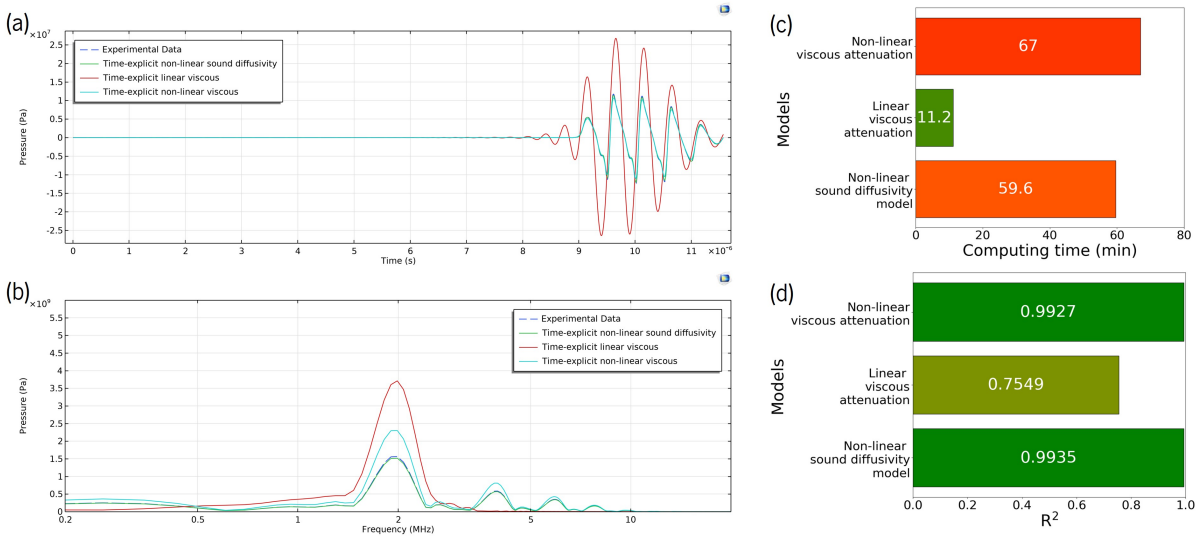



Figure 161: Experimental and simulated pressure responses for acoustic wave propagation in skin at $2$ MHz: (a) time-domain signals, (b) frequency spectra, (c) computational time, and (d) model fit ($R^2$).

overestimating both time-domain amplitudes and spectral peaks, with consistently low correlation ($R^2 \approx 0.74$), confirming that its limitations intensify with increasing frequency. The non-linear models, while still providing the best agreement, begin to show a slight degradation in accuracy compared to lower frequencies ($R^2 \approx 0.97$–$0.98$), reflecting the growing complexity of accurately capturing high-frequency propagation in dissipative biological media. In the frequency domain, the experimental response exhibits clear attenuation and spectral smoothing, which are only reproduced by the non-linear formulations, although with minor discrepancies relative to the near-perfect agreement observed at $500$ kHz and $1$ MHz. Computational cost increases substantially, reaching hour-scale simulations, with the non-linear viscous model remaining the most demanding, followed by the non-linear sound diffusivity approach, which continues to offer a favorable balance between accuracy and efficiency.

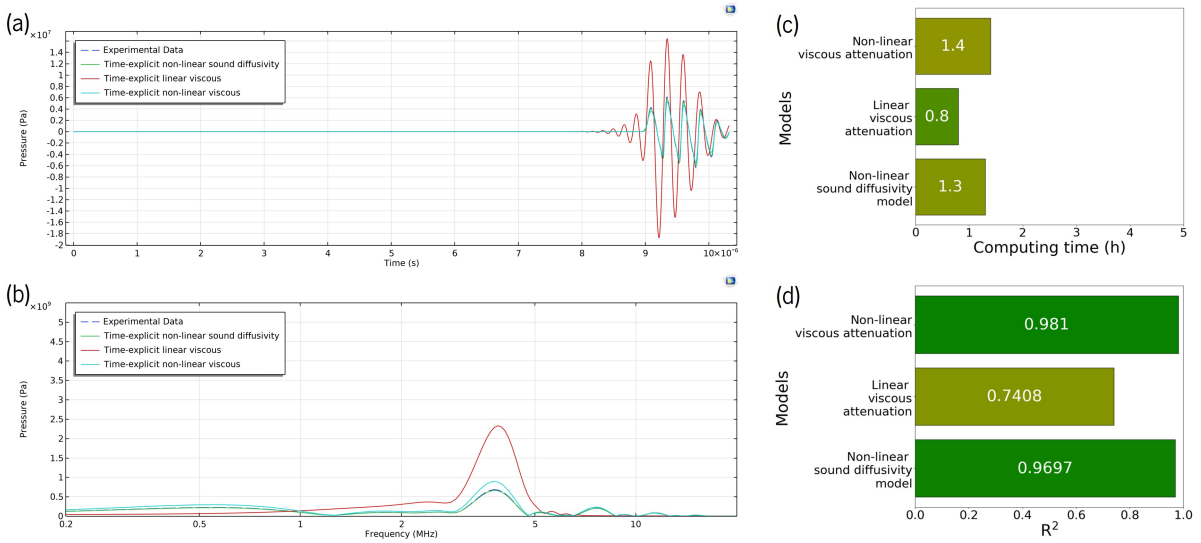



Figure 162: Experimental and simulated pressure responses for acoustic wave propagation in skin at $4$ MHz: (a) time-domain signals, (b) frequency spectra, (c) computational time, and (d) model fit ($R^2$).

At $5MHz$ (figure 163), the propagation behavior enters a regime where attenuation and non-linear effects overwhelmingly govern the response, extending the trends observed from $500$ kHz through $4$ MHz. The linear viscous model remains fundamentally inadequate, significantly overestimating amplitudes and failing to reproduce the spectral peak near the excitation frequency, with consistently low agreement ($R^2$≈$0.75$), similar to previous frequencies but now clearly detached from the experimental behavior. In contrast, the non-linear models continue to provide excellent agreement ($R^2$≈$0.99$), accurately capturing the attenuated waveform and the broadened spectral content, with only minor deviations relative to the near-perfect fits observed at lower frequencies. Compared to $4$ MHz, the accuracy of the non-linear models stabilizes rather than degrades further, suggesting that while the system is highly dissipative, the dominant physics are still well represented by the current formulations. However, the computational cost becomes significantly more restrictive, reaching several hours per simulation, reinforcing the practical limitations of high-frequency modeling. When viewed across all frequencies, a coherent pattern emerges: increasing frequency amplifies attenuation, suppresses higher harmonics, and exposes the limitations of linear assumptions, while non-linear formulations remain essential for predictive accuracy. Among them, the non-linear sound diffusivity model consistently achieves a near-equivalent representation of the full non-linear viscous behavior at a lower computational cost, making it the most viable approach for high-frequency acoustic simulations in biological tissues.

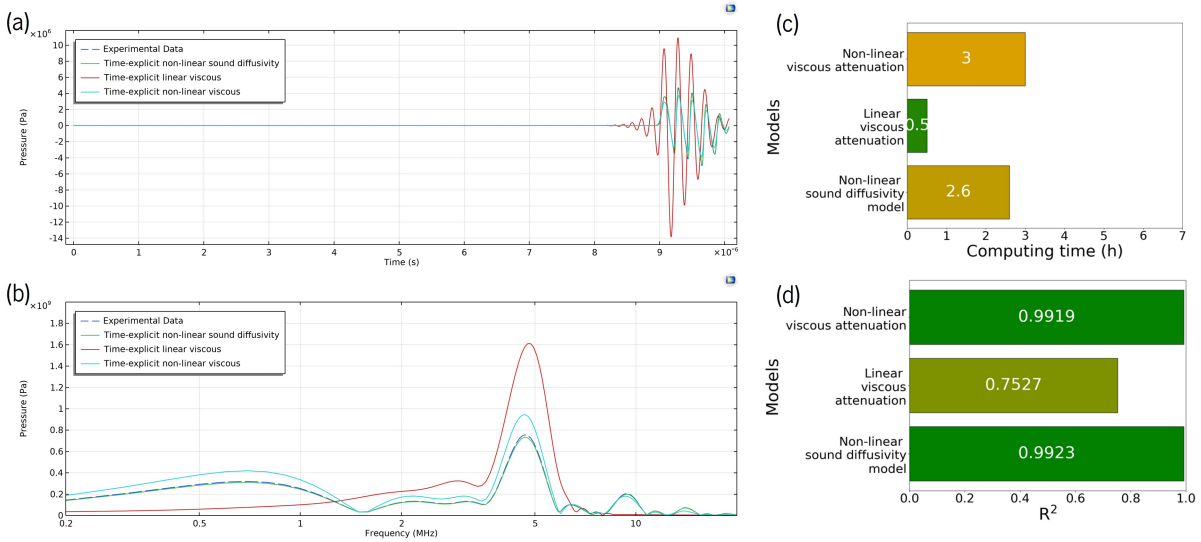



Figure 163: Experimental and simulated pressure responses for acoustic wave propagation in skin at $5$ MHz: (a) time-domain signals, (b) frequency spectra, (c) computational time, and (d) model fit ($R^2$).

### B.1.2 Adipose Tissue

For acoustic wave propagation in adipose tissue at $500$ kHz (figure 164), the overall behavior follows trends similar to those observed in skin, although with subtle differences attributable to the lower stiffness

and distinct attenuation characteristics of adipose tissue. The linear viscous model again exhibits clear limitations, overestimating the pressure amplitude and failing to accurately reproduce the spectral peak, leading to a reduced correlation with experimental data ($R^2 \approx 0.72$). In contrast, both non-linear models achieve excellent agreement ($R^2 \approx 0.998$), closely matching the waveform evolution and capturing the distribution of energy across the fundamental frequency and higher harmonics. Notably, the spectral content in adipose tissue shows a slightly more distributed harmonic structure compared to skin at the same frequency, which is effectively reproduced only by the non-linear formulations. From a computational perspective, the same hierarchy is maintained, with the linear model being significantly faster, while the non-linear viscous model is the most computationally demanding and the non-linear sound diffusivity model offering a comparable level of accuracy at a moderately reduced cost.

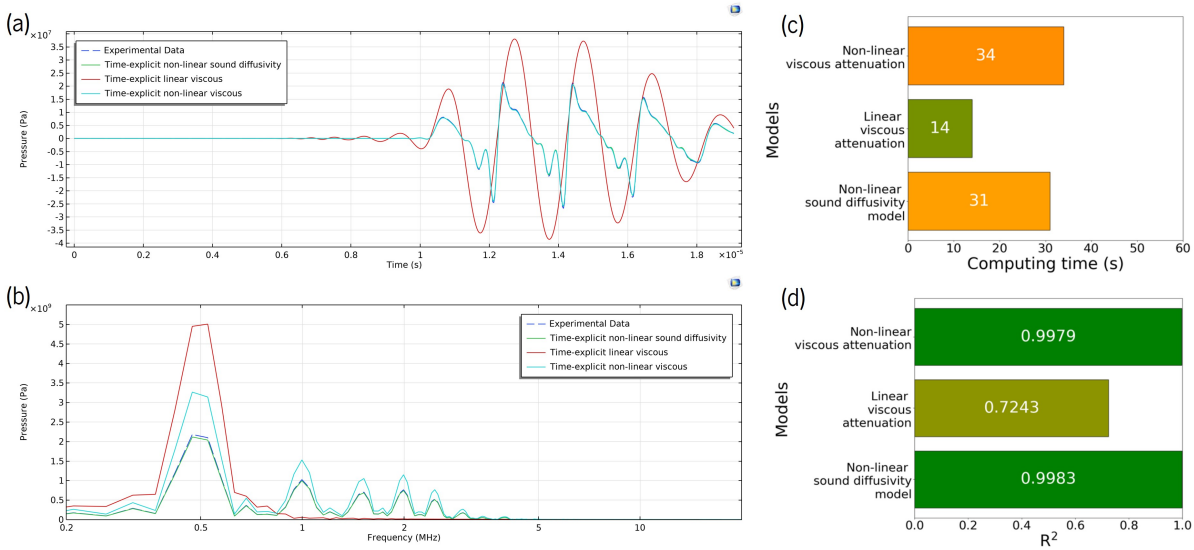



Figure 164: Experimental and simulated pressure responses for acoustic wave propagation in adipose tissue at $500$ kHz: (a) time-domain signals, (b) frequency spectra, (c) computational time, and (d) model fit ($R^2$).

At $1$ MHz (figure 165), acoustic wave propagation in adipose tissue preserves the same fundamental behavior observed at $500$ kHz, while exhibiting increased sensitivity to attenuation and non-linear effects. The linear viscous model continues to significantly overestimate the pressure amplitude and distort the spectral peak around the excitation frequency, resulting in limited agreement with experimental data ($R^2 \approx 0.75$), consistent with its performance at $500$ kHz. In contrast, both non-linear models achieve near-perfect agreement ($R^2 \approx 0.999$), accurately reproducing the temporal waveform and the spectral distribution, including the presence and relative amplitude of higher harmonics. Compared to $500$ kHz, the spectral content at $1$ MHz shows a more pronounced attenuation of higher-frequency components, reflecting the expected frequency-dependent dissipative behavior of adipose tissue, which is effectively captured only by the non-linear formulations. Computationally, all models exhibit a marked increase in cost due to the higher frequency resolution requirements, with the non-linear viscous model remaining

the most demanding and the non-linear sound diffusivity model offering a slightly more efficient alternative while maintaining equivalent accuracy.

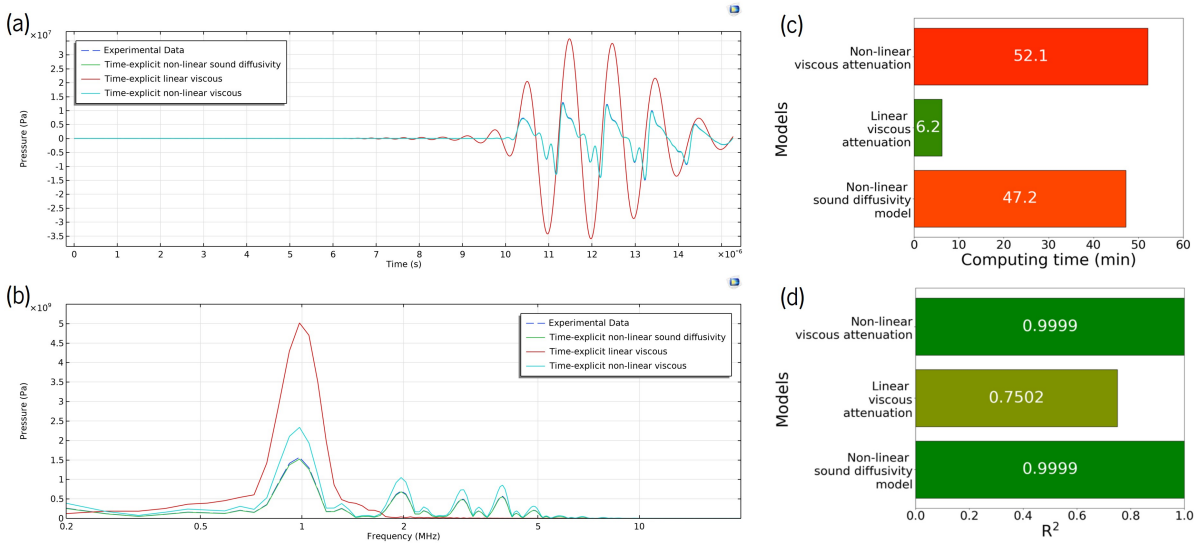



Figure 165: Experimental and simulated pressure responses for acoustic wave propagation in adipose tissue at 1 MHz: (a) time-domain signals, (b) frequency spectra, (c) computational time, and (d) model fit ($R^2$).

At $2$ MHz (figure 166), acoustic wave propagation in adipose tissue exhibits a further intensification of the trends already observed at $500$ kHz and $1$ MHz, with attenuation and non-linear effects playing an increasingly dominant role. The linear viscous model continues to provide a poor representation of the experimental response, significantly overestimating the pressure amplitude and producing a distorted spectral peak, maintaining low agreement ($R^2{\approx}0.75$), consistent across all frequencies. In contrast, both non-linear models retain excellent predictive capability ($R^2{\approx}0.998$), accurately reproducing the attenuated waveform and the spectral distribution, including the progressive smoothing and reduction of higher harmonics. Compared to $1$ MHz and especially $500$ kHz, the spectral content at $2$ MHz shows a clear attenuation-driven narrowing and damping of higher-frequency components, which is only captured by the non-linear formulations. Computational cost increases further due to the higher resolution requirements, with the non-linear viscous model remaining the most demanding and the non-linear sound diffusivity model offering a slightly more efficient alternative with comparable accuracy.

At $4$ MHz (figure 167), acoustic wave propagation in adipose tissue shows a clearer dominance of attenuation and cumulative non-linear effects than at $2$ MHz, $1$ MHz, and $500$ kHz, making the separation between the modeling approaches more evident. The linear viscous model again overestimates the time-domain amplitude and produces a broadened, exaggerated spectral peak, maintaining poor agreement with the experimental data ($R^2{\approx}0.72$), in line with its consistently limited performance across all frequencies. In contrast, both non-linear formulations still reproduce the experimental response far more accurately, although their correlation decreases relative to $2$ MHz and

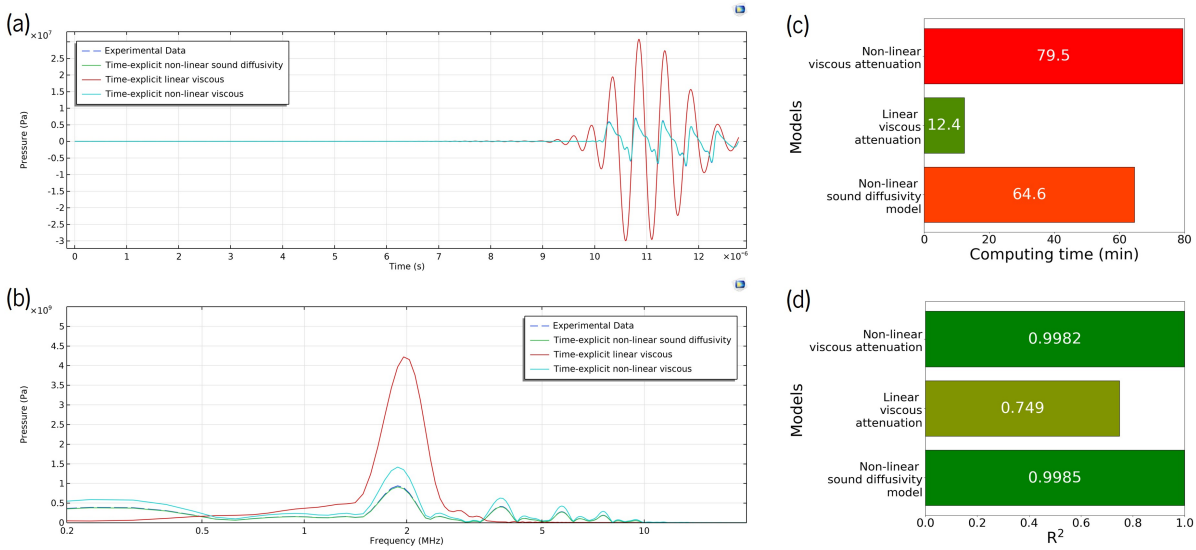



Figure 166: Experimental and simulated pressure responses for acoustic wave propagation in adipose tissue at 2 MHz: (a) time-domain signals, (b) frequency spectra, (c) computational time, and (d) model fit ($R^2$).

especially to $1$ MHz and $500$ kHz, with $R^2$ values now around $0.97$–$0.98$. This indicates that, at $4$ MHz, the propagation problem becomes more sensitive to the precise representation of dissipation and non-linear distortion, and minor discrepancies between model and experiment become more apparent. The frequency-domain response also reflects stronger attenuation and smoothing of higher-order spectral components than at lower frequencies, a trend that is captured only by the non-linear models. Computationally, the cost rises into the hour scale, with the non-linear viscous model remaining slightly more expensive than the non-linear sound diffusivity model, while the latter still provides the best balance between accuracy and efficiency.

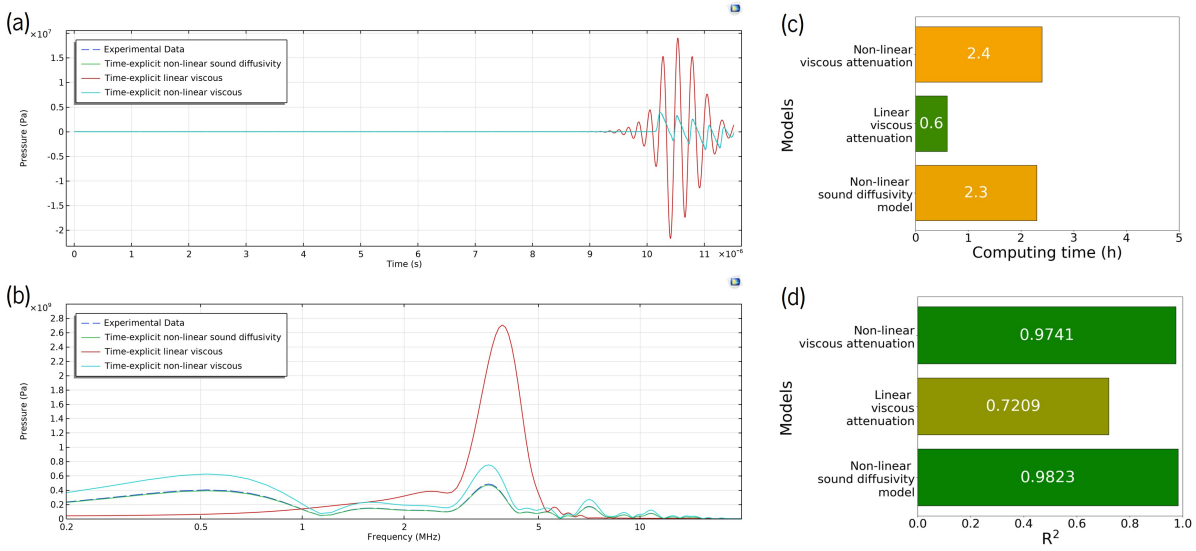



Figure 167: Experimental and simulated pressure responses for acoustic wave propagation in adipose tissue at $4$ MHz: (a) time-domain signals, (b) frequency spectra, (c) computational time, and (d) model fit ($R^2$).

At $5$ MHz (figure 168), acoustic wave propagation in adipose tissue is strongly governed by

attenuation and non-linear effects, representing the most demanding regime among all tested frequencies. The linear viscous model remains unable to capture the experimental behavior, significantly overestimating amplitudes and distorting the spectral peak, with consistently low agreement ($R^2 \approx 0.75$), unchanged from lower frequencies and confirming its systematic inadequacy. In contrast, both non-linear models maintain excellent agreement with the experimental data ($R^2 \approx 0.999$), accurately reproducing the attenuated waveform and the smoothed spectral distribution, even under severe dissipative conditions. Compared to $4$ MHz, the accuracy of the non-linear models improves slightly, indicating that while attenuation dominates, the governing physics remain well captured by the implemented formulations. Relative to $2$ MHz, $1MHz$, and $500$ kHz, the spectral response at $5$ MHz exhibits the strongest attenuation and suppression of higher harmonics, a trend consistently reproduced only by the non-linear approaches. Computational cost remains high, in the order of hours, with the non-linear viscous model being the most expensive and the non-linear sound diffusivity model offering a slightly more efficient alternative without compromising accuracy. Across all frequencies, a clear pattern emerges: increasing frequency amplifies attenuation-driven behavior and exposes the failure of linear assumptions, while non-linear formulations remain robust, with the sound diffusivity model consistently providing an optimal balance between computational efficiency and predictive capability in adipose tissue.

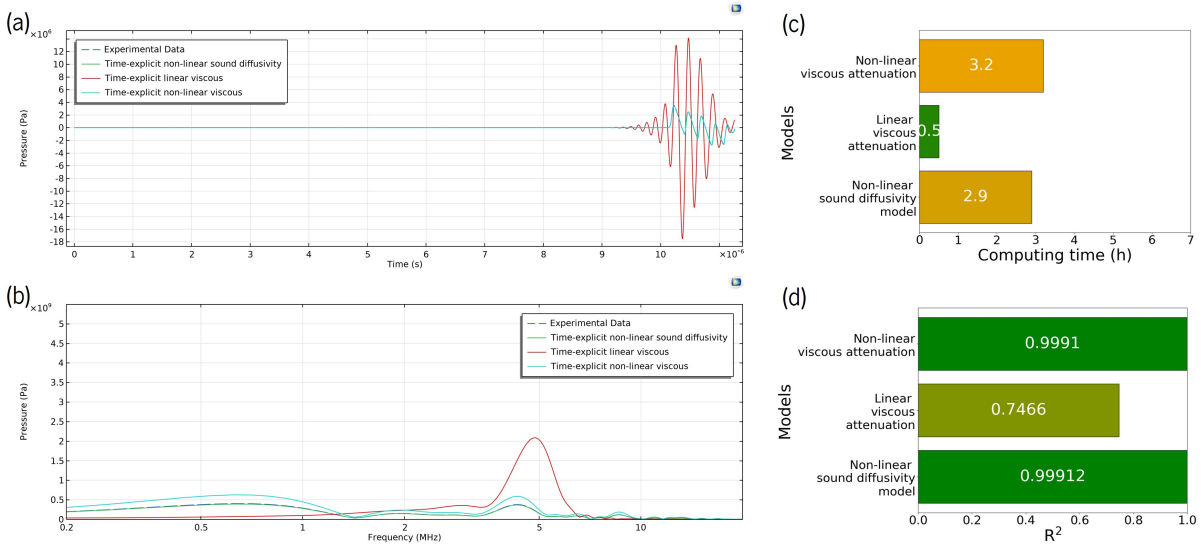



Figure 168: Experimental and simulated pressure responses for acoustic wave propagation in adipose tissue at $5$ MHz: (a) time-domain signals, (b) frequency spectra, (c) computational time, and (d) model fit ($R^2$).

### B.1.3 Skeletal Muscle ($\perp$ fibres)

For acoustic wave propagation in skeletal muscle perpendicular to the fiber direction at $500kHz$ (figure 169), the overall behavior is consistent with other soft tissues, though influenced by the anisotropic structure of muscle. The linear viscous model again overestimates the pressure amplitude and fails to accurately reproduce the spectral peak and harmonic distribution, resulting in limited agreement with experimental data ($R^2{\approx}0.73$). In contrast, both non-linear models provide a significantly improved representation ($R^2{\approx}0.997$), closely matching the waveform evolution and capturing the spectral content, including secondary harmonic components. Compared to adipose tissue at the same frequency, the spectral response in muscle appears slightly more structured, reflecting differences in mechanical properties and wave interaction with the fibrous architecture, which are better captured by the non-linear formulations. Computational performance follows the same trend observed previously, with the linear model being the least expensive and the non-linear viscous model the most demanding, while the non-linear sound diffusivity model offers a comparable level of accuracy with reduced computational cost.

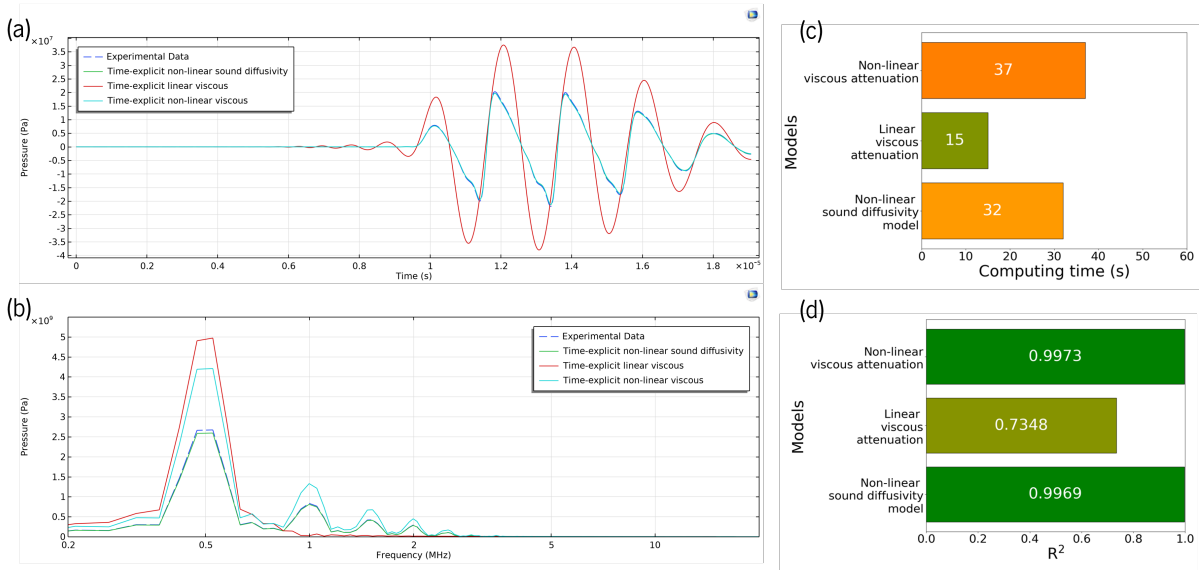



Figure 169: Experimental and simulated pressure responses for acoustic wave propagation in skeletal muscle ($\perp$ fibers) at $500$ kHz: (a) time-domain signals, (b) frequency spectra, (c) computational time, and (d) model fit ($R^2$).

At $1$ MHz (figure 170), acoustic wave propagation in skeletal muscle perpendicular to the fiber direction maintains the same qualitative trends observed at $500$ kHz, while showing increased sensitivity to attenuation and non-linear effects. The linear viscous model again overestimates the pressure amplitude and produces a distorted spectral peak, resulting in poor agreement with experimental data ($R^2{\approx}0.71$), consistent with its behavior at $500kHz$. In contrast, both non-linear models achieve excellent agreement ($R^2{\approx}0.996$–$0.997$), accurately reproducing the waveform evolution and capturing

the spectral content, including higher-order harmonics. Compared to $500$ kHz, the response at $1$ MHz exhibits stronger attenuation and a slight smoothing of the spectral peaks, reflecting the expected frequency-dependent dissipative behavior of muscle tissue, which is effectively captured only by the non-linear formulations. The influence of tissue anisotropy remains evident in the structured spectral response, although its relative impact diminishes slightly as attenuation becomes more dominant. Computational cost increases due to higher resolution requirements, with the non-linear viscous model remaining the most expensive and the non-linear sound diffusivity model offering a more efficient alternative with comparable accuracy.

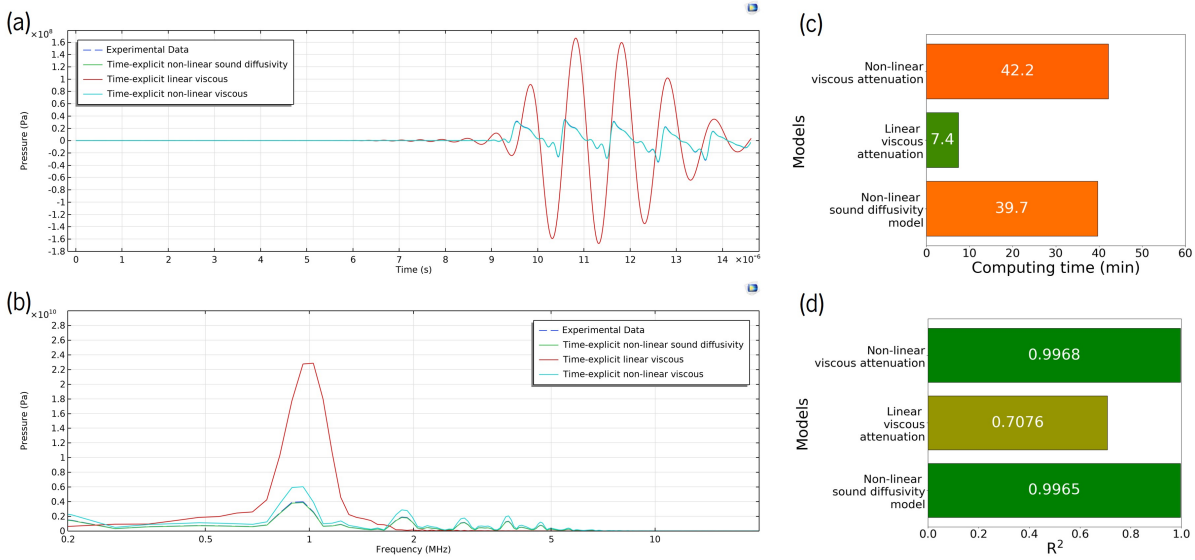



Figure 170: Experimental and simulated pressure responses for acoustic wave propagation in skeletal muscle (perpendicular to fibers) at $1$ MHz: (a) time-domain signals, (b) frequency spectra, (c) computational time, and (d) model fit ($R^2$).

At $2$ MHz (figure 171), acoustic wave propagation in skeletal muscle perpendicular to the fiber direction shows a further increase in attenuation-dominated and non-linear behavior relative to $1$ MHz and $500$ kHz. The linear viscous model remains unable to reproduce the experimental response, markedly overestimating the pressure amplitude and broadening the main spectral peak, which results in poor agreement with the measurements ($R^2 \approx 0.71$), essentially maintaining the same limitation already observed at the lower frequencies. In contrast, both non-linear models continue to provide excellent agreement ($R^2 \approx 0.995$–$0.996$), accurately reproducing the attenuated waveform and the spectral distribution, including the reduced amplitude and smoothing of higher-order components. Compared with $1$ MHz and especially $500$ kHz, the $2$ MHz response exhibits stronger damping and a more concentrated spectral behavior around the excitation frequency, indicating the increasing dominance of dissipative mechanisms over the more structured harmonic response observed at lower frequencies. Computational cost also rises substantially, with the non-linear viscous model remaining the

most expensive and the non-linear sound diffusivity model preserving a slightly lower computational burden while maintaining comparable predictive accuracy.

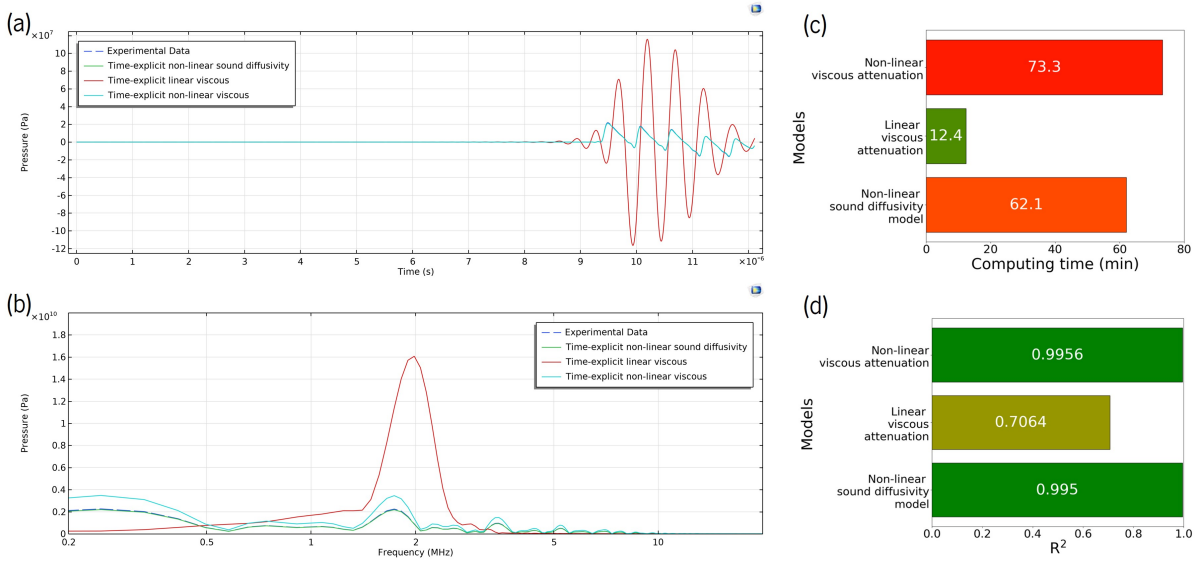



Figure 171: Experimental and simulated pressure responses for acoustic wave propagation in skeletal muscle (perpendicular to fibers) at 2 MHz: (a) time-domain signals, (b) frequency spectra, (c) computational time, and (d) model fit ($R^2$).

At $4$ MHz (figure 172), acoustic wave propagation in skeletal muscle perpendicular to the fiber direction is strongly governed by attenuation and non-linear effects, extending the trends observed at $2$ MHz, $1$ MHz, and $500$ kHz. The linear viscous model shows a pronounced inability to reproduce the experimental response, significantly overestimating the pressure amplitude and generating an exaggerated spectral peak, resulting in the lowest agreement among the tested frequencies ($R^2 \approx 0.68$), indicating a progressive degradation compared to its already limited performance at lower frequencies. In contrast, both non-linear models continue to capture the overall waveform and spectral behavior, although with a noticeable reduction in accuracy ($R^2 \approx 0.97–0.99$) relative to $2$ MHz and especially to $1$ MHz and $500$ kHz, reflecting the increased sensitivity of high-frequency propagation to the precise modeling of dissipation and non-linear distortion. The frequency-domain response shows stronger attenuation and smoothing of higher-order components compared to lower frequencies, reducing the structured harmonic content observed at $500$ kHz and $1$ MHz, and indicating that dissipative mechanisms dominate over anisotropic effects in this regime. Computational cost increases further, reaching hour-scale simulations, with the non-linear viscous model remaining the most demanding and the non-linear sound diffusivity model providing a slightly more efficient alternative while preserving comparable predictive capability.

At $5$ MHz (figure 173), acoustic wave propagation in skeletal muscle perpendicular to the fiber direction reaches a regime strongly dominated by attenuation and non-linear effects, extending and intensifying the trends observed from $500kHz$ through $4$ MHz. The linear viscous model remains fundamentally inadequate, significantly overestimating time-domain amplitudes and producing an

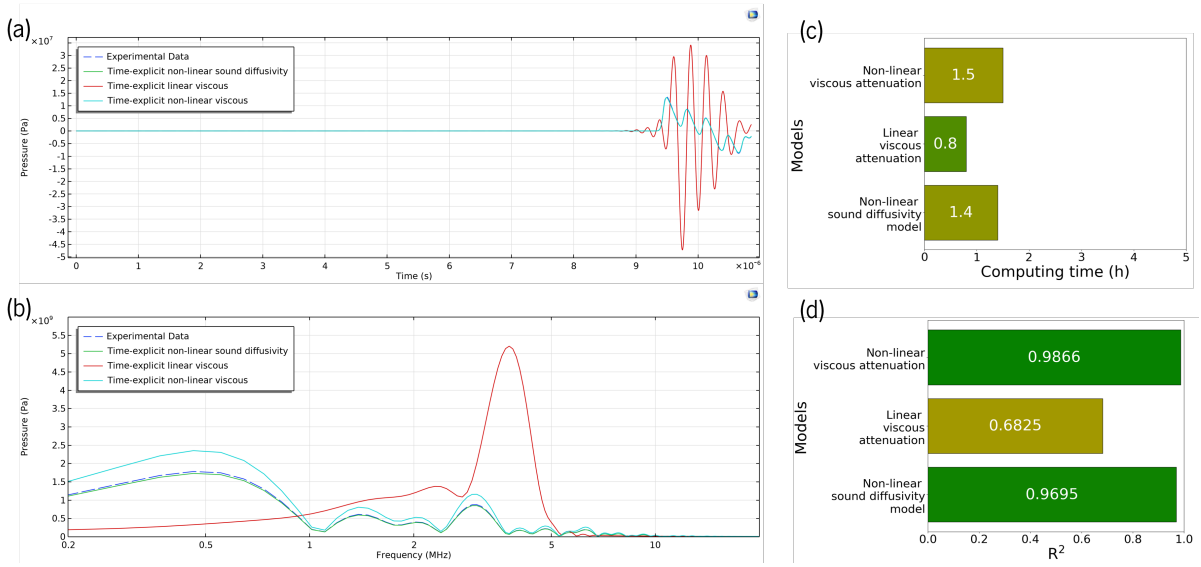



Figure 172: Experimental and simulated pressure responses for acoustic wave propagation in skeletal muscle (perpendicular to fibers) at $4$ MHz: (a) time-domain signals, (b) frequency spectra, (c) computational time, and (d) model fit ($R^2$).

exaggerated and shifted spectral peak, with persistently low agreement ($R^2 \approx 0.70$), consistent across all frequencies but increasingly disconnected from the experimental response. In contrast, both non-linear models continue to capture the essential physics, maintaining high agreement ($R^2 \approx 0.994$), although with a slight reduction in accuracy compared to $4$ MHz, indicating growing sensitivity to model assumptions at this frequency. The frequency-domain response shows strong attenuation and substantial smoothing of higher-order components, with the harmonic structure observed at $500$ kHz and $1$ MHz largely suppressed, confirming that dissipative mechanisms dominate over anisotropic effects in this regime. Compared to $4$ MHz, $2$ MHz, $1$ MHz, and $500$ kHz, this represents the most attenuated and least structured spectral response, while still being well approximated by the non-linear formulations. Computational cost remains high, at the hour scale, with the non-linear viscous model being the most demanding and the non-linear sound diffusivity model offering a slightly more efficient alternative with comparable accuracy. Overall, the progression across frequencies demonstrates a clear transition from structured, moderately non-linear propagation at lower frequencies to highly attenuated, diffusion-dominated behavior at $5$ MHz, where non-linear modeling remains essential and linear assumptions fail entirely.

### B.1.4 Skeletal Muscle ($\parallel$ fibers)

For acoustic wave propagation in skeletal muscle parallel to the fiber direction at $500$ kHz (figure 174), the results show that the linear viscous model remains unable to accurately reproduce the experimental response, as it clearly overestimates the pressure amplitude in the time domain and exaggerates the

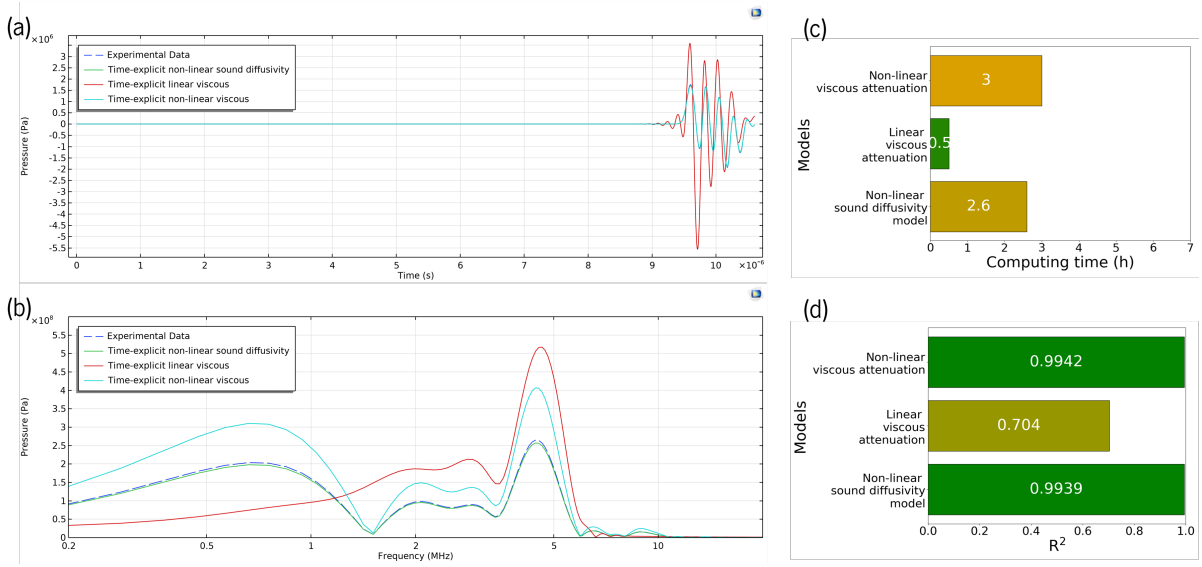



Figure 173: Experimental and simulated pressure responses for acoustic wave propagation in skeletal muscle (perpendicular to fibers) at $5$ MHz: (a) time-domain signals, (b) frequency spectra, (c) computational time, and (d) model fit ($R^2$).

main spectral peak, leading to substantially lower agreement with the measurements ($R^2 \approx 0.75$). In contrast, both non-linear models provide a much closer representation of the experimental signal, with $R^2$ values close to $0.997$, accurately capturing both the waveform evolution and the dominant spectral content. Compared with the previously discussed perpendicular-to-fibers case at the same frequency, the parallel configuration appears less spectrally structured, with a response more strongly concentrated around the fundamental component and with less pronounced secondary peaks, suggesting a directional influence of the muscle architecture on wave propagation. The computational trend is unchanged, with the linear model being the least expensive, the non-linear viscous attenuation model the most demanding, and the non-linear sound diffusivity model offering nearly identical predictive accuracy at a slightly lower computational cost.

At $1$ MHz (figure 175), acoustic wave propagation in skeletal muscle parallel to the fiber direction follows the same general trends observed at $500$ kHz, with an increased influence of attenuation and non-linear effects. The linear viscous model continues to overestimate the pressure amplitude and exaggerate the dominant spectral peak, leading to poor agreement with the experimental data ($R^2 \approx 0.71$), consistent with its performance at $500$ kHz. In contrast, both non-linear models maintain high accuracy ($R^2 \approx 0.996$), successfully reproducing the waveform evolution and capturing the main spectral content. Compared to $500$ kHz, the $1$ MHz response exhibits a slightly more attenuated and smoother spectral distribution, with reduced prominence of secondary harmonic components, indicating stronger dissipative effects along the fiber direction. The directional influence of the muscle structure remains evident, with the parallel configuration showing a more concentrated spectral response than the perpendicular case. Computational cost increases due to higher frequency resolution requirements, with

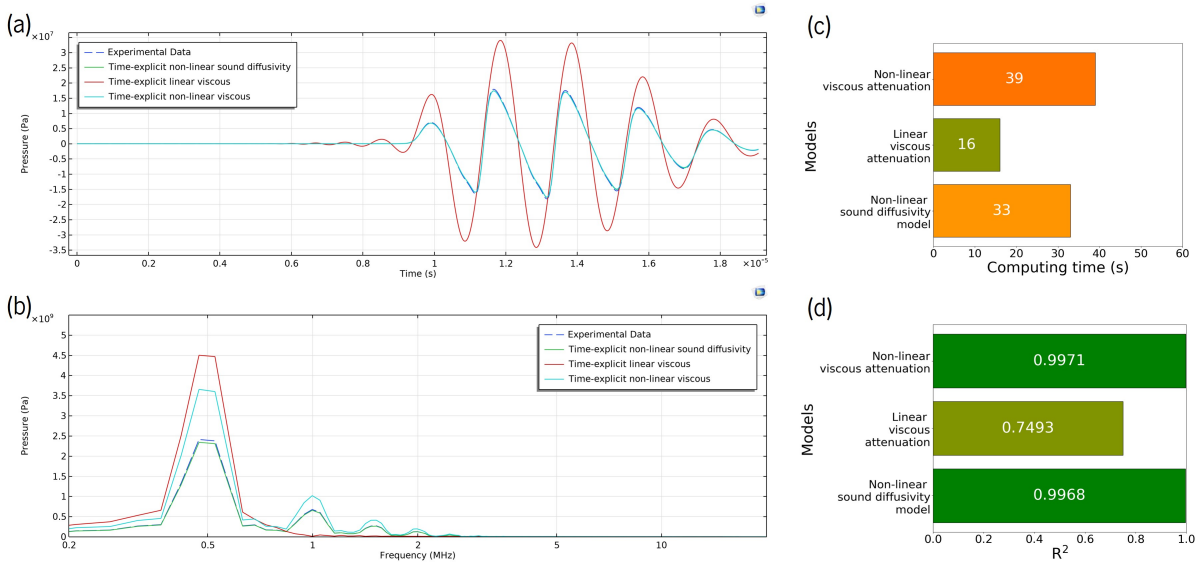



Figure 174: Experimental and simulated pressure responses for acoustic wave propagation in skeletal muscle (parallel to fibers) at $500$ kHz: (a) time-domain signals, (b) frequency spectra, (c) computational time, and (d) model fit ($R^2$).

the non-linear viscous model remaining the most expensive and the non-linear sound diffusivity model providing a more efficient alternative while preserving comparable predictive performance.

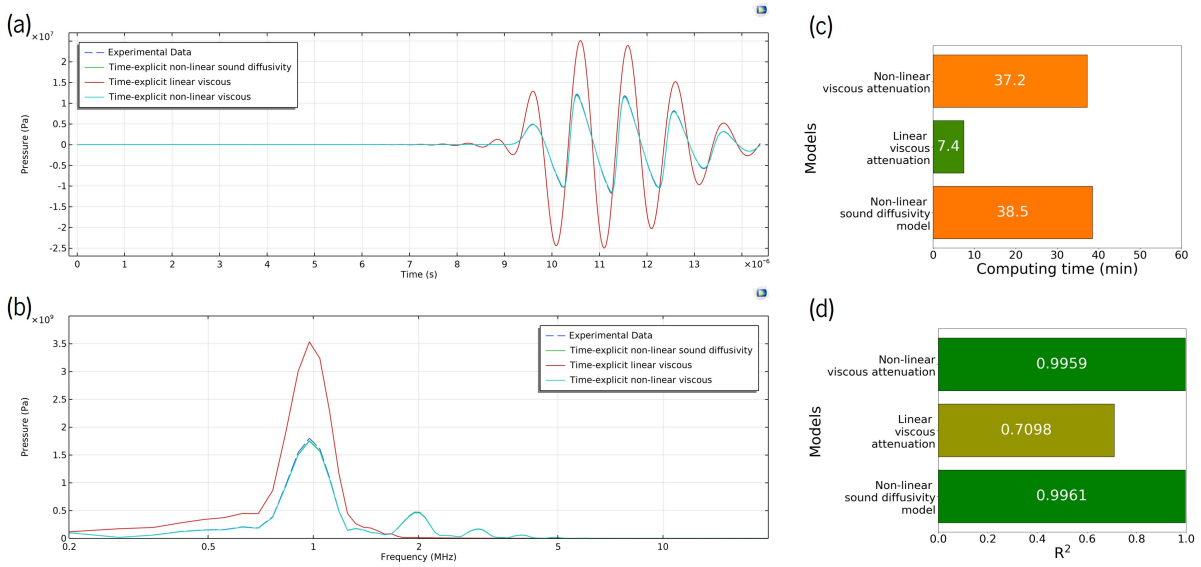



Figure 175: Experimental and simulated pressure responses for acoustic wave propagation in skeletal muscle (parallel to fibers) at $1$ MHz: (a) time-domain signals, (b) frequency spectra, (c) computational time, and (d) model fit ($R^2$).

At $2$ MHz (figure 176), acoustic wave propagation in skeletal muscle parallel to the fiber direction shows a clear progression from the behavior observed at $500$ kHz and $1$ MHz, with attenuation and non-linear effects becoming more dominant. The linear viscous model continues to overestimate the pressure amplitude and produce an exaggerated spectral peak, resulting in poor agreement with the experimental data ($R^2 \approx 0.71$), consistent with its systematic limitations across frequencies. In contrast, both non-linear models maintain high accuracy ($R^2 \approx 0.994$–$0.995$), successfully reproducing the waveform and capturing the main spectral characteristics, including the attenuation-induced smoothing of the response.

Compared to $1$ MHz and especially to $500$ kHz, the spectral content at $2$ MHz is more concentrated around the excitation frequency, with reduced prominence of higher-order harmonics, reflecting stronger dissipative effects along the fiber direction. The anisotropic influence remains present but is increasingly overshadowed by attenuation as frequency increases. Computational cost rises accordingly, with the non-linear viscous model remaining the most demanding and the non-linear sound diffusivity model offering a slightly more efficient alternative while preserving comparable predictive performance.

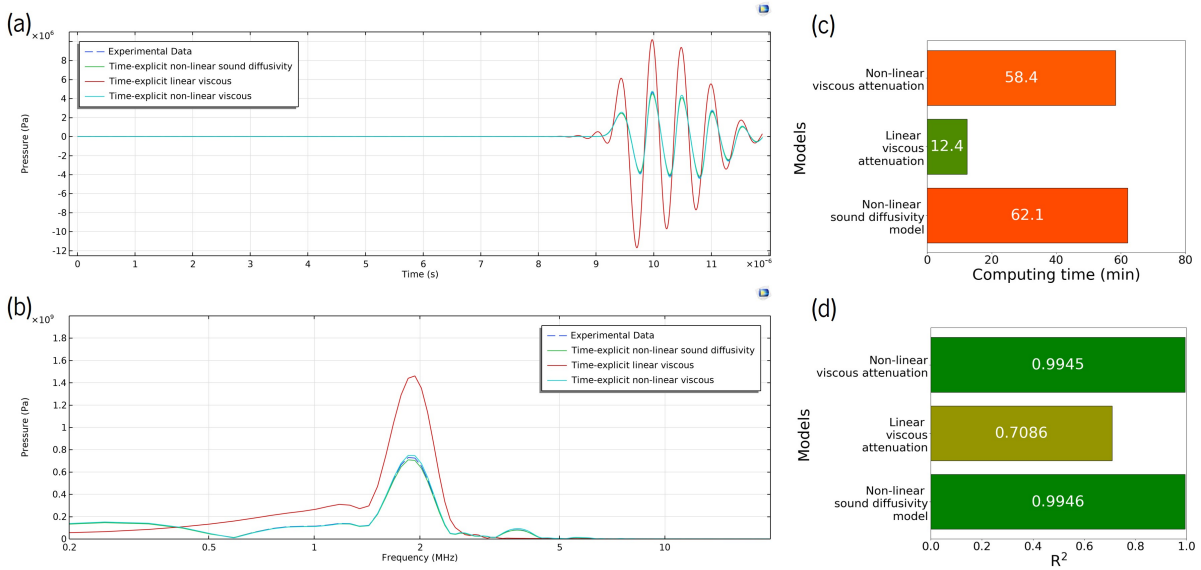



Figure 176: Experimental and simulated pressure responses for acoustic wave propagation in skeletal muscle (parallel to fibers) at $2$ MHz: (a) time-domain signals, (b) frequency spectra, (c) computational time, and (d) model fit ($R^2$).

At $4$ MHz (figure 177), acoustic wave propagation in skeletal muscle parallel to the fiber direction exhibits a markedly more attenuated and spectrally redistributed response than at $2$ MHz, $1$ MHz, and $500$ kHz, confirming the stronger dominance of dissipative mechanisms at higher frequency. The linear viscous model again fails to reproduce the experimental behavior, showing clear mismatch in both the time-domain amplitude and the frequency-domain distribution, with substantially lower agreement ($R^2 \approx 0.69$). In contrast, the two non-linear models remain far more accurate, with the non-linear viscous attenuation model providing the best overall fit ($R^2 \approx 0.98$) and the non-linear sound diffusivity model also maintaining high agreement, though with a slightly larger deviation than at lower frequencies. Compared with $2$ MHz and below, the spectrum is less concentrated around a single sharp fundamental peak and instead shows a broader redistributed response over the lower-frequency range, while the time-domain signal remains strongly attenuated and temporally compact. This indicates that, in the parallel-to-fiber direction, high-frequency propagation becomes increasingly sensitive to the precise representation of attenuation and non-linear losses. Computational cost also rises to the hour scale, with both non-linear models becoming much more demanding than the linear one.

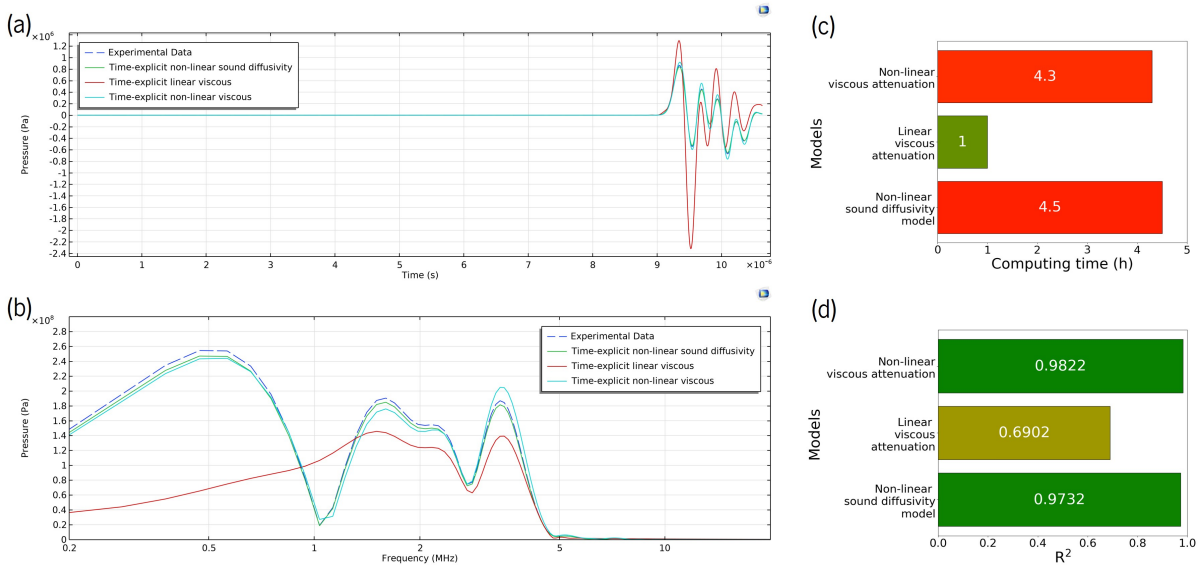



Figure 177: Experimental and simulated pressure responses for acoustic wave propagation in skeletal muscle (parallel to fibers) at $4$ MHz: (a) time-domain signals, (b) frequency spectra, (c) computational time, and (d) model fit ($R^2$).

At $5$ MHz (figure 178), acoustic wave propagation in skeletal muscle parallel to the fiber direction reaches a highly attenuated regime, further extending the trends observed from $500$ kHz through $4$ MHz. The linear viscous model continues to significantly misrepresent the experimental response, overestimating the pressure amplitude and failing to capture the spectral distribution, resulting in consistently low agreement ($R^2 \approx 0.71$). In contrast, both non-linear models maintain strong predictive capability ($R^2 \approx 0.993$), accurately reproducing the attenuated waveform and the redistributed spectral content. Compared with $4$ MHz, the accuracy of the non-linear models decreases slightly, indicating increased sensitivity to the modeling of dissipation and non-linear effects at this frequency. Relative to $2$ MHz, $1$ MHz, and $500$ kHz, the spectral response at $5$ MHz is broader and more diffused, with energy concentrated at lower frequencies and a strong suppression of higher-order harmonics, reflecting dominant attenuation along the fiber direction. The time-domain response is correspondingly more compact and damped. Computational cost remains high, in the order of several hours, with the non-linear viscous model being the most expensive and the non-linear sound diffusivity model offering a slightly more efficient alternative with comparable accuracy. Overall, the comparison across all frequencies confirms a clear transition toward attenuation-controlled propagation at high frequencies, where anisotropic effects become less pronounced and non-linear modeling remains essential for accurate representation.

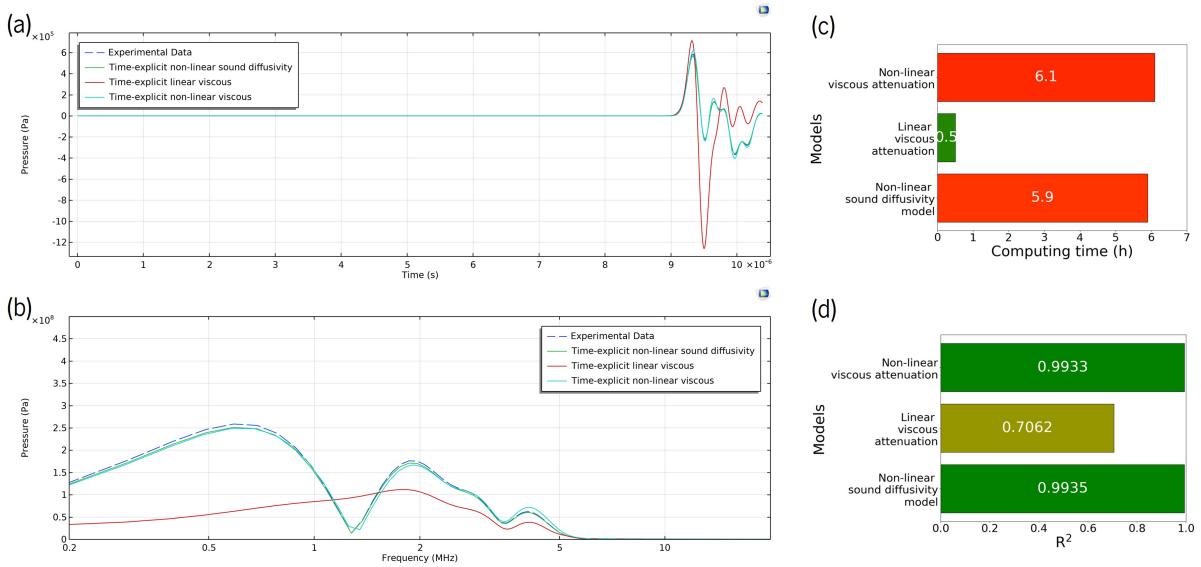



Figure 178: Experimental and simulated pressure responses for acoustic wave propagation in skeletal muscle (parallel to fibers) at $5$ MHz: (a) time-domain signals, (b) frequency spectra, (c) computational time, and (d) model fit ($R^2$).

### B.1.5 Tendon

For acoustic wave propagation in tendon at $500$ kHz (figure 179), the results show a well-defined waveform and a strongly concentrated spectral response around the excitation frequency, consistent with the relatively low attenuation and high structural organization of the tissue. The linear viscous model significantly overestimates the pressure amplitude in the time domain and produces an exaggerated spectral peak, resulting in poor agreement with experimental data ($R^2 \approx 0.62$). In contrast, both non-linear models closely match the experimental signal, accurately reproducing the waveform evolution and the dominant spectral content, with high correlation ($R^2 \approx 0.99$). The frequency-domain response is sharply peaked near$0.5MHz$ with limited higher-order harmonic content, indicating that, at this frequency, tendon exhibits a more coherent and less diffusive propagation behavior compared to softer tissues. Computational performance follows the expected trend, with the linear model being the least expensive, while the non-linear viscous attenuation model requires the highest computational effort, and the non-linear sound diffusivity model provides a comparable level of accuracy with slightly reduced cost.

At $1$ MHz (figure 180), acoustic wave propagation in tendon exhibits a pronounced frequency-centered response with increased attenuation and dispersion compared to lower frequencies, while still maintaining a coherent waveform structure. In the time domain, the linear viscous model substantially overestimates the pressure amplitude and fails to capture the damping behavior, whereas both non-linear models closely reproduce the experimental waveform, with only minor deviations in later oscillations. In the frequency domain, a dominant peak is observed near $1$ MHz, accompanied by limited secondary content, indicating

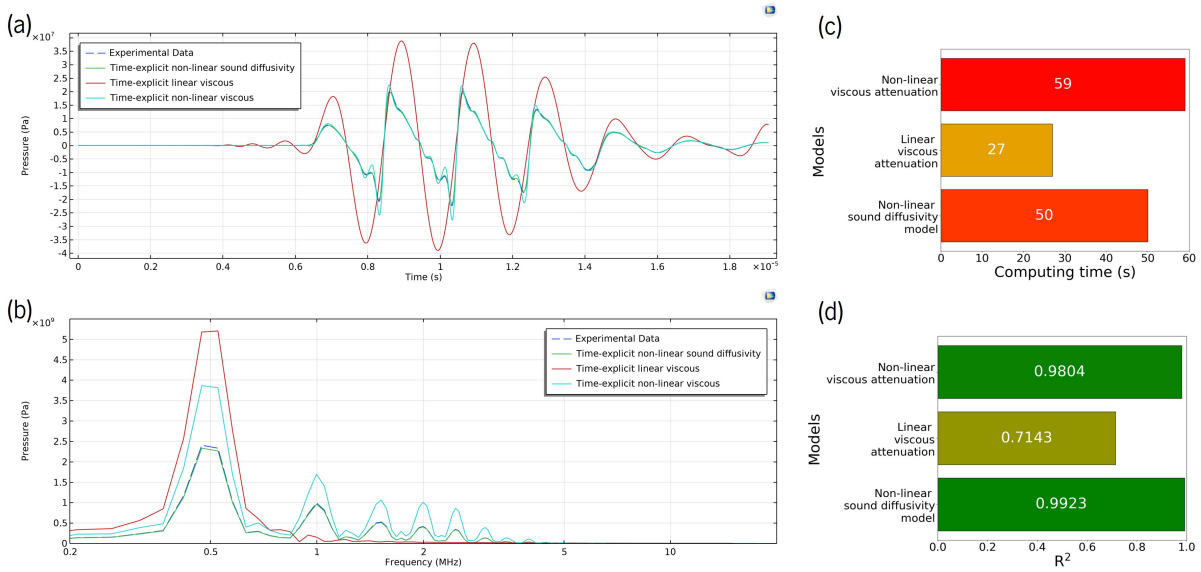



Figure 179: Experimental and simulated pressure responses for acoustic wave propagation in tendon at $500$ kHz: (a) time-domain signals, (b) frequency spectra, (c) computational time, and (d) model fit ($R^2$).

that energy remains relatively concentrated despite some broadening due to microstructural interactions. The linear viscous model produces an exaggerated and overly sharp peak, while the non-linear sound diffusivity and non-linear viscous attenuation models align closely with the experimental amplitude and bandwidth. This is reflected in the goodness-of-fit values, where both non-linear approaches achieve excellent agreement ($R^2 \approx 0.99$), in contrast to the significantly lower performance of the linear model ($R^2 \approx 0.57$). Computationally, the linear viscous model remains the most efficient ( $7.4$ min), while both non-linear models require longer but comparable times ( $37$ min).

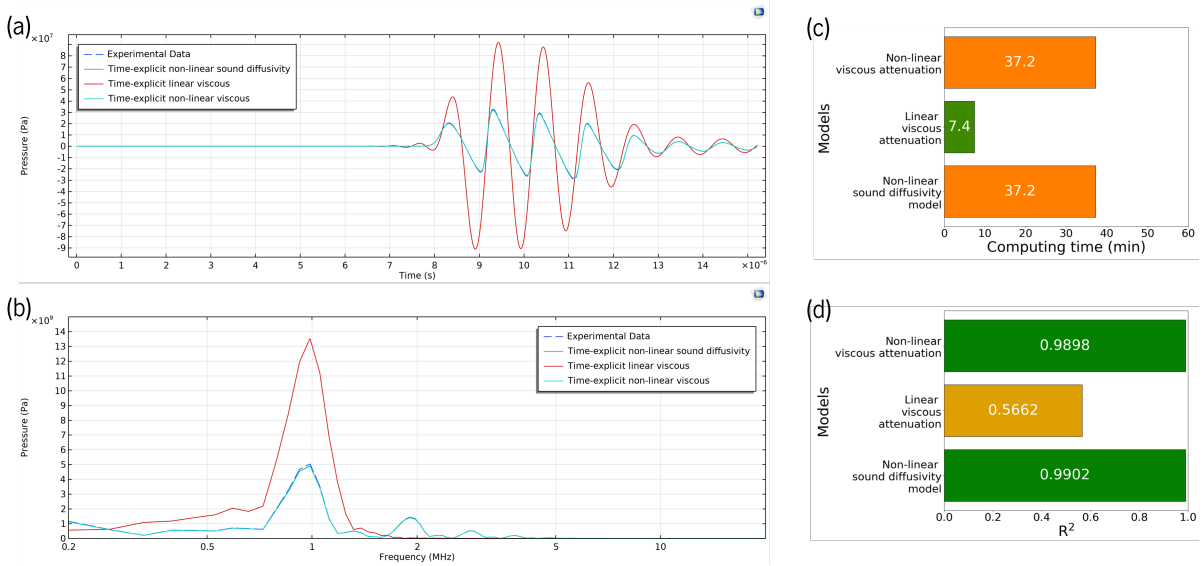



Figure 180: Experimental and simulated pressure responses for acoustic wave propagation in tendon at $1$ MHz: (a) time-domain signals, (b) frequency spectra, (c) computational time, and (d) model fit ($R^2$).

At $2$ MHz (figure 181), acoustic wave propagation in tendon shows a clear intensification of frequency-dependent effects compared to $1$ MHz and $500$ kHz, with increased attenuation, stronger dispersion, and

a more localized spectral response. In the time domain, the waveform becomes more rapidly damped and slightly more distorted, while the linear viscous model again overpredicts the amplitude and fails to capture the correct decay behavior; in contrast, both non-linear models closely follow the experimental signal, preserving both amplitude and phase with high fidelity. In the frequency domain, the dominant peak shifts to around $2$ MHz and becomes sharper and more pronounced than at $1$ MHz, indicating stronger energy concentration at the excitation frequency, while secondary components are further suppressed relative to $500$ kHz, reflecting reduced low-frequency contributions. The linear viscous model produces an exaggerated peak and poor spectral agreement, whereas the non-linear sound diffusivity and non-linear viscous attenuation models accurately reproduce both the peak amplitude and spectral bandwidth. This is consistent with the goodness-of-fit values, where both non-linear models maintain excellent agreement ($R^2 \approx 0.99$), while the linear model drops significantly ($R^2 \approx 0.57$). Computational cost remains similar to the $1$ MHz case ( $37$ min for non-linear models versus $7.4$ min for the linear model).

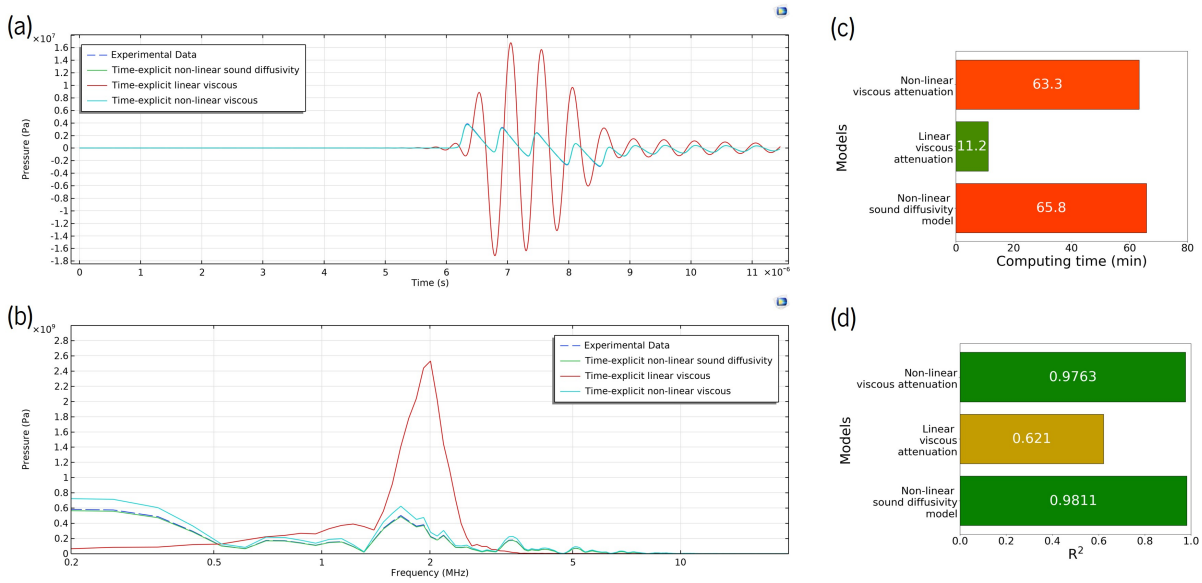



Figure 181: Experimental and simulated pressure responses for acoustic wave propagation in tendon at $2$ MHz: (a) time-domain signals, (b) frequency spectra, (c) computational time, and (d) model fit ($R^2$).

At $4$ MHz (figure 182), acoustic wave propagation in tendon clearly transitions into a strongly attenuation-dominated regime, with pronounced damping, reduced waveform coherence, and significant spectral reshaping compared to $2$ MHz, $1$ MHz, and $500$ kHz. In the time domain, the signal exhibits rapid decay and increased distortion, with the linear viscous model severely overestimating peak amplitudes and failing to capture the correct phase and damping behavior, while both non-linear models remain closely aligned with the experimental response despite minor deviations at later times. In the frequency domain, the energy distribution broadens substantially and shifts away from a simple dominant peak, with the main spectral content becoming less sharply defined than at lower frequencies,

indicating stronger scattering and internal friction mechanisms within the tendon structure; the linear model again produces an unrealistic, overly smooth and amplified response, whereas the non-linear models better reproduce both the magnitude and spread of the experimental spectrum. This is reflected in the reduced but still high goodness-of-fit values for the non-linear approaches ($R^2 \approx 0.96$), compared to the significantly poorer performance of the linear model ($R^2 \approx 0.55$). Computational cost remains comparable to lower-frequency cases ( $1.3$–$1.4$ h for non-linear models versus $0.8$ h for the linear model), but with diminishing gains in predictive simplicity.

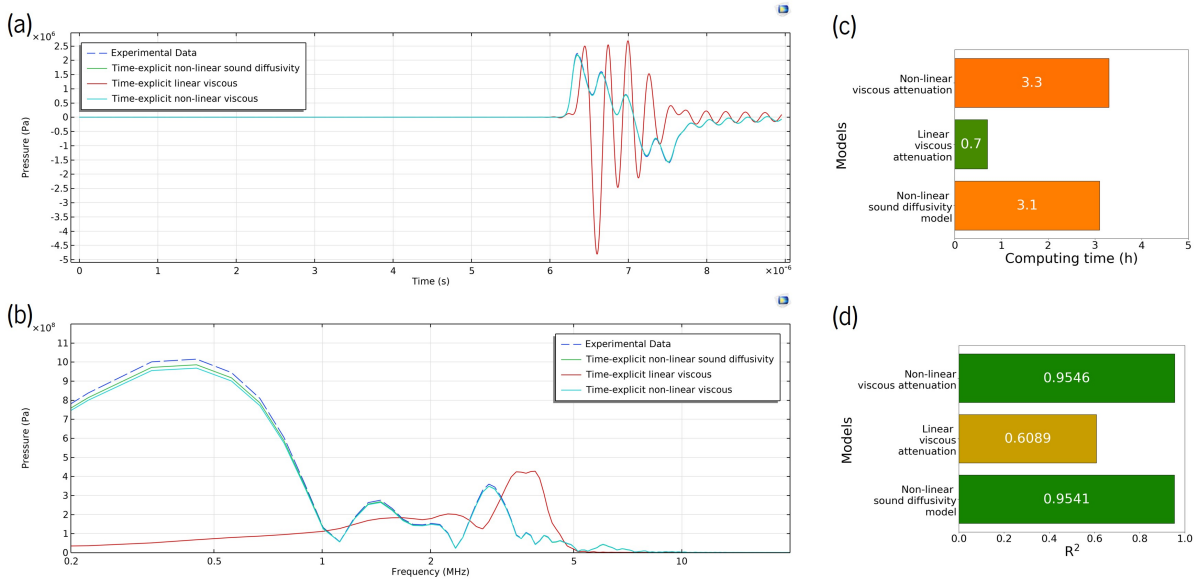



Figure 182: Experimental and simulated pressure responses for acoustic wave propagation in tendon at $4$ MHz: (a) time-domain signals, (b) frequency spectra, (c) computational time, and (d) model fit ($R^2$).

At $5$ MHz (figure 183), acoustic wave propagation in tendon remains strongly governed by attenuation and non-linear effects, continuing the high-frequency behavior observed at $4$ MHz while showing a slightly improved agreement between the non-linear models and the experimental response. In the time domain, the signal is highly damped and temporally compact, and the linear viscous model again fails to reproduce the waveform, strongly overestimating the negative pressure excursion and misrepresenting the decay pattern, whereas both non-linear formulations closely follow the measured response. In the frequency domain, the spectrum is broadly redistributed, with most energy concentrated at lower frequencies and only reduced secondary peaks around higher harmonics, confirming that at $5$ MHz the propagating wave is heavily filtered by the dissipative nature of the tendon. This trend is more pronounced than at $2$ MHz and $1$ MHz, and markedly different from the sharper, more coherent response observed at $500$ kHz, while remaining qualitatively similar to the strongly attenuated regime already seen at $4$ MHz. The goodness-of-fit values show that both non-linear models still provide excellent agreement ($R^2 \approx 0.987$–$0.988$), substantially outperforming the linear model

($R^2 \approx 0.56$), although the accuracy remains slightly below the values obtained at $1$–$2$ MHz. Computational cost also reaches its highest level, with the non-linear models requiring about $5.6$–$6.2$ h compared to only about $0.4$ h for the linear model. Overall, compared with $4$ MHz, $2$ MHz, $1$ MHz, and $500$ kHz, the $5$ MHz case confirms a clear transition toward a severely attenuation-dominated propagation regime in tendon, where non-linear diffusion and viscous mechanisms control the response and must be included for reliable prediction.

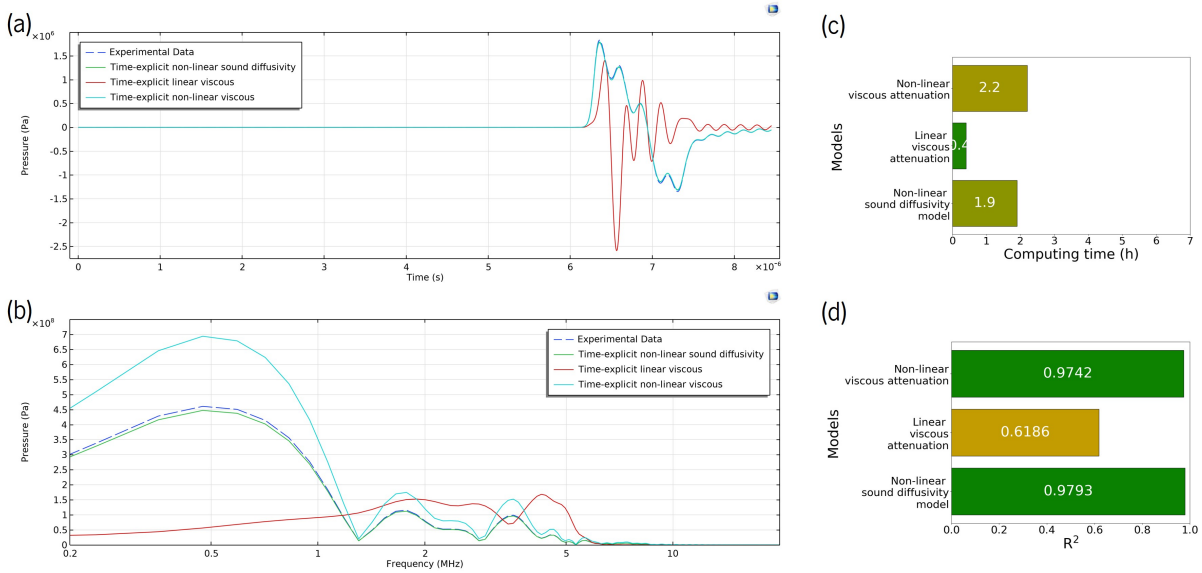



Figure 183: Experimental and simulated pressure responses for acoustic wave propagation in tendon at $5$ MHz: (a) time-domain signals, (b) frequency spectra, (c) computational time, and (d) model fit ($R^2$).

### B.1.6 Ligament

For acoustic wave propagation in ligament at $500$ kHz (figure 184), the response is characterized by a well-defined oscillatory waveform and a dominant spectral peak centered near the excitation frequency, consistent with the organized fibrous nature of the tissue. The linear viscous model clearly overestimates the pressure amplitude in the time domain and produces an exaggerated spectral peak, leading to only moderate agreement with the experimental data ($R^2 \approx 0.63$). In contrast, both non-linear models reproduce the measured response very closely, capturing both the waveform evolution and the narrow frequency-domain peak with high fidelity, as reflected by the near-unity coefficients of determination ($R^2 \approx 0.998$–$0.999$). The spectrum is strongly concentrated around $500$ kHz, with only limited secondary content, indicating relatively coherent propagation at this frequency. Computationally, the linear viscous model remains the fastest, while the non-linear viscous attenuation model is the most expensive, and the non-linear sound diffusivity model achieves nearly identical predictive accuracy at a somewhat lower computational cost.

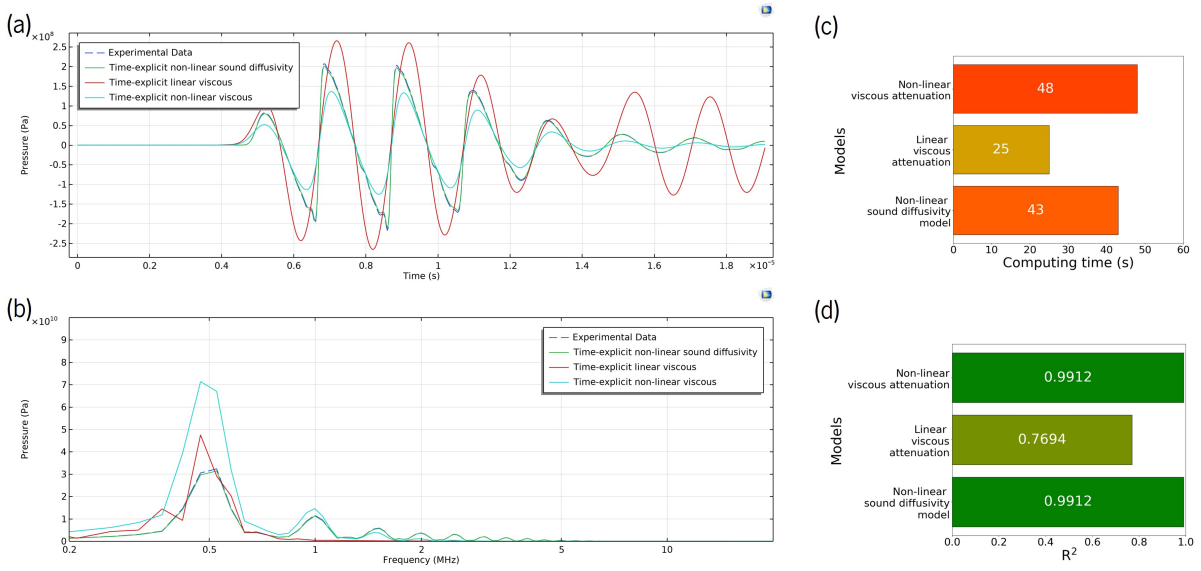



Figure 184: Experimental and simulated pressure responses for acoustic wave propagation in ligament at $500$ kHz: (a) time-domain signals, (b) frequency spectra, (c) computational time, and (d) model fit ($R^2$).

At $1$ MHz (figure 185), acoustic wave propagation in ligament shows a clear shift toward stronger attenuation and reduced waveform coherence compared to $500kHz$, while still maintaining a well-defined oscillatory structure. In the time domain, the linear viscous model again overpredicts the pressure amplitude and fails to capture the correct damping behavior, whereas both non-linear models closely reproduce the experimental waveform, accurately matching both amplitude and phase. In the frequency domain, the dominant peak shifts to approximately $1$ MHz and becomes slightly broader than at $500$ kHz, indicating increased energy redistribution and interaction with the ligament microstructure; secondary harmonics are present but remain limited, reflecting relatively controlled dispersion. The linear viscous model produces an exaggerated and overly sharp peak, while the non-linear sound diffusivity and non-linear viscous attenuation models align closely with the experimental spectrum. This is confirmed by the goodness-of-fit values, where both non-linear approaches achieve near-perfect agreement ($R^2 \approx 0.999–1.000$), significantly outperforming the linear model ($R^2 \approx 0.57$). Computational cost increases substantially compared to $500$ kHz, with non-linear models requiring $42–44$ min versus $8.7$ min for the linear model.

At $2$ MHz (figure 186), ligament exhibits a pronounced increase in attenuation and waveform distortion relative to both $1$ MHz and $500$ kHz, marking a transition toward a more strongly dissipative regime. In the time domain, the experimental signal shows reduced amplitude and faster decay, with noticeable asymmetry and phase distortion, which are accurately captured by the non-linear models; the linear viscous model again significantly overestimates the peak pressure and fails to reproduce the damping behavior. In the frequency domain, the main spectral peak shifts to approximately $2$ MHz and

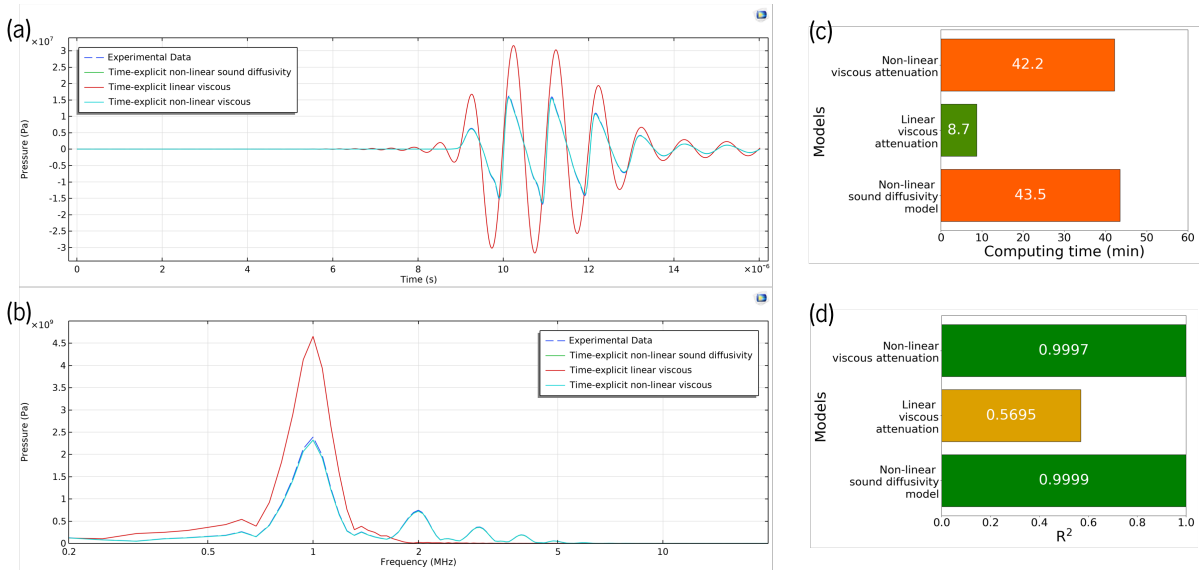



Figure 185: Experimental and simulated pressure responses for acoustic wave propagation in ligament at $1$ MHz: (a) time-domain signals, (b) frequency spectra, (c) computational time, and (d) model fit ($R^2$).

becomes broader and less sharply defined compared to lower frequencies, indicating enhanced scattering and frequency-dependent absorption; secondary components are more attenuated, and energy is redistributed over a wider bandwidth. The linear viscous model produces an unrealistically sharp and amplified peak, while both non-linear formulations closely match the experimental spectrum. This is reflected in the $R^2$ values, where the non-linear viscous attenuation and non-linear sound diffusivity models maintain excellent agreement ($R^2 \approx 0.998$–$0.999$), whereas the linear model remains significantly lower ($R^2 \approx 0.57$). Computational cost continues to increase with frequency, with non-linear models requiring approximately $52$–$56$ minutes compared to $11$ minutes for the linear model.

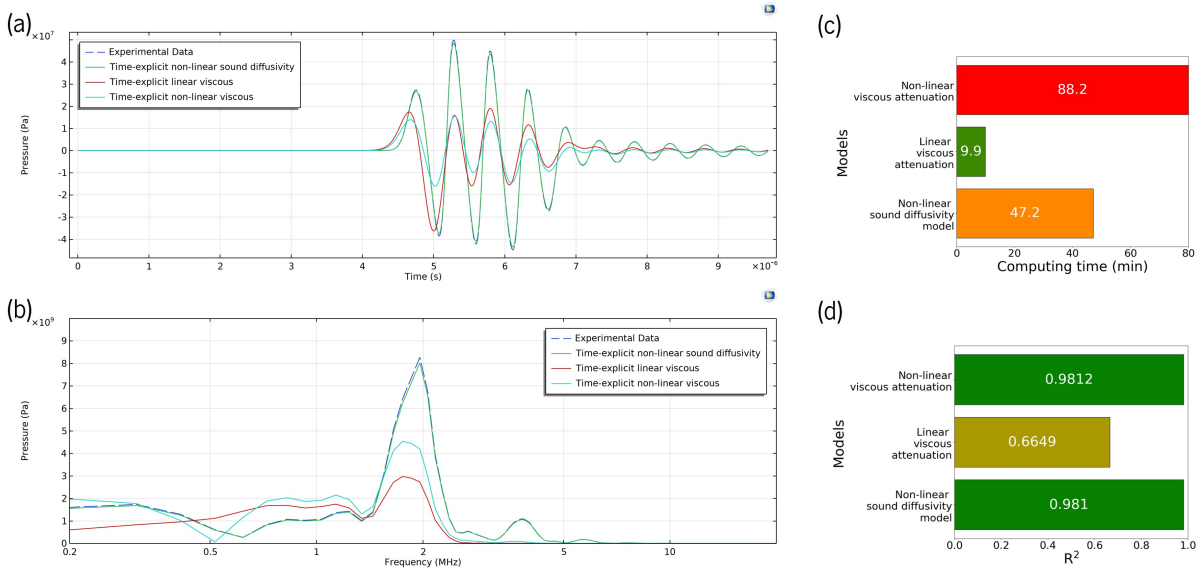



Figure 186: Experimental and simulated pressure responses for acoustic wave propagation in ligament at $2$ MHz: (a) time-domain signals, (b) frequency spectra, (c) computational time, and (d) model fit ($R^2$).

At $4$ MHz (figure 187), ligament behavior clearly enters a highly attenuated and strongly dispersive

regime, where wave propagation is dominated by rapid energy dissipation and loss of coherence. In the time domain, the experimental signal exhibits a sharp initial peak followed by rapid decay and pronounced waveform distortion; the non-linear models reproduce both the amplitude envelope and phase evolution with good fidelity, while the linear viscous model again overpredicts peak amplitudes and fails to capture the damping rate. In the frequency domain, the spectral energy shifts toward higher frequencies (≈$4$–$5$ MHz) but becomes significantly broadened and flattened, with reduced peak sharpness compared to $2$ MHz, indicating increased scattering and frequency-dependent attenuation. The linear viscous formulation produces an exaggerated and narrow spectral peak, whereas both non-linear approaches follow the experimental distribution more closely. This is reflected in the fit metrics, where the non-linear sound diffusivity ($R^2$≈$0.9749$) and non-linear viscous attenuation ($R^2$≈$0.9692$) maintain strong agreement, while the linear model degrades further ($R^2$≈$0.5395$). Computational cost increases substantially, reaching approximately $1.5$–$1.7$ hours for the non-linear models versus $0.8$ hours for the linear model.

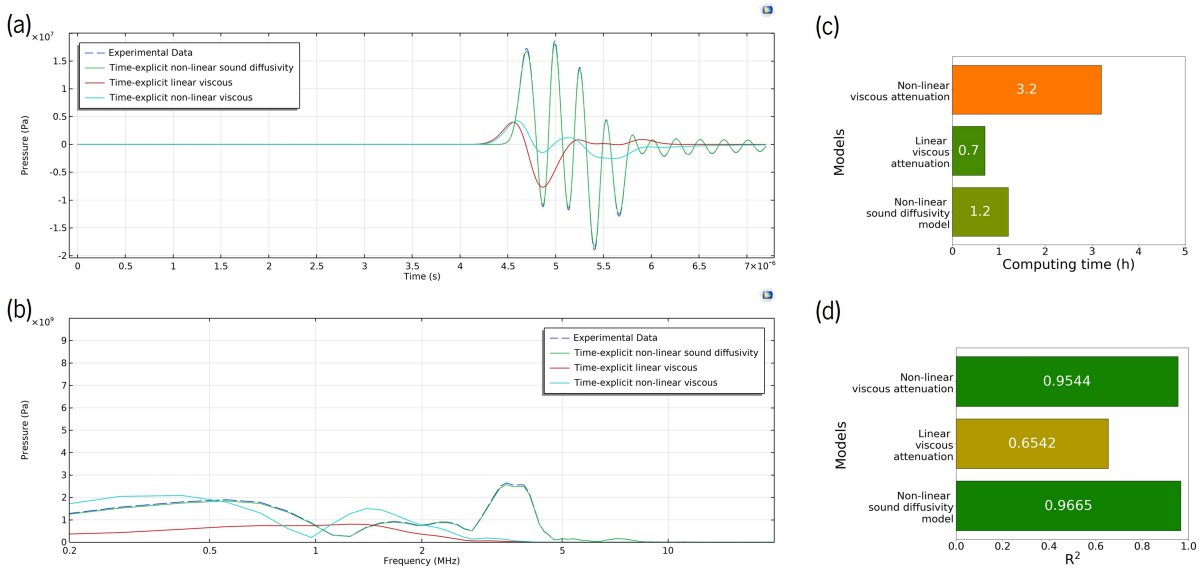



Figure 187: Experimental and simulated pressure responses for acoustic wave propagation in ligament at $4$ MHz: (a) time-domain signals, (b) frequency spectra, (c) computational time, and (d) model fit ($R^2$).

At $5$ MHz (figure 188), ligament demonstrates an extreme attenuation-dominated regime, where propagation becomes highly localized and strongly distorted. In the time domain, the experimental signal is characterized by a sharp, high-frequency burst followed by rapid decay and significant asymmetry, indicating intense energy dissipation; both non-linear models capture this transient behavior well, including the envelope and phase distortion, while the linear viscous model again overestimates peak amplitudes and fails to reproduce the damping characteristics. In the frequency domain, the dominant spectral peak shifts toward $5$ MHz but becomes broader and less coherent, with a clear reduction in

harmonic structure compared to $4$ MHz and lower frequencies, reflecting increased scattering and frequency-dependent absorption. The linear viscous model produces an unrealistically amplified and narrow peak, whereas the non-linear viscous attenuation and sound diffusivity models closely track the experimental spectrum. This is quantitatively confirmed by the $R^2$ values, which remain high for the non-linear models ($R^2 \approx 0.9971$–$0.9973$) and significantly lower for the linear model ($R^2 \approx 0.5659$). Computational cost continues to rise, reaching approximately $2.3$–$2.4$ hours for the non-linear models compared to $0.5$ hours for the linear approach. Compared with $4$ MHz, $2$ MHz, $1$ MHz, and $500$ kHz, the results reveal a clear monotonic transition: increasing frequency leads to stronger attenuation, reduced waveform coherence, and greater spectral broadening, with ligament behavior increasingly governed by non-linear and diffusive mechanisms; consequently, the inadequacy of linear viscous models becomes more pronounced, while non-linear formulations remain robust across the entire frequency range.

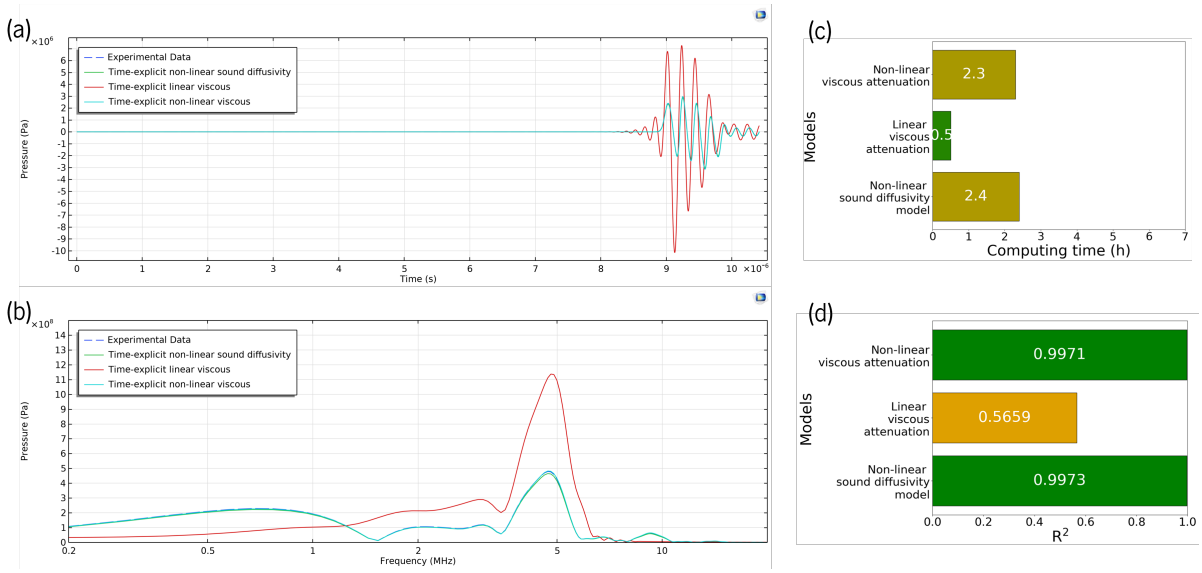



Figure 188: Experimental and simulated pressure responses for acoustic wave propagation in ligament at $5$ MHz: (a) time-domain signals, (b) frequency spectra, (c) computational time, and (d) model fit ($R^2$).

### B.1.7 Cartilage

At $500$ kHz (figure 189), cartilage exhibits comparatively low attenuation and a more coherent wave propagation regime relative to fibrous tissues such as ligament and tendon. In the time domain, the experimental waveform retains a smooth, quasi-sinusoidal structure with moderate damping, indicating limited energy loss; both non-linear models reproduce the phase and amplitude evolution well, although with slightly reduced peak amplitudes compared to the experimental signal. In contrast, the linear viscous model significantly overestimates the oscillation amplitude and fails to capture the correct

attenuation rate. In the frequency domain, a dominant and well-defined peak is observed around $500$ kHz, with minimal spectral broadening and weak higher-order components, reflecting relatively low scattering and frequency-dependent losses. The non-linear sound diffusivity model shows excellent agreement with the experimental spectrum ($R^2 \approx 0.9906$), while the non-linear viscous attenuation model provides a reasonable but less accurate fit ($R^2 \approx 0.9534$). The linear viscous model again performs poorly ($R^2 \approx 0.5153$), producing an underestimated peak width and incorrect amplitude distribution. Computationally, the linear model remains the most efficient ( $7s$), while the non-linear models require increased time ( $15–19s$), though still modest compared to higher-frequency cases.

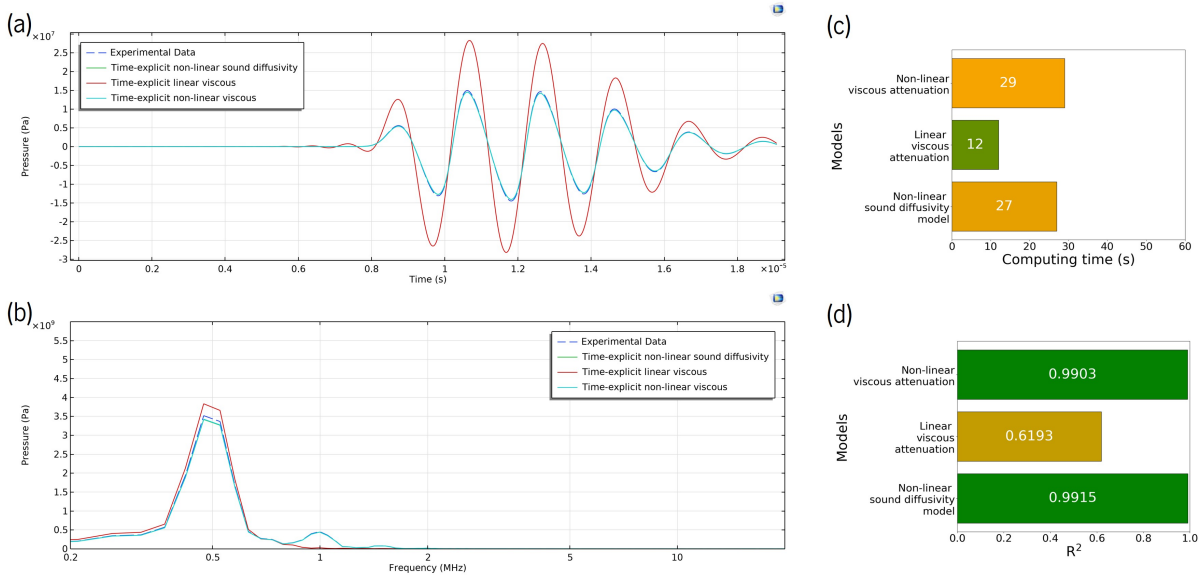



Figure 189: Experimental and simulated pressure responses for acoustic wave propagation in cartilage at $500$ kHz: (a) time-domain signals, (b) frequency spectra, (c) computational time, and (d) model fit ($R^2$).

At $1$ MHz (figure 190), cartilage begins to exhibit a clearer influence of attenuation and dispersion compared to $500$ kHz, while still maintaining a relatively coherent propagation regime. In the time domain, the experimental waveform shows increased damping and reduced amplitude relative to lower frequency, with slight phase distortion; the non-linear models capture both the attenuation and waveform shape effectively, whereas the linear viscous model again overestimates peak amplitudes and introduces unrealistic oscillation magnitudes. In the frequency domain, the dominant peak shifts to approximately $1$ MHz and becomes slightly broader than at $500$ kHz, indicating the onset of stronger frequency-dependent losses and mild scattering; secondary spectral features remain weak but more visible than in the lower-frequency case. The non-linear sound diffusivity and non-linear viscous attenuation models closely reproduce the spectral peak and its width, yielding strong agreement ($R^2 \approx 0.987–0.9873$), while the linear viscous model shows a marked degradation in accuracy ($R^2 \approx 0.4722$), with incorrect amplitude scaling and peak definition. Computational time increases

substantially compared to $500$ kHz, with non-linear models requiring approximately $52$–$55$ minutes versus $8.7$ minutes for the linear model.

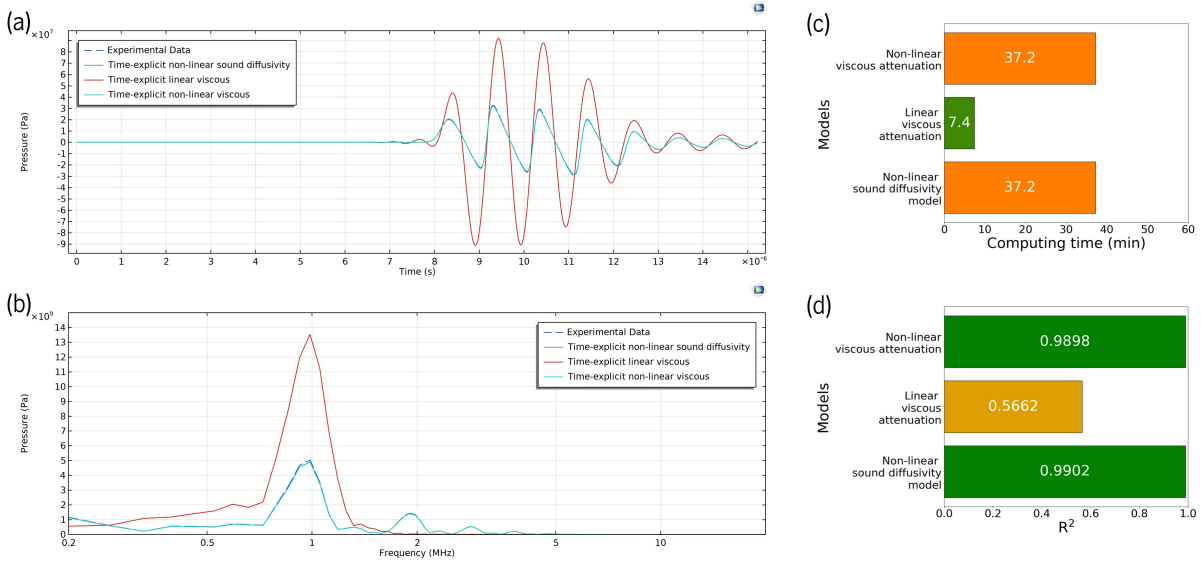



Figure 190: Experimental and simulated pressure responses for acoustic wave propagation in cartilage at $1$ MHz: (a) time-domain signals, (b) frequency spectra, (c) computational time, and (d) model fit ($R^2$).

At $2$ MHz (figure 191), cartilage exhibits a clear shift towards higher attenuation and dispersive propagation regime compared to $1$ MHz and $500$ kHz. In the time domain, the experimental signal shows stronger damping, reduced amplitude, and more evident phase distortion, with a shorter effective propagation window; the non-linear models capture both the decay and waveform shape with good agreement, while the linear viscous model again significantly overestimates peak amplitudes and fails to reproduce the attenuation rate. In the frequency domain, the dominant peak shifts to approximately $2$ MHz and becomes broader and less symmetric than at $1$ MHz, indicating increased frequency-dependent absorption and moderate scattering; higher-frequency components are strongly suppressed. The linear viscous model produces an exaggerated and narrow peak, whereas both non-linear formulations follow the experimental spectral distribution more closely. This is reflected in the fit metrics, where the non-linear viscous attenuation and non-linear sound diffusivity models maintain strong agreement ($R^2 \approx 0.985$–$0.986$), while the linear model remains substantially lower ($R^2 \approx 0.47$). Computational cost increases further relative to $1$ MHz, with non-linear models requiring approximately $52$–$53$ minutes compared to $12$ minutes for the linear model.

At $4$ MHz (figure 192), cartilage clearly enters a more strongly attenuated and spectrally redistributed regime than at $2$ MHz, $1$ MHz, and $500$ kHz. In the time domain, the signal becomes more temporally compact and more sensitive to damping and phase distortion, and the linear viscous model again fails to reproduce the experimental behavior, showing a pronounced amplitude mismatch and an incorrect waveform evolution. In contrast, both non-linear formulations remain closely aligned with the measured

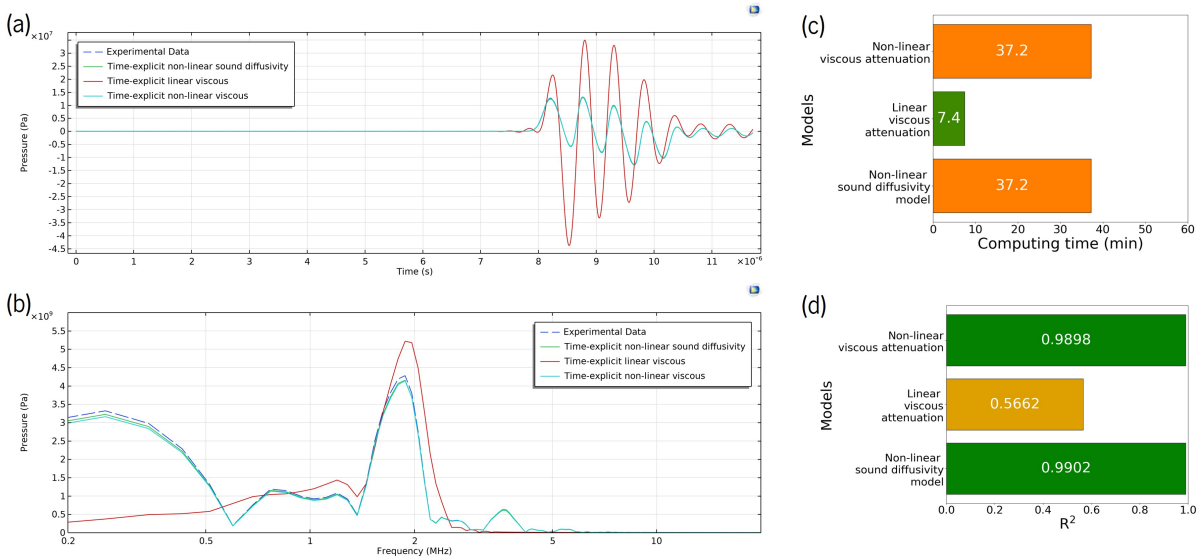



Figure 191: Experimental and simulated pressure responses for acoustic wave propagation in cartilage at 2 MHz: (a) time-domain signals, (b) frequency spectra, (c) computational time, and (d) model fit ($R^2$).

response, capturing the oscillation envelope and decay with good fidelity. In the frequency domain, the energy is no longer concentrated in a narrowband around the excitation frequency as in the lower-frequency cases; instead, it is redistributed over a broader range, with a strong peak in the higher-frequency region and a more complex low-frequency background, indicating stronger attenuation, dispersion, and energy transfer mechanisms. This trend is more pronounced than at 2 MHz and markedly different from the more coherent spectra observed at 1 MHz$and especially 500 kHz$. The goodness-of-fit values confirm this behavior: both non-linear models still provide strong agreement ($R^2 \approx 0.966$), whereas the linear model performs poorly ($R^2 \approx 0.457$). Computational cost also rises substantially, reaching approximately $2.4$–$3.1$ h for the non-linear models compared with about 1 h for the linear case.

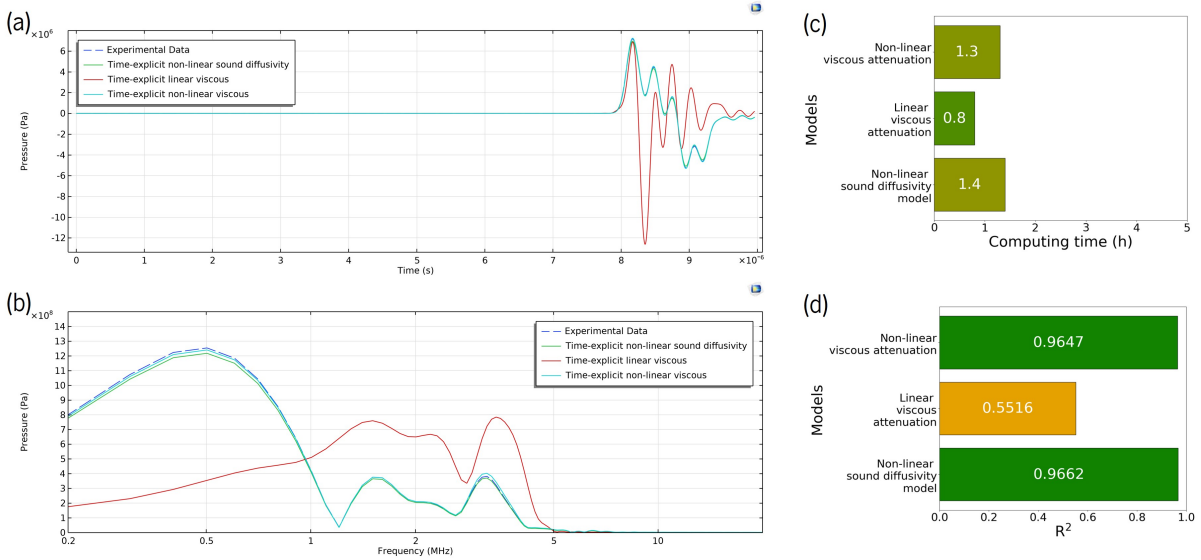



Figure 192: Experimental and simulated pressure responses for acoustic wave propagation in cartilage at 4 MHz: (a) time-domain signals, (b) frequency spectra, (c) computational time, and (d) model fit ($R^2$).

At $5$ MHz (figure 193), cartilage reaches a strongly attenuation-dominated regime, where wave propagation becomes highly localized and increasingly distorted compared to $4$ MHz, $2$ MHz, $1$ MHz, and $500$ kHz. In the time domain, the signal is characterized by a sharp, high-frequency burst followed by rapid decay and reduced oscillatory coherence; both non-linear models reproduce this transient behavior with good agreement, while the linear viscous model significantly misrepresents the amplitude and damping, producing exaggerated peaks and incorrect waveform evolution. In the frequency domain, the energy is concentrated on the excitation frequency ( $5$ MHz) but with noticeable broadening and reduced spectral sharpness compared to lower frequencies, indicating stronger frequency-dependent attenuation and enhanced energy redistribution; the lower-frequency content is diminished, and the spectrum appears more fragmented than at $4$ MHz. The non-linear sound diffusivity and non-linear viscous attenuation models closely follow the experimental spectral shape, whereas the linear model underestimates the complexity of the response. This is confirmed by the fit metrics, where the non-linear models maintain strong agreement ($R^2 \approx 0.984$–$0.985$), while the linear viscous model remains significantly lower ($R^2 \approx 0.4686$). Computational cost increases further, reaching approximately $2.8$–$4.5$ h for the non-linear models compared to $0.5$ h for the linear formulation. Compared with $4$ MHz, $2$ MHz, $1$ MHz, and $500$ kHz, the results show a consistent progression in cartilage toward increased attenuation, reduced waveform coherence, and broader spectral distributions with frequency, reinforcing that non-linear and diffusive mechanisms become increasingly dominant and are essential for accurately capturing high-frequency acoustic propagation.

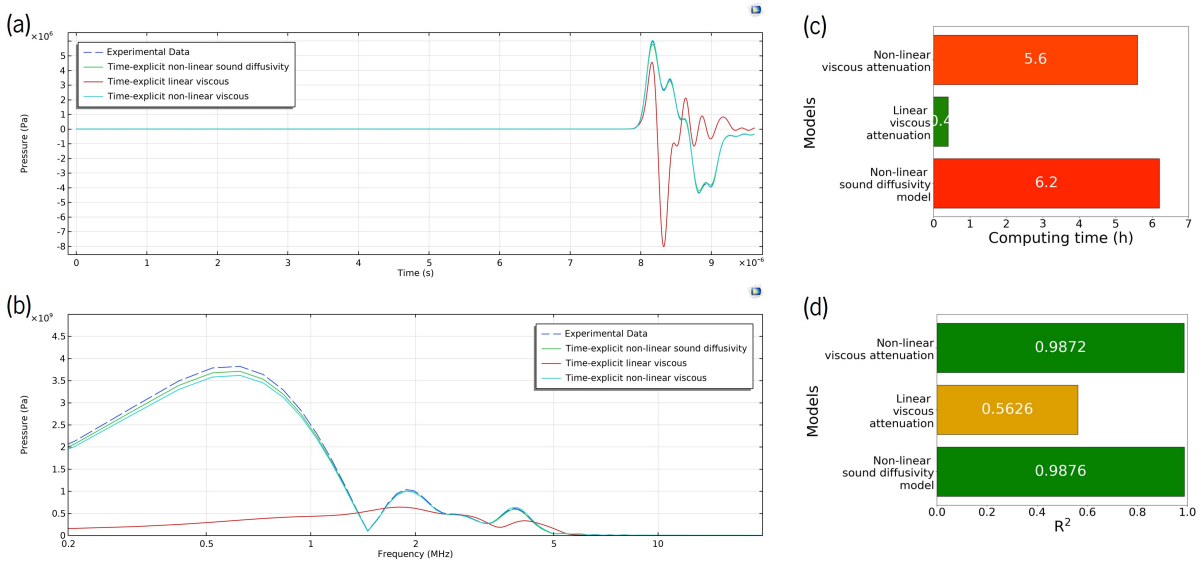



Figure 193: Experimental and simulated pressure responses for acoustic wave propagation in cartilage at $5$ MHz: (a) time-domain signals, (b) frequency spectra, (c) computational time, and (d) model fit ($R^2$).

### B.1.8 Trabecular Bone

At $500$ kHz (figure 194), acoustic wave propagation in trabecular bone is characterized by a complex but still moderately coherent response, where the experimental signal exhibits clear oscillatory behavior with noticeable attenuation and slight waveform distortion in the time domain. The linear viscous model significantly overestimates the amplitude of the propagating wave and fails to capture the damping observed experimentally, resulting in exaggerated peaks and poor phase agreement. In contrast, both non-linear formulations closely follow the experimental waveform, accurately reproducing both amplitude decay and phase evolution, with only minor deviations in peak sharpness. In the frequency domain, the experimental spectrum is dominated by a primary peak around $500$ kHz, accompanied by secondary harmonics and a broadened spectral distribution indicative of scattering and microstructural heterogeneity. The non-linear models successfully capture this dominant peak and the secondary spectral content, whereas the linear viscous model overpredicts the main peak magnitude and suppresses higher-frequency contributions. The goodness-of-fit metrics reflect these observations, with the non-linear sound diffusivity model ($R^2 \approx 0.9923$) and the non-linear viscous model ($R^2 \approx 0.9804$) showing excellent agreement with the experimental data, while the linear viscous model performs significantly worse ($R^2 \approx 0.7143$). From a computational standpoint, the linear viscous model remains the most efficient ($\approx 27$ s), while the non-linear models require increased computation time ($\approx 50$–$59$ s) due to the additional complexity associated with non-linear and diffusive mechanisms.

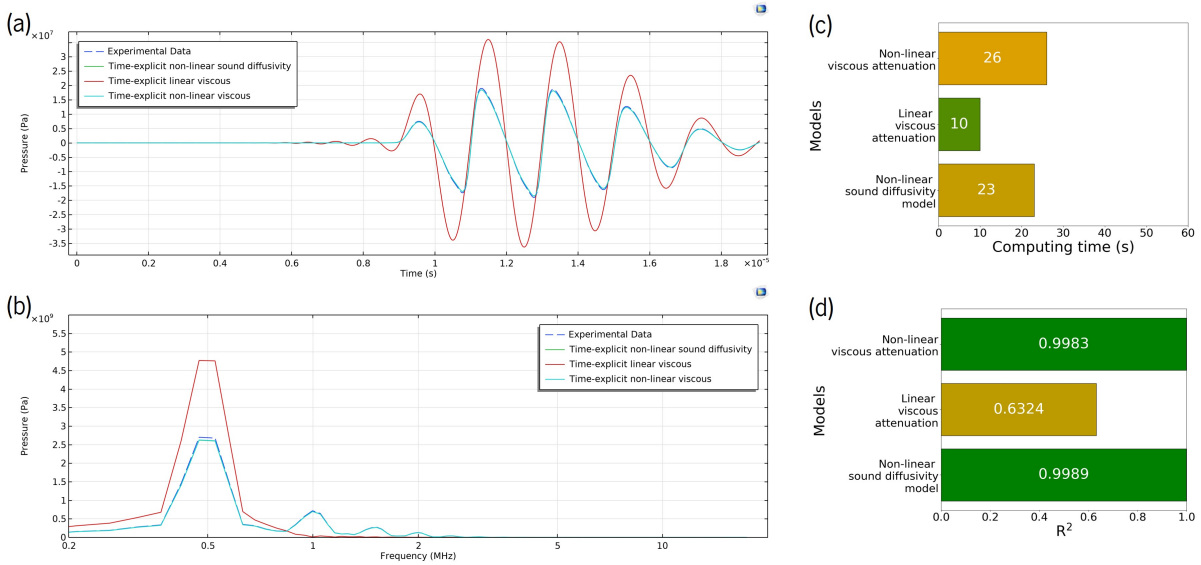



Figure 194: Experimental and simulated pressure responses for acoustic wave propagation in trabecular bone at $500$ kHz: (a) time-domain signals, (b) frequency spectra, (c) computational time, and (d) model fit ($R^2$).

At $1$ MHz (figure 195), acoustic wave propagation in trabecular bone exhibits a clear transition toward stronger attenuation and increased spectral selectivity when compared to the $500$ kHz case. In

the time domain, the experimental waveform shows a more rapidly damped response with reduced persistence of oscillations, indicating enhanced energy dissipation within the porous microstructure. The linear viscous model again significantly overestimates the amplitude and fails to reproduce the observed decay, producing exaggerated oscillations and incorrect phase behavior. In contrast, both non-linear models provide a substantially improved representation of the signal, with the non-linear sound diffusivity model most closely matching the experimental amplitude and decay envelope, while the non-linear viscous formulation slightly underestimates peak amplitudes but still captures the overall waveform evolution. In the frequency domain, the response becomes more concentrated around the fundamental frequency near $1$ MHz, with a pronounced peak and diminished higher-order contributions compared to $500$ kHz, reflecting increased attenuation of scattered components at higher frequencies. The linear viscous model overpredicts the magnitude of this dominant peak and fails to reproduce the reduced spectral richness, whereas the non-linear models more accurately capture both the peak amplitude and the attenuation of higher-frequency content. Quantitatively, the goodness-of-fit improves for the non-linear formulations, with $R^2 \approx 0.9829$ for the non-linear sound diffusivity model and approximately $0.9778$ for the non-linear viscous model, while the linear viscous model remains significantly less accurate ($R^2 \approx 0.6222$). Computationally, the linear model remains the most efficient ( $7.4$ min), whereas the non-linear models require longer runtimes ( $39.7$–$48.4$ min), consistent with their increased physical fidelity.

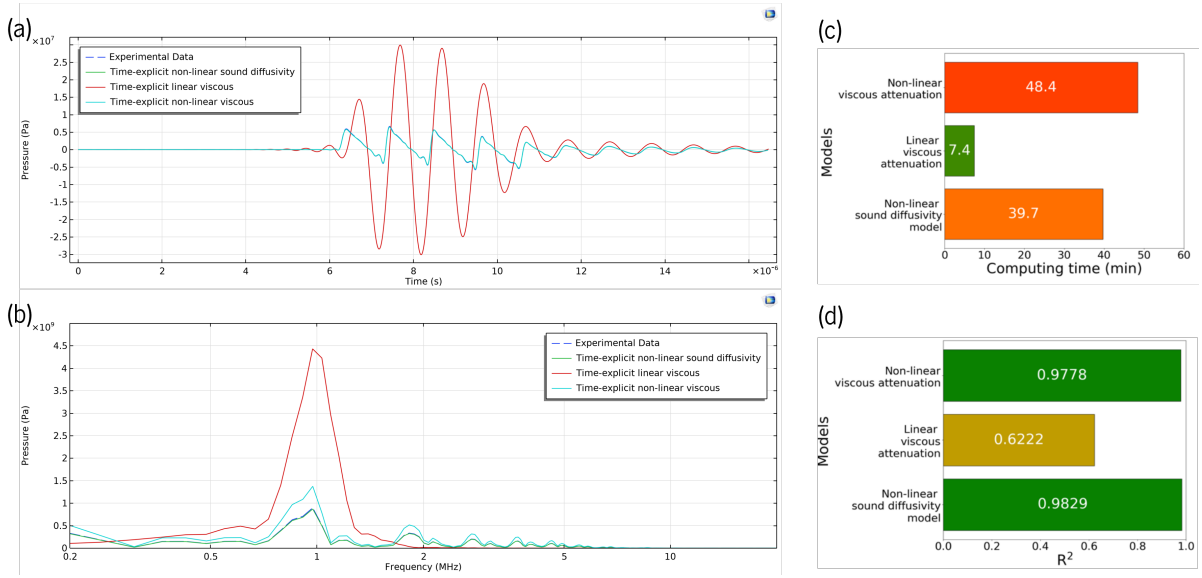



Figure 195: Experimental and simulated pressure responses for acoustic wave propagation in trabecular bone at $1$ MHz: (a) time-domain signals, (b) frequency spectra, (c) computational time, and (d) model fit ($R^2$).

At $2$ MHz (figure 196), acoustic wave propagation in trabecular bone shows a further intensification of attenuation and loss of temporal coherence relative to both $1$ MHz and $500$ kHz, reflecting the strong

frequency dependence of scattering and viscous losses in the porous microstructure. In the time domain, the experimental signal is more rapidly damped, with fewer sustained oscillations and a sharper decay envelope, indicating that energy is dissipated over shorter propagation distances. The linear viscous model continues to overestimate the amplitude and produces non-physical oscillation magnitudes, failing to capture both the attenuation rate and phase evolution. In contrast, the non-linear sound diffusivity and non-linear viscous models closely track the experimental waveform, with the diffusivity model providing the best agreement in both amplitude and decay behavior, while the non-linear viscous model slightly underestimates peak amplitudes but maintains accurate phase alignment. In the frequency domain, the spectral response shifts toward a dominant peak near $2$ MHz with significantly reduced bandwidth and suppressed higher-order components compared to lower frequencies, evidencing stronger filtering of scattered energy. The linear viscous model again overpredicts the magnitude of this peak and fails to represent the attenuated spectral tail, whereas the non-linear models better capture both the reduced amplitude and spectral distribution. Quantitatively, the superiority of the non-linear approaches remains evident, with $R^2 \approx 0.9811$ for the non-linear sound diffusivity model and approximately $0.9763$ for the non-linear viscous model, compared to approximately $0.621$ for the linear viscous formulation. Computational cost increases with frequency, with the linear model remaining the fastest ( $11.2$ min) and the non-linear models requiring substantially longer runtimes ( $63$–$66$ min). When compared to $1$ MHz and $500$ kHz, the $2$ MHz results highlight a clear progression: increasing frequency leads to stronger attenuation, reduced temporal persistence, and greater reliance on non-linear and diffusive mechanisms to accurately reproduce the observed behavior.

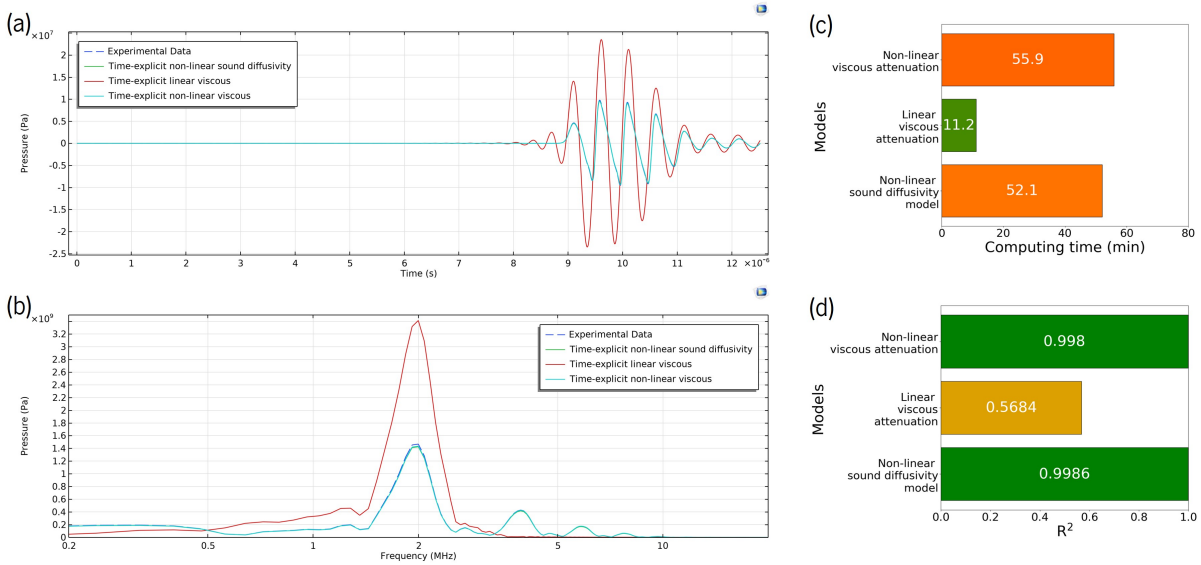



Figure 196: Experimental and simulated pressure responses for acoustic wave propagation in trabecular bone at $2$ MHz: (a) time-domain signals, (b) frequency spectra, (c) computational time, and (d) model fit ($R^2$).

At $4$ MHz (figure 197), acoustic wave propagation in trabecular bone enters a distinctly more

attenuated and spectrally redistributed regime than at $2$ MHz, $1$ MHz, and $500$ kHz. In the time domain, the experimental response becomes more localized and rapidly damped, with a short burst-like waveform followed by strong decay, indicating that propagation is increasingly dominated by microstructural scattering and energy loss. The linear viscous model again fails to reproduce this behavior, generating a markedly exaggerated oscillatory response and substantial amplitude mismatch, whereas both non-linear models follow the measured signal much more closely, capturing the compact waveform and its rapid attenuation. In the frequency domain, the response is no longer dominated by a narrow peak around the excitation frequency, but instead shows a broader redistribution of energy with strong low-frequency content and a more complex spectral shape, reflecting intense filtering and mode conversion within the trabecular architecture. This contrasts with the more coherent and narrower responses observed at $500$ kHz and $1$ MHz, and extends the attenuation trend already visible at $2MHz$. Quantitatively, the non-linear models still provide good agreement, with $R^2 \approx 0.955$ for both formulations, while the linear viscous model remains substantially less accurate ($R^2 \approx 0.609$). Computational cost also rises to the hour scale, with the non-linear models requiring about $3.1$–$3.3$ h compared with about $0.7$ h for the linear model.

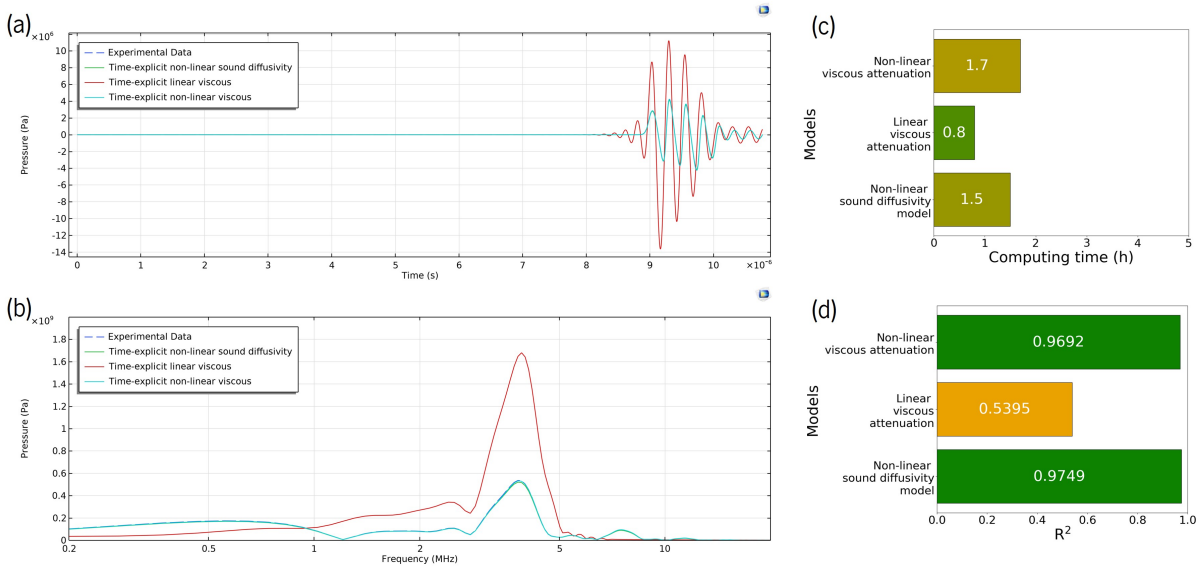



Figure 197: Experimental and simulated pressure responses for acoustic wave propagation in trabecular bone at $4$ MHz: (a) time-domain signals, (b) frequency spectra, (c) computational time, and (d) model fit ($R^2$).

At $5$ MHz (figure 198), acoustic wave propagation in trabecular bone reaches a regime dominated by severe attenuation, strong scattering, and pronounced spectral redistribution, extending the trends observed at $4$ MHz, $2$ MHz, $1$ MHz, and $500$ kHz. In the time domain, the experimental signal is highly localized, with a short-duration, rapidly decaying waveform and minimal sustained oscillations, indicating that energy is dissipated almost immediately after propagation begins. The linear viscous model again fails to capture this behavior, producing exaggerated oscillations and significant amplitude errors,

particularly in the negative pressure peaks. In contrast, the non-linear models reproduce the overall waveform structure more accurately, with the non-linear sound diffusivity model providing the closest agreement in both amplitude and decay, while the non-linear viscous model captures the general trend but shows slight deviations in peak magnitude and phase. In the frequency domain, the response is no longer centered around a sharp excitation peak; instead, energy is redistributed toward lower frequencies with a broad, smooth spectrum and suppressed high-frequency content, reflecting strong frequency-dependent attenuation and multiple scattering within the trabecular network. This represents a clear evolution from the narrower and more defined peaks observed at $500$ kHz and $1$ MHz, through the partially broadened response at $2$ MHz, to the highly diffused spectrum at $4$ MHz. The goodness-of-fit metrics remain high for the non-linear models ($R^2 \approx 0.9793$ for sound diffusivity and approximately $0.9742$ for non-linear viscous attenuation), while the linear viscous model continues to underperform ($R^2 \approx 0.6186$). Computationally, the cost remains substantial for the non-linear models ( $1.9$–$2.2$ h), compared to the significantly lower runtime of the linear model ( $0.7$ h). Overall, relative to all lower frequencies, the $5$ MHz case confirms that trabecular bone behaves as a strongly attenuating, scattering-dominated medium where wave propagation becomes increasingly diffusive in nature, and where accurate modeling requires the inclusion of non-linear attenuation and diffusivity mechanisms to capture both the rapid temporal decay and the broadened spectral response.

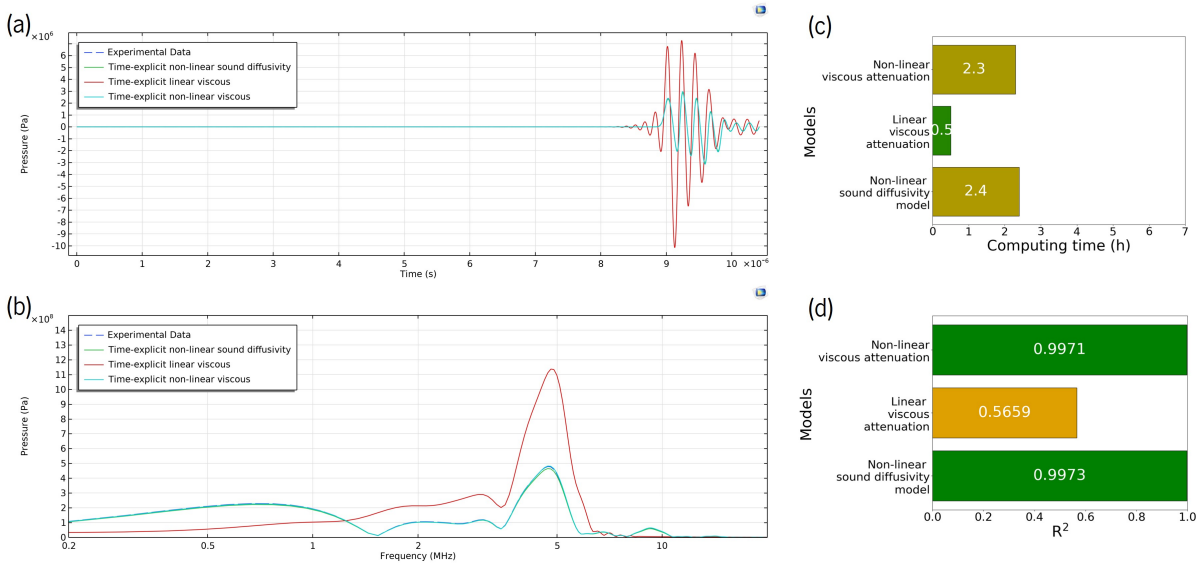



Figure 198: Experimental and simulated pressure responses for acoustic wave propagation in trabecular bone at $5$ MHz: (a) time-domain signals, (b) frequency spectra, (c) computational time, and (d) model fit ($R^2$).

### B.1.9 Cortical Bone

At $500$ kHz (figure 199), acoustic wave propagation in cortical bone exhibits a more coherent and less scattering-dominated response than in cortical bone, consistent with its dense and relatively homogeneous structure. In the time domain, the experimental signal presents a well-defined oscillatory waveform with gradual attenuation, indicating that energy dissipation is primarily governed by intrinsic material damping rather than strong structural scattering. The linear viscous model overestimates the oscillation amplitude and introduces noticeable deviations in the decay envelope, although its performance is improved relative to porous bone cases. Both non-linear models provide a close match to the experimental waveform, accurately reproducing the amplitude, phase, and attenuation characteristics, resulting in nearly identical goodness-of-fit values ($R^2 \approx 0.991$). In the frequency domain, the response is dominated by a sharp peak around $500$ kHz with limited spectral spreading, reflecting the lower scattering and more waveguide-like propagation typical of cortical bone. The non-linear models capture both the peak magnitude and the secondary harmonic content with good accuracy, whereas the linear viscous model distorts the peak amplitude and underrepresents the spectral structure. It is also observed that the non-linear viscous formulation slightly overpredicts the dominant spectral peak compared to the sound diffusivity model, despite similar overall agreement. In terms of computational performance, the linear model remains the most efficient ( $25$ s), while the non-linear viscous attenuation and sound diffusivity models require longer runtimes ( $48$ s and $43$ s, respectively).

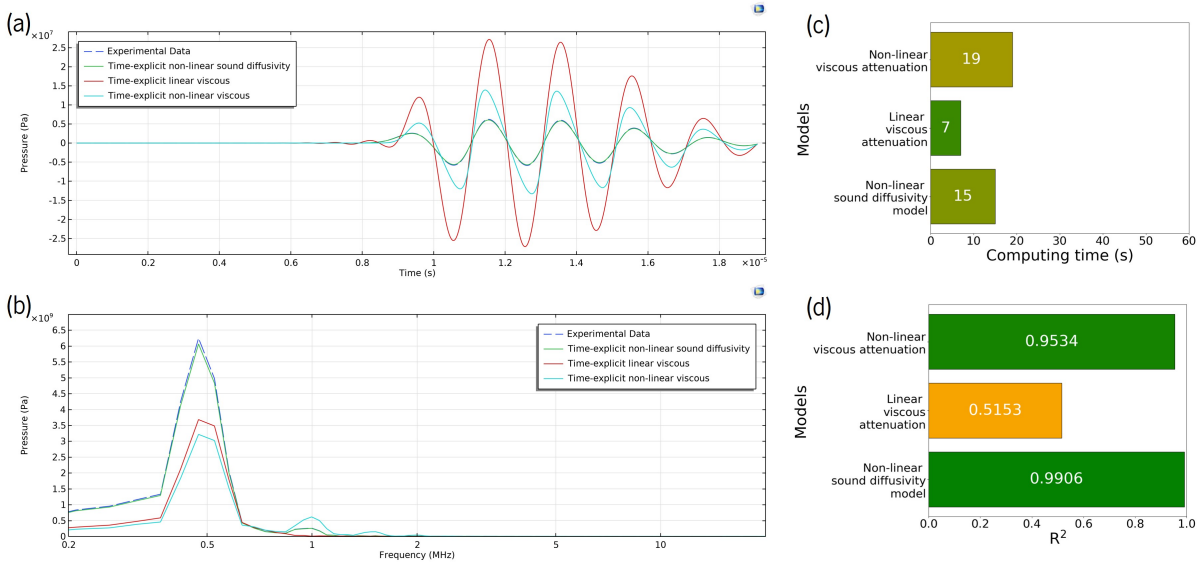



Figure 199: Experimental and simulated pressure responses for acoustic wave propagation in cortical bone at $500$ kHz: (a) time-domain signals, (b) frequency spectra, (c) computational time, and (d) model fit ($R^2$).

At $1$ MHz (figure 200), acoustic wave propagation in cortical bone exhibits a more rapidly attenuated and temporally confined response compared to $500$ kHz, reflecting the stronger frequency-dependent

damping inherent to dense mineralized tissue. In the time domain, the experimental signal shows a shorter-lived oscillatory behavior, which is accurately captured by both non-linear models, while the linear viscous model overestimates amplitude and introduces phase discrepancies. In the frequency domain, the dominant peak shifts toward $1$ MHz and becomes broader, with reduced low-frequency contributions, indicating increased attenuation and slight spectral spreading; this behavior is well reproduced by the non-linear formulations, whereas the linear model underestimates peak magnitude and fails to capture higher-frequency content, resulting in a lower fit quality. Quantitatively, both non-linear models achieve high agreement with the experimental data ($R^2 \approx 0.982$), significantly outperforming the linear viscous approach ($R^2 \approx 0.666$), while also revealing that diffusive and viscous non-linear effects converge at this frequency. From a computational perspective, the linear viscous model remains the most efficient ( $7.4$ min), but the non-linear sound diffusivity model ( $36$ min) provides a substantial reduction in cost compared to the non-linear viscous model ( $55.9$ min) without compromising accuracy, confirming it as the most effective balance between fidelity and efficiency as frequency increases from $500$ kHz to $1$ MHz.

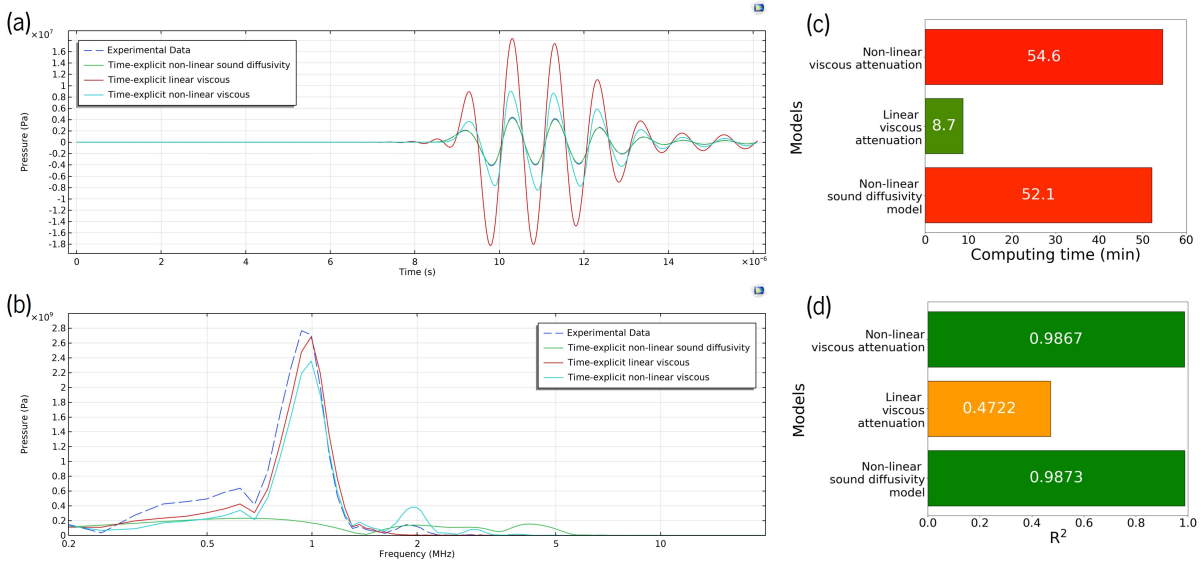



Figure 200: Experimental and simulated pressure responses for acoustic wave propagation in cortical bone at $1$ MHz: (a) time-domain signals, (b) frequency spectra, (c) computational time, and (d) model fit ($R^2$).

At $2$ MHz (figure 201), acoustic wave propagation in cortical bone exhibits a further increase in attenuation and temporal localization compared to $1$ MHz and $500$ kHz, with the time-domain response showing a sharper, more rapidly decaying oscillatory wave packet, indicative of strong frequency-dependent energy dissipation in the dense mineral matrix. The non-linear models closely reproduce both the amplitude and phase of the experimental signal, capturing the pronounced peaks and rapid decay, while the linear viscous model significantly underestimates the waveform amplitude and fails to represent the correct oscillatory structure. In the frequency domain, the dominant spectral peak shifts to approximately $2$ MHz and becomes narrower and more intense relative to lower

frequencies, reflecting increased energy concentration around the excitation frequency and reduced low-frequency content; this behavior is accurately captured by the non-linear formulations, whereas the linear model underpredicts peak magnitude and exhibits a poorer spectral match. Quantitatively, both non-linear approaches maintain high predictive accuracy ($R^2 \approx 0.981$), substantially outperforming the linear viscous model ($R^2 \approx 0.665$), with minimal differences between the non-linear viscous and sound diffusivity formulations, indicating convergence of attenuation mechanisms at higher frequencies. In terms of computational cost, the linear viscous model remains the most efficient ( $9.9$ min), while the non-linear sound diffusivity model ( $47.2$ min) provides a significantly faster alternative to the non-linear viscous model ( $88.2$ min) without loss of accuracy,

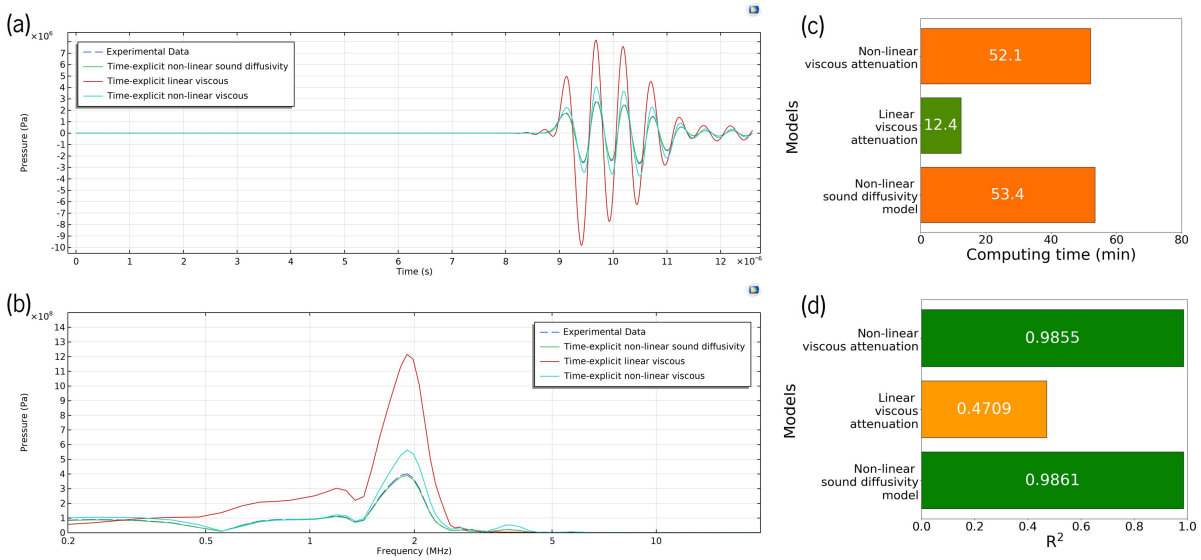



Figure 201: Experimental and simulated pressure responses for acoustic wave propagation in cortical bone at $2$ MHz: (a) time-domain signals, (b) frequency spectra, (c) computational time, and (d) model fit ($R^2$).

At $4$ MHz (figure 202), acoustic wave propagation in cortical bone becomes strongly attenuated and highly localized in time, with the waveform exhibiting a short, high-frequency oscillatory burst that decays rapidly, reflecting the dominance of frequency-dependent losses in dense mineralized tissue; compared to $2$ MHz, $1$ MHz, and $500$ kHz, this represents a clear progression toward reduced penetration depth and diminished temporal persistence. The non-linear models continue to capture the experimental signal with good fidelity, although slight deviations in peak amplitude and phase become more apparent at this higher frequency, particularly for the non-linear viscous formulation, while the linear viscous model significantly underestimates the response amplitude and fails to reproduce the oscillatory structure. In the frequency domain, the energy is concentrated around $4$–$5$ MHz with a broader and more attenuated spectral peak than at lower frequencies, indicating increased scattering and absorption, and while both non-linear models reproduce the general spectral shape, discrepancies in peak magnitude are more noticeable, leading to a modest reduction in fit quality ($R^2 \approx 0.966$ for sound diffusivity and approximately $0.954$ for non-linear

viscous) compared to the near-ideal agreement observed at lower frequencies, whereas the linear model remains substantially less accurate ($R^2 \approx 0.654$). From a computational perspective, the linear viscous model remains the fastest ( $0.7h$), while the non-linear sound diffusivity model ( $1.2$ h) offers a significantly reduced cost compared to the non-linear viscous model ( $3.2$ h), maintaining a favorable balance between efficiency and accuracy.

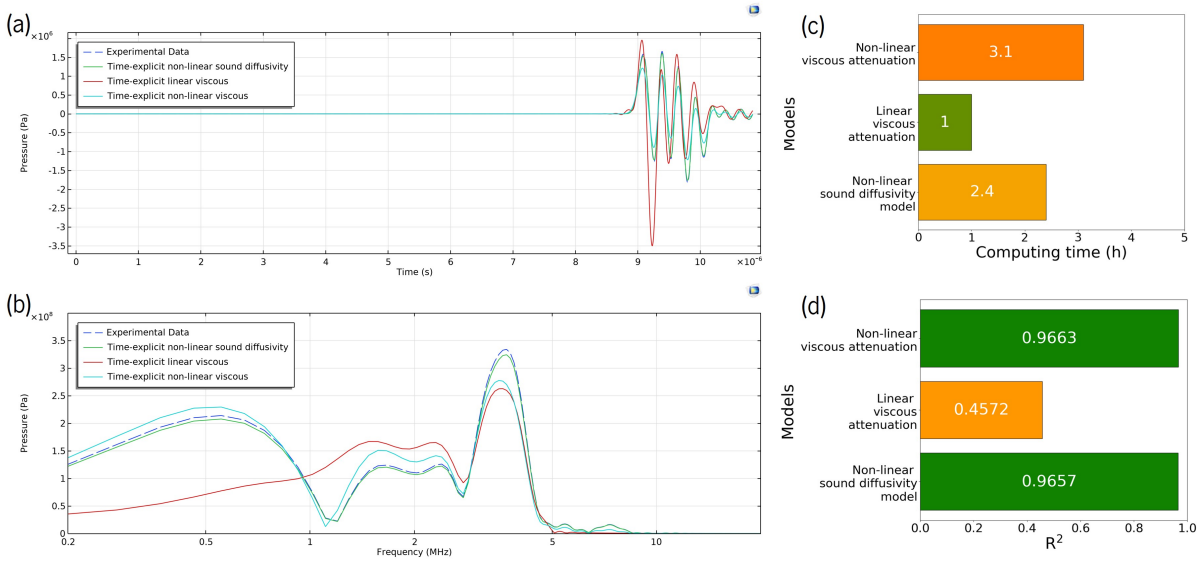



Figure 202: Experimental and simulated pressure responses for acoustic wave propagation in cortical bone at $4$ MHz: (a) time-domain signals, (b) frequency spectra, (c) computational time, and (d) model fit ($R^2$).

At $5$ MHz (figure 203), acoustic wave propagation in cortical bone reaches the most strongly attenuated and spectrally redistributed regime among all tested frequencies, extending the progression already observed from $500$ kHz to $4$ MHz. In the time domain, the experimental response becomes a highly localized, rapidly decaying burst with pronounced high-frequency oscillations, indicating that propagation is increasingly dominated by intrinsic damping and frequency-dependent losses; both non-linear models reproduce this behavior closely, whereas the linear viscous model fails almost completely, severely underestimating the oscillatory structure and providing only a smoothed low-amplitude response. In the frequency domain, the energy is concentrated on the high-frequency range near the excitation frequency but is also distributed across multiple secondary peaks, revealing a more complex and fragmented spectral pattern than at $4$ MHz, $2$ MHz, $1$ MHz, and especially $500$ kHz, where the response was more coherent and narrowly centered. This growing spectral complexity is still captured well by the non-linear formulations, which yield high and nearly identical agreement with the experiments ($R^2 \approx 0.979$), while the linear model remains markedly less accurate ($R^2 \approx 0.663$). Computationally, the linear viscous model remains the least expensive, but the non-linear sound diffusivity model provides a much better balance between fidelity and efficiency than the non-linear viscous attenuation model, requiring about $1.6$ h instead of $4.3$ h while preserving the same predictive

quality. Overall, compared with $4$ MHz, $2$ MHz, $1$ MHz, and $500$ kHz, the $5$ MHz results confirm that cortical bone propagation becomes increasingly attenuation-controlled and spectrally complex as frequency rises, and that accurate representation at high frequency requires non-linear modeling, with the sound diffusivity approach remaining the most efficient robust option.

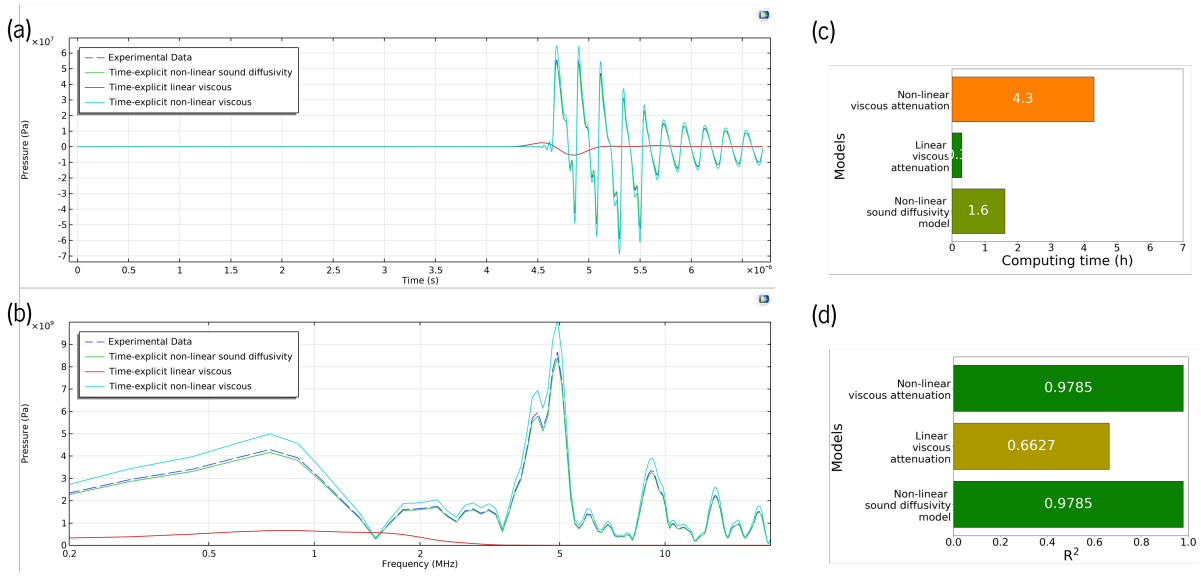



Figure 203: Experimental and simulated pressure responses for acoustic wave propagation in cortical bone at $5$ MHz: (a) time-domain signals, (b) frequency spectra, (c) computational time, and (d) model fit ($R^2$).

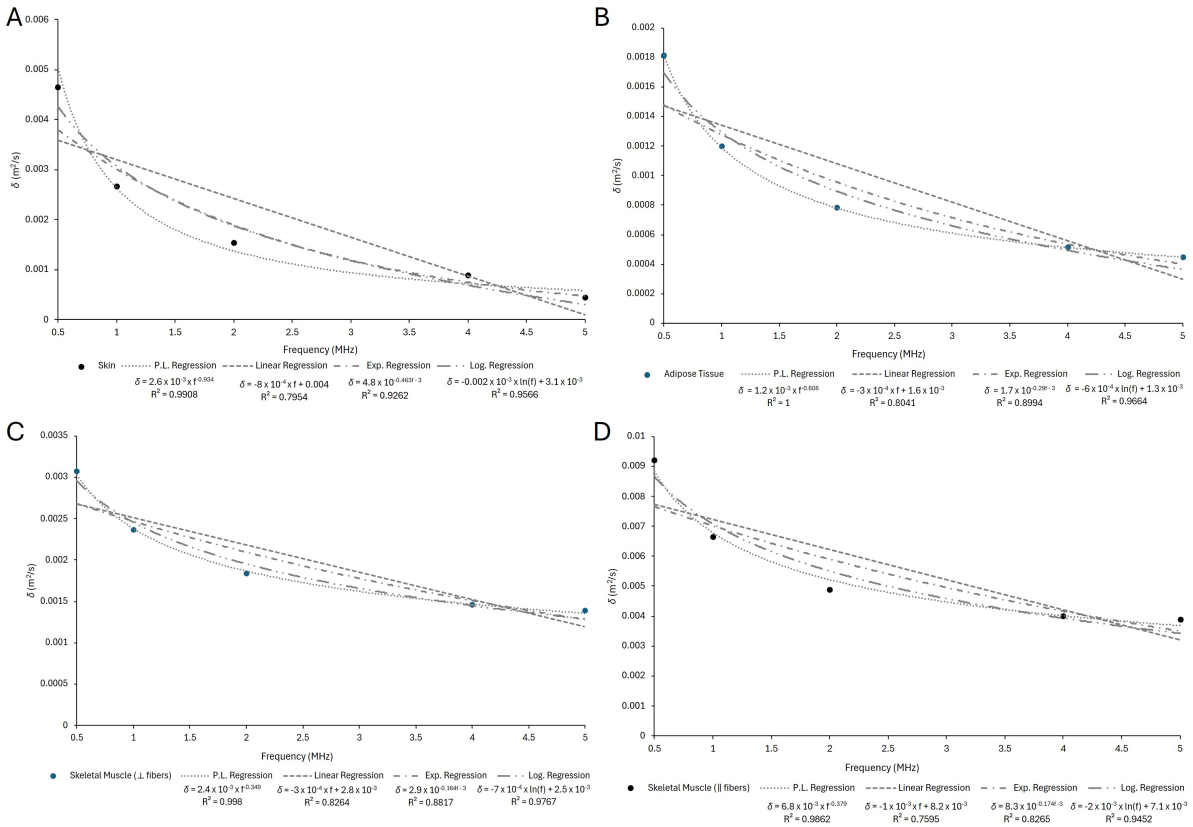



Figure 204: Frequency-dependent sound diffusivity for soft tissues: (A) skin, (B) adipose tissue, (C) skeletal muscle perpendicular to fibers, and (D) skeletal muscle parallel to fibers, including regression model comparisons.

## B.2 Sound Diffusivity Regression Curves

This section will present the inverse estimation results for sound diffusivity.

In skin and adipose tissue (figure 204 A–B), $\delta$ decreases smoothly with frequency, reflecting relatively homogeneous and isotropic structures. Skin presents higher diffusivity values compared to adipose tissue, which may be attributed to its layered architecture and higher collagen content, promoting increased scattering and viscoelastic dissipation. Adipose tissue, being more compliant and less structurally organized, exhibits lower diffusivity and a more gradual decay.

Skeletal muscle introduces a clear anisotropic effect (figure 204 C–D). Diffusivity is consistently higher when wave propagation occurs perpendicular to the fiber direction compared to parallel propagation. This behavior is consistent with the known microstructural organization of muscle, where aligned fibers act as preferential pathways for wave transmission, reducing scattering and energy dissipation in the longitudinal direction. Conversely, transverse propagation encounters repeated impedance mismatches at fiber boundaries, increasing attenuation. Despite these directional differences, both orientations follow a similar decreasing trend with frequency, reinforcing the dominant role of frequency-dependent dissipation mechanisms.

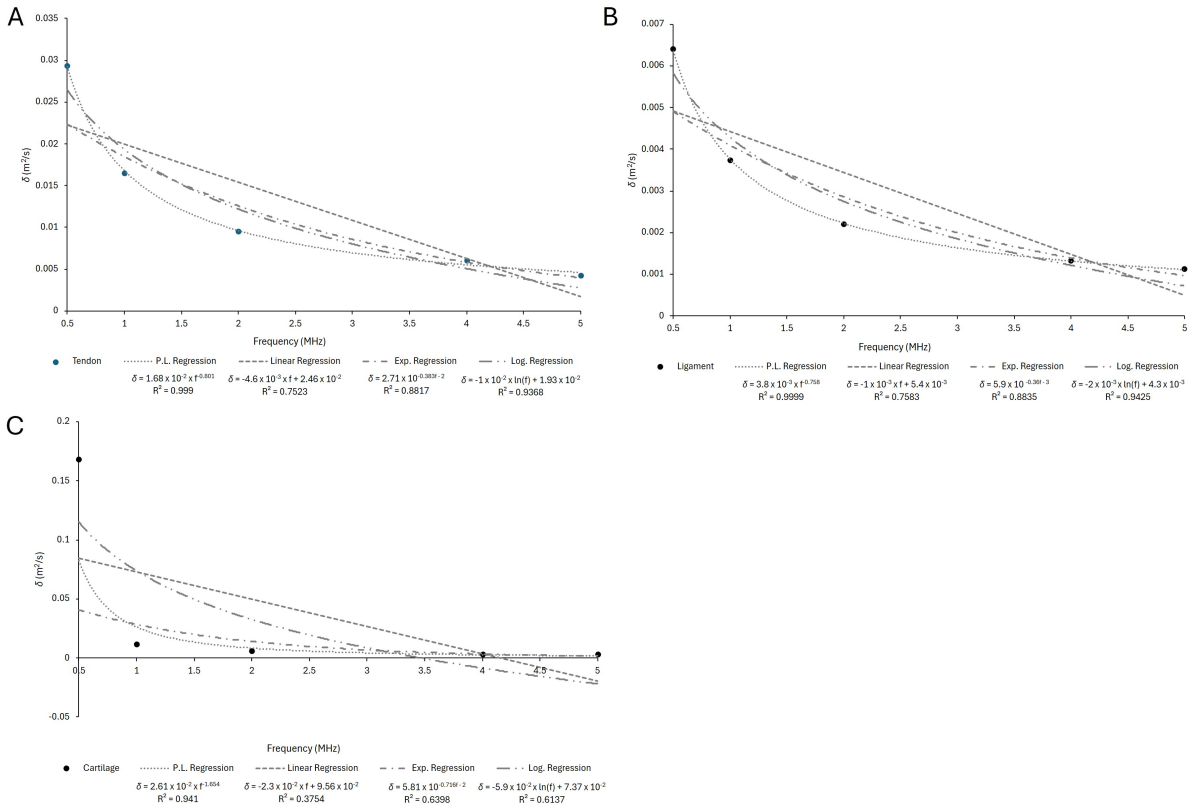



Figure 205: Frequency-dependent sound diffusivity for fibrous and poroelastic tissues: (A) tendon, (B) ligament, and (C) cartilage, including regression model comparisons.

The behavior of tendon and ligament (figure 205 A–B) reflects their highly organized collagen structure. Both tissues exhibit higher diffusivity values compared to soft tissues, with a pronounced decay at low frequencies followed by a more gradual decrease. Tendon generally shows slightly higher $\delta$ values than ligament, which may be linked to its denser and more aligned fiber architecture, enhancing scattering and internal friction mechanisms.

Cartilage (figure 205 C) presents a distinct response characterized by a very steep decrease in diffusivity between $0.5$ and $1MHz$, followed by a rapid stabilization at higher frequencies. This behavior is indicative of strong initial energy dissipation mechanisms, likely associated with its poroelastic nature, where fluid-solid interactions dominate at lower frequencies. As frequency increases, fluid mobility becomes restricted, and the system transitions toward a more elastic-dominated response, resulting in reduced sensitivity of $\delta$ to further frequency increases. Compared to tendon and ligament, cartilage exhibits significantly higher diffusivity at low frequencies, highlighting its strong dissipative capacity in this regime.

Bone tissues (figure 206 A–B) display the highest diffusivity values among all investigated materials, reflecting their complex hierarchical and heterogeneous structure. Cortical bone, in particular, exhibits markedly higher $\delta$ values than trabecular bone, especially at lower frequencies. This difference can be

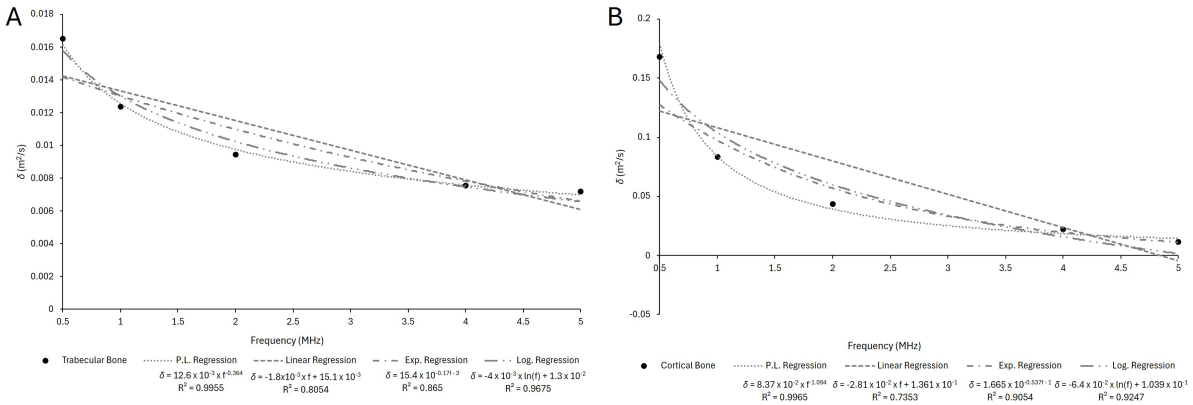



Figure 206: Frequency-dependent sound diffusivity for hard tissues: (A) trabecular bone and (B) cortical bone, with corresponding regression model fits.

attributed to its dense mineralized matrix and the presence of microstructural features such as osteons and pores, which contribute to increased scattering and absorption.

Both bone types show a clear decrease in diffusivity with increasing frequency, although the rate of decay is less pronounced than in softer tissues. This suggests that, while frequency-dependent mechanisms remain relevant, structural heterogeneity plays a dominant role in governing attenuation in bone. The persistence of relatively high $\delta$ values even at higher frequencies indicates that scattering effects remain significant across the studied frequency range.

# Appendix C

# Supplemental Simulation Framework Data

# C.1 Imaging processing results

Figures 207-214 present the segmentation results obtained from MRI data of the knee joint for the analyzed subjects. Each figure illustrates the spatial delineation of the principal anatomical components, namely skin, adipose tissue, skeletal muscle, tendon, bone, and cartilage, following the image-processing workflow described previously. The segmented domains are represented as binary masks, enabling clear identification of tissue boundaries and geometric features relevant for subsequent computational modelling.

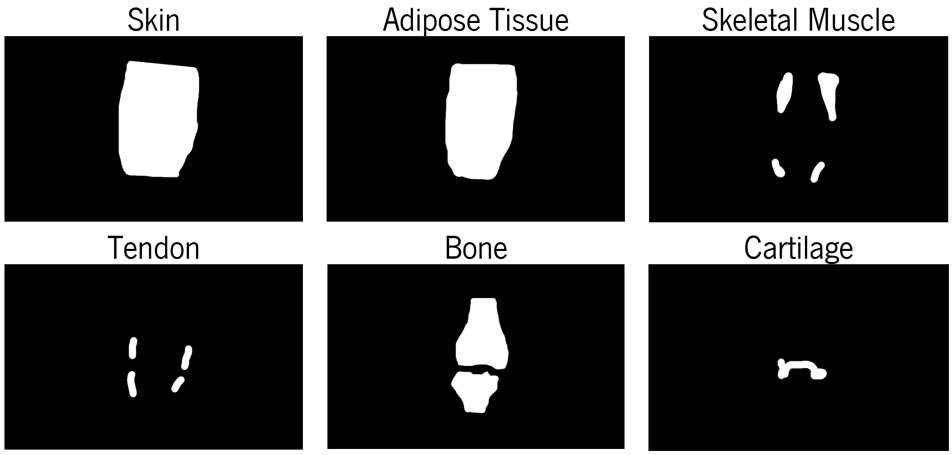



Figure 207: Processing results of the MRI scan of the knee joint for the different organs of patient A.

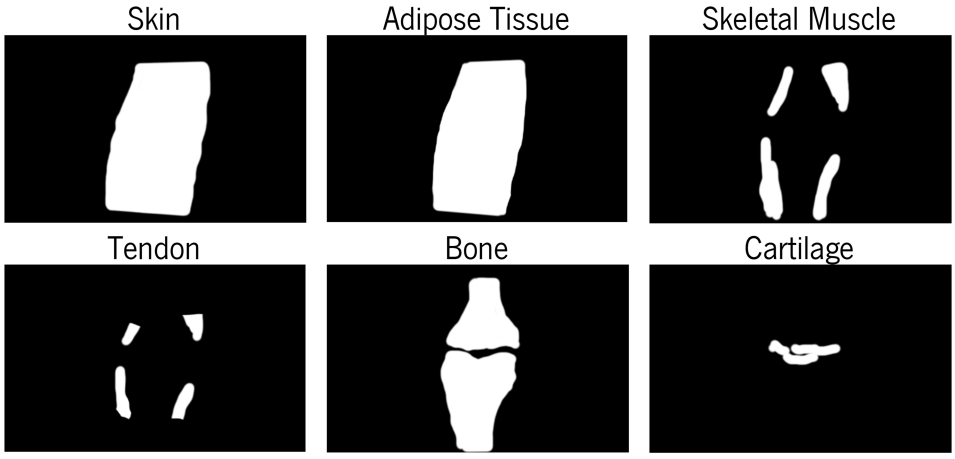



Figure 208: Processing results of the MRI scan of the knee joint for the different organs of patient B.

Across all subjects, the segmentation procedure successfully isolates both soft and hard tissues, preserving the overall anatomical structure of the joint while highlighting inter-patient variability in morphology. Differences are particularly evident in the distribution and thickness of soft tissues, as well as in cartilage geometry and joint spacing, which are critical parameters influencing acoustic wave propagation and mechanical response. The skeletal muscle and tendon regions exhibit more fragmented

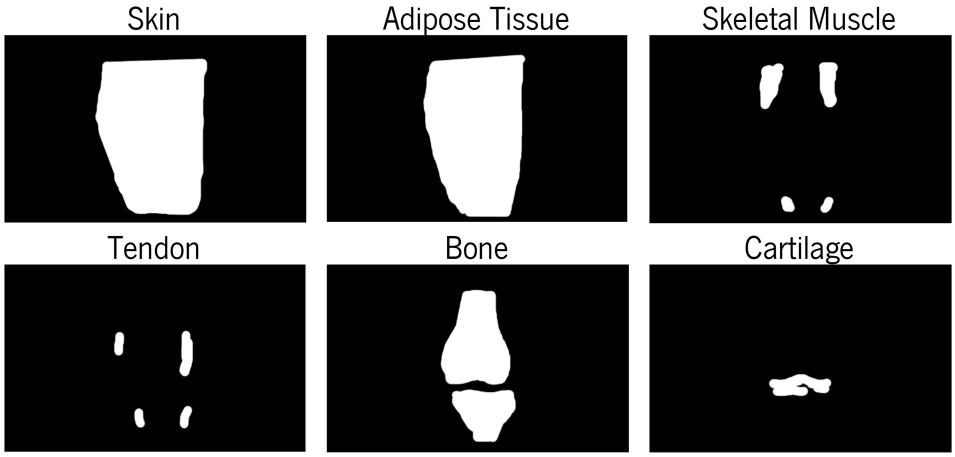



Figure 209: Processing results of the MRI scan of the knee joint for the different organs of patient C.

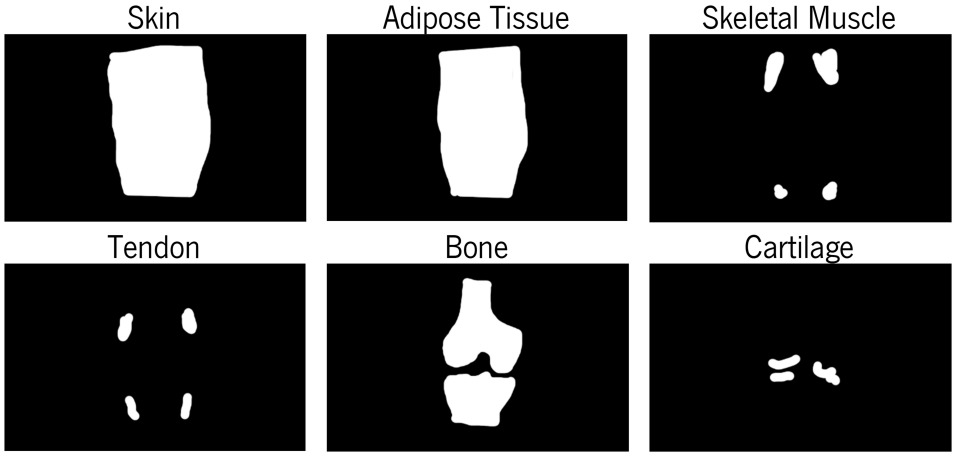



Figure 210: Processing results of the MRI scan of the knee joint for the different organs of patient D.

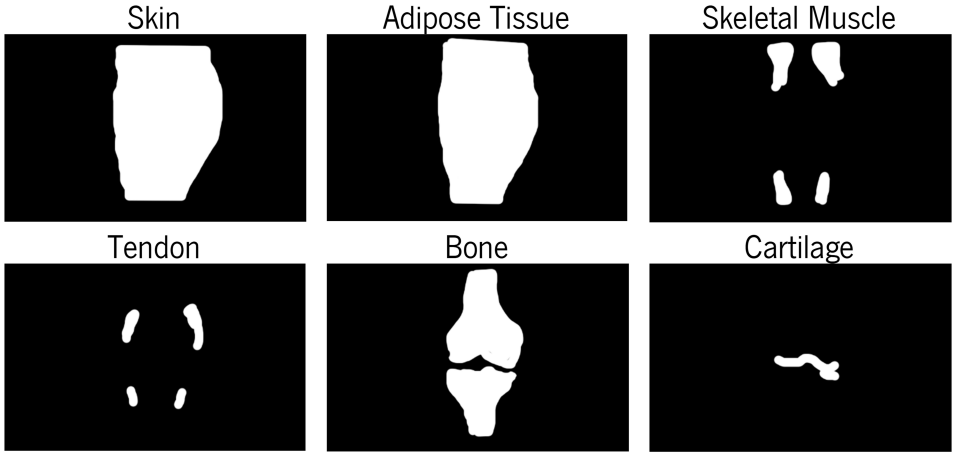



Figure 211: Processing results of the MRI scan of the knee joint for the different organs of patient E.

patterns due to their anatomical complexity and orientation-dependent appearance in the imaging plane, whereas bone structures remain well-defined and continuous across all cases.

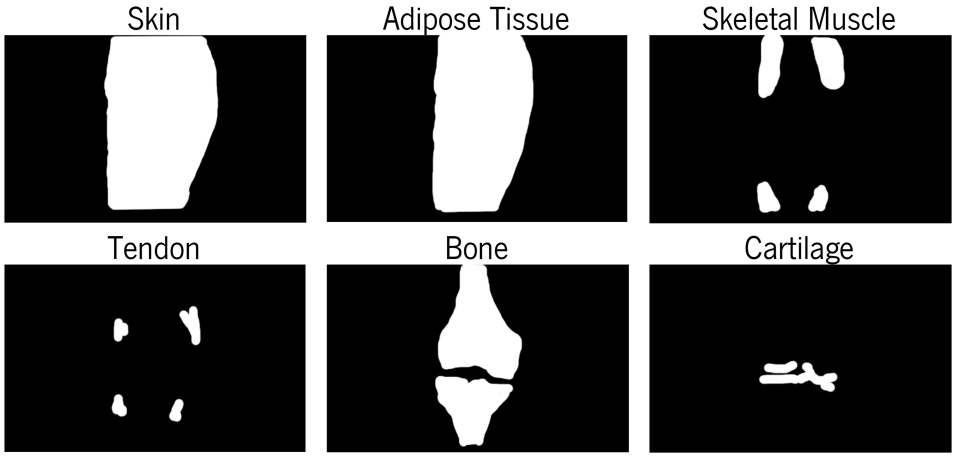



Figure 212: Processing results of the MRI scan of the knee joint for the different organs of patient F.

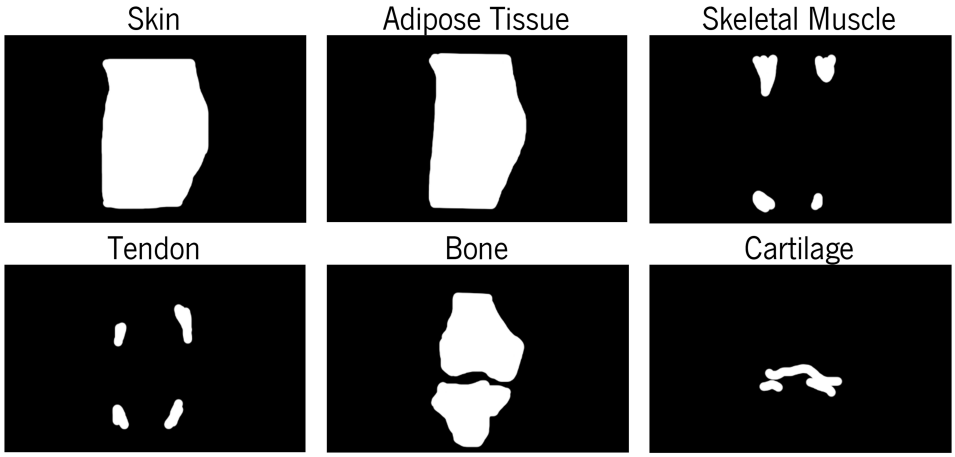



Figure 213: Processing results of the MRI scan of the knee joint for the different organs of patient G.

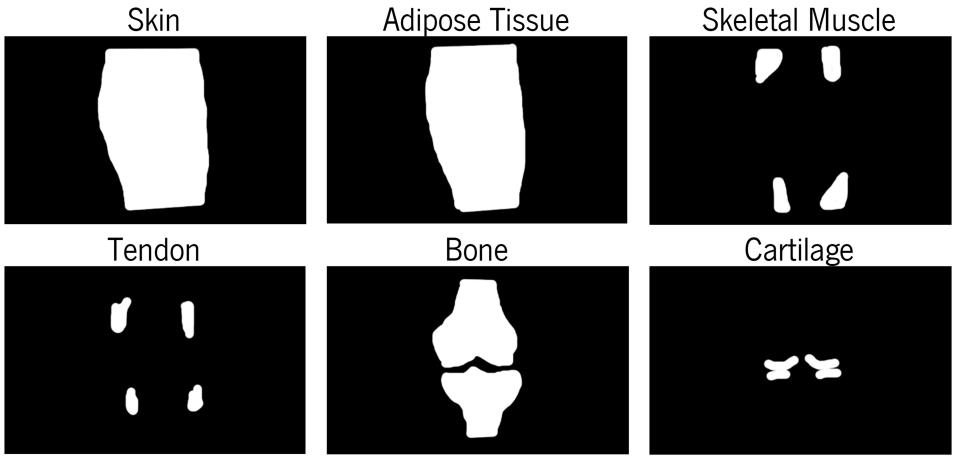



Figure 214: Processing results of the MRI scan of the knee joint for the different organs of patient H.

## C.2 Transfer Function Magnitude from Transducer to Cartilage for the Remaining Patients

Figures 215–221 present the transfer function magnitude $|H_{pp}|$ from the transducer to the cartilage as a function of frequency for Patients B–H, considering transducer diameters ranging from $30$ to $75$ mm.

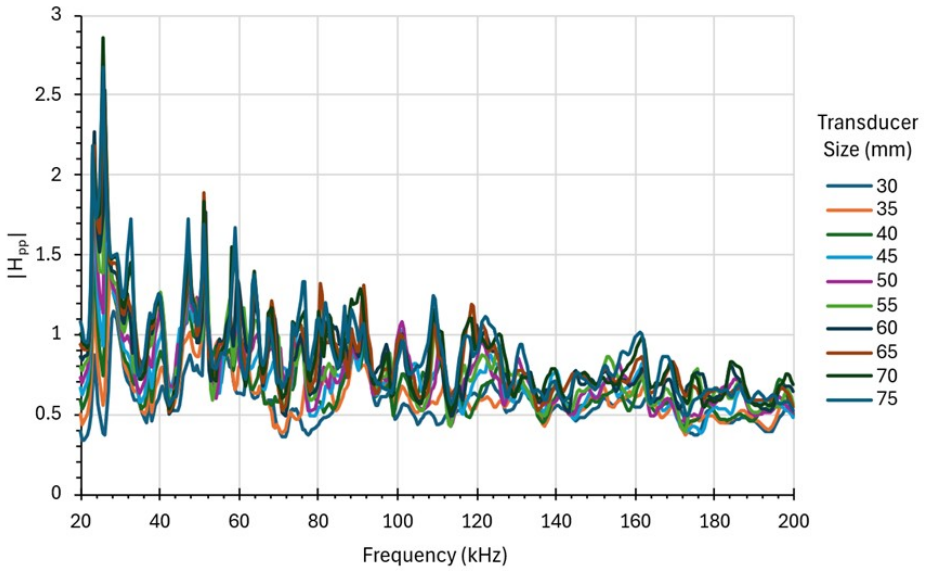



Figure 215: Transfer function magnitude $|H_{pp}|$ from transducer to cartilage for Patient B as a function of frequency for varying transducer diameters ($30$–$75$ mm).

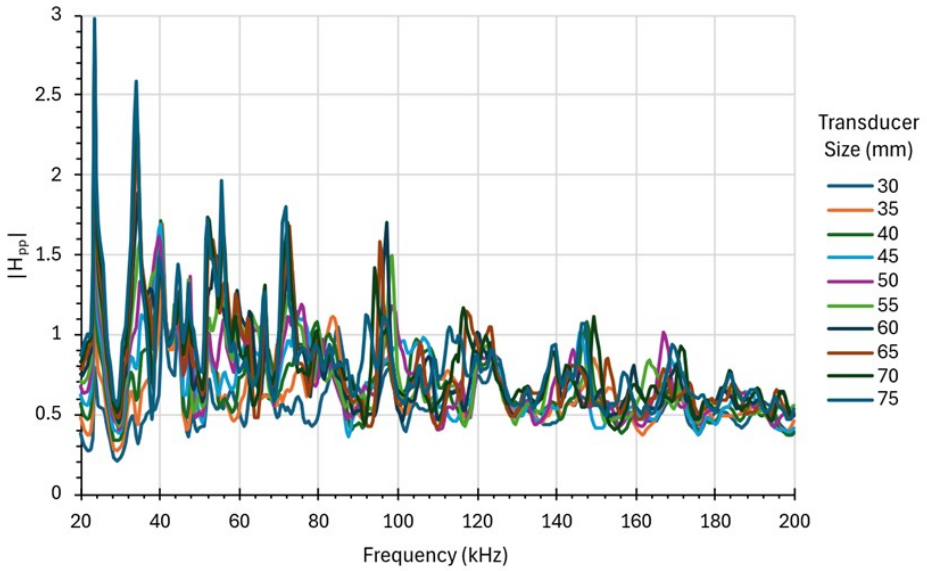



Figure 216: Transfer function magnitude $|H_{pp}|$ from transducer to cartilage for Patient C as a function of frequency for varying transducer diameters ($30$–$75$ mm).

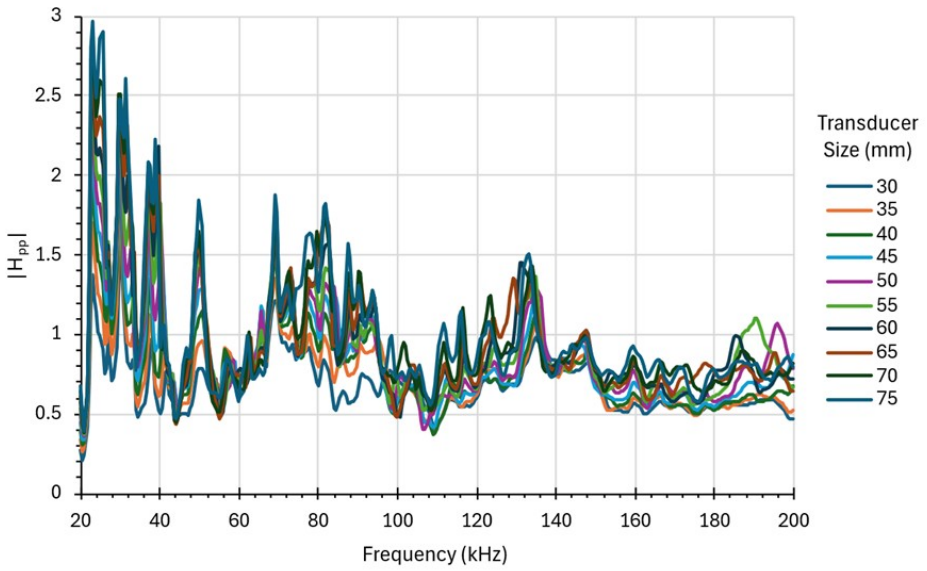



Figure 217: Transfer function magnitude $|H_{pp}|$ from transducer to cartilage for Patient D as a function of frequency for varying transducer diameters ($30$–$75$ mm).

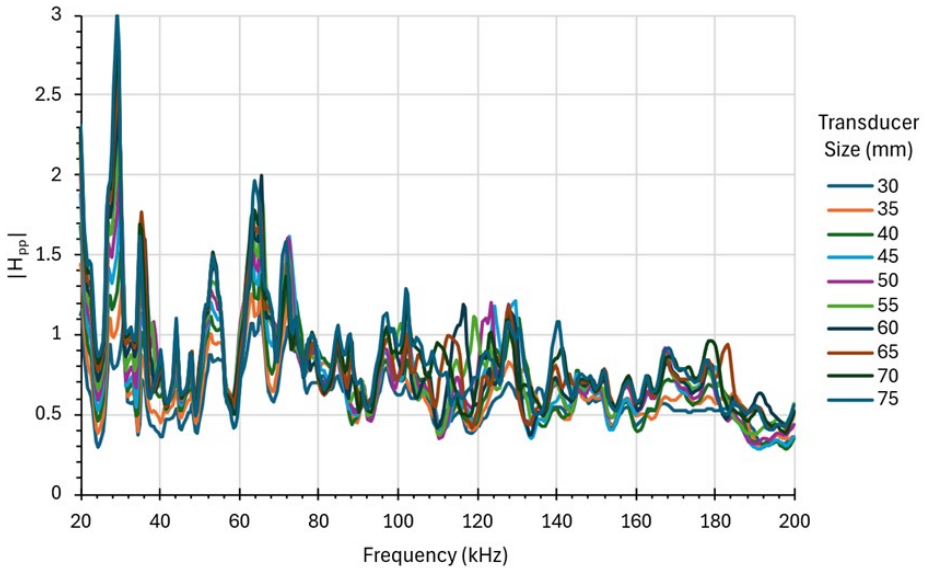



Figure 218: Transfer function magnitude $|H_{pp}|$ from transducer to cartilage for Patient E as a function of frequency for varying transducer diameters ($30$–$75$ mm).

Across all subjects, the acoustic response exhibits a consistent frequency-dependent behavior, characterized by higher transmissibility in the low-frequency range (approximately $20$–$60$ kHz), followed by a gradual attenuation and stabilization at higher frequencies.

For smaller transducer diameters, moderate variability in amplitude is observed, particularly within the low-frequency region, where peak magnitudes show sensitivity to transducer size and positioning. However, as the transducer diameter increases beyond approximately $60$ mm, the response curves tend to converge, indicating that the influence of source geometry on transmissibility becomes progressively less significant. In this regime, both the magnitude and location of the dominant peaks remain largely

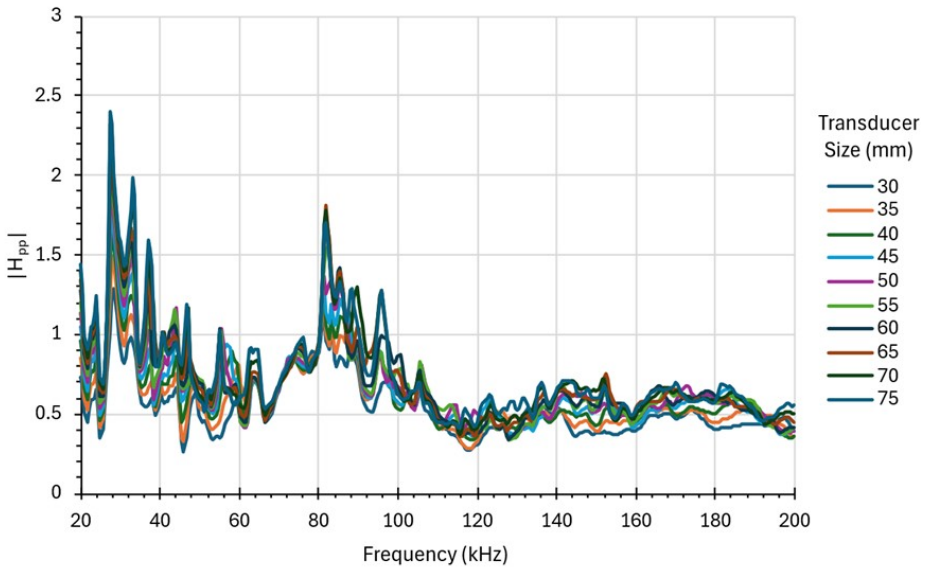



Figure 219: Transfer function magnitude $|H_{pp}|$ from transducer to cartilage for Patient F as a function of frequency for varying transducer diameters ($30$–$75$ mm).

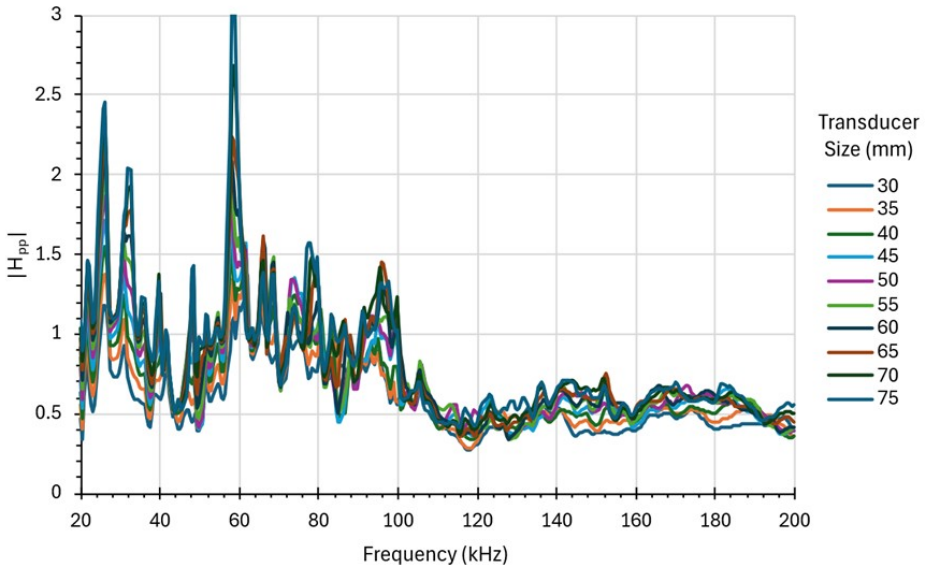



Figure 220: Transfer function magnitude $|H_{pp}|$ from transducer to cartilage for Patient G as a function of frequency for varying transducer diameters ($30$–$75$ mm).

unchanged across configurations.

Despite patient-specific differences in anatomical geometry, which result in variations in peak amplitude and minor frequency shifts, the overall spectral shape and decay trend are preserved across all cases. The dominant amplification regions consistently occur within comparable frequency bands, while higher-frequency responses exhibit reduced variability and lower transmissibility.

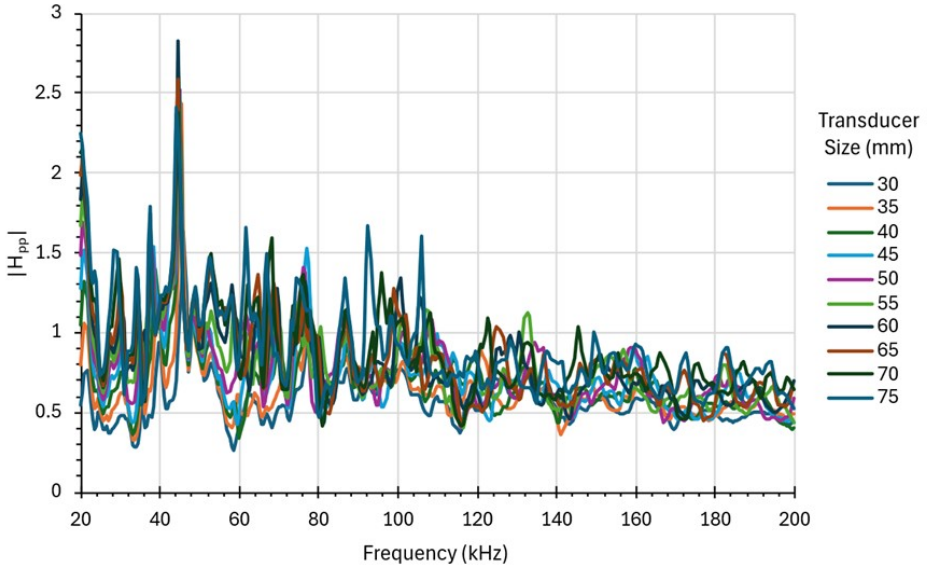



Figure 221: Transfer function magnitude $|H_{pp}|$ from transducer to cartilage for Patient H as a function of frequency for varying transducer diameters ($30$–$75$ mm).

## C.3 Acoustic pressure distribution for the remaining patients

Figures 222–228 illustrate the spatial distribution of the RMS acoustic pressure within the knee joint of Patients B–H under varying excitation frequencies and transducer sizes. The results are presented for three dominant frequencies and transducer diameters ranging from $30$ to $75$ mm, with the color scale indicating the pressure amplitude (Pa $\times 10^2$).

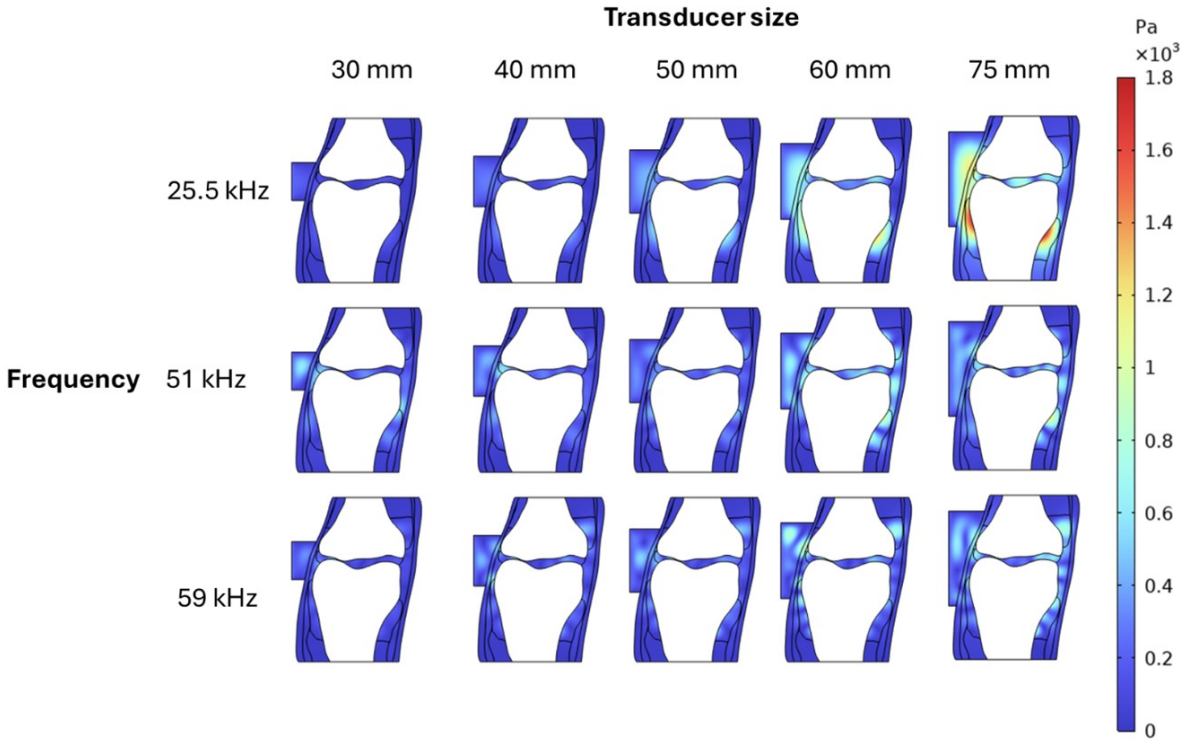



Figure 222: RMS acoustic pressure distribution for Patient B under varying excitation conditions. The color scale represents pressure amplitude (Pa $\times 10^2$).

At the lowest frequency, the acoustic fields exhibit pronounced spatial heterogeneity, with localized regions of elevated pressure emerging near tissue interfaces, particularly at the cartilage boundaries and adjacent bone structures. As the transducer size increases, these high-amplitude regions become more prominent and spatially extended, indicating enhanced energy coupling and partial focusing within the joint space.

At intermediate and higher frequencies, the pressure fields become more diffuse, with lower peak amplitudes and reduced localization. Although regions of amplification are still observable near structural interfaces, their intensity and spatial extent are diminished compared to the lower-frequency case. This behavior reflects increased attenuation and reduced constructive interference at higher frequencies.

Across all excitation conditions, the general propagation pathway remains consistent, with acoustic energy entering through the soft tissue layers and interacting with internal structures before reaching the cartilage. However, both the magnitude and spatial distribution of the pressure field are strongly influenced

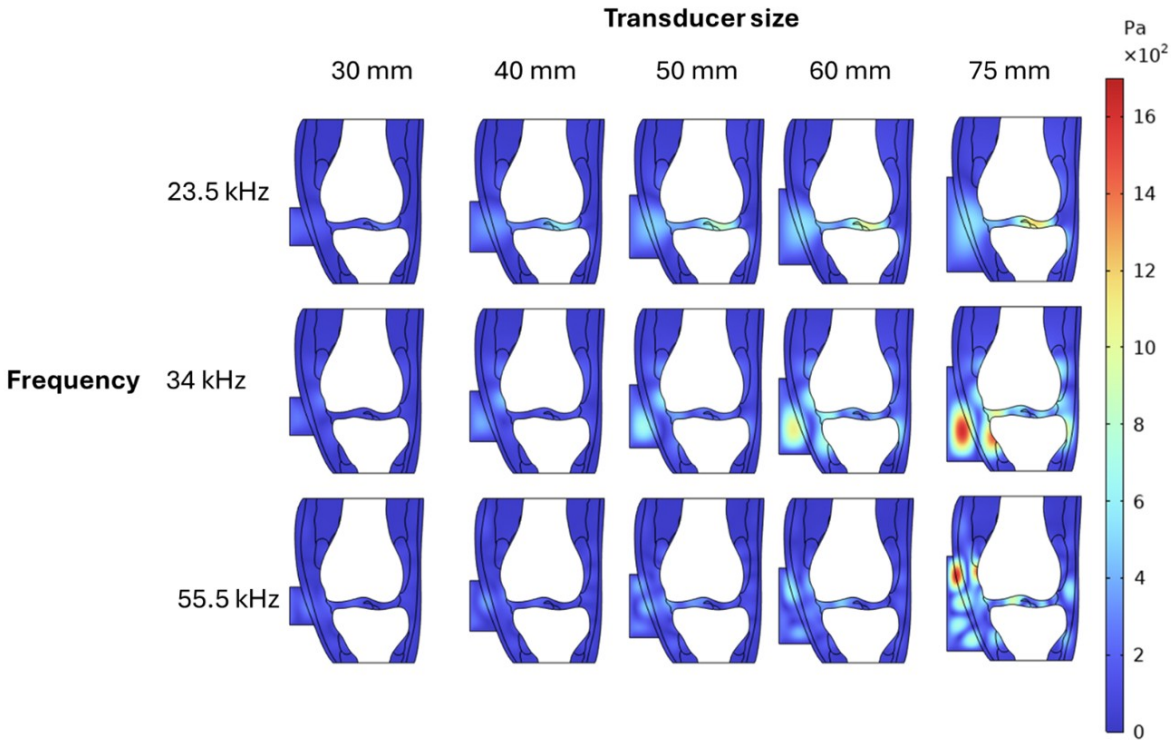



Figure 223: RMS acoustic pressure distribution for Patient C under varying excitation conditions. The color scale represents pressure amplitude (Pa $\times 10^2$).

by frequency and transducer size. Larger transducers tend to promote broader energy distribution and slightly increased pressure levels, whereas smaller transducers produce more confined and less intense fields.

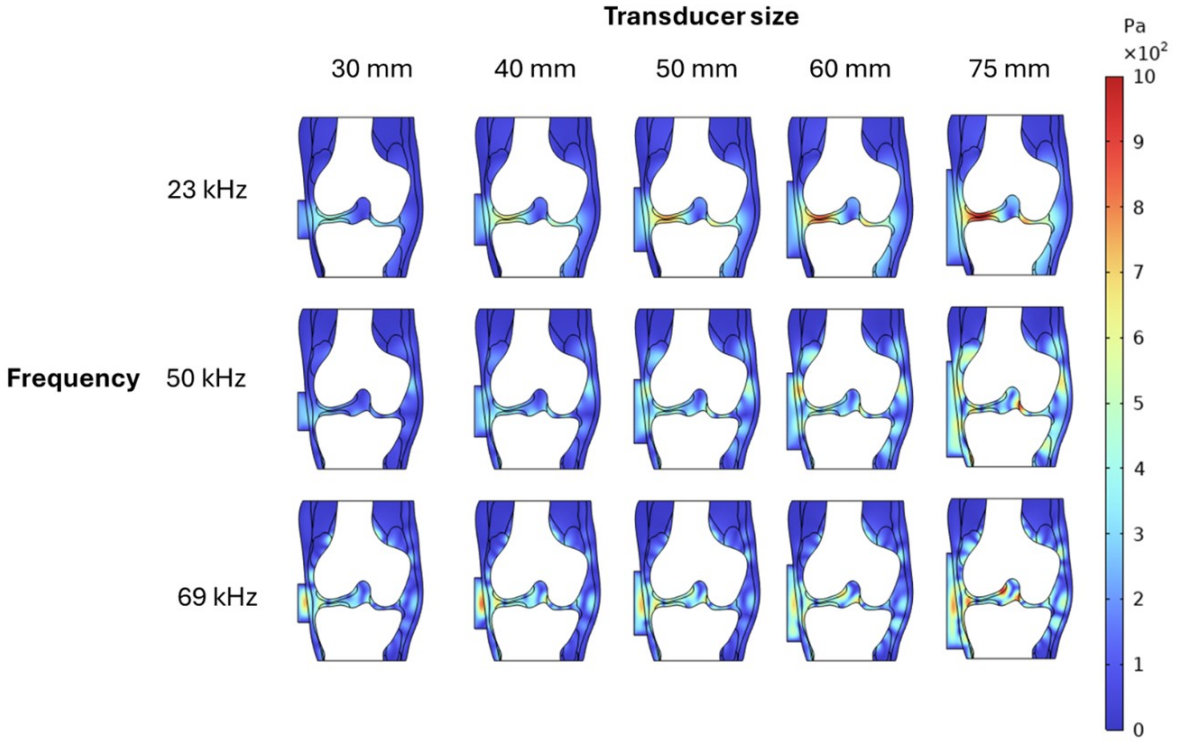



Figure 224: RMS acoustic pressure distribution for Patient D under varying excitation conditions. The color scale represents pressure amplitude (Pa $\times 10^2$).

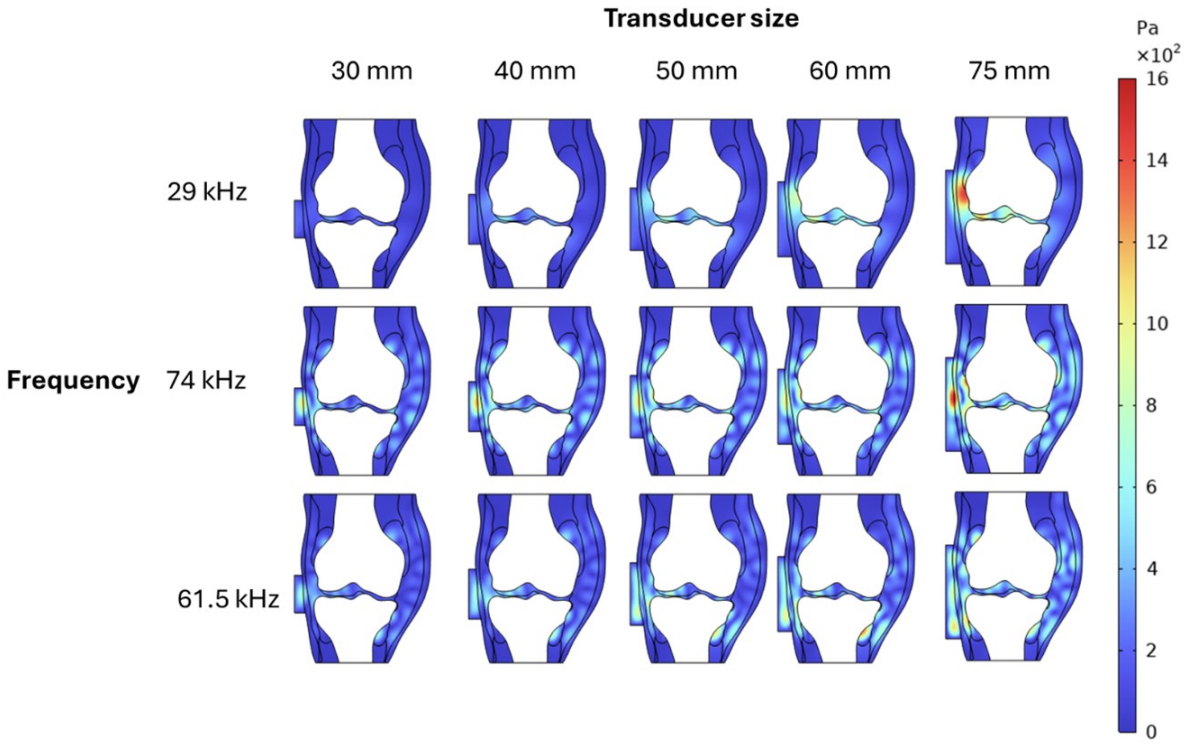



Figure 225: RMS acoustic pressure distribution for Patient E under varying excitation conditions. The color scale represents pressure amplitude (Pa $\times 10^2$).

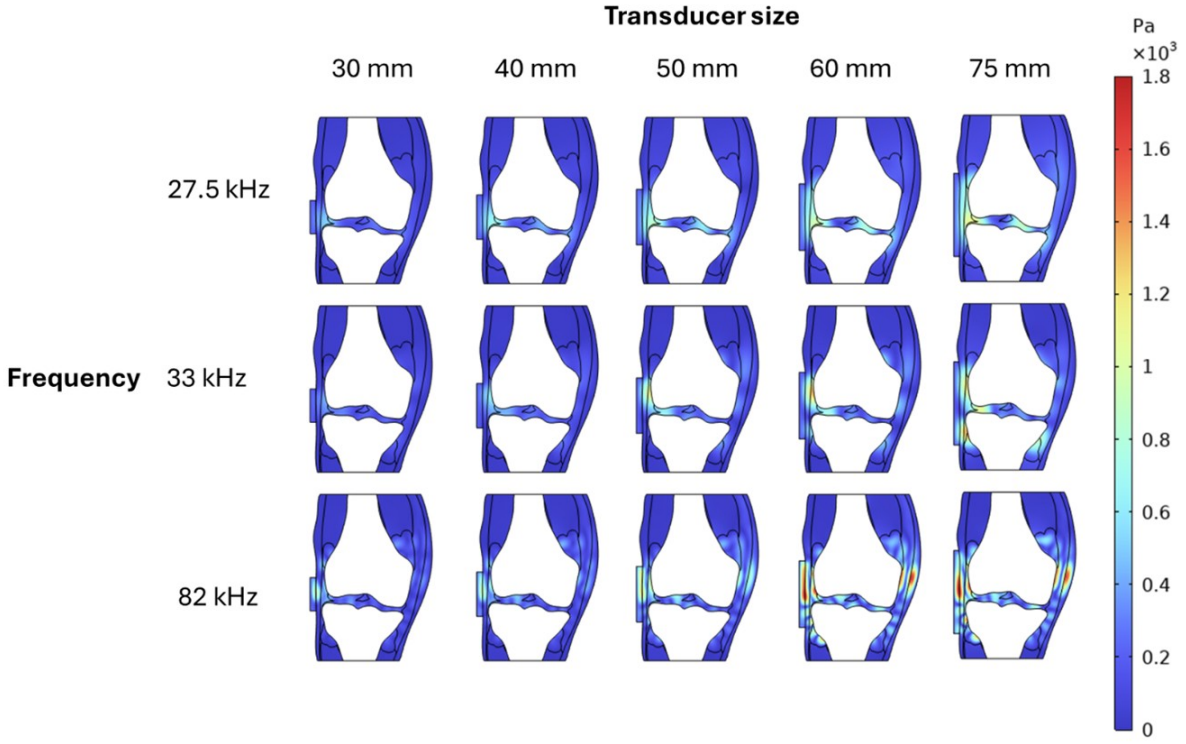



Figure 226: RMS acoustic pressure distribution for Patient F under varying excitation conditions. The color scale represents pressure amplitude (Pa $\times 10^2$).

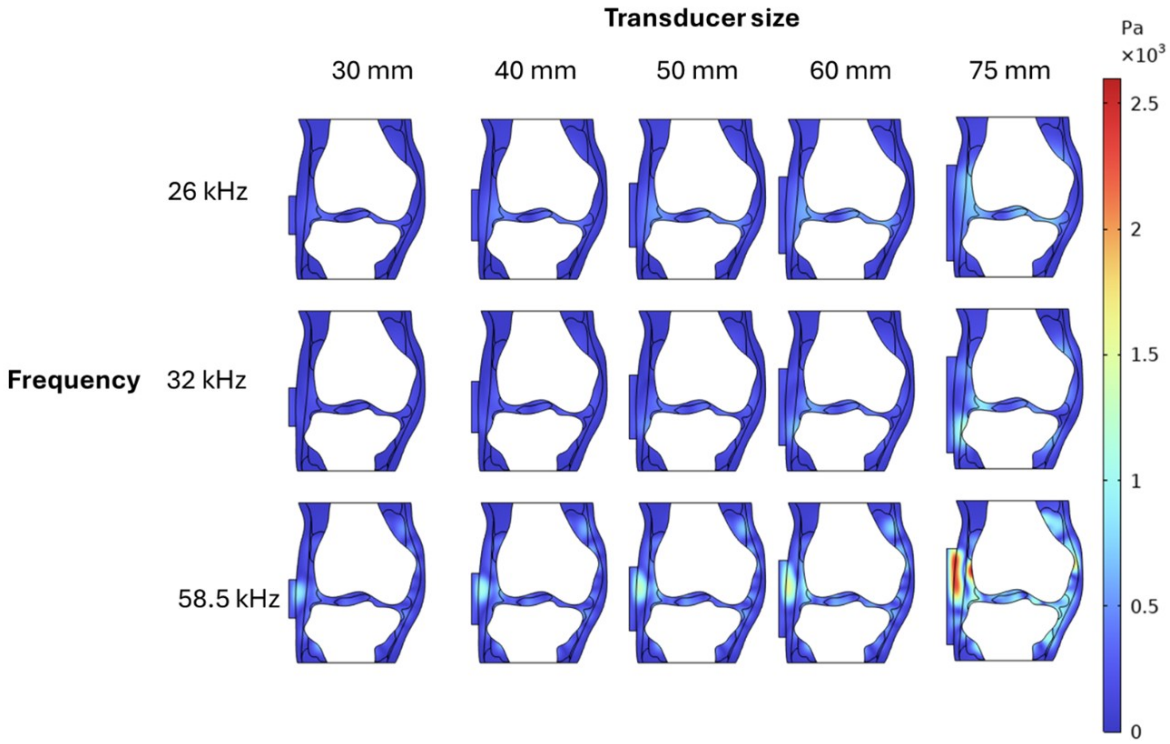



Figure 227: RMS acoustic pressure distribution for Patient G under varying excitation conditions. The color scale represents pressure amplitude (Pa $\times 10^2$).

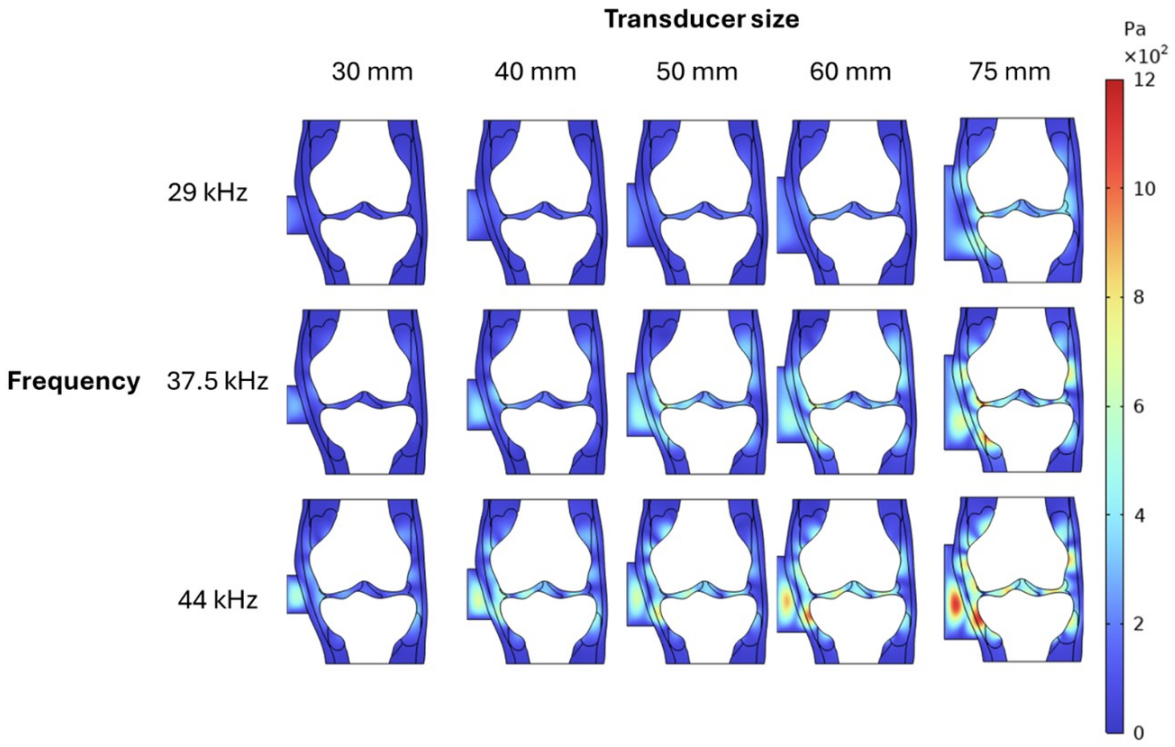



Figure 228: RMS acoustic pressure distribution for Patient H under varying excitation conditions. The color scale represents pressure amplitude (Pa $\times 10^2$).

# Appendix D

# Supplemental Experimental Validation Data

# D.1 Additional Tissue-mimicking Phantom Characterization Data

## D.1.1 Silicone Phantoms Additional Materials and Methods

To design composite medical phantoms capable of reproducing the anisotropic mechanical and acoustic behaviour of fibrous biological tissues, this study adopted an integrated methodology combining computational modelling with experimental validation. The framework was based on an iterative design strategy, in which numerical simulations guided material selection, composite architecture, and expected tissue-mimicking performance, while experimental characterization was used to verify the predicted behaviour and refine the modelling assumptions. Initially, the mechanical response of the silicone matrix was characterized and fitted using hyperelastic constitutive models, providing the basis for simulating tissue-like deformation under physiologically relevant loading conditions. These simulations supported the design of anisotropic composite structures by enabling the influence of fiber orientation and volume fraction to be controlled. The resulting configurations were then implemented through a custom fabrication process to ensure reproducible sample production. In parallel, viscoelastic and acoustic wave propagation simulations were performed to estimate the frequency-dependent and direction-dependent behaviour of the phantoms, thereby defining relevant targets for elastography and ultrasound-based validation. The manufacturing procedure and experimental protocols were designed to reproduce the numerical conditions as closely as possible, ensuring consistency between model predictions and physical testing. Overall, this approach ensured that the theoretical assumptions and computational outputs were experimentally grounded, supporting the development of bioinspired phantoms with validated mechanical and acoustic performance.

### D.1.1.1 Computational Methods

Computational modelling was used at three key stages of this study to define appropriate reference conditions and support the design of the composite phantom materials. All numerical simulations were performed in COMSOL Multiphysics 5.3, while Python 3.13.2 was used for post-processing and data analysis. First, biological tissues were simulated under the same loading and testing conditions applied to the phantoms, allowing direct comparison between native tissue behaviour and the developed tissue-mimicking materials. Second, the mechanical response of the elastomeric matrix was modelled

by fitting the experimentally measured behaviour to appropriate hyperelastic constitutive laws. Finally, the numerical framework was used to iteratively optimize the phantom formulation by adjusting fiber content and architecture, with the objective of reproducing the acoustic and mechanical anisotropy of the target tissues.

**Tensile Hyperelastic Model Curve Fitting**

The mechanical response of the elastomeric matrix was evaluated from uniaxial tensile data and subsequently fitted to several hyperelastic constitutive models using the Cauchy stress formulation. The identification of hyperelastic material parameters can be complex, particularly when volumetric deformation is considered. For this reason, elastomeric materials are commonly approximated as nearly incompressible, which is a suitable assumption for most rubber-like polymers. Under this condition, the strain energy density function may be decomposed into an isochoric contribution, $W_{\text{iso}}$, associated with distortional deformation, and a volumetric contribution, $W_{\text{vol}}$, associated with changes in volume. For an incompressible material, the volume ratio is constrained to $J = 1$, and the incompressibility condition is enforced through the Lagrange multiplier $p$, as expressed in Equation 273.

$$W_s = W_{\text{vol}} + W_{\text{iso}} = W_{\text{iso}} - p(J-1) \tag{273}$$

The second Piola–Kirchhoff stress tensor can then be written as a function of the isochoric strain energy density, the volume ratio $J$, and the right Cauchy–Green deformation tensor $C$, according to Equation 274.

$$S = -pJC^{-1} + 2\frac{\partial W_{\text{iso}}}{\partial C} \tag{274}$$

By expanding this expression in terms of the invariants of the isochoric Cauchy–Green tensor, $\bar{C} = J^{-2/3}C$, the second Piola–Kirchhoff stress may be expressed as:

$$\begin{aligned} S = -pJC^{-1} + 2\Bigg[ & J^{-2/3}\left(\frac{\partial W_{\text{iso}}}{\partial \bar{I}_1} + \bar{I}_1\frac{\partial W_{\text{iso}}}{\partial \bar{I}_2}\right) - J^{-4/3}\frac{\partial W_{\text{iso}}}{\partial \bar{I}_2}C \\ & - \left(\frac{\bar{I}_3}{3}\frac{\partial W_{\text{iso}}}{\partial \bar{I}_1} + \frac{2\bar{I}_3}{3}\frac{\partial W_{\text{iso}}}{\partial \bar{I}_2}\right)C^{-1}\Bigg] \end{aligned} \tag{275}$$

The first Piola–Kirchhoff stress tensor, $P$, and the Cauchy stress tensor, $\sigma$, are related to the second Piola–Kirchhoff stress tensor through the deformation gradient $F$, as shown in Equation 276.

$$P = FS, \qquad \sigma = J^{-1}FSF^T \tag{276}$$

In hyperelasticity, both the strain energy density and the resulting stress measures are commonly formulated as functions of the stretch ratio, $\lambda$. In a uniaxial tensile test, this quantity is defined as

$\lambda = L/L_0$, where $L$ and $L_0$ are the deformed and initial lengths, respectively. For a general multiaxial deformation state, the principal stretches $\lambda_a$, with $a = 1, 2, 3$, may be defined along the principal material directions $\hat{N}_a$. The spectral representation of the right Cauchy–Green tensor is then given by Equation 277.

$$C = \sum_{a=1}^{3} \lambda_a^2 \hat{N}_a \otimes \hat{N}_a \tag{277}$$

For an incompressible isotropic material subjected to uniaxial extension, the principal stretches are defined as:

$$\lambda_1 = \lambda, \qquad \lambda_2 = \lambda_3 = \lambda^{-1/2} \tag{278}$$

Accordingly, the deformation gradient can be written as:

$$F = \begin{bmatrix} \lambda & 0 & 0 \\ 0 & \lambda^{-1/2} & 0 \\ 0 & 0 & \lambda^{-1/2} \end{bmatrix} \tag{279}$$

Assuming uniaxial extension and imposing the transverse stress-free conditions $S_2 = S_3 = 0$, the pressure term can be eliminated. The resulting expressions for the axial second Piola–Kirchhoff stress, first Piola–Kirchhoff stress, and Cauchy stress are presented in Equation 280.

$$S_1 = 2\left(\frac{1}{\lambda} - \frac{1}{\lambda^4}\right)\left(\lambda \frac{\partial W_{\text{iso}}}{\partial \bar{I}_{1,\text{uni}}} + \frac{\partial W_{\text{iso}}}{\partial \bar{I}_{2,\text{uni}}}\right), \qquad P_1 = \lambda S_1, \qquad \sigma_1 = \lambda^2 S_1 \tag{280}$$

The isochoric invariants for uniaxial deformation are defined in terms of the stretch ratio as:

$$\bar{I}_{1,\text{uni}} = \lambda^2 + \frac{2}{\lambda}, \qquad \bar{I}_{2,\text{uni}} = 2\lambda + \frac{1}{\lambda^2} \tag{281}$$

To determine the most appropriate constitutive representation for the silicone matrix, the experimental stress–stretch data were fitted to four hyperelastic models: Neo-Hookean, two-parameter Mooney–Rivlin, five-parameter Mooney–Rivlin, and Ogden. The incompressible Neo-Hookean strain energy density is given by equation 282, where $\mu$ is the material constant obtained through curve fitting.

$$W_{\text{iso}} = \frac{1}{2}\mu(\bar{I}_1 - 3) \tag{282}$$

For incompressible uniaxial deformation, the first Piola–Kirchhoff stress predicted by the Neo-Hookean model becomes:

$$P_{1,\text{uniaxial}} = \mu(\lambda - \lambda^{-2}) \tag{283}$$

The corresponding first Piola–Kirchhoff stress for the two-parameter Mooney–Rivlin model is given by:

$$P_{1,\text{uniaxial}} = 2(1 - \lambda^{-3})(\lambda C_{10} + C_{01}) \tag{284}$$

The five-parameter Mooney–Rivlin model extends this formulation by including higher-order terms associated with the isochoric invariants. Its uniaxial stress expression is:

$$P_{1,\text{uniaxial}} = 2(1-\lambda^{-3})\Big[\lambda C_{10} + 2C_{20}\lambda(I_{1,\text{uni}}-3) + C_{11}\lambda(I_{2,\text{uni}}-3) + C_{01} + 2C_{02}(I_{2,\text{uni}}-3) + C_{11}(I_{1,\text{uni}}-3)\Big] \tag{285}$$

The Ogden model describes nonlinear elastic behaviour using a stretch-based spectral formulation. For uniaxial deformation, the first Piola–Kirchhoff stress is expressed as:

$$P_{1,\text{uniaxial}} = \sum_{p=1}^{n} \mu_p \left(\lambda^{\alpha_p - 1} - \lambda^{-\frac{\alpha_p}{2}-1}\right) \tag{286}$$

The material parameters of each constitutive model were identified using a least-squares fitting procedure. This method minimized the sum of squared residuals between the experimentally measured stresses and the stresses predicted by each model over the full stretch range. The fitted parameters obtained for each formulation are presented and compared in the Results section.

The tensile test was also reproduced numerically to match the experimental configuration. The simulation was performed using the Solid Mechanics interface within the Structural Mechanics Module, including the Nonlinear Structural Materials formulation. The specimen geometry was defined with a length of 120 mm, width of 20 mm, and thickness of 2 mm. To reproduce the grip conditions used during the experimental test, the model was divided into three regions, with 40 mm assigned to the lower grip, 40 mm to the upper grip, and the remaining central region corresponding to the deformable gauge section.

The lower grip region was fixed, while a prescribed displacement was applied to the upper grip at a constant velocity of 10 mm/min, matching the experimental loading rate. The time history recorded during the tensile test was used to define the simulation duration. A cross-sectional plane was placed at the centre of the specimen to extract the average Cauchy stress, which was then compared with the experimental stress response. A mesh convergence analysis was conducted, and a triangular mesh with an element size of 1 mm was selected as the optimal compromise between numerical accuracy and computational stability.

**Micro- and Macromechanical Composite Formulation** In macroscopic structural analyses, explicitly representing microscale heterogeneity is often computationally inefficient and may be unnecessary when the objective is to describe the global material response. For this reason, heterogeneous materials are commonly replaced by an equivalent homogeneous medium with effective properties obtained through homogenization. In COMSOL Multiphysics, this procedure can be

implemented using the cell periodicity approach, which is based on the RVE concept and referred to as the Repeating Unit Cell (RUC) method. The RUC defines a periodic domain that captures the relevant microstructural features of the composite. For a periodic material, the displacement field can be decomposed into a macroscopic contribution associated with the average strain tensor, $\bar{\varepsilon}$, and a periodic fluctuation term, $u^*$, as expressed in Equation 287.

$$u = \bar{\varepsilon} X + u^* \tag{287}$$

Because the periodic unit cells represent a continuous material system, displacement compatibility must be enforced across opposite boundaries of the RUC. In COMSOL, this is implemented through boundary pairs, where opposing parallel faces are defined as source and destination boundaries. The displacement field on each paired boundary is expressed as:

$$u_{\text{dst}} = \bar{\varepsilon} X_{\text{dst}} + u^*, \qquad u_{\text{src}} = \bar{\varepsilon} X_{\text{src}} + u^* \tag{288}$$

Thus, periodic displacement continuity is imposed by requiring that the displacement difference between paired boundaries depends only on the imposed macroscopic strain and on the relative position of the two boundaries, as shown in Equation 289.

$$u_{\text{dst}} - u_{\text{src}} = \bar{\varepsilon} \left( X_{\text{dst}} - X_{\text{src}} \right) \tag{289}$$

The material properties used in the composite simulations were assigned independently to the elastomeric matrix and fiber phases. The matrix parameters were obtained from the hyperelastic curve-fitting procedure described in the previous section, whereas the fiber properties were determined experimentally. The complete set of parameters used for the fiber-reinforced RUC model is presented in Table 28.

Table 28: Material parameters used for the fiber-reinforced RUC simulations.

| Parameter | Value |
|---|---|
| Density (kg/m$^3$) | 1200 |
| Poisson's ratio (transverse strain due to axial load) | 0.2 |
| Poisson's ratio (out-of-plane strain due to in-plane load) | 0.05 |
| Young's modulus (longitudinal/along fiber direction) (MPa) | 202 |
| Young's modulus (transverse/perpendicular to fiber direction) (MPa) | 11 |

After defining the microscale geometry, its effective behaviour was transferred to the macroscale through homogenization. Six independent loading cases were applied to the RUC to determine the full effective elasticity matrix. This procedure allows the heterogeneous composite cell to be represented as an equivalent continuous material. The macroscopic stress tensor, $\bar{\sigma}$, and strain tensor, $\bar{\varepsilon}$, were obtained

by volume averaging the corresponding microscopic fields over the periodic cell volume, $V$, according to Equation 290.

$$\bar{\sigma} = \frac{1}{V}\int_V \sigma \, dV, \qquad \bar{\varepsilon} = \frac{1}{V}\int_V \varepsilon \, dV \tag{290}$$

The effective macroscopic elasticity tensor, $\bar{C}$, was then defined from the relationship between the averaged stress and strain tensors:

$$\bar{\sigma} = \bar{C} : \bar{\varepsilon} \tag{291}$$

This homogenization framework was used to guide the design of the composite phantom materials. The simulated mechanical response of each formulation was compared with constitutive descriptions of fibrous biological tissues reported in the literature. The analyses were performed using the Solid Mechanics interface within the Structural Mechanics Module, together with the Composite Materials Module. By comparing the homogenized composite response with the target tissue behaviour, the most suitable formulation was identified according to its capacity to reproduce the mechanical characteristics of native anisotropic tissues.

**Dynamic Mechanical Response Calculation**

To evaluate the dynamic response of fibrous biological tissues, namely human skin and skeletal muscle, a numerical compressive test was implemented in COMSOL Multiphysics using the Solid Mechanics interface within the Structural Mechanics Module. The model considered viscoelastic energy dissipation, which is a relevant feature of soft biological tissues under cyclic loading. A rectangular specimen with dimensions of $20$ mm $\times$ $20$ mm $\times$ $2$ mm was defined, with one face fixed and the opposite face subjected to a sinusoidal compressive load. The analysis was performed over a frequency range of 10–100 Hz using the Finite Element Method, allowing the frequency-dependent mechanical response of the material to be evaluated.

The viscoelastic behaviour of the simulated tissues was described using the Kelvin–Voigt formulation, which is commonly used to represent the dynamic response of soft biological materials. This model combines an elastic spring and a viscous damper in parallel, allowing the instantaneous elastic response and time-dependent dissipative behaviour to be represented simultaneously. The constitutive relation is given by equation 292,

$$\sigma = E\varepsilon + \eta\dot{\varepsilon} \tag{292}$$

where $\sigma$ is the stress, $E$ is the elastic modulus, $\varepsilon$ is the strain, $\eta$ is the viscosity coefficient, and $\dot{\varepsilon}$ is the strain rate. This formulation enables the material to store part of the mechanical energy elastically while

dissipating another part through viscous effects, reproducing the main features of cyclic loading in soft tissues.

The material properties and Kelvin–Voigt model parameters used in the simulations are summarized in Table 29. Instead of assigning a single deterministic value to each parameter, a range of values was considered to account for the natural variability and heterogeneity of biological tissues. Several parametric sweeps were therefore performed to identify the range of mechanical responses expected for fibrous tissues under dynamic compression.

Table 29: Simulation parameters for dynamic mechanical compressive tests of skin and skeletal muscle.

| Parameter | Human skin | | Skeletal muscle | |
|---|---|---|---|---|
| | Value | Source | Value | Source |
| Density [kg/m$^3$] | 1100–1270 | [1] | 1300–1350 | [1] |
| Poisson's ratio | 0.35–0.43 | [1] | 0.28–0.47 | [2] |
| Young's modulus [kPa] | 100–130 | [3] | 100–200 | [4] |
| Viscosity coefficient [Pa·s] | 5–10 | [3] | 4.5–9 | [4] |

The main outputs of the simulation were the storage modulus, loss modulus, and complex modulus across the selected frequency range. The storage modulus represents the elastic component of the response, associated with recoverable energy storage, whereas the loss modulus describes viscous dissipation during cyclic deformation. The complex modulus combines both contributions and provides a global description of the frequency-dependent viscoelastic behaviour. Model convergence was assessed to ensure numerical stability and adequate precision of the computed results.

### Acoustic Wave Propagation Calculation

Acoustic wave propagation in the composite phantom materials was simulated in COMSOL Multiphysics using a time-explicit formulation. The model combined the Solid Mechanics interface, within the Structural Mechanics Module, with the Acoustics Module to describe coupled elastic and acoustic wave transmission. In the acoustic domains, wave propagation was solved using a discontinuous Galerkin finite element formulation of the acoustic wave equation 293,

$$\frac{1}{\rho_0 c^2}\frac{\partial^2 p}{\partial t^2} + \nabla \cdot \left(-\frac{1}{\rho_0}\nabla p\right) = 0 \tag{293}$$

where $\rho_0$ is the medium density, $c$ is the speed of sound, $p$ is the acoustic pressure, and $t$ is time.

The phantom sample was represented using the time-explicit elastic wave formulation, with material properties derived from the equivalent composite response. This approach solves the governing equations for a general linear elastic medium through a velocity–strain formulation:

$$\rho\frac{\partial \mathbf{v}}{\partial t} - \nabla \cdot \mathbf{S} = \mathbf{F}_v \tag{294}$$

$$\frac{\partial \mathbf{E}}{\partial t} - \frac{1}{2}\left[\nabla \mathbf{v} + (\nabla \mathbf{v})^T\right] = 0 \tag{295}$$

$$\mathbf{S} = \mathbf{C} : \mathbf{E} \tag{296}$$

where $\mathbf{v}$ is the particle velocity, $\rho$ is the material density, $\mathbf{S}$ is the stress tensor, $\mathbf{E}$ is the strain tensor, $\mathbf{C}$ is the stiffness tensor, and $\mathbf{F}_v$ represents the applied body force.

The transducer components were also modelled using the time-explicit elastic wave formulation. The exception was the PZT disc, which was described using the Piezoelectric Waves, Time Explicit interface coupled with the Electrostatics interface. This allowed the electromechanical conversion between the applied electrical excitation and the resulting mechanical wave generation to be represented within the same numerical framework.

To ensure numerical stability and adequate spatial resolution, the mesh was defined according to the Courant–Friedrichs–Lewy (CFL) criterion. For quartic elements, at least 1.5 elements per minimum wavelength were used. Accordingly, the maximum admissible element size was estimated as:

$$h_{\text{max}} = \frac{\lambda_{\text{min}}}{1.5} = \frac{c_{\text{min}}}{1.5 f_{\text{max}}} \tag{297}$$

where $h_{\text{max}}$ is the maximum element size, $\lambda_{\text{min}}$ is the minimum wavelength, $c_{\text{min}}$ is the lowest wave speed in the model, and $f_{\text{max}}$ is the highest frequency considered in the analysis.

An axisymmetric configuration was adopted to model the transducer and phantom specimen, reducing computational cost while preserving the main propagation direction. The sample geometry was defined with a thickness of 2 mm and a width of 40 mm. A single acoustic pulse was emitted by the transducer, and two observation points were placed within the solid domain. One point was aligned with the longitudinal propagation direction to determine the longitudinal wave speed (LWS), while the second was positioned to evaluate the transverse response and estimate the shear wave speed (SWs). The LWS values were intended for comparison with ultrasound measurements, whereas the SWs values were used as reference quantities for elastography-based validation.

Attenuation was not included in these simulations, since the required frequency-dependent damping parameters could not be established before experimental acoustic characterization. Consequently, the numerical analysis was performed at 500 kHz only. Under the assumption of linear elastic propagation without attenuation, wave velocity is independent of frequency, allowing this frequency to be used as a representative case for estimating longitudinal and shear wave speeds.

#### D.1.1.2 Material Characterization Methods

**Tensile Testing Methods**

Tensile tests were performed using a Mecmesin MultiTest-i universal testing machine equipped with a 10 kN load cell. The tests were conducted to characterize the mechanical response of the elastomeric matrix, whose behaviour is strongly nonlinear and therefore cannot be adequately described using only Young's modulus and Poisson's ratio. Consequently, the experimental analysis focused on obtaining the Cauchy stress, or true stress, rather than the first Piola–Kirchhoff stress, in order to generate suitable input data for fitting nonlinear hyperelastic constitutive models in COMSOL Multiphysics.

The specimens had dimensions of 120 mm in length, 20 mm in width, and 2 mm in thickness, with a gauge length of 50 mm, following ASTM D412[5]. The samples were tested with their longitudinal axis aligned with the loading direction. A constant displacement rate of 10 mm/s was applied during the tests. For each material condition, five replicate specimens were tested, and the results were reported in terms of average strain and tensile strength.

Due to the high deformability of the elastomeric samples, the use of a conventional extensometer was not feasible. In addition, the application of a speckle pattern for digital image correlation was not effective for the tested material surface. Therefore, sample deformation was recorded using a high-definition camera (Basler acA2440-75um, Ahrensburg, Germany). The camera operated at 75 fps and provided a resolution of $2448 \times 2048$ pixels, corresponding to 5 MP, using a $2/3''$ CMOS sensor. Image acquisition was carried out with VIC-Snap software, version 6.

To improve image contrast, a white background was positioned behind the specimen during testing. Before acquisition, the camera was aligned so that its optical axis was perpendicular to the specimen plane. Brightness and focus were adjusted to ensure clear visualization of the sample boundaries. A physical reference marker was included in the field of view to allow conversion between pixel dimensions and real-world length units.

The recorded images were processed using a custom Python routine, available online[6]. Initially, each frame was cropped to reduce the computational domain and limit the number of processed pixels. A manually adjustable contrast threshold was then applied to binarize the image, assigning the specimen to black pixels and the background to white pixels. A second cropping operation was used to isolate the gauge region, based on the width difference between the gripped and free sections of the sample. For each frame, the number of black pixels was counted along each horizontal line to determine the local specimen width. The minimum width identified in each frame was assumed to correspond to the necking region and was used to compute the instantaneous Cauchy stress (figure 229).

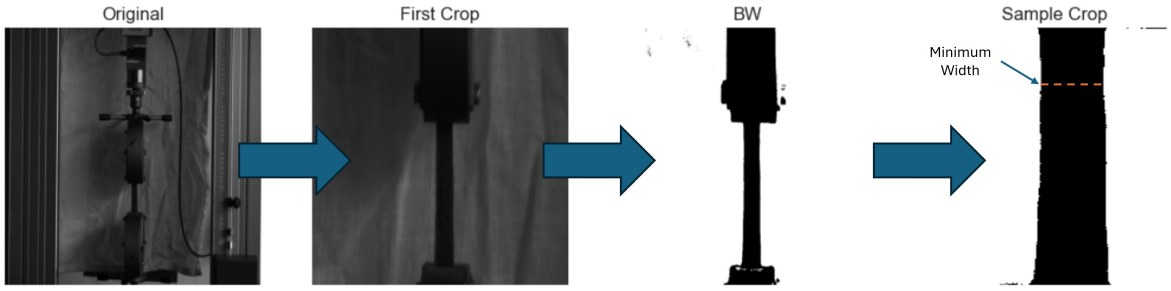



Figure 229: Image-processing workflow used to determine the instantaneous specimen width during tensile testing. The original camera frame was first cropped to isolate the specimen region, followed by grayscale thresholding and binary conversion to distinguish the sample from the background. A second crop was then applied to extract the gauge section, where the minimum width was identified and used to estimate the local necking region for Cauchy stress calculation.

The data acquired from the universal testing machine and the image-based measurements were synchronized through interpolation. After temporal alignment, the datasets were downsampled to reduce dimensionality and facilitate subsequent analysis, since the deformation evolution was smooth and continuous throughout the test. The resulting synchronized stress–strain data were then used for the identification of the hyperelastic material parameters.

Specimens were prepared as rectangular strips with dimensions of $20$ mm in width, $120$ mm in length, and a nominal thickness of $2$ mm. Dynamic compressive tests were performed using an electrodynamic shaker system (V650, M8-CE, Brüel & Kjær, Nærum, Denmark) equipped with a load cell (221B02, PCB Piezotronics, Depew, NY, USA). A sinusoidal displacement input was applied with an amplitude selected to produce approximately $2\%$ compressive strain, corresponding to a displacement of $0.04$ mm.

**Dynamic Mechanical Response Methods**

The shaker was mounted in a pendulum configuration, using a stinger selected to minimize the risk of buckling during excitation. The mass of the shaker assembly provided stable contact with the specimens throughout testing. Displacement was obtained by double integration of the differential acceleration signal measured by two triaxial accelerometers (356A14, PCB Piezotronics, Depew, NY, USA), positioned before and after the sample. This arrangement allowed the deformation of the specimen to be isolated from base motion and system vibrations, as illustrated in Figure 230.

Dynamic characterization was conducted at excitation frequencies of 3, 4, 5, 7, and $10$ Hz. For each frequency, 100 loading cycles were acquired. To ensure that the analysis represented steady-state behaviour, the first and last five cycles were excluded, and the intermediate 90 cycles were retained for post-processing. The stress–strain data of each hysteresis loop were offset so that both stress and strain remained positive during the analysis.

The storage modulus, $E'$, and loss modulus, $E''$, were calculated from the hysteresis loops using

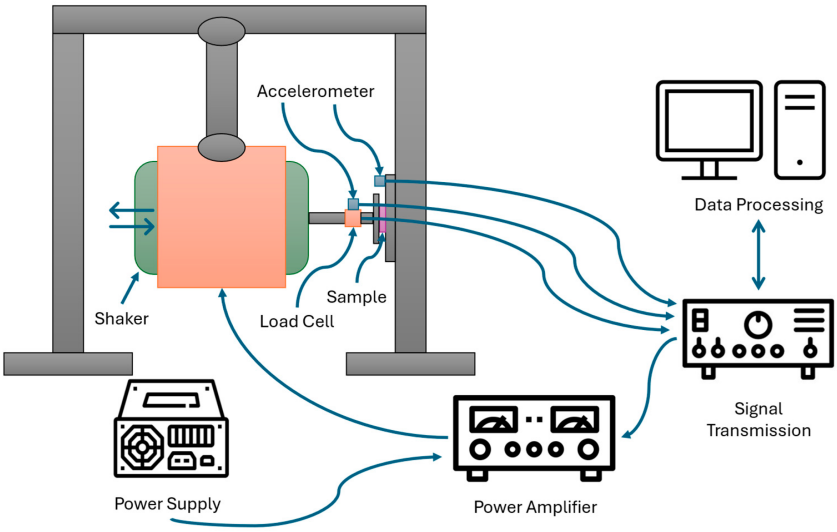



Figure 230: Experimental setup used for dynamic mechanical characterization, consisting of an electrodynamic shaker, load cell, and accelerometers for real-time force and displacement acquisition.

custom Python routines. First, the dissipated energy per cycle, $W_d$, was obtained by numerical integration of the stress–strain loop using Simpson's rule:

$$W_d = \oint \sigma \, d\varepsilon \tag{298}$$

where $\sigma$ is the compressive stress and $\varepsilon$ is the compressive strain.

The elastically stored energy over one loading cycle, $W_s$, was estimated from the maximum stress and strain amplitudes, $\sigma_0$ and $\varepsilon_0$, according to:

$$W_s = \frac{\pi \sigma_0 \varepsilon_0}{2} \tag{299}$$

The loss tangent was then used to estimate the phase angle, $\delta$, between the stress and strain responses:

$$\tan(\delta) = \frac{E''}{E'} = \frac{W_d}{2\pi W_s} \quad \Longleftrightarrow \quad \delta = \arctan\left(\frac{W_d}{2\pi W_s}\right) \tag{300}$$

Finally, the storage modulus, loss modulus, and complex modulus, $E^*$, were calculated as:

$$E' = \frac{\sigma_0}{\varepsilon_0}\cos(\delta) \tag{301}$$

$$E'' = \frac{\sigma_0}{\varepsilon_0}\sin(\delta) \tag{302}$$

$$E^* = \sqrt{(E')^2 + (E'')^2} \tag{303}$$

This procedure enabled the frequency-dependent viscoelastic response of the samples to be quantified from the measured hysteresis behaviour, with $E'$ representing the recoverable elastic component and $E''$ describing the dissipative contribution associated with cyclic loading.

**Shear Wave Elastography Methods**

Shear wave elastography (SWE) measurements were performed using a LOGIQ E9 ultrasound system (GE Healthcare, Milwaukee, WI, USA) equipped with an L3-12-RS linear array probe (GE Healthcare, Milwaukee, WI, USA), operating over a frequency range of 2.0–11.0 MHz. To minimize compression-induced artifacts and improve measurement repeatability, the probe was fixed using a universal articulated support arm, maintaining a stable position perpendicular to the phantom surface. A thin and uniform layer of commercial ultrasound coupling gel was applied to the scanning interface and between phantom layers to improve acoustic coupling and prevent the presence of air gaps.

The tested phantom samples had in-plane dimensions of $120$ mm $\times$ $150$ mm. Skin-mimicking specimens had a thickness of 2 mm, whereas muscle-mimicking samples were produced with a thickness of 10 mm to provide sufficient volume for elastographic assessment. Before each acquisition, the ultrasound system settings were standardized by selecting the "small parts" imaging preset and activating the shear wave elastography mode. The region of interest was positioned at the centre of each sample at a fixed depth to ensure consistency between measurements.

Before data collection, the system and samples were allowed to stabilize for at least 5 min to reduce the influence of temperature-dependent variations in stiffness. For each specimen, five consecutive shear wave speed (SWs) measurements were recorded in $\mathrm{m}/\mathrm{s}$. The region of interest was slightly repositioned within the central area between acquisitions to improve measurement robustness and reduce the influence of local heterogeneity. To evaluate anisotropic behaviour, measurements were performed both parallel and perpendicular to the fiber orientation.

All measurements were carried out by the same experienced operator under controlled laboratory conditions, with temperature maintained at $23 \pm 1$ °C and relative humidity at $50 \pm 5\%$. The mean and standard deviation of the five measurements were calculated for each sample and orientation, providing a quantitative assessment of the elastographic response of the developed phantom materials.

## D.1.2 Silicone Phantoms Additional Results and Discussion

### D.1.2.1 Tensile Testing and Composite Formulation Results

The tensile testing results and the corresponding constitutive curve-fitting parameters are presented in Figure 231. Four hyperelastic formulations were evaluated: the Neo-Hookean model, the two-parameter Mooney–Rivlin model, the five-parameter Mooney–Rivlin model, and the Ogden model.

The Neo-Hookean model, shown in Figure 231a, provided an adequate description of the experimental response only at low strain levels, particularly for strains below 0.5. In this region, the

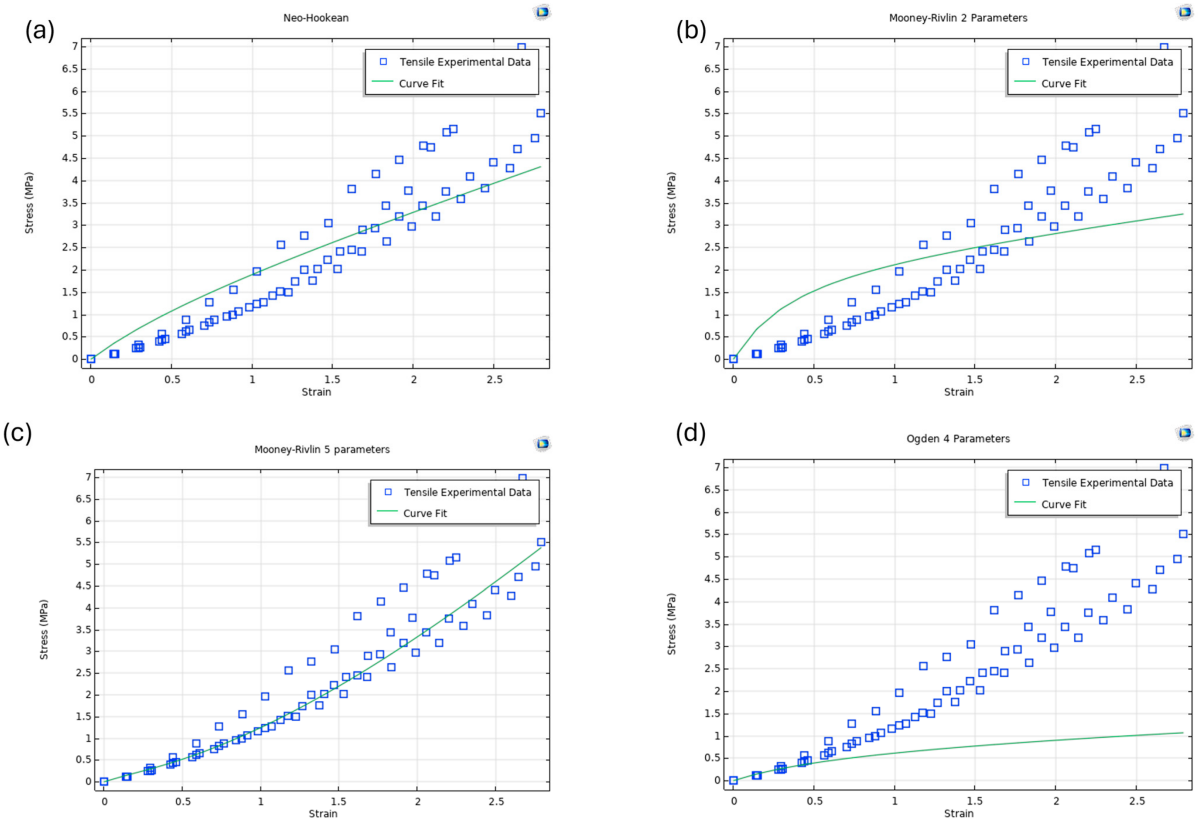



Figure 231: Curve-fitting results obtained for four hyperelastic constitutive models: (a) Neo-Hookean, (b) two-parameter Mooney–Rivlin, (c) five-parameter Mooney–Rivlin, and (d) Ogden model.

material behaviour remained close to a linear elastic response. However, the model progressively underestimated the measured stress at moderate and large deformations, indicating that a single-parameter formulation was insufficient to represent the strain-stiffening behaviour of the elastomeric matrix.

The two-parameter Mooney–Rivlin model, presented in Figure 231b, improved the agreement over a wider deformation range. Nevertheless, it also failed to reproduce the pronounced stress increase observed at strains above approximately 1.5. This deviation suggests that the two-parameter formulation did not provide enough flexibility to fully capture the nonlinear response of the material, particularly under large stretch conditions.

The five-parameter Mooney–Rivlin model, shown in Figure 231c, produced the best agreement with the experimental tensile data. This model closely followed the measured stress–strain response over the complete deformation range and accurately represented the nonlinear hardening observed at high strains. The inclusion of higher-order invariant terms provided greater flexibility, allowing the constitutive model to describe the complex mechanical behaviour of the silicone matrix more effectively.

The Ogden model, presented in Figure 231d, did not provide a satisfactory fit for the tested material under the selected fitting conditions. Although this formulation is commonly used for large-strain

hyperelasticity, it underestimated the experimental stress response across most of the strain range. This may be related to parameter sensitivity, inadequate initial estimates, or convergence toward a local minimum during the fitting procedure. Therefore, despite its theoretical suitability for nonlinear elastomeric materials, the Ogden formulation was not selected for subsequent simulations.

Overall, the five-parameter Mooney–Rivlin model provided the most accurate representation of the elastomeric matrix. Its capacity to reproduce the full stress–strain response makes it the most appropriate constitutive description for the numerical modelling of the composite phantom materials. The fitted material parameters used in the subsequent simulations are presented in Table 30.

Table 30: Fitted parameters for the five-parameter Mooney–Rivlin model.

| **Parameter** | **Value** |
|---|---|
| Density (kg/m$^3$) | 1038 |
| $C_{10}$ (kPa) | 44.658 |
| $C_{01}$ (kPa) | 146.25 |
| $C_{11}$ (kPa) | 2.6260 |
| $C_{20}$ (kPa) | 75.213 |

After fitting the elastomeric matrix to an appropriate hyperelastic constitutive model, the composite phantom formulations were further optimized to reproduce the mechanical behaviour of fibrous biological tissues. The optimization focused on shear wave propagation speed, with the objective of adjusting the fiber volume fraction until the predicted response matched values reported for human skin and skeletal muscle. Based on this process, and considering the geometries and material formulations described previously, the target fiber volume fractions were determined as 6.07% for the skin-mimicking composite and 0.53% for the muscle-mimicking composite. These values provided a compromise between directional mechanical biofidelity, fabrication feasibility, and compatibility with ultrasound-based characterization.

Figure 232 shows the six independent loading conditions applied to the repeating unit cell (RUC) to compute the effective material properties of the skeletal muscle phantom. These load cases were required to determine the homogenized stiffness matrix of the fiber–elastomer composite.

The three normal loading cases, shown in Figure 232a–c, were applied independently along the $x$, $y$, and $z$ directions. These simulations describe the response of the microstructure under axial deformation and enable extraction of the principal stiffness terms of the effective elasticity tensor. The stress concentrations observed near the fiber region arise from the stiffness contrast between the reinforcement and the elastomeric matrix, as well as from the imposed fiber orientation.

The three shear loading cases, shown in Figure 232d–f, represented shear deformation in the $xy$, $yz$, and $xz$ planes. These simulations were used to determine the shear components of the homogenized stiffness matrix, which are essential for describing the anisotropic behaviour introduced by

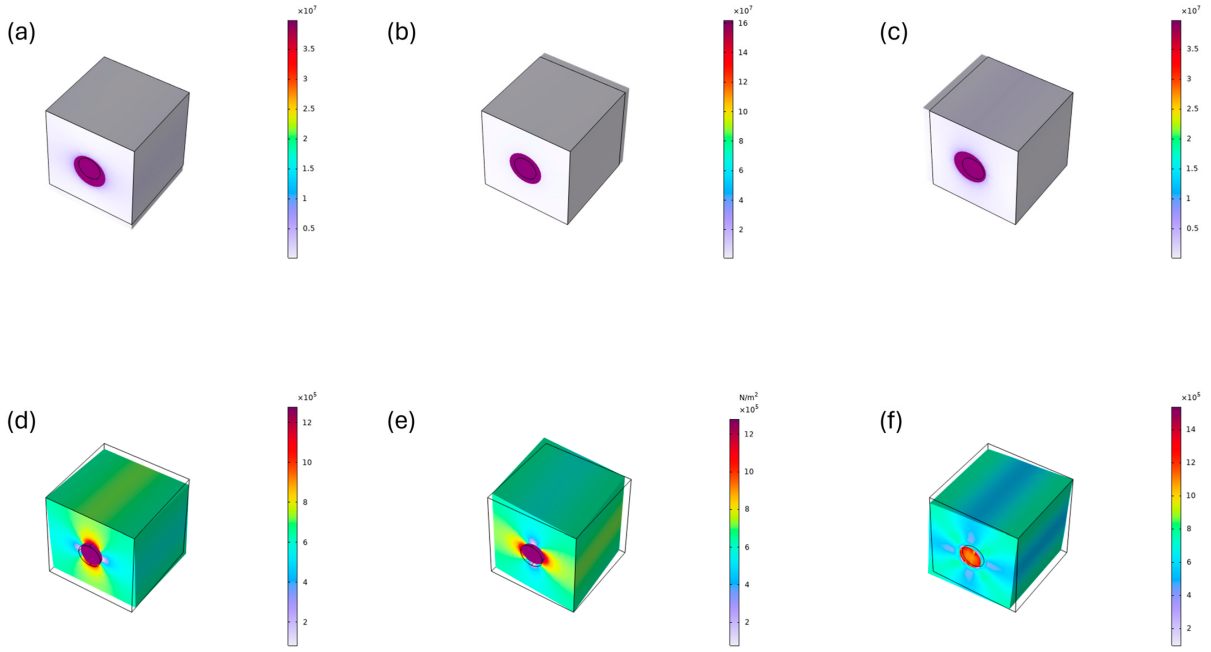



Figure 232: Six independent loading cases applied to the RUC for homogenization. Subfigures (a–c) correspond to normal loading along the principal directions, while subfigures (d–f) represent shear loading cases.

the embedded fibers. The localization of shear stress near the fiber–matrix interface indicates that reinforcement distribution and interfacial mechanics strongly influence the shear response of the composite.

Together, these six simulations allowed the complete homogenized stiffness matrix, $\bar{C}_{ij}$, to be obtained. This matrix was then used to represent the heterogeneous composite as an equivalent anisotropic material at the macroscale, enabling multiscale modelling of the phantom response.

To compare the developed materials with biological tissue data and numerical predictions, tensile tests were performed on the skin- and muscle-mimicking phantom samples, as shown in Figure 233. For comparison with literature values, Young's modulus was calculated using the second Piola–Kirchhoff stress tensor.

Figure 233a demonstrates that the skin-mimicking composite reproduced the anisotropic stiffness response reported for human skin. Biological skin data showed substantial variability, particularly in the direction parallel to collagen fiber alignment, where the standard deviation exceeded $\pm 3.0$ MPa. This variability is consistent with the heterogeneous nature of skin and may be influenced by anatomical location, donor characteristics, age, hydration, and testing protocol. The composite phantom containing approximately 6% natural fibers reproduced the expected directional dependence of stiffness. In the parallel direction, the measured modulus was 11.04 MPa, slightly below the simulated value but close to the reported human skin mean of approximately 10.5 MPa. The values obtained at $45^\circ$ and perpendicular to the fiber direction, $7.36 \pm 0.554$ MPa and $7.16 \pm 0.45$ MPa, respectively, also

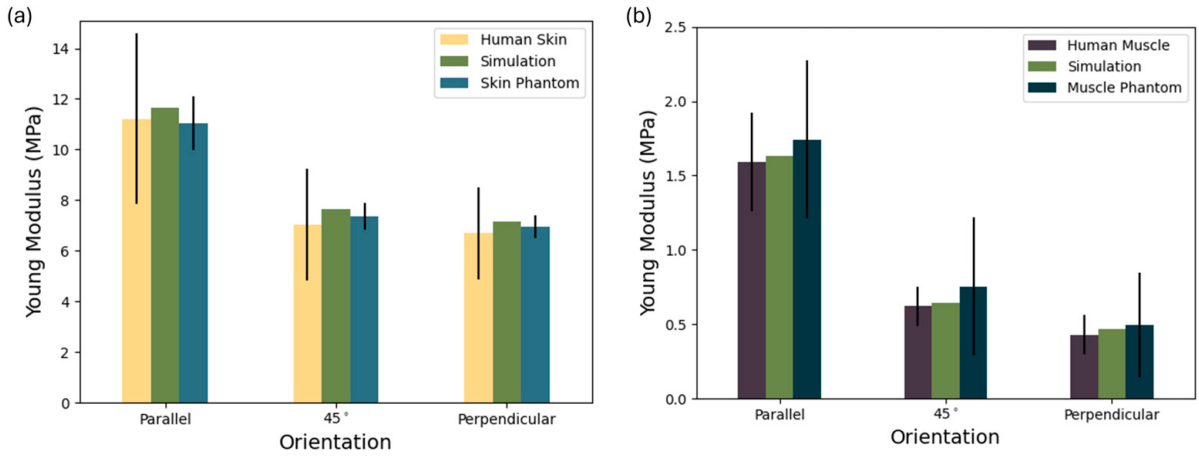



Figure 233: Young's modulus of (a) skin-mimicking and (b) muscle-mimicking phantoms compared with biological tissue data and numerical predictions across different fiber orientations.

remained close to the biological reference range.

The relatively low variability observed in the skin phantom, together with the agreement between experimental, numerical, and literature values, supports the effectiveness of the simulation-guided design approach. These results indicate that natural fiber reinforcement can be used to tune mechanical anisotropy in silicone-based phantoms. Consequently, the developed composite is suitable for applications where direction-dependent stiffness is relevant, including skin-mimicking ultrasound phantoms, surgical training models, and elastography validation platforms.

Figure 233b compares the Young's modulus of human skeletal muscle with the simulated and fabricated muscle-mimicking composite in three orientations: parallel, $45°$, and perpendicular to the fiber direction. The biological data exhibited a clear anisotropic response, with the highest modulus along the fiber direction, $1.743 \pm 0.312$ MPa, followed by lower values at $45°$, $0.754 \pm 0.465$ MPa, and in the transverse direction, $0.494 \pm 0.352$ MPa. This behaviour reflects the structural organization of skeletal muscle, which is optimized to resist tensile loading along the fiber axis.

The muscle phantom reproduced both the magnitude and directional trend of the biological tissue. In the parallel direction, the experimental value slightly exceeded the numerical prediction, while maintaining a relatively controlled standard deviation, indicating satisfactory fabrication repeatability. At $45°$ and perpendicular to the fiber orientation, the expected reduction in modulus was preserved. Although variability increased in these orientations, likely due to fiber misalignment or local fiber–matrix interfacial effects, the measured and simulated values remained within the variability reported for human muscle. This indicates that the composite formulation provides a mechanically representative approximation of passive skeletal muscle anisotropy.

The observed variability in the muscle-mimicking material is likely related to the very low fiber

volume fraction required for this formulation, approximately 0.5%. At such low reinforcement contents, small inconsistencies in fiber mass, dispersion, or alignment can have a disproportionate influence on the mechanical response. Accurate fiber measurement is also more difficult in small-scale samples, even when a high-precision balance is used, which may contribute to increased standard deviation. This limitation is expected to decrease when producing larger structures, since higher absolute fiber quantities improve weighing accuracy and reduce the relative effect of material loss during handling.

Finally, the fabrication strategy allows the thickness of each phantom layer to be adjusted according to the intended anatomical target. This enables future patient-specific designs in which layer depths are defined from imaging data, rather than being restricted to the fixed dimensions used in the present study.

### D.1.2.2 Dynamic Mechanical Response Results

The viscoelastic response of the fabricated phantoms was evaluated by experimentally determining the storage modulus, $E'$, loss modulus, $E''$, and complex modulus, $E^*$, over a frequency range of 3–10 Hz. These parameters were obtained from the stress–strain hysteresis loops generated during cyclic compression testing and are presented in Figure 234.

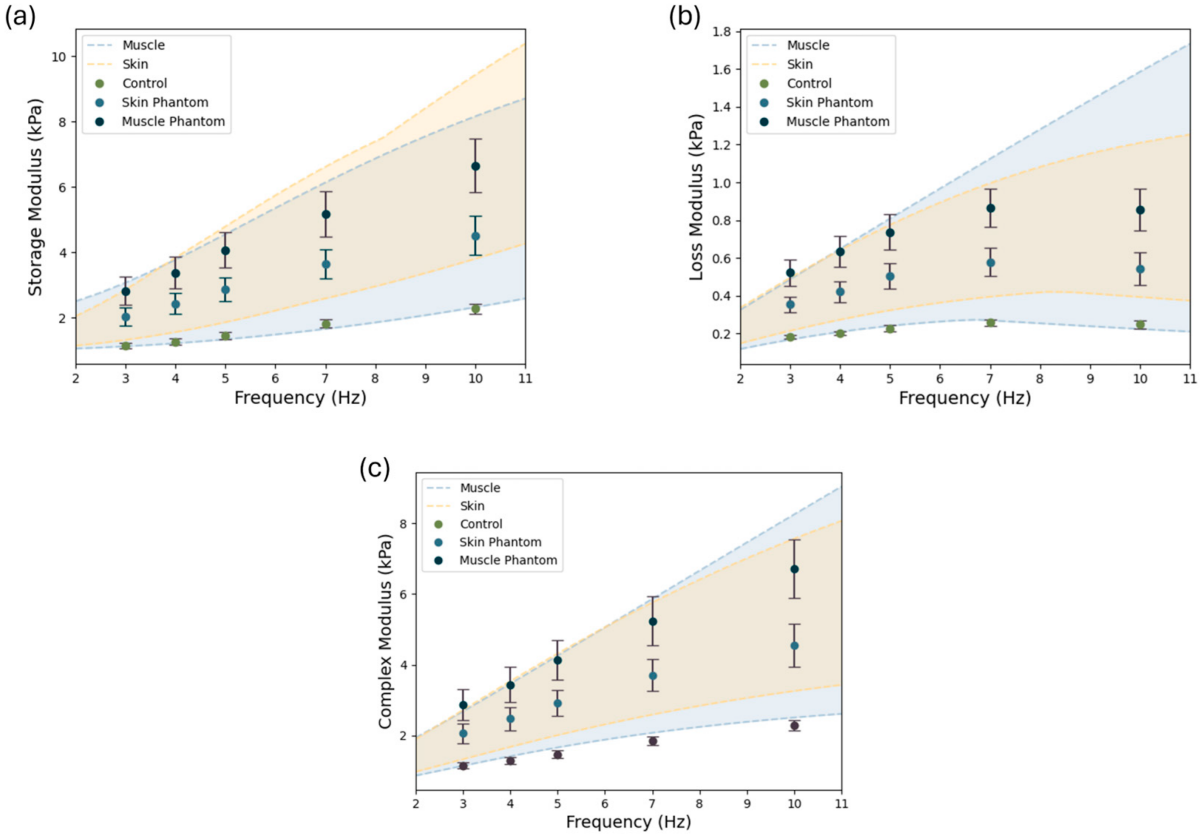



Figure 234: Viscoelastic characterization of the control silicone, skin-mimicking, and muscle-mimicking phantoms as a function of frequency between 3 and 10 Hz: (a) storage modulus, $E'$; (b) loss modulus, $E''$; and (c) complex modulus, $E^*$. The shaded regions represent the simulated physiological ranges for skin and skeletal muscle. Data are shown as mean $\pm$ standard deviation.

The storage modulus, shown in Figure 234a, represents the recoverable elastic energy stored during each loading cycle. The control silicone exhibited the lowest $E'$ values throughout the tested frequency range, increasing from 1.135 to 2.274 kPa. These values remained below the lower limit of the physiological range defined for skin. The incorporation of natural fibers increased the stiffness of the skin-mimicking phantom, with $E'$ values ranging from 2.032 to 4.521 kPa. This response was consistent with the simulated skin range and showed a frequency-dependent increase in stiffness, which is characteristic of viscoelastic soft tissues. The skeletal muscle phantom showed a stronger frequency-dependent response, with $E'$ increasing from 2.819 to 6.652 kPa. This trend reproduces the dynamic stiffening commonly observed in skeletal muscle and indicates that the composite formulation can approximate both the static and rate-dependent mechanical behaviour of fibrous tissue surrogates.

The increase in storage modulus after fiber incorporation is mainly attributed to the reinforcing action of the natural fibers within the silicone matrix. Since the fibers are stiffer than the elastomeric phase, they contribute to load transfer and restrict matrix deformation during cyclic loading. This increases the capacity of the composite to store elastic energy. Moreover, the interaction between the fibers and the surrounding matrix enhances stress transfer and introduces microstructural resistance to deformation. Even when the fibers are not perfectly aligned with the loading direction, their presence contributes to anisotropic reinforcement and becomes increasingly relevant at higher frequencies, where the apparent dynamic stiffness is amplified.

The loss modulus, $E''$, presented in Figure 234b, quantifies the energy dissipated as heat during each cycle. The control silicone again showed the lowest response, with $E''$ values between 0.1813 and 0.2495 kPa. Although this indicates measurable damping, the values remained below the physiological ranges of both skin and skeletal muscle, which is consistent with the comparatively low dissipative behaviour of unreinforced silicone. The skin-mimicking phantom exhibited higher damping, with $E''$ ranging from 0.3546 to 0.5453 kPa. This increase suggests that even moderate fiber reinforcement enhances viscous dissipation, most likely through fiber–matrix friction, local interfacial deformation, and microscale shear mechanisms.

The muscle-mimicking phantom showed the highest loss modulus values, ranging from 0.5226 to 0.8546 kPa. This behaviour indicates greater internal energy dissipation and agrees with the expected response of fibrous biological tissues under oscillatory loading. The increase in damping is likely associated with enhanced interfacial friction, micro-slip between the fibers and matrix, local stress concentrations, and viscoelastic drag during cyclic deformation. The observed peak followed by a slight reduction at higher frequencies may indicate the onset of dynamic saturation or reduced mobility of the reinforcing fibers.

Overall, the simultaneous increase in $E'$ and $E''$ demonstrates that fiber reinforcement improves both load-bearing capacity and energy dissipation.

The complex modulus, $E^*$, shown in Figure 234c, combines the elastic and viscous components of the response and therefore represents the overall resistance of the material to dynamic deformation. The control silicone remained below the biological reference ranges, with $E^*$ values between 2.139 and 3.376 kPa. In contrast, the skin and muscle phantoms showed a pronounced increase with frequency, with $E^*$ ranging from 4.087 to 7.083 kPa and from 5.938 to 10.829 kPa, respectively. This clear separation between formulations indicates that the reinforcement strategy allowed the dynamic mechanical impedance of the phantoms to be adjusted according to the target tissue. The frequency-dependent increase in $E^*$ further supports the suitability of the composites for applications requiring tissue-like viscoelastic behaviour, including ultrasound phantoms, biomechanical surrogates, and elastography validation.

The experimental results are consistent with the viscoelastic behaviour reported by Manickam et al. for agar-based tissue phantoms[7], where the storage modulus exceeded the loss modulus. This relationship is commonly observed in soft tissues and indicates a predominantly elastic response with a measurable dissipative component. While Manickam et al. achieved mechanical tuning by varying agar concentration, the present work demonstrates that similar control can be obtained through structural reinforcement using natural fibers. Their observation that dynamic parameters, such as $E''$ and $E^*$, are more sensitive than static stiffness for distinguishing tissue-mimicking materials is also supported by the present findings.

Comparison with Kazemirad et al.[8] requires consideration of both loading mode and frequency range. Their study reported shear storage moduli, $G'$, between 1.5 and 2.5 kPa over 200–1000 Hz, which is consistent with soft gel behaviour under shear loading. In the present work, the measured storage moduli, $E'$, were obtained under uniaxial cyclic compression at lower frequencies, 3–10 Hz. Although the absolute values differ due to loading mode, geometry, and material formulation, both studies show that reinforcement increases stiffness and damping. The increase in damping reported by Kazemirad et al., reflected by a rise in $\tan\delta$ from 0.11 to 0.26, is consistent with the increase in $E''$ observed in the fiber-reinforced silicone phantoms.

The results also differ from those reported by Guo et al.[9] for a PVA-based phantom, which exhibited an elastic modulus of $1.34 \pm 0.28$ kPa and a viscosity of $9.67 \pm 3.00$ Pa·s. The higher stiffness and damping observed in the present silicone-based composites are expected, given the different material system, structural reinforcement, and cyclic compression test configuration. Guo et al. targeted liver tissue, with elasticities between 0.9 and 2.9 kPa and viscosities up to 14.4 Pa·s, whereas the present

phantoms were designed to mimic fibrous tissues such as skin and skeletal muscle, which generally exhibit greater resistance to deformation. These differences highlight the importance of selecting both the matrix and reinforcement strategy according to the mechanical regime of the target tissue.

A further distinction can be made with the gelatine–castor oil phantoms described by Nguyen et al. [62]. In that study, the addition of castor oil reduced the shear modulus from 2.01 to 0.88 kPa while producing a modest increase in viscosity. Conversely, the fiber-reinforced silicone composites developed here showed simultaneous increases in stiffness and damping. This contrast reflects two different material design strategies: oil addition softens the gel matrix, whereas fiber incorporation increases load-bearing capacity and enhances internal dissipation. Consequently, the proposed composites are more appropriate for reproducing the viscoelastic response of fibrous biological structures, where stiffness and damping are both relevant.

Overall, the results demonstrate that natural fiber-reinforced silicone composites provide a controllable route for tuning viscoelastic properties. Compared with conventional gel-based phantoms, these materials allow simultaneous adjustment of stiffness and damping while offering improved structural stability, lower material cost, and the potential for more sustainable fabrication through the use of natural reinforcements. This supports their applicability as durable and structurally tunable tissue-mimicking materials for ultrasound and biomechanical validation studies.

#### D.1.2.3 Shear Wave Elastography Results

Figure 235 shows clear differences in shear wave speed (SWs) among the tested phantom formulations. These differences indicate that the mechanical stiffness and anisotropic response of the materials were successfully adjusted to approximate the behaviour of the target biological tissues.

The ultrasound images revealed distinct structural features between the different phantom types. The control phantom, shown in Figure 235a, presented a uniform appearance, consistent with a homogeneous and isotropic silicone material without internal fiber reinforcement. In contrast, the laminated skin phantom, shown in Figure 235b,c, exhibited two clearly distinguishable layers. The upper layer, composed only of silicone, appeared homogeneous, whereas the lower fiber-reinforced layer showed visible internal structure. This contrast confirmed the successful fabrication of the layered architecture and the differentiation between the silicone and composite regions.

For the skin-mimicking phantom, the presence of natural fibers influenced shear wave propagation and produced a direction-dependent elastographic response. When the measurement was performed parallel to the fiber orientation, the internal fiber architecture was clearly visible in the ultrasound image

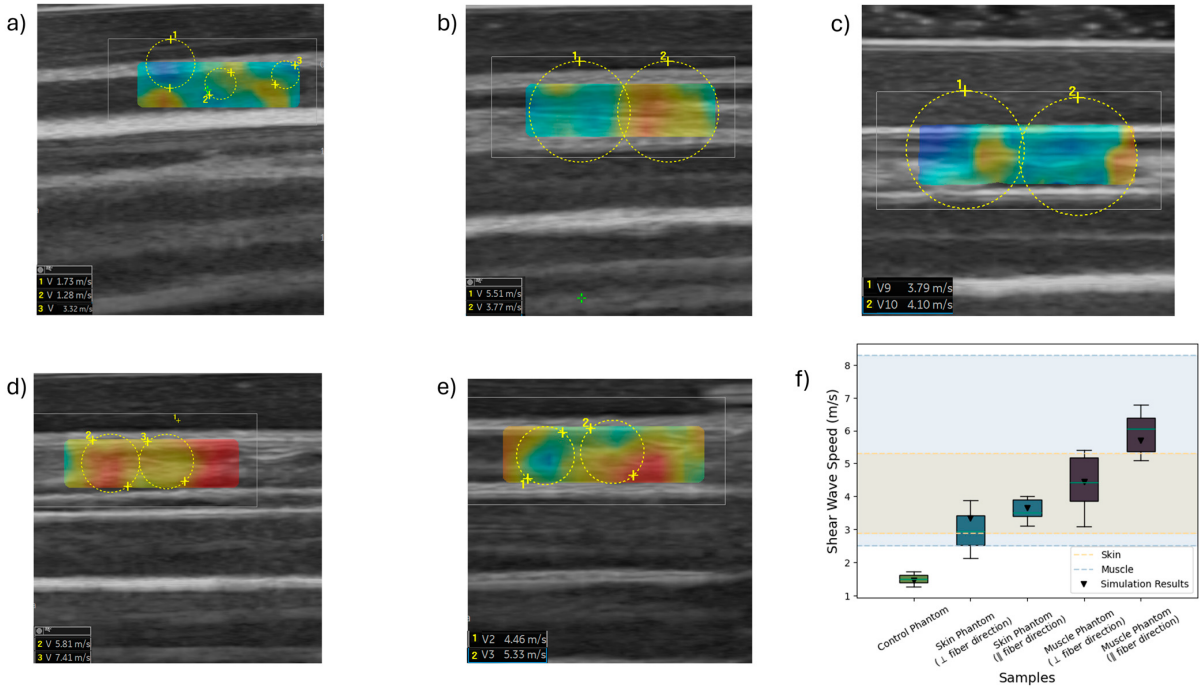



Figure 235: Shear wave speed measurements obtained for: (a) control phantom, (b) laminated skin phantom measured parallel to the fiber direction, (c) laminated skin phantom measured perpendicular to the fiber direction, (d) muscle phantom measured parallel to the fiber direction, and (e) muscle phantom measured perpendicular to the fiber direction. (f) Box plot comparing the SWs values obtained for all samples. The circles in the elastography images indicate the regions of interest used for SWs measurement.

and the measured SWs reached $2.98 \pm 0.72$ m/s. When the measurement direction was perpendicular to the fibers, the SWs changed to $3.58 \pm 0.33$ m/s. This directional variation demonstrates the anisotropic behaviour introduced by the reinforcement and indicates that the fibers acted both as mechanical stiffening elements and as microstructural features capable of modifying shear wave propagation.

The muscle-mimicking phantom, shown in Figure 235d,e, also presented anisotropic behaviour, with a heterogeneous ultrasound appearance associated with fiber alignment and local variations in fiber distribution. When the ultrasound assessment was performed parallel to the fibers, the structure of the reinforcement was more clearly identified, producing an image qualitatively similar to the fascicular organization of skeletal muscle. In this orientation, the measured SWs was $4.43 \pm 0.74$ m/s. In the perpendicular direction, the fiber structure was less distinct and the SWs reached $5.93 \pm 0.62$ m/s. These results further support the role of the fibers in producing anisotropic wave propagation and increasing the apparent stiffness of the composite.

The use of coupling gel between layers also contributed to the imaging appearance of the phantoms by creating interfaces that resembled adipose-like regions in ultrasound. This effect increased the anatomical realism of the multilayer construct and improved the visual distinction between material domains. Overall, the elastography results demonstrate that the fibers served a dual function: they reinforced the silicone matrix mechanically and altered the propagation of shear waves through the composite. This combination

is essential for reproducing the anisotropic response of fibrous tissues such as skin and skeletal muscle.

The control phantom exhibited the lowest SWs, $1.5 \pm 0.22$ m/s, with values consistently below $2$ m/s. This response is consistent with a soft isotropic silicone matrix and represents the expected baseline behaviour of the unreinforced material. The corresponding numerical simulation predicted a SWs of $1.46$ m/s, showing close agreement with the experimental measurements and supporting the validity of the material parameters used to model the silicone matrix.

The skin phantom presented SWs values of $3.65 \pm 0.51$ m/s, which fall within the reported range for human skin, $2.87$–$5.31$ m/s[10]. The relatively narrow dispersion of the measurements suggests a consistent stiffness distribution and indicates that the composite formulation was appropriately tuned to reproduce skin-like elastographic behaviour. The simulated SWs for this formulation was $3.74$ m/s, which closely matched the experimental result and further supports the assumptions used in the numerical model.

The muscle phantom showed higher and more variable SWs values, reaching $5.93 \pm 0.62$ m/s. This value lies within the broad physiological range reported for skeletal muscle, $2.5$–$8.3$ m/s[11]. The larger variability is consistent with the anisotropic nature of muscle, where stiffness depends strongly on the direction of measurement relative to the fiber axis. The corresponding simulation predicted a SWs of $5.44$ m/s, which remained within the experimental range and indicates that the model captured the magnitude of shear wave propagation in the anisotropic composite.

Tsai et al. investigated scar elasticity using high-frequency ultrasound elastography with a Lamb wave model and reported SWs values of $1.66 \pm 0.05$ m/s and $2.69 \pm 0.03$ m/s for gelatine-based phantoms[12]. The phantoms developed in the present study achieved comparable or higher shear wave speeds while also introducing tunable anisotropy through natural fiber reinforcement. This provides an advantage over homogeneous gelatine systems when the objective is to reproduce the directional mechanical behaviour of fibrous tissues.

Many ultrasound phantoms simplify the anatomical structure by grouping skin, muscle, and adipose tissue into a single homogeneous layer. Although useful for basic imaging and calibration, this approach reduces anatomical realism and may affect the reliability of shear wave elastography, Doppler evaluation, and training procedures. Simplified models do not adequately reproduce the mechanical impedance differences between tissue layers, which may alter wave propagation and introduce calibration errors[13]. The multilayer silicone-based composites developed in this work address this limitation by separating the skin-like layer from the underlying tissue structure and by incorporating fiber reinforcement to reproduce anisotropy.

Dong et al. developed 3D-printed alginate-based skeletal muscle phantoms using a modified hydrogel approach and reported an average SWs of approximately $4.08$ m/s[14]. In comparison, the silicone–fiber muscle phantoms developed in this study produced a broader and higher range of shear wave speeds, indicating greater mechanical tunability. Tsuchida et al. reported an average SWs of $2.2$ m/s for a phantom jelly material[15], which is lower than values typically associated with skeletal muscle and fibrous soft tissues. The present silicone-based composite therefore provides a closer approximation to the expected elastographic response of skeletal muscle.

Aristizábal et al. developed anisotropic gelatine-based phantoms using fibrous inclusions and fishing lines, reporting SWs values between 2.44 and $4.10$ m/s, depending on fiber orientation and gelatine concentration[16]. In particular, their 14% gelatine fibrous composites showed SWs values of $4.10 \pm 0.11$ m/s at $0°$ and $3.90 \pm 0.02$ m/s at $90°$. The silicone-based muscle phantom developed here achieved higher and more directionally sensitive values, suggesting stronger anisotropic behaviour and broader tunability. This difference highlights the limitations of purely gelatine-based systems for replicating stiffer fibrous tissues and supports the use of fiber-reinforced silicone composites for more durable anisotropic phantoms.

Compared with hydrogel-, alginate-, and gelatine-based phantoms, the use of silicone provides improved durability, dimensional stability, and suitability for repeated ultrasound measurements. The incorporation of natural fibers further enables mechanical anisotropy to be tuned while maintaining a low-cost and potentially more sustainable material strategy. Therefore, the developed silicone-based anisotropic phantoms provide a reusable and structurally representative platform for ultrasound elastography, imaging calibration, training, and biomechanical research involving fibrous tissues such as skin and skeletal muscle.

### D.1.3 Speed of Sound of Gelatine Phantoms

The measured speed of sound of the gelatin phantoms in function of frequency is described in figure 236.

The results show that the speed of sound of the hydrogel-based soft tissue phantoms is formulation-dependent but only weakly frequency-dependent within the tested range of 0.5–5 MHz. Most formulations present relatively stable values across frequency, suggesting limited acoustic dispersion in this range. This is desirable for ultrasound phantom applications, since biological soft tissues are often treated as weakly dispersive media over diagnostic and therapeutic ultrasound frequencies.

The 5Gel formulation showed the lowest speed of sound, ranging approximately from 1510 to 1535

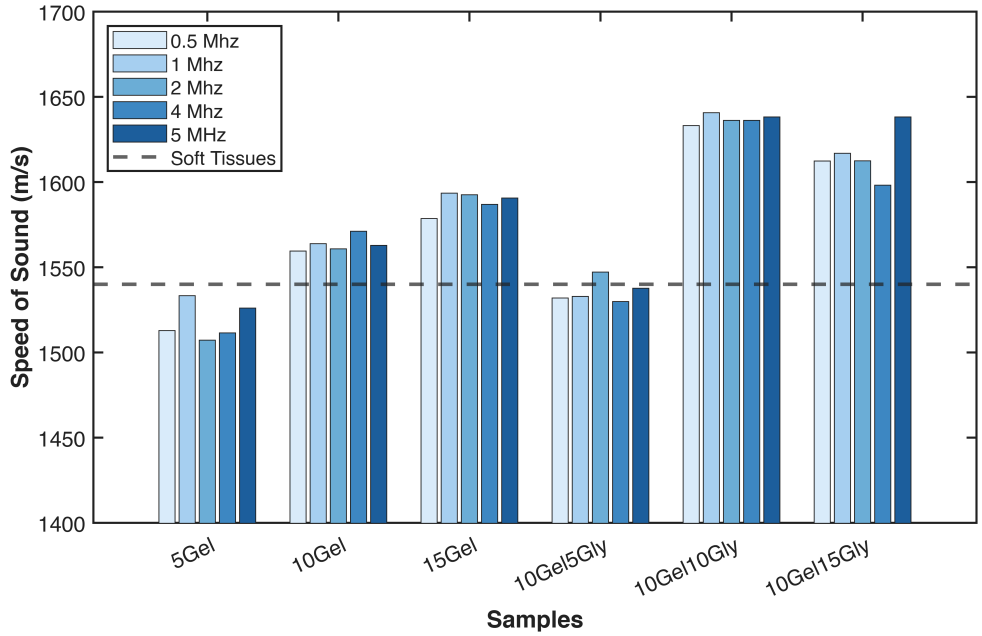



Figure 236: Measured speed of sound of the gelatin phantoms across a frequency range of 0.5 to 5 MHz. The results show that the speed of sound is relatively constant, with values around 1540 m/s, which is consistent with typical values for soft biological tissues.

m/s. These values are slightly below the reference soft tissue value of 1540 m/s, indicating that this formulation is somewhat more water-like and may underestimate the acoustic velocity of average soft tissue. The 10Gel formulation increased the speed of sound to approximately 1560–1570 m/s, placing it slightly above the reference value but still within a reasonable soft-tissue-mimicking range. The 15Gel formulation showed a further increase, with values close to 1580–1595 m/s, proposing that increasing gelatin content increases acoustic velocity, most likely due to the higher solid fraction and increased stiffness of the hydrogel network.

The addition of glycerol also influenced the speed of sound. The 10Gel5Gly formulation remained close to the reference line, with values around 1530–1550 m/s, making it the best match to generalized soft tissue among the tested formulations. In contrast, 10Gel10Gly and 10Gel15Gly showed substantially higher values, mostly between 1600 and 1640 m/s. These formulations may therefore overestimate the speed of sound of average soft tissue, although they could be suitable for mimicking tissues with higher acoustic velocity, such as muscle-like or more collagen-rich tissues.

Across the frequency range, the variations within each formulation were relatively small compared with the differences between formulations. This indicates that composition had a stronger effect on speed of sound than excitation frequency. Some minor fluctuations are visible, particularly for 5Gel and 10Gel15Gly, but no strong monotonic frequency-dependent trend is observed. These variations may arise from experimental uncertainty, signal processing differences between frequencies, or small coupling and time-of-flight measurement errors.

## D.2 Additional Tissue-mimicking Phantom Characterization Data

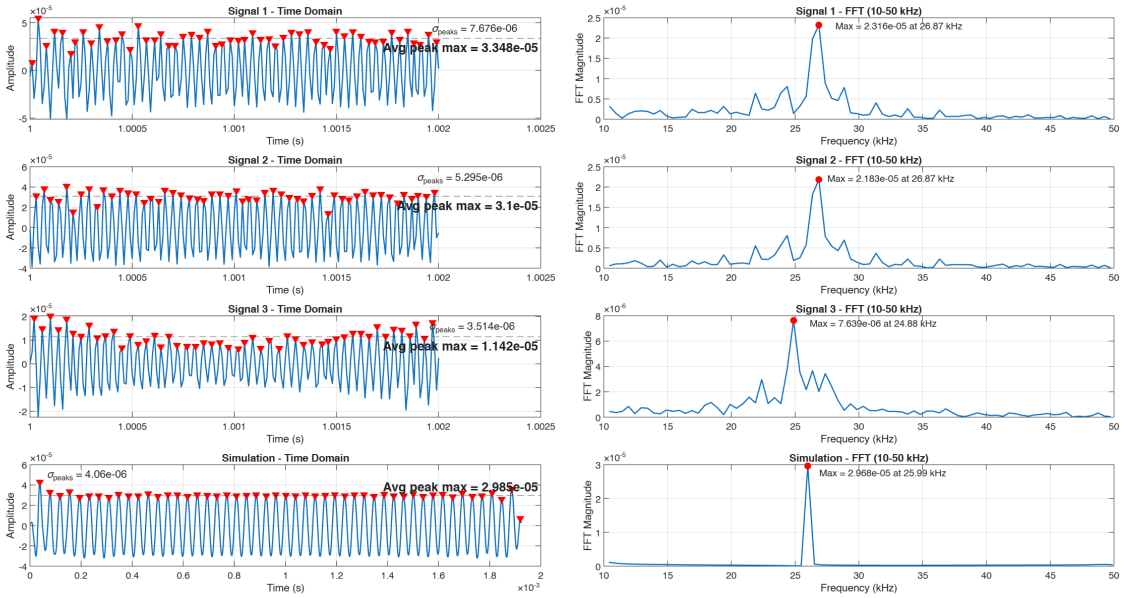



Figure 237: Time- and frequency-domain responses of three experimental LDV measurements and the corresponding numerical simulation. Red markers indicate detected signal peaks in the time domain and the dominant spectral peak in the FFT domain. The experimental signals showed maximum average peak amplitudes of $3.348 \times 10^{-5}$, $3.10 \times 10^{-5}$, and $1.142 \times 10^{-5}$, with dominant frequencies of 26.87, 26.87, and 24.88 kHz, respectively. The simulation predicted an average peak amplitude of $2.985 \times 10^{-5}$ and a dominant frequency of 25.99 kHz.

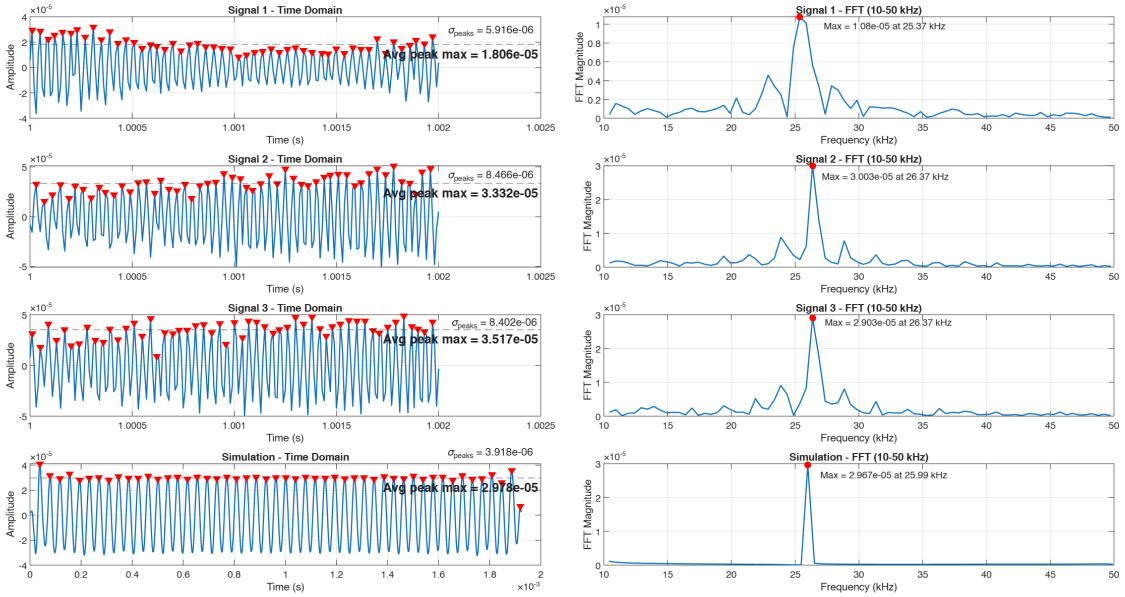



Figure 238: Time- and frequency-domain responses of three experimental LDV measurements and the corresponding numerical simulation. Red markers indicate detected signal peaks in the time domain and the dominant spectral peak in the FFT domain. The experimental signals showed maximum average peak amplitudes of $3.348 \times 10^{-5}$, $3.10 \times 10^{-5}$, and $1.142 \times 10^{-5}$, with dominant frequencies of 26.87, 26.87, and 24.88 kHz, respectively. The simulation predicted an average peak amplitude of $2.985 \times 10^{-5}$ and a dominant frequency of 25.99 kHz.

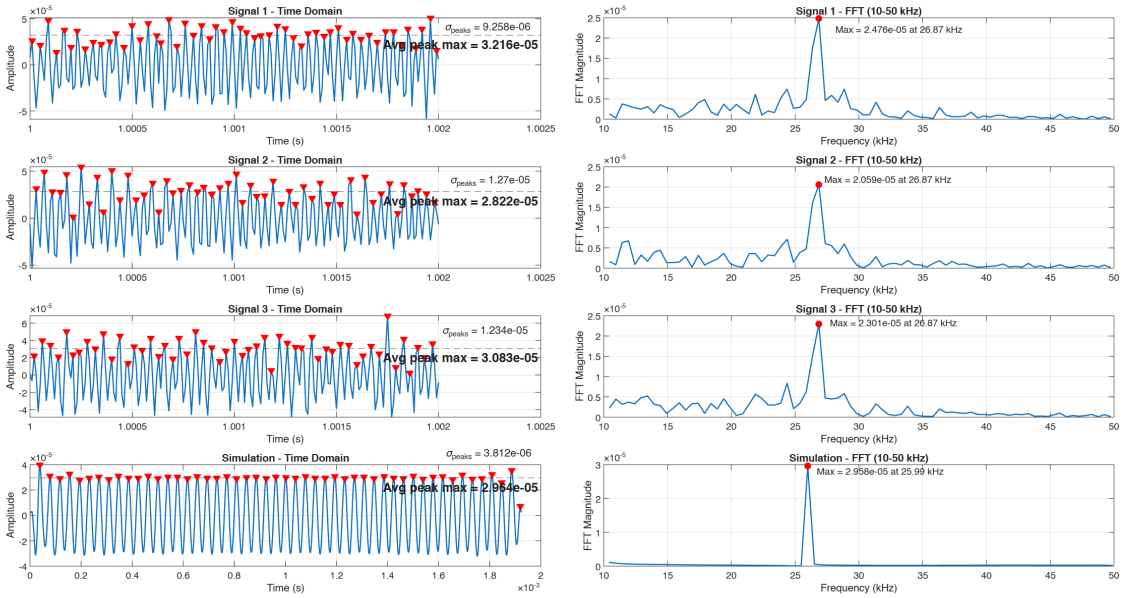



Figure 239: Time- and frequency-domain responses of three experimental LDV measurements and the corresponding numerical simulation. Red markers indicate detected signal peaks in the time domain and the dominant spectral peak in the FFT domain. The experimental signals showed maximum average peak amplitudes of $3.348 \times 10^{-5}$, $3.10 \times 10^{-5}$, and $1.142 \times 10^{-5}$, with dominant frequencies of 26.87, 26.87, and 24.88 kHz, respectively. The simulation predicted an average peak amplitude of $2.985 \times 10^{-5}$ and a dominant frequency of 25.99 kHz.

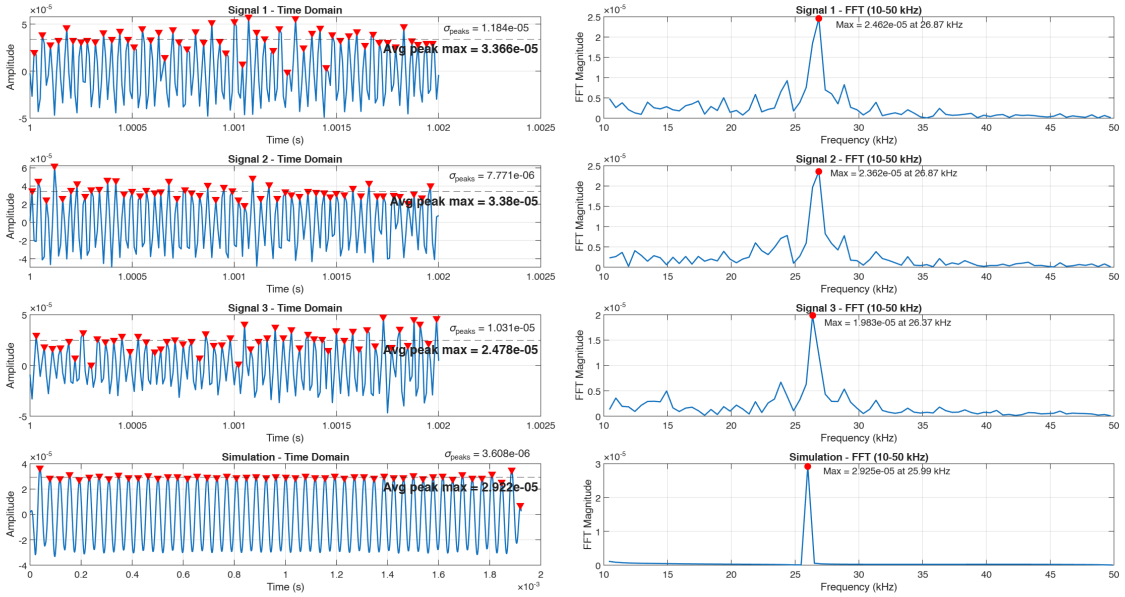



Figure 240: Time- and frequency-domain responses of three experimental LDV measurements and the corresponding numerical simulation. Red markers indicate detected signal peaks in the time domain and the dominant spectral peak in the FFT domain. The experimental signals showed maximum average peak amplitudes of $3.348 \times 10^{-5}$, $3.10 \times 10^{-5}$, and $1.142 \times 10^{-5}$, with dominant frequencies of 26.87, 26.87, and 24.88 kHz, respectively. The simulation predicted an average peak amplitude of $2.985 \times 10^{-5}$ and a dominant frequency of 25.99 kHz.

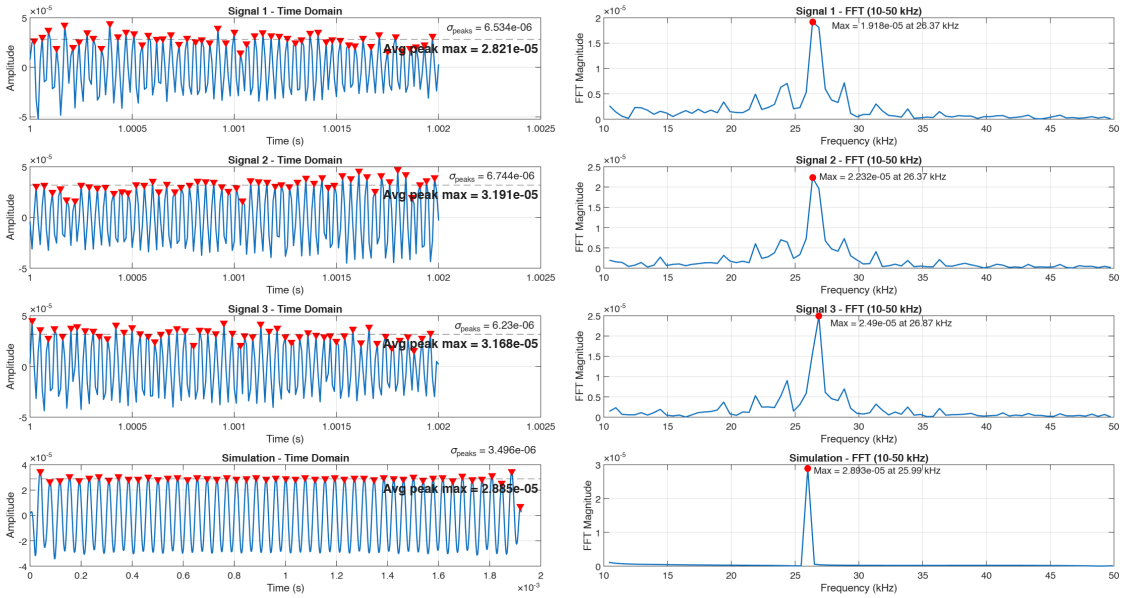



Figure 241: Time- and frequency-domain responses of three experimental LDV measurements and the corresponding numerical simulation. Red markers indicate detected signal peaks in the time domain and the dominant spectral peak in the FFT domain. The experimental signals showed maximum average peak amplitudes of $3.348 \times 10^{-5}$, $3.10 \times 10^{-5}$, and $1.142 \times 10^{-5}$, with dominant frequencies of 26.87, 26.87, and 24.88 kHz, respectively. The simulation predicted an average peak amplitude of $2.985 \times 10^{-5}$ and a dominant frequency of 25.99 kHz.

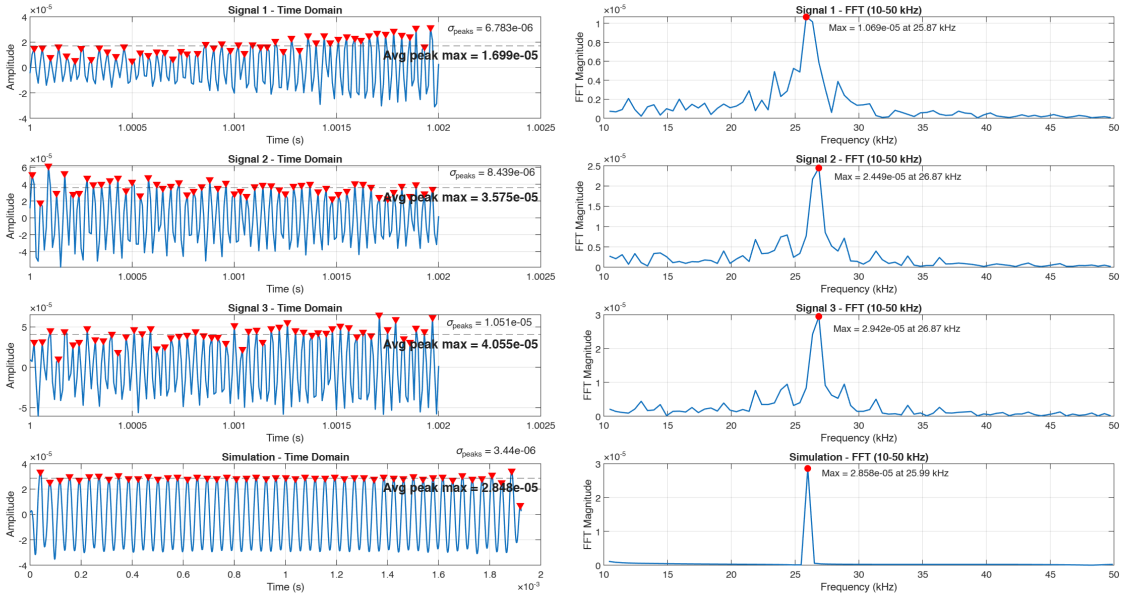



Figure 242: Time- and frequency-domain responses of three experimental LDV measurements and the corresponding numerical simulation. Red markers indicate detected signal peaks in the time domain and the dominant spectral peak in the FFT domain. The experimental signals showed maximum average peak amplitudes of $3.348 \times 10^{-5}$, $3.10 \times 10^{-5}$, and $1.142 \times 10^{-5}$, with dominant frequencies of 26.87, 26.87, and 24.88 kHz, respectively. The simulation predicted an average peak amplitude of $2.985 \times 10^{-5}$ and a dominant frequency of 25.99 kHz.

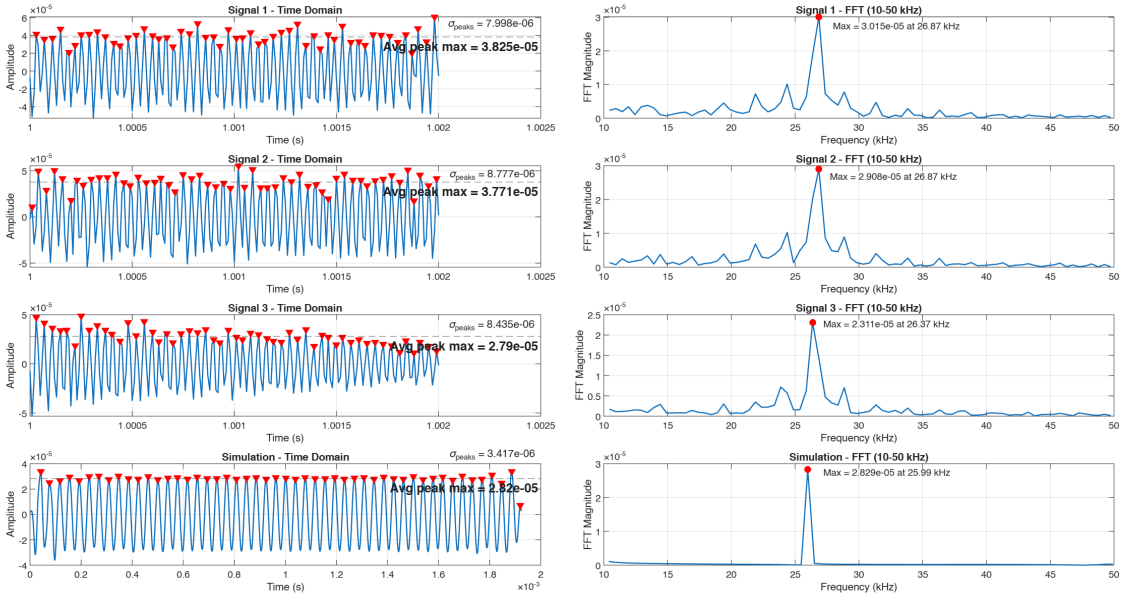



Figure 243: Time- and frequency-domain responses of three experimental LDV measurements and the corresponding numerical simulation. Red markers indicate detected signal peaks in the time domain and the dominant spectral peak in the FFT domain. The experimental signals showed maximum average peak amplitudes of $3.348 \times 10^{-5}$, $3.10 \times 10^{-5}$, and $1.142 \times 10^{-5}$, with dominant frequencies of 26.87, 26.87, and 24.88 kHz, respectively. The simulation predicted an average peak amplitude of $2.985 \times 10^{-5}$ and a dominant frequency of 25.99 kHz.

## D.3 Bibliography

[1] "Measuring the Skin", in *Measuring the skin*, edited by P. Agache and P. Humbert (Springer, Berlin Heidelberg, 2004), Chapter 24.

[2] M. Takaza, K. M. Moerman, J. Gindre, G. Lyons, and C. K. Simms, "The anisotropic mechanical behaviour of passive skeletal muscle tissue subjected to large tensile strain", J. Mech. Behav. Biomed. Mater. **17**, 209–220 (2013) 10.1016/j.jmbbm.2012.09.001.

[3] G. Boyer, H. Zahouani, A. Le Bot, and L. Laquieze, "In vivo characterization of viscoelastic properties of human skin using dynamic micro-indentation", in 2007 29th Annu. Int. Conf. IEEE Eng. Med. Biol. Soc. (Aug. 2007), pp. 4584–4587, 10.1109/IEMBS.2007.4353360.

[4] M. J. Kang, B.-s. Kim, S. Hwang, and H. H. Yoo, "Experimentally derived viscoelastic properties of human skin and muscle in vitro", Med. Eng. Phys. **61**, 25–31 (2018) 10.1016/j.medengphy.2018.08.001.

[5] D11 Committee, *Test Methods for Vulcanized Rubber and Thermoplastic ElastomersTension*, 10.1520/D0412-16R21.

[6] N. A. T. C. Fernandes, *Nnunofernandes/Cauchy-Stress-Tensile-Test-Post-Processing: First Release*, version 1.0.0, Zenodo, May 24, 2026, 10.5281/ZENODO.20369750.

[7] K. Manickam, R. R. Machireddy, and S. Seshadri, "Characterization of biomechanical properties of agar based tissue mimicking phantoms for ultrasound stiffness imaging techniques", J. Mech. Behav. Biomed. Mater. **35**, 132–143 (2014) 10.1016/j.jmbbm.2014.03.017.

[8] S. Kazemirad, S. Bernard, S. Hybois, A. Tang, and G. Cloutier, "Ultrasound Shear Wave Viscoelastography: Model-Independent Quantification of the Complex Shear Modulus", IEEE Trans. Ultrason. Ferroelectr. Freq. Control **63**, 1399–1408 (2016) 10.1109/TUFFC.2016.2583785.

[9] K. Guo, Y. Zhu, J. Wang, C. Jiang, and J. Yu, "Characterizing the viscoelastic properties of a tissue mimicking phantom for ultrasound elasticity imaging studies", IOP Conf. Ser. Mater. Sci. Eng. **490**, 022035 (2019) 10.1088/1757-899X/490/2/022035.

[10] C. P. Carvalho, J. F. S. Costa-Júnior, C. D. S. Rangel, and W. C. D. A. Pereira, "Measurement of Shear Wave Speed and Normalized Elastic Modulus of Human Skin with and without Dermal Striae Using Shear Wave Elastography", Ultrasound Med. Biol. **47**, 454–470 (2021) 10.1016/j.ultrasmedbio.2020.11.014.

[11]L. A. Chernak, R. J. DeWall, K. S. Lee, and D. G. Thelen, "Length and activation dependent variations in muscle shear wave speed", Physiol. Meas. **34**, 713–721 (2013) 10.1088/0967-3334/34/6/713.

[12]W.-Y. Tsai, Y.-Y. Hsueh, P.-Y. Chen, K.-S. Hung, and C.-C. Huang, "High-Frequency Ultrasound Elastography for Assessing Elastic Properties of Skin and Scars", IEEE Trans. Ultrason. Ferroelectr. Freq. Control **69**, 1871–1880 (2022) 10.1109/TUFFC.2022.3154235.

[13]C. Gaudette, H. Cho, M. J. Saikia, and B. J. Ranger, "Mimicry of skeletal muscle tissue with layered phantom for ultrasound imaging", in 2022 IEEE MIT Undergrad. Res. Technol. Conf. URTC (Sept. 30, 2022), pp. 1–6, 10.1109/URTC56832.2022.10002212.

[14]J. Dong, J. Zhao, X. Liu, and W.-N. Lee, "Nondestructive ultrasound evaluation of microstructure-related material parameters of skeletal muscle: an in silico and in vitro study", J. Mech. Behav. Biomed. Mater. **142**, 105807 (2023) 10.1016/j.jmbbm.2023.105807.

[15]W. Tsuchida, Y. Yamakoshi, S. Matsuo, M. Asakawa, K. Sugahara, T. Fukaya, E. Yamanaka, Y. Asai, N. Nitta, T. Ooie, and S. Suzuki, "Application of the novel estimation method by shear wave elastography using vibrator to human skeletal muscle", Sci. Rep. **10**, 22248 (2020) 10.1038/s41598-020-79215-z.

[16]S. Aristizabal, C. Amador, B. Qiang, R. R. Kinnick, I. Z. Nenadic, J. F. Greenleaf, and M. W. Urban, "Shear wave vibrometry evaluation in transverse isotropic tissue mimicking phantoms and skeletal muscle", Phys. Med. Biol. **59**, 7735–7752 (2014) 10.1088/0031-9155/59/24/7735.

*"I suffer this no longer*

*I'll put an end to*

*This I swear*

*This I swear*

*The sun will shine"*

**Metallica**, The day that never comes - Death Magnetic